

Solid Mechanics and Its Applications

Volume 215

Series Editors

J. R. Barber

Ann Arbor, Michigan, USA

Anders Klarbring

Linköping, Sweden

The fundamental questions arising in mechanics are: Why?, How?, and How much? The aim of this series is to provide lucid accounts written by authoritative researchers giving vision and insight in answering these questions on the subject of mechanics as it relates to solids. The scope of the series covers the entire spectrum of solid mechanics. Thus it includes the foundation of mechanics; variational formulations; computational mechanics; statics, kinematics and dynamics of rigid and elastic bodies; vibrations of solids and structures; dynamical systems and chaos; the theories of elasticity, plasticity and viscoelasticity; composite materials; rods, beams, shells and membranes; structural control and stability; soils, rocks and geomechanics; fracture; tribology; experimental mechanics; biomechanics and machine design. The median level of presentation is the first year graduate student. Some texts are monographs defining the current state of the field; others are accessible to final year undergraduates; but essentially the emphasis is on readability and clarity.

Springer and Professors Barber and Klarbring welcome book ideas from authors. Potential authors who wish to submit a book proposal should contact Nathalie Jacobs, Publishing Editor, Springer (Dordrecht), e-mail: Nathalie.Jacobs@springer.com

Indexed by SCOPUS and Springerlink

More information about this series at <http://www.springer.com/series/6557>

Lester W. Schmerr Jr.

Fundamentals of Ultrasonic Phased Arrays

Lester W. Schmerr Jr.
Iowa State University
Center for Nondestructive Evaluation
and the Dept. of Aerospace Engineering
Ames
Iowa
USA

The online version of this chapter (doi:10.1007/978-3-319-07272-2_14) contains supplementary material, which is available to authorized users.

ISBN 978-3-319-34465-2 ISBN 978-3-319-07272-2 (eBook)
DOI 10.1007/978-3-319-07272-2
Springer Cham Heidelberg New York Dordrecht London

© Springer International Publishing Switzerland 2015
Softcover reprint of the hardcover 1st edition 2015

This work is subject to copyright. All rights are reserved by the Publisher, whether the whole or part of the material is concerned, specifically the rights of translation, reprinting, reuse of illustrations, recitation, broadcasting, reproduction on microfilms or in any other physical way, and transmission or information storage and retrieval, electronic adaptation, computer software, or by similar or dissimilar methodology now known or hereafter developed. Exempted from this legal reservation are brief excerpts in connection with reviews or scholarly analysis or material supplied specifically for the purpose of being entered and executed on a computer system, for exclusive use by the purchaser of the work. Duplication of this publication or parts thereof is permitted only under the provisions of the Copyright Law of the Publisher's location, in its current version, and permission for use must always be obtained from Springer. Permissions for use may be obtained through RightsLink at the Copyright Clearance Center. Violations are liable to prosecution under the respective Copyright Law.

The use of general descriptive names, registered names, trademarks, service marks, etc. in this publication does not imply, even in the absence of a specific statement, that such names are exempt from the relevant protective laws and regulations and therefore free for general use.

While the advice and information in this book are believed to be true and accurate at the date of publication, neither the authors nor the editors nor the publisher can accept any legal responsibility for any errors or omissions that may be made. The publisher makes no warranty, express or implied, with respect to the material contained herein.

Printed on acid-free paper

Springer is part of Springer Science+Business Media (www.springer.com)

Preface

This is the third book I have written on ultrasonic waves and their applications to the nondestructive evaluation (NDE) of materials and structures. The first book (Schmerr, L.W., *Fundamentals of Ultrasonic Nondestructive Evaluation—A Modeling Approach*, Plenum Press, New York, N.Y., 1998) covered the behavior of elastic waves (primarily bulk waves) in terms of their generation, propagation, scattering, and reception in an NDE system and described the use of models in applications such as flaw classification and sizing. The second book, with Prof. Sung-Jin Song, (Schmerr, L.W. and S-J. Song, *Ultrasonic Nondestructive Evaluation Systems—Models and Measurements*, Springer, New York, N.Y., 2007) was a more complete systems-level effort to use a combination of models and measurements to describe in detail all the elements that go into forming the signals that we measure in an ultrasonic NDE test. In both of those books the primary focus was on ultrasonic measurements with single element piezoelectric transducers. The present book arose out of a realization that ultrasonic phased array systems, which are now starting to see significant NDE applications in industry, have many unique characteristics and issues that have not been adequately described except in journal papers and conference proceedings.

In organizing the structure of this book and writing it I have had three purposes in mind. First, while I did not want to generate a textbook I did want to introduce some of the basic physics behind ultrasonic phased arrays in a simple context so that the important aspects these systems could be readily accessible to students, engineers, and technical workers. Thus, many of the initial discussions of phased array topics such as beam steering, delay laws, apodization, etc. are in terms of 1-D array elements radiating waves in two dimensions. Second, I wanted to follow the basic philosophy of the previous books by showing how all the components of an ultrasonic phased array system can either be measured or modeled, using a combination of reciprocity relations, linear systems theory, and wave propagation and scattering theory. This approach allows one to develop *ultrasonic measurement models* for NDE phased array systems in the same fashion as done previously for inspections with single element transducers. These measurement models demonstrate explicitly how signals are produced in ultrasonic phased array systems and in particular how the responses of flaws are contained in those signals, so that those flaw responses

can be extracted and used for quantitative flaw detection, sizing and characterization purposes. Third, because of the importance of imaging applications with phased arrays, I wanted to introduce a new, rational approach to how images are produced and what they mean. Currently, phased array images are often formed with ad-hoc *delay-and-sum methods* such as the synthetic aperture focusing technique (SAFT) and the total focusing method (TFM). I have re-examined the image formation process to understand why those delay-and-sum methods often work so well and to place them in a more fundamental context based on the physics of the measurement process. Specifically, I show that one can start with ultrasonic measurement models and, with relatively few assumptions, based on a model of the waves that contribute to an image, formally invert those measurement models to form flaw images that are explicit functions of the surface geometry and reflectivity of the flaw. These images are related to the measured signals and the wave propagation processes and electro-acoustical components present in a phased array experiment in a form called an *imaging measurement model*. Imaging measurement models are developed that are generalizations of both SAFT and TFM. These models describe the images produced in physical terms and define those aspects of the imaging process that SAFT and TFM ignore. For small flaws it is shown that the imaging measurement models are also generalizations of the physical optics far field inverse scattering (POFFIS) method originally developed by Bojarski and later modified by Bleistein. Thus, the imaging measurement models described here provide for the first time a unified framework for understanding some of the most commonly used NDE phased array imaging methods.

To help make some of the phased array models described in the book more accessible to the reader, MATLAB[®] functions and scripts¹ are also provided. Most of these MATLAB[®] resources describe simple 2-D and 3-D scalar problems that one can use to conduct a variety of parametric studies. The intent here was not to produce a comprehensive set of phased array software but to provide some software tools for examining and understanding phased arrays. Listings of the MATLAB[®] functions and scripts can be found in Appendix C and the m-files are also available by sending an e-mail with subject titled “Phased Array Codes” to the author at lschmerr@cnde.iastate.edu.

Finally, I would like to thank my longtime colleague and friend, Alex Sedov, for his contributions and for reading and helping to edit the entire book. I also want to acknowledge the research efforts of Dr. Ruiju Huang and Brady Engle which have helped to make this work possible.

¹ MATLAB[®] is a registered trademark of the The MathWorks, Inc.

Article note

MATLAB[®] is a registered trademark of the The MathWorks, Inc.

All program examples and figures presented in this book have been generated with MATLAB[®] version 7.12.0.635 (R2011a)

All illustrated examples of MATLAB[®] dialog boxes, figures and graphic interfaces have been reprinted with permission from The MathWorks, Inc.

For MATLAB[®] and Simulink[®] product information, please contact:

The MathWorks, Inc.

3 Apple Hill Drive

Natick, MA 01760-2098, USA

Tel: 508-647-7000

Fax: 508-647-7001

E-mail: info@mathworks.com

Web: mathworks.com

Contents

1	Introduction	1
1.1	An Overview	1
1.2	Linear and 2-D Arrays	5
1.3	Modeling Ultrasonic Phased Array Systems	7
1.4	Book Outline	13
	References	15
2	Acoustic Field of a 1-D Array Element	17
2.1	Single Element Transducer Models (2-D)	17
2.2	Far Field Waves	23
2.3	Numerical Piston Element Models	27
2.4	Line Source Models	33
2.5	Radiation Through a Planar Interface	36
	References	44
3	Large, Single Element Transducer Models	45
3.1	The Paraxial Approximation and a Fresnel Integral Model	45
3.2	Beam Steering and Focusing of a Large Element	47
3.2.1	Beam Steering	48
3.2.2	Steering in the Far Field	50
3.2.3	Beam Focusing	51
3.2.4	Beam Steering and Focusing	57
3.3	Amplitude Weighting	60
3.4	Multi-Gaussian Beam Model	65
3.5	Summary	71
	References	72
4	Phased Array Beam Modeling (1-D Elements)	73
4.1	Phased Array Beam Models	73
4.1.1	Far Field Behavior of an Array	76
4.2	Array Beam Steering	80
4.3	Array Beam Focusing	85

4.4	Array Amplitude Weighting	87
4.5	Array Beam Modeling Examples	89
4.6	Use of Gaussians for Modeling Phased Array Beam Fields	91
4.7	Beam Steering and Focusing through a Planar Interface	94
	References	98
5	Time Delay Laws (2-D)	99
5.1	Delay Laws for a Single Medium	99
5.2	Steering and Focusing Through a Planar Interface	102
	References	111
6	Acoustic Field of a 2-D Array Element	113
6.1	Single Element Transducer Models (3-D)	113
6.2	Far Field Waves	117
6.3	Numerical Point Source Piston Model	119
6.4	Contact Transducer Element Modeling	122
6.5	Radiation Through a Planar Interface	124
6.6	Gaussian Beam Equivalent Point Source Modeling	138
	References	146
7	Phased Array Beam Modeling (2-D Elements)	147
7.1	Phased Array Beam Models—Single Medium	147
7.1.1	Far Field Behavior of an Array	151
7.1.2	Beam Steering in 3-D	152
7.2	Radiation Through a Planar Interface	156
7.3	Array Beam Modeling Examples	160
	Reference.....	168
8	Time Delay Laws (3-D)	169
8.1	Beam Steering in 3-D	169
8.2	Beam Steering and Focusing in 3-D	170
8.3	Beam Steering Through a Planar Interface	172
8.4	Beam Steering and Focusing Through a Planar Interface	173
	Reference.....	177
9	Linear System Modeling of Phased Arrays	179
9.1	Linear System Modeling and Sound Generation	180
9.2	Linear System Modeling and Sound Reception	184
9.3	The Reception Process and Grating Lobes	189
9.4	Linear System Model of the Complete Ultrasonic Measure- ment Process	191
	References	193

10 Phased Array System Functions	195
10.1 Acoustic/Elastic Transfer Function Models	195
10.2 Array Element System Functions	206
Reference.....	209
11 Measurement Models for Ultrasonic Arrays	211
11.1 Reciprocity Relations	212
11.2 An Ultrasonic Measurement Model for Immersion Setups	216
11.3 An Ultrasonic Measurement Model for Contact Setups	217
11.4 A Reduced Measurement Model for Small Flaws	218
11.5 Measurement Models for Quantitative Imaging	224
11.6 Measurement Models for 2-D Problems	234
References	240
12 Imaging with Phased Arrays—An Introduction	241
12.1 SAFT Imaging	241
12.2 TFM Imaging	244
12.3 The Image Formation Process	246
12.4 Far Field Imaging Measurement Models (2-D)	249
12.5 Imaging Simulations	263
References	277
13 Imaging Measurement Models	279
13.1 Pulse-Echo Imaging	279
13.2 Full Matrix Imaging	287
13.3 2-D Imaging with a Linear Array	293
13.4 Discussion	302
13.5 Summary of Imaging Measurement Models	304
References	310
14 Element Boundary Conditions and Other Modeling Issues	313
14.1 Finite Impedance Baffle Model	313
14.2 Line Source Model of an Element in a Finite Impedance Baffle ...	318
14.3 Other Modeling Issues	325
References	326
Appendices	327
A The Beylkin Determinant	327
A.1 The Beylkin Determinant for 3-D Imaging (Common Source Case)	327
A.2 The Beylkin Determinant for 3-D Imaging (Pulse-Echo Case)	330
A.3 The Beylkin Determinant for 2-D Imaging	331
A.4 References	334

B Angle-Area Ratios	334
B.1 Ratios for Inspection in a Single Medium	334
B.2 Ratios for Inspection Through a Planar Interface	335
B.3 References	339
C MATLAB [®] Functions and Scripts	340
C.1 Beam Models for Single Elements	340
C.2 Delay Laws and Apodization Laws	341
C.3 Beam Models for Arrays	341
C.4 Miscellaneous Functions	342
C.5 Code Listings	343
Index	375

Chapter 1

Introduction

1.1 An Overview

In the medical field, ultrasound is used for performing noninvasive examinations of patients. Similarly, in industry ultrasound is used for conducting nondestructive evaluation (NDE) inspections of materials and structures. Ultrasonic methods are fast, safe, and relatively inexpensive—characteristics that have led ultrasound to being one of the most frequently used techniques in both medical and industrial applications. Like many other diagnostic and inspection methods, however, ultrasonic methods are indirect methods. The term “indirect” means that the measured outputs, which are usually in the form of electrical voltage versus time signals, are the result of complex transformations of the acoustic energy that is generated and received, making it difficult to connect the characteristics of the measured signals directly with the properties of the object being examined. To illustrate this difficulty, consider the simple ultrasonic system outlined in Fig. 1.1, where a single element ultrasonic transducer is placed in a fluid.

The element of this transducer is typically made of a piezoelectric material that converts electrical energy into mechanical motion of the element and vice-versa. Thus, if the transducer is excited by an electrical pulse, as shown in Fig. 1.1a, a traveling pulse of sound will be generated in the water in the form of an acoustic wave. If this wave strikes an object such as a spherical reflector, as shown in Fig. 1.1b, then waves will be scattered from the sphere in all directions and some of that scattered acoustic energy will return to the transducer and will be converted back into electrical energy, amplified, and output as a voltage versus time pulse. Knowing the wave speed of the fluid and the time of arrival of this pulse we can easily determine the distance to the sphere, but other quantitative information such as the size of the sphere, its mechanical properties, etc. are not directly obvious from the measured signal. If one mechanically moves this single element transducer and changes its position and/or orientation, then a collection of measured signals can be obtained and used to help better determine such quantitative information. In fact, with sufficient information obtained from such mechanical motion of the transducer one can even synthesize an ultrasonic image of the sphere. However, mechanical scanning is slow and expensive to perform with a single element transducer setup. A more

Fig. 1.1 **a** A single element ultrasonic transducer generating a traveling wave, and **b** the same transducer receiving the waves scattered from a spherical reflector

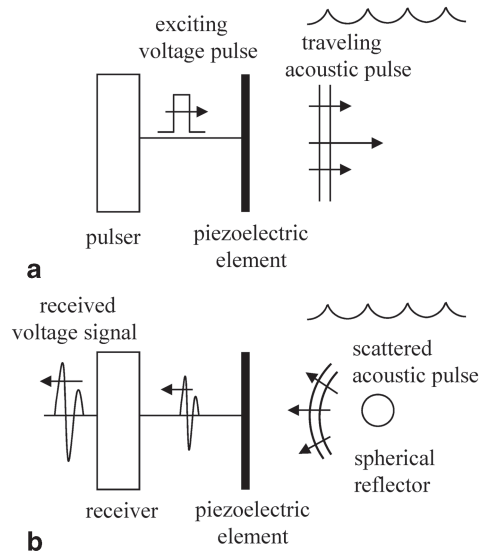
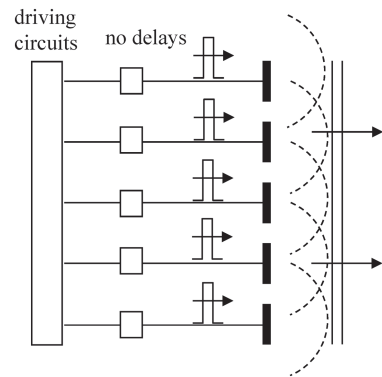


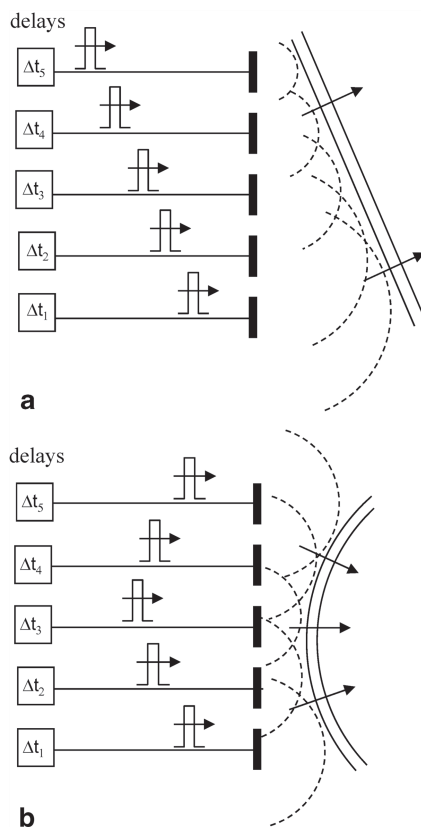
Fig. 1.2 An ultrasonic phased array, where the driving electrical pulses for each element arrive in unison, i.e. with no time delay relative to each other



effective approach to conduct inspections and form images is to use an ultrasonic phased array, where the sound beam can be manipulated electronically. Even with phased arrays, however, one must overcome the indirect nature of the measurement process. Thus, the primary purpose of this book is to describe in detail how the signals and images are formed with ultrasonic phased array systems so that one can extract quantitative information from those phased array measurements and images.

In a phased array setup (Fig. 1.2), the ultrasonic transducer is composed of an array of small piezoelectric elements, where each element can be separately driven and the response of each element independently received. If each of the elements is driven in an identical fashion so that the driving electrical pulses travel in unison and all arrive at the piezoelectric elements at the same time (no relative delay between pulses) then each small element of the array acts effectively like a point source and radiates a spherical wave (the dashed lines in Fig. 1.2 represent the

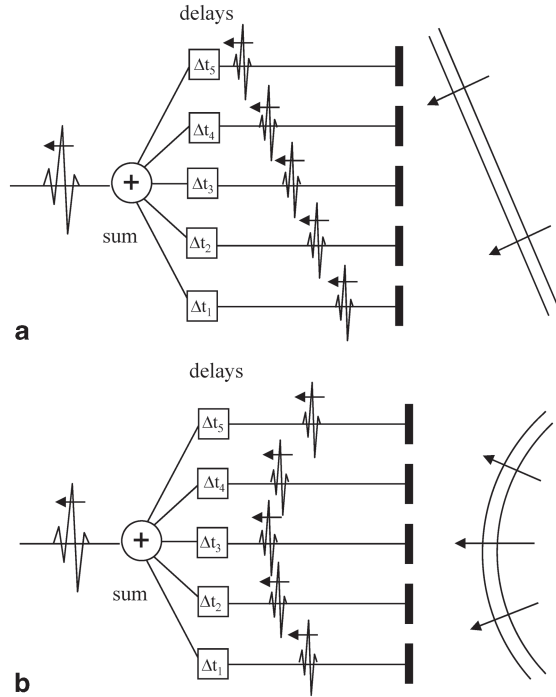
Fig. 1.3 **a** An ultrasonic phased array where a set of delays are used to steer the sound beam of the array and, **b** the case where a set of delays produce a focusing of the sound beam



spherical wave fronts), and these spherical waves combine to form a traveling wave pulse, as shown in Fig. 1.2. Except in a region close to the array the sound beam of the array is similar to the beam generated by a single element transducer of the same size as that of the entire array. However, by varying the relative time delays, Δt_i , of the driving pulses (where the ensemble of delays is called a *delay law*), the ultrasonic phased array is able to electronically steer the sound beam generated in different directions, as shown in Fig. 1.3a without requiring any motion of the transducer itself. With an appropriate non-linear delay law, the same array can also generate a focused sound beam as shown in Fig. 1.3b. A more complex combination of these delay laws can simultaneously perform both beam steering and focusing. This flexibility of ultrasonic phased arrays to electronically control the properties of the sound beam can make the collection and use of many ultrasonic measurements rapid and cost-effective. This same flexibility also allows one to rapidly form ultrasonic images, a capability that has been used for many years in clinical applications and is seeing a much broader use recently in industrial NDE inspections.

Relative time delays for each element can also be used for modifying the characteristics of the signals received by an array. Fig. 1.4a shows the case where a plane wave front arrives at an array. As this wave strikes each element of the array in

Fig. 1.4 a Applying variable time delays and a summation on reception for receiving a wave arriving at angle to the array, and **b** applying variable time delays and a summation on reception for receiving a curved wave front arriving at the array

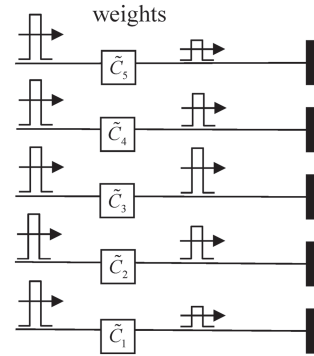


succession, a series of electrical pulses will be generated as shown. If relative time delays, Δt_i , are applied to these received signals so that all of the signals occur at the same time, then they can be summed to generate a single, large output signal. Note that this summed signal is similar to what would be measured by a single element transducer whose face was at normal incidence to the incoming wave so that the entire surface of the transducer was excited simultaneously by the incident wave. Thus, this reception delay law effectively acts much the same as a single element receiving transducer oriented to face the incoming wave. Similarly, in Fig. 1.4b, where the incident wave front is curved, relative time delays can be applied on reception to align all the signals from the elements so they also can be summed. This delay law is then analogous to what would happen with a focused single element transducer on reception.

Because an ultrasonic phased array can transmit/receive with each element of the array independently of the other elements, it also is possible to apply individual amplitude weights, \tilde{C}_i , to the elements on either sound generation and reception (or both) (see Fig. 1.5). The ensemble of such amplitude weights is called an *apodization law*. In Chap. 3, we will describe the most common apodization laws that are used to tailor the important acoustic radiation characteristics of a phased array.

The ability to use general delay laws and apodization laws on generation and reception makes an ultrasonic phased array a very versatile and effective device for conducting ultrasonic tests. It is important that engineers and scientists who use

Fig. 1.5 An ultrasonic phased array where amplitude weights are applied to the driving pulses, corresponding to an apodization law applied to the sending elements



this ultrasonic phased array technology understand the basic principles that govern the behavior of phased arrays and the important parameters that control their performance. It is also important to know how the characteristics of ultrasonic phased array systems can be exploited to help overcome the indirect nature of measured ultrasonic responses and better determine the properties of the object being examined, as discussed previously.

This book will describe in detail the fundamentals of ultrasonic phased array systems, using a combination of models and measurements to characterize the behavior of the arrays that are typically used in NDE inspections of materials and structures. Two references to those fundamental concepts we will mention often are the books listed as [1, 2] in the References at the end of this Chapter. Throughout this book those two references will be listed simply as [Schmerr] and [Schmerr-Song], respectively. Since our focus is on the use of phased arrays in NDE settings the behavior of ultrasonic arrays when interacting with biological systems and medical applications of arrays will not be discussed here but the reader can find a number of other very good sources for those important topics [3, 4, 5]. Also, see [6] for an overview of ultrasonic NDE applications.

1.2 Linear and 2-D Arrays

The shape of the piezoelectric elements in an array can be quite general but rectangular elements are often used in practice because they are cost effective to manufacture. Figure 1.6 shows a set of identical rectangular elements where the length of each element in the x -direction, l_x , is much smaller than its length in the y -direction, l_y . This configuration is called a *linear array*. The gap length, g_x , between elements in the x -direction is normally the same for all pairs of elements in such an array. This gap length is also called the *kerf* of the array. Another important parameter is the element-to-element spacing, s_x , as shown in Fig. 1.6. This parameter is called the *pitch* of the array. Obviously, from the geometry the pitch is $s_x = l_x + g_x$. Because there are multiple elements in only one dimension in a linear array, time delay laws

Fig. 1.6 The elements of a linear array

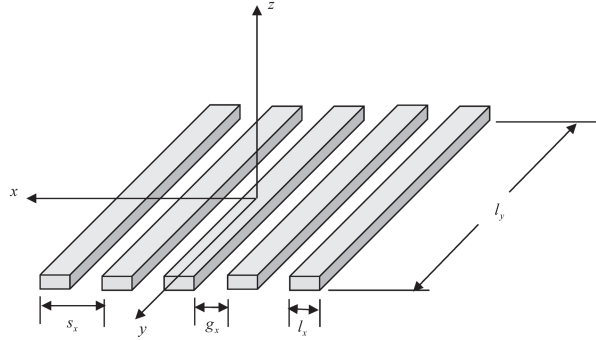
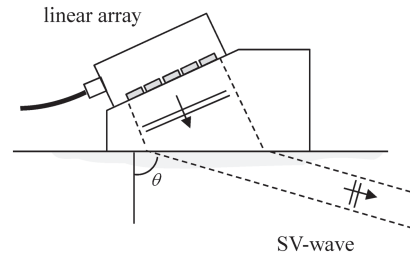


Fig. 1.7 An array-based angle beam shear wave inspection setup



applied to the elements of a linear array can only steer the beam in the x - z plane and generate cylindrical focusing along lines parallel the y -axis that pass through various points in the x - z plane. Even with this restriction a linear array can be a very effective tool for conducting NDE inspections.

One common application of such linear arrays is to place the array on a low speed wedge in contact with an adjacent solid, as shown in Fig. 1.7, to generate an array-based angle beam vertical-shear (SV) wave inspection setup, where phasing of the array allows the shear wave to be steered and focused at various angles, θ , in the solid.

Figure 1.8 shows a two-dimensional array of small, identical rectangular elements of lengths l_x and l_y , respectively, in the x - and y -directions and where there are uniform gap lengths g_x and g_y between elements in each of the x - and y -directions so that the pitches in each of these directions are given by $s_x = l_x + g_x$, $s_y = l_y + g_y$. Since time delays that vary in both the x - and y -directions can be applied to the elements of a two-dimensional array, it is possible to steer and focus the beam of a 2-D array in a very general manner.

Other array configurations (annular arrays, segmented circular arrays, etc.) can also be considered but the linear and two-dimensional rectangular arrays shown in Figs. 1.6 and 1.8 are the types most commonly used in NDE tests so they will be the types of arrays we will consider in this book.

Fig. 1.8 A two-dimensional array of uniformly spaced, identical rectangular elements

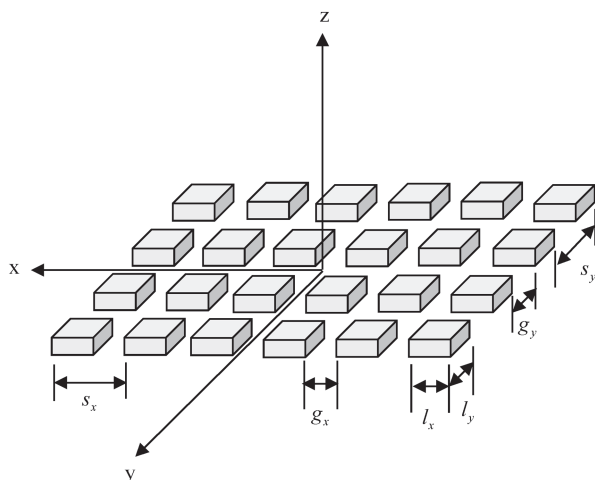
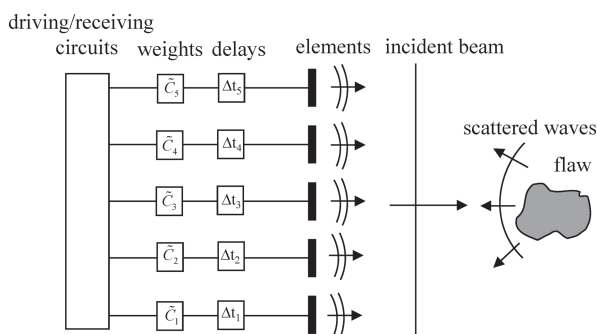


Fig. 1.9 Components of an ultrasonic phased array measurement system

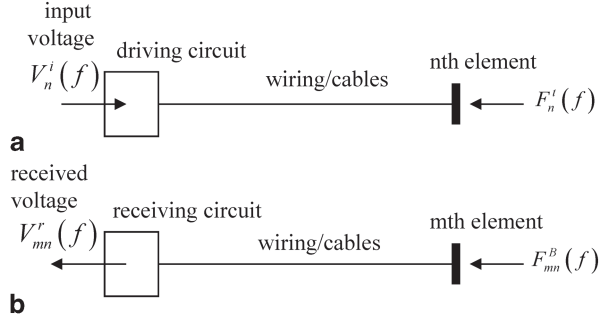


1.3 Modeling Ultrasonic Phased Array Systems

This book will exam in detail all the components of an ultrasonic phased array flow measurement system (see Fig. 1.9) and describe the models and measurements necessary for describing those components. We will develop a comprehensive system model that will quantify the generation and reception of sound with the phased array transducer(s) and instrumentation, the propagation of the beam of ultrasound in the material being inspected, and the scattering of waves from any flaws that may be present. The approach we will take is similar to the one we used previously in describing ultrasonic systems that use large, single element transducers [Schmerr-Song] and many of the concepts discussed here can be found in that reference. However, there are unique modeling and measurement issues associated with arrays and we will also outline some of those issues in this book.

In an ultrasonic phased array system, time-dependent (time domain) driving electrical signals are used to produce time-dependent traveling waves. Time domain wave signals are, in turn, converted back into time-dependent voltages. However, it is convenient not to directly model these time domain signals but to work instead

Fig. 1.10 **a** 1-D model of the generation of sound at an array element, and **b** 1-D model of the reception of sound at an element and the conversion to a received electrical signal



in terms of their frequency components (frequency domain), which can be easily obtained with the use of the Fast Fourier Transform (FFT) [Schmerr-Song]. Thus, throughout this book we will characterize all the components of a phased array system in the frequency domain where the system parameters will be functions of the frequency, f , normally measured in millions of cycles per second (or megaHertz (MHz)).

First, consider the electrical and electromechanical parts of the phased array system, both on sound generation and reception (Fig. 1.10) when no delays or apodization weights are present. During sound generation the driving circuits produce a voltage pulse which travels down the wiring and cabling to the element (usually a piezoelectric material) where the electrical signals (voltage, current) are transformed into acoustic pulses (force, velocity). If we assume the driving circuits are linear, then for the circuit driving the n th element in an array (Fig. 1.10a) we can model the source of electrical energy in those driving circuits as a Thévenin equivalent voltage source, $V_n^i(f)$, [Schmerr-Song]. This equivalent voltage source will produce a time dependent transmitted compressive force at the face of the n th element whose frequency domain response is denoted in Fig. 1.10a as $F_n^t(f)$. We can write this compressive force as

$$F_n^t(f) = t_n^g(f)V_n^i(f), \quad (1.1)$$

where $t_n^g(f)$ is called the sound generation transfer function. This transfer function is a function of the electrical impedance of the driving circuits, the electrical properties of the wiring/cabling connecting the driving circuits to the piezoelectric element, and the electrical impedance and sensitivity of the array element [Schmerr-Song]. When the acoustic pulses generated by the n th element interact with scattering objects (such as surfaces of a component being inspected or flaws) and travel back to the array they are received by the m th element of the array and converted to a received voltage pulse. We can relate the frequency components of this received voltage, $V_m^r(f)$, to the *blocked force*, $F_m^B(f)$ (Fig. 1.10b), generated by the incident waves for each pair of sending and receiving elements through a sound reception transfer function, $t_m^r(f)$, i.e.

$$V_{mn}^r(f) = t_m^r(f) F_{mn}^B(f) \quad (1.2)$$

This receiving transfer function is a function of the electrical impedance and gain present in the receiving circuits, the wiring/cabling present, and the electrical impedance and sensitivity of the m th piezoelectric element [Schmerr-Song]. The blocked force appearing in Eq. (1.2) is defined as the force exerted on the face of the receiving element when the face of that element is held rigidly fixed. In [Schmerr-Song] and in Chap. 9 it is shown how this blocked force arises naturally in describing the sound reception process for an ultrasonic system.

From Eqs. (1.1) and (1.2) we see that in an ultrasonic measurement process involving a pair of elements, where the waves are generated by the n th element and received by the m th element, the received voltages, V_{mn}^r , are given by

$$\begin{aligned} V_{mn}^r(f) &= \frac{V_{mn}^r(f)}{F_{mn}^B(f)} \frac{F_{mn}^B(f)}{F_n^t(f)} \frac{F_n^t(f)}{V_n^i(f)} V_n^i(f) \\ &= t_m^r(f) t_n^g(f) t_{mn}^a(f) V_n^i(f) \\ &= s_{mn}(f) t_{mn}^a(f) \end{aligned} \quad (1.3)$$

where the *acoustic/elastic transfer functions*, $t_{mn}^a(f)$, are defined as $t_{mn}^a \equiv F_{mn}^B / F_n^t$ and the *system functions*, $s_{mn}(f)$, are given by

$$s_{mn}(f) = t_m^r(f) t_n^g(f) V_n^i(f) \quad (1.4)$$

If we apply time delays, $(\Delta t_n^g, \Delta t_m^r)$ on sound generation and reception, respectively, and also apodization weights $(\tilde{C}_n^g, \tilde{C}_m^r)$, on sound generation and reception, respectively, then in the frequency domain these effects can easily be incorporated into Eq. (1.3) (see Chaps. 4 and 7) as

$$V_{mn}^r(f) = \tilde{C}_n^g \tilde{C}_m^r \exp(2\pi i f \Delta t_n^g) \exp(2\pi i f \Delta t_m^r) s_{mn}(f) t_{mn}^a(f). \quad (1.5)$$

Equation (1.5) is a very general model for an ultrasonic phased array measurement system as it describes the voltages received by all possible pairs of sending and receiving elements. This equation also shows that all the electrical and electromechanical parts of the system response can be characterized by the system functions, $s_{mn}(f)$ and all the wave propagation and scattering processes present can be characterized by the acoustic/elastic transfer functions, $t_{mn}^a(f)$.

In Chap. 10 it will be shown that the system functions can be obtained experimentally by measuring the received voltage, $V_{mn}^r(f)$, for various element pairs in a reference configuration where the acoustic/elastic transfer functions, $t_{mn}^a(f)$ are known. These acoustic/elastic transfer functions will also be derived in Chap. 10 for a convenient calibration setup. Then from Eq. (1.3) we have formally

$$s_{mn}(f) = \frac{V_{mn}^r(f)}{t_{mn}^a(f)}. \quad (1.6)$$

In practice, the direct division in Eq. (1.6) is replaced by a Wiener filter to desensitize this deconvolution process to noise [Schmerr-Song]. If $M = N$ so there are M transmitting and receiving elements, then a total of M^2 different system functions are needed to characterize the behavior of the entire array. Even if one assumes that the system functions and acoustic/elastic transfer functions are symmetric, one still has a total of $M(M+1)/2$ different system functions that would have to be obtained from Eq. (1.6). For a 16 element linear array, for example, this would correspond to 136 different calibration experiments that would be needed to characterize the entire array. Fortunately, however, phased arrays are normally made with nominally identical driving and receiving circuits, wiring, and piezoelectric elements, so it is not surprising, as found in Chap. 10, that the measured system functions may also be nominally identical, i.e. $s_{mn}(f) \equiv s(f)$. In this case only one calibration experiment is needed to obtain this system function and Eq. (1.3) becomes

$$V_{mn}^r(f) = s(f)t_{mn}^a(f) \quad (1.7)$$

and the general model of a phased array system with time delay law and apodization laws, Eq. (1.5) becomes

$$V_{mn}^r(f) = \tilde{C}_n^g \tilde{C}_m^r \exp\left(2 \text{ if } \Delta t_n^g\right) \exp\left(2 \text{ if } \Delta t_m^r\right) s(f) t_{mn}^a(f). \quad (1.8)$$

Equation (1.8) shows that if the system function is determined experimentally and the time delays and apodization weights specified, knowledge of all the acoustic/elastic transfer functions present is required to simulate the received voltage. These transfer functions are functions of the waves generated by the driving elements and propagating in the media present, the waves scattered by a reflector or flaw present, and the waves propagated to the receiving elements. It is not possible to determine these propagating and scattered waves experimentally so that it is necessary to have explicit models of these wave processes and how they contribute to the acoustic/elastic transfer functions.

In order to describe the ultrasonic wave fields generated by the driving elements in the acoustic/elastic transfer function it is necessary to develop an appropriate mathematical model of the array as a set of acoustical sources. In the frequency domain these field quantities are all functions of the spatial variables (x, y, z) and the frequency, f . For a large, single element transducer such as the one shown in Fig. 1.11a a simple but effective frequency domain model that has been used assumes that the transducer acts like a velocity source with the normal velocity, $v_z(x, y, z = 0, f)$, on the face of the transducer given by

$$v_z(x, y, z = 0, f) = \begin{cases} v_0(f) & \text{on } S \\ 0 & \text{otherwise} \end{cases}, \quad (1.9)$$

where S is the active area of the transducer face (see Fig. 1.11a). This model assumes that the entire face of the transducer acts in unison in a piston-like manner, i.e. it is a *piston transducer model*. Piston behavior has been successfully used to

Fig. 1.11 **a** A large, single element *rectangular* transducer, and **b** its representation as a piston velocity source acting over the area S that is embedded in an infinite, rigid baffle

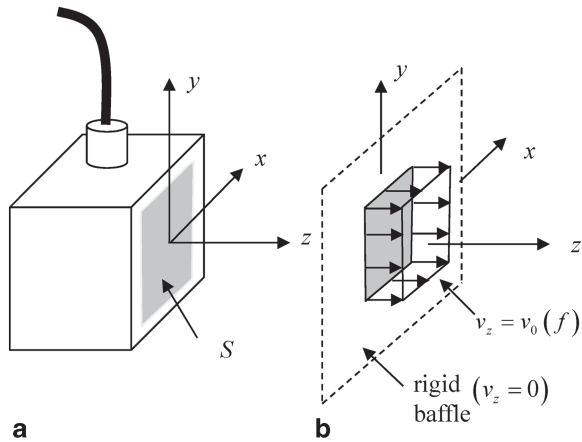
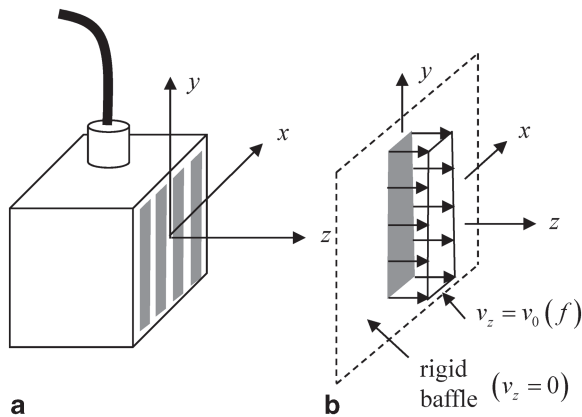
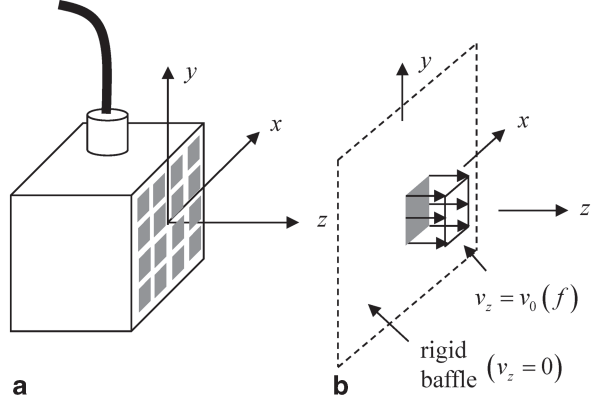


Fig. 1.12 **a** A linear phased array and **b** a model of an individual element as a piston velocity source embedded in a rigid baffle



model many large single element transducers [Schmerr], [Schmerr-Song]. In our transducer array modeling we will also assume that each element of the array also acts like a piston. Equation (1.9) shows that in this piston transducer model the piston source is embedded in an infinite planar rigid baffle, as shown in Fig. 1.11b. It is possible to replace the actual 3-D geometry of the transducer in Fig. 1.11a by a piston source acting in a planar rigid baffle since for large single element transducers the transducer crystal is supported along its edges by a relatively rigid case. Also, as we will see, for example in Chaps. 3 and 6, for large, single element transducers, which typically operate at MHz frequencies in NDE tests, the beam of sound generated by the transducer is well-collimated, i.e. it is significant only in a relatively small region directly ahead of the transducer. Thus, the fields on the plane $z=0$ outside the region S are typically very small anyway, so that the rigid baffle assumption does not affect the fields significantly. For phased arrays such as the linear and 2-D arrays shown in Figs. 1.12a and 1.13a, however, the phased array elements are separated by gaps filled with an epoxy-like material (which is

Fig. 1.13 **a** A 2-D phased array and **b** a model of an individual element as a piston velocity source embedded in a rigid baffle



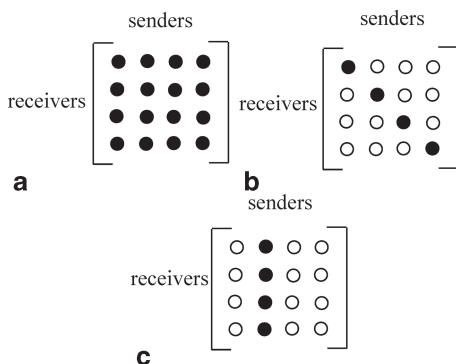
not as rigid as the elements themselves) and at MHz frequencies each element of the array does not generate a well-collimated beam of sound in all directions so one should examine the validity of applying the rigid baffle model of Eq. (1.9) to each element of the array. In modeling phased arrays in this book we will still assume that each element is surrounded by a rigid baffle, as shown in Figs. 1.12b and 1.13b but in Chap. 14 we will model the radiation of an element when it is surrounded by a finite acoustic impedance baffle and discuss how to determine experimentally if such effects are important. Other modeling issues associated with arrays will also be discussed in Chap. 14.

The voltages, $V_{mn}^r(f)$ ($m = 1, 2, \dots, M$), ($n = 1, 2, \dots, N$), are all the possible measurements that can be made with a phased array system having M sending elements and N receiving elements. If the data from the measurement of all these voltages separately is available, the measurement is said to be one of *full matrix capture* (FMC). Full matrix capture provides the largest amount of information that is available from a phased array system and is shown in Fig. 1.14a as a fully filled information matrix of senders and receivers. If only the same individual element is used as both a sender and receiver, then the collection of these pulse-echo responses is shown in the information matrix of Fig. 1.14b. In Chap. 13 we will develop imaging methods based on both full-matrix capture as well as the pulse-echo responses. In developing the FMC case, we will also need to consider the case of a single sending element and multiple receiving elements, as shown in Fig. 1.14c. This case is known in the seismology literature as a common shot response. Of course, many other combinations of the sending and receiving elements can be used for measurements and imaging, but the FMC and pulse-echo cases are those most commonly found in practice.

In an ultrasonic measurement, if the responses of all M sending elements and N receiving elements are measured then we can simply sum all these responses to obtain a single response, $V^r(f)$, given by

$$V^r(f) = \sum_{m=1}^M \sum_{n=1}^N \tilde{C}_n^g \tilde{C}_m^r \exp(2\pi i f \Delta t_n^g) \exp(2\pi i f \Delta t_m^r) s_{mn}(f) t_{mn}^a(f). \quad (1.10)$$

Fig. 1.14 Information matrices showing the data available with combinations of sending and receiving elements for **a** full matrix capture (all element pairs), **b** pulse-echo responses (same sending/receiving pairs), and **c** a single sending element used with all the receivers



This measured voltage is then analogous to what would be measured by a single element transducer of a size comparable to the whole array, but where the array transducer beam can be tailored by the steering, focusing and apodization terms. Commercial phased array systems typically provide this summed signal as an output, as well as standard images formed with the array signals such as B-scans, S-scans, etc. However, with full matrix capture capabilities, a phased array system allows the user to manipulate the array data and form images in ways that are not possible with the output signal of Eq. (1.10).

1.4 Book Outline

This book is divided into essentially three sections. The first section, covering Chaps. 2–5, idealizes arrays as 1-D elements radiating waves in two dimensions. This assumption allows us to discuss many modeling issues and important concepts such as beam steering, focusing, and the existence of grating lobes in a very simple framework. This section also provides an ideal source of materials for introducing students to phased arrays and describes some MATLAB[®] functions and scripts that can be used to simulate the behavior of a phased array.

The second section of the book, in Chaps. 6–11, develops a complete model of a phased array ultrasonic measurement system. Phased array beam models are developed in detail in Chaps. 6 and 7 and the time delay laws that can be used to control the behavior of an array are obtained in Chap. 8. A complete linear systems model of an ultrasonic phased array measurement system is developed in Chap. 9 where the system response is divided into a *system function* that describes the electrical and electro-mechanical parts of the system associated with a sending and receiving pair of elements, and an *acoustic/elastic transfer function* that describes all the acoustic and elastic wave propagation and scattering fields present between those sending and receiving elements, as discussed earlier in this Chapter. Chapter 10 shows how the system function for each element can

be measured experimentally in a calibration setup while Chap. 11 uses reciprocity relations to obtain an expression for the acoustic/elastic transfer function for a flaw measurement system in terms of the incident and scattered waves at the flaw surface in a form similar to that originally developed by Auld [7]. The combination of the system function and the acoustic/elastic transfer function then gives an explicit expression for the measured voltage from each pair of sending/receiving elements. This expression is called an *ultrasonic measurement model*. It is also shown in Chap. 11 how for small flaws this general measurement model can be reduced to a Thompson-Gray type of form [8] where the flaw response is obtained as an explicit and separate part of the overall expression for the received voltage. Examples are given of how this reduced measurement model can be used to predict the measured response of some simple reflectors.

Since ultrasonic phased array flaw measurement systems are commonly used to generate images of the flaws present, the third section of the book, Chaps. 12 and 13, are devoted to the fundamentals of imaging. In Chap. 12, two commonly used ad-hoc imaging methods, the Synthetic Aperture Focusing Technique (SAFT) and the Total Focusing Method (TFM) are first discussed. Then it is shown how, for simple 2-D problems, Thompson-Gray measurement models can be inverted to produce an explicit image of the surface geometry and reflectivity of a flaw in a form called an *imaging measurement model*. These imaging measurement models are shown to be closely related to the Physical Optics Far Field Inverse Scattering (POFFIS) method and also to SAFT and TFM imaging. The nature of the images generated with imaging measurement models are also described in Chap. 12 through a number of “exact” simulations. In Chap. 13 imaging measurement models are more fully developed for both large and small flaws in 3-D, leading to a unified framework of imaging that generalizes SAFT, TFM, and POFFIS imaging and rationally describes the terms inherently present in the imaging process. The implications that these imaging measurement models have on quantitative flaw characterization are also discussed.

Finally, in Chap. 14, some of the explicit assumptions used in the development of the array beam models used in the previous Chapters are re-examined. Specifically, as discussed previously in Sect. 1.3, the assumption that an array element acts as a velocity source in a surrounding rigid baffle is relaxed and a more general model is developed where the baffle is allowed to have finite acoustic impedance.

There are also three Appendices. Appendices A and B provide detailed derivations of several factors that appear in the development of imaging measurement models. Appendix C gives complete Code Listings for the MATLAB[®] functions and scripts described in the book.

References [1] and [2] will be referred to often in this book and are listed as [Schmerr] and [Schmerr-Song], respectively, in this and later Chapters.

References

1. L.W. Schmerr, *Fundamentals of Ultrasonic Nondestructive Evaluation—A Modeling Approach* (Plenum Press, New York, 1998)
2. L.W. Schmerr, S.-J. Song, *Ultrasonic Nondestructive Evaluation Systems—Models and Measurements* (Springer, New York, 2007)
3. T.L. Szabo, *Diagnostic Ultrasound: Inside Out* (Academic Press, New York, 2004)
4. K.K. Shung, *Diagnostic Ultrasound: Imaging and Blood Flow Measurements* (CRC Press, Boca Raton, 2006)
5. P.N.T. Wells, Ultrasonic imaging of the human body. *Rep. Prog. Phys.* **62**, 671–722 (1999)
6. N. Dube, Introduction to Phased Array Technology Applications. R/D Tech. (2004). (available from www.olympus-ims.com Advanced NDT Series Books)
7. B.A. Auld, General electromechanical reciprocity relations applied to the calculation of elastic wave scattering coefficients. *Wave Motion*. **1**, 3–10 (1979)
8. R.B. Thompson, T. A. Gray, A model relating ultrasonic scattering measurements through liquid-solid interfaces to unbounded medium scattering amplitudes. *J. Acoust. Soc. Am.* **74**, 140–146 (1983)

Chapter 2

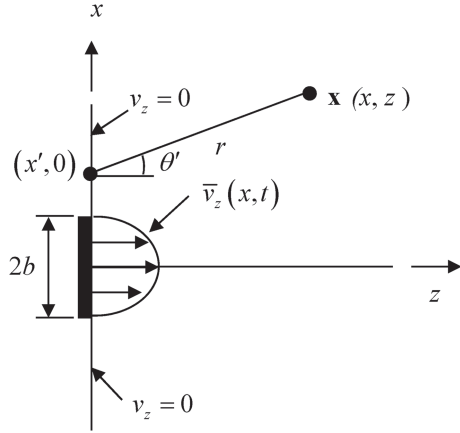
Acoustic Field of a 1-D Array Element

As discussed in Chap. 1, an ultrasonic phased array is composed of many small acoustic sending and receiving elements, each of which acts as an individual sending or receiving transducer. In this Chapter we will develop models of the acoustic waves generated by a single element and describe how the nature of this wave field depends on the size of the element and its motion. Models that simulate the radiation of a single array element will be generated explicitly in MATLAB®. The superposition of a number of these single element models with different driving excitations will then give us a complete model of a multi-element phased array transducer, as shown in Chap. 4. To keep the discussion as simple as possible in this Chapter the single element will be treated as a 1-D source of sound radiating two-dimensional waves into a fluid or through a planar interface between two fluids. Although both linear and 2-D arrays are composed of 2-D elements which produce sound waves traveling in three dimensions, the physics of wave propagation is similar for both 1-D and 2-D elements so that we can learn much of the fundamentals of sound generation with these simplified models. In Chaps. 6 and 7 we will discuss the corresponding three-dimensional models and wave fields of single elements and phased arrays.

2.1 Single Element Transducer Models (2-D)

The basic setup we will use to describe a single element transducer is shown in Fig. 2.1. We will treat the transducer as a velocity source located on the plane $z=0$ where a normal velocity, $\bar{v}_z(x,t)$, as a function of the location, x , and time, t , is generated over a finite length $[-b, b]$ in the x -direction and $[-\infty, +\infty]$ in the y -direction. The normal velocity is assumed to be zero over the remainder of the plane. This type of model is called a *rigid baffle model* since the element is assumed to be embedded in an otherwise motionless plane, as discussed in Chap. 1. The motion of the element radiates a 2-D pressure wave field $p(x,z,t)$ into an ideal compressible fluid medium that occupies the region $z \geq 0$.

Fig. 2.1 Model of a 1-D element radiating into a fluid with density and wave speed, (ρ, c) , respectively



As shown in many texts (see [Schmerr], for example) the application of Newton's law ($\sum \mathbf{F} = m\mathbf{a}$) to a small fluid element yields the equations of motion (for no body forces) of the fluid given by:

$$-\nabla p = \rho \frac{\partial^2 \mathbf{u}}{\partial t^2}, \quad (2.1)$$

Where ρ is the density of the fluid, $\mathbf{u}(x, z, t)$ is the vector displacement, and the 2-D gradient operator $\nabla = \mathbf{e}_x \frac{\partial}{\partial x} + \mathbf{e}_z \frac{\partial}{\partial z}$, and $(\mathbf{e}_x, \mathbf{e}_z)$ are unit vectors in the x - and z -directions, respectively. For an ideal compressible fluid the pressure in the fluid is related to the fluid motion by the constitutive equation

$$p = -\lambda_b \nabla \cdot \mathbf{u}, \quad (2.2)$$

where λ_b is the bulk modulus of the fluid. The quantity $\nabla \cdot \mathbf{u}$ appearing in Eq. (2.2) is called the dilatation. Physically, it represents the relative change of volume per unit volume of a small fluid element and it is also called the volumetric strain of the fluid element [Schmerr]. The minus sign is present in Eq. (2.2) because a positive pressure causes a decrease in the volume of a compressible fluid.

If one takes the divergence ($\nabla \cdot$) of both sides of Eq. (2.1) and uses Eq. (2.2), it follows that the pressure $p(x, z, t)$ must satisfy the wave equation:

$$\frac{\partial^2 p}{\partial x^2} + \frac{\partial^2 p}{\partial z^2} - \frac{1}{c^2} \frac{\partial^2 p}{\partial t^2} = 0, \quad (2.3)$$

where the wave speed, c , in the fluid is given by

$$c = \sqrt{\lambda_B / \rho}. \quad (2.4)$$

In modeling waves in the fluid, we will assume that all the waves have a harmonic time dependency $\exp(-i\omega t)$ so that

$$p(x, z, t) = \tilde{p}(x, z, \omega) \exp(-i\omega t). \quad (2.5)$$

Placing this relationship into Eq. (2.3) shows that $\tilde{p}(x, z, \omega)$ must satisfy the Helmholtz equation

$$\frac{\partial^2 \tilde{p}}{\partial x^2} + \frac{\partial^2 \tilde{p}}{\partial z^2} + \frac{\omega^2}{c^2} \tilde{p} = 0. \quad (2.6)$$

Alternatively, we can view a solution $\tilde{p}(x, z, \omega)$ of Eq. (2.6) as the Fourier transform (frequency domain spectrum) of a time dependent wave field $p(x, z, t)$, where

$$\tilde{p}(x, z, \omega) = \int_{-\infty}^{+\infty} p(x, z, t) \exp(+i\omega t) dt \quad (2.7)$$

and

$$p(x, z, t) = \frac{1}{2\pi} \int_{-\infty}^{+\infty} \tilde{p}(x, z, \omega) \exp(-i\omega t) d\omega, \quad (2.8)$$

since if we take the Fourier transform of the wave equation it follows that the transformed pressure $\tilde{p}(x, z, \omega)$ also must satisfy the Helmholtz equation.

We will solve our models of transducer behavior in this and later Chapters for the fields $\tilde{p}(x, z, \omega)$. Since we will be working almost exclusively with frequency domain wave fields in this book, we will henceforth drop the tilde on our frequency domain variables and simply write fields such as the pressure or velocity as $p(x, z, \omega)$ or $\mathbf{v}(x, z, \omega)$, etc. with the understanding that an additional time dependent term $\exp(-i\omega t)$ is also always present implicitly if we want to recover a time domain solution (see Eq. (2.8)) or if we consider these fields as harmonic wave fields.

To solve for the waves generated in the geometry of Fig. 2.1, we first note that the Helmholtz equation has harmonic wave solutions given by

$$p = \exp(ik_x x + ik_z z), \quad (2.9)$$

where

$$k_z = \begin{cases} \sqrt{k^2 - k_x^2} & k \geq k_x \\ i\sqrt{k_x^2 - k^2} & k < k_x \end{cases} \quad (2.10)$$

and $k = \omega / c$ is the *wave number*. For the real value of k_z given in Eq. (2.10), the solution of Eq. (2.9) represents a plane wave traveling at an angle θ with respect to the z -axis, where $k_x = k \sin \theta$, $k_z = k \cos \theta$. The imaginary value of k_z corresponds to an *inhomogeneous wave* traveling in the plus or minus x -direction (depending on the sign of k_x) and decaying exponentially in amplitude in the z -direction. Since the waves given by Eq. (2.9) are solutions of the Helmholtz equation, we can also form up a more general solution by simply a superposition of these waves traveling with different values of k_x , i.e. we can let

$$p(x, z, \omega) = \frac{1}{2\pi} \int_{-\infty}^{+\infty} P(k_x) \exp(ik_x x + ik_z z) dk_x. \quad (2.11)$$

This type of solution is called an *angular spectrum of plane waves*, although as we have seen it is really a combination of both plane waves and inhomogeneous waves.

We will use this type of solution to represent the waves generated by the element model of Fig. 2.1. If we let $v_z(x, 0, \omega)$ be the Fourier transform of $v_z(x, 0, t)$ (on the plane $z=0$) then

$$v_z(x, 0, \omega) = \int_{-\infty}^{+\infty} v_z(x, 0, t) \exp(i\omega t) dt \quad (2.12)$$

and we see that

$$v_z(x, 0, \omega) = \begin{cases} \bar{v}_z(x, 0, \omega) & -b < x < b \\ 0 & \text{otherwise} \end{cases}, \quad (2.13)$$

where

$$\bar{v}_z(x, 0, \omega) = \int_{-\infty}^{+\infty} \bar{v}_z(x, 0, t) \exp(i\omega t) dt. \quad (2.14)$$

Note that from the equation of motion (Eq. (2.1)) we have

$$-\frac{\partial p}{\partial z} = -\rho \omega^2 u_z = -i\omega \rho v_z \quad (2.15)$$

so that

$$v_z(x, 0, \omega) = \frac{1}{i\omega \rho} \left. \frac{\partial p(x, z, \omega)}{\partial z} \right|_{z=0}. \quad (2.16)$$

Thus, from Eq. (2.11) we find

$$\begin{aligned}
 v_z(x, 0, \omega) &= \frac{1}{2\pi} \int_{-\infty}^{+\infty} \frac{ik_z}{i\omega\rho} P(k_x) \exp(ik_x x) dk_x \\
 &= \frac{1}{2\pi} \int_{-\infty}^{+\infty} V(k_x) \exp(ik_x x) dk_x,
 \end{aligned} \tag{2.17}$$

where

$$V(k_x) = \frac{ik_z P(k_x)}{i\omega\rho}. \tag{2.18}$$

Equation (2.17) shows that $v_z(x, 0, \omega)$ can be treated as a spatial inverse Fourier transform of $V(k_x)$ so that from the corresponding forward spatial transform we have

$$V(k_x) = \int_{-\infty}^{+\infty} v_z(x, 0, \omega) \exp(-ik_x x) dx. \tag{2.19}$$

Since the velocity on $z=0$ is known (Eq. (2.13)) the spatial Fourier transform $V(k_x)$ is also known and we can write the pressure anywhere in the fluid from Eq. (2.11) and Eq. (2.18) as

$$p(x, z, \omega) = \frac{\omega\rho}{2\pi} \int_{-\infty}^{+\infty} \frac{V(k_x)}{k_z} \exp(ik_x x + ik_z z) dk_x. \tag{2.20}$$

Now, Eq. (2.20) is in the form of a spatial inverse Fourier transform of a product of functions $G(k_x, z, \omega)$ and $H(k_x, \omega)$, i.e.

$$p(x, z, \omega) = \frac{1}{2\pi} \int_{-\infty}^{+\infty} G(k_x, z, \omega) H(k_x, \omega) \exp(ik_x x) dk_x, \tag{2.21}$$

where

$$G(k_x, z, \omega) = \frac{\exp(ik_z z)}{k_z}, \quad H(k_x, \omega) = \omega\rho V(k_x). \tag{2.22}$$

But by the convolution theorem [Schmerr] the inverse Fourier transform of a product of transformed functions is the convolution of the functions themselves, so that in this case the convolution theorem gives

$$p(x, z, \omega) = \int_{-\infty}^{+\infty} h(x', \omega) g(x - x', z, \omega) dx', \tag{2.23}$$

where

$$g(x, z, \omega) = \frac{1}{2\pi} \int_{-\infty}^{+\infty} \frac{1}{k_z} \exp(ik_x x + ik_z z) dk_x \quad (2.24)$$

and

$$h(x, \omega) = \frac{\rho\omega}{2\pi} \int_{-\infty}^{+\infty} V(k_x) \exp(ik_x x) dk_x. \quad (2.25)$$

First, examine Eq. (2.25). Since $V(k_x)$ is the spatial Fourier transform of $v_z(x, 0, \omega)$, it follows that

$$h(x, \omega) = \rho\omega v_z(x, 0, \omega). \quad (2.26)$$

Now, consider Eq. (2.24). This is the inverse Fourier transform of an explicit function and can be shown to be proportional to a Hankel function of zeroth order and type one [1]. Specifically,

$$g(x, z, \omega) = \frac{H_0^{(1)}\left(k\sqrt{x^2 + z^2}\right)}{2}, \quad (2.27)$$

where again $k = \omega/c$ is the wave number. Placing these results into Eq. (2.21) then gives

$$p(\mathbf{x}, \omega) = \frac{\omega\rho}{2} \int_{-\infty}^{+\infty} v_z(x', 0, \omega) H_0^{(1)}(kr) dx', \quad (2.28)$$

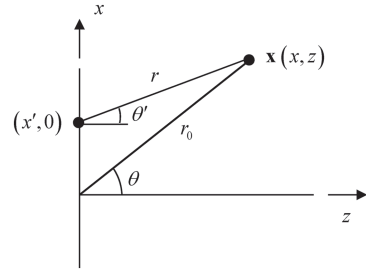
where $r = \sqrt{(x - x')^2 + z^2}$ is the distance from a point $(x', 0)$ on the plane $z=0$ to a point $\mathbf{x} = (x, z)$ in the fluid (see Fig. 2.1). Since the velocity on the plane $z=0$ is given by Eq. (2.13), we find

$$p(\mathbf{x}, \omega) = \frac{\omega\rho}{2} \int_{-b}^{+b} \bar{v}_z(x', 0, \omega) H_0^{(1)}(kr) dx' \quad (2.29)$$

in terms of the velocity on the face of the element, which is assumed to be known. Equation (2.29) gives the pressure anywhere in the fluid generated by the motion of the face of the element so it is a complete ultrasonic model for the waves generated by a single element radiating into a single fluid medium.

Physically, Eq. (2.29) represents the wave field of the transducer element in terms of a weighted superposition of cylindrical waves arising from concentrated sources acting over the length of the transducer. This can be seen more explicitly by

Fig. 2.2 Geometry parameters for defining the far field response



assuming the distance r to a point in the fluid is many wavelengths away from the element so that $kr \gg 1$. Then, since the Hankel function has the asymptotic value [2]

$$H_0^{(1)}(u) = \sqrt{\frac{2}{\pi u}} \exp[i(u - \pi/4)] \quad (2.30)$$

for $u \gg 1$, Eq. (2.30) becomes

$$p(\mathbf{x}, \omega) = \frac{k\rho c \exp(-i\pi/4)}{2} \int_{-b}^{+b} \bar{v}_z(x', 0, \omega) \sqrt{\frac{2}{\pi kr}} \exp(ikr) dx' \quad (2.31)$$

in terms of a superposition of the cylindrical wave terms $\exp(ikr)/\sqrt{r}$ over the length of the element.

2.2 Far Field Waves

From the law of cosines (see Fig. 2.2) we have

$$r = \sqrt{r_0^2 + (x')^2 - 2x'r_0 \sin \theta}. \quad (2.32)$$

Continuing to keep the high frequency approximation $kr \gg 1$ the *far field* of the element is defined as the region far enough from the element so that $x'/r_0 \ll 1$ are valid and we can expand Eq. (2.32) to only first order as

$$r = r_0 - x' \sin \theta. \quad (2.33)$$

If we place this approximation into Eq. (2.30) we obtain

$$p(\mathbf{x}, \omega) = \frac{k\rho c}{2} \sqrt{\frac{2}{\pi kr_0}} \exp(-i\pi/4) \exp(ikr_0) \int_{-\infty}^{+\infty} \bar{v}_z(x', 0, \omega) \exp(-ik \sin \theta x') dx', \quad (2.34)$$

or equivalently, in terms of the spatial Fourier transform of the velocity field,

$$p(\mathbf{x}, \omega) = \sqrt{\frac{k}{2\pi i}} \rho c V(k_x) \frac{\exp(ikr_0)}{\sqrt{r_0}} \quad (2.35)$$

with $k_x = k \sin \theta$.

Equation (2.35) shows that in the far field region the element behaves like a concentrated source emitting a single cylindrical wave so we could call this region the *cylindrical wave region* of the element.

In most cases we will model the motion on the face of an element as if it acted as a *piston source*, i.e. as if the element had a spatially uniform velocity over the entire length of the element:

$$v_z(x', 0, \omega) = \begin{cases} v_0(\omega) & -b < x' < b \\ 0 & \text{otherwise} \end{cases} \quad (2.36)$$

In this case the spatial Fourier transform is

$$\begin{aligned} V(k_x) &= \int_{-b}^{+b} v_0(\omega) \exp(-ik_x x') dx' \\ &= \frac{2v_0(\omega) \sin(k_x b)}{k_x} = \frac{2v_0(\omega) \sin(kb \sin \theta)}{k \sin \theta} \end{aligned} \quad (2.37)$$

and the far field piston element response can be written as

$$p(\mathbf{x}, \omega) = \rho c v_0(\omega) \sqrt{\frac{2}{\pi i}} (kb) \frac{\sin(kb \sin \theta)}{kb \sin \theta} \frac{\exp(ikr_0)}{\sqrt{kr_0}} \quad (2.38)$$

Equation (2.38) shows that in the far field the piston element response has a directivity function, $D_b(\theta)$, where

$$D_b(\theta) = \frac{\sin(kb \sin \theta)}{kb \sin \theta} \quad (2.39)$$

This directivity function is strongly controlled by the non-dimensional wave number, kb , as shown in Fig. 2.3. [Note: For brevity of notation in later expressions this kb dependency will be omitted in the argument of D_b but it should be implicitly understood that it is still present in this and in other directivities that will be discussed in later Chapters.] For a value of $kb=0.314$ where the length, $2b$, of the element is one tenth of a wavelength, λ , (Fig. 2.3a), the sound radiation of the element is nearly uniform in all directions ($-90^\circ \leq \theta \leq 90^\circ$). At $kb=1.57$ (element length=one half a wavelength) there begins to be some significant changes in directivity with angle (Fig. 2.3b) but the radiation pattern is still broad. At a value $kb=3.14$ (element

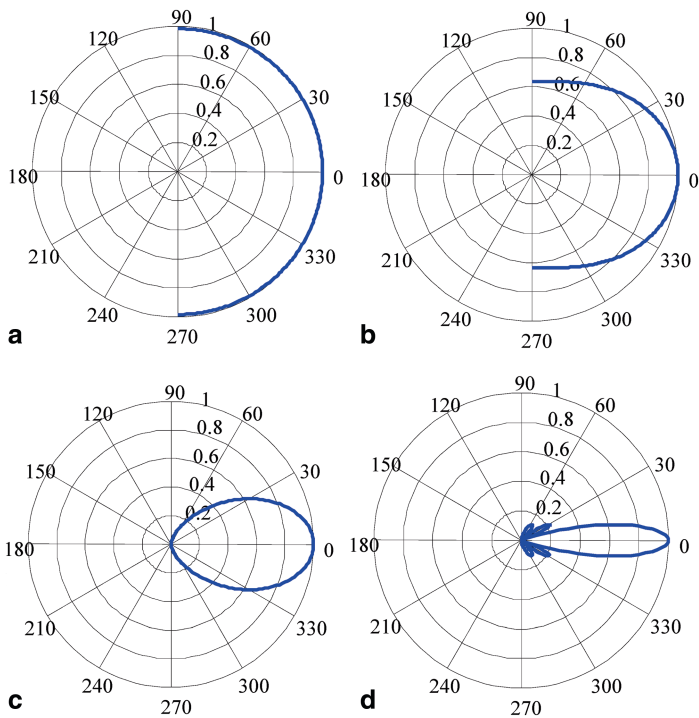


Fig. 2.3 The directivity function for an element of **a** length $2b/\lambda = 0.1$, **b** $2b/\lambda = 0.5$, **c** $2b/\lambda = 1.0$, and **d** $2b/\lambda = 3.0$

Table 2.1 Directivities of some elements of various sizes

Element size, $2b/\lambda$	$\theta_{-6\text{ dB}}$ (degrees)
1.0	36.9
3.0	11.5
10.0	3.4

length=one wavelength) Fig. 2.3c shows that now most of the radiation is in an angular region of $\pm 30^\circ$ about the normal to the element and at $kb=9.42$ (element length=three wavelengths) the sound is confined primarily to a highly directed beam, with the appearance of small side lobes, as shown in Fig. 2.3d. Most NDE phased array transducers operate at MHz frequencies and with element sizes that are larger than one half a wave length so that directivity of the element plays an important role in the sound field generated and appears as a part of the overall response of an array of elements.

It is customary to define the size of the main “lobe” of the far field sound beam generated by an element in terms of the angle at which the pressure first drops to one half (−6 dB) of its value along the z-axis ($\theta = 0$). For the sinc function, $\sin x/x$, this one half value occurs at $x=1.8955$ so that from Eq. (2.39) we see the −6 dB angle is given by

$$\theta_{-6\text{ dB}} = \sin^{-1} \left[0.6 \frac{\lambda}{2b} \right], \quad (2.40)$$

which always has a root as long as $2b > 0.6\lambda$. Table 2.1 shows the results for cases (c) and (d) of Fig. 2.3 which agree with the angular patterns shown in Fig. 2.3. Also shown in Table 2.1 are the results for an element that is ten wave lengths long, where it can be seen that the directivity becomes quite small. Large, single element transducers used in NDE applications are normally tens of wavelengths in diameter so that they are highly directional and generate sound beams that are well collimated, i.e. most of the sound propagates normal to the face of the transducer. However, for the smaller elements present in phased array transducers the far field directivity can vary considerably, depending on the size of the elements.

It is important to know when the far field approximation we have been using in this section is valid. Recall, in Eq. (2.32) we expanded the radius r to only first order Eq. (2.33) which led us to the explicit far field results. Let us go back to Eq. (2.32) and examine when the remaining terms in the expansion are negligible. First, we rewrite the radius r as

$$r = r_0 \sqrt{1 + \frac{(x')^2 - 2x'r_0 \sin \theta}{r_0^2}}, \quad (2.41)$$

which is in a form that can be expanded to three terms since by the binomial expansion of a square root

$$\sqrt{1+b} \approx \left(1 + \frac{b}{2} - \frac{b^2}{8} + \dots \right), \quad |b| < 1. \quad (2.42)$$

In the case of Eq. (2.41) if we use Eq. (2.42) and keep only quadratic terms at most in the expansion we find

$$r \approx r_0 - x' \sin \theta + \frac{(x')^2 \cos^2 \theta}{2r_0}. \quad (2.43)$$

Equation (2.43) shows that in order to keep only the first order term of Eq. (2.33) in the phase term of Eq. (2.1.31) we must have the complex exponential $\exp(ik(x')^2 \cos^2 \theta / 2r_0)$ term near unity, which will only be possible if $k(x')^2 \cos^2 \theta / 2r_0 \ll 1$. This condition will certainly be satisfied if we replace x' and $\cos^2 \theta$ by their largest possible values of b and one, respectively, and require

$$\frac{kb^2}{2r_0} = \frac{\pi b^2}{\lambda r_0} \ll 1. \quad (2.44)$$

So the far field conditions should be well satisfied if

$$r_0 \gg \frac{\pi b^2}{\lambda}. \quad (2.45)$$

For large single element transducers radiating waves in 3-D the far field occurs when the transducer wave field is well approximated by a point source radiating a single spherical wave. For a circular transducer of radius b the far field of the transducer is also given by Eq. (2.45) where the quantity $N = b^2/\lambda$ is called the near field distance [Schmerr]. The quantity $D = \pi b^2/\lambda$ can be rewritten as $D = kb^2/2$ which is called the *Rayleigh distance* [Schmerr-Song]. We see that the far field of a 1-D element also occurs for distances greater than the Rayleigh distance.

2.3 Numerical Piston Element Models

Although we can obtain explicit results for the wave field of an element in the far field, for other points in the wave field it is not possible to analytically perform the integrations present in either Eq. (2.29) or Eq. (2.31). However, it is relatively easy to compute the pressure wave field numerically from Eq. (2.29) as long as z is not too near the element face ($z=0$) where the Hankel function can become singular. At or near the element face one needs to perform the integration more carefully, but generally we are only interested in the radiated wave field at some finite distance from the element face where such singular behavior is not present. For piston behavior we have:

$$p(\mathbf{x}, \omega) = \frac{k \rho c v_0(\omega)}{2} \int_{-b}^{+b} H_0^{(1)}(kr) dx', \quad (2.46)$$

where $k = \omega/c$ is the wave number. First, we break up the face of the element into N equal segments of length $\Delta d = 2b/N$. The centroids of these segments will be located at the positions

$$x'_n = -b + \frac{\Delta d}{2} + (n-1)\Delta d \quad (n = 1, 2, \dots, N) \quad (2.47)$$

or, in normalized form

$$\bar{x}_n = \frac{x'_n}{b} = -1 + \frac{2}{N} \left(n - \frac{1}{2} \right). \quad (2.48)$$

If we assume that the segments are small enough that the Hankel function can be taken as a constant over each segment, then Eq. (2.46) can be written as

$$\frac{p(\mathbf{x}, \omega)}{\rho c v_0} = \frac{kb}{N} \sum_{n=1}^N H_0^{(1)}(kb \bar{r}_n), \quad (2.49)$$

where

$$\bar{r}_n = \sqrt{(x/b - \bar{x}_n)^2 + (z/b)^2}. \quad (2.50)$$

We will call the beam model of Eq. (2.49) the *Hankel function model*.

Since for large kb values the Hankel function is a highly oscillatory function, to treat it as a constant over each segment we will typically have to keep the segment size, Δd , to about a tenth of a wavelength, λ , or less. If we take frequency, f , in MHz, the wave speed, c , in m/sec, and dimensions of b and Δd in mm, then the criterion

$$\Delta d \leq \frac{\lambda}{10} \quad (2.51)$$

is equivalent to the requirement that N must satisfy

$$N = \begin{cases} \text{ceil}\left(\frac{20 \times 10^3 fb}{c}\right) & 2b > \lambda/10 \\ 1 & 2b \leq \lambda/10 \end{cases}, \quad (2.52)$$

where the MATLAB[®] function *ceil()* rounds the value of its argument towards infinity to the nearest integer. Note that Eq. (2.52) also guarantees that for element lengths less than a tenth of a wavelength we must have at least one segment ($N=1$). For $b=6$ mm, $f=5$ MHz, and $c=1500$ m/sec we obtain $N=400$. This example shows that even in this 2-D problem when computing the integral of Eq. (2.46) for element sizes comparable to large, single element NDE transducers one needs to compute a relatively large number of terms. For the much smaller element sizes used in phased arrays the number of terms needed is greatly reduced. The MATLAB[®] function *rs_2Dv* given in Code Listing C.1 (see Appendix C) implements the Hankel function model. Its calling sequence is

$$>> p = \text{rs_2Dv}(b, f, c, e, x, z, \text{Nopt});$$

This function uses Eq. (2.49) to calculate the normalized pressure field, $p(x, z)/\rho c v_0$ at a point (x, z) , measured in mm, for a piston element of length $2b$ mm radiating waves into a fluid whose wave speed is c (in m/sec) at a frequency, f , given in MHz. In anticipation that this function will also be used to model a single element in an array where the center of the element may not be located at $x' = 0$, Eq. (2.50) has been modified to be

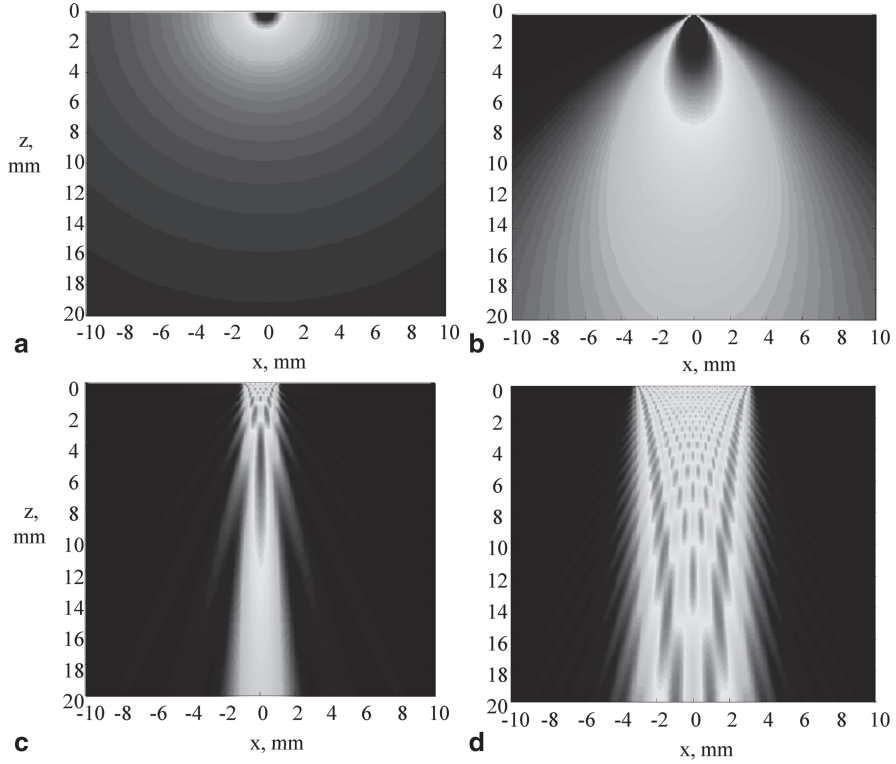


Fig. 2.4 The magnitude of the normalized pressure, $p/\rho cv_0$, generated at 5 MHz, $c=1500$ m/sec, for an element where **a** $2b=.03$ mm ($2b/\lambda=0.1$), **b** $2b=0.3$ mm ($2b/\lambda=1.0$), **c** $2b=2.0$ mm ($2b/\lambda=6.67$), and **d** $2b=6.35$ mm ($2b/\lambda=21.2$)

$$\bar{r}_n = \sqrt{(x/b - \bar{x}_n - e/b)^2 + (z/b)^2}, \quad (2.53)$$

where the offset of the element in the x -direction, e , (in mm) is also specified as an input parameter of `rs_2Dv`. The parameter, `Nopt`, is an optional input argument for this function. If `Nopt` is not specified, the number of segments used to calculate the wave field is given by Eq. (2.52). Otherwise `Nopt` is used for the number of segments instead. This gives the user some flexibility in controlling the calculations but, as we will show shortly, when choosing `Nopt` there are some limits to how large the element segments can be.

Figure 2.4 shows the magnitude of the pressure wave field generated by elements of different sizes. In all these cases the frequency was taken to be 5 MHz and the wave speed (nominally that of water) was given as 1500 m/sec. The `Nopt` parameter was not specified. Figure 2.4a shows the case for an element of total length $2b=0.03$ mm, which corresponds to $2b/\lambda=0.1$. For this case in the far field we saw the directivity of the element was uniform in all directions and this behavior is also true for much of

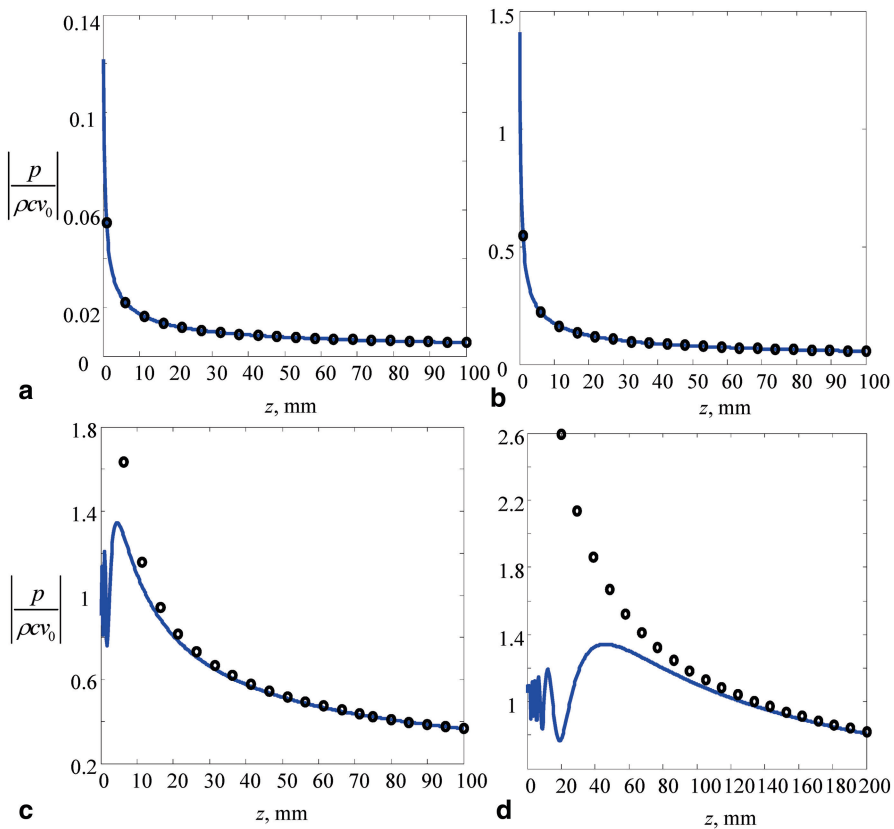


Fig. 2.5 The magnitude of the normalized on-axis pressure, $p/\rho c v_0$, versus z generated at 5 MHz, $c=1500$ m/sec, for an element where **a** $2b=.03$ mm ($2b/\lambda = 0.1$), **b** $2b=0.3$ mm ($2b/\lambda = 1.0$), **c** $2b=2.0$ mm ($2b/\lambda = 6.67$), and **d** $2b=6.35$ mm ($2b/\lambda = 21.2$). Solid line—using Eq. (2.49). Circles—using the far field expression, Eq. (2.38), for $\theta = 0$. Note the changing scales in these cases

the entire wave field of the element as seen in Fig. 2.4a. In Fig. 2.4b the length of the element was $2b=0.3$ mm ($2b/\lambda = 1.0$) and one now sees a very broad beam but with some directivity, in agreement with the far field behavior of Fig. 2.3c. Figure 2.4c is for $2b=2.0$ mm ($2b/\lambda = 6.67$) and now the element generates a highly directional beam, as expected. In Fig. 2.4d, the element size is typical of many large, single element transducers, $2b=6.35$ mm ($2b/\lambda = 21.2$), and the wave field remains highly collimated, with much internal structure in the main “beam” of the element visible.

These results show that the nature of the waves generated by a small phased array element will be quite different from that of a large, single element transducer. The wave fields of small phased array elements will individually exhibit very broad radiation patterns, while large elements are quite directional in their response. When many small elements are combined in a multi-element phased array transducer, these wave fields will be combined to give the overall array sound beam. As we will

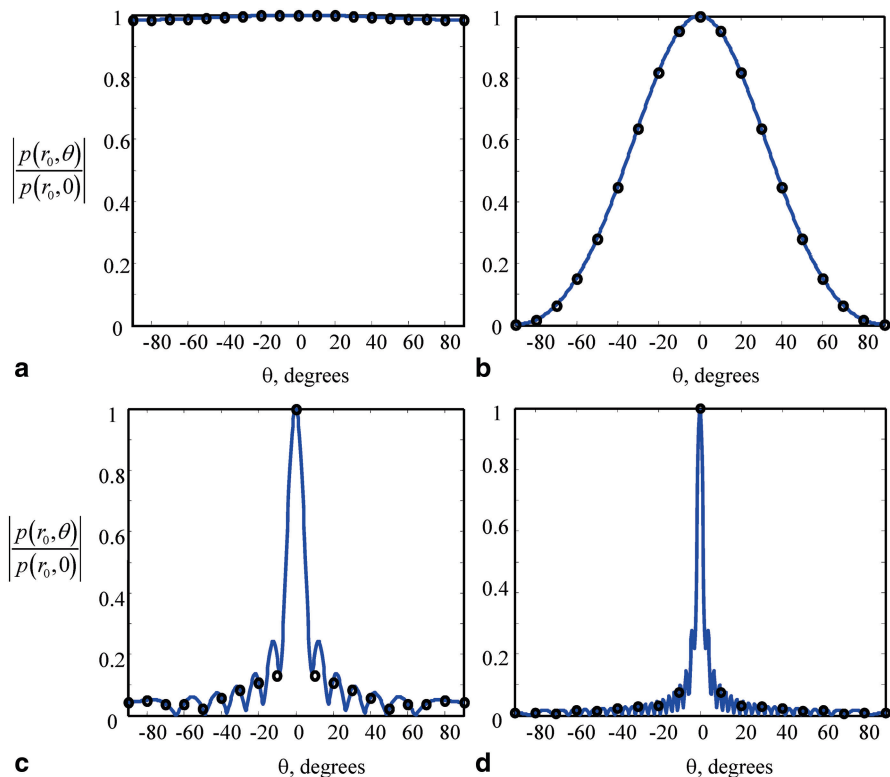
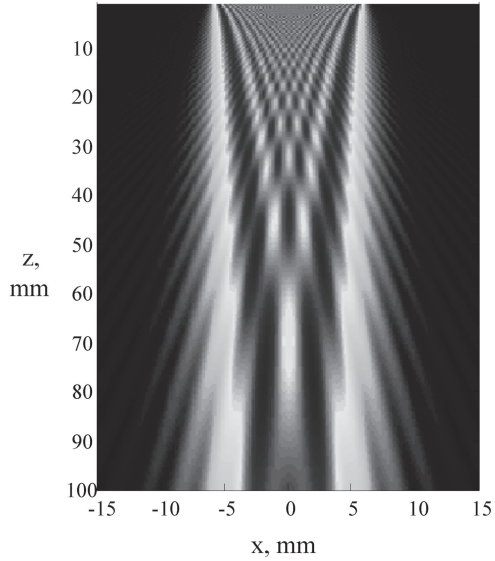


Fig. 2.6 The magnitude of the normalized pressure, $p(r_0, \theta)/p(r_0, 0)$, generated at 5 MHz, $c = 1500$ m/sec, at a fixed distance, r_0 , for an element where **a** $r_0 = 5$ mm, $2b = .03$ mm ($2b/\lambda = 0.1$), **b** $r_0 = 5$ mm, $2b = 0.3$ mm ($2b/\lambda = 1.0$), **c** $r_0 = 15$ mm, $2b = 2.0$ mm ($2b/\lambda = 6.67$), and **d** $r_0 = 100$ mm, $2b = 6.35$ mm ($2b/\lambda = 21.2$). *Solid line*—using Eq. (2.49). *Circles*—using the far field expression, Eq. (2.38), for $\theta = 0$

see in Chap. 5, by appropriately delaying the broadly generated wave fields of such small elements we can easily adjust their combined effect to both steer and focus the overall sound beam of the array. However, such steering and focusing becomes more difficult as the element size gets larger because we are then combining elements wave fields that are more highly directional themselves. Practical considerations in the manufacture of commercial phased array elements may require that the elements be large enough so that element directivity effects are present. This, in turn, may affect the steering and focusing capability of commercial arrays.

It is also instructive to examine the behavior of the pressure wave field along the central axis of an element and compare it to the far field values of Eq. (2.38) (for $\theta = 0$). The results are shown in Fig. 2.5 for the same four cases considered in Fig. 2.4. It can be seen that for elements of lengths equal to one wavelength or less the “exact” numerical values follow the far field values essentially throughout the

Fig. 2.7 The magnitude of the normalized pressure, $p/\rho c v_0$, generated at 5 MHz in water ($c=1480$ m/sec) for a 12 mm long element where the element is divided into segments whose length is one tenth of a wavelength



entire wave field. For the larger element sizes there is a near field oscillatory structure in the numerical results close to the element but at larger distances the numerical and far field results again agree.

Since the on-axis exact and far field results are identical for cases (a) and (b) in Fig. 2.5 one would expect that off-axis results would agree also. This is the case, as shown in Fig. 2.6 where the angular behavior of the normalized pressure wave field for a fixed radius $r_0 = \sqrt{x^2 + z^2}$ is plotted versus the angle $\theta = \tan^{-1}(x/z)$ from both Eq. (2.49) and Eq. (2.38). For an element length of one tenth of a wavelength (Fig. 2.6a) at a distance $r_0 = 5$ mm the directivity is nearly uniform, while there is more directivity at the same radius for an element length of one wavelength (Fig. 2.6b). In both cases the exact results and the far field results agree closely and show the same behavior of directivity that we have seen previously in the polar plots of Fig. 2.3. For the larger elements of Fig. 2.6c and d, the exact and far field results again agree as long as the radius r_0 is in the cylindrically spreading region. From the on-axis results of Fig. 2.5 we saw that for case (c) the two curves merge at approximately $z=15$ mm while they merge for approximately $z=100$ mm for case (d). Thus, these distances were used for the r_0 values in Fig. 2.6c and d. Although the spacing of the discrete far field results shown in Fig. 2.6c and d is too large to show the detailed behavior of the directivity for these cases, at the angular locations evaluated here there was good agreement with the exact results.

Using Eq. (2.52) to determine the number of segments for an element is generally a conservative choice so that one can often obtain acceptable solutions with a smaller number of segments. However, if the length of the segment exceeds a wavelength, fictitious side beams (called grating lobes) will appear in wave field. These side lobes are simply the result of inadequate sampling of the element and can

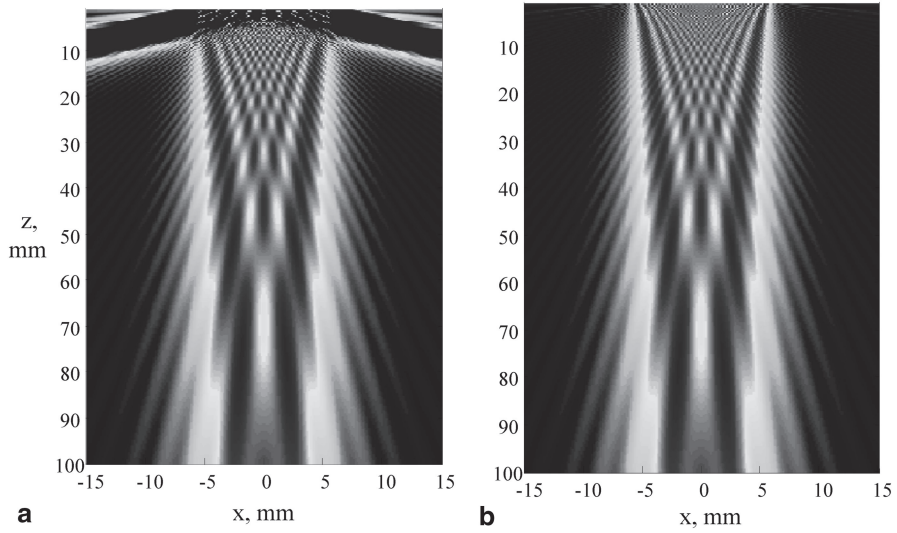


Fig. 2.8 The magnitude of the normalized pressure, $p/\rho cv_0$, generated at 5 MHz in water ($c=1480$ m/sec) for a 12 mm long element where the field calculations are performed with **a** thirty five sub-element segments, each 1.14 wave lengths long, and **b** 50 sub-element segments, each 0.8 wave lengths long

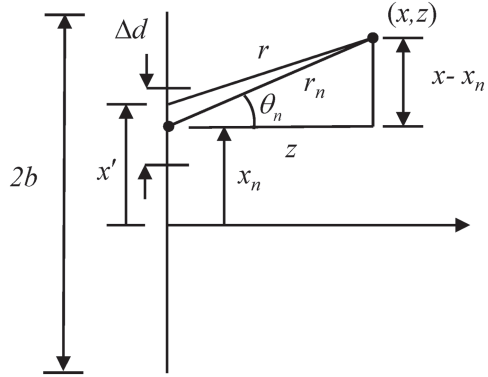
also appear in the response of multi-element phased arrays, as discussed in some detail in Chap. 4. We can easily see this behavior by making different choices of the N_{opt} parameter. Consider, for example, a 12 mm long element radiating into water ($c=1480$ m/sec) at 5 MHz. An image of the pressure wave field (magnitude) is shown in Fig. 2.7 when Eq. (2.52) is used to guarantee that the segment size is one tenth a wavelength. If, instead we evaluate this wave field with $N_{opt}=35$, the size of a segment is 1.14 wavelengths and the field is shown in Fig. 2.8a. We see that the main structure of the radiated beam in Fig. 2.8 is identical to that of Fig. 2.7 but outward radiating side beams (grating lobes) also appear as well. These grating lobes can be eliminated by choosing $N_{opt}=50$ so that the size of each segment is 0.8 wavelengths, as shown in Fig. 2.8b.

2.4 Line Source Models

Studies such as those described in the previous section show that as long as we are at a distance of about 3 near field lengths or greater from an element the entire wave field of an element is well described by the far field results of Eq. (2.38) given here as

$$p(\mathbf{x}, \omega) = \rho cv_0(\omega) \sqrt{\frac{2}{\pi i}} (kb) D_b(\theta) \frac{\exp(ikr_0)}{\sqrt{kr_0}} \quad (2.54)$$

Fig. 2.9 The geometrical parameters defining the n th segment of length Δd for an element of total length $2b$. The distance x_n is to the centroid of the n th segment and $\Delta d = 2b/N$ where N is the number of segments



in terms of the element directivity, $D_b(\theta)$. If we use this single term to represent the waves generated by an array element we will call this model an array *single line source model*. We should note that some authors discuss phased arrays by using single line source models for each array element where the directivity function is equal to one. As we have seen, this is permissible only for element lengths one tenth of a wavelength or less, which is much smaller than what is practical to make in most commercial NDE phased arrays so that for NDE applications one needs to include this directivity in the single line source model. When the fields are needed for an element in a region where the far field values of Eq. (54) are not adequate one can superimpose a number of such far field results over the length of the element. This is equivalent to using the high frequency model of Eq. (2.31) for a piston element given as

$$p(\mathbf{x}, \omega) = \frac{k\rho c \exp(-i\pi/4)v_0(\omega)}{2} \int_{-b}^{+b} \sqrt{\frac{2}{\pi kr}} \exp(ikr) dx' \quad (2.55)$$

and then breaking the element length into N segments in exactly the same fashion as done for our original Hankel function element model (see Eq. (2.49)) but where now within each segment (see Fig. 2.9) we have from the law of cosines

$$\begin{aligned} r &= \sqrt{r_n^2 - 2(x' - x_n)r_n \sin \theta_n + (x' - x_n)^2} \\ &\equiv r_n [1 - (x' - x_n) \sin \theta_n / r_n]. \end{aligned} \quad (2.56)$$

Keeping only the leading term in Eq. (2.56) for the $1/\sqrt{r}$ term of Eq. (2.55) and both terms in the exponential of that equation we obtain

$$p(\mathbf{x}, \omega) = \frac{k\rho c \exp(-i\pi/4)v_0(\omega)}{2} \sum_{n=1}^N \sqrt{\frac{2}{\pi kr_n}} \exp(ikr_n) \int_{-\Delta d/2}^{+\Delta d/2} \exp(-ikv \sin \theta_n) dv, \quad (2.57)$$

where $v = x' - x_n$. But the integral in Eq. (2.57) is just equal to $\Delta d D_{k\Delta d/2}(\theta_n)$, where

$$D_{\Delta d/2}(\theta_n) = \frac{\sin [k(\Delta d/2) \sin \theta_n]}{k(\Delta d/2) \sin \theta_n} \quad (2.58)$$

(see Eqs. (2.38) and (2.39)), so we find

$$p(\mathbf{x}, \omega) = \rho c v_0(\omega) \frac{k\Delta d}{2} \sqrt{\frac{2}{\pi i}} \sum_{n=1}^N D_{\Delta d/2}(\theta_n) \frac{\exp(ikr_n)}{\sqrt{kr_n}} \quad (2.59)$$

which, comparing with Eq. (2.54), shows that the wave field of the element can be calculated as the superposition of single line source terms for each segment. Equation (2.59) gives us an expression for evaluating the wave field of any element, large or small, similar to the Hankel function model, as long as the segments are chosen to be small enough. We will call this model the *multiple line source model*.

As with the Hankel function model we can write Eq. (2.59) in non-dimensional form to give

$$\frac{p(\mathbf{x}, \omega)}{\rho c v_0(\omega)} = \frac{1}{N} \sqrt{\frac{2kb}{\pi i}} \sum_{n=1}^N D_{b/N}(\theta_n) \frac{\exp(ikb\bar{r}_n)}{\sqrt{\bar{r}_n}}, \quad (2.60)$$

where the normalized distance to the centroid of each segment, \bar{r}_n , is again given by Eq. (2.50).

The MATLAB® function `ls_2Dv` given in Code Listing C.2 uses Eq. (2.60) to calculate the normalized pressure field, $p(x, z)/\rho c v_0$ for a piston element where the center of the element can be offset a distance, e , in the x -direction so that the distance \bar{r}_n is again replaced by the modified expression of Eq. (2.53). The calling sequence for this function is very similar to that of `rs_2Dv`:

```
>>p=ls_2Dv(b, f, c, e, x, z, Nopt);
```

The optional function argument, `Nopt`, gives the number of segments. For `Nopt=1`, the function implements a single line source model for the element. If this argument is not specified then the number of segments, N , is chosen so that a segment is never larger than one wavelength:

$$N = \begin{cases} \text{ceil}\left(\frac{2 \times 10^3 fb}{c}\right) & 2b > \lambda \\ 1 & 2b \leq \lambda \end{cases}, \quad (2.61)$$

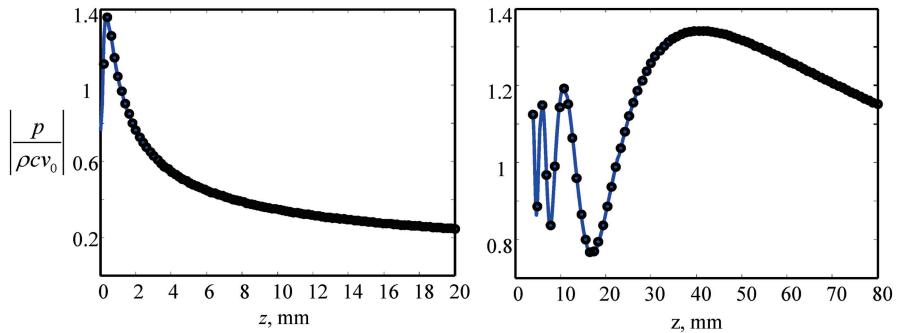


Fig. 2.10 Comparison of the magnitude of the on-axis normalized pressure, $p/\rho c v_0$, versus on-axis distance, z , where the Hankel function model (*solid line*) and multiple line source model (*circles*) were used to model the waves from an element for **a** $2b = 0.6$ mm ($2b/\lambda = 2.0$), **b** $2b = 6$ mm ($2b/\lambda = 20$). Other parameters: $f = 5$ MHz, $c = 1500$ m/sec

which eliminates the possibility of grating lobes arising from choosing inadequate segment size when representing an element (recall b here is in mm, f is in MHz, c is in m/sec). However, in Chap. 4 we will show that regardless of the smallness of the segments used to represent an element, if the element size itself and gap size of an array combine to give a value of the array pitch that is greater than only one half a wavelength then similar grating lobes can appear in the wave field of the entire array.

Figure 2.10 shows the magnitude of the on-axis pressure for both a small and large piston element as calculated with either the Hankel function model or the multiple line source model (using Eq. (2.61) for determining N). It can be seen that the multiple line source model accurately predicts the response even at small distances from the element where near field effects are present. Similar agreement between the two models can be shown to exist for all points in the wave field except in a very small region directly adjacent to the face of the element for both large and small elements, so that the multiple line source model is an accurate and versatile model for both array elements and for large, single element transducers.

2.5 Radiation Through a Planar Interface

The behavior of a phased array element can be best described in the simple context of radiation into a single medium, but in practice arrays are often used in setups where an interface exists between the element and the point at which the fields are being evaluated. Thus, in this section we will examine how to include a planar interface in modeling the radiated wave field.

Consider the setup of Fig. 2.11 where a planar element located in a fluid medium radiates sound into a second fluid medium through a plane interface. In [Schmerr] this type of problem was analyzed using both an angular plane wave spectrum in-

Fig. 2.11 Radiation of waves from an element in 2-D through a planar interface between two fluids

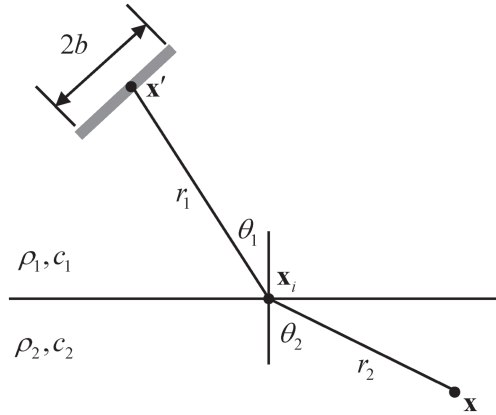
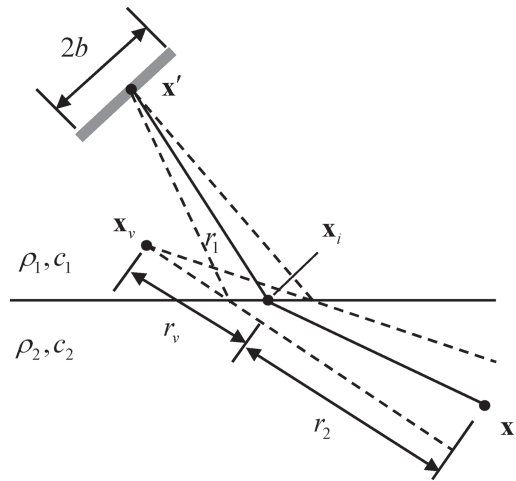


Fig. 2.12 Geometry of a bundle of rays that travels on a Snell's law path from a point on the element to a point in the second medium



tegral and a Kirchhoff approximation approach in conjunction with the method of stationary phase. However, it was also shown that both of these methods, which involve rather complex derivations, are equivalent to the use of simple high frequency ray theory methods so we will directly apply those ray methods here.

According to ray theory, at high frequencies the pressure at point \mathbf{x} due to a cylindrical wave propagating from a point \mathbf{x}' on the face of the element can be calculated by following a bundle of rays as it propagates along a path from \mathbf{x}' to a point \mathbf{x}_i on the interface and then to \mathbf{x} , where the path must satisfy Snell's law [3]. Such a bundle is shown as the dashed lines in Fig. 2.12. If we assume the element acts as a piston velocity source, then at the interface point, \mathbf{x}_i , the incident pressure in the first fluid for a cylindrical wave traveling from \mathbf{x}' to a point \mathbf{x}_i for a small segment dx' of that element, $p_1(\mathbf{x}_i)$, is just

$$p_1(\mathbf{x}_i) = \rho_1 c_1 v_0(\omega) \sqrt{\frac{k_1}{2\pi i}} \frac{\exp(ik_1 r_1)}{\sqrt{r_1}} dx' \quad (2.62)$$

(see Eq. (2.55) which is just an integral superposition of this type of term). The pressure at point \mathbf{x}_i for the wave that is transmitted into the second medium, $p_2(\mathbf{x}_i)$, is then

$$p_2(\mathbf{x}_i) = \rho_1 c_1 v_0(\omega) T_p \sqrt{\frac{k_1}{2\pi i}} \frac{\exp(ik_1 r_1)}{\sqrt{r_1}} dx', \quad (2.63)$$

where T_p is the plane wave transmission coefficient (based on pressure ratios). As shown in Fig. 2.12, a bundle of these transmitted waves appears to originate from a virtual source point, \mathbf{x}_v , located at a distance r_v along the refracted ray. It is easy to show, using Snell's law that this distance is given by

$$r_v = \frac{c_1}{c_2} \frac{\cos^2 \theta_2}{\cos^2 \theta_1} r_1 \quad (2.64)$$

(the proof follows identical lines to the proof of Eq. (B.40) given in Appendix B for the virtual distance in the plane of incidence for rays traveling in 3-D). In propagating from \mathbf{x}_i to \mathbf{x} along the refracted ray, the ratio of the magnitude of the pressures at these two points is inversely proportional to the ratio of the square roots of the distances from the virtual source [3] so that we have

$$\frac{p_2(\mathbf{x})}{p_2(\mathbf{x}_i)} = \frac{\sqrt{r_v}}{\sqrt{r_v + r_2}} \exp(ik_2 r_2). \quad (2.65)$$

Placing Eq. (2.63) into Eq. (2.65) gives

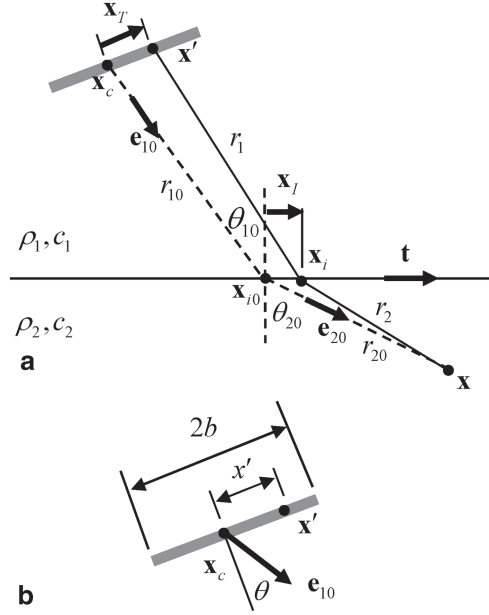
$$p_2(\mathbf{x}) = \rho_1 c_1 v_0(\omega) T_p \sqrt{\frac{k_1}{2\pi i}} \frac{\exp(ik_1 r_1 + ik_2 r_2)}{\sqrt{r_1 + \frac{c_2}{c_1} \frac{\cos^2 \theta_1}{\cos^2 \theta_2} r_2}} dx'. \quad (2.66)$$

Summing all the small segments over the length of the array element, the total pressure at \mathbf{x} from the element, $p(\mathbf{x})$, is

$$p(\mathbf{x}) = \rho_1 c_1 v_0(\omega) \sqrt{\frac{k_1}{2\pi i}} \int_{-b}^{+b} T_p \frac{\exp(ik_1 r_1 + ik_2 r_2)}{\sqrt{r_1 + \frac{c_2}{c_1} \frac{\cos^2 \theta_1}{\cos^2 \theta_2} r_2}} dx'. \quad (2.67)$$

Equation (2.67) is the foundation for generating a multiple line source model for our two medium problem. This is in a very similar form to Eq. (2.55) for a single

Fig. 2.13 **a** The geometry for a pair of nearby rays traveling from an element to a point in the second medium, and **b** the definition of parameters at the radiating element



medium and reduces to that equation when both media are identical. Evaluating Eq. (2.67), however, is more complex than Eq. (2.55) since the angles (θ_1, θ_2) and the distances (r_1, r_2) are not known explicitly until the Snell's law ray path from any point \mathbf{x}' to \mathbf{x} is known. Such paths are determined once the locations of the points \mathbf{x}_i on the interface are obtained. In Chap. 5, in discussing the development of time delay laws for steering and focusing through a planar interface, the location of the point \mathbf{x}_i is found by explicitly solving for the zero of a function $g(\mathbf{x}_i)$ (see Eq. (5.18)). The same approach can be used here to obtain (θ_1, θ_2) and (r_1, r_2) for use in Eq. (2.67).

Consider now the case when the element is small enough so that the distances (r_1, r_2) are approximately equal to (r_{10}, r_{20}) as measured along a Snell's law ray path from the center of the element, \mathbf{x}_c , to point \mathbf{x} in the second medium (Fig. 2.13a). From the geometry of Fig. 2.13a we see that

$$\begin{aligned}
 \frac{r_1}{c_1} &= \frac{\sqrt{(r_{10}\mathbf{e}_{10} + \mathbf{x}_I - \mathbf{x}_T) \cdot (r_{10}\mathbf{e}_{10} + \mathbf{x}_I - \mathbf{x}_T)}}{c_1} \\
 &= \frac{\sqrt{r_{10}^2 + 2r_{10}\mathbf{e}_{10} \cdot (\mathbf{x}_I - \mathbf{x}_T) + |\mathbf{x}_I - \mathbf{x}_T|^2}}{c_1} \\
 &\cong \frac{r_{10} + \mathbf{e}_{10} \cdot (\mathbf{x}_I - \mathbf{x}_T)}{c_1}
 \end{aligned} \tag{2.68}$$

and, similarly,

$$\begin{aligned} \frac{r_2}{c_2} &= \frac{\sqrt{(r_{20}\mathbf{e}_{20} - \mathbf{x}_I) \cdot (r_{20}\mathbf{e}_{20} - \mathbf{x}_I)}}{c_2} \\ &= \frac{\sqrt{r_{20}^2 - 2r_{20}\mathbf{e}_{20} \cdot \mathbf{x}_I + |\mathbf{x}_I|^2}}{c_2} \\ &\equiv \frac{r_{20} - \mathbf{e}_{20} \cdot \mathbf{x}_I}{c_2}, \end{aligned} \quad (2.69)$$

where $(\mathbf{e}_{10}, \mathbf{e}_{20})$ are unit vectors along the Snell's law path from \mathbf{x}_c to \mathbf{x} in the first medium and second medium, respectively. Combining Eq. (2.68) and Eq. (2.69) gives

$$\frac{r_1}{c_1} + \frac{r_2}{c_2} \equiv \frac{r_{10}}{c_1} + \frac{r_{20}}{c_2} - \frac{\mathbf{e}_{10} \cdot \mathbf{x}_I}{c_1} + \left(\frac{\mathbf{e}_{10} \cdot \mathbf{t}}{c_1} - \frac{\mathbf{e}_{20} \cdot \mathbf{t}}{c_2} \right) x_I, \quad (2.70)$$

where we have written $\mathbf{x}_I = x_I \mathbf{t}$, with \mathbf{t} being a unit vector along the interface, as shown in Fig. 2.13a. But the term in parentheses in Eq. (2.70) vanishes because it is merely a statement of Snell's law for the path from \mathbf{x}_c to \mathbf{x} , so that

$$\frac{r_1}{c_1} + \frac{r_2}{c_2} \equiv \frac{r_{10}}{c_1} + \frac{r_{20}}{c_2} - \frac{\mathbf{e}_{10} \cdot \mathbf{x}_I}{c_1}. \quad (2.71)$$

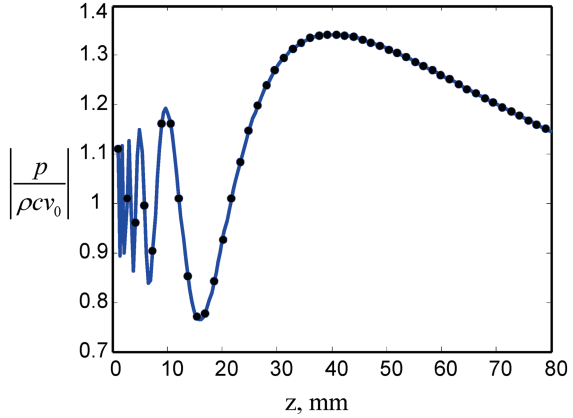
If we use this approximation in the phase term of Eq. (2.67) and replace the amplitude terms by their values along the ray from \mathbf{x}_c to \mathbf{x} , we find

$$p(\mathbf{x}) = \rho_1 c_1 v_0(\omega) \sqrt{\frac{k_1}{2\pi i}} \frac{T_{p0} \exp(ik_1 r_{10} + ik_2 r_{20})}{\sqrt{r_{10} + \frac{c_2 \cos^2 \theta_{10}}{c_1 \cos^2 \theta_{20}} r_{20}}} \int_{-b}^{+b} \exp(-ik_1 \sin \theta x') dx', \quad (2.72)$$

where T_{p0} is the plane wave transmission coefficient along this ray and we have written $\mathbf{e}_{10} \cdot \mathbf{x}_I = x' \sin \theta$ with θ being the angle that the unit vector \mathbf{e}_{10} makes with respect to the normal to the element, as shown in Fig. 2.13b. The remaining integral, however, is just the length of the element multiplied by the element far field directivity (see Eq. (2.39)) so that we find, finally

$$\begin{aligned} p(\mathbf{x}) &= \rho_1 c_1 v_0(\omega) \sqrt{\frac{k_1}{2\pi i}} \frac{T_{p0} \exp(ik_1 r_{10} + ik_2 r_{20})}{\sqrt{r_{10} + \frac{c_2 \cos^2 \theta_{10}}{c_1 \cos^2 \theta_{20}} r_{20}}} 2b \frac{\sin(k_1 b \sin \theta)}{k_1 b \sin \theta} \\ &= \rho_1 c_1 v_0(\omega) \sqrt{\frac{k_1}{2\pi i}} \frac{T_{p0} \exp(ik_1 r_{10} + ik_2 r_{20})}{\sqrt{r_{10} + \frac{c_2 \cos^2 \theta_{10}}{c_1 \cos^2 \theta_{20}} r_{20}}} 2b D_b(\theta), \end{aligned} \quad (2.73)$$

Fig. 2.15 Comparison of the magnitude of the on-axis normalized pressure, $p/\rho c v_0$, versus z where the multiple line source model for radiation through an interface (solid line) and the Hankel function model for a single medium (circles) were used to model the waves from an element: $2b=6$ mm, $f=5$ MHz, $D_{t0}=1$ mm, $\theta_i=0^\circ$, $\rho_1=\rho_2=1.0$ gm/cm³, $c_1=c_2=1500$ m/s



so that they are never larger than one wavelength. Otherwise, the value of N_{opt} given is used as the number of segments. This function uses the auxiliary function `pts_2Dintf` (Code Listing C.4) to calculate the distance, x_i , at which a ray (satisfying Snell's law) intersects the interface when traveling from the centroid of an element segment (see Fig. 2.14) to the point (x, z) in the second medium. The calling sequence for this auxiliary function is

```
>> xi=pts_2Dintf(b, e, xn, angf, Dt0, c1,c2, x, z);
```

where x_n is the distance, x_{cn} , from the center of the element to the center of the n th element segment (Fig. 2.14) and $(c1,c2)$ are the wave speeds contained in `mat`. The function `pts_2Dint` evaluates the distance, x_i , by solving for the zero of a function $g(\mathbf{x}_i)$ with Ferrari's method which is coded in the MATLAB[®] function `ferrari2` (Code Listing C.5) used in Chap. 5 to develop the time delay laws for steering and focusing through a planar interface (see Eq. (5.18) and the following discussion in Chap. 5). The function `pts_2Dint` also uses a function `init_xi` (Code Listing C.6) to determine, based on the sizes of the vectors or matrices present in the (x, z) variables, the size of the corresponding vector or matrix needed to hold the x_i calculations. The calling sequence for this function is

```
>> [xi, V1, V2] =init_xi(x, z);
```

where `V1` and `V2` are the number of rows and columns in the initial matrix, `xi`, of zeros that will subsequently be used to hold the calculated `xi` values for each element segment.

It is assumed that (x, z) can be (vector, scalar) or (scalar, vector) pairs or equal sized vectors or arrays. Unless N_{opt} is specified, the frequency, f , must be a scalar. Figure 2.15 shows the magnitude of the on-axis normalized pressure calculated with `ls_2Dint` for a large element ($b=3$ mm) at $f=5$ MHz where both media have identical properties: $\rho_1=\rho_2=1.0$ gm/cm³ and $c_1=c_2=1500$ m/s. The center of the ele-

Fig. 2.16 Comparison of the magnitude of the cross-axis normalized pressure, $p/\rho c v_0$, versus x at $z=15$ mm where the multiple line source model for radiation through an interface (*solid line*) and the Hankel function model for a single medium (*circles*) were used to model the waves from an element: $2b=6$ mm, $f=5$ MHz, $D_{i0}=1$ mm, $\theta_i=0^\circ$, $\rho_1=\rho_2=1.0$ gm/cm³, $c_1=c_2=1500$ m/s

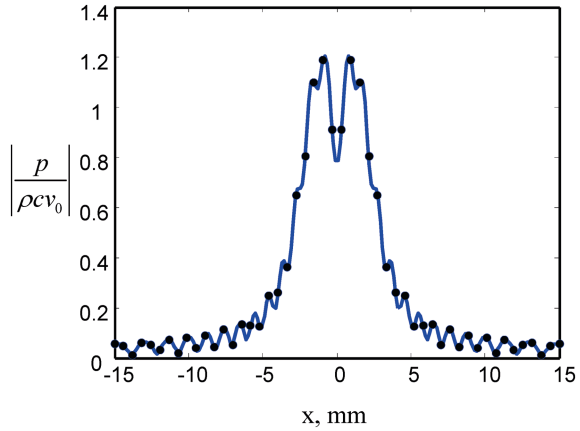
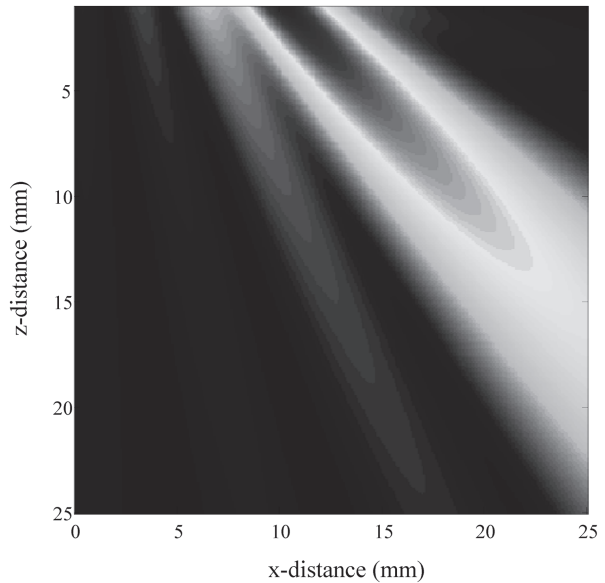


Fig. 2.17 The magnitude of the normalized pressure, $p/\rho c v_0$, in “steel” ($\rho_2=7.9$ gm/cm³, $c_2=5900$ m/s) generated by an element in water ($\rho_1=1.0$ gm/cm³, $c_1=1480$ m/s) with $2b=6$ mm, $f=5$ MHz, $\theta_i=10.217^\circ$, $D_{i0}=50.8$ mm



ment is located at a distance of $D_{i0}=1$ mm from the interface at an angle $\theta_i=0^\circ$. In Fig. 2.15 the results are compared to the Hankel function model for a single medium (see also Fig. 2.10b which considers this same case using multiple line source and Hankel function models for a single medium). Figure 2.16 shows a comparisons of cross-axis pressure values at a distance $z=15$ mm in the “second” medium for the same case. As expected, there is close agreement between both models in these test cases. Figure 2.17 shows an image of the magnitude of the normalized pressure wave field for the same large element ($b=3$ mm) located in water and radiating at oblique incidence through a plane interface at $f=5$ MHz. Although the model used

here is for an interface between two fluids, we have let the properties of the second fluid to be that of steel so that we could consider a case similar to what might be encountered at a water/steel interface. In Chap. 7 we will develop the array beam model needed for such fluid/solid cases. The angle of the element was chosen here to be $\theta_i = 10.217^\circ$ which corresponds to a refracted angle of 45° in the “steel”. The distance $D_{i0} = 50.8$ mm in this case. It can be seen in Fig. 2.17 that the main beam in the “steel” does propagate in the 45° direction but there are also some smaller refracted lobes as well.

References

1. P. Morse, H. Feshbach, *Methods of Theoretical Physics, I* (McGraw-Hill, New York, 1953), p. 823
2. M. Abramovitch, I.A. Stegun, *Handbook of Mathematical Functions*. (Dover, New York, 1965)
3. N. Bleistein, *Mathematical Methods for Wave Phenomena*. (Academic Press, New York, 1984)

Chapter 3

Large, Single Element Transducer Models

The last Chapter showed that the superposition of multiple high frequency line sources generated an effective model of the acoustic wave field of an element. While that model can be used for any size element, there are a number of alternate models available for large, single element transducers that are useful for understanding the overall behavior of an array of small elements. Thus, in this Chapter we will consider such alternative models and demonstrate the principles behind beam steering and focusing with those models. A similar approach was used by Ziomek [1, 2] to describe sound beams in underwater acoustics. As in Chap. 2, we will treat the element as a 1-D source of sound radiating waves in two dimensions.

3.1 The Paraxial Approximation and a Fresnel Integral Model

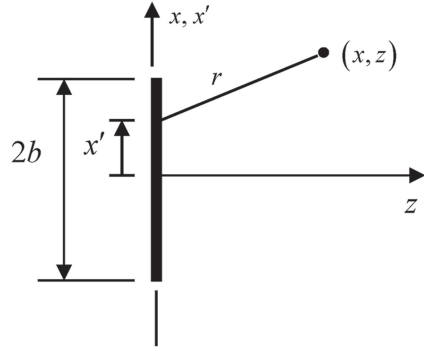
Consider a single element transducer of length $2b$ (see Fig. 3.1) where the length is very large in comparison to the wave length ($2b / \lambda \gg 1$). As seen in Chap. 2, a large transducer will generate a highly directional (well-collimated) beam of sound that travels in a direction normal to the face of the transducer. We will start from the high frequency ($kr \gg 1$) model of Eq. (2.31) which can be written as:

$$p(\mathbf{x}, \omega) = \rho c \sqrt{\frac{k}{2i\pi}} \int_{-b}^{+b} \bar{v}_z(x', \omega) \frac{\exp(ikr)}{\sqrt{r}} dx'. \quad (3.1)$$

The radius $r = \sqrt{(x - x')^2 + z^2}$ but since the sound beam is essentially traveling in the z -direction, if we are not too close to the face of the transducer the beam will primarily be in the region where $(x - x') / z \ll 1$ and r can be expanded in that small parameter. This approximation is called the paraxial approximation. In this approximation the radius is given by

$$r = z \sqrt{1 + \frac{(x - x')^2}{z^2}} \cong z \left[1 + \frac{(x - x')^2}{2z^2} \right] \quad (3.2)$$

Fig. 3.1 A large single element transducer radiating into the region $z > 0$



so Eq. (3.2) becomes

$$p(\mathbf{x}, \omega) = \rho c \sqrt{\frac{k}{2i\pi}} \frac{\exp(ikz)}{\sqrt{z}} \int_{-b}^{+b} \bar{v}_z(x', \omega) \exp\left[\frac{ik(x-x')^2}{2z}\right] dx'. \quad (3.3)$$

If we make the change of variables $u = (x-x')\sqrt{k/\pi z}$ and assume we have piston behavior then

$$p(\mathbf{x}, \omega) = -\rho c v_0(\omega) \sqrt{\frac{1}{2i}} \exp(ikz) \int_{\sqrt{\frac{k}{\pi z}}(x+b)}^{\sqrt{\frac{k}{\pi z}}(x-b)} \exp\left(\frac{i\pi u^2}{2}\right) du, \quad (3.4)$$

which can be written as the difference of two Fresnel integrals as

$$p(x, z, \omega) = \rho c v_0 \sqrt{\frac{1}{2i}} \exp(ikz) \left[F\left(\sqrt{\frac{k}{\pi z}}(x+b)\right) - F\left(\sqrt{\frac{k}{\pi z}}(x-b)\right) \right], \quad (3.5)$$

where the Fresnel integral, $F(x)$, is defined as

$$F(x) = \int_0^x \exp\left(\frac{i\pi u^2}{2}\right) du. \quad (3.6)$$

The MATLAB[®] function `fresnel_int(x)` defined in Code Listing C.8 evaluates the Fresnel integral numerically. This function is used in the beam model `fresnel_2D(b, f, c, e, x, z)`, given in Code Listing C.7, which computes the normalized pressure wave field of a large 1-D piston element transducer. The calling sequence for this function is

```
>>p=Fresnel_2D(b, f, c, x, z);
```

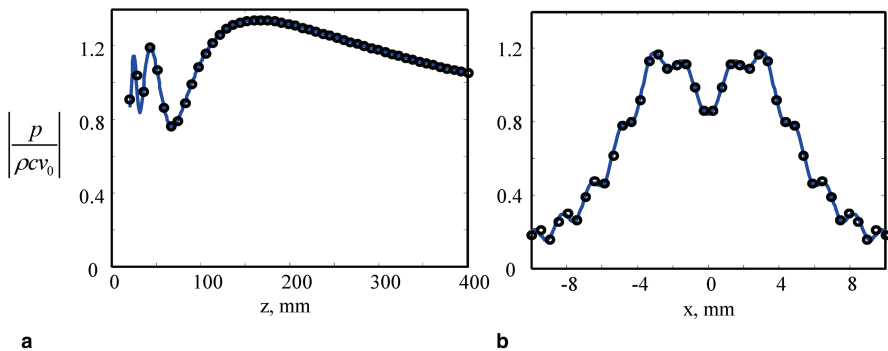



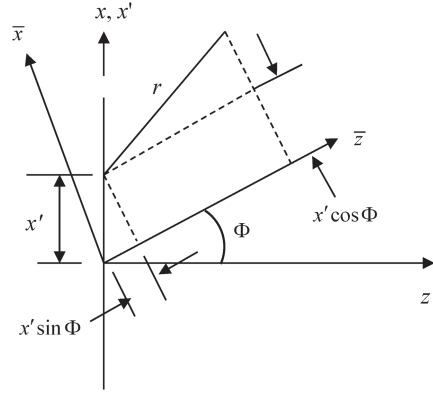
Fig. 3.2 Comparison of the multiple line source model with the Fresnel integral model for the transducer parameters; $b=6$ mm, $f=5$ MHz, $c=1500$ m/s. **a** The on-axis normalized pressure versus distance z , and **b** the cross-axis normalized pressure at $z=60$ mm versus the distance, x . *Solid line*—multiple line source model, *Circles*—Fresnel integral model

where $2b$ is the length of the element (in mm), f is the frequency (in MHz), c is the wave speed (in m/s), and (x, z) are the coordinates (in mm) in the fluid at which the normalized pressure, $p / \rho c v_0$, is calculated. Figure 3.2 shows a comparison of both on-axis and cross-axis pressure profiles for a 12 mm long element radiating at 5 MHz into water as computed with the Fresnel integral model and the multiple line source model. It can be seen that the Fresnel integral model accurately predicts the wave field in these plots. This is because the paraxial approximation is well satisfied for the highly directional beam emitted by an element that is large with respect to the wavelength. For the small elements present in arrays, this approximation can only be used in a much more limited sense. However, the Fresnel integral model gives us a direct way to use a model of a large, single element transducer to study the phasing effects used by arrays to steer and focus beams, as will be shown in the next section.

3.2 Beam Steering and Focusing of a Large Element

As discussed in Chap. 1, an array of elements can be steered and/or focused by applying an appropriate set of delays, called a *delay law*, to the elements. A delay in a time domain response, however, corresponds to multiplying the frequency domain response (frequency spectrum of the time domain signal) by a phase term that is linear in frequency and proportional to that delay. This is just the consequence of the properties of the Fourier transform since if a time domain function, $f(t)$, has a frequency spectrum (Fourier transform), $F(\omega)$, then a delayed signal, $f(t - \Delta t_d)$, where Δt_d is the delay, has a spectrum $\exp(i\omega\Delta t_d) F(\omega)$ [Schmerr]. In an array lying on the x -axis, this delay can be expressed as a function of the discrete centroid coordinate, x_n , of each element. To study the effects of different delay laws, in this

Fig. 3.3 Rotated coordinates for defining the wave field of a linearly phased element



section we will consider a large, single element transducer on the x -axis where we imagine applying a continuous time delay, $\Delta t_d(x')$, on the face, $-b \leq x' \leq b$, of that element. In practice, it is not possible to actually apply such continuous delays to a single element but this idealized case mimics the effects of the discrete delays that are applied to arrays and provides a means to study their effects on the generated sound beam.

3.2.1 Beam Steering

We will again start with the high frequency expression for the sound field of an element derived in the last Chapter, Eq. (2.31), which is in the form:

$$p(\mathbf{x}, \omega) = \frac{k\rho c \exp(-i\pi/4)}{2} \int_{-b}^{+b} \bar{v}_z(x', 0, \omega) \sqrt{\frac{2}{\pi k r}} \exp(ikr) dx' \quad (3.7)$$

and write the radius, r , in terms of a rotated set of coordinates, (\bar{x}, \bar{z}) , (see Fig. 3.3) i.e.

$$r = \sqrt{(\bar{z} - x' \sin \Phi)^2 + (\bar{x} - x' \cos \Phi)^2}, \quad (3.8)$$

which can be expanded in the exact form

$$r = \sqrt{\bar{z}^2 - 2x'\bar{z}\sin\Phi - 2x'\bar{x}\cos\Phi + \bar{x}^2 + (x')^2}. \quad (3.9)$$

We are using rotated coordinates since in this section we will examine delay laws that steer the beam produced by a large element to directions away from the z -axis. In this case the beam will be best described in a rotated set of coordinates. If the steered beam is well-collimated in the \bar{z} -direction, then it makes sense to apply the paraxial approximation to the radius r in that direction. In our expansion of the

radius in Eq. (3.2), we used the expansion $r = z\sqrt{1+\varepsilon} \cong z(1+\varepsilon/2)$. If we write Eq. (3.9) in a similar form as $r = \bar{z}\sqrt{1+\varepsilon}$, where

$$\varepsilon = \frac{(x')^2 + \bar{x}^2 - 2x'\bar{z}\sin\Phi - 2x'\bar{x}\cos\Phi}{\bar{z}^2}, \quad (3.10)$$

the appearance of \bar{z} in the numerator of the ε term means that if we expand r for $x'/\bar{z} \ll 1$ and wish to keep all quantities to $O(x'/\bar{z})^2$ we must also include the next term in the expansion, namely

$$r = \bar{z}\sqrt{1+\varepsilon} \cong \bar{z}\left(1 + \frac{\varepsilon}{2} - \frac{\varepsilon^2}{8} + \dots\right). \quad (3.11)$$

Using this expansion we obtain

$$r \cong \bar{z}\left[1 + \frac{(x')^2 \cos^2\Phi}{2\bar{z}^2} + \frac{\bar{x}^2}{2\bar{z}^2} - \frac{\bar{x}x'\cos\Phi}{\bar{z}^2} - \frac{x'\sin\Phi}{\bar{z}}\right] \quad (3.12)$$

which, when placed into Eq. (3.7) gives

$$p(\mathbf{x}, \omega) = \rho c \sqrt{\frac{k}{2\pi i \bar{z}}} \exp(ik\bar{z}) \cdot \int_{-b}^{+b} \bar{v}_z(x', 0, \omega) \exp\left\{ik\left[\frac{(x'\cos\Phi - \bar{x})^2}{2\bar{z}} - x'\sin\Phi\right]\right\} dx'. \quad (3.13)$$

Now, suppose the velocity on the face of the element has a constant amplitude, $v_0(\omega)$, (piston behavior) but also with a phase term, i.e.

$$\bar{v}_z = v_0(\omega) \exp(ikx'\sin\Phi), \quad (3.14)$$

which corresponds to specifying a continuous, linearly varying time delay, $\Delta t_d(x') = x'\sin\Phi/c$, over the face of the transducer element. Then we see that this phase term just cancels the one appearing in Eq. (3.13) and if we write that equation in terms of the variable $w = x'\cos\Phi$, it becomes

$$p(\mathbf{x}, \omega) = \frac{\rho c v_0}{\cos\Phi} \sqrt{\frac{k}{2\pi i \bar{z}}} \exp(ik\bar{z}) \int_{-b\cos\Phi}^{+b\cos\Phi} \exp\left\{ik\left(\frac{(w-\bar{x})^2}{2\bar{z}}\right)\right\} dw. \quad (3.15)$$

The integral of Eq. (3.15) is of the same form as Eq. (3.3) so that we can follow the same steps used with that equation to write the pressure in terms of Fresnel integrals. The result, in the (\bar{x}, \bar{z}) coordinates, is explicitly:

$$p(\bar{x}, \bar{z}, \omega) = \frac{\rho c v_0}{\cos \Phi} \sqrt{\frac{1}{2i}} \exp(ik\bar{z}) \cdot \left[F\left(\sqrt{\frac{k}{\pi\bar{z}}}(\bar{x} + b \cos \Phi)\right) - F\left(\sqrt{\frac{k}{\pi\bar{z}}}(\bar{x} - b \cos \Phi)\right) \right] \quad (3.16)$$

If we compare Eq. (3.16) with Eq. (3.5) for the radiated field of a piston transducer, we see that the linear time delay law $\Delta t_d(x') = x' \sin \Phi / c$ produces a wave field of a “virtual” rotated transducer (Fig. 3.4) of length $2b \cos \Phi$ having a driving velocity of $v_0 / \cos \Phi$ on its face.

Thus, a spatially varying time delay on the face of the element that is linear (in x') of the form

$$\Delta t_d(x') = x' \sin \Phi / c \quad (3.17)$$

steers the entire beam of the transducer along an axis that makes an angle, Φ , with respect to the z -axis. We should note that the “delay” law of Eq. (3.17) actually involves both delays (for x' positive) and advances (for x' negative). It is not physically possible to generate time advances in a phased array but by simply adding a positive, constant term to Eq. (3.17) one can generate a steering law consisting of delays only.

3.2.2 Steering in the Far Field

In Chap. 2 we obtained explicit results for the wave field in the far field of the element. We found the far field pressure was given by Eq. (2.35):

$$p(\mathbf{x}, \omega) = \sqrt{\frac{k}{2\pi i}} \rho c V(k_x) \frac{\exp(ikr_0)}{\sqrt{r_0}}, \quad (3.18)$$

where

$$V(k_x) = \int_{-b}^{+b} \bar{v}_z(x', \omega) \exp(-ik_x x') dx' \quad (3.19)$$

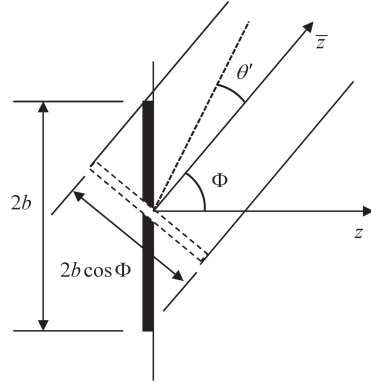
and $k_x = k \sin \theta$. If we apply the velocity of Eq. (3.14) to the face of the element, then the integral yields instead

$$V(k_x) = 2v_0(\omega) \frac{\sin[(k_x - k \sin \Phi)b]}{(k_x - k \sin \Phi)}, \quad (3.20)$$

which shows that the far field pressure is

$$p(\mathbf{x}, \omega) = \rho c v_0(\omega) \sqrt{\frac{2}{\pi i}} (kb) \frac{\sin[(k_x - k \sin \Phi)b]}{(k_x - k \sin \Phi)b} \frac{\exp(ikr_0)}{\sqrt{kr_0}} \quad (3.21)$$

Fig. 3.4 The rotated “virtual” transducer that generates the same wave field as a linearly phased element in the paraxial approximation



and the directivity of the element is now

$$D_b(\theta) = \frac{\sin[kb(\sin \theta - \sin \Phi)]}{kb(\sin \theta - \sin \Phi)}. \quad (3.22)$$

Since the directivity is governed by the sinc function, $\text{sinc } x \equiv \sin x / x$, which has its maximum at $x=0$, it is clear from Eq. (3.22) that that maximum (and hence the entire directivity function) has been steered to the $\theta = \Phi$ direction by the linear phasing of the element.

We can also relate these results with those of the last section by noting that in the rotated (\bar{x}, \bar{z}) coordinates we have wave numbers $(k_{\bar{x}}, k_{\bar{z}})$ where $k_x = k_{\bar{z}} \sin \Phi + k_{\bar{x}} \cos \Phi$. But in the paraxial approximation $k_{\bar{z}} = \sqrt{k^2 - k_{\bar{x}}^2} \cong k$ so that $k_x = k \sin \Phi + k_{\bar{x}} \cos \Phi$ and we can write Eq. (3.21) in the rotated coordinates as

$$p(\mathbf{x}, \omega) = \rho c \frac{v_0(\omega)}{\cos \Phi} \sqrt{\frac{2}{\pi i}} (kb \cos \Phi) \frac{\sin[k_{\bar{x}} b \cos \Phi]}{k_{\bar{x}} b \cos \Phi} \frac{\exp(ikr_0)}{\sqrt{kr_0}}, \quad (3.23)$$

where $k_{\bar{x}} = k \sin \theta'$ and θ' is measured from the \bar{z} -axis (Fig. 3.4). Comparing Equation (3.23) with the far field expression of Eq. (2.38) for an element without steering shows that in the paraxial approximation the far field response of the linear phased element in the rotated coordinates is identical to the far field from a virtual transducer of length $2b \cos \Phi$ which has a velocity $v_0 / \cos \Phi$ acting on its face, which is consistent with our results in the previous section.

3.2.3 Beam Focusing

For a large single element piston transducer, one way that focusing can be achieved in two dimensions is to place a set of uniform normal velocity sources on a circular aperture of radius R_0 instead of a straight aperture, as shown in Fig. 3.5. This is the 2-D equivalent of the O'Neil model for a spherically focused transducer [3], [Schmerr]. The same focusing effect, however, can also be simulated by applying

Fig. 3.5 A focused piston transducer consisting of a set of uniform velocity sources on a circular line of radius R_0

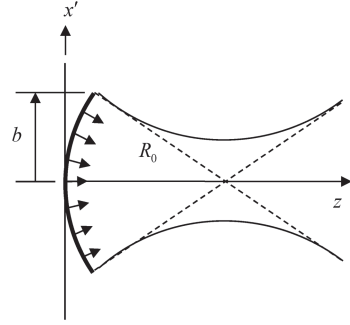
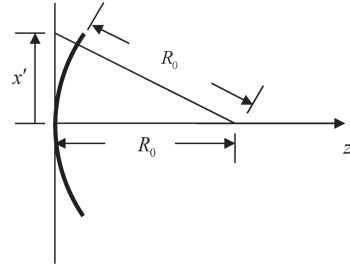


Fig. 3.6 Geometry for defining the phasing needed to focus the waves from an unfocused element to a point on the z -axis



the uniform sources over the straight aperture (located at $z=0$) and changing the time of arrival of the waves from different locations on the transducer face so that they are all in phase on the circular aperture, just as they are in the configuration of Fig. 3.5. First, consider a wave that has traveled from a point x' at $z=0$ to the location of the geometrical focus on the z -axis (see Fig. 3.6). Then consider the same wave traveling on the same path from the circular aperture to the focus. The time difference between these two cases is simply

$$\Delta t(x') = \frac{\sqrt{R_0^2 + (x')^2} - R_0}{c}. \quad (3.24)$$

In the paraxial approximation ($x' / R_0 \ll 1$) this time difference is approximately

$$\begin{aligned} \Delta t(x') &= \frac{R_0 \left[\sqrt{1 + (x' / R_0)^2} - 1 \right]}{c} \\ &\cong \frac{R_0 \left[1 + (x' / R_0)^2 / 2 + \dots - 1 \right]}{c} \\ &= \frac{(x')^2}{2R_0 c}, \end{aligned} \quad (3.25)$$

corresponding to a propagation phase delay term given by

$$\exp[i\omega\Delta t] = \exp\left[ik\frac{(x')^2}{2R_0}\right]. \quad (3.26)$$

Thus, if on the planar aperture we specify a velocity field given by

$$v_z(x', 0, \omega) = \begin{cases} v_0(\omega) \exp\left[-ik\frac{(x')^2}{2R_0}\right] & -b \leq x' \leq b \\ 0 & \text{otherwise} \end{cases}, \quad (3.27)$$

we will produce the same cylindrical focusing effect of the circular aperture. Note that the phase term in Eq. (3.27) has a negative sign since for all x' on the plane $z=0$ we need to *advance* the arrival time of the waves relative to the arrival at the focus from the point $x' = 0$ to have them arrive in phase on the circular element. Thus, our “delay” law is the negative of the time differences appearing in Eqs. (3.25) and (3.26), i.e.

$$\Delta t_d(x') = -\frac{(x')^2}{2R_0 c}. \quad (3.28)$$

Again, in this form we do not have a physically possible delay law but by simply adding a constant delay term to Eq. (3.28) we can turn these advances into a law with delays only.

Now, consider the wave field of a large element where the velocity on the element face is given by Eq. (3.27). Then from Eq. (3.7) the pressure is given by

$$p(\mathbf{x}, \omega) = \rho c v_0(\omega) \sqrt{\frac{k}{2\pi i}} \int_{-b}^{+b} \exp\left[-ik\frac{(x')^2}{2R_0}\right] \frac{\exp(ikr)}{\sqrt{r}} dx'. \quad (3.29)$$

In the paraxial approximation (see Eq. (3.2)) then we have

$$p(\mathbf{x}, \omega) = \rho c v_0(\omega) \sqrt{\frac{k}{2\pi i}} \frac{\exp(ikz)}{\sqrt{z}} \exp\left(ik\frac{x^2}{2z}\right) \int_{-b}^{+b} \exp\left\{\frac{ik}{2z}\left[u_0(x')^2 - 2xx'\right]\right\} dx', \quad (3.30)$$

where

$$u_0 = (1 - z/R_0). \quad (3.31)$$

But we can “complete the square” in the phase term appearing in the integrand of Eq. (3.30) and rewrite that equation as

$$p(\mathbf{x}, \omega) = \rho c v_0(\omega) \sqrt{\frac{k}{2\pi i}} \frac{\exp(ikz)}{\sqrt{z}} \exp\left(-ik\frac{x^2}{2u_0 R_0}\right) \int_{-b}^{+b} \exp\left\{\frac{iku_0}{2z}\left(x' - \frac{x}{u_0}\right)^2\right\} dx'. \quad (3.32)$$

Now, consider first the case when u_0 is positive ($z < R_0$). If we let $u = (x' - x / u_0) \sqrt{ku_0} / \pi z$ then Eq. (3.32) can be put in the form

$$p(\mathbf{x}, \omega) = \rho c v_0(\omega) \sqrt{\frac{1}{2i} \frac{\exp(ikz)}{\sqrt{u_0}}} \exp\left(-ik \frac{x^2}{2u_0 R_0}\right) \int_{u = -\sqrt{\frac{ku_0}{\pi z}}(b+x/u_0)}^{u = \sqrt{\frac{ku_0}{\pi z}}(b-x/u_0)} \exp\left(\frac{i\pi u^2}{2}\right) du, \quad (3.33)$$

which can again be expressed as two Fresnel integrals:

$$p(\mathbf{x}, \omega) = \frac{\rho c v_0(\omega) \exp(ikz)}{\sqrt{|u_0|}} \sqrt{\frac{1}{2i}} \cdot \exp\left(-ik \frac{x^2}{2|u_0| R_0}\right) \left\{ F\left[\sqrt{\frac{k|u_0|}{\pi z}} \left(\frac{x}{|u_0|} + b\right)\right] - F\left[\sqrt{\frac{k|u_0|}{\pi z}} \left(\frac{x}{|u_0|} - b\right)\right] \right\} \quad (3.34)$$

and we have let $u_0 = |u_0|$ to emphasize that it is positive.

If u_0 is negative ($z > R_0$) then we can write $u_0 = -|u_0|$ in Eq. (3.32) and follow the same steps that led to Eq. (3.34). In this case we find

$$p(\mathbf{x}, \omega) = \frac{\rho c v_0(\omega) \exp(ikz)}{\sqrt{|u_0|}} \sqrt{\frac{1}{2i}} \exp\left(-ik \frac{x^2}{2|u_0| R_0}\right)^* \cdot \left\{ F\left[\sqrt{\frac{k|u_0|}{\pi z}} \left(\frac{x}{|u_0|} + b\right)\right] - F\left[\sqrt{\frac{k|u_0|}{\pi z}} \left(\frac{x}{|u_0|} - b\right)\right] \right\}^*. \quad (3.35)$$

The $(\cdot)^*$ here indicates the complex conjugate.

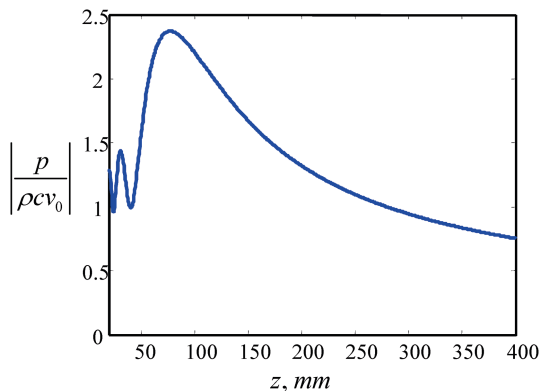
Now, consider the on-axis response of the element in the paraxial approximation. This response can be obtained from Eqs. (3.34) and (3.35) by setting $x=0$ to obtain

$$p(z, \omega) = \frac{\rho c v_0(\omega) \exp(ikz)}{\sqrt{|u_0|}} \sqrt{\frac{2}{i}} \begin{cases} F\left[\sqrt{\frac{k|u_0|}{\pi z}} b\right] & z < R_0 \\ F^*\left[\sqrt{\frac{k|u_0|}{\pi z}} b\right] & z > R_0 \end{cases}. \quad (3.36)$$

Equation (3.36) is very similar in form to the unfocused on-axis response. To obtain the comparable on-axis fields in the unfocused case we can set $x=0$ in Eq. (3.5) to obtain

$$p(z, \omega) = \rho c v_0(\omega) \exp(ikz) \sqrt{\frac{2}{i}} F\left[\sqrt{\frac{kb^2}{\pi z}}\right]. \quad (3.37)$$

Fig. 3.7 The magnitude of the on-axis normalized pressure of a 12 mm long, 100 mm focal length element radiating at 5 MHz into water



If we set $R_0 = \infty$ in Eq. (3.36) then $u_0 = 1$ and Eq. (3.36) just reduces to the unfocused case of Eq. (3.37).

The presence of the $\sqrt{|u_0|}$ term in both the Fresnel integral and its coefficient for the focused case causes the pressure to increase near the geometrical focus at $z = R_0$. Although the $\sqrt{|u_0|}$ term in the denominator appears to make the pressure singular at the geometric focus, the presence of the same term in the Fresnel integral cancels this behavior and the pressure is well behaved and finite at the geometric focus ($z = R_0$), where

$$p(R_0, \omega) = \rho c v_0 \sqrt{kb \frac{2}{i\pi} \frac{b}{R_0}} \exp(ikR_0). \quad (3.38)$$

The MATLAB® function `on_axis_foc2D` given in Code Listing C.9 uses Eq. (3.36) to compute the normalized pressure, $p / \rho c v_0$, and uses the explicit value given by Eq. (3.38) near the geometric focus. The calling sequence for this function is

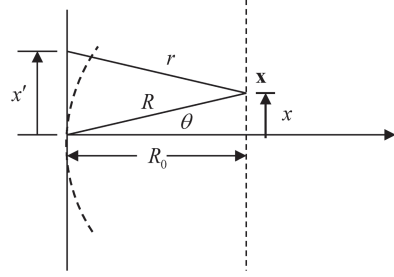
$$\gg p = \text{on_axis_foc2D}(b, R, f, c, z);$$

where $2b$ is the length of the element (in mm), R is the focal length (in mm), f is the frequency (in MHz), c is the wave speed (in m/s), and z is the on-axis distance (in mm). Figure 3.7 plots the magnitude of the on-axis response for a 5 MHz, 12 mm long transducer radiating into water as considered in Fig. 3.2 but where now the transducer is cylindrically focused with a focal length of 100 mm. It can be seen from that figure that the amplitude is indeed larger in a region about the geometrical focus.

It is possible to examine the cross-axis behavior of the pressure field explicitly at the geometric focus $z = R_0$. In that case, we start from Eq. (3.7) and express the radius r as (see Fig. 3.8)

$$r = \sqrt{R^2 + (x')^2 - 2R \sin \theta x'}. \quad (3.39)$$

Fig. 3.8 Geometrical parameters for examining the pressure field along a cross-sectional axis at the geometrical focus



We will expand Eq. (3.39), assuming $x' / R \ll 1$ (paraxial approximation) and also assume the angle θ will be small in anticipation that the field near the focus will be confined to a relatively small region about the z -axis. In this case, we can also let $R \cong z = R_0$ and write

$$r \cong R_0 + \frac{(x')^2}{2R_0} - x' \sin \theta \quad (3.40)$$

and place this approximation into Eq. (3.7) to obtain

$$p(\mathbf{x}, \omega) = \rho c \sqrt{\frac{k}{2\pi i}} \frac{\exp(ikR_0)}{\sqrt{R_0}} \int_{-b}^{+b} v_z(x', 0, \omega) \exp \left[ik \frac{(x')^2}{2R_0} \right] \exp(ikx' \sin \theta) dx'. \quad (3.41)$$

However, if the velocity field is given by Eq. (3.27) then Eq. (3.41) reduces to

$$\begin{aligned} p(\mathbf{x}, \omega) &= \rho c v_0 \sqrt{\frac{k}{2\pi i}} \frac{\exp(ikR_0)}{\sqrt{R_0}} \int_{-b}^{+b} \exp(ikx' \sin \theta) dx' \\ &= \rho c v_0 \sqrt{\frac{2}{\pi i}} (kb) \frac{\sin(kb \sin \theta)}{kb \sin \theta} \frac{\exp(ikR_0)}{\sqrt{kR_0}}, \end{aligned} \quad (3.42)$$

which is identical in form to the far-field behavior of the planar piston probe (see Eq. (2.38)). We can use Eq. (3.42) and the results from Chap. 2 for the far field of a planar transducer to estimate the width of the focused beam at the geometrical focus since the magnitude of the pressure drops to one half its on-axis value at $kb \sin \theta_{-6dB} = 1.8955$ and, since $\sin \theta_{-6dB} = x_{-6dB} / R$ (see Fig. 3.8) and $R \cong R_0$, we have approximately

$$x_{-6dB} = 0.6 \frac{\lambda R_0}{2b}. \quad (3.43)$$

It is certainly not obvious how these explicit results on the plane of the geometrical focus are compatible with the Fresnel integral expressions (Eqs. (3.34) and (3.35)), which are valid for both $z < R_0$ and $z > R_0$, respectively. Since on the plane of the geometrical focus $u_0 \rightarrow 0$, we need to examine that limit for the terms

$$G = \frac{1}{\sqrt{|u_0|}} \exp\left(-ik \frac{x^2}{2|u_0|R_0}\right) \left\{ F\left[\sqrt{\frac{k|u_0|}{\pi z}} \left(\frac{x}{|u_0|} + b\right)\right] - F\left[\sqrt{\frac{k|u_0|}{\pi z}} \left(\frac{x}{|u_0|} - b\right)\right] \right\}, \quad (3.44)$$

which appear in both of those expressions. When the argument of the Fresnel integral is large, that integral behaves asymptotically as [4]

$$F(x) \sim \frac{1+i}{2} - \frac{i}{\pi x} \exp\left(\frac{i\pi x^2}{2}\right) \quad (3.45)$$

so that the leading constant terms in Eq. (3.45) cancel in Eq. (3.44) and near $z = R_0$ we have

$$G \sim -i \sqrt{\frac{1}{\pi k R_0}} \frac{R_0}{x} \exp\left(-ik \frac{x^2}{2|u_0|R_0}\right) \cdot \left\{ \exp\left[\frac{i\pi k|u_0|}{2\pi R_0} \left(\frac{x^2}{|u_0|^2} + 2b \frac{x}{|u_0|} + b^2\right)\right] - \exp\left[\frac{i\pi k|u_0|}{2\pi R_0} \left(\frac{x^2}{|u_0|^2} - 2b \frac{x}{|u_0|} + b^2\right)\right] \right\}. \quad (3.46)$$

But the terms involving $|u_0|b^2$ vanish on the geometric focal plane and $x/R_0 = \sin \theta$ (see Fig. 3.8) so we can reduce and rewrite Eq. (3.46) as

$$\begin{aligned} G &= -i \sqrt{\frac{1}{\pi k R_0}} \frac{1}{\sin \theta} \left\{ \exp[ikb \sin \theta] - \exp[-ikb \sin \theta] \right\} \\ &= 2 \sqrt{\frac{1}{\pi k R_0}} \frac{1}{\sin \theta} \sin(kb \sin \theta), \end{aligned} \quad (3.47)$$

which is real so from either Eq. (3.34) or (3.35) we find the same result, namely

$$p(\mathbf{x}, \omega) = \rho c v_0(\omega) \sqrt{\frac{2}{i\pi}} \frac{\sin(kb \sin \theta)}{\sin \theta} \sqrt{\frac{1}{kR_0}} \exp(ikR_0), \quad (3.48)$$

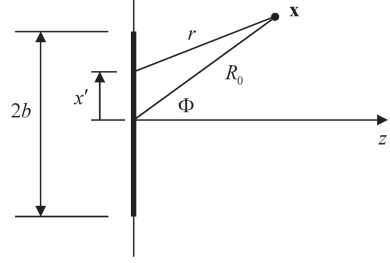
which is identical to the focal plane expression previously obtained in Eq. (3.42).

3.2.4 Beam Steering and Focusing

From the results of the previous sections it might appear that to both steer and focus a large single element transducer then one needs only add the time delays for steering and focusing to obtain a delay law

$$\Delta t_d = \frac{x' \sin \Phi}{c} - \frac{(x')^2}{2R_0 c} \quad (3.49)$$

Fig. 3.9 Geometry for steering and focusing a single element transducer to a point \mathbf{x} in a fluid



but this result is incorrect! To see why, consider the single element transducer in Fig. 3.9 where we want to focus the waves at a distance R_0 and at an angle Φ as shown. The propagation time delay for a wave going from a point on the transducer face to the point \mathbf{x} in the fluid is just

$$\Delta t = \frac{r - R_0}{c} = \frac{\sqrt{R_0^2 + (x')^2 - 2x'R_0 \sin \Phi} - R_0}{c}, \quad (3.50)$$

where we have included a constant term to make the total propagation time delay equal to zero at $x' = 0$. In the paraxial approximation $x' / R_0 \ll 1$ so if we expand the square root in Eq. (3.50) using three terms in the expansion (see Eq. (3.11)) again, we obtain

$$\Delta t = \frac{-\sin \Phi}{c} x' + \frac{(x')^2 \cos^2 \Phi}{2R_0 c}. \quad (3.51)$$

To steer the transducer beam to an angle Φ and focus at a distance R_0 , we must cancel these propagation delays by applying the negative of these values at the transducer face, giving the time delay law

$$\Delta t_d = \frac{\sin \Phi}{c} x' - \frac{(x')^2 \cos^2 \Phi}{2R_0 c}. \quad (3.52)$$

This result can be interpreted as follows. The first term in Eq. (3.52) steers the beam of the transducer in the Φ direction and produces the field of the virtual transducer shown in Fig. 3.4. To focus this virtual transducer at a distance R_0 , we must then apply a quadratic time delay across the face of this virtual transducer, i.e. along the \bar{x} axis of Fig. 3.4, not along the original transducer face (the x' axis), as Eq. (3.49) assumes. This simply corresponds to replacing x' distance in Eq. (3.49) by $\bar{x} = x' \cos \Phi$, to obtain the correct focusing term of Eq. (3.52).

If we use the time delays of Eq. (3.52) in the velocity field on the face of the transducer, i.e. if we set

$$v_z(x', 0, \omega) = \begin{cases} v_0(\omega) \exp \left[ikx' \sin \Phi - ik \frac{(x')^2 \cos^2 \Phi}{2R_0} \right] & -b < x' < b \\ 0 & \text{otherwise} \end{cases} \quad (3.53)$$

and place this velocity in Eq. (3.7) and expand the radius r in rotated coordinates (\bar{x}, \bar{z}) as done previously in Eq. (3.12), then we find

$$p(\mathbf{x}, \omega) = \rho c v_0(\omega) \sqrt{\frac{k}{2\pi i}} \frac{\exp(ik\bar{z})}{\sqrt{\bar{z}}} \exp\left(ik \frac{\bar{x}^2}{2\bar{z}}\right) \int_{-b}^{+b} \exp\left\{\frac{ik}{2\bar{z}} [\bar{u}_0(x')^2 \cos^2 \Phi - 2\bar{x}x' \cos \Phi]\right\} dx', \quad (3.54)$$

where

$$\bar{u}_0 = 1 - \bar{z} / R_0. \quad (3.55)$$

But letting $w = x' \cos \Phi$ gives

$$p(\mathbf{x}, \omega) = \frac{\rho c v_0(\omega)}{\cos \Phi} \sqrt{\frac{k}{2\pi i}} \frac{\exp(ik\bar{z})}{\sqrt{\bar{z}}} \exp\left(ik \frac{\bar{x}^2}{2\bar{z}}\right) \int_{-b \cos \Phi}^{+b \cos \Phi} \exp\left\{\frac{ik}{2\bar{z}} [\bar{u}_0 w^2 - 2\bar{x}w]\right\} dw. \quad (3.56)$$

Equation (3.56) is in the same form as Eq. (3.30) for the focused case. Taking the same steps as in that case we find for both steering and focusing

$$p(\mathbf{x}, \omega) = \frac{\rho c v_0(\omega)}{\cos \Phi} \frac{\exp(ik\bar{z})}{\sqrt{|\bar{u}_0|}} \sqrt{\frac{1}{2i}} \cdot \exp\left(-ik \frac{\bar{x}^2}{2|\bar{u}_0|R_0}\right) \left\{ F\left[\sqrt{\frac{k|\bar{u}_0|}{\pi\bar{z}}} \left(\frac{\bar{x}}{|\bar{u}_0|} + b \cos \Phi\right)\right] - F\left[\sqrt{\frac{k|\bar{u}_0|}{\pi\bar{z}}} \left(\frac{\bar{x}}{|\bar{u}_0|} - b \cos \Phi\right)\right] \right\} \quad (3.57)$$

for $\bar{u}_0 \geq 0$ ($\bar{z} \leq R_0$), and

$$p(\mathbf{x}, \omega) = \frac{\rho c v_0(\omega)}{\cos \Phi} \frac{\exp(ik\bar{z})}{\sqrt{|\bar{u}_0|}} \sqrt{\frac{1}{2i}} \cdot \exp\left(-ik \frac{\bar{x}^2}{2|\bar{u}_0|R_0}\right) \left\{ F^*\left[\sqrt{\frac{k|\bar{u}_0|}{\pi\bar{z}}} \left(\frac{\bar{x}}{|\bar{u}_0|} + b \cos \Phi\right)\right] - F^*\left[\sqrt{\frac{k|\bar{u}_0|}{\pi\bar{z}}} \left(\frac{\bar{x}}{|\bar{u}_0|} - b \cos \Phi\right)\right] \right\}^* \quad (3.58)$$

for $\bar{u}_0 < 0$ ($\bar{z} > R_0$).

These results again are in the form of a virtual rotated transducer as discussed previously. If we set $\bar{x} = 0$, we obtain the pressure along the central (\bar{z}) axis of the steered and focused transducer, which has the much simpler form

$$p(\bar{z}, \omega) = \frac{\rho c v_0 \exp(ik\bar{z})}{\cos \Phi \sqrt{|\bar{u}_0|}} \sqrt{\frac{2}{i}} \begin{cases} F\left[\sqrt{\frac{k|\bar{u}_0| b^2 \cos^2 \Phi}{\pi\bar{z}}}\right] & \bar{z} \leq R_0 \\ F^*\left[\sqrt{\frac{k|\bar{u}_0| b^2 \cos^2 \Phi}{\pi\bar{z}}}\right] & \bar{z} > R_0 \end{cases}, \quad (3.59)$$

which (compare to Eq. (3.36)) is indeed just the on-axis wave field of a virtual rotated piston element of length $2b \cos \Phi$ having a velocity $v_0 / \cos \Phi$ on its face and focused at $\bar{z} = R_0$.

3.3 Amplitude Weighting

In phased arrays, in addition to delaying the individual elements of the array to generate beam steering and focusing, one can weight each element differently by providing different gains to the elements during either sound generation, reception, or both. This weighting is called *apodization*. Here, we will examine the analogous situation where we specify continuous amplitude profiles on the face of a large, single element transducer.

For a single element transducer the far-field behavior was given by Eq. (3.18) in terms of the Fourier transform of the velocity field on the face of the transducer, $V(k_x)$, where recall

$$V(k_x) = \int_{-\infty}^{+\infty} v_z(x', 0, \omega) \exp(-ik_x x') dx' \quad (3.60)$$

and $k_x = k \sin \theta$. Now, let the velocity field be defined in a separable form by an amplitude term, $v_0(\omega)$, and a spatial distribution terms, $\tilde{C}(x')$, i.e.

$$v_z(x', 0, \omega) = v_0(\omega) \tilde{C}(x'). \quad (3.61)$$

Then

$$V(k_x) = v_0(\omega) C(k_x), \quad (3.62)$$

where $C(k_x)$ is the corresponding spatial Fourier transform of $\tilde{C}(x')$ given by

$$C(k_x) = \int_{-\infty}^{+\infty} \tilde{C}(x') \exp(-ik_x x') dx'. \quad (3.63)$$

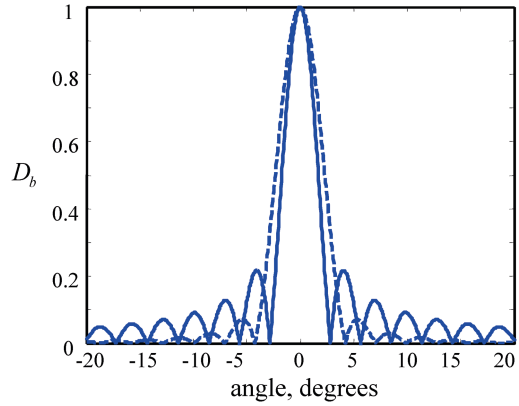
Rewriting Eq. (3.18) in terms of this transform, the far-field pressure can be expressed as

$$p(\mathbf{x}, \omega) = \rho c v_0(\omega) \sqrt{\frac{k}{2\pi i}} C(k_x) \frac{\exp(ikr_0)}{\sqrt{r_0}}. \quad (3.64)$$

Consistent with how we defined the total directivity of the array (see Eqs. (2.38) and (2.39)) the far-field pressure can also be expressed in terms of the far-field directivity, $D_b(\theta)$ of the single element transducer as

$$p(\mathbf{x}, \omega) = \rho c v_0(\omega) \sqrt{\frac{1}{2\pi i}} (2kb) D_b(\theta) \frac{\exp(ikr_0)}{\sqrt{kr_0}}. \quad (3.65)$$

Fig. 3.10 The far field directivity for a 12 mm long element radiating at 5 MHz into water. *Solid line*—piston transducer, *Dashed line*—cosine window



Comparing Eq. (3.65) with Eq. (3.64) we see that

$$D_b(\theta) = \frac{1}{2b} C(k_x). \quad (3.66)$$

For a piston transducer of radius b , $\tilde{C}(x') = \text{rect}(x', b)$, where

$$\text{rect}(x', b) = \begin{cases} 1 & -b < x' < b \\ 0 & \text{otherwise} \end{cases}, \quad (3.67)$$

the spatial Fourier transform, $C(k_x)$, then has the form (see Eq. (2.37) with $v_0 = 1$)

$$C(k_x) = 2b \frac{\sin(k_x b)}{k_x b} = 2b \frac{\sin(kb \sin \theta)}{kb \sin \theta}. \quad (3.68)$$

Figure 3.10 plots this directivity for a 12 mm long ($b = 6$ mm) piston transducer radiating into water at 5 MHz. As is typically the case for a large single element transducer or for an array, in the far field one will see a beam structure with a large main lobe as well as smaller side lobes. It is possible to reduce the amplitude of the side lobes appearing in Figure 3.10 relative to the main lobe by tailoring the spatial amplitude behavior. This is generally the purpose behind amplitude weighting in a phased array. For example, let the amplitude profile be given by

$$\tilde{C}(x') = C_0 \cos(\pi x' / L) \text{rect}(x', b), \quad (3.69)$$

where C_0 and L are two arbitrary constants. This profile is called a *cosine window*. We can write this cosine window in the alternate form

$$\tilde{C}(x') = \frac{C_0}{2} (\exp(i\pi x' / L) + \exp(-i\pi x' / L)) \text{rect}(x', b), \quad (3.70)$$

so that the Fourier transform is given directly by

$$\begin{aligned} C(k_x) &= \frac{C_0}{2} \left\{ \int_{-b}^{+b} \exp \left[i \left(-\frac{\pi}{L} - k_x \right) x' \right] dx' + \int_{-b}^{+b} \exp \left[i \left(\frac{\pi}{L} - k_x \right) x' \right] dx' \right\} \\ &= bC_0 \left\{ \frac{\sin(k_x b + \pi b / L)}{(k_x b + \pi b / L)} + \frac{\sin(k_x b - \pi b / L)}{(k_x b - \pi b / L)} \right\}. \end{aligned} \quad (3.71)$$

Normally one chooses $L=2b$ so that the amplitude is tapered to zero at $x = \pm b$. In that case, since $\sin(k_x b \pm \pi / 2) = \pm \cos(k_x b)$ we find

$$\begin{aligned} C(k_x) &= bC_0 \left[\frac{\sin(k_x b + \pi / 2)}{(k_x b + \pi / 2)} + \frac{\sin(k_x b - \pi / 2)}{(k_x b - \pi / 2)} \right] \\ &= \frac{4bC_0}{\pi} \frac{\cos(k_x b)}{[1 - (2k_x b / \pi)^2]} = \frac{2C_0 L}{\pi} \frac{\cos(k_x L / 2)}{[1 - (k_x L / \pi)^2]}. \end{aligned} \quad (3.72)$$

If we let $C_0 = \pi / 2$ from Eq. (3.66) we see that we will generate a “normalized” directivity associated with this case that will have a maximum amplitude of one at $k_x = 0$, just as in the piston case. This normalized directivity is also plotted in Fig. 3.10 so that it can be compared to the directivity of the uniform amplitude (piston) case plot in that figure. It can be seen that the cosine amplitude weighting does indeed reduce the amplitude of the side lobes, but Fig. 3.10 also shows that with this side lobe reduction comes some broadening of the main lobe. Thus, other types of weighting functions (windows) may be considered that have different effectiveness in balancing these two effects. For example, the continuous *Hanning* amplitude window function (also known as the *Hann* window, the raised cosine window or the cosine squared window) is given by

$$\begin{aligned} \tilde{C}(x') &= C_0 \cos^2(\pi x' / L) \text{rect}(x', L / 2) \\ &= \frac{C_0}{2} [1 + \cos(2\pi x' / L)] \text{rect}(x', L / 2), \end{aligned} \quad (3.73)$$

while the *Hamming* amplitude window is

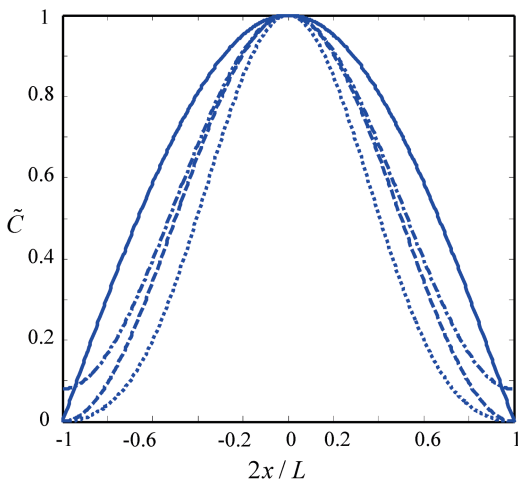
$$\tilde{C}(x') = C_0 [0.54 + 0.46 \cos(2\pi x' / L)] \text{rect}(x', L / 2) \quad (3.74)$$

and the *Blackman* amplitude window is

$$\tilde{C}(x') = C_0 [0.42 + 0.5 \cos(2\pi x' / L) + 0.08 \cos(4\pi x' / L)] \text{rect}(x', L / 2). \quad (3.75)$$

Figure 3.11 shows each of these window functions. We have written these three windows in terms of a length, L . For the single element transducer case one generally sets $L = 2b$. With this choice all of these windows (except the Hamming window) tapers to zero at the ends of the element, as can be seen in Fig. 3.11. However, as

Fig. 3.11 Plots of the cosine window (solid line), Hanning (cosine-squared) window (dashed line), Hamming window (dashed-dotted line), and the Blackman window (dotted line). In all cases the constant $C_0 = 1$



shown in the next Chapter, for an array which uses discrete versions of these amplitude weights, the tapering to zero is normally done at the centroids of the first and last elements, which leads to a different choice for L . The spatial Fourier transforms of all these windows can be obtained in the same fashion as done for the cosine window (by writing the cosine terms in the form of a sum of complex exponentials which allows us to perform the Fourier transforms directly). We find:

Hanning window:

$$C(k_x) = C_0 \frac{L \sin(k_x L / 2)}{2 (k_x L / 2)} \left[\frac{1}{1 - (k_x L / 2\pi)^2} \right], \quad (3.76)$$

Hamming window:

$$C(k_x) = C_0 \frac{L \sin(k_x L / 2)}{2 (k_x L / 2)} \left[\frac{1.08 - 0.16(k_x L / 2\pi)^2}{1 - (k_x L / 2\pi)^2} \right], \quad (3.77)$$

Blackman window:

$$C(k_x) = C_0 \frac{L \sin(k_x L / 2)}{2 (k_x L / 2)} \left[0.84 + \frac{(k_x L / 2\pi)^2}{1 - (k_x L / 2\pi)^2} - \frac{0.16(k_x L / 4\pi)^2}{1 - (k_x L / 4\pi)^2} \right]. \quad (3.78)$$

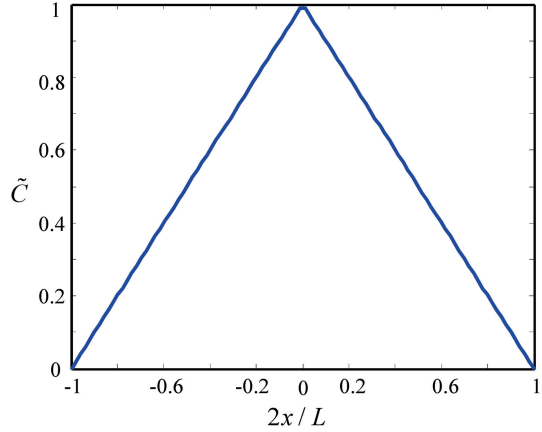
Another commonly discussed window is the triangular window (Fig. 3.12) where

$$\tilde{C}(x) = C_0 (1 - 2|x'|/L) \text{rect}(x', L/2). \quad (3.79)$$

To obtain the spatial Fourier transform of this window, it is convenient to use a property of the Fourier transform involving differentiation, namely

$$C(k_x) = \int_{-\infty}^{+\infty} \tilde{C}(x') \exp(-ik_x x') dx' = \frac{1}{(ik_x)^n} \int_{-\infty}^{+\infty} \frac{d^n \tilde{C}(x')}{dx'^n} \exp(-ik_x x') dx'. \quad (3.80)$$

Fig. 3.12 A triangular window function



This is useful for the triangular window since two derivatives of that window gives a form in terms of delta functions only:

$$\frac{d^2 \tilde{C}(x')}{dx'^2} = \frac{2C_0}{L} \delta(x' + L/2) - 2\delta(x') + \delta(x' - L/2) \quad (3.81)$$

whose spatial Fourier transform can be obtained directly to give

$$C(k_x) = \frac{-2C_0}{k_x^2 L} [\exp(ik_x L/2) - 2 + \exp(-ik_x L/2)]. \quad (3.82)$$

But the term in brackets in Eq. (3.82) can be rewritten in terms of the square of difference of two terms, i.e.

$$C(k_x) = \frac{-2C_0}{k_x^2 L} [\exp(ik_x L/4) - \exp(-ik_x L/4)]^2, \quad (3.83)$$

which then can be put in the even simpler form:

$$C(k_x) = \frac{C_0 L}{2} \left[\frac{\sin(k_x L/4)}{k_x L/4} \right]^2. \quad (3.84)$$

To compare the performance of these various windows we have plotted in Fig. 3.13 their normalized directivities, D_N , obtained by choosing the constant C_0 so that the magnitude of the directivities were all equal to one at $\theta = 0$. Figure 3.13a compares the rectangular (piston) window with the cosine and triangular windows, while Fig. 3.13b compares the rectangular window with the Hanning, Hamming, and Blackman windows. From the amplitude curves of Fig. 3.13 one can calculate the -6 dB angular width of the main lobe of the far field response and also determine how small the amplitude of the first lobe is relative to the main lobe amplitude. Table 3.1 summarizes these results.

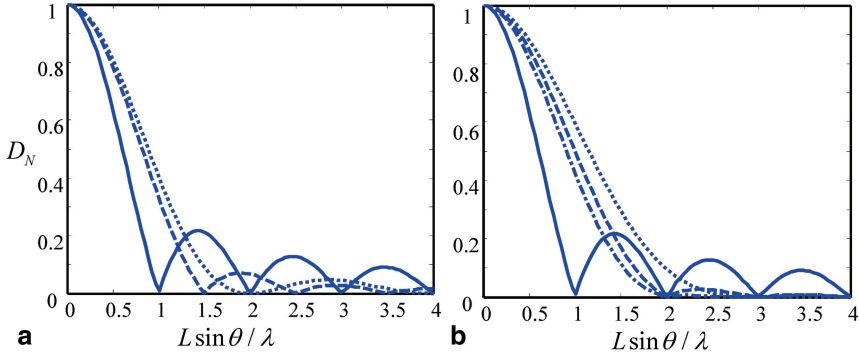


Fig. 3.13 The normalized directivities for different amplitude weighting windows. **a** Comparison of the rectangular window (*solid line*), cosine window (*dashed line*), and triangular window (*dotted line*). **b** Comparison of the rectangular window (*solid line*), Hanning window (*dashed line*), Hamming window (*dash-dot line*), and Blackman window (*dotted line*).

Table 3.1 The -6 dB angular width of the far field directivity main lobe and the amplitude of the first side lobe relative to the amplitude of the main lobe for different choices of the window function

Window function	θ_{-6B} width of main lobe	First side lobe amplitude (dB)
Rectangular	$\sin^{-1}(0.600\lambda / L)$	-13.3
Cosine	$\sin^{-1}(0.817\lambda / L)$	-23.0
Triangular	$\sin^{-1}(0.885\lambda / L)$	-26.5
Hanning	$\sin^{-1}(0.997\lambda / L)$	-31.5
Hamming	$\sin^{-1}(0.905\lambda / L)$	-44.0
Blackman	$\sin^{-1}(1.149\lambda / L)$	-58.1

Generally, Table 3.1 shows that a window that reduces the amplitude of the side lobes also increases the width of the main lobe. The Hamming window, however, is an exception to that rule as it has both a smaller main lobe width and first side lobe amplitude in comparison to the Hanning window. The windows discussed in this section are the “classical” functions often described in the literature. However, there are alternative windows that may be better for a particular application [5].

3.4 Multi-Gaussian Beam Model

For large, single element transducers in addition to the Fresnel integral models one can use a superposition of a small number of Gaussian beams to represent the radiated field of a piston transducer. As will be shown here, multi-Gaussian beam models also can provide an effective tool for modeling both beam steering and focusing.

If we let the pressure $p(x, z, \omega) = P(x, z, \omega) \exp(ikz)$ in Helmholtz’s equation (Eq. (2.6)) we find

$$\frac{\partial^2 P}{\partial x^2} + \frac{\partial^2 P}{\partial z^2} + 2ik \frac{\partial P}{\partial z} = 0. \quad (3.85)$$

If the waves are all traveling in approximately the z -direction then we can make the paraxial approximation, which is equivalent to the mathematical condition [Schmerr-Song]

$$\frac{\partial^2 P}{\partial z^2} \ll 2ik \frac{\partial P}{\partial z}, \frac{\partial^2 P}{\partial x^2}, \quad (3.86)$$

and Eq. (3.85) becomes the 2-D paraxial wave equation for P given by:

$$\frac{\partial^2 P}{\partial x^2} + 2ik \frac{\partial P}{\partial z} = 0. \quad (3.87)$$

One solution of Eq. (3.87) is in the form of a Gaussian given by

$$P(x, z) = \tilde{P}(z) \exp\left(ik \frac{x^2}{2q(z)}\right). \quad (3.88)$$

Placing this solution into Eq. (3.87) we obtain the two equations

$$\begin{aligned} \frac{dq}{dz} &= 1 \\ 2 \frac{d\tilde{P}}{dz} + \frac{\tilde{P}}{q} &= 0, \end{aligned} \quad (3.89)$$

which can both be solved to find

$$\begin{aligned} q(z) &= z + q_0 \\ \tilde{P}(z) &= \frac{P_0}{\sqrt{q(z)}}, \end{aligned} \quad (3.90)$$

where (P_0, q_0) are constants. Thus, the pressure is given by a Gaussian beam of the form

$$p(x, z, \omega) = \frac{P_0}{\sqrt{q(z)}} \exp(ikz) \exp\left(\frac{ikx^2}{2q(z)}\right). \quad (3.91)$$

At $z=0$ we see the pressure is given in terms of the (P_0, q_0) constants as

$$p = \frac{P_0}{\sqrt{q_0}} \exp\left(\frac{ikx^2}{2q_0}\right), \quad (3.92)$$

which can be expressed in terms of constants (A, B) as

$$\frac{p}{\rho c v_0} = A \exp(-Bx^2/b^2). \quad (3.93)$$

Comparing Eqs. (3.92) and (3.93) gives the relations between these constants:

$$\begin{aligned} q_0 &= \frac{-ikb^2}{2B} \\ P_0 &= \rho c v_0 A \sqrt{q_0}. \end{aligned} \quad (3.94)$$

Using Eq. (3.94) the propagating 2-D Gaussian beam of Eq. (3.91) can be written in terms of (A, B) as

$$p(x, z, \omega) = \rho c v_0 A \sqrt{\frac{q_0}{z + q_0}} \exp(ikz) \exp\left(\frac{ikx^2}{2(z + q_0)}\right). \quad (3.95)$$

Another way to obtain this propagating Gaussian beam directly is to use Eq. (2.29) for the pressure in terms of a Hankel function, i.e.

$$p(\mathbf{x}, \omega) = \frac{\omega p}{2} \int_{-\infty}^{+\infty} v_z(x', 0, \omega) H_0^{(1)}(kr) dx'. \quad (3.96)$$

If we replace the Hankel function by its high frequency asymptotic value to obtain

$$p(\mathbf{x}, \omega) = \frac{k \rho c \exp(-i\pi/4)}{2} \int_{-\infty}^{+\infty} v_z(x', 0, \omega) \sqrt{\frac{2}{\pi kr}} \exp(ikr) dx' \quad (3.97)$$

and assume that the normal velocity on the surface at $z=0$ is given by the Gaussian velocity profile

$$\bar{v}_z = v_0(\omega) A \exp(-B(x')^2/b^2) \quad (3.98)$$

then the pressure wave field is given by

$$p(\mathbf{x}, \omega) = \frac{k \rho c v_0(\omega) \exp(-i\pi/4) A}{2} \int_{-\infty}^{+\infty} \exp\left[-B(x')^2/b^2\right] \sqrt{\frac{2}{\pi kr}} \exp(ikr) dx', \quad (3.99)$$

where A, B , and b are constants, $v_0(\omega)$ is a velocity spectrum, and the radius $r = \sqrt{(x-x')^2 + z^2}$. Now assume $x, x' \ll z$ in this radius expression. This is equivalent to saying all the waves are propagating in the z -direction, i.e. we are again using the paraxial approximation. Then we have, approximately,

$$\frac{p(\mathbf{x}, \omega)}{\rho c v_0(\omega)} = \sqrt{\frac{k}{2\pi iz}} A \exp(ikz) \int_{-\infty}^{+\infty} \exp\left[-\frac{B(x')^2}{b^2}\right] \exp\left[ik \frac{(x-x')^2}{2z}\right] dx'. \quad (3.100)$$

When the second exponential in Eq. (3.100) is expanded out we obtain

$$\frac{p(\mathbf{x}, \omega)}{\rho c v_0(\omega)} = \sqrt{\frac{k}{2\pi iz}} A \exp(ikz) \exp\left[ik \frac{x^2}{2z}\right] \cdot \int_{-\infty}^{+\infty} \exp\left[i\left(\frac{k}{2z} + \frac{iB}{b^2}\right)(x')^2\right] \exp\left[-ik \frac{xx'}{z}\right] dx'. \quad (3.101)$$

However, this integral can be evaluated exactly [Schmerr-Song]. After combining terms and some algebra one finds

$$\frac{p(\mathbf{x}, \omega)}{\rho c v_0(\omega)} = \sqrt{\frac{-ikb^2 / 2B}{(z - ikb^2 / 2B)}} A \exp(ikz) \exp\left[ik \frac{x^2}{2(z - ikb^2 / 2B)}\right], \quad (3.102)$$

which is of exactly the same form as Eq. (3.95) in terms of the constants A and B . This result shows that if we generate a Gaussian velocity profile on $z=0$ in the paraxial approximation this Gaussian profile simply launches a Gaussian beam traveling in the fluid for $z > 0$. In the paraxial approximation the pressure and velocity, v_z , satisfy the plane wave relationship $p = \rho c v_z$ [Schmerr-Song] so the velocity is also in this same form:

$$\frac{v_z(\mathbf{x}, \omega)}{v_0(\omega)} = \sqrt{\frac{-ikb^2 / 2B}{(z - ikb^2 / 2B)}} A \exp(ikz) \exp\left[ik \frac{x^2}{2(z - ikb^2 / 2B)}\right]. \quad (3.103)$$

In 1988 Wen and Breazeale [6] showed that one could model the wave field of a circular piston transducer radiating waves in three dimensions by superimposing ten Gaussian beams having different complex coefficients (A_n, B_n) . These coefficients were obtained with a non-linear least squares optimization procedure to find the (A_n, B_n) that best matched a constant piston profile on the transducer face given by

$$\frac{v_z}{v_0} = \text{circ}(\rho^2 / b^2) = \begin{cases} 1 & \rho / b \leq 1 \\ 0 & \text{otherwise} \end{cases}, \quad (3.104)$$

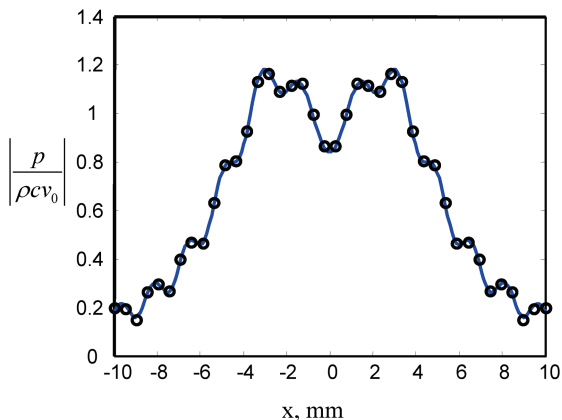
where ρ was a radial coordinate and b was the radius of the transducer. In 1990, Wen and Breazeale improved the accuracy of their model with a slightly larger set of 15 Gaussian beams [7]. If we simply set $\rho = x$ we can use this same set of coefficients for our 2-D problem for a 1-D transducer of length $2b$.

Using Eq. (3.102) and the 15 Wen and Breazeale coefficients the pressure wave field in our 2-D problem can be written compactly as

$$p(x, z, \omega) = \sum_{n=1}^{15} \rho c v_0 A_n \sqrt{\frac{(q_0)_n}{z + (q_0)_n}} \exp(ikz) \exp\left(\frac{ikx^2}{2(z + (q_0)_n)}\right), \quad (3.105)$$

where

Fig. 3.14 Comparison of the multi-Gaussian beam model with the Fresnel integral model for the transducer parameters; $b = 6$ mm, $f = 5$ MHz, $c = 1500$ m/s. Shown is the cross-axis normalized pressure at $z = 60$ mm versus the distance, x . *Solid line*—Fresnel integral model, *Circles*—multi-Gaussian beam model (see Fig. 3.2b for a similar comparison)



$$(q_0)_n = \frac{-ikb^2}{2B_n}. \quad (3.106)$$

The MATLAB[®] function Gauss_2D(b, f, c, x, z) in Code Listing C.10 uses Eq. (3.106) and the 15 Wen and Breazeale coefficients obtained from the MATLAB[®] function gauss_c15 (Code Listing C.11) to implement a 2-D multi-Gaussian beam model for a piston transducer of length $2b$. The calling sequence for this function is

$$>> p = \text{Gauss_2D}(b, f, c, x, z);$$

where $2b$ is the element length (in mm), f is the frequency (in MHz), c is the wave speed (in m/s), and (x, z) is a point in the fluid (in mm) at which the normalized pressure, $p / \rho v_0$, is calculated. Figure 3.14 shows a comparison of a beam profile calculated with the multi-Gaussian beam model and the Fresnel integral model. Both beam models are based on the paraxial approximation but recall in Fig. 3.2b a similar comparison was also made with a multiple line source model. From these figures it can be seen that both paraxial models accurately predict the wave field of the large ($b = 6$ mm) element. Similar results can be found with beam models based on the paraxial approximation for points about a diameter away from the face of the element [Schmerr-Song].

Now, consider the case where a linear phase variation of the form $\exp(ikx' \sin \Phi)$ is applied to a Gaussian velocity profile $Av_0 \exp(-B(x')^2 / b^2)$ on the surface of a 1-D transducer. Then a Gaussian beam of exactly the same form as found in Eq. (3.102) is generated traveling in the \bar{z} -direction with amplitude $Av_0 / \cos \Phi$ and where $b \rightarrow b \cos \Phi$. This result can be obtained directly by using this velocity profile in Eq. (3.97):

$$p(\mathbf{x}, \omega) = \frac{k \rho c v_0(\omega) \exp(-i\pi/4) A}{2} \int_{-\infty}^{+\infty} \exp(ikx' \sin \Phi) \exp[-B(x')^2 / b^2] \sqrt{\frac{2}{\pi k r}} \exp(ikr) dx'. \quad (3.107)$$

Placing the approximation for the radius r in the (\bar{x}, \bar{z}) coordinates obtained previously in Eq. (3.12) we then obtain

$$\frac{p(\mathbf{x}, \omega)}{\rho c v_0(\omega)} = \sqrt{\frac{k}{2\pi i \bar{z}}} A \exp(ik\bar{z}) \int_{-\infty}^{+\infty} \exp\left[-\frac{B(x')^2}{b^2}\right] \exp\left[ik \frac{(\bar{x} - x' \cos \Phi)^2}{2\bar{z}}\right] dx', \quad (3.108)$$

and letting $w = x' \cos \Phi$ again, we find

$$\frac{p(\mathbf{x}, \omega)}{\rho c v_0(\omega)} = \sqrt{\frac{k}{2\pi i \bar{z}}} \frac{A}{\cos \Phi} \exp(ik\bar{z}) \int_{-\infty}^{+\infty} \exp\left[-\frac{Bw^2}{(b \cos \Phi)^2}\right] \exp\left[ik \frac{(\bar{x} - w)^2}{2\bar{z}}\right] dw, \quad (3.109)$$

which is similar to Eq. (3.100) so following the same steps taken following that equation, we see this linearly phased Gaussian velocity profile at $z' = 0$ generates a Gaussian beam traveling in the fluid given by

$$\frac{p(\mathbf{x}, \omega)}{\rho c v_0(\omega)} = \sqrt{\frac{-ik(\bar{b})^2 / 2B}{(\bar{z} - ik(\bar{b})^2 / 2B)}} \tilde{A} \exp(ik\bar{z}) \exp\left[ik \frac{\bar{x}^2}{2(\bar{z} - ik(\bar{b})^2 / 2B)}\right], \quad (3.110)$$

where in terms of $\bar{b} = b \cos \Phi$, $\tilde{A} = A / \cos \Phi$ we have exactly the same form as Eq. (3.102).

It is easy in a Gaussian beam model to include the effects of both steering and focusing because in the paraxial approximation focusing can be introduced in addition to steering by adding a term on the transducer face with a quadratic phase variation $-(x')^2 \cos^2 \Phi / 2R_0 c$ (see Eq. (3.52)). But this additional phase term changes Eq. (3.109) to

$$\frac{p(\mathbf{x}, \omega)}{\rho c v_0(\omega)} = \sqrt{\frac{k}{2\pi i \bar{z}}} \frac{A}{\cos \Phi} \exp(ik\bar{z}) \int_{-\infty}^{+\infty} \exp\left[-\frac{ikw^2}{2R_0} - \frac{Bw^2}{(b \cos \Phi)^2}\right] \exp\left[ik \frac{(\bar{x} - w)^2}{2\bar{z}}\right] dw. \quad (3.111)$$

so that if we define a \tilde{B} coefficient as

$$\tilde{B} = B + \frac{ik\bar{b}^2}{2R_0} \quad (3.112)$$

Equation (3.112) becomes

$$\frac{p(\mathbf{x}, \omega)}{\rho c v_0(\omega)} = \sqrt{\frac{k}{2\pi i \bar{z}}} \frac{A}{\cos \Phi} \exp(ik\bar{z}) \int_{-\infty}^{+\infty} \exp\left[-\frac{\tilde{B}w^2}{(b \cos \Phi)^2}\right] \exp\left[ik \frac{(\bar{x} - w)^2}{2\bar{z}}\right] dw, \quad (3.113)$$

which is identical in form to Eq. (3.109) so that the steered and focused Gaussian beam is in the same form as Eq. (3.110) with \tilde{B} simply replacing B to obtain

$$\frac{p(\mathbf{x}, \omega)}{\rho c v_0(\omega)} = \sqrt{\frac{-ik(\bar{b})^2 / 2\tilde{B}}{(\bar{z} - ik(\bar{b})^2 / 2\tilde{B})}} \tilde{A} \exp(ik\bar{z}) \exp\left[ik \frac{\bar{x}^2}{2(\bar{z} - ik(\bar{b})^2 / 2\tilde{B})}\right]. \quad (3.114)$$

Using 15 modified Wen and Breazeale coefficients $\tilde{A}_n = A_n / \cos \Phi$, $\tilde{B}_n = B_n + ik\bar{b}^2 / 2R_0$, we can then obtain the pressure wave field of a steered and focused 1-D piston transducer of length $2b$ as

$$p(x, z, \omega) = \sum_{n=1}^{15} \rho c v_0 \tilde{A}_n \sqrt{\frac{(\tilde{q}_0)_n}{\bar{z} + (\tilde{q}_0)_n}} \exp(ik\bar{z}) \exp\left(\frac{ik\bar{x}^2}{2(\bar{z} + (\tilde{q}_0)_n)}\right), \quad (3.115)$$

where

$$(\tilde{q}_0)_n = \frac{-ik(\bar{b})^2}{2\tilde{B}_n}. \quad (3.116)$$

3.5 Summary

In this chapter we have seen how applying a linear time delay law to the face of a large single element piston transducer can steer the sound beam, while applying a quadratic delay can produce focusing of the beam. Explicit expressions for the steered and focused beams were found using both a Fresnel integral beam model and a multi-Gaussian beam model. Both of those beam models showed that the steered wave field was equivalent to the wave field of a rotated virtual transducer (Fig. 3.4) with a driving velocity on its face increased by a factor of $1 / \cos \Phi$. This amplitude increase occurs because the effective transducer size is reduced in width as a result of steering.

We should note that the quadratic time delay law used here to demonstrate focusing was only an approximate focusing delay law since it was obtained with the paraxial approximation. This approximation was consistent with the Fresnel integral model and the multi-Gaussian beam models used to discuss steering and focusing since those models also relied on the paraxial approximation. However, when developing focusing laws or combined steering and focusing laws for a phased array it is not necessary to use the paraxial approximation. In Chaps. 5 and 8 we will see how the discrete delays applied to array elements can be obtained from more exact delay laws.

Both the Fresnel integral beam model and the multi-Gaussian beam model are very useful beam models for describing the wave fields of large, single element transducers and the multi-Gaussian beam model in particular is a very powerful model for simulating wave fields in very complex testing situations [Schmerr-Song]. However, without modifications these are generally not suitable beam models for describing the wave fields of the small elements present in phased arrays. This is because, as shown in Chap. 2, such small elements produce significant beam spreading that is not consistent with the paraxial approximation. One way to overcome this limitation is to use as the basis functions Gaussian beams together with a linear phasing over an element, an approach that has been used successfully to simulate linear arrays [8]. In the next Chapter we will examine a beam model that

uses Gaussians without assuming the paraxial approximation. In Chap. 6 we will discuss another modeling approach which replaces the spherical waves generated by point sources with equivalent Gaussian beams.

References

1. L.J. Ziomek, *Underwater Acoustics—A Linear Systems Theory Approach* (Academic, New York, 1985)
2. L.J. Ziomek, *Fundamentals of Acoustic Field Theory and Space-Time Signal Processing* (CRC Press, Boca Raton, 1995)
3. H.T. O Neil, Theory of focusing radiators. *J. Acoust. Soc. Am.* **21**, 516–526 (1949)
4. M. Abramovich, I.A. Stegun, *Handbook of Mathematical Functions* (Dover Publications, New York, 1965)
5. K.J. Parker, Apodization and windowing functions. *IEEE Trans. Ultrason. Ferroelectr. Freq. Control.* **60**, 1263–1271 (2013)
6. J.J. Wen, M.A. Breazeale, A diffraction beam field expressed as the superposition of Gaussian beams. *J. Acoust. Soc. Am.* **83**, 1752–1756 (1988)
7. J.J. Wen, M.A. Breazeale, in *Computational Acoustics: Scattering, Gaussian Beams, and Aero-acoustics*, vol 2, ed. by D. Lee, A. Cakmak, R. Vichnevetsky. Computer optimization of the Gaussian beam description of an ultrasonic field (North Holland, Amsterdam, 1990), pp. 181–196
8. R. Huang, L.W. Schmerr, A. Sedov, Modeling the radiation of ultrasonic phased-array transducers with Gaussian beams. *IEEE Trans. Ultrason Ferroelectr. Freq. Control.* **55**, 2692–2702 (2008)

Chapter 4

Phased Array Beam Modeling (1-D Elements)

In Chap. 2 we developed beam models for a single element radiating waves in two dimensions. By superimposing M of these solutions we can develop corresponding M -element array models. In this chapter we will model the 2-D acoustic wave field generated by an array of 1-D elements and examine how the properties of this wave field are affected by choices of parameters such as element size and spacing. We will also discuss how discrete time delays applied to the array elements can implement beam steering and focusing and how discrete amplitude weights can affect beam characteristics for arrays. These discrete time delay laws and apodization windows will be sampled values of the continuous functions discussed in Chap. 3 for a large, single element transducer.

4.1 Phased Array Beam Models

Figure 4.1 shows an array of M elements where M is an even number and the center of the array is assumed to lie on the z -axis. Let each element length be $2b$ and assume the elements are all separated from each other by Δ , a constant spacing distance. The total length of the entire array will be taken as $2B$. In this case, the centroid of the first element is located at an x -distance of $e_1 = -B + b$ and the distance between centroids is $\Delta + 2b$ so the x -location of the centroid of the m th element is

$$e_m = -B + b + (\Delta + 2b)(m - 1). \quad (4.1)$$

But the distance B is given by

$$B = \frac{M}{2}(2b) + \left(\frac{M}{2} - 1\right)\Delta + \frac{\Delta}{2}, \quad (4.2)$$

where the first term on the right of Eq. (4.2) represents the contribution to B from half of the total elements ($M/2$). The second terms represents the contribution to B from the number of full gaps present, Δ , and the last term represents the half gap

Fig. 4.1 An array of M transducer elements, each of length $2b$ and separated by a distance, Δ , where M is an even number and the z -axis is located at the center of the array. The total length of the entire array is $2B$

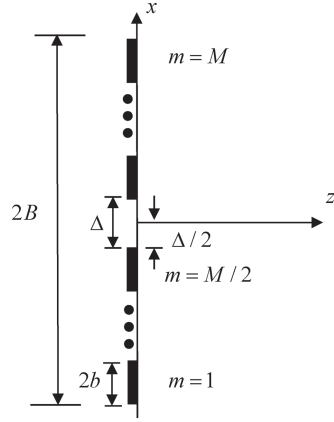
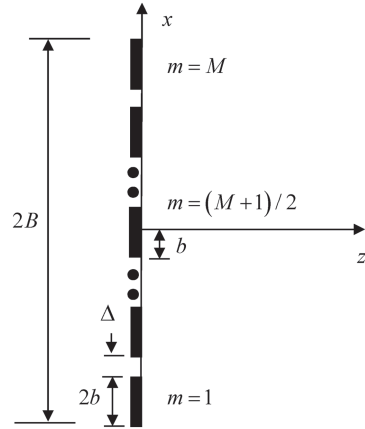


Fig. 4.2 An array of M transducer elements, each of length $2b$ and separated by a distance, Δ , where M is an odd number and the z -axis is located at the center of the array. The total length of the entire array is $2B$



length from the z -axis to the $m = M/2$ element (see Fig. 4.1). Combining Eqs. (4.1) and (4.2) then gives the x -location of the centroid of the m th element in the array as

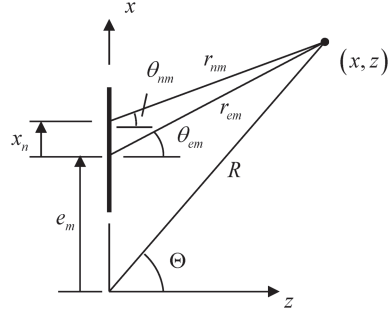
$$e_m = (\Delta + 2b) \left(\frac{2m - 1 - M}{2} \right). \quad (4.3)$$

If, instead, there are an odd number of elements in the array then with the z -axis again located at the center of the array (see Fig. 4.2), the centroid of the first element is again located at an x -distance of $e_1 = -B + b$ and the distance between centroids is still $\Delta + 2b$ so Eq. (4.1) holds. In this case

$$B = \frac{(M-1)}{2} (\Delta + 2b) + b, \quad (4.4)$$

since there are $(M-1)/2$ elements and gaps on each side of the center element and

Fig. 4.3 Geometry parameters for the m th element of an array for use in multiple and single line source array beam models and for considering the far field response of the array. The distance e_m is measured from the origin (taken as the center of the array) to the centroid of the m th element while x_n is the distance measured from this element centroid to the center of the n th segment of this element



an additional distance b on each side from the center element (Fig. 4.2). Comparing Eqs. (4.2) and (4.4) we see they are identical. This is to be expected since for either an even or odd number of elements we have M elements and $(M-1)$ gaps so that the total length of the array is

$$2B = M(2b) + (M-1)\Delta, \quad (4.5)$$

which also is identical with Eqs. (4.2) and (4.4). Thus it follows that the centroid location expression of Eq. (4.3) is valid for arrays with either an odd or even number of elements. The distance $s = 2b + \Delta$ which appears in Eq. (4.3) is called the *pitch* of the array. This particular distance, as we will see, plays an important role in describing the properties of the wave field of the array. In terms of the pitch, s , the centroid locations then are given simply by

$$e_m = \left(\frac{2m-1-M}{2} \right) s. \quad (4.6)$$

With Eq. (4.2) and the beam models developed in Chap. 2 for a single element piston transducer it now is possible to develop models for a 2-D transducer array. Each element in the array is typically driven by a separate circuit so that the driving voltages and the corresponding velocities on the faces of the elements can be different, i.e. $v_0(\omega) \rightarrow v_{0m}(\omega)$ for the m th element. Here, we will let $v_{0m}(\omega) = v_0(\omega)\tilde{C}_m$ so that the only differences between elements in the driving velocities will be apodization values, \tilde{C}_m , which are discrete values of the continuous apodization windows discussed in Chap. 3. Also, we will assume a different time delay, Δt_m , at each element that will produce an additional complex exponential term $\exp(i\omega\Delta t_m)$ for the m th element in the array model. We can sample the continuous time delays of Chap. 3 to generate discrete delay laws for beam steering and focusing of arrays or use the more general time delay laws developed in the next chapter.

Consider using our multiple line source model (Eq. 2.59) to represent each element of an array. Then for the wave field of the entire array we have (see Fig. 4.3)

$$\frac{p(\mathbf{x}, \omega)}{\rho c v_0(\omega)} = \sum_{m=1}^M \tilde{C}_m \exp(i\omega \Delta t_m) \left[\frac{kb}{N} \sqrt{\frac{2}{\pi i}} \sum_{n=1}^N D_{b/N}(\theta_{nm}) \frac{\exp(ikb\bar{r}_{nm})}{\sqrt{kb\bar{r}_{nm}}} \right], \quad (4.7)$$

where there are M elements and the acoustic field of each element is calculated with N segments over the element. The normalized distances, \bar{r}_{nm} , are given by

$$\bar{r}_{nm} = \sqrt{[(x - x_n - e_m) / b]^2 + (z / b)^2} \quad (4.8)$$

and the angles θ_{nm} are measured from the centroid of each segment of a given element (Fig. 4.3), i.e.

$$\sin[\theta_{nm}] = \frac{x - x_n - e_m}{b\bar{r}_{nm}}. \quad (4.9)$$

The model of Eq. (4.7) we will call the multiple line source array beam model. In many cases we are interested in calculating the wave field of the array only at distances which are in the far field region of each element. In that case we can set $N = 1$ in Eq. (4.7) and take $x_n = 0$ to obtain

$$\frac{p(\mathbf{x}, \omega)}{\rho c v_0(\omega)} = \sum_{m=1}^M \tilde{C}_m \exp(i\omega \Delta t_m) \left[kb \sqrt{\frac{2}{\pi i}} D_b(\theta_{em}) \frac{\exp(ikb\bar{r}_{em})}{\sqrt{kb\bar{r}_{em}}} \right], \quad (4.10)$$

where now the radii and angles are

$$\begin{aligned} \bar{r}_{em} &= \sqrt{(x / b - e_m / b)^2 + (z / b)^2} \\ \sin(\theta_{em}) &= \frac{x - e_m}{b\bar{r}_{em}}, \end{aligned} \quad (4.11)$$

as measured from the centroid of each element (see Fig. 4.3). We will call the model of Eq. (4.10) the single line source array beam model. This model will be used in the next section as the basis for discussing the existence of grating lobes in the radiated wave field of an array.

4.1.1 Far Field Behavior of an Array

If the point (x, z) in the fluid is in the far-field of the entire array, then a single line source is adequate to represent every element of the array and in the single line source array beam model we can set (see Fig. 4.3)

$$\begin{aligned} r_{em} &= \sqrt{R^2 + e_m^2 - 2Re_m \sin \Theta} \\ &\cong R - e_m \sin \Theta \end{aligned} \quad (4.12)$$

and

$$\theta_{em} \cong \Theta \quad (4.13)$$

so Eq. (4.10) becomes, approximately,

$$p(\mathbf{x}, \omega) = \sum_{m=1}^M \tilde{C}_m \exp(i\omega \Delta t_m) \left[\rho c v_0 \sqrt{\frac{2}{\pi i}} k b D_b(\Theta) \frac{\exp(ikR)}{\sqrt{kR}} \exp(-ike_m \sin \Theta) \right]. \quad (4.14)$$

Now consider the case where there is no apodization or delay law imposed, i.e. $\tilde{C}_m = 1$, $\Delta t_m = 0$. Then we find

$$p(\mathbf{x}, \omega) = \rho c v_0 \sqrt{\frac{2}{\pi i}} k b D_b(\Theta) \sum_{m=1}^M [\exp(-ike_m \sin \Theta)] \frac{\exp(ikR)}{\sqrt{kR}}. \quad (4.15)$$

But, using Eq. (4.6) for the distances to the centroid, e_m , Eq. (4.15) reduces to

$$\begin{aligned} p(\mathbf{x}, \omega) &= \rho c v_0 \sqrt{\frac{2}{\pi i}} k b D_b(\Theta) \exp \left[iks \left(\frac{M+1}{2} \right) \sin \Theta \right] \\ &\cdot \sum_{m=1}^M [\exp(-iks \sin \Theta m)] \frac{\exp(ikR)}{\sqrt{kR}} \end{aligned} \quad (4.16)$$

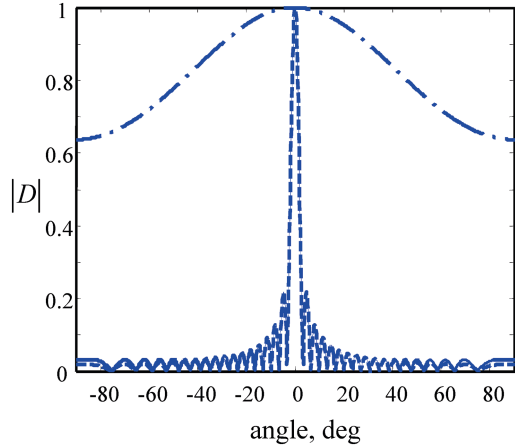
In this case we can perform the sum since

$$\sum_{m=1}^M a^m = \frac{a(1-a^M)}{1-a}. \quad (4.17)$$

Letting $a = \exp(-iks \sin \Theta)$ we find

$$\begin{aligned} &\sum_{m=1}^M [\exp(-iks \sin \Theta m)] \\ &= \exp(-iks \sin \Theta) \frac{[1 - \exp(-iks \sin \Theta M)]}{[1 - \exp(-iks \sin \Theta)]} \\ &= \exp \left[-iks \left(\frac{M+1}{2} \right) \sin \Theta \right] \frac{\sin[(Mks \sin \Theta) / 2]}{\sin[(ks \sin \Theta) / 2]} \end{aligned} \quad (4.18)$$

Fig. 4.4 The magnitude of the directivity for a single element of a 5 MHz, 32 element array radiating into water versus angle (*dashed-dotted line*). The magnitude of the directivity of the discrete sources of the array (*solid line*) compared to the directivity of a single element transducer of the same overall size as the array (*dashed line*). $M=32$, $2b/\lambda = 0.5$, $\Delta/2b = 0.1$, $f=5$ MHz



and Eq. (4.16) becomes

$$p(\mathbf{x}, \omega) = \rho c v_0 \sqrt{\frac{2}{\pi i}} (kbM) D_b(\Theta) \frac{\sin[(M ks \sin \Theta) / 2]}{M \sin[(ks \sin \Theta) / 2]} \frac{\exp(ikR)}{\sqrt{kR}}. \quad (4.19)$$

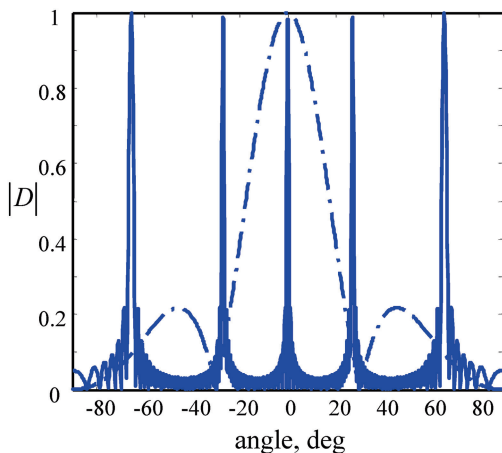
Equation (4.19) shows that in the far-field of the array the wave field acts like a cylindrically spreading wave with a total angular directivity, $D(\Theta) = D_b(\Theta) D_s(\Theta)$, where

$$\begin{aligned} D_b(\Theta) &= \frac{\sin(kb \sin \Theta)}{kb \sin \Theta}, \\ D_s(\Theta) &= \frac{\sin[(Mks \sin \Theta) / 2]}{M \sin[(ks \sin \Theta) / 2]}. \end{aligned} \quad (4.20)$$

While the directivity function $D_b(\Theta)$ represents the directivity of an individual element the directivity $D_s(\Theta)$ can be considered to be due to a discrete array of “point” sources, each separated by the distance, s . One can see this since if b is very small, each element reduces to a “point” and in this limit $D_b \cong 1$ so the total directivity of these very small “point” elements is just $D(\Theta) \cong D_s(\Theta)$. For arrays where the element size and pitch are fractions of a wavelength the directivity function of the element, $D_b(\Theta)$, is slowly varying in angle while the directivity of the discrete sources, $D_s(\Theta)$, behaves similar to the directivity of a single element transducer having the size of the entire array ($2B$). This can be seen in Fig. 4.4 which plots these directivities as a function of the angle, Θ for the 5 MHz, 32 element array with an element length which is one half a wavelength. Figure 4.4 also shows the directivity of a single element transducer having the same overall size as the entire array, i.e.

$$D_B(\Theta) = \frac{\sin(kB \sin \Theta)}{kB \sin \Theta}, \quad (4.21)$$

Fig. 4.5 The magnitude of the directivity versus angle of a single element of a 5 MHz, 32 element array radiating into water (dashed-dotted line) and the magnitude of the directivity versus angle of the discrete sources of the array (*solid line*). $M=32$, $2b/\lambda = 2.0$, $\Delta/2b = 0.1$, $f=5$ MHz



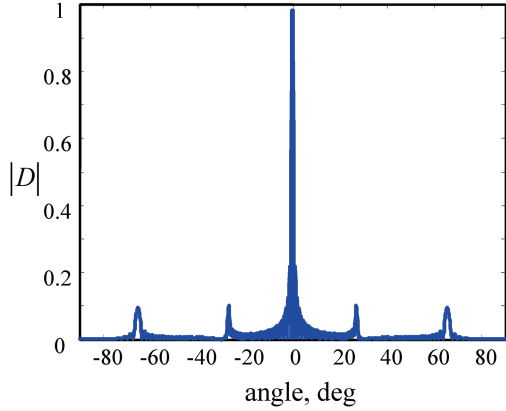
where it can be seen that there is little difference between $D_b(\Theta)$ and $D_s(\Theta)$. From Fig. 4.4 it would appear that the overall far-field behavior of the array, which is determined by the product of these directivity functions, will be very similar to that of a single element transducer of the same size. However, this is only true because in the example considered the pitch was only about one half a wavelength. If the element size was two wavelengths instead but all other parameters were left unchanged, the corresponding directivity plots of $D_b(\Theta)$ and $D_s(\Theta)$ would be as shown in Fig. 4.5. In this case the directivity of an element is more concentrated about $\Theta = 0$ since the element is larger and itself produces a more highly collimated beam, but the striking difference is in the directivity of discrete array sources, which now looks again like the overall directivity of a single element transducer of the same size as the entire array but where this directivity is periodically repeated as a function of angle. Since the total directivity function of the array is the product of these two directivities, additional “lobes” in the directivity function $D(\Theta) = D_b(\Theta)D_s(\Theta)$ will appear in the far-field wave field as shown in Fig. 4.6. These lobes are called *array grating lobes*. Similar lobes appeared in Chap. 2 when modeling large, single element transducers if the element segments were too large. Since the elements themselves in an array act as similar segments of the entire array it is not surprising that array grating lobes appear also if the element size is too large. The conditions for the existence of grating lobes can be found by noting that the directivity function D_s is a function of the variable $ks \sin \Theta$ given by

$$D_s(ks \sin \Theta) = \frac{1}{M} \exp \left[iks \sin \Theta \left(\frac{M+1}{2} \right) \right] \sum_{m=1}^M \exp(-iks \sin \Theta m). \quad (4.22)$$

Equation (4.22) shows that the magnitude of this directivity function is a periodic function since

$$|D_s(ks \sin \Theta)| = |D_s(ks \sin \Theta \pm 2n\pi)|. \quad (4.23)$$

Fig. 4.6 The magnitude of the total directivity versus angle of an array radiating into water versus angle of a 5 MHz, 32 element array radiating into water. $M=32$, $2b/\lambda = 2.0$, $\Delta/2b = 0.1$, $f=5$ MHz



Thus, the same maximum value of the directivity function which occurs at $\Theta = 0$ where $ks \sin \Theta = 0$ will also occur at angles Θ_n where $ks \sin \Theta_n = \pm 2n\pi$ ($n = 1, 2, \dots$) provided that we can find a real solution or solutions of

$$\Theta_n = \sin^{-1} \left(\pm \frac{n\lambda}{s} \right) \quad (n = 1, 2, \dots). \quad (4.24)$$

Equation (4.24) shows that as long as $s < \lambda$ there are no solutions except $\Theta = 0$. For $s > \lambda$, other solutions (lobes of the response) can exist. A similar situation was found in Chap. 2 when breaking an element up into segments. There it was found that the segment size had to be less than one wavelength to prevent extraneous lobes from appearing. Here, we need to keep the pitch of the array less than a wavelength instead. In the next section we will show that if we use a delay law to steer the beam of an array the conditions needed to prevent grating lobes will be even more restrictive (the pitch will have to be less than one half a wavelength). Manufacturing and economic constraints present when producing commercial NDE phased arrays may dictate that the array pitch be more than a wavelength, so that in practice one may have to deal with an array where grating lobes are inherently present and can affect the test results.

4.2 Array Beam Steering

Since the individual elements of an array transducer are driven independently, it is possible to excite each element with a different time delay. These delays can be used to electronically steer and focus the ultrasound. In this section we will examine beam steering by examining the far-field behavior of an array, first using the single line source model of Eq. (4.10) with the amplitude coefficients, \tilde{C}_m , taken to

be unity. If we use the continuous beam steering law of Eq. (3.17) and sample that function at the centroid locations of the array elements given by Eq. (4.6) we find the discrete delays, Δt_m , given by

$$\Delta t_m = \frac{s \sin \Phi}{c} \left[(m-1) - \frac{M-1}{2} \right] \quad (4.25)$$

If these delays are placed into the far field values of the single line source model Eq. (4.14) with $\tilde{C}_m = 1$ we obtain

$$p(\mathbf{x}, \omega) = \rho c v_0 \sqrt{\frac{2}{\pi i}} (kbM) D_b(\Theta) \frac{\exp(ikR)}{\sqrt{kR}} \cdot \frac{1}{M} \exp \left[iks(\sin \Theta - \sin \Phi) \frac{M+1}{2} \right] \sum_{m=1}^M \exp[-iks(\sin \Theta - \sin \Phi)m], \quad (4.26)$$

which shows that we have a point source directivity, $D_s(\Theta, \Phi)$, given by

$$D_s(\Theta, \Phi) = \frac{1}{M} \exp \left[iks(\sin \Theta - \sin \Phi) \frac{M+1}{2} \right] \sum_{m=1}^M \exp[-iks(\sin \Theta - \sin \Phi)m]. \quad (4.27)$$

Again, we can sum this series using Eq. (4.17) to obtain

$$D_s(\Theta, \Phi) = \frac{\sin[Mks(\sin \Theta - \sin \Phi)/2]}{M \sin[ks(\sin \Theta - \sin \Phi)/2]}. \quad (4.28)$$

This directivity of the steered array is very similar in form to that of the array without steering (see Eq. (4.20)) so this new directivity function has the same type of lobe structure as seen previously for the case with no delays but we see that the main lobe at $\Theta = 0$ in the non-delayed case now occurs when $\Theta = \Phi$ so that the beam of the array has been shifted (steered) and Φ is just the steering angle as shown schematically in Fig. 4.7. The directivity is plotted in Fig. 4.8 for the same case considered in Fig. 4.4, but where now the steering angle $\Phi = 30^\circ$. Since the pitch is only slightly greater than one half a wave length in this case, no significant grating lobes appear in Fig. 4.8.

Now, consider the grating lobe structure of the array when it is steered. We can take the steering angle as positive since, as Eq. (4.28) shows, $D_s(-\Theta, -\Phi) = D_s(\Theta, \Phi)$ so that the behavior of the directivity function for negative steering angles can be easily obtained from that for positive steering angles. Equation (4.28) shows that the maximum magnitude of D_s occurs at $\Theta = \Phi$ where $ks(\sin \Theta - \sin \Phi) = 0$, but additional maxima can also occur when

$$ks(\sin \Theta - \sin \Phi) = \pm 2n\pi \quad (n = 1, 2, \dots), \quad (4.29)$$

Fig. 4.7 A linear distribution of realizable time delays applied to an array that steer the beam to an angle $\Phi > 0$ in the far field

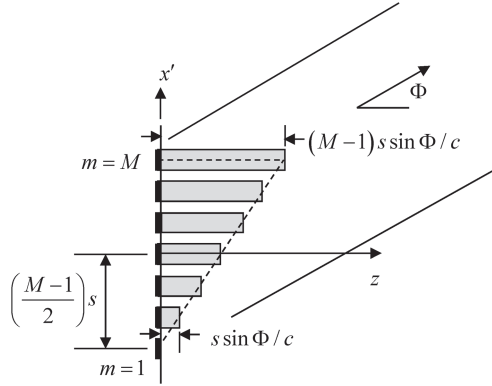
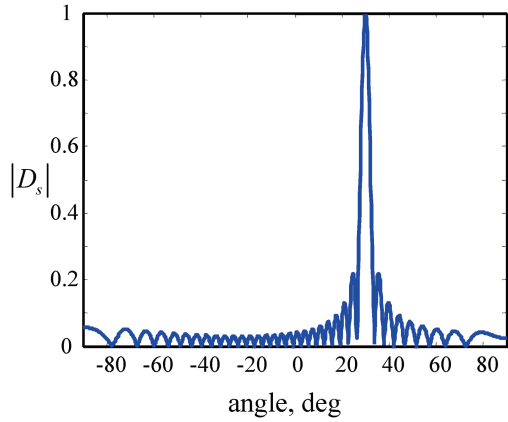


Fig. 4.8 The magnitude of the directivity of the discrete sources of an array for a steering angle $\Phi = 30^\circ$, $M=32$, $2b/\lambda = 2.0$, $\Delta/2b = 0.1$, $f=5$ MHz. This directivity can be compared to the same case (Fig. 4.4) with no steering

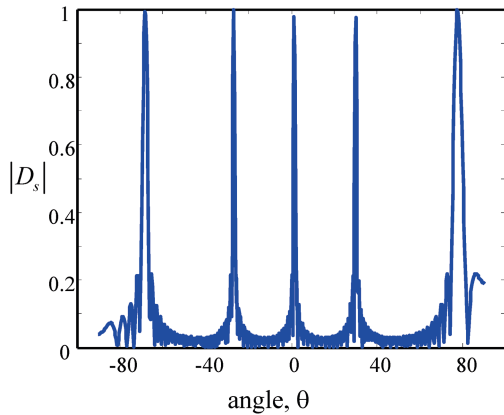


corresponding to the angles

$$\Theta_n = \sin^{-1} \left(\sin \Phi \pm \frac{n\lambda}{s} \right) \quad (n = 1, 2, \dots). \quad (4.30)$$

In this case, one can see that if $s < \lambda/2$ then there will be no real values of Eq. (4.30) for steering angles $0^\circ \leq \Phi \leq 90^\circ$ (and similarly for $-90^\circ \leq \Phi \leq 0^\circ$). Note that this condition is more restrictive than the case $s < \lambda$ found when no beam steering was present so that we must keep the pitch less than half a wavelength to prevent grating lobes from existing, regardless of the angle to which we steer the array beam. The point source array directivity is plotted in Fig. 4.9 for the same case considered in Fig. 4.5 where grating lobes are present, but with a steering angle $\Phi = 30^\circ$. It can be seen that the main lobe is shifted, as expected, but there are also shifted grating lobes off the main steering direction as well.

Fig. 4.9 The magnitude of the directivity of the discrete sources of an array for a steering angle $\Phi = 30^\circ$, $M=32$, $2b/\lambda = 2.0$, $\Delta/2b = 0.1$, $f=5$ MHz. **This directivity can be compared to the same case (Fig. 4.5) with no steering**



Although we have only examined the case where all the array elements are weighted equally ($\tilde{C}_m = 1$), for other weighting factors the magnitude of the array directivity without any time delays is given by

$$|D_s(ks \sin \Theta)| = \left| \frac{1}{M} \sum_{m=1}^M \tilde{C}_m \exp(-iks \sin \Theta m) \right|, \quad (4.31)$$

whereas, with steering time delays, we have

$$|D_s(ks(\sin \Theta - \sin \Phi))| = \left| \frac{1}{M} \sum_{m=1}^M \tilde{C}_m \exp[-iks(\sin \Theta - \sin \Phi)m] \right| \quad (4.32)$$

so that the array far-field wave field is steered in exactly the same manner for an array driven with any set of \tilde{C}_m amplitude factors.

In implementing beam steering in an array we cannot use the time delay law of Eq. (4.25) since it contains advances as well as delays. However, we note that if $\Phi \geq 0$ the largest negative term occurs for $m = 1$. Thus, if we add a constant (positive) term of $s \sin \Phi (M - 1) / 2c$ to this law we obtain a proper steering delay law for $\Phi \geq 0$ given by

$$\Delta t_m = \frac{s \sin \Phi}{c} (m - 1). \quad (4.33)$$

These discrete delays are the ones shown schematically on the elements of the array in Fig. 4.7. If $\Phi < 0$ then the largest negative terms in Eq. (4.25) occur for $m = M$ and we must subtract a constant (negative) term of $s \sin \Phi (M - 1) / 2c$ to give the proper delay law

$$\Delta t_m = \frac{s |\sin \Phi|}{c} (M - m). \quad (4.34)$$

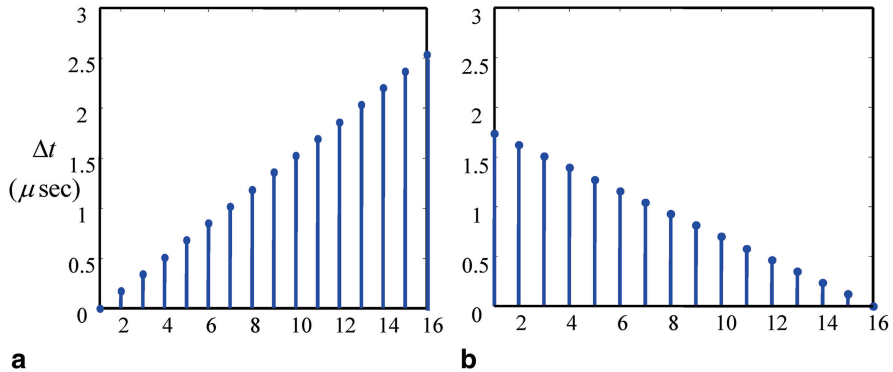


Fig. 4.10 Time delays for steering a 16 element array with pitch $s = 0.5$ mm in water for (a) a steering angle of 30° , and (b) a steering angle of -20°

Combining these terms we arrive at a complete and realizable beam steering law

$$\Delta t_m = \begin{cases} \frac{s \sin \Phi}{c} (m-1) & \Phi \geq 0 \\ \frac{s |\sin \Phi|}{c} (M-m) & \Phi < 0 \end{cases} \quad (4.35)$$

Note that adding or subtracting constant terms in the original delay law of Eq. (4.25) only generates additional constant phase terms in the point source directivity so that they have no effect on the criterion for grating lobes discussed previously.

In the next chapter we will discuss beam steering in a much more general context where we can have both steering and focusing occurring simultaneously. The MATLAB® function `delay_laws2D` given in Code Listing C.12 generates the delays laws for an array that is both steered and focused in a single medium radiating waves in two dimensions. The calling sequence for this function is

```
>>td=delay_laws2D(M, s, Phi, F,c);
```

This function generates the time delays (in microseconds) for an array with M elements that has a pitch s (mm) and is steered to a focal point F (mm) through the angle Φ (degrees) for a single medium with wave speed c (m/s) (see the discussion in Chap. 5). If the focal length F in this function is specified as $F = \text{inf}$ (infinity) then the steering only law is that of Eq. (4.35). Figure 4.10a shows the time delays generated by this function for a 16 element array steered in water to an angle of 30° where the function inputs are $M = 16$, $s = 0.5$ mm, $\Phi = 30^\circ$, $F = \text{inf}$, and $c = 1480$ m/s. Figure 4.10b shows the delays for the same array steered in the -20° direction.

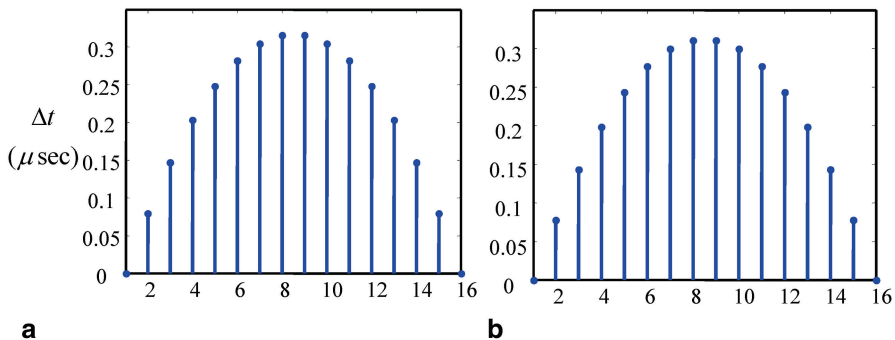


Fig. 4.11 Time delays for focusing a 16 element array with pitch $s=0.5$ mm in water (without steering) at a focal length of 15 mm using (a) the paraxial law of Eq. (4.39), and (b) an exact focusing law as implemented in the MATLAB function `delay_laws2D`

4.3 Array Beam Focusing

For an array, focusing can be achieved by evaluating the continuous time “delay” focusing law we obtained in Chap. 3 (using the paraxial approximation) at the centroids, e_m , of each element given by Eq. (4.6). That continuous delay law was

$$\Delta t_d(x') = -\frac{(x')^2}{2R_0c}. \quad (4.36)$$

Thus, we obtain the discrete delays

$$\Delta \tilde{t}_m \equiv \Delta t(e_m) = -\frac{s^2}{2R_0c} \left[(m-1) - \frac{M-1}{2} \right]^2. \quad (4.37)$$

However, again these “delays” are really time advances that cannot be implemented electronically in practice so that adding a constant delay term, T , to each element of the array, where

$$T = \frac{s^2}{2R_0c} \left[\frac{M-1}{2} \right]^2, \quad (4.38)$$

we obtain a realizable set of time delays, $\Delta t_m = \Delta \tilde{t}_m + T$ given by

$$\Delta t_m = \frac{s^2}{2R_0c} (m-1)(M-m). \quad (4.39)$$

Figure 4.11a shows a set of proper discrete focusing delays for a 16 element array obtained by using Eq. (4.39) for an array with a pitch $s=0.5$ mm focused into water ($c=1480$ m/s) at a focal length of $R_0=15$ mm. Equation (4.39) is, however,

only an approximate expression since it was developed using the paraxial approximation. The MATLAB[®] function `delay_laws2D` discussed in the previous section implements focusing (and combined beam steering and focusing) without such paraxial approximations. Fig. 4.11b shows the delays generated with this function for the same parameters as used in Fig. 4.11a ($M = 16$, $s = 0.5$ mm, $\Phi = 0^\circ$, $F = 15$ mm, $c = 1480$ m/s). Differences between these two delay laws, while present, are small enough to not be readily visible for the scale of Fig. 4.11.

To see the effect of the focusing law on the sound beam generated by the array, consider the single line source array beam model of Eq. (4.10) which we rewrite here as

$$\frac{p(\mathbf{x}, \omega)}{\rho c v_0(\omega)} = \sum_{m=1}^M \tilde{C}_m \exp(i\omega \Delta t_m) \left[kb \sqrt{\frac{2}{\pi i}} D_b(\theta_{em}) \frac{\exp(ikr_{em})}{\sqrt{kr_{em}}} \right], \quad (4.40)$$

where (see Eq. (4.12))

$$\begin{aligned} r_{em} &= \sqrt{R^2 + e_m^2 - 2R e_m \sin \Theta} \\ \sin \theta_{em} &= \frac{x - e_m}{r_{em}}. \end{aligned} \quad (4.41)$$

Since the entire array will generate a well collimated beam we can use the paraxial approximation on both r_{em} and θ_{em} (see Fig. 4.3). In this approximation we will assume that e_m/R is small so that $\theta_{em} \cong \Theta$ and expand the square root in Eq. (4.41) to second order as

$$r_{em} \cong R \left[1 + \frac{e_m^2 - 2R e_m \sin \Theta}{2R^2} - \frac{e_m^2 \sin^2 \Theta}{2R^2} + \dots \right]. \quad (4.42)$$

But, because the angle Θ itself is assumed to be small, in the paraxial approximation we can drop the last term in Eq. (4.42), giving

$$r_{em} = R - e_m \sin \Theta + \frac{e_m^2}{2R}. \quad (4.43)$$

Placing this result into Eq. (4.40) we have

$$\frac{p(\mathbf{x}, \omega)}{\rho c v_0(\omega)} = \sum_{m=1}^M \tilde{C}_m \exp(i\omega \Delta t_m) \exp\left(ik \frac{e_m^2}{R}\right) \left[kb \sqrt{\frac{2}{\pi i}} \right] \exp(-ike_m \sin \Theta) D_b(\Theta) \frac{\exp(ikR)}{\sqrt{kR}}. \quad (4.44)$$

However, if we use the paraxial focusing delay law (Eq. (4.37)) and let $R = R_0$, we see that the phase terms involving e_m^2 cancel and the pressure at the focal distance is just

$$p = \sum_{m=1}^M \rho c v_0(\omega) \tilde{C}_m \left[kb \sqrt{\frac{2}{\pi i}} \right] \exp(-ike_m \sin \Theta) D_b(\Theta) \frac{\exp(ikR_0)}{\sqrt{kR_0}}. \quad (4.45)$$

Comparing Eq. (4.45) with Eq. (4.14) we see that the pressure field at the focal distance is now just the same as the far field pressure of the entire array with no delays applied to the elements. This is consistent with what we found in Chap. 3 (Sect. 3.2) when examining focusing behavior in the paraxial approximation with a large, single element transducer.

4.4 Array Amplitude Weighting

The continuous amplitude weights discussed in Chap. 3 can be sampled to generate the discrete weights, \tilde{C}_m , needed for arrays. The cosine, Hanning, Hamming, and Blackman windows all contain the functions $\cos(n\pi x' / L)$ ($n = 1, 2, 4$). If we let $x' = e_m$, the centroid location of the m th element in an array, and choose $L = 2(B - b)$ so that all the windows (except the Hanning window) taper to zero at the centroids of the first and last element in the array, then from Eq. (4.4) we have $L = s(M - 1)$ and it follows that

$$\cos\left(\frac{n\pi x'}{L}\right) \rightarrow \cos\left[\frac{n\pi s\{m-1-(M-1)/2\}}{s(M-1)}\right] = \cos\left[\frac{n\pi(m-1)}{M-1} - \frac{n\pi}{2}\right], \quad (4.46)$$

so that

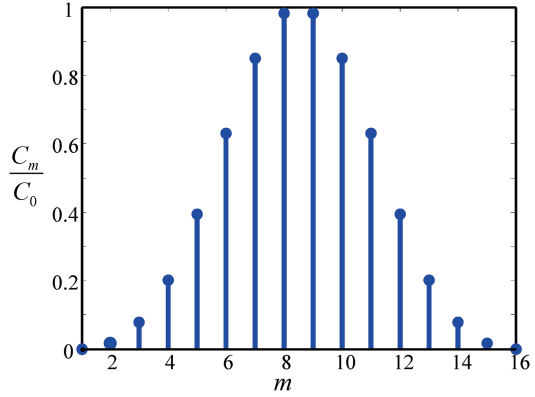
$$\begin{aligned} \cos\left(\frac{\pi x'}{L}\right) &\rightarrow \sin\left[\frac{\pi(m-1)}{M-1}\right] \\ \cos\left(\frac{2\pi x'}{L}\right) &\rightarrow -\cos\left[\frac{2\pi(m-1)}{M-1}\right] \\ \cos\left(\frac{4\pi x'}{L}\right) &\rightarrow \cos\left[\frac{4\pi(m-1)}{M-1}\right] \end{aligned} \quad (4.47)$$

and the discrete forms of these windows become:

Cosine Window

$$\tilde{C}_m = C_0 \sin\left[\frac{\pi(m-1)}{M-1}\right], \quad (4.48)$$

Fig. 4.12 The normalized amplitude weights using the Blackman window



Hanning Window

$$\tilde{C}_m = C_0 \sin^2 \left[\frac{\pi(m-1)}{M-1} \right], \quad (4.49)$$

Hamming Window

$$\tilde{C}_m = C_0 \left\{ 0.54 - 0.46 \cos \left[\frac{2\pi(m-1)}{M-1} \right] \right\}, \quad (4.50)$$

Blackman Window

$$\tilde{C}_m = C_0 \left\{ 0.42 - 0.5 \cos \left[\frac{2\pi(m-1)}{M-1} \right] + 0.08 \cos \left[\frac{4\pi(m-1)}{M-1} \right] \right\}. \quad (4.51)$$

For the triangular window the same choices of $x' = e_m$ and $L = s(M-1)$ gives

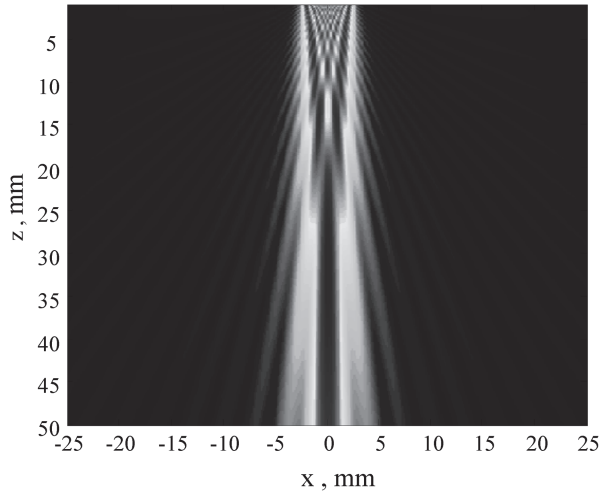
$$\tilde{C}_m = C_0 \left\{ 1 - \left| \frac{2(m-1)}{M-1} - 1 \right| \right\}. \quad (4.52)$$

The MATLAB[®] function `discrete_windows` given in Code Listing C.13 generates normalized discrete weights (i.e. with $C_0 = 1$). The calling sequence for this function is

```
>> amp=discrete_windows(M, type);
```

The function outputs the non-dimensional amplitudes $\text{amp} = \tilde{C}_m / C_0$ for M elements and windows of type 'cos' (cosine), 'Han' (Hanning), 'Ham' (Hamming), 'Blk' (Blackman), 'tri' (triangle) and 'rect' (rectangular). The case 'rect' is where all elements have equal weights of one, i.e. there is no apodization. Figure 4.12 shows an example of the discrete weights generated with this function using the Blackman window for a 16 element array.

Fig. 4.13 A 32 element array radiating into water at 5 MHz. Element size is one half a wavelength with a gap size equal to one tenth of an element length



4.5 Array Beam Modeling Examples

The multiple line source model of Eq. (4.7) can be combined with appropriate delay laws and apodization laws to generate a complete beam model for an array. The MATLAB[®] script `mls_array_modeling` given in Code Listing C.14 uses such a combination to produce images of the array wave field. The calling sequence of the script is simply

```
>> mls_array_modeling
```

The script uses the multiple line source beam model for each element contained in the function `ls_2Dv` and obtains the time delay law and apodization law from the functions `delay_laws2D` and `discrete_windows` discussed previously. The script also contains the MATLAB[®] function `elements` (Code Listing C.15) which has the calling sequence

```
>> [D, d, g, e] = elements(f, c, dl, gd, M);
```

where f is the frequency (in MHz), c is the wave speed (in m/s), $dl = 2b / \lambda$ is the length of the element, $d = 2b$, divided by the wavelength, λ . The parameter $gd = \Delta / 2b$ is the gap size, Δ , divided by the element length, and M is the total number of elements in the array. This function returns the total length of the array aperture $D = 2B$ (in mm), the length of each element $d = 2b$ (in mm), the gap size, $g = \Delta$, (in mm), and a $[1 \times M]$ vector e whose m th term is the location of the centroid of the m th element, e_m , (in mm) given by Eq. (4.6).

To apply this script, let us first consider a 32 element array radiating into water ($c = 1480$ m/s) with an element size of one half a wavelength and with no delay laws or apodization laws. Figure 4.13 show an image of the magnitude of the pressure

Fig. 4.14 A 32 element array radiating into water at 5 MHz. Element size is two wave lengths with a gap size equal to one tenth of an element length

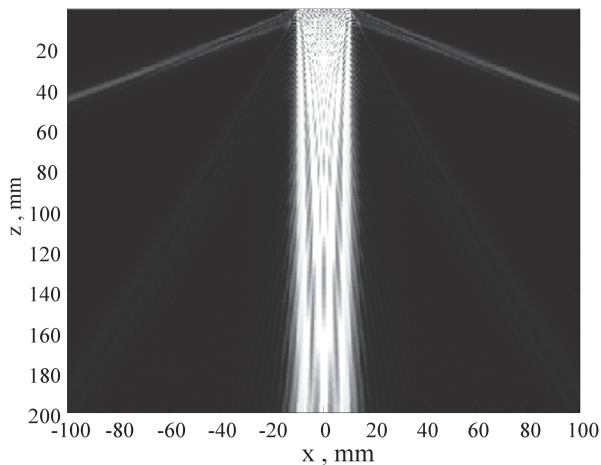
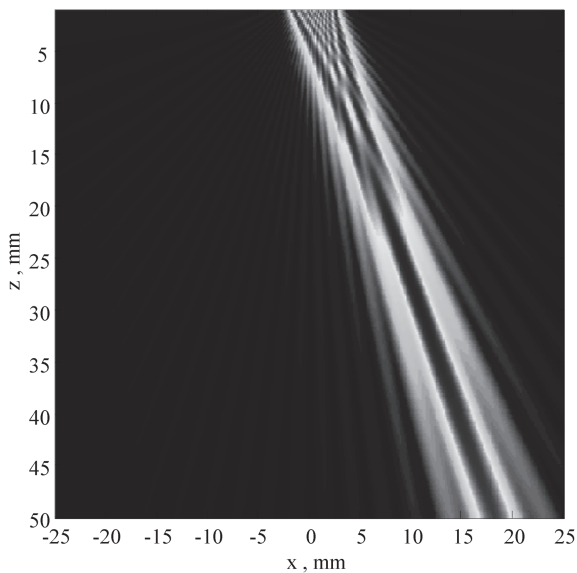


Fig. 4.15 A 32 element array radiating into water at 5 MHz with a delay law to produce a steering angle of 20° and no focusing ($\Phi = 20^\circ$, $F = \infty$). Element size is one half a wave length with a gap size equal to one tenth of an element length



generated by this array. It can be seen that there are no grating lobes visible and the array generates a near field beam structure similar to that of a single element transducer. However, if one changes the element length to be two wavelengths, with all other parameters staying the same, then we see definite grating lobes in addition to the main beam (Fig. 4.14). If we apply a steering law only to the array considered in Fig. 4.13 the wave field in Fig. 4.15 looks as if it was coming from a rotated transducer as discussed in Chap. 3. Figure 4.16 shows the 32 element array considered in Fig. 4.13 when a focusing delay law is used to focus the beam at a distance of 20 mm. It can be seen that the beam does develop a beam “waist” near the specified focal point. As a final example, consider the array example of Fig. 4.13 again

Fig. 4.16 A 32 element array radiating into water at 5 MHz with a delay law to produce focusing and no steering ($\Phi=0$, $F=20$ mm). Element size is one half a wave length with a gap size equal to one tenth of an element length

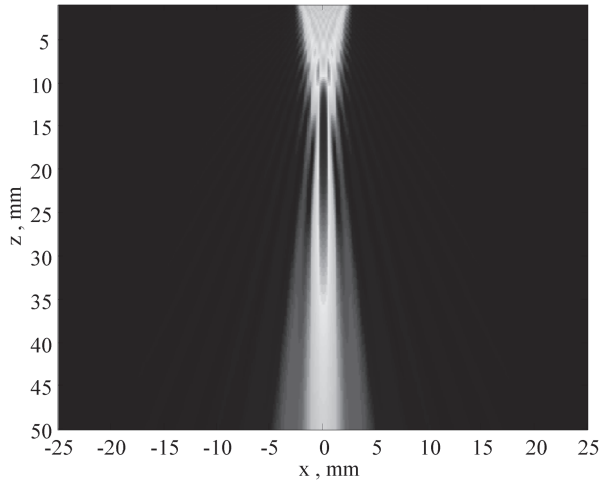
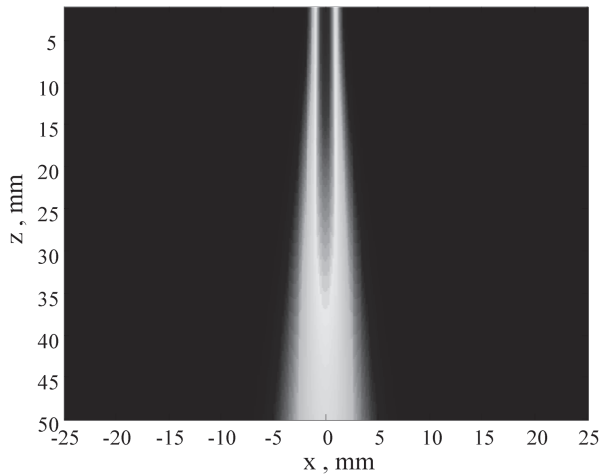


Fig. 4.17 A 32 element array radiating into water at 5 MHz. Element size is one half a wave length with a gap size equal to one tenth of an element length. A Blackman apodization law is applied to the elements



but where we apply Blackman apodization weights to the array. As can be seen in Fig. 4.17, this apodization produces a beam with a much smoother profile and without the visible side lobes of Fig. 4.13.

4.6 Use of Gaussians for Modeling Phased Array Beam Fields

In Chap. 3 we showed that a multi-Gaussian beam model is an effective model for large single element transducers. Because of the use of the paraxial approximation in the multi-Gaussian beam model, which assumed that the entire beam of the

element was contained in a narrow region centered around the z -axis (normal to the element), that model cannot accurately predict the fields at large angles from the z -axis of small elements, as is required in phased arrays when significant beam steering is present. However, it is still possible to use the Gaussian basis functions developed by Wen and Breazeale in conjunction with a high frequency line source model to model properly the wave field at large angles of small elements by using a non-paraxial expansion [6]. To see this, we start from the high frequency line source model with a Gaussian velocity profile on the surface at $z=0$ (see Eq. (3.99)), which we rewrite as

$$p(\mathbf{x}, \omega) = \rho c v_0(\omega) A \sqrt{\frac{k}{2\pi i}} \int_{-\infty}^{+\infty} \exp\left[-B(x')^2 / b^2\right] \frac{\exp(ikr)}{\sqrt{r}} dx', \quad (4.53)$$

where $\mathbf{x} = (x, z)$ and $r = \sqrt{(x - x')^2 + z^2}$. However, instead of expanding the radius, r , about the z -axis, as is done with the paraxial approximation, we let

$$\begin{aligned} r &= \sqrt{x^2 + z^2 - 2xx' + (x')^2} \\ &= \sqrt{r_0^2 - 2xx' + (x')^2} \\ &= r_0 \sqrt{1 + \frac{(x')^2 - 2xx'}{r_0^2}}, \end{aligned} \quad (4.54)$$

where $r_0 = \sqrt{x^2 + z^2}$ and assume that $x' / r_0 \ll 1$ (which is valid for a small element if we are not too close to the element). This same expansion was discussed in Chap. 2 when looking at the validity of the far field approximation (see Eqs. (2.39), (2.40), and (2.41)) and we found that to keep at least quadratic terms in the expansion we had to use three terms in the binomial expansion to find

$$r \cong r_0 - \frac{xx'}{r_0} + \frac{(x')^2 \cos^2 \theta}{2r_0}, \quad (4.55)$$

where $\cos \theta = z / r_0$ and θ is the angle that the radius r_0 makes with respect to the z -axis. Note that the original derivation [6] of this approach kept only two terms in the expansion which had the effect of making the replacement $\cos^2 \theta \rightarrow 1$. Placing the correct second order approximation of Eq. (4.55) into Eq. (4.53) then gives

$$p(\mathbf{x}, \omega) = \rho c v_0(\omega) \sqrt{\frac{k}{2\pi i}} A \frac{\exp(ikr_0)}{\sqrt{r_0}} \int_{-\infty}^{+\infty} \exp\left[ik(x')^2 \left(\frac{\cos^2 \theta}{2R} + \frac{iB}{kb^2}\right)\right] \exp\left[\frac{-ikxx'}{R}\right] dx'. \quad (4.56)$$

But the integral in Eq. (4.56) can be done [Schmerr-Song], leading to the explicit expression

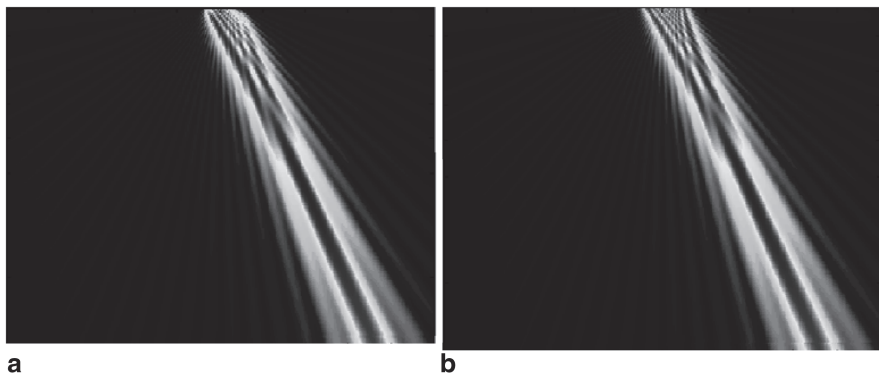


Fig. 4.18 A 32 element array radiating into water at 5 MHz with a delay law to produce a steering angle of 20° and no focusing ($\Phi = 20, F = \infty$). Element size is one half a wave length with a gap size equal to one tenth of an element length. This is the same case considered in Fig. 4.15 where the wave field was calculated with a multiple line source model. Here, the wave field is calculated with (a) a non-paraxial Gaussian model and (b) with a Hankel function model.

$$p(\mathbf{x}, \omega) = \frac{\rho c v_0(\omega) A \exp(ikr_0)}{\sqrt{\cos^2 \theta + iBr_0 / D}} \exp\left[\frac{-ikx^2}{2r_0(\cos^2 \theta + iBr_0 / D)}\right], \quad (4.57)$$

where $D = kb^2 / 2$ is the *Rayleigh distance* [Schmerr-Song]. Here we will use the 10 rather than the 15 Wen and Breazeale coefficients for piston behavior [7] in order to keep the calculation times to a minimum. We then have a complete beam model for an element in the form

$$p(\mathbf{x}, \omega) = \sum_{n=1}^{10} \frac{\rho c v_0(\omega) A_n \exp(ikr_0)}{\sqrt{\cos^2 \theta + iB_n r_0 / D}} \exp\left[\frac{-ikx^2}{2r_0(\cos^2 \theta + iB_n r_0 / D)}\right]. \quad (4.58)$$

The MATLAB[®] function NPGauss_2D (Code Listing C.16) which has the calling sequence

```
>>p=NPGauss_2D(b, f, c, e, x, z);
```

implements Eq. (4.58) for an element whose center is offset a distance, e , in the x -direction, so that $r_0 = \sqrt{(x-e)^2 + z^2}$. It uses the ten Wen and Breazeale coefficients which are contained in the MATLAB[®] function gauss_c10 (Code Listing C.17). One can replace the multiple line source beam model ls_2Dv in the MATLAB[®] script mls_array_model with NPGauss_2D to generate comparable results for phased arrays. Figure 4.18a shows the same setup considered in Fig. 4.15 (a 32 element array radiating into water at 5 MHz with a delay law to produce a steering angle of 20° and no focusing. The element size was one half a wave length with a gap size equal

to one tenth of an element length) but with the use of the non-paraxial Gaussian model in the MATLAB[®] script `mls_array_model` in place of `ls_2Dv`. Figure 4.18b shows again the same results but with the Hankel function beam model (contained in the MATLAB[®] function `rs_2Dv`) used in place of `ls_2Dv` in the same script. It can be seen from Figs. 4.15 and 4.18 that the Hankel function model and multiple line source model results appear identical and the non-paraxial Gaussian model also agrees quite well with the other two models but with some differences appearing in the very near field region adjacent to the face of the array where the expansion of Eq. (4.55) cannot be expected to be accurate. However, the non-paraxial Gaussian model took 13 times longer to evaluate than the multiple line source model and the Hankel function model took 8.3 times longer than the multiple line source model so the multiple line source model appears to be the best overall choice for simulating phased arrays in 2-D problems. This is not surprising since the multiple line source model uses only a single line source term for the small element size considered here (element length less than a wavelength) whereas the other models use multiple element segments or basis functions in their calculations. Even for larger array elements the multiple line source model remains efficient, losing its advantage only when the element length is tens of wavelengths, as found in large, single element transducers. In contrast, for large, single element circular transducers a paraxial multi-Gaussian beam model only needs ten or fifteen Gaussians to produce accurate wave field calculations [Schmerr-Song] so it is typically the fastest beam model available for those cases, particularly when calculating the fields through interfaces.

4.7 Beam Steering and Focusing through a Planar Interface

In Chap. 2 we also described modeling the radiation of an element through a planar interface. We can use that model and combine it with the beam steering and focusing laws developed in Chap. 5 for this case and the discrete apodization laws of Sect. 4.4 to simulate array wave fields with an interface present. All these elements are combined in the MATLAB[®] script `mls_array_int` (Code Listing C.18) which is very similar in structure to the `mls_array_modeling` script for a single medium used in Sect. 4.5. The calling sequence for this script is simply

```
>>mls_array_int
```

The script uses the beam modeling MATLAB[®] function `ls_2Dint` discussed in Chap. 2 as well as the MATLAB[®] `discrete_windows` function for the apodization laws. The time delay laws are generated in the MATLAB[®] function `delay_laws_2D_int` (Code Listing C.19) developed in Chap. 5. The calling sequence for this delay law function is

```
td=delay_laws2D_int(M, s, angt, ang20, DT0, DF, c1, c2, n)
```


Fig. 4.19 Geometry and material parameters for steering and focusing an array through a planar interface

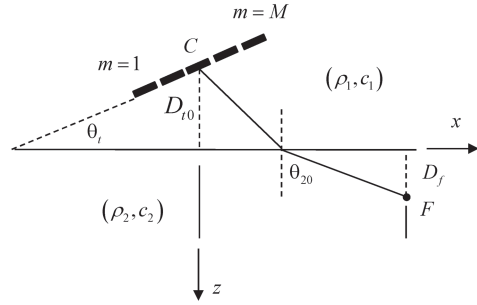
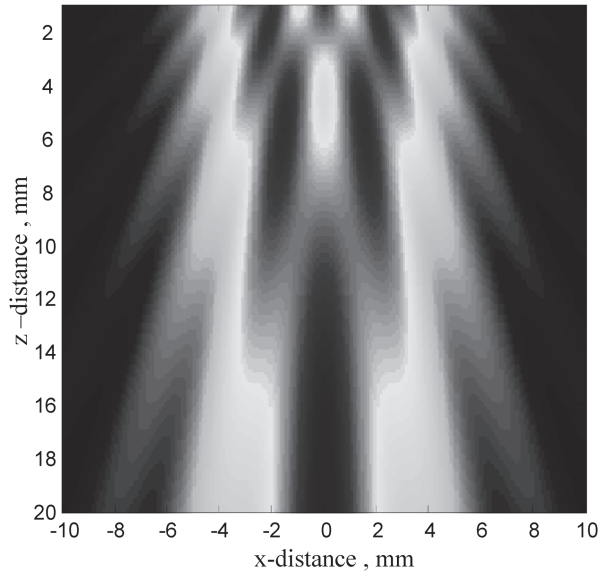


Fig. 4.20 Normalized pressure wave field in steel for a 32 element array located in water at a distance of $D_{t0} = 25.4$ mm from a water-steel interface. Other setup parameters are: $d = 2b = 0.25$ mm, $\Delta = 0.05$ mm, $\theta_i = 0^\circ$, $f = 5$ MHz, no apodization or steering/focusing



where td holds the delay times (in microseconds), M is the number of elements in the array, s is the array pitch (in mm), $angt = \theta_i$ is the angle the array makes with the interface (in degrees), $ang20 = \theta_{20}$ is the specified steering angle (in degrees) as measured in the second medium, $DTO = D_{t0}$ is the distance of the center of the array from the interface (in mm), $DF = D_f$ is the specified focal depth in the second medium (in mm). If $DF = \text{inf}$ is specified then steering without focusing is present. The variables $(c1, c2)$ are the wave speeds in the first and second media, respectively, in m/s. The final input string parameter ('y' or 'n') specifies if a plot of the rays corresponding to the delay law parameters is wanted. Figure 4.19 illustrates these various parameters and Chap. 5 gives more details of this function.

To illustrate the use of this script, consider the case of a 32 element array in water located 25.4 mm from a water-steel interface and oriented parallel to the interface ($\theta_i = 0^\circ$). Figure 4.20 shows results for the case where the element length is 0.25 mm, the gap length is 0.05 mm, the frequency is 5 MHz, and no apodization or

Fig. 4.21 Normalized pressure wave field in steel for a 32 element array located in water at a distance of $D_{t0} = 25.4$ mm from a water-steel interface. Other setup parameters are: $d = 2b = 0.25$ mm, $\Delta = 0.05$ mm, $\theta_i = 0^\circ$, $f = 5$ MHz, $\theta_{20} = 30^\circ$, $D_f = \text{inf}$, no apodization

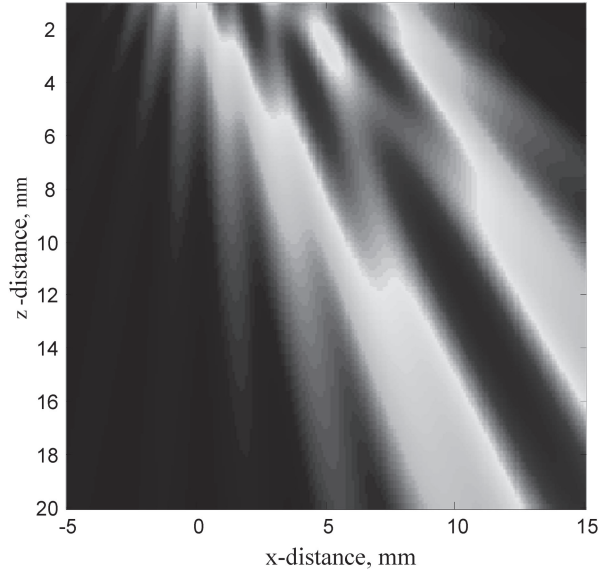
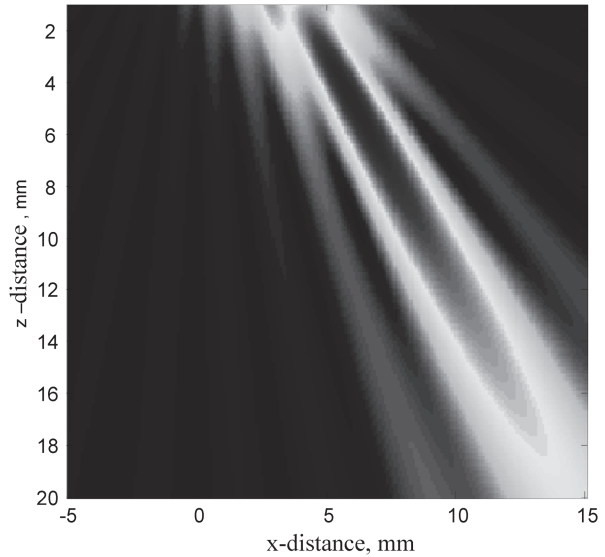


Fig. 4.22 Normalized pressure wave field in steel for a 32 element array located in water at a distance of $D_{t0} = 25.4$ mm from a water-steel interface. Other setup parameters are: $d = 2b = 0.25$ mm, $\Delta = 0.05$ mm, $\theta_i = 0^\circ$, $f = 5$ MHz, $\theta_{20} = 30^\circ$, $D_f = 8$ mm, no apodization



delay law is specified for the array. The near field structure of this array wave field in the steel can be clearly seen in Fig. 4.20. Figure 4.21 shows the same setup as in Fig. 4.20 but where now a delay law is chosen to steer the array, without focusing, at an angle $\theta_{20} = 30^\circ$ in the steel. Figure 4.22 is for the case where a steering angle $\theta_{20} = 30^\circ$ is again specified, along with a focal depth $D_f = 8$ mm. Steering and focusing effects consistent with these choices of the delay law are clearly evident. Figure 4.23 shows the wave field of a 16 element array where the element length is 0.325 mm and the gap length is 0.05 mm but where $D_{t0} = 50.8$ mm the array is now

Fig. 4.23 Normalized pressure wave field in steel for a 16 element array located in water at a distance of $D_{t0} = 50.8$ mm from a water-steel interface, $\theta_t = 10.217^\circ$. Other setup parameters are: $d = 2b = 0.325$ mm, $\Delta = 0.05$ mm, $f = 5$ MHz, $\theta_{20} = 45^\circ$ (no steering), $D_f = \text{inf}$, no apodization

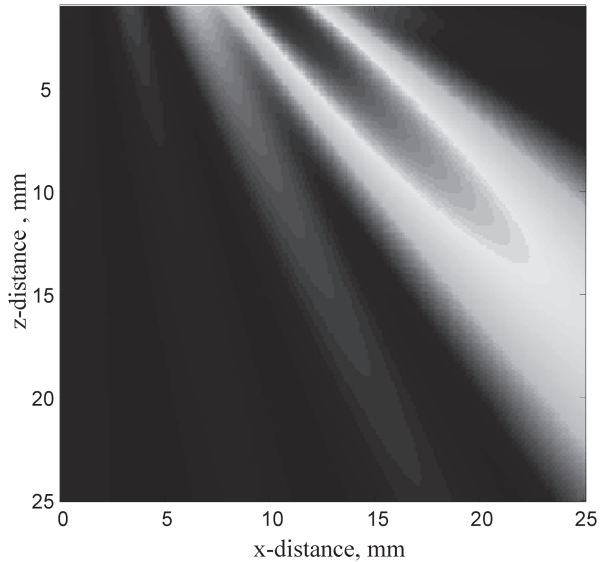
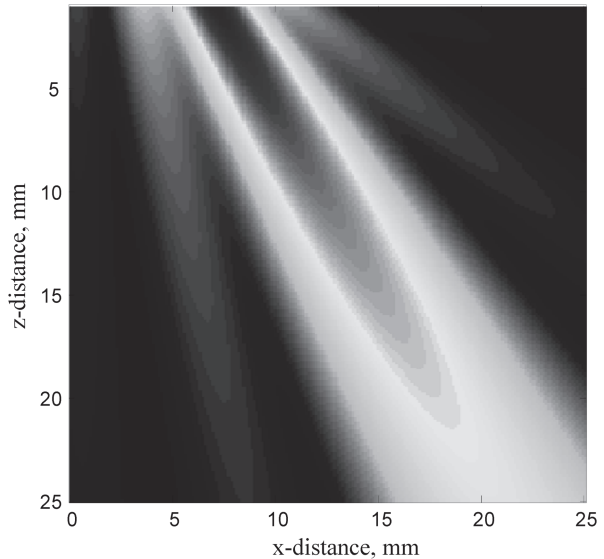


Fig. 4.24 Normalized pressure wave field in steel for a 16 element array located in water at a distance of $D_{t0} = 50.8$ mm from a water-steel interface, $\theta_t = 10.217^\circ$. Other setup parameters are $d = 2b = 0.325$ mm, $\Delta = 0.05$ mm, $f = 5$ MHz, $\theta_{20} = 30^\circ$, $D_f = \text{inf}$, no apodization



at an angle $\theta_t = 10.217^\circ$ from the interface. By Snell's law this will generate a refracted beam at 45° in the steel. In this case the time delay law parameters were chosen to be $\theta_{20} = 45^\circ$, $D_f = \text{inf}$, so that there is no steering or focusing. The size of this array is the same as the large single element transducer example shown in Fig. 2.17 so it is not surprising that without steering or focusing the wave field images are very similar. Figure 4.24 shows the same array of Fig. 4.23 but with beam steering specified as $\theta_{20} = 30^\circ$. It can be seen that the wave field has indeed been shifted to the new specified refracted angle. The 2-D modeling studies of this chapter are in

the spirit of those done by Wooh et al [1–3]. See also [4–5] for some similar modeling simulations and discussions of efficiency.

References

1. S.-C. Wooh, Y. Shi, A simulation study of the beam steering characteristics for linear phased arrays. *J. Nondestr. Eval.* **18**, 39–57 (1999).
2. A. Clay, S.-C. Wooh, L. Azar, J.-Y. Wang, Experimental study of phased array beam steering characteristics. *J. Nondestr. Eval.* **18**, 59–71 (1999).
3. S.-C. Wooh, Y. Shi, Optimum beam steering of linear phased arrays. *Wave. Motion.* **29**, 245–265 (1999).
4. E. Kuhnicke, Plane arrays—fundamental investigations for correct steering by means of sound field calculations. *Wave. Motion.* **44**, 248–261 (2007).
5. P. Crombie, A.J. Bascom, R. Cobbold, Calculating the pulsed response of linear arrays: accuracy versus computational efficiency. *IEEE T. Ultrason. Ferr.* **44**, 997–1009 (1997).
6. X. Zhao, T. Gang, Non-paraxial multi-Gaussian beam models and measurement models for phased array transducers. *Ultrasonics.* **49**, 126–130 (2009).
7. J.J. Wen, M.A. Breazeale, A diffraction beam field expressed as a superposition of Gaussian beams. *J. Acoust. Soc. Am.* **83**, 1752–1756 (1988).

Chapter 5

Time Delay Laws (2-D)

In Chap. 3 we introduced continuous time delay laws for beam steering and focusing of large, single element transducers and we obtained discrete versions of those laws in Chap. 4 for phased arrays. The explicit focusing delay laws discussed in both previous chapters used the paraxial approximation. This approximation gave us a simple delay law to implement and it was consistent with the paraxial approximation used in the beam models in Chap. 3. However, there is no requirement to introduce such approximations in the delay laws designed for phased arrays. In this chapter we will derive exact delay laws for combined steering and focusing in a single medium and describe the case where the steered/focused beam must pass through a planar interface. In all cases, we will limit our discussion in this chapter to 1-D arrays radiating waves in two-dimensions. The corresponding delays laws for 2-D arrays radiating into three dimensions will be discussed in Chap. 8.

5.1 Delay Laws for a Single Medium

In designing a delay law for steering and focusing a 1-D array in two dimensions, one can parameterize the delay law in several ways. One way is to specify the steering angle, Φ , as measured along the central axis of the entire array, and the focal distance, F , as measured along this axis (see Fig. 5.1a and b). For both cases shown in Fig. 5.1 the distance from the center of the array to the center of the first element is $B - b = (M - 1)s / 2$, where $2B$ is the total length of the array, $2b$ is the length of an element, and s is the pitch of the array (see Eq. (4.5)). The quantity $(M - 1) / 2$ will appear frequently in our delay law expressions so we will abbreviate that quantity as \bar{M} :

$$\bar{M} = \frac{(M - 1)}{2}. \quad (5.1)$$

The distance to the centroid of the m th element, e_m , in terms of \bar{M} is then

$$e_m = [(m - 1) - \bar{M}]s. \quad (5.2)$$

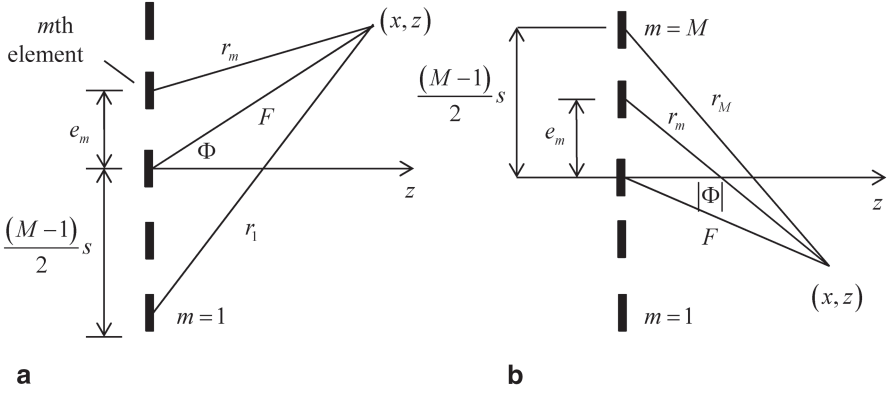


Fig. 5.1 **a** Geometrical parameters for steering and focusing an array when $\Phi \geq 0$, and **b** when $\Phi < 0$

Consider first the case when $\Phi \geq 0$ (Fig. 5.1a). To obtain the delay law to steer and focus the beam to the point (x, z) we first calculate the times it takes to propagate from the centroid of the m th element to (x, z) , $\Delta t_m = r_m / c$, where c is the wave speed. If we apply the negative of these times (representing time advances) to all the elements then all of the waves from the elements will arrive at (x, z) at the same time. To turn this result into a proper delay law we must also add a positive, constant term so that all of these time values are time delays, not advances. It is obvious from Fig. 5.1a that the distance from the first element to (x, z) , r_1 , is the largest distance for the entire array, so that a proper delay law is simply

$$\Delta t_d = r_1 / c - r_m / c. \quad (5.3)$$

From the geometry of Fig. 5.1a and the law of cosines, we then have

$$\begin{aligned} r_1 &= \sqrt{F^2 + (\bar{M}s)^2 + 2F\bar{M}s \sin \Phi} \\ r_m &= \sqrt{F^2 + (e_m)^2 - 2Fe_m \sin \Phi} \end{aligned} \quad (5.4)$$

and the delay law becomes

$$\Delta t_d = \frac{1}{c} \left[\sqrt{F^2 + (\bar{M}s)^2 + 2F\bar{M}s \sin \Phi} - \sqrt{F^2 + (e_m)^2 - 2Fe_m \sin \Phi} \right]. \quad (5.5)$$

In comparison, for $\Phi < 0$, if we use the geometry of Fig. 5.1b we find instead

$$\begin{aligned} \Delta t_d &= r_M / c - r_m / c \\ &= \frac{1}{c} \left[\sqrt{F^2 + (\bar{M}s)^2 + 2F\bar{M}s \sin |\Phi|} - \sqrt{F^2 + (e_m)^2 + 2Fe_m \sin |\Phi|} \right]. \end{aligned} \quad (5.6)$$

It should be noted that although Fig. 5.1 shows a geometry for an array with an odd number of elements, there is nothing in the expressions used in the derivation that restricts our results to that case and so these delay laws are valid for arrays with either an even or odd number of elements. Azar et. al. [1] used a similar approach to develop these delay laws, which are also applicable to linear arrays operating in a 3-D setting since such arrays can only be steered and focused in a plane with the 2-D delay laws given here.

We can compare these exact laws with our previous results which used the paraxial approximation. If we are focusing the beam to a point well removed from the face of the array then we can expand Eqs. (5.5) and (5.6) for F large and obtain to second order (keeping three terms in the expansion as shown in Eq. (2.42)) For $\Phi \geq 0$ we find

$$\begin{aligned}\Delta t_d &= \frac{F}{c} \left[\sqrt{1 + \frac{(\bar{M}s)^2 + 2F\bar{M}s \sin \Phi}{F^2}} - \sqrt{1 + \frac{(e_m)^2 - 2Fe_m \sin \Phi}{F^2}} \right] \\ &\cong \frac{F}{c} \left[1 + \frac{(\bar{M}s)^2 + 2F\bar{M}s \sin \Phi}{2F^2} - \frac{1}{8} \frac{4(\bar{M}s)^2 \sin^2 \Phi}{F^2} \right. \\ &\quad \left. - 1 - \frac{(e_m)^2 - 2Fe_m \sin \Phi}{2F^2} + \frac{1}{8} \frac{4(e_m)^2 \sin^2 \Phi}{F^2} \right],\end{aligned}\quad (5.7)$$

whereas for $\Phi < 0$ we have

$$\begin{aligned}\Delta t_d &= \frac{F}{c} \left[\sqrt{1 + \frac{(\bar{M}s)^2 + 2F\bar{M}s \sin |\Phi|}{F^2}} - \sqrt{1 + \frac{(e_m)^2 + 2Fe_m \sin |\Phi|}{F^2}} \right] \\ &\cong \frac{F}{c} \left[1 + \frac{(\bar{M}s)^2 + 2F\bar{M}s \sin |\Phi|}{2F^2} - \frac{1}{8} \frac{4(\bar{M}s)^2 \sin^2 \Phi}{F^2} \right. \\ &\quad \left. - 1 - \frac{(e_m)^2 + 2Fe_m \sin |\Phi|}{2F^2} + \frac{1}{8} \frac{4(e_m)^2 \sin^2 \Phi}{F^2} \right].\end{aligned}\quad (5.8)$$

Using the definition of \bar{M} and e_m from Eqs. (5.1) and (5.2) and collecting terms and simplifying we obtain, for $\Phi \geq 0$

$$\Delta t_d \cong \frac{1}{c} \left[\frac{(m-1)(M-m)s^2 \cos^2 \Phi}{2F} + (m-1)s \sin \Phi \right], \quad (5.9)$$

and, for $\Phi < 0$

$$\Delta t_d \cong \frac{1}{c} \left[\frac{(m-1)(M-m)s^2 \cos^2 \Phi}{2F} + (M-m)s \sin |\Phi| \right], \quad (5.10)$$

which are a combination of the steering laws and focusing laws developed previously in the paraxial approximation (see Eqs. (4.35) and (4.39) and let $\sin|\Phi| = |\sin\Phi|$ and $F = R_0$).

If we want to use the combined steering and focusing laws of Eqs. (5.5) and (5.6) for steering only, we have to let $F \rightarrow \infty$. It can be seen from Eqs. (5.9) and (5.10) that we do recover the proper limit but only because of canceling infinities in Eqs. (5.7) and (5.8), a procedure which is difficult to implement in software. Thus, it is best to treat steering only as a special case.

Parameterization of the delay laws by specifying (F, Φ) is a logical choice but another convenient way to design the delay law is to specify the point (x, z) in the medium to which we want to steer and focus the beam. Since $F = \sqrt{x^2 + z^2}$, $\sin\Phi = x/F$, we could specify that point and then use these relations in the delay laws Eqs. (5.5) and (5.6). However, we could also simply write the time delay as

$$\begin{aligned}\Delta t_d &= \max \left\{ \frac{r_m}{c} \right\} - \frac{r_m}{c} \\ &= \max \left\{ \frac{\sqrt{(x - e_m)^2 + z^2}}{c} \right\} - \frac{\sqrt{(x - e_m)^2 + z^2}}{c},\end{aligned}\quad (5.11)$$

which will also give a proper delay law.

The function `td=delay_laws2D(M, s, Phi, F, c)` discussed in the last Chapter (Code Listing C.12) implements Eqs. (5.5) and (5.6) to generate the delays, `td`, in microseconds needed to produce steering to a focal point at an angle Φ (Phi) (in degrees) and focusing at a distance F (in mm) for an array of M elements with a pitch, s , (in mm) and for a medium of wave speed c (in m/s). If F is specified as infinity ($F=\text{inf}$) the steering only delay law of Eq. (4.35) is used instead.

5.2 Steering and Focusing Through a Planar Interface

As seen in the last section, in a single medium it is relatively simple to set up the general time delay law based on the angle of beam steering (from the center of the transducer) and the desired focal point. In radiation through a plane interface, however, the relationship becomes more complex, particularly when focusing is involved.

We will begin by considering the case of beam steering only for the configuration shown in Fig. 5.2 where an array radiates at an angle through a plane interface. This type of setup can be used to model an immersion test where the array is placed in a water bath and radiates into a solid component or in an angle beam inspection where the array sits on a plastic wedge and radiates into the solid. In either of those cases the wave speed of second medium is larger, i.e. $c_2 > c_1$, which is a condition we will assume here. We will let the angle of the face of the array relative to the

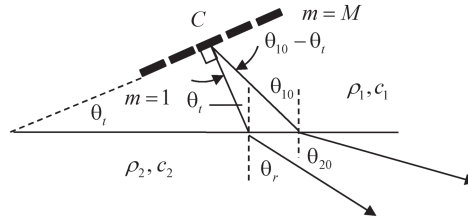


Fig. 5.2 A phased array radiating at oblique incidence to a planar interface, showing a reference ray that is normal to the face of the array and a ray which makes a specified angle, θ_{20} , relative to the normal of the interface

plane interface be θ_t as shown in Fig. 5.2. At high frequencies, each element of the array will radiate a wave field through the interface that will satisfy Snell's law [Schmerr]. Figure 5.2 shows a ray path of a wave that travels from the center point C of the array along a direction normal to the face of the array in the first medium and is refracted into the second medium at an angle θ_r . Just as we used the z -axis as the reference axis for no steering in a single medium we will use this central ray axis to define the case of no steering in this configuration. From Snell's law, then the refracted angle, θ_r , for the no steering case must satisfy

$$\frac{\sin \theta_r}{c_2} = \frac{\sin \theta_t}{c_1}, \quad (5.12)$$

where c_1 and c_2 are the wave speeds in the first and second media, respectively. Now, suppose we want to steer the beam so that the refracted angle is specified as θ_{20} instead. In this case from Snell's law the incident angle in the first medium must satisfy

$$\frac{\sin \theta_{10}}{c_2} = \frac{\sin \theta_{20}}{c_1}, \quad (5.13)$$

which can always be solved for a real angle θ_{10} as long as $c_2 > c_1$. At the array, this corresponds to steering the array in medium one at an angle $\theta_{10} - \theta_t$ relative to the reference ray in medium one. Thus, we can steer the array with the single medium delay law (see Eq. (4.2.12)):

$$\Delta t_m = \begin{cases} \frac{s \sin(\theta_{10} - \theta_t)}{c_1} (m-1) & (\theta_{10} - \theta_t) \geq 0 \\ \frac{s |\sin(\theta_{10} - \theta_t)|}{c_1} (M-m) & (\theta_{10} - \theta_t) < 0 \end{cases}, \quad (5.14)$$

with θ_{10} given in terms of θ_{20} by Eq. (5.13). Thus, with the use of Eq. (5.13) we can consider this a steering delay law parameterized in terms of (θ_t, θ_{20}) and the wave speeds of the two media. Note, however, that the specified angle θ_{20} is

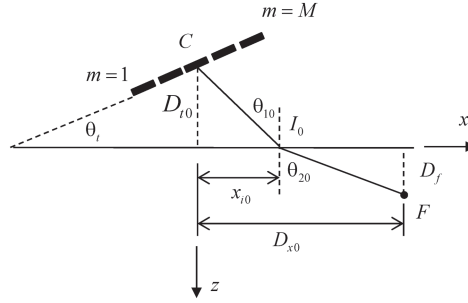


Fig. 5.3 Geometry parameters for steering and focusing a beam through a plane interface at a refracted angle, θ_{20} , and to a depth, D_f

relative to a refracted ray which is different from the reference ray chosen for no steering (see Fig. 5.2).

Now consider the case of both steering and focusing (Fig. 5.3). Again we will assume the array makes an angle, θ_t , relative to the interface and we will let D_{t0} be the vertical distance of the center point C of the array above the interface. Our beam steering and focusing law will be based on parameters $(D_{t0}, D_f, \theta_{20})$ that describe a ray path from C to a point I_0 on the interface and then from I_0 to point F at a refracted angle, θ_{20} , and to a depth, D_f , in the second medium. Although there are an infinite number of paths that one could take going from C to I_0 and then from I_0 to F , at high frequencies the waves travel along the straight line paths that satisfy Snell's law, so that Eq. (5.13) is satisfied. In this case the specific path from C to F is completely specified since the angle θ_{10} is given by Eq. (5.13) which then also determines the location of the point I_0 on the interface as well as the horizontal distance, D_{x0} , to the point F , i.e. we have

$$\begin{aligned} x_{t0} &= D_{t0} \tan \theta_{10} \\ D_{x0} &= x_{t0} + D_f \tan \theta_{20}, \end{aligned} \quad (5.15)$$

where x_{t0} is the horizontal distance to the point I_0 on the interface from C (see Fig. 5.3). Note that as in the steering only case this Snell's law path is not in general normal to the transducer in medium 1, so that $\theta_{10} \neq \theta_t$ and there will be steering present unless one specifically chooses $\theta_t = \sin^{-1}(c_1 \sin \theta_{20}/c_2)$.

In this discussion we can give the location of the point F (relative to point C) to which we want the beam to be steered and focused by specifying the three parameters $(D_{t0}, D_f, \theta_{20})$. Specifying the angle θ_{20} is analogous to specifying the beam steering angle, Φ , in a single medium, and specifying the distances (D_{t0}, D_f) is analogous to specifying the distance, F , to the focal point in a single medium. We could, however, also parameterize the beam steering and focusing with three other parameters such as (D_{t0}, D_f, D_{x0}) , for example, but here we will develop our time delays only with the set $(D_{t0}, D_f, \theta_{20})$.

Once we have located the point F in this manner then we must determine the corresponding Snell's law path from the centroid of an element located at point P on

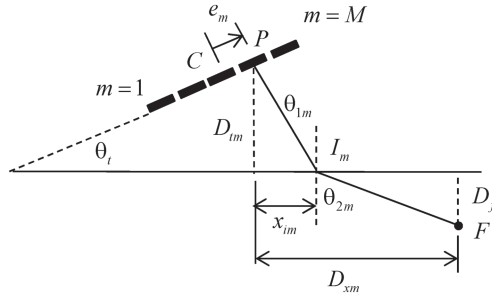


Fig. 5.4 Snell's law path from the centroid, P , of the m th element in an array to the point F at which we want to steer and focus the array

the transducer surface to the point F where we want to focus the array (see Fig. 5.4). Since point P is located a distance e_m from C , the vertical distance from P to the interface is D_{tm} and the horizontal distance from P to F is D_{xm} , where

$$\begin{aligned} D_{tm} &= D_{t0} + e_m \sin \theta_t \\ D_{xm} &= D_{x0} - e_m \cos \theta_t. \end{aligned} \quad (5.16)$$

Both of these distances are known if the parameters $(D_{t0}, D_f, \theta_{20}, e_m, \theta_t)$ are given. Here the angles $(\theta_{1m}, \theta_{2m})$ are unknown, as well as the distance x_{im} to the point I_m where a Snell's law path from the m th element intersects the plane interface (Fig. 5.4). However, Snell's law can be written in a form where satisfying it is equivalent to determining a value x_{im} that is the location of the zero of a function, $f(x_{im})$, since from the geometry of Fig. 5.4

$$\begin{aligned} f(x_{im}) &= \frac{\sin \theta_{2m}}{c_2} - \frac{\sin \theta_{1m}}{c_1} \\ &= \frac{1}{c_2} \frac{(D_{xm} - x_{im})}{\sqrt{D_f^2 + (D_{xm} - x_{im})^2}} - \frac{1}{c_1} \frac{x_{im}}{\sqrt{x_{im}^2 + D_{tm}^2}}. \end{aligned} \quad (5.17)$$

$= 0$

An equivalent form of Eq. (5.17) normalized by the distance D_{xm} is:

$$g(x_{im}) = \frac{(D_{xm} - x_{im})\sqrt{x_{im}^2 + D_{tm}^2} - (c_2 / c_1)x_{im}\sqrt{(D_{xm} - x_{im})^2 + D_f^2}}{D_{xm}} = 0. \quad (5.18)$$

There are several methods available to solve for x_{im} from Eq. (5.18) in MATLAB®. The function g goes from a positive value of $g = D_{tm}$ at $x_{im} = 0$ to a negative value $g = -(c_2 / c_1)D_f$ at $x_{im} = D_{xm}$ and there is a zero value in the interval $[0, D_{xm}]$. Thus, one method is to use the MATLAB® function `fzero` to determine the location x_{im}

of this zero of $g(x_{im})$ iteratively with Newton's method. A second approach is to eliminate the square roots in either Eq. (5.17) or Eq. (5.18) by squaring to generate a quartic equation in x_{im} of the form

$$a_4 x_{im}^4 + a_3 x_{im}^3 + a_2 x_{im}^2 + a_1 x_{im} + a_0 = 0, \quad (5.19)$$

where

$$\begin{aligned} a_4 &= [1 - (c_2 / c_1)^2] \\ a_3 &= 2[(c_2 / c_1)^2 - 1] D_{xm} \\ a_2 &= D_{xm}^2 + D_{im}^2 - (c_2 / c_1)^2 (D_{xm}^2 + D_f^2) \\ a_1 &= -2 D_{xm} D_{im}^2 \\ a_0 &= D_{xm}^2 D_{im}^2. \end{aligned} \quad (5.20)$$

The MATLAB[®] function `roots` can then be used to find the four roots of this quartic or one can use Ferrari's method [2, 3], to obtain the four roots directly. Two extraneous roots will be complex while one extraneous real root will lie outside the interval $[0, D_{xm}]$ so that one needs only to identify the one real root in that interval to obtain the proper value for x_{im} . The built in MATLAB[®] functions `fzero` and `roots` are both viable methods, but the use of Ferrari's method with the function `ferrari2` defined in Code Listing C.5 is more direct and will be the one implemented here. The calling sequence for this function is

$$>> xi = ferrari2(cr, DF, DT, DX);$$

where xi is the distance x_{im} , cr is the ratio of the wave speeds in the two media, $(c_r = c_1 / c_2)$, DF is the distance D_f , DT is the distance D_{im} , and DX is the distance D_{xm} (see Fig. 5.4). The function `ferrari2` is faster than the use of either `fzero` or `roots`. For example, in evaluating the ray paths to a set of 200×200 values of D_{x0} and D_f (which would be necessary when determining the delays needed for forming an image at these points—see Chaps. 12 and 13) the use of Ferrari's method is approximately 1.9 times faster than the use of `roots`, and 15.1 times faster than the use of `fzero`.

Once x_{im} is found, then the angles $(\theta_{1m}, \theta_{2m})$ are given by

$$\begin{aligned} \theta_{1m} &= \tan^{-1} \left(\frac{x_{im}}{D_{im}} \right) \\ \theta_{2m} &= \tan^{-1} \left(\frac{D_{xm} - x_{im}}{D_f} \right) \end{aligned} \quad (5.21)$$

and the propagation time in going from P to F , t_m^{PF} , is

$$t_m^{PF} = \frac{\sqrt{x_{im}^2 + D_{im}^2}}{c_1} + \frac{\sqrt{D_f^2 + (D_{xm} - x_{im})^2}}{c_2}. \quad (5.22)$$

If we subtract these propagation times from every path going from P to F , then the waves for all these paths (and all the elements) will arrive at point F at the same time, i.e. we will have steered the array at an angle θ_{20} and focused it at point F . However, this would correspond to applying time advances $\Delta t_m = -t_m^{PF}$. As in the single medium case we can simply add a constant value to these delays that makes all the Δt_m values positive and we do have a realizable beam steering/focal law time delay, Δt_m^d , given by

$$\Delta t_m^d = \left(t_m^{PF} \right)_{\max} - t_m^{PF}. \quad (5.23)$$

The MATLAB[®] function `delay_laws2D_int` given in Code Listing C.19 implements the delay law for steering, Eq. (5.14) and for steering and focusing, Eq. (5.23), through a plane interface. The calling sequence for this function is:

```
>>td=delay_laws2D_int(M, s, angt, ang20, DT0, DF, c1, c2, plt);
```

where `td` is the delay times for the elements (in μ s), `M` is the number of elements, `s` is the pitch of the array (in mm), `angt` is the angle θ_t (in degrees), `ang20` is the specified refracted angle, θ_{20} , for the central ray (in degrees), `DT0` is the height of the center of the array above the interface, D_{i0} , (in mm), `DF` is the depth to the focal point in the second medium, D_f , (in mm) and (`c1`, `c2`) are the wave speeds of the incident and refracted media, (c_1, c_2), (in m/s). The final argument, `plt`, is a string used to optionally plot ray paths for the parameters chosen, where `plt` = 'y' or 'n' for plot generation or not, respectively. Both `DT0` and `DF` must be specified as positive numbers while `angt` and `ang20` can individually be positive or negative. Figure 5.5a–d show the array parameters for various choices of θ_t and θ_{20} . For both θ_t and θ_{20} positive angles are measured in a counterclockwise sense. Also note that when θ_t is positive the first element of the array ($m=1$) is nearest element to the interface, but it is the farthest element when θ_t is negative. If one does not want this change to happen, then one can simply re-order the time delays. Figure 5.6a, b show the ray paths and time delays, respectively, for a 16 element array with $\theta_t = 5^\circ$, $\theta_{20} = 60^\circ$, $D_{i0} = D_f = 10$ mm, and $c_1 = 1480$ m/s, $c_2 = 5900$ m/s. In contrast, Fig. 5.7a, b changes (θ_t, θ_{20}) to $(-5, -60)$ degrees, respectively, with all other parameters remaining the same. It can be seen that the delay law in Fig. 5.7 is “flipped” from that of Fig. 5.6 because of the ordering of

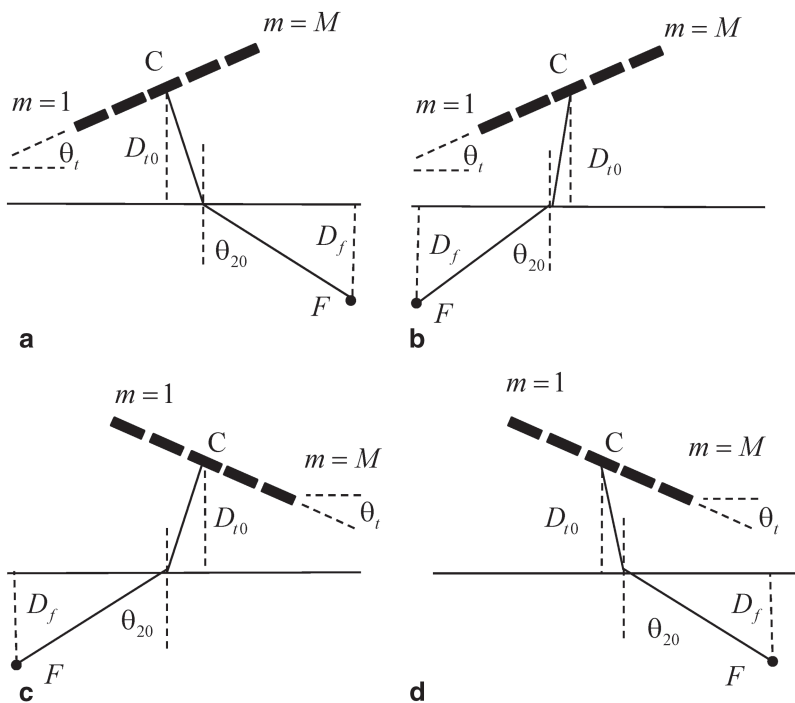


Fig. 5.5 The array parameters for the cases where: **a** the angles (θ_t, θ_{20}) are both positive, **b** the angle θ_t is positive but θ_{20} is negative, **c** the angles (θ_t, θ_{20}) are both negative, and **d** the angle θ_t is negative but θ_{20} is positive

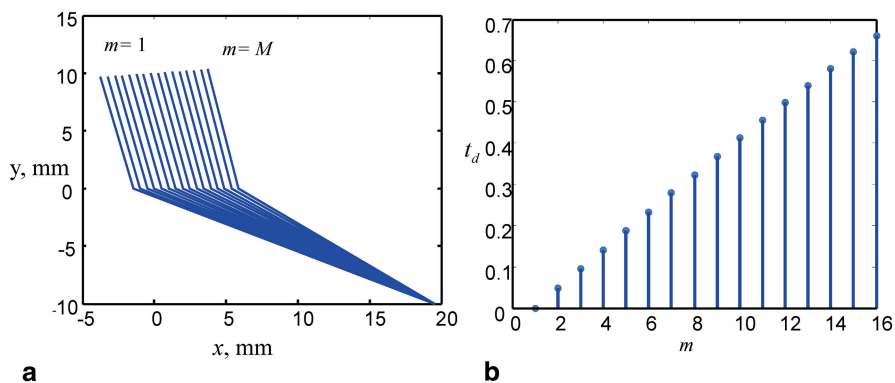


Fig. 5.6 **a** The ray paths for an array with $M=16$ elements, $s=0.5$ mm, $\text{angt}=5^\circ$, $\text{ang20}=60^\circ$, $\text{DTO}=10$ mm, $D_f=10$ mm, $c_1=1480$ m/s, $c_2=5900$ m/s, **b** the corresponding time delays, measured in μs

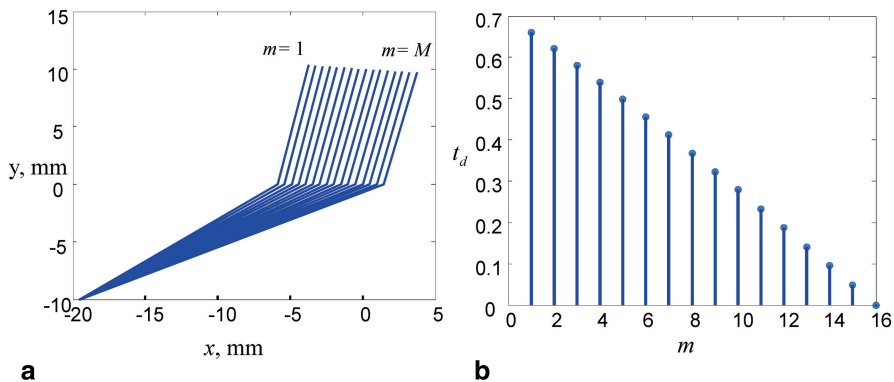


Fig. 5.7 **a** The ray paths for an array with $M=16$ elements, $s=0.5$ mm, $\text{angt}=-5^\circ$, $\text{ang20}=-60^\circ$, $\text{DTO}=10$ mm, $\text{Df}=10$ mm, $c_1=1480$ m/s, $c_2=5900$ m/s, **b** the corresponding time delays, measured in μs

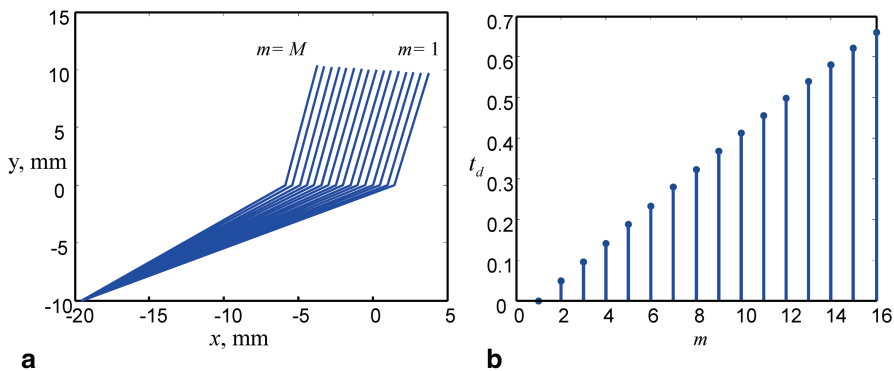


Fig. 5.8 **a** The ray paths for an array with $M=16$ elements, $s=0.5$ mm, $\text{angt}=-5^\circ$, $\text{ang20}=-60^\circ$, $\text{DTO}=10$ mm, $\text{DF}=10$ mm, $c_1=1480$ m/s, $c_2=5900$ m/s, **b** the corresponding time delays, measured in μs . The order of the elements has been changed so that the first element is nearest to the interface, giving the same delay law as seen in Fig. 5.6

the elements. This ordering can be easily changed in MATLAB® with the built-in function `fliplr`:

```
>> tdf = fliplr(td);
```

which results in the time delay law of Fig. 5.8, which is now identical with that of Fig. 5.6.

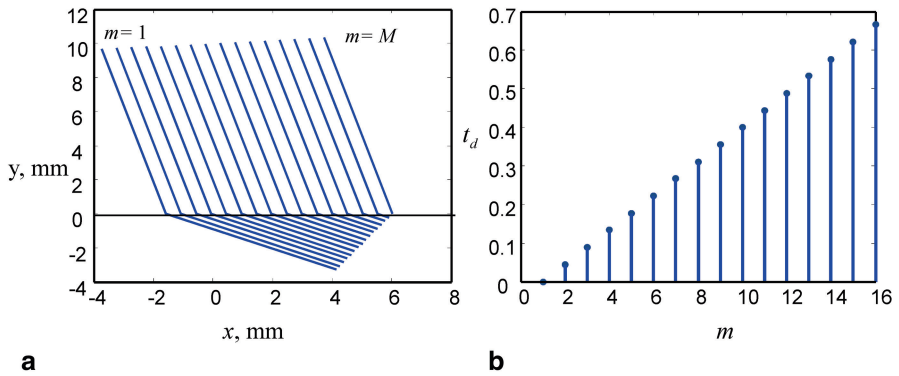


Fig. 5.9 **a** The ray paths for pure steering of an array with $M=16$ elements, $s=0.5 \text{ mm}$, $\text{angt}=5^\circ$, $\text{ang20}=60^\circ$, $\text{DTO}=10 \text{ mm}$, $\text{DF}=\text{inf}$, $c_1=1480 \text{ m/s}$, $c_2=5900 \text{ m/s}$, **b** the corresponding time delays, measured in μs

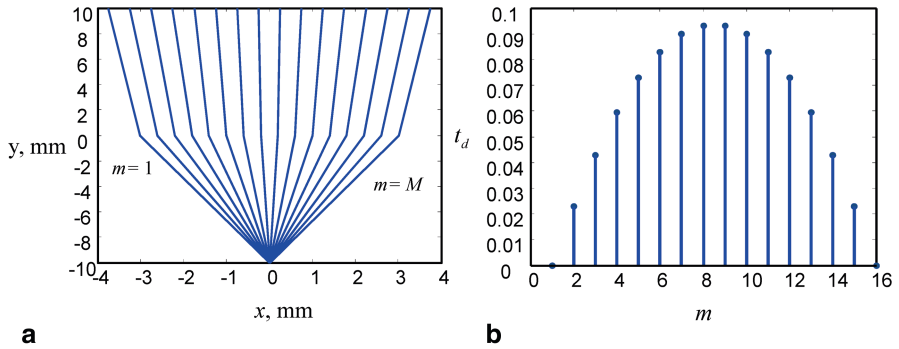


Fig. 5.10 **a** The ray paths for pure focusing of an array with $M=16$ elements, $s=0.5 \text{ mm}$, $\text{angt}=0^\circ$, $\text{ang20}=0^\circ$, $\text{DTO}=10 \text{ mm}$, $\text{DF}=10 \text{ mm}$, $c_1=1480 \text{ m/s}$, $c_2=5900 \text{ m/s}$, **b** the corresponding time delays, measured in μs

Figures 5.9 and 5.10 show the rays and delays for several other cases. Figure 5.9 considers the case of pure steering for a 16 element array with $\theta_t = 5^\circ$, $\theta_{20} = 60^\circ$, $D_{t0} = 10 \text{ mm}$, $D_f = \text{inf}$, and $c_1 = 1480 \text{ m/s}$, $c_2 = 5900 \text{ m/s}$. Figure 5.10 shows a pure focusing case where the 16 element array is at normal incidence, i.e. $\theta_t = 0^\circ$, $\theta_{20} = 0^\circ$, and where $D_{t0} = 10 \text{ mm}$, $D_f = 10 \text{ mm}$, and $c_1 = 1480 \text{ m/s}$, $c_2 = 5900 \text{ m/s}$.

References

1. L. Azar, Y. Shi, S.-C. Wooh, Beam focusing behavior of linear phased arrays. *NDT&E Int.* **33**, 189–198, (2000)
2. M. Weston, P. Mudge, C. Davis, A. Peyton, Time-efficient auto-focussing algorithms for ultrasonic inspection of dual-layered media using full matrix capture. *NDT&E Int.* **47**, 43–50, (2012)
3. http://exampleproblems.com/wiki/index.php/Quartic_equation

Chapter 6

Acoustic Field of a 2-D Array Element

In previous chapters we considered 1-D elements radiating two dimensional waves into a fluid as this simple configuration can explain many of the fundamental issues associated with arrays such as grating lobes, steering and focusing, etc. In this chapter we will develop models that describe the radiation of a 2-D array element in three dimensions. This is a more practical configuration that can be used to directly model the radiation characteristics of the linear and 2-D matrix arrays often used in practice. We will employ many of the same methods and models used in Chap. 2, where now they will be implemented for fully 3-D problems. As done earlier, we will describe radiation in both a single medium and through a planar interface.

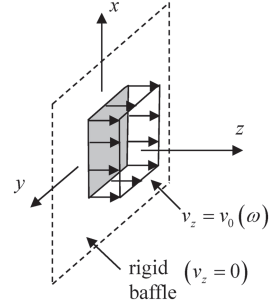
6.1 Single Element Transducer Models (3-D)

The basic setup we will use to describe a single element of an array is shown in Fig. 6.1. As done in Chap. 2, we will treat the element as a velocity source located on the plane $z=0$ where now a normal velocity, $\bar{v}_z(x, y, t)$, is generated over finite area, S , of the plane and the velocity over the remainder of the plane is assumed to be zero (rigid baffle model). The element will radiate waves into a fluid which occupies the half space $z \geq 0$. Following the same steps used in Chap. 2, from the equations of motion and constitutive equation one can show that the pressure, $p(x, y, z, t)$, in the fluid will satisfy the 3-D wave equation [Schmerr]

$$\frac{\partial^2 p}{\partial x^2} + \frac{\partial^2 p}{\partial y^2} + \frac{\partial^2 p}{\partial z^2} - \frac{1}{c^2} \frac{\partial^2 p}{\partial t^2} = 0, \quad (6.1)$$

where the wave speed is given by Eq. (2.4). We will again typically model wave propagation for these three dimensional problems in the frequency domain. Taking the Fourier transform on time of Eq. (6.1) gives the three dimensional Helmholtz equation

Fig. 6.1 Model of an element as a velocity source in an infinite, motionless rigid baffle radiating into a fluid occupying the region $z \geq 0$, where the specific velocity distribution shown is spatially uniform over the face of the element (piston model)



$$\frac{\partial^2 \tilde{p}}{\partial x^2} + \frac{\partial^2 \tilde{p}}{\partial y^2} + \frac{\partial^2 \tilde{p}}{\partial z^2} + \frac{\omega^2}{c^2} \tilde{p} = 0 \quad (6.2)$$

for $\tilde{p}(x, y, z, \omega)$, where consistent with Chap. 2 we define the forward and inverse Fourier transforms on time here as:

$$\begin{aligned} \tilde{p}(x, y, z, \omega) &= \int_{-\infty}^{+\infty} p(x, y, z, t) \exp(i\omega t) dt \\ p(x, y, z, t) &= \frac{1}{2\pi} \int_{-\infty}^{+\infty} \tilde{p}(x, y, z, \omega) \exp(-i\omega t) d\omega. \end{aligned} \quad (6.3)$$

Once again, since our 3-D models will primarily be described in the frequency domain we will drop the tilde on the Fourier transformed pressure (and the Fourier transform of other variables such as the velocity) and simply express that transform as $p(x, y, z, \omega)$.

The 3-D Helmholtz equation has wave solutions given as

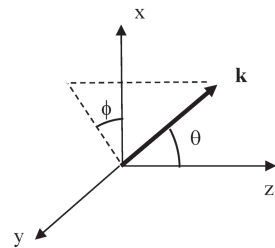
$$p = \exp(ik_x x + ik_y y + ik_z z), \quad (6.4)$$

with

$$k_z = \begin{cases} \sqrt{k^2 - k_x^2 - k_y^2} & k_x^2 + k_y^2 \leq k^2 \\ i\sqrt{k_x^2 + k_y^2 - k^2} & k_x^2 + k_y^2 > k^2 \end{cases} \quad (6.5)$$

and $k = \omega/c$. For $k_x^2 + k_y^2 \leq k^2$ Eq. (6.4) represents harmonic plane waves traveling with a positive z -component, $k_z = k \cos \theta$, and with components (k_x, k_y) coordinates $k_x = k \cos \phi \sin \theta$, $k_y = k \sin \phi \sin \theta$ (in spherical coordinates—see Fig. 6.2). For $k_x^2 + k_y^2 > k^2$ Eq. (6.4) represents an inhomogeneous wave which decays exponentially in the z -direction. To form a more general solution of Helmholtz's equation we can consider a superposition of these plane and inhomogeneous waves in the form

Fig. 6.2 Description of the wave number vector, \mathbf{k} , in spherical coordinates



$$p(\mathbf{x}, \omega) = \left(\frac{1}{2\pi} \right)^2 \int_{-\infty}^{+\infty} \int_{-\infty}^{+\infty} P(k_x, k_y) \exp[i(k_x x + k_y y + k_z z)] dk_x dk_y, \quad (6.6)$$

with $\mathbf{x} = (x, y, z)$. Equation (6.6) is a 3-D angular plane wave spectrum representation analogous to Eq. (2.10). It can be seen from Eq. (6.6) that the amplitude term $P(k_x, k_y)$ is a two dimensional spatial Fourier transform of the pressure on the plane $z = 0$ since we have the transform pair:

$$p(x, y, 0, \omega) = \left(\frac{1}{2\pi} \right)^2 \int_{-\infty}^{+\infty} \int_{-\infty}^{+\infty} P(k_x, k_y) \exp(ik_x x + ik_y y) dk_x dk_y$$

$$P(k_x, k_y) = \int_{-\infty}^{+\infty} \int_{-\infty}^{+\infty} p(x, y, 0, \omega) \exp(-ik_x x - ik_y y) dx dy. \quad (6.7)$$

To obtain the z -component of the velocity on the plane $z = 0$ (see Eq. 2.15), since

$$v_z(x, y, 0, \omega) = \frac{1}{i\omega\rho} \frac{\partial p(x, y, z, \omega)}{\partial z} \Big|_{z=0}, \quad (6.8)$$

we have

$$v_z(x, y, z = 0, \omega) = \left(\frac{1}{2\pi} \right)^2 \int_{-\infty}^{+\infty} \int_{-\infty}^{+\infty} \frac{k_z P(k_x, k_y)}{\omega\rho} \exp[i(k_x x + k_y y)] dk_x dk_y \quad (6.9)$$

and if we let

$$V(k_x, k_y) = \frac{k_z P(k_x, k_y)}{\rho\omega} \quad (6.10)$$

we have

$$v_z(x, y, z=0, \omega) = \left(\frac{1}{2\pi} \right)^2 \int_{-\infty}^{+\infty} \int_{-\infty}^{+\infty} V(k_x, k_y) \exp[i(k_x x + k_y y)] dk_x dk_y. \quad (6.11)$$

We recognize $V(k_x, k_y)$ as the two dimensional spatial Fourier transform of the velocity, v_z , on the plane $z=0$, i.e.

$$V(k_x, k_y) = \int_{-\infty}^{+\infty} \int_{-\infty}^{+\infty} v_z(x, y, 0, \omega) \exp(-ik_x x - ik_y y) dx dy. \quad (6.12)$$

Since we wish to write the pressure in the fluid in terms of this velocity, from Eqs. (6.6) and (6.10) we have

$$p(\mathbf{x}, \omega) = \left(\frac{1}{2\pi} \right)^2 \int_{-\infty}^{+\infty} \int_{-\infty}^{+\infty} \frac{\rho \omega V(k_x, k_y)}{k_z} \exp[i(k_x x + k_y y + ik_z z)] dk_x dk_y. \quad (6.13)$$

We can now use the convolution theorem [Schmerr] for two dimensional Fourier transforms to turn Eq. (6.13) into a more explicit relationship between the pressure and the velocity on the plane $z=0$. The convolution theorem states that if a function $f(x, y)$ can be expressed as the inverse 2-D Fourier transform of a product of transforms, $H(k_x, k_y)$ and $G(k_x, k_y)$, i.e.

$$f(x, y) = \left(\frac{1}{2\pi} \right)^2 \int_{-\infty}^{+\infty} \int_{-\infty}^{+\infty} H(k_x, k_y) G(k_x, k_y) \exp[i(k_x x + k_y y)] dk_x dk_y, \quad (6.14)$$

then $f(x, y)$ is also equal to the 2-D convolution of the functions $h(x, y)$ and $g(x, y)$ given as:

$$f(x, y) = \int_{-\infty}^{+\infty} \int_{-\infty}^{+\infty} h(x', y') g(x - x', y - y') dx' dy', \quad (6.15)$$

where $h(x, y)$ is the inverse Fourier transform of $H(k_x, k_y)$ and $g(x, y)$ is the inverse Fourier transform of $G(k_x, k_y)$. We can use this theorem directly for Eq. (6.13) if we let

$$\begin{aligned} H(k_x, k_y) &= -i\omega \rho V(k_x, k_y) \\ G(k_x, k_y) &= \frac{\exp[ik_z z]}{-ik_z}. \end{aligned} \quad (6.16)$$

Since $V(k_x, k_y)$ is the Fourier transform of $v_z(x, y, 0, \omega)$ it follows that here

$$h(x, y) = -i\omega \rho v_z(x, y, 0, \omega). \quad (6.17)$$

The transform $G(k_x, k_y)$ can be identified as the transform of a spherical wave from the Weyl representation [1]

$$\frac{\exp\left(ik\sqrt{x^2 + y^2 + z^2}\right)}{\sqrt{x^2 + y^2 + z^2}} = \left(\frac{1}{2\pi}\right)^2 \int_{-\infty}^{+\infty} \int_{-\infty}^{+\infty} \left[\frac{\exp(ik_z z)}{-ik_z} \right] \exp(ik_x x + ik_y y) dk_x dk_y \quad (6.18)$$

so that the convolution theorem gives the pressure in the fluid as

$$p(\mathbf{x}, \omega) = \frac{-i\omega\rho}{2\pi} \int_{-\infty}^{+\infty} \int_{-\infty}^{+\infty} v_z(x', y', 0, \omega) \frac{\exp(ikr)}{r} dx' dy', \quad (6.19)$$

where

$$r = \sqrt{(x - x')^2 + (y - y')^2 + z^2}. \quad (6.20)$$

Equation (6.19) is a Rayleigh-Sommerfeld integral representation of the pressure wave field of an element in terms of an integral superposition of spherical waves over the plane $z=0$ [Schmerr]. When the velocity field is a spatial constant, $v_0(\omega)$, over the surface, S , of an element, then we find the Rayleigh-Sommerfeld form for a piston transducer:

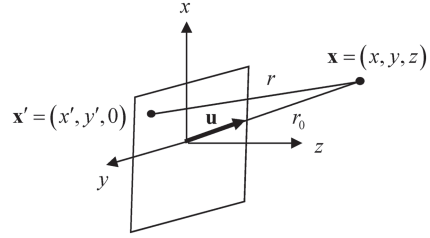
$$p(\mathbf{x}, \omega) = \frac{-i\omega\rho v_0(\omega)}{2\pi} \int_S \frac{\exp(ikr)}{r} dx' dy'. \quad (6.21)$$

6.2 Far Field Waves

When the distance from the element to the point in the fluid where the pressure is being calculated is sufficiently large, the distance, r , can be approximated to first order as (see Fig. 6.3):

$$\begin{aligned} r &= \sqrt{r_0^2 + \mathbf{x}' \cdot \mathbf{x}' - 2\mathbf{x}' \cdot r_0 \mathbf{u}} \\ &\approx r_0 - \mathbf{x}' \cdot \mathbf{u}, \end{aligned} \quad (6.22)$$

Fig. 6.3 Geometry for obtaining the far field behavior of an element



where $\mathbf{x}' = (x', y', 0)$ and \mathbf{u} is a unit vector from the centroid of the element to the point (x, y, z) in the fluid. If we keep only the first term in Eq. (6.22) for the $1/r$ amplitude part in Eq. (6.19) and both terms in the phase kr , we obtain

$$p(\mathbf{x}, \omega) = \frac{-i\omega\rho}{2\pi} \frac{\exp(ikr_0)}{r_0} \int_{-\infty}^{+\infty} \int_{-\infty}^{+\infty} v_z(x', y', 0, \omega) \exp(-ik_x x' - ik_y y') dx' dy', \quad (6.23)$$

where $k_x = ku_x$, $k_y = ku_y$. But from Eq. (6.12) we recognize the integral as just the 2-D Fourier transform of the normal velocity on the plane $z=0$, so the far field pressure is given by

$$p(\mathbf{x}, \omega) = \frac{-i\omega\rho}{2\pi} V(k_x, k_y) \frac{\exp(ikr_0)}{r_0}. \quad (6.24)$$

For a rectangular piston element of length l_x in the x -direction and length l_y in the y -direction

$$\begin{aligned} V(k_x, k_y) &= v_0(\omega) \int_{-l_x/2}^{+l_x/2} \int_{-l_y/2}^{+l_y/2} \exp(-ik_x x' - ik_y y') dx' dy' \\ &= v_0(\omega) l_x l_y \frac{\sin(k_x l_x / 2)}{k_x l_x / 2} \frac{\sin(k_y l_y / 2)}{k_y l_y / 2} \end{aligned} \quad (6.25)$$

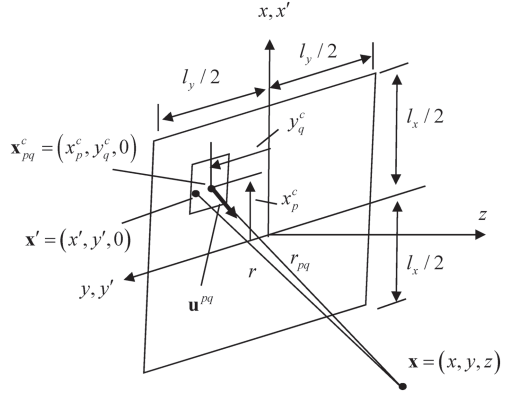
so the far field pressure is

$$p(\mathbf{x}, \omega) = \frac{\rho c v_0(\omega)}{2\pi} (-ik l_x l_y) \frac{\sin(k_x l_x / 2)}{k_x l_x / 2} \frac{\sin(k_y l_y / 2)}{(k_y l_y / 2)} \frac{\exp(ikr_0)}{r_0}. \quad (6.26)$$

In terms of spherical coordinates (θ, ϕ) we have $k_x = ku_x = k \cos \phi \sin \theta$, $k_y = ku_y = k \sin \phi \sin \theta$. In those coordinates we can write Eq. (6.26) as

$$p(\mathbf{x}, \omega) = \frac{\rho c v_0(\omega)}{2\pi} (-ik l_x l_y) D_l(\theta, \phi) \frac{\exp(ikr_0)}{r_0}, \quad (6.27)$$

Fig. 6.4 Parameters for evaluating the Rayleigh–Sommerfeld model of an element radiating into a fluid



which represents a spherically spreading wave from the element with a directivity, $D_l(\theta, \phi)$, given by

$$D_l(\theta, \phi) = \frac{\sin(kl_x \cos \phi \sin \theta / 2)}{kl_x \cos \phi \sin \theta / 2} \frac{\sin(kl_y \sin \phi \sin \theta / 2)}{kl_y \sin \phi \sin \theta / 2}. \quad (6.28)$$

6.3 Numerical Point Source Piston Model

To evaluate the Rayleigh–Sommerfeld model of Eq. (6.21) numerically we can break a rectangular element of length l_x in the x -direction and length l_y in the y -direction into P equal length segments along the x -axis and Q equal length segments along the y -axis (see Fig. 6.4). The lengths of these segments, therefore, will be $\Delta d_x = l_x / P$ in the x -direction and $\Delta d_y = l_y / Q$ in the y -direction. In this case, the coordinates of the centroid (x_p^c, y_q^c) of the pq th rectangular segment can be defined as

$$\begin{aligned} x_p^c &= -\frac{l_x}{2} + \Delta d_x \left(p - \frac{1}{2} \right) \quad (p = 1, \dots, P) \\ y_q^c &= -\frac{l_y}{2} + \Delta d_y \left(q - \frac{1}{2} \right) \quad (q = 1, \dots, Q). \end{aligned} \quad (6.29)$$

A unit vector, \mathbf{u}^{pq} , is defined to be along the axis from this centroid $\mathbf{x}_{pq}^c = (x_p^c, y_q^c, 0)$ to a point $\mathbf{x} = (x, y, z)$ in the fluid (Fig. 6.4). If we let an arbitrary point in this rectangular segment be $\mathbf{x}' = (x', y', 0)$ then the distance, r , from \mathbf{x}' to \mathbf{x} is given by

$$\begin{aligned} r &= \sqrt{(\mathbf{x}_{pq}^c - \mathbf{x}' + r_{pq} \mathbf{u}^{pq}) \cdot (\mathbf{x}_{pq}^c - \mathbf{x}' + r_{pq} \mathbf{u}^{pq})} \\ &= \sqrt{r_{pq}^2 + 2(\mathbf{x}_{pq}^c - \mathbf{x}') \cdot r_{pq} \mathbf{u}^{pq} + |\mathbf{x}' - \mathbf{x}_{pq}^c|^2} \\ &\equiv r_{pq} + (\mathbf{x}_{pq}^c - \mathbf{x}') \cdot \mathbf{u}^{pq} \end{aligned} \quad (6.30)$$

since we will also assume the segment dimensions Δd_x and Δd_y are small relative to the distance, r_{pq} , at which we will want to evaluate the pressure wave field. In this approximation Eq. (6.21) can then be written as a sum given by

$$p(\mathbf{x}, \omega) = \frac{-i\omega\rho v_0(\omega)}{2\pi} \sum_{p=1}^P \sum_{q=1}^Q \frac{\exp(ikr_{pq})}{r_{pq}} \int_{S_{pq}} \exp\left[ik(\mathbf{x}_{pq} - \mathbf{x}') \cdot \mathbf{u}^{pq}\right] dS, \quad (6.31)$$

where the integral is over the area of the segment, S_{pq} . If we let $x' - x_p^c = s$, $y' - y_q^c = t$ then Eq. (6.31) becomes

$$p(\mathbf{x}, \omega) = \frac{-i\omega\rho v_0(\omega)}{2\pi} \sum_{p=1}^P \sum_{q=1}^Q \frac{\exp(ikr_{pq})}{r_{pq}} \int_{-\Delta d_x/2}^{+\Delta d_x/2} \int_{-\Delta d_y/2}^{+\Delta d_y/2} \exp(-iks u_x^{pq}) \exp(-ikt u_y^{pq}) ds dt. \quad (6.32)$$

But, integrals of similar form have been done before (see Eq. 6.25 for example) so we obtain

$$p(\mathbf{x}, \omega) = \frac{\rho c v_0(\omega)}{2\pi} \sum_{p=1}^P \sum_{q=1}^Q (-ik\Delta d_x \Delta d_y) \frac{\sin(ku_x^{pq} \Delta d_x / 2)}{ku_x^{pq} \Delta d_x / 2} \frac{\sin(ku_y^{pq} \Delta d_y / 2)}{ku_y^{pq} \Delta d_y / 2} \frac{\exp(ikr_{pq})}{r_{pq}}. \quad (6.33)$$

If we compare this result with Eq. (6.26) we see the product of the sinc function terms in Eq. (6.33) is just the far field directivity for each segment of the element. These directivities multiply a spherically spreading wave from the centroid of each segment. A similar form for 2-D problems (see Eq. (2.59)) involved a directivity and a cylindrically spreading wave. We called that model a multiple line source model. Since the spherical wave term in Eq. (6.33) represents waves from a point source, the 3-D model obtained in Eq. (6.33) will be similarly called a *multiple point source model*. In this model the centroid terms (x_p^c, y_q^c) are given by Eq. (6.29), the distance, r_{pq} , is simply

$$r_{pq} = \sqrt{(x - x_p^c)^2 + (y - y_q^c)^2 + z^2} \quad (6.34)$$

and the components of the unit vector, \mathbf{u}^{pq} , are

$$u_x^{pq} = \frac{x - x_p^c}{r_{pq}}, \quad u_y^{pq} = \frac{y - y_q^c}{r_{pq}}. \quad (6.35)$$

As in our discussion of the multiple line source model, there is a minimum number of segments needed to avoid grating lobes and aliasing. In the 3-D case for a rectangular element we must keep $\Delta d_x < \lambda$, $\Delta d_y < \lambda$, where λ is the wavelength. We can do this by choosing

$$\begin{aligned}
 P &= \begin{cases} \text{ceil}\left(\frac{1000fl_x}{c}\right) & (l_x > \lambda) \\ 1 & (l_x \leq \lambda) \end{cases}, \\
 Q &= \begin{cases} \text{ceil}\left(\frac{1000fl_y}{c}\right) & (l_y > \lambda) \\ 1 & (l_y \leq \lambda) \end{cases},
 \end{aligned} \tag{6.36}$$

where f is in MHz, (l_x, l_y) in mm, and c is in m/s.

Equation (6.33) has been implemented in the 3-D point source MATLAB[®] function `ps_3Dv` (Code Listing C.20) where the centroid of the element is assumed to have offsets (e_x, e_y) in the (x, y) directions, respectively. The calling sequence for this function is

$$p = \text{ps_3Dv}(lx, ly, f, c, ex, ey, x, y, z, P_{\text{opt}}, Q_{\text{opt}});$$

where (lx, ly) are the lengths of the elements in the x - and y -directions (in mm), f is the frequency (in MHz), c is the wave speed (in m/s), (ex, ey) are the offsets of the center of the element from the center of the array (in mm), (x, y, z) are the coordinates of the point at which the normalized pressure, $p / \rho c v_0$, is to be calculated. P_{opt} and Q_{opt} are optional input parameters discussed below.

The form of Eq. (6.33) used in this function is still the same, but in this case Eqs. (6.34) and (6.35) are changed to include the offsets:

$$\begin{aligned}
 r_{pq} &= \sqrt{(x - x_p^c - e_x)^2 + (y - y_q^c - e_y)^2 + z^2} \\
 u_x^{pq} &= \frac{x - x_p^c - e_x}{r_{pq}}, \quad u_y^{pq} = \frac{y - y_q^c - e_y}{r_{pq}}.
 \end{aligned} \tag{6.37}$$

In implementing the criteria of Eq. (6.36) for determining the number of element segments in the function `ps_3Dv` the frequency, f , is assumed to be a scalar so that to synthesize the spectrum of a pulse with this function one must call the function for each frequency component in the spectrum. At high frequencies, these P and Q values may be prohibitively large so one must be careful to evaluate the fields only over the bandwidth of the transducer when implementing the function in this manner. The function, however, also has a pair of optional arguments, P_{opt} , Q_{opt} , that allows the user to specify the number of segments directly regardless of the frequency. When calling the function with these optional arguments, the frequency, f , can be vector. The choice $P_{\text{opt}} = 1$, $Q_{\text{opt}} = 1$ is the simple case of a *single point source model*, where the pressure is given by Eq. (6.27).

To show a fairly stringent test of the use of `ps_3Dv`, consider the case of a large single element where $l_x = 6$ mm, $l_y = 12$ mm, $f = 5$ MHz, $c = 1480$ m/s, $e_x = e_y = 0$, $x = y = 0$, $z = \text{linspace}(5, 100, 500)$, and P_{opt} , Q_{opt} are not specified. Figure 6.5 compares a plot of this case with the case where $P_{\text{opt}} = 203$, $Q_{\text{opt}} = 406$

Fig. 6.5 The on-axis pressure variation for a 6×12 mm rectangular element radiating into water ($c = 1480$ m/s) at 5 MHz. *Solid line*—one segment per wavelength (P_{opt} and Q_{opt} are not specified), *dashed line*— $P_{\text{opt}} = 203$, $Q_{\text{opt}} = 406$ (ten segments per wavelength in both directions). There is no discernible difference between the two cases

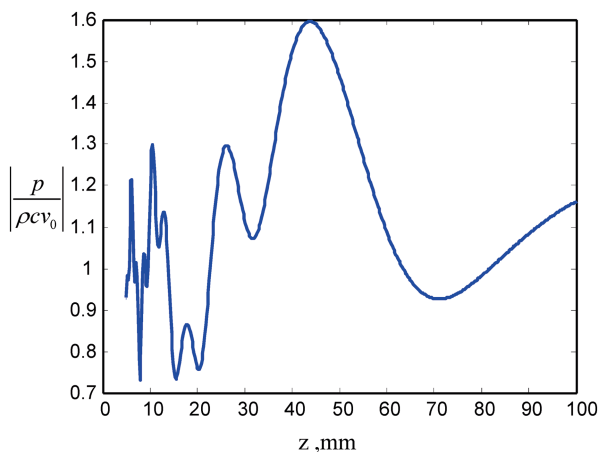
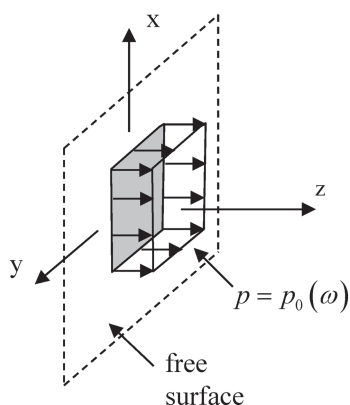


Fig. 6.6 Model of an array element in contact with an elastic solid as a uniform pressure distribution on an otherwise stress-free surface

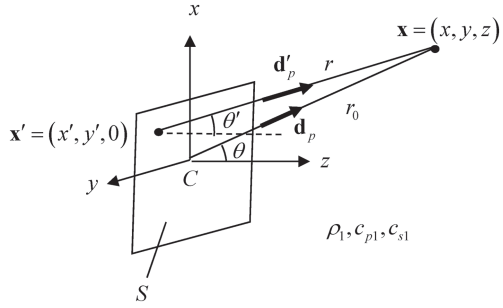


which corresponds to choosing ten segments per wavelength in both dimensions to represent this element. It can be seen that there is no visible difference between the two cases even in the near field of the element.

6.4 Contact Transducer Element Modeling

If an array is used in contact testing, the array element is in direct contact with a solid, with a thin layer of fluid couplant between the element and the solid. In this case, a more appropriate model for the boundary conditions is to assume that the element exerts a pressure distribution (usually assumed to be uniform) over the face of the element on an otherwise stress-free surface (Fig. 6.6). This pressure distribution generates a number of waves, including bulk P-waves and S-waves,

Fig. 6.7 Parameters for the modeling a contact element radiating into a solid



Head waves, and Rayleigh surface waves [Schmerr]. At high frequencies the bulk P-waves, which are generally the waves used most often in contact inspections, can also be modeled in the form of a Rayleigh-Sommerfeld type of integral [Schmerr] where the velocity, $\mathbf{v}(\mathbf{x}, \omega)$, in a solid due to a uniform pressure, $p_0(\omega)$ over a surface area, S , is given by

$$\mathbf{v}(\mathbf{x}, \omega) = \frac{-ik_{p1}P_0(\omega)}{2\pi\rho_1c_{p1}} \int_S K_p(\theta') \mathbf{d}'_p \frac{\exp(ik_{p1}r_1)}{r} dS, \quad (6.38)$$

where $K_p(\theta')$ is a directivity function given by

$$K_p(\theta') = \frac{\cos \theta' \kappa^2 (\kappa^2 / 2 - \sin^2 \theta')}{2G(\sin \theta')}. \quad (6.39)$$

Here θ' is an angle measured from the element normal, as shown in Fig. 6.7 and

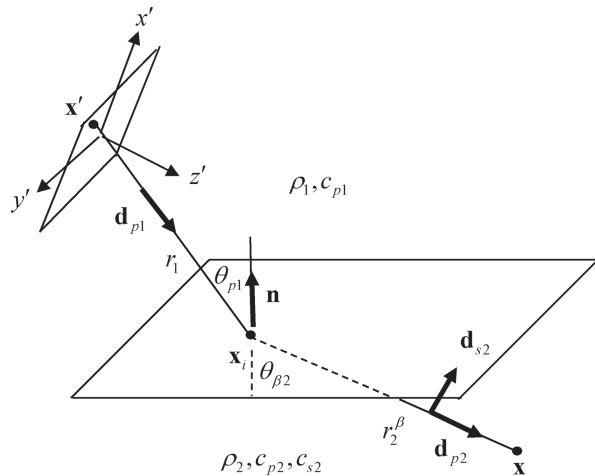
$$G(x) = (x^2 - \kappa^2 / 2)^2 + x^2 \sqrt{1 - x^2} \sqrt{\kappa^2 - x^2}, \quad (6.40)$$

where $\kappa = c_{p1} / c_{s1}$ is the ratio of the compressional and shear wave speeds in the solid. The unit vector \mathbf{d}'_p is the polarization vector along a ray from an arbitrary point \mathbf{x}' on the element face to a point \mathbf{x} in the solid.

In the far field of the element one can approximate the integrand in exactly the same manner as done for the fluid case so we will omit the intermediate steps and simply write the result for a rectangular element as:

$$\mathbf{v}(\mathbf{x}, \omega) = \frac{-ik_{p1}P_0(\omega)}{2\pi\rho_1c_{p1}} K_p(\theta) l_x l_y D_l(\theta, \phi) \mathbf{d}_p \frac{\exp(ik_{p1}r_1)}{r_0}, \quad (6.41)$$

Fig. 6.8 Geometry for the radiation of waves from an array element through a plane, liquid-solid interface



where the angle θ , the polarization \mathbf{d}_p , and the distance r_0 , are all measured relative to a ray from the centroid of the element to the point \mathbf{x} , as shown in Fig. 6.7. The directivity function $D_l(\theta, \phi)$ is given by Eq. (6.28). Aside from the extra directivity function, $K_p(\theta)$, and the polarization vector, \mathbf{d}_p , Eq. (6.41) is of very similar form to Eq. (6.27) for the fluid case. Equation (6.41) gives us a *single point source model* for a contact element radiating P-waves into a solid.

6.5 Radiation Through a Planar Interface

Many NDE applications of phased arrays involve either immersion testing or angle beam testing where the array sits on a solid wedge in contact with the material to be examined. In both these cases the waves must travel through an interface. In this section we will develop beam models for an array radiating through a planar interface. These models will be 3-D models equivalent to the 2-D cases considered in Chap. 2.

Consider first the case of an immersion setup where an element in a fluid radiates waves across a planar interface into an elastic solid, as shown in Fig. 6.8. In Chap. 2 we showed that for 2-D waves we could use ray theory to develop a beam model for the transmitted waves. In this section we will follow the same approach for the 3-D case. [For a very complete description of ray theory for both scalar and elastic wave problems, see the book by Červený [2] on seismic ray theory.] If we model the pressure waves incident on the interface through the Rayleigh-Sommerfeld equation for a piston source, a small segment of the element of area $dx'dy'$ will act as a point source and produce an incident pressure, $p_1(\mathbf{x}_i, \omega)$, at the interface given by (see Eq. 6.21):

$$p_1(\mathbf{x}_i, \omega) = \frac{-i\omega\rho_1 v_0(\omega)}{2\pi} \frac{\exp(ik_{p1}r_1)}{r_1} d\mathbf{x}'d\mathbf{y}'. \quad (6.42)$$

The velocity in this incident wave, from the equation of motion of the fluid, is given as

$$\mathbf{v}_1 = \frac{1}{i\omega\rho_1} \nabla p_1, \quad (6.43)$$

but at high frequencies the gradient of the pressure is primarily due to the derivative of the complex exponential phase term in Eq. (6.42) so that we have

$$\mathbf{v}_1(\mathbf{x}_i, \omega) = \frac{-ik_{p1}v_0(\omega)}{2\pi} \frac{\exp(ik_{p1}r_1)}{r_1} \nabla r_1 d\mathbf{x}'d\mathbf{y}' \quad (6.44)$$

or, equivalently,

$$\mathbf{v}_1(\mathbf{x}_i, \omega) = \frac{-ik_{p1}v_0(\omega)}{2\pi} \frac{\exp(ik_{p1}r_1)}{r_1} \mathbf{d}_{p1} d\mathbf{x}'d\mathbf{y}', \quad (6.45)$$

since the polarization vector of these pressure waves is just $\mathbf{d}_{p1} = \nabla r_1$. This incident wave at high frequencies will produce transmitted waves at the interface of type β ($\beta = p, s$) whose velocity, $\mathbf{v}_2(\mathbf{x}_i, \omega)$, is

$$\mathbf{v}_2(\mathbf{x}_i, \omega) = \frac{-ik_{p1}v_0(\omega)}{2\pi} \frac{\exp(ik_{p1}r_1)}{r_1} T_{fs}^{\beta,p} \mathbf{d}_{\beta 2} d\mathbf{x}'d\mathbf{y}', \quad (6.46)$$

where $T_{fs}^{\beta,p}$ is the plane wave transmission coefficient (based on velocity ratios) for a transmitted wave of type β due the incident P-wave for a plane fluid-solid interface and $\mathbf{d}_{\beta 2}$ is a unit vector describing the polarization of a wave of type β traveling in the solid.

According to ray theory, the pressure at \mathbf{x} from a small “point” source at \mathbf{x}' can be determined by following a bundle of rays on a Snell’s law path from \mathbf{x}' to \mathbf{x} . However, this bundle spreads differently in the plane of incidence (POI) and outside that plane, as shown in Fig. 6.9a and b, respectively. In the POI a bundle of waves appear to originate from a virtual point source located at a distance ρ_{vi}^β from point \mathbf{x}_i along the refracted ray. Outside the POI the bundle appears to originate at a distance ρ_{vo}^β instead. Following the same steps shown in Appendix B it is easy

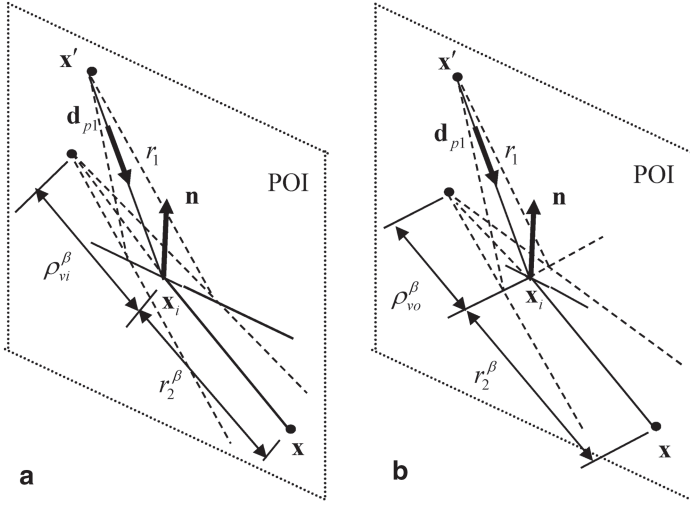


Fig. 6.9 **a** Spreading of a bundle of rays in the plane of incidence (POI), and **b** spreading of a bundle of rays outside the POI

to calculate these distances from the geometry and Snell's law, so we will just state the result here, namely

$$\begin{aligned}\rho_{vi}^{\beta} &= \frac{c_{p1}}{c_{\beta2}} \frac{\cos^2 \theta_{\beta2}}{\cos^2 \theta_{p1}} r_1 \\ \rho_{vo}^{\beta} &= \frac{c_{p1}}{c_{\beta2}} r_1.\end{aligned}\quad (6.47)$$

In propagating from \mathbf{x}_i to \mathbf{x} , the velocity at \mathbf{x} according to ray theory is just

$$\mathbf{v}_2(\mathbf{x}, \omega) = \mathbf{v}_2(\mathbf{x}_i, \omega) \frac{\sqrt{\rho_{vi}^{\beta} \rho_{vo}^{\beta}}}{\sqrt{(\rho_{vi}^{\beta} + r_2^{\beta})(\rho_{vo}^{\beta} + r_2^{\beta})}} \exp(ik_{\beta2} r_2^{\beta}). \quad (6.48)$$

So, from Eqs. (6.46) and (6.47),

$$\mathbf{v}_2(\mathbf{x}, \omega) = \frac{-ik_{p1} v_0(\omega)}{2\pi} \frac{\exp(ik_{p1} r_1 + ik_{\beta2} r_2^{\beta})}{\sqrt{\left(r_1 + \frac{c_{\beta2}}{c_{p1}} \frac{\cos^2 \theta_{p1}}{\cos^2 \theta_{\beta2}} r_2^{\beta}\right) \left(r_1 + \frac{c_{\beta2}}{c_{p1}} r_2^{\beta}\right)}} T_{fs}^{\beta,p} \mathbf{d} dx' dy'. \quad (6.49)$$

Summing up these velocities over the entire element face we then find the total velocity in the solid, $\mathbf{v}(\mathbf{x}, \omega)$, is

$$\mathbf{v}(\mathbf{x}, \omega) = \frac{-ik_{p1}v_0(\omega)}{2\pi} \int_S \frac{\exp(ik_{p1}r_1 + ik_{\beta 2}r_2^\beta)}{\sqrt{\left(r_1 + \frac{c_{\beta 2}}{c_{p1}} \frac{\cos^2 \theta_{p1}}{\cos^2 \theta_{\beta 2}} r_2^\beta\right) \left(r_1 + \frac{c_{\beta 2}}{c_{p1}} r_2^\beta\right)}} T_{fs}^{\beta,p} \mathbf{d}_{\beta 2} dx' dy'. \quad (6.50)$$

As in the 2-D case, here the distances (r_1, r_2^β) and angles $(\theta_{p1}, \theta_{\beta 2})$ need to be determined by finding the Snell's law path from \mathbf{x}' to \mathbf{x} . Again, this path is determined once the point on the interface, \mathbf{x}_i , along the ray is found. In Chap. 8, as part of the process of determining the time delay laws for steering and focusing an array through a plane interface, this interface location is determined from Snell's law following the same approach used previously in 2-D models. We will discuss more explicitly how \mathbf{x}_i is found later in this section.

The plane wave transmission coefficients (based on velocity ratios) for a fluid-solid interface used in Eq. (6.50) are [Schmerr-Song]

$$\begin{aligned} T_{fs}^{p;p} &= \frac{2 \cos \theta_{p1} [1 - 2(\sin \theta_{s2})^2]}{\cos \theta_{p2} + \frac{\rho_2 c_{p2}}{\rho_1 c_{p1}} \cos \theta_{p1} \Delta_1}, \\ T_{fs}^{s;p} &= \frac{-4 \cos \theta_{p1} \cos \theta_{p2} \sin \theta_{s2}}{\cos \theta_{p2} + \frac{\rho_2 c_{p2}}{\rho_1 c_{p1}} \cos \theta_{p1} \Delta_1}, \end{aligned} \quad (6.51)$$

where

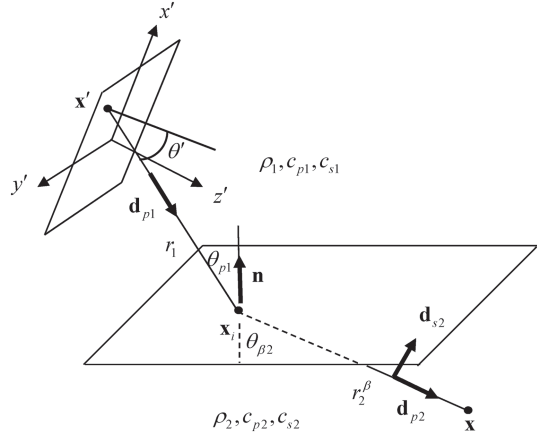
$$\Delta_1 = \left[4 \left(\frac{c_{s2}}{c_{p2}} \right)^2 \sin \theta_{s2} \cos \theta_{s2} \sin \theta_{p2} \cos \theta_{p2} + 1 - 4(\sin \theta_{s2} \cos \theta_{s2})^2 \right] \quad (6.52)$$

and the angles $(\theta_{p1}, \theta_{p2}, \theta_{s2})$ are all related through Snell's law, i.e.

$$\frac{\sin \theta_{p1}}{c_{p1}} = \frac{\sin \theta_{p2}}{c_{p2}} = \frac{\sin \theta_{s2}}{c_{s2}}. \quad (6.53)$$

In the case of angle beam testing with an array placed on a solid wedge, we can develop a very similar model for the transmitted waves since the array generates primarily P-waves in the wedge and the geometry is as shown in Fig. 6.10. For a small

Fig. 6.10 Geometry for the radiation of waves in an angle beam setup where an array element sits on a solid wedge in smooth contact with an adjacent solid



segment area $dx'dy'$ of the element in contact with the wedge then the incident velocity field in the wedge at point \mathbf{x}_i on the interface is given by (see Eq. 6.38)

$$\mathbf{v}_1(\mathbf{x}_i, \omega) = \frac{-ik_{p1}p_0(\omega)}{2\pi\rho_1c_{p1}} K_p(\theta') \mathbf{d}_{p1} \frac{\exp(ik_{p1}r_1)}{r_1} dx'dy' \quad (6.54)$$

and the velocity field of the transmitted wave in the adjacent solid at the interface point \mathbf{x}_i is

$$\mathbf{v}_2(\mathbf{x}_i, \omega) = \frac{-ik_{p1}p_0(\omega)}{2\pi\rho_1c_{p1}} K_p(\theta') \mathbf{d}_{\beta 2} \frac{\exp(ik_{p1}r_1)}{r_1} T_{ss}^{\beta;p} dx'dy', \quad (6.55)$$

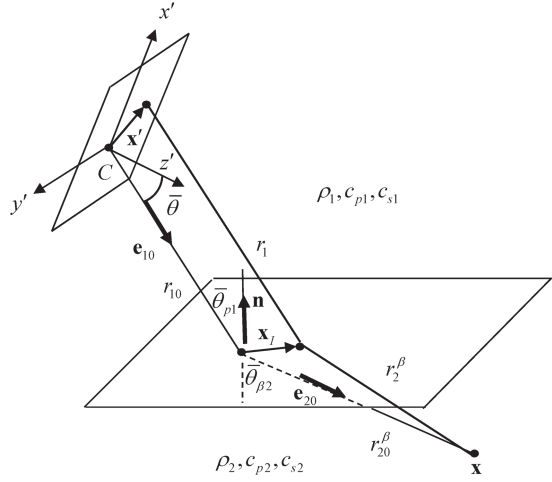
where $T_{ss}^{\beta;p}$ is the plane wave transmission coefficient (based on velocity ratios) for two elastic solids in smooth contact [Schmerr-Song], which is appropriate since in angle beam testing a thin fluid couplant layer exists between the wedge and the underlying solid.

The same ray expressions used in the fluid-solid case to obtain the total field from the element apply here also, so the velocity at point \mathbf{x} generated from the velocity field of Eq. (6.55) at the interface is

$$\mathbf{v}(\mathbf{x}, \omega) = \frac{-ik_{p1}p_0(\omega)}{2\pi\rho_1c_{p1}} \int_S \frac{\exp(ik_{p1}r_1 + ik_{\beta 2}r_2^\beta)}{\sqrt{\left(r_1 + \frac{c_{\beta 2}}{c_{p1}} \frac{\cos^2 \theta_{p1}}{\cos^2 \theta_{\beta 2}} r_2^\beta\right) \left(r_1 + \frac{c_{\beta 2}}{c_{p1}} r_2^\beta\right)}} K_p(\theta') T_{ss}^{\beta;p} \mathbf{d}_{\beta 2} dx'dy'. \quad (6.56)$$

Here, the plane wave transmission coefficients are given by

Fig. 6.11 Geometry for calculating the phase term in the far field of an element



$$T_{ss}^{p;p} = \frac{2 \cos \theta_{p1} [1 - 2(\sin \theta_{s2})^2] [1 - 2(\sin \theta_{s1})^2]}{\cos \theta_{p2} \Delta_2 + \frac{\rho_2 c_{p2}}{\rho_1 c_{p1}} \cos \theta_{p1} \Delta_1}, \quad (6.57)$$

$$T_{ss}^{s;p} = \frac{-4 \cos \theta_{p1} \cos \theta_{p2} \sin \theta_{s2} [1 - 2(\sin \theta_{s1})^2]}{\cos \theta_{p2} \Delta_2 + \frac{\rho_2 c_{p2}}{\rho_1 c_{p1}} \cos \theta_{p1} \Delta_1},$$

where Δ_1 is again given by Eq. (6.52) and

$$\Delta_2 = \left[4 \left(\frac{c_{s1}}{c_{p2}} \right)^2 \sin \theta_{s1} \cos \theta_{s1} \sin \theta_{p1} \cos \theta_{p1} + 1 - 4(\sin \theta_{s1} \cos \theta_{s1})^2 \right]. \quad (6.58)$$

Snell's law is again satisfied for all the angles appearing in Eq. (6.57), i.e.

$$\frac{\sin \theta_{p1}}{c_{p1}} = \frac{\sin \theta_{s1}}{c_{s1}} = \frac{\sin \theta_{p2}}{c_{p2}} = \frac{\sin \theta_{s2}}{c_{s2}}. \quad (6.59)$$

It is easy to see that these transmission coefficients reduce to those of the fluid-solid interface by setting $\sin \theta_{s1} = 0$ in Eq. (6.57).

When we are in the far field of an element we can approximate the phase term $k_{p1} r_{p1} + k_{\beta 2} r_{\beta 2}$ to first order about a ray that travels to \mathbf{x} from the centroid C of the

element and approximate all other amplitude terms to zeroth order about that central ray. From the geometry of Fig. 6.11 we have

$$\begin{aligned}
 k_{p1}r_1 + k_{\beta2}r_2^\beta &= k_{p1}\sqrt{(r_{10}\mathbf{e}_{10} + \mathbf{x}_I - \mathbf{x}') \cdot (r_{10}\mathbf{e}_{10} + \mathbf{x}_I - \mathbf{x}')} \\
 &\quad + k_{\beta2}\sqrt{(r_{20}^\beta\mathbf{e}_{20} - \mathbf{x}_I) \cdot (r_{20}^\beta\mathbf{e}_{20} - \mathbf{x}_I)} \\
 &\cong k_{p1}\sqrt{r_{10}^2 + 2\mathbf{e}_{10} \cdot (\mathbf{x}_I - \mathbf{x}')} + k_{\beta2}\sqrt{(r_{20}^\beta)^2 - 2\mathbf{e}_{20} \cdot \mathbf{x}_I} \\
 &\cong k_{p1}r_{10} + k_{\beta2}r_{20}^\beta - k_{p1}(\mathbf{e}_{10} \cdot \mathbf{x}') + \left[k_{p1}(\mathbf{e}_{10} \cdot \mathbf{t}) - k_{p2}(\mathbf{e}_{20} \cdot \mathbf{t}) \right] x_I,
 \end{aligned} \tag{6.60}$$

where we have written $\mathbf{x}_I = x_I \mathbf{t}$ with \mathbf{t} being a unit vector in the plane of the interface. But the term in the square brackets in Eq. (6.60) vanishes because it is just a statement of Snell's law, so we have

$$k_{p1}r_1 + k_{\beta2}r_2^\beta \cong k_{p1}r_{10} + k_{\beta2}r_{20}^\beta - k_{p1}(\mathbf{e}_{10} \cdot \mathbf{x}'). \tag{6.61}$$

Placing this approximation in the immersion case, Eq. (6.50), we find

$$\begin{aligned}
 \mathbf{v}(\mathbf{x}, \omega) &= \frac{-ik_{p1}v_0(\omega)}{2\pi} \frac{\exp(ik_{p1}r_{10} + ik_{\beta2}r_{20}^\beta)}{\sqrt{\left(r_{10} + \frac{c_{\beta2}}{c_{p1}} \frac{\cos^2 \bar{\theta}_{p1}}{\cos^2 \bar{\theta}_{\beta2}} r_{20}^\beta\right) \left(r_{10} + \frac{c_{\beta2}}{c_{p1}} r_{20}^\beta\right)}} \bar{T}_{fs}^{\beta;p} \bar{\mathbf{d}}_{\beta2} \\
 &\quad \cdot \int_S \exp[-ik_{p1}\mathbf{e}_{10} \cdot \mathbf{x}'] d\mathbf{x}' dy'.
 \end{aligned} \tag{6.62}$$

Similarly, the contact case, Eq. (6.56) becomes

$$\begin{aligned}
 \mathbf{v}(\mathbf{x}, \omega) &= \frac{-ik_{p1}p_0(\omega)}{2\pi\rho_1 c_{p1}} K_p(\bar{\theta}) \bar{T}_{ss}^{\beta;p} \bar{\mathbf{d}}_{\beta2} \frac{\exp(ik_{p1}r_{10} + ik_{\beta2}r_{20}^\beta)}{\sqrt{\left(r_{10} + \frac{c_{\beta2}}{c_{p1}} \frac{\cos^2 \bar{\theta}_{p1}}{\cos^2 \bar{\theta}_{\beta2}} r_{20}^\beta\right) \left(r_{10} + \frac{c_{\beta2}}{c_{p1}} r_{20}^\beta\right)}} \\
 &\quad \cdot \int_S \exp[ik_{p1}(\mathbf{e}_{10} \cdot \mathbf{x}')] d\mathbf{x}' dy',
 \end{aligned} \tag{6.63}$$

where the bar over the various parameters indicates that they are calculated along the central ray from the centroid of the element to point \mathbf{x} .

We have calculated the integrals in Eqs. (6.62) and (6.63) before (see Eq. 6.23) where we obtained the directivity function of the element, so using those results here we find

$$\mathbf{v}(\mathbf{x}, \omega) = \frac{-ik_{p1}v_0(\omega)l_x l_y}{2\pi} \bar{T}_{fs}^{\beta;p} \bar{\mathbf{d}}_{\beta 2} \frac{\sin(k_{p1}u_{x'}l_x/2)}{k_{p1}u_{x'}l_x/2} \frac{\sin(k_{p1}u_y l_y/2)}{k_{p1}u_y l_y/2} \frac{\exp(ik_{p1}r_{10} + ik_{\beta 2}r_{20}^\beta)}{\sqrt{\left(r_{10} + \frac{c_{\beta 2}}{c_{p1}} \frac{\cos^2 \bar{\theta}_{p1}}{\cos^2 \bar{\theta}_{\beta 2}} r_{20}^\beta\right) \left(r_{10} + \frac{c_{\beta 2}}{c_{p1}} r_{20}^\beta\right)}} \quad (6.64)$$

for the immersion case, and

$$\mathbf{v}(\mathbf{x}, \omega) = \frac{-ik_{p1}p_0(\omega)l_x l_y}{2\pi\rho_1 c_{p1}} K_p(\bar{\theta}) \bar{T}_{ss}^{\beta;p} \bar{\mathbf{d}}_{\beta 2} \frac{\sin(k_{p1}u_{x'}l_x/2)}{k_{p1}u_{x'}l_x/2} \frac{\sin(k_{p1}u_y l_y/2)}{k_{p1}u_y l_y/2} \frac{\exp(ik_{p1}r_{10} + ik_{\beta 2}r_{20}^\beta)}{\sqrt{\left(r_{10} + \frac{c_{\beta 2}}{c_{p1}} \frac{\cos^2 \bar{\theta}_{p1}}{\cos^2 \bar{\theta}_{\beta 2}} r_{20}^\beta\right) \left(r_{10} + \frac{c_{\beta 2}}{c_{p1}} r_{20}^\beta\right)}} \quad (6.65)$$

for the contact case, where $\mathbf{e}_{10} = \mathbf{u} = (u_{x'}, u_{y'}, u_{z'})$.

We can use these results to also develop a numerical point source model for an element radiating through a planar fluid-solid interface by breaking the element up into R segments along the x' -axis and Q segments along the y' -axis. Then for the immersion case we have

$$\mathbf{v}(\mathbf{x}, \omega) = \frac{-ik_{p1}v_0(\omega)\Delta d_x \Delta d_y}{2\pi} \sum_{r=1}^R \sum_{q=1}^Q \bar{T}_{fs}^{\beta;p}(\bar{\theta}_1^{rq}) \bar{\mathbf{d}}_{\beta 2}^{rq} \frac{\sin(k_{p1}u_{x'}^{rq}\Delta d_x/2)}{k_{p1}u_{x'}^{rq}\Delta d_x/2} \frac{\sin(k_{p1}u_{y'}^{rq}\Delta d_y/2)}{k_{p1}u_{y'}^{rq}\Delta d_y/2} \frac{\exp(ik_{p1}r_1^{rq} + ik_{\beta 2}r_2^{\beta;rq})}{\sqrt{\left(r_1^{rq} + \frac{c_{\beta 2}}{c_{p1}} \frac{\cos^2 \bar{\theta}_1^{rq}}{\cos^2 \bar{\theta}_2^{rq}} r_2^{\beta;rq}\right) \left(r_1^{rq} + \frac{c_{\beta 2}}{c_{p1}} r_2^{\beta;rq}\right)}}, \quad (6.66)$$

[Note that $x_c'^{rq}$ is in reality a function of r only and $y_c'^{rq}$ is a function of q only, but we have used both superscripts in these parameters to emphasize they are calculated for all the segments present in the element. Both \tilde{D} and D_s are also functions of both r and q but for economy of notation we will not explicitly indicate those dependencies.]

From these distances and knowledge of the point of intersection of the ray with the interface in terms of the distance \tilde{x}_i^{rq} we can then calculate the incident and refracted angles, i.e.

$$\bar{\theta}_1^{rq} = \tan^{-1} \left(\frac{\tilde{x}_i^{rq}}{D_s} \right), \quad \bar{\theta}_2^{rq} = \tan^{-1} \left(\frac{\tilde{D} - x_i^{rq}}{z} \right), \quad (6.70)$$

which are always well-behaved since we must have $D_s > 0$ to make sure the array segment is always above the interface and we will only evaluate rays in the second medium at points where $z > 0$. Finding the distance \tilde{x}_i^{rq} is similar to the 2-D case discussed in Chaps. 2 and 5. We can also evaluate the ray path lengths:

$$\begin{aligned} r_1^{rq} &= \sqrt{D_s^2 + (\tilde{x}_i^{rq})^2} \\ r_2^{rq} &= \sqrt{(\tilde{D} - \tilde{x}_i^{rq})^2 + z^2} \end{aligned} \quad (6.71)$$

and the segment lengths are simply $\Delta d_x = l_x / R$, $\Delta d_y = l_y / Q$. To get the components of \mathbf{u}^{rq} along the (x', y', z') axes, we can first locate the interface point, \mathbf{x}_I , in terms of the points \mathbf{x}_Q and \mathbf{x}_R as

$$\mathbf{x}_I = \frac{\tilde{x}_i^{rq}}{\tilde{D}} (\mathbf{x}_Q - \mathbf{x}_R) + \mathbf{x}_R. \quad (6.72)$$

But in (x, y, z) coordinates we have

$$\begin{aligned} \mathbf{x}_R &= (e_{x'} + x_c'^{rq}) \cos \theta_r \mathbf{i} + (e_{y'} + y_c'^{rq}) \mathbf{j}, \\ \mathbf{x}_Q &= x \mathbf{i} + y \mathbf{j}, \end{aligned} \quad (6.73)$$

where $(\mathbf{i}, \mathbf{j}, \mathbf{k})$ are unit vectors along the (x, y, z) axes, respectively so that we have

$$\mathbf{x}_I = \left[\frac{\tilde{x}_i^{rq} x}{\tilde{D}} + \left(1 - \frac{\tilde{x}_i^{rq}}{\tilde{D}} \right) (e_{x'} + x_c'^{rq}) \cos \theta_r \right] \mathbf{i} + \left[\frac{\tilde{x}_i^{rq} y}{\tilde{D}} + \left(1 - \frac{\tilde{x}_i^{rq}}{\tilde{D}} \right) (e_{y'} + y_c'^{rq}) \right] \mathbf{j}. \quad (6.74)$$

Then, since $\mathbf{u} = (\mathbf{x}_I - \mathbf{x}_s) / r_1^{rq}$, where

$$\mathbf{x}_s = (e_{x'} + x_c'^{rq}) \cos \theta_T \mathbf{i} + (e_{y'} + y_c'^{rq}) \mathbf{j} - D_s \mathbf{k}, \quad (6.75)$$

we find

$$\mathbf{u} = \frac{\tilde{x}_i^{rq}}{\tilde{D} r_1^{rq}} \left[x - (e_{x'} + x_c'^{rq}) \cos \theta_T \right] \mathbf{i} + \frac{\tilde{x}_i^{rq}}{\tilde{D} r_1^{rq}} \left[y - (e_{y'} + y_c'^{rq}) \right] \mathbf{j} + \frac{D_s}{r_1^{rq}} \mathbf{k}. \quad (6.76)$$

To get the components in the (x', y', z') system we first write unit vectors $(\mathbf{i}', \mathbf{j}', \mathbf{k}')$ along these axes as

$$\begin{aligned} \mathbf{i}' &= \cos \theta_T \mathbf{i} - \sin \theta_T \mathbf{k} \\ \mathbf{j}' &= \mathbf{j} \\ \mathbf{k}' &= \sin \theta_T \mathbf{i} + \cos \theta_T \mathbf{k}, \end{aligned} \quad (6.77)$$

giving

$$\begin{aligned} u_{x'} &= \mathbf{u} \cdot \mathbf{i}' = \frac{\tilde{x}_i^{rq} \cos \theta_T}{\tilde{D} r_1^{rq}} \left[x - (e_{x'} + x_c'^{rq}) \cos \theta_T \right] - \frac{D_s \sin \theta_T}{r_1^{rq}}, \\ u_{y'} &= \mathbf{u} \cdot \mathbf{j}' = \frac{\tilde{x}_i^{rq}}{\tilde{D} r_1^{rq}} \left[y - (e_{y'} + y_c'^{rq}) \right], \\ u_{z'} &= \mathbf{u} \cdot \mathbf{k}' = \frac{\tilde{x}_i^{rq} \sin \theta_T}{\tilde{D} r_1^{rq}} \left[x - (e_{x'} + x_c'^{rq}) \cos \theta_T \right] + \frac{D_s \cos \theta_T}{r_1^{rq}}. \end{aligned} \quad (6.78)$$

Note that it is possible that a ray travels through the interface at normal incidence. In that case $\tilde{D} = 0$, $\tilde{x}_i^{rq} = 0$, $D_s = r_1^{rq}$, and

$$\begin{aligned} u_{x'} &= -\sin \theta_T \\ u_{y'} &= 0 \\ u_{z'} &= \cos \theta_T. \end{aligned} \quad (6.79)$$

To find the polarization vectors $(\bar{\mathbf{d}}_{s2}^{rq}, \bar{\mathbf{d}}_{p2}^{rq})$, we first must have the P-wave polarization compatible with the direction assumed when calculating the transmission coefficient, $(\bar{T}_{fs}^{p;p}$ or $\bar{T}_{ss}^{p;p})$. This polarization is normally taken in the direction of propagation, as shown in Fig. 6.12, so we have $\bar{\mathbf{d}}_{p2}^{rq} = (\mathbf{x} - \mathbf{x}_I) / r_2^{rq}$ with

$$\mathbf{x} = x\mathbf{i} + y\mathbf{j} + z\mathbf{k}, \quad (6.80)$$

and the P-wave polarization is

$$\begin{aligned}\bar{\mathbf{d}}_{p2}^{rq} = & d_{px}\mathbf{i} + d_{py}\mathbf{j} + d_{pz}\mathbf{k} = \frac{1}{r_2^{rq}} \left(1 - \frac{\tilde{x}_i^{rq}}{\tilde{D}} \right) \left[x - (e_{x'} + x_c'^{rq}) \cos \theta_T \right] \mathbf{i} \\ & + \frac{1}{r_2^{rq}} \left(1 - \frac{\tilde{x}_i^{rq}}{\tilde{D}} \right) \left[y - (e_{y'} + y_c'^{rq}) \right] \mathbf{j} + \frac{z}{r_2^{rq}} \mathbf{k}.\end{aligned}\quad (6.81)$$

The shear wave polarization, which is also compatible with the direction assumed in calculating the plane wave transmission coefficient ($\bar{T}_{fs}^{s;p}$ or $\bar{T}_{ss}^{s;p}$), for this wave (see Fig. 6.12), is

$$\bar{\mathbf{d}}_{s2}^{rq} = \frac{\mathbf{d}_{p2}^{rq} \times \mathbf{i}}{|\mathbf{d}_{p2}^{rq} \times \mathbf{i}|} \times \bar{\mathbf{d}}_{p2}^{rq} = \sqrt{d_{py}^2 + d_{pz}^2} \mathbf{i} - \frac{d_{px} d_{py}}{\sqrt{d_{py}^2 + d_{pz}^2}} \mathbf{j} - \frac{d_{px} d_{pz}}{\sqrt{d_{py}^2 + d_{pz}^2}} \mathbf{k}, \quad (6.82)$$

which is always well-behaved since we will always assume the fields are calculated for $z > 0$ and hence d_{pz} is never zero. For contact problems we also need to calculate the transducer directivity $K_p(\bar{\theta}^{rq})$. But we have $u_{z'} = \cos \bar{\theta}^{rq}$ so we can calculate the additional angle needed for this directivity from

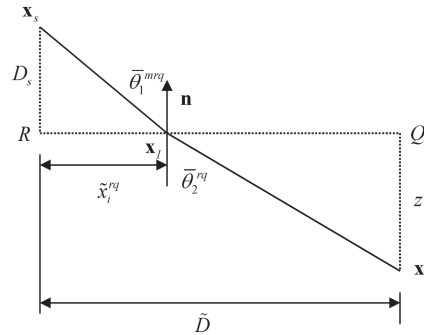
$$\bar{\theta}^{rq} = \cos^{-1}(u_{z'}). \quad (6.83)$$

The MATLAB® function `ps_3Dint` (Code Listing C.23) uses these relations to evaluate the normalized velocity wave field of an array element radiating through a fluid/solid interface. The calling sequence for this function is

`[vx, vy, vz]=ps_3Dint(lx, ly, f, mat, ex, ey, ang, Dt0, x, y, z, Ropt, Qopt);`

where (vx, vy, vz) are the velocity components in the second medium divided by the driving velocity on the face of the element, as measured in the (x, y, z) axes of Fig. 6.12. The parameters (lx, ly) are the lengths (in mm), of the rectangular element in the x' - and y' -directions, respectively, and f is the frequency (in MHz). The frequency must be a scalar so if one wants to simulate a pulse one must make multiple calls to the function at different frequencies. The input parameter mat is a MATLAB® row vector given as `mat=[d1, cp1, d2, cp2, cs2, type]` where d1 is the density of the first (fluid) medium in arbitrary units and cp1 is its compressional wave speed (in m/s). Similarly, d2, cp2, cs2, are the density, compressional wave speed (in m/s), and shear wave speed (in m/s), respectively for the second medium, and type is a string that specifies the type of refracted wave we are considering, where type can be 'p' or 's' for a P-wave or an S-wave, respectively. The distances ex and ey are the distances of the element in the x' - and y' -directions from the center of the array, $(e_{x'}, e_{y'})$, measured in mm. The variable ang is the angle of the transducer, θ_T , (in degrees) and Dt0 is the vertical distance, D_{t0} , of the center of the entire array from the interface (in mm). The parameters (x, y, z) are the coordinate locations (in mm) at which the normalized velocity fields are to be evaluated in

Fig. 6.13 A Snell's law ray path as seen in the plane of incidence (see Fig. 6.12)



the second medium. These variables can be scalars, vectors or 2-D matrices, so that with one call to `ps_3Dint` one can produce 2-D data in the x - z , y - z , or x - y planes. Similarly, with one call to the function one can produce data along the x -, y -, or z -axes or along a general line in 3-D. To produce fully 3-D data one must evaluate the velocity fields one plane at a time with multiple calls to the function to cover the third dimension. The distance, z , must always have a non-zero positive value or values. The parameters `Ropt` and `Qopt` are optional inputs that specify the number of segments used in the x' and y' directions, respectively. If one or both of these parameters are not specified then the number of segments in the direction where the number of segments is not specified is calculated so that the segment size is no larger than one wavelength.

The function `ps_3Dint` uses the function `T_fluid_solid` (Code Listing C.29) to calculate the plane wave transmission coefficients for the waves that propagate across a plane fluid-solid interface. The calling sequence for this function is

```
>> [tpp, tps]=T_fluid_solid(d1, cp1, d2, cp2, cs2, theta1);
```

where `theta1` is the angle (in degrees) of the incident waves at the interface and (`tpp`, `tps`) are the transmission coefficients (based on velocity ratios—see Eq. 6.51) for the P-to-P and P-to-SV wave transmission, respectively.

The function `ps_3Dint` also uses the function `pts_3Dint` (Code Listing C.24) to calculate the distances, \tilde{x}_i^{rq} , at which the rays intersect the interface. The calling sequence for this function is

```
>> xi=pts_3Dint(ex, ey, xc, yc, ang1, Dt0, c1, c2, x, y, z);
```

where `xi` is the distance \tilde{x}_i^{rq} (Fig. 6.13), `xc` is the distance x_c^{rq} to the center of the rq th segment in the x' direction and `yc` is the corresponding distance y_c^{rq} in the y' direction. Parameters (`c1`, `c2`) are the wave speeds for the waves traveling in the first and second medium, respectively. The remaining parameters are the same as described for the function `ps_3Dint`. The function `pts_3Dint` uses a function `init_xi3D` (Code Listing C.25) to determine, based on the sizes of the vectors or matrices present in the (x, y, z) variables, the size of the corresponding vector or

Fig. 6.14 The magnitude of the total P-wave velocity in steel as seen in the x - z plane for a 6×12 mm element radiating waves at 5 MHz through a planar water-steel interface. The parameters chosen were: $c_{p1} = 1480$ m/s, $c_{p2} = 5900$ m/s, $c_{s2} = 3200$ m/s, $\rho_1 = 1.0$ gm/cm³, $\rho_2 = 7.9$ gm/cm³, $\theta_T = 10.217^\circ$, $D_{i0} = 50.8$ mm, $e_x = e_y = 0$

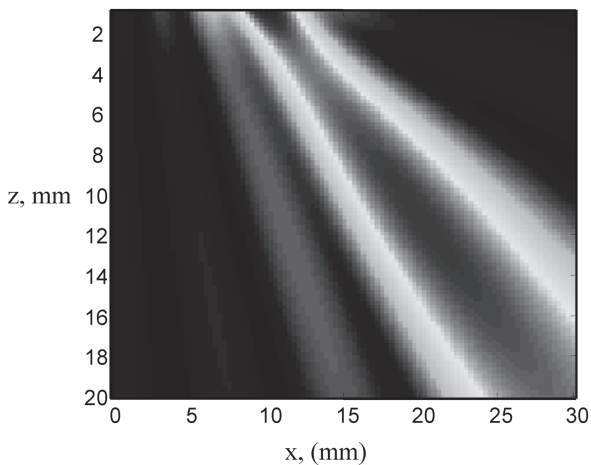
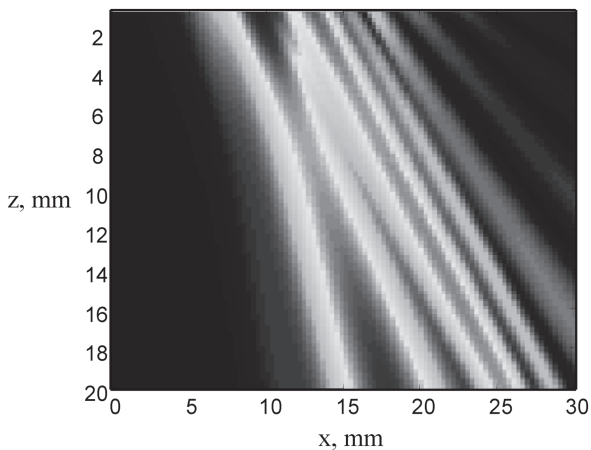


Fig. 6.15 The magnitude of the total S-wave velocity in steel as seen in the x - z plane for a 6×12 mm element radiating waves at 5 MHz through a planar water-steel interface. The other parameters here are the same as in Fig. 6.14



matrix needed to hold the corresponding \tilde{x}_i^{rq} calculations for each element segment. The calling sequence for this function is

$$\gg [\text{xi}, \text{V1}, \text{V2}] = \text{init_xi3D}(\text{x}, \text{y}, \text{z});$$

where xi here is a matrix of zeros having V1 rows and V2 columns. The function pts_3Dint then fills in this matrix of zeros with \tilde{x}_i^{rq} values by following the same approach used in Chaps. 5 and 8. Briefly, this approach writes Snell's law for a ray in terms of the parameters seen in the plane of incidence (Fig. 6.13) as (see Eq. 8.18)

$$g(\tilde{x}_i^{rq}) = \frac{(\tilde{D} - \tilde{x}_i^{rq})\sqrt{(\tilde{x}_i^{rq})^2 + D_s^2} - (c_2 / c_1)\tilde{x}_i^{rq}\sqrt{(\tilde{D} - \tilde{x}_i^{rq})^2 + z^2}}{\tilde{D}} = 0. \quad (6.84)$$

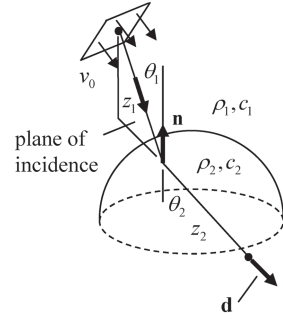
Solving for the value \tilde{x}_i^{rq} at the zero of this $g(\tilde{\mathbf{x}}_i^{rq})$ function then is done with the MATLAB® function `ferrari2` (Code Listing C.5) which was used in Chaps. 5 and 8 to develop the time delay laws for steering and focusing through a planar interface (for more details see Eq. (5.18) and the following discussion in Chap. 5).

As an example of the use of `ps_3Dint`, Fig. 6.14 shows an image in the x - z plane of the magnitude of the velocity at a frequency of 5 MHz in steel for a transmitted P-wave when the center of a 6×12 mm rectangular element in water is located 50.8 mm above a planar water/steel interface and the element is oriented at an angle $\theta_T = 10.217^\circ$. According to Snell's law this element angle will produce a transmitted P-wave at a refracted angle of 45° , which is indeed the angle along which the transmitted beam seen in Fig. 6.14 propagates. Figure 6.15 shows the corresponding magnitude of velocity for the refracted shear wave in the steel instead, which according to Snell's law should travel at a refracted angle of 22.5° . It can be seen from Fig. 6.15 that the main beam does travel in that direction but relatively strong side lobes are also transmitted into the steel.

6.6 Gaussian Beam Equivalent Point Source Modeling

Point source beam models have been frequently used to describe ultrasonic phased arrays. As shown in the previous sections, a relatively simple point source beam model can be developed for radiation through planar interfaces by combining a Rayleigh/Sommerfeld integral approach with high frequency approximations such as ray theory. A similar ray theory approach can be used in more complex problems such as the radiation through curved interfaces by explicitly modeling the behavior of the waves in the neighborhood of a ray (called pencils) with the paraxial approximation [3]. Unfortunately, for curved interfaces the interface itself can produce focusing of the waves, resulting in singularities in the pencil expressions for the wave amplitudes at points or along lines. One can use more exact uniform high frequency expansions to eliminate such singularities but this approach results in a much more complex beam model. Gaussian beam expressions are always non-singular even when radiating through curved interfaces. This property, plus the fact that a multi-Gaussian beam model is numerically very efficient makes it the ideal beam model for modeling large, single element transducers, as discussed in Chap. 3, even where point source models in conjunction with high frequency ray theory fails. However, as seen in Chap. 4, multi-Gaussian beam models rely on the paraxial approximation, an approximation that hinders their use as an effective beam model for modeling the wide radiation patterns of small elements in an array. The non-paraxial multi-Gaussian beam model discussed Chap. 4 can remove this restriction but as seen in that Chapter a non-paraxial multi-Gaussian beam model is less efficient than a point source beam model for single medium problems. Furthermore, non-paraxial multi-Gaussian beam models are not readily extendable to radiation through interfaces. There is an alternate approach that can use Gaussian beams while avoiding the limitations of the paraxial approximation. The basic idea is to replace a beam model that uses point sources and ray theory with one that uses Gaussian beams and ray

Fig. 6.16 Radiation of pressure waves by an array element through a spherical interface between two fluid media



theory. In this section we will show that such a replacement is possible, resulting in a Gaussian beam equivalent point source (GBEPS) model [4].

To see the basis of the GBEPS model, consider a harmonic spherical wave radiating from a point source in a fluid, where the pressure, p , is given by

$$p = \frac{\exp(ikr)}{r}. \quad (6.85)$$

If we take the z -axis to be along a particular direction and let $r = \sqrt{\rho^2 + z^2}$, where ρ is the perpendicular distance from the z -axis, then in the paraxial approximation near that axis we have, approximately

$$p \cong \frac{\exp(ikz)}{z} \exp\left(\frac{ik\rho^2}{2z}\right). \quad (6.86)$$

Alternatively, if we consider a Gaussian beam propagating along the z -axis, then [Schmerr-Song]

$$p = \frac{A(-ik/2B)}{(z - ik/2B)} \exp(ikz) \exp\left[\frac{ik\rho^2}{2(z - ik/2B)}\right], \quad (6.87)$$

where the constants A and B define the specific characteristics of the Gaussian beam. Comparing Eqs. (6.86) and (6.87), we see they will be essentially identical if

$$\left|\frac{k}{2B}\right| \ll z, \quad A(-ik/2B) = 1. \quad (6.88)$$

Under these conditions, we see that the propagation characteristics of the spherical wave and the Gaussian beam are indistinguishable. In the GBEPS model, the wave field of an array element is first modeled as a superposition of spherical wave (point source) responses. The spherical waves are then replaced by their Gaussian beam equivalents, satisfying Eq. (6.88), and the well-behaved propagation and transmission/reflection laws for Gaussian beams are used to model the transducer

wave field after interactions with complex geometries. To see how this replacement works, consider the propagation of waves from an element radiating through a fluid-fluid interface. In order to keep the expressions involved from being too algebraically complex, we will also assume in this example that the interface is spherical so that the plane of incidence is always aligned with a principal axis of the curved spherical interface (Fig. 6.16). In this case, the velocity, \mathbf{v} , in the second medium can be represented by a point source model and high frequency ray theory (see Eq. (6.49) for the comparable planar interface fluid-solid model) as [Schmerr]

$$\mathbf{v} = \frac{-ik_1 v_0}{2\pi} \int_S \frac{T_{12} \mathbf{d} \exp(ik_1 z_1 + ik_2 z_2)}{\sqrt{\phi_1} \sqrt{\phi_2}} dS, \quad (6.89)$$

where

$$\begin{aligned} \phi_1 &= z_1 + \frac{c_2 \cos^2 \theta_1}{c_1 \cos^2 \theta_2} z_2 + \frac{z_1 z_2}{R} \left(\frac{c_2 \cos \theta_1}{c_1} - \cos \theta_2 \right) \\ \phi_2 &= z_1 + \frac{c_2}{c_1} z_2 + \frac{z_1 z_2}{R} \left(\frac{c_2 \cos \theta_1}{c_1} - \cos \theta_2 \right). \end{aligned} \quad (6.90)$$

Here, v_0 is the velocity on the surface, S , of the element, $k_m = \omega / c_m$ ($m=1,2$) are the wave numbers for waves traveling in the first and second media, respectively, with c_m the corresponding wave speeds, z_m ($m=1,2$) are the distances traveled along a Snell's law ray path from a point on the transducer surface to a point in the solid where the velocity is to be evaluated, T_{12} is an ordinary plane wave transmission coefficient (based on a velocity ratio) along this ray path, and R is the radius of curvature of the spherical interface. The vector \mathbf{d} is the polarization of the compressional wave in the second medium (Fig. 6.16). The problem with this point source model is readily evident from Eq. (6.90). The terms ϕ_1 or ϕ_2 can become zero for the case of a focusing spherical interface which occurs if $R > 0$ and $c_1 > c_2$ or $R < 0$ and $c_2 > c_1$ [Schmerr], so that the velocity expressions will become singular at those points. However, if we replace the spherical waves in the first medium by an equivalent Gaussian beam, i.e. one that satisfies Eq. (6.88), and use the laws of propagation and transmission of that Gaussian beam through the spherical interface [Schmerr-Song], in place of Eq. (6.89) we find

$$\mathbf{v} = \frac{-ik_1 v_0}{2\pi} \int_S \frac{T_{12} \mathbf{d} \exp(ik_1 z_1 + ik_2 z_2)}{\sqrt{\psi_1} \sqrt{\psi_2}} dS, \quad (6.91)$$

where

$$\begin{aligned} \psi_1 &= (z_1 - ik/2B) + \frac{c_2 \cos^2 \theta_1}{c_1 \cos^2 \theta_2} z_2 + \frac{(z_1 - ik/2B)z_2}{R} \left(\frac{c_2 \cos \theta_1}{c_1} - \cos \theta_2 \right) \\ \psi_2 &= (z_1 - ik/2B) + \frac{c_2}{c_1} z_2 + \frac{(z_1 - ik/2B)z_2}{R} \left(\frac{c_2 \cos \theta_1}{c_1} - \cos \theta_2 \right) \end{aligned} \quad (6.92)$$

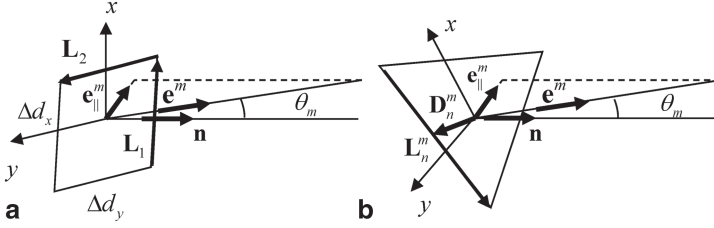


Fig. 6.17 The definition of parameters that define the far field directivity of **a** a rectangular segment, and **b** a triangular segment

and now the velocity is always well-behaved everywhere in the second medium.

As done previously with a point source model we can use Eq. (6.91) and break S up into M segments, ΔS , and perform the phase integration to first order over the elements exactly for small polygonal elements (rectangles, triangles). We have shown this previously for a small rectangular element radiating through a planar interface, (see Eq. (6.62), for example) and the curvature of the interface in the present case does not change those first order results [Schmerr]. Thus, in the far field approximation for a segment the surface integration of Eq. (6.91) in terms of M segments yields

$$\mathbf{v} = v_0 \sum_{m=1}^M \mathbf{d}^m T_{12}^m D_R^m \frac{\exp(ik_1 z_1^m + ik_2 z_2^m)}{\sqrt{\psi_1^m} \sqrt{\psi_2^m}} \quad (6.93)$$

in terms of a directivity function, D_R^m ($m = 1, \dots, M$). For a rectangular segment this directivity is given as [Schmerr]

$$D_R^m = \frac{-ik_1 \Delta d_x \Delta d_y}{2\pi} \frac{\sin[k_1 \sin \theta_m (\mathbf{e}_{||}^m \cdot \mathbf{L}_1) / 2]}{k_1 \sin \theta_m (\mathbf{e}_{||}^m \cdot \mathbf{L}_1) / 2} \frac{\sin[k_1 \sin \theta_m (\mathbf{e}_{||}^m \cdot \mathbf{L}_2) / 2]}{k_1 \sin \theta_m (\mathbf{e}_{||}^m \cdot \mathbf{L}_2) / 2}, \quad (6.94)$$

where, $\mathbf{L}_1, \mathbf{L}_2$ are vectors $\mathbf{L}_1 = \Delta d_x \mathbf{e}_x$, $\mathbf{L}_2 = \Delta d_y \mathbf{e}_y$, and $\Delta d_x, \Delta d_y$ are the lengths of the segment in the x - and y -directions, respectively, and $\mathbf{e}_x, \mathbf{e}_y$ are unit vectors along those same directions. The unit vector $\mathbf{e}_{||}^m$ is along the projection of a unit vector, \mathbf{e}^m , along a ray path in the first medium onto the x - y plane as shown in Fig. 6.17a, and θ_m is the angle of this ray path from the element unit normal, \mathbf{n} . Note that this directivity is slightly different from those defined previously as it also contains a coefficient (the first term on the right side of Eq. (6.94)) as well as the sinc functions that appeared in previously defined directivities. Similarly, for a triangular segment (see Fig. 6.17b) the directivity is [Schmerr]

$$D_R^m = \sum_{n=1}^3 \frac{1}{2\pi} \frac{(\mathbf{n} \times \mathbf{e}^m) \cdot \mathbf{L}_n^m}{\sin^2 \theta_m} \exp[-ik_1 \sin \theta_m (\mathbf{e}_{||}^m \cdot \mathbf{D}_n^m)] \frac{\sin[k_1 \sin \theta_m (\mathbf{e}_{||}^m \cdot \mathbf{L}_n^m) / 2]}{[k_1 \sin \theta_m (\mathbf{e}_{||}^m \cdot \mathbf{L}_n^m) / 2]}, \quad (6.95)$$

where \mathbf{D}_n^m is the vector distance from the centroid of the m th segment to the center of the n th side and \mathbf{L}_n^m are vectors along the segment sides. The triangular element case is also shown here since it is an important building block for modeling segments of large, single element non-rectangular transducers and could also be used to model segments of non-rectangular array elements as well.

This example was for a very specific case but Gaussian beams can be used to model much more general problems. For example, Gaussian beams can be propagated, transmitted and reflected through multiple media and explicit expressions written for the Gaussian beam wave field after these complex interactions. For example, after beam interactions with P curved interfaces the velocity along the central ray in the $(P+1)$ th medium, \mathbf{v}_{P+1} , of a Gaussian beam can be written as [Schmerr-Song]

$$\mathbf{v}_{P+1} = A v_0 \frac{\sqrt{\det[\mathbf{M}_{P+1}(z_{P+1})]}}{\sqrt{\det[\mathbf{M}_{P+1}(0)]}} \left[\prod_{p=P}^{p=1} \mathbf{T}_p \mathbf{d}_1 \frac{\sqrt{\det[\mathbf{M}_p(z_p)]}}{\sqrt{\det[\mathbf{M}_p(0)]}} \right] \exp \left[i \omega \sum_{p=1}^{p=P} \frac{z_p}{c_p} \right], \quad (6.96)$$

where one can write down explicit expressions for the 2×2 \mathbf{M}_p matrices and the 3×3 \mathbf{T}_p matrices contain the appropriate plane wave transmission/reflection coefficients for the given ray path and \mathbf{d}_1 is the polarization in the first medium (at the array element). The distances z_p are the propagation distances in each medium along a ray path. The velocity amplitude of the Gaussian beam on the element face is v_0 .

If we use Eq. (6.96) in our GBEPS modeling approach, then the general form of the GBEPS model for the velocity \mathbf{v} generated by an element with M segments (with $A = 2iB/k$) is:

$$\mathbf{v} = v_0 \sum_{m=1}^{m=M} \left\{ A D_R^m \frac{\sqrt{\det[\mathbf{M}_{P+1}^m(z_{P+1}^m)]}}{\sqrt{\det[\mathbf{M}_{P+1}^m(0)]}} \left[\prod_{p=P}^{p=1} \mathbf{T}_p^m \mathbf{d}_1 \frac{\sqrt{\det[\mathbf{M}_p^m(z_p^m)]}}{\sqrt{\det[\mathbf{M}_p^m(0)]}} \right] \exp \left[i \omega \sum_{p=1}^{p=P} \frac{z_p^m}{c_p} \right] \right\}. \quad (6.97)$$

The success of the GBEPS model relies on having constants A and B that accurately simulate the behavior of a spherical wave. To obtain such best-fit A , B values it is convenient to use Prony's method [5, 6] because it is a fast and direct method. In this approach, a Gaussian beam is matched with the spherical wave in the neighborhood of a particular axis, which we will take as the z -axis. Thus, we want to satisfy

$$p = \frac{\exp(ik\sqrt{\rho^2 + z^2})}{\sqrt{\rho^2 + z^2}} = A \frac{1}{1 + 2iBz/k} \exp(ikz) \exp \left[\frac{ik\rho^2}{2(z - ik/2B)} \right], \quad (6.98)$$

where ρ is the perpendicular distance from the z -axis. We sample these functions at a known fixed z value and for M values of ρ , ρ_m , given by $\rho_m = m^2 \varepsilon^2$, where ε is a constant that controls the spacing of points. Then, Eq. (6.98) at these sampled values gives

$$p_m = \frac{\exp\left(ik\sqrt{\rho_m^2 + z^2}\right)}{\sqrt{\rho_m^2 + z^2}} = A \frac{1}{1 + 2iBz/k} \exp(ikz) \exp\left[\frac{ikm\varepsilon}{2(z - ik/2B)}\right], \quad (6.99)$$

which we write as the M sampled values in the form

$$p_m = C \exp(mD) \quad (6.100)$$

with

$$\begin{aligned} C &= A \frac{1}{1 + 2iBz/k} \exp(ikz), \\ D &= \frac{ik\varepsilon}{2(z - ik/2B)}. \end{aligned} \quad (6.101)$$

Expressing sampled values of a variable in terms of a single best fit complex exponential with C and D parameters is a special case of the more general fitting of the samples to multiple complex exponentials with N values of C and D . These parameters are easily obtained with Prony's method by solving for the roots of a polynomial and a system of linear equations [5, 6]. For example, let the frequency $f = 5\text{MHz}$, the distance $z = 200\text{ mm}$, and the wave speed (of water) $c = 1480\text{ m/s}$ and consider $M = 4$ sampled values of the pressure for ρ values from 0 to 6.5 mm (using $\varepsilon = 0.637$). This range of ρ values is well within the paraxial region where the Gaussian beam solution is valid. The values obtained from Prony's method for these choices were

$$A = 10.51 + 9.11i; B = 96.67 - 111.50i, \quad (6.102)$$

which do satisfy $A = 2iB/k$. At other frequencies it is not necessary to recalculate these A and B values since one can simply use the B obtained here and scale the A value appropriately. Note that to satisfy the inequality $z \gg |k/2B|$, our choice of parameters gives $z \gg 0.07\text{mm}$, approximately, so that this single Gaussian beam should accurately represent the spherical wave for z -distances of, say, 1 mm or greater. This can be shown to indeed be the case by simply plotting the exact magnitude of the pressure in a spherical wave versus the radial (z -distance) and comparing it to that of the single Gaussian beam. Thus, except in a very small region near the origin of the spherical wave, this single Gaussian beam and a spherical wave for all practical purposes are indistinguishable. The size of the region where the inequality is violated will of course grow as the frequency increases but generally

Fig. 6.18 Steering angles for **a** an array radiating directly into a fluid, and **b** for the case where the array is on a solid Lucite wedge radiating into steel

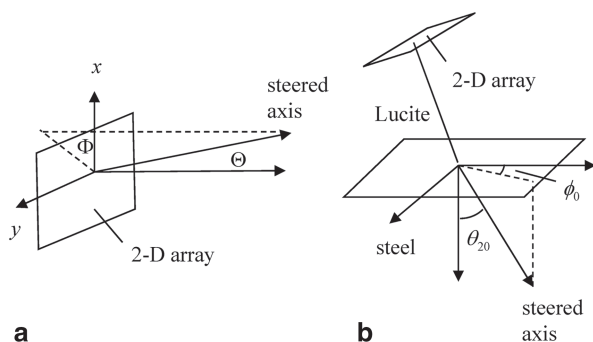
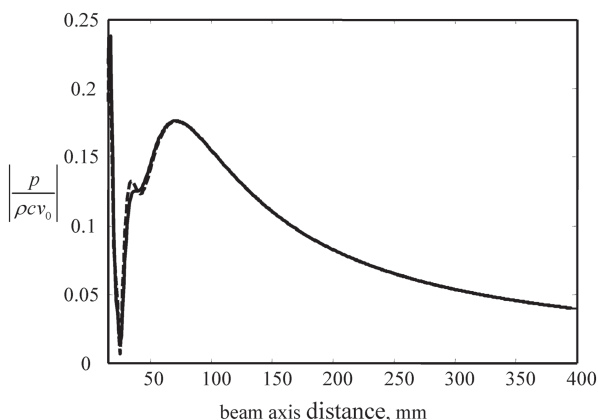


Fig. 6.19 Magnitude of the on-axis pressure for a 5 MHz, 8×4 array radiating into a fluid where the array is phased to steer the beam in the $\Phi = -90^\circ$, $\Theta = 20^\circ$ direction and focused at 150 mm. *Solid line*: point source model “exact” result, *dashed line*: GBEPS model results



this is not a problem as the frequency content in most ultrasonic NDE signals is roughly of the order of the 5 MHz value used here to obtain these A and B values. If one wishes to use arrays with significantly higher frequencies (much greater than 20 MHz, for example) one can simply re-compute a new set of A and B values suitable for those higher frequencies.

The GBEPS model has been examined for a wide variety of problems with excellent results. Here, we will show some selected examples of the performance of this method similar to those given in [4]. First, consider a phased array radiating directly into water (see Fig. 6.18a), where phasing will be used to both focus the beam and steer it in the (Θ, Φ) directions. We modeled a 5 MHz, 8×4 rectangular array where the elements were 0.8×2.4 mm rectangles with a gap size between elements of 0.2 mm in both directions. A delay law was applied to this array to steer it in the $\Theta = -90^\circ$, $\Phi = 20^\circ$ direction and focus it at a distance of 150 mm along the steering direction. The magnitude of the normalized pressure along the steered axis is shown in Fig. 6.19 for both the GBEPS model and an result obtained by a very detailed integration of a point source model, which was used as The “gold standard”. It can be seen from that figure that the GBEPS model gave very good results in spite of

Fig. 6.20 Magnitude of the on-axis velocity for a 5 MHz, 16×16 array placed on a Lucite wedge and radiating into steel, plotted versus the distance along the steered beam axis. The array was phased to focus at a depth of 50 mm in the steel and steered to the angles $\phi_0 = 30^\circ$, $\theta_{20} = 30^\circ$. *Solid line*—point source model “exact” results; *dashed line*—GBEPS model results

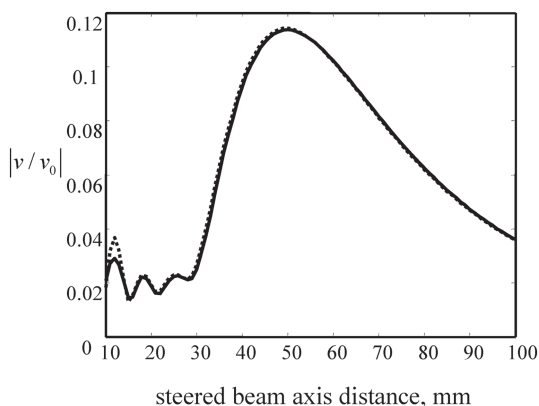
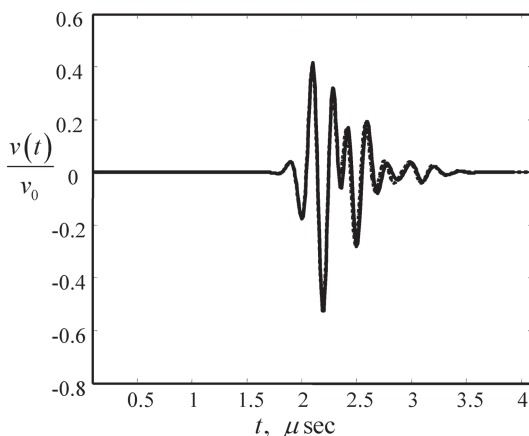


Fig. 6.21 Simulated pulse at a distance of 6.25 mm in steel for a 5 MHz, 8×8 array placed on a Lucite wedge. *Solid line*—point source beam model “exact” results. *Dashed line*—GBEPS model results



the fact that it used only one segment per array element, where the array elements were rather large (approximately 2.7×8 wavelengths). Even the small differences in the near-field could be improved by simply using more segments in the larger element dimension. Figure 6.18b shows a more complex modeling setup where an array is placed on a Lucite wedge and radiates into steel. In this angle beam setup, the wedge angle was chosen to generate a 45° P-wave in the wedge without any phasing (a shear wave also was generated, but the results shown will only be for the P-wave beam). In this example a 5 MHz square 16×16 array was placed on the wedge with elements having dimensions of 1.6×1.6 mm and there was a gap size of 0.2 mm between elements in both directions. The distance from the center of the array to the interface (along a direction normal to the array) was 24.86 mm. Figure 6.20 shows a plot of the magnitude of the normalized velocity (normalized by the velocity on the face of the transducer) along the steered beam axis where the time delay law was chosen to focus the beam at a depth of 50 mm and steered to the

angles ($\phi_0 = 30^\circ$, $\theta_{20} = 30^\circ$). Both the GBEPS results and that for the point source standard are plotted in Fig. 6.20, showing that again the GBEPS model gave excellent agreement even though only one segment per array element was used and each side of the array element was about 3.7 wavelengths in length.

If the GBEPS model is used to simulate a time domain pulse, the performance and accuracy of the model are also very good. Consider the same angle beam setup described previously where without steering present a 45° P-wave is radiated into steel. The transducer on the wedge in this case was a square 8×8 array with square elements having side lengths of 3.2 mm and the gap between elements was 0.2 mm in both directions. In this case the response at a fixed point ($z=6.25$ mm) along the steered axis was calculated at a single frequency and multiplied by a Gaussian window having a center frequency of 5 MHz and a -6 dB bandwidth of 60% to generate a response spectrum. This spectrum was then inverted into time to simulate a pulsed response. In this case the focus was placed at 50 mm and the beam was steered in the ($\phi_0 = 0^\circ$, $\theta_{20} = 60^\circ$) direction. The “gold standard” model was again a point source model where each array element was divided into 40×40 segments, giving each segment a length of about a fifth of a wavelength. As Fig. 6.21 shows, the GBEPS model very closely models that of the point source model.

The examples discussed above were chosen to illustrate the ability of the GBEPS model to accurately simulate beam steering and focusing of some typical arrays. All the cases examined were for single medium or planar interface problems where point source models are well-behaved so that we could compare GBEPS models with a well-known “standard”. Since a GBEPS model, however, is not restricted to those geometries and can in fact also be applied to much more complicated cases such as anisotropic or inhomogeneous media, curved interfaces, etc. the GBEPS beam model approach can be considered to be the extension of the point source beam models presented in this book to more complex NDE bulk wave inspection problems.

References

1. W.C. Chew, *Waves and Fields in Inhomogeneous Media* (Van Nostrand Reinhold, New York, 1990)
2. V. Červený, *Seismic Ray Theory* (Cambridge University Press, Cambridge, 2001)
3. N. Gengembre, A. Lhémy, Pencil method in elastodynamics: application to ultrasonic field computation. *Ultrasonics* **38**, 495–499 (2000)
4. L.W. Schmerr, R. Huang, A. Sedov, The simulation of ultrasonic beams with a Gaussian beam equivalent point source model. *Chin. J. Acoust.* **29**, 97–106 (2010)
5. M.D. Prange, R.G. Shenoy, A fast Gaussian beam description of ultrasonic fields based on Prony’s method. *Ultrasonics* **34**, 117–119 (1996)
6. L.W. Schmerr, A.L. Lopez-Sanchez, A. Sedov, K-Space Prony’s method for generating basis functions of multi-Gaussian beam models. *Ultrasonics* **50**, 600–605 (2010)

Chapter 7

Phased Array Beam Modeling (2-D Elements)

The models developed in Chap. 6 for a single element will be used in this Chapter to develop a model of a complete 2-D or linear array. As done in Chap. 4 for 2-D problems, we will discuss steering and focusing in 3-D for these arrays.

7.1 Phased Array Beam Models—Single Medium

Consider first a 2-D array of identical rectangular elements radiating directly into a single fluid medium. We will assume that the array has $n = (1, 2, \dots, L_1)$ elements in the x -direction and $l = (1, 2, \dots, L_2)$ elements in the y -direction. The lengths of the element are (l_x, l_y) in the x - and y -directions, respectively and the corresponding gap widths in those directions are (g_x, g_y) . The geometry for one of those elements is shown in Fig. 7.1. We can use the multiple point source model developed in Chap. 6 (see Eq. (6.33)) to represent each element. The pressure wave field of the entire array can then be written as

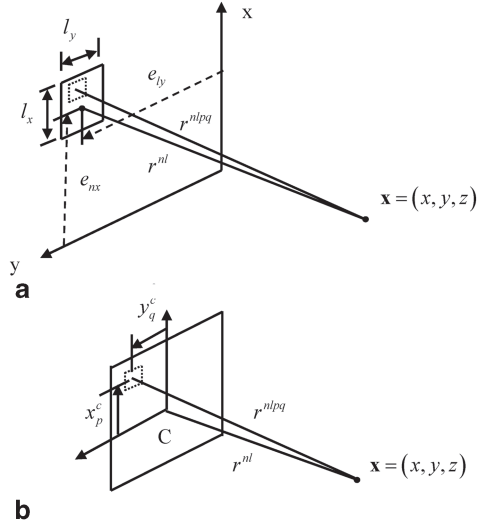
$$p(\mathbf{x}, \omega) = \rho c v_0(\omega) \sum_{n=1}^{L_1} \sum_{l=1}^{L_2} \tilde{C}_n \tilde{C}_l \exp(i\omega \Delta t_{nl}) p_e(x, y, z, \omega, e_{nx}, e_{ly}), \quad (7.1)$$

where $(\tilde{C}_n, \tilde{C}_l)$ are the apodization constants in the x - and y -directions, respectively, and Δt_{nl} are the time delays and where $p_e(x, y, z, \omega, e_{nx}, e_{ly})$ is the normalized pressure, $p / \rho c v_0$, of a single element in the multiple point source model of Eq. (6.33) as implemented in the MATLAB[®] function `ps_3Dv` (Code Listing C.20), that is,

$$p_e(\mathbf{x}, \omega) = \frac{1}{2\pi} \sum_{p=1}^P \sum_{q=1}^Q (-ik \Delta d_x \Delta d_y) \frac{\sin(ku_x^{nlpq} \Delta d_x / 2)}{(ku_x^{nlpq} \Delta d_x / 2)} \frac{\sin(ku_y^{nlpq} \Delta d_y / 2)}{(ku_y^{nlpq} \Delta d_y / 2)} \frac{\exp(ikr^{nlpq})}{r^{nlpq}} \quad (7.2)$$

The various parameters appearing in Eq. (7.2) are:

Fig. 7.1 **a** Geometry parameters for an element of a 2-D array radiating into a fluid, and **b** details of the element segment parameters within each element



$$\begin{aligned}
 r^{nlpq} &= \sqrt{(x - x_p^c - e_{nx})^2 + (y - y_q^c - e_{ly})^2 + z^2} \\
 u_x^{nlpq} &= \frac{x - x_p^c - e_{nx}}{r^{nlpq}}, u_y^{nlpq} = \frac{y - y_q^c - e_{ly}}{r^{nlpq}} \\
 x_p^c &= -\frac{l_x}{2} + \Delta d_x \left(p - \frac{1}{2} \right) \\
 y_q^c &= -\frac{l_y}{2} + \Delta d_y \left(q - \frac{1}{2} \right) \\
 e_{nx} &= \left(\frac{2n-1-L_1}{2} \right) s_x \\
 e_{ly} &= \left(\frac{2l-1-L_2}{2} \right) s_y,
 \end{aligned} \tag{7.3}$$

where $\Delta d_x = l_x / P$, $\Delta d_y = l_y / Q$ are the lengths of the element segments in the x - and y -directions, respectively, and $s_x = l_x + g_x$, $s_y = l_y + g_y$ are the array pitches in the x - and y -directions.

The model for a contact array radiating P-waves into an elastic solid is very similar to the fluid case. If we compare the original Rayleigh-Sommerfeld model of Eq. (6.21) with the corresponding contact model of Eq. (6.38) or, equivalently, the far field models of Eqs. (6.26) and (6.41) we see that we can get the contact case from the fluid case by making the replacement $\rho_1 c_{p1} v_0 \rightarrow p_0 / \rho_1 c_{p1}$ to go from a model of a pressure field to one for a velocity field, and including an extra term $K_p \mathbf{d}_p$ to account for the additional directivity and polarization terms present in the velocity field for the contact case. However, since the segments are typically very

small we can approximate this additional term by its value at the centroid of each segment, in which case $K_p(\theta') \equiv K_p(u_z^{nlpq})$ and $\mathbf{d}_p = (u_x^{nlpq}, u_y^{nlpq}, u_z^{nlpq})$, where

$$u_z^{nlpq} = \frac{z}{r^{nlpq}} \quad (7.4)$$

and (see Eqs. (6.39) and (6.40))

$$K_p(u_z^{nlpq}) = \frac{u_z^{nlpq} \kappa^2 \left(\kappa^2 / 2 - 1 + (u_z^{nlpq})^2 \right)}{2G} \quad (7.5)$$

$$G = \left(1 - (u_z^{nlpq})^2 - \kappa^2 / 2 \right)^2 + \left(1 - (u_z^{nlpq})^2 \right)^2 u_z^{nlpq} \sqrt{\kappa^2 - 1 + (u_z^{nlpq})^2},$$

and, recall, $\kappa = c_{p1}/c_{s1}$ is the ratio of the compressional and shear wave speeds in the solid. Making these changes to Eq. (7.2), our model for the contact array gives the velocity field in the solid as

$$\mathbf{v}(\mathbf{x}, \omega) = \frac{p_0(\omega)}{2\pi\rho_1 c_{p1}} \sum_{n=1}^{L_1} \sum_{l=1}^{L_2} \tilde{C}_n \tilde{C}_l \exp(i\omega\Delta t_{nl}) \left\{ \sum_{p=1}^P \sum_{q=1}^Q (-ik\Delta d_x \Delta d_y) \mathbf{d}^{nlpq} K_p(u_z^{nlpq}) \right. \\ \left. \cdot \frac{\sin(ku_x^{nlpq} \Delta d_x / 2)}{(ku_x^{nlpq} \Delta d_x / 2)} \frac{\sin(ku_y^{nlpq} \Delta d_y / 2)}{(ku_y^{nlpq} \Delta d_y / 2)} \frac{\exp(ikr^{nlpq})}{r^{nlpq}} \right\} \quad (7.6)$$

with

$$\mathbf{d}^{nlpq} = (u_x^{nlpq}, u_y^{nlpq}, u_z^{nlpq}). \quad (7.7)$$

Generally, we would expect that both K_p and \mathbf{d}^{nlpq} will also vary very slowly over the element, so if we approximate those parameters by their values at the centroid C of the element (see Fig. 7.1), we can write Eq. (7.6) instead as

$$\mathbf{v}(\mathbf{x}, \omega) = \frac{p_0(\omega)}{2\pi\rho_1 c_{p1}} \sum_{n=1}^{L_1} \sum_{l=1}^{L_2} \tilde{C}_n \tilde{C}_l \exp(i\omega\Delta t_{nl}) \mathbf{d}^{nl} K_p(u_z^{nl}) \left\{ \sum_{p=1}^P \sum_{q=1}^Q (-ik\Delta d_x \Delta d_y) \right. \\ \left. \cdot \frac{\sin(ku_x^{nlpq} \Delta d_x / 2)}{(ku_x^{nlpq} \Delta d_x / 2)} \frac{\sin(ku_y^{nlpq} \Delta d_y / 2)}{(ku_y^{nlpq} \Delta d_y / 2)} \frac{\exp(ikr^{nlpq})}{r^{nlpq}} \right\}, \quad (7.8)$$

where $\mathbf{d}^{nl} = (u_x^{nl}, u_y^{nl}, u_z^{nl})$ and

$$\begin{aligned} u_x^{nl} &= \frac{x - e_{nx}}{r^{nl}}, u_y^{nl} = \frac{y - e_{ly}}{r^{nl}}, u_z^{nl} = \frac{z}{r^{nl}} \\ r^{nl} &= \sqrt{(x - e_{nx})^2 + (y - e_{ly})^2 + z^2}, \end{aligned} \quad (7.9)$$

which then can also be simply rewritten in terms of the normalized pressure as

$$\mathbf{v}(\mathbf{x}, \omega) = \frac{p_0(\omega)}{\rho_1 c_{p1}} \sum_{n=1}^{L_1} \sum_{l=1}^{L_2} \tilde{C}_n \tilde{C}_l \exp(i\omega \Delta t_{nl}) \mathbf{d}^{nl} K_p(u_z^{nl}) p_e(x, y, z, \omega, e_{nx}, e_{ly}). \quad (7.10)$$

If the element itself is less than a wavelength in length in both the x - and y -directions then we expect that we can use a single point source model for each element. In this case, the single point source model for the array gives

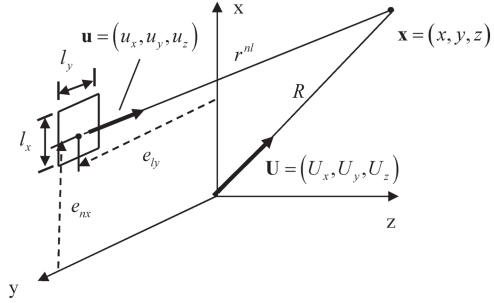
$$\begin{aligned} p(\mathbf{x}, \omega) &= \frac{\rho c v_0(\omega)}{2\pi} \sum_{n=1}^{L_1} \sum_{l=1}^{L_2} \tilde{C}_n \tilde{C}_l \exp(i\omega \Delta t_{nl}) (-ik l_x l_y) \\ &\cdot \frac{\sin(ku_x^{nl} l_x / 2)}{(ku_x^{nl} l_x / 2)} \frac{\sin(ku_y^{nl} l_y / 2)}{(ku_y^{nl} l_y / 2)} \frac{\exp(ikr^{nl})}{r^{nl}} \end{aligned} \quad (7.11)$$

for the immersion case, and

$$\begin{aligned} \mathbf{v}(\mathbf{x}, \omega) &= \frac{p_0(\omega)}{2\pi \rho_1 c_{p1}} \sum_{n=1}^{L_1} \sum_{l=1}^{L_2} \tilde{C}_n \tilde{C}_l \exp(i\omega \Delta t_{nl}) \mathbf{d}^{nl} K_p(u_z^{nl}) (-ik l_x l_y) \\ &\cdot \frac{\sin(ku_x^{nl} l_x / 2)}{(ku_x^{nl} l_x / 2)} \frac{\sin(ku_y^{nl} l_y / 2)}{(ku_y^{nl} l_y / 2)} \frac{\exp(ikr^{nl})}{r^{nl}} \end{aligned} \quad (7.12)$$

for the contact case. These are simply special cases of Eqs. (7.2) and (7.10), respectively, for these small element sizes. For the immersion case, Eq. (7.11) is implemented automatically by the MATLAB[®] function `ps3Dv` when both element lengths are less than a wavelength, as discussed in Chap. 6. One could also use a single point source model for larger elements by specifying $P_{opt} = Q_{opt} = 1$ when evaluating the normalized pressure with `ps_3Dv` but this must be done with care since a single point source model will lose accuracy as the element size increases unless one is computing fields sufficiently far from the element so that one is in the far field of the element.

Fig. 7.2 Parameters for defining the behavior of an array element in the far field



7.1.1 Far Field Behavior of an Array

We can certainly use the single point source models to examine the wave field of the array when we are in the far field of the entire array. In this case, we can approximate r^{nl} as (see Fig. 7.2)

$$\begin{aligned} r^{nl} &= \sqrt{(x - e_{nx})^2 + (y - e_{ly})^2 + z^2} \\ &\cong R - e_{nx} U_x - e_{ly} U_y \\ (u_x^{nl}, u_y^{nl}, u_z^{nl}) &\cong (U_x, U_y, U_z), \end{aligned} \quad (7.13)$$

where

$$\begin{aligned} R &= \sqrt{x^2 + y^2 + z^2} \\ U_x &= \frac{x}{R}, U_y = \frac{y}{R}, U_z = \frac{z}{R}. \end{aligned} \quad (7.14)$$

If we consider the immersion case, Eq. (7.11), we then have

$$\begin{aligned} p(\mathbf{x}, \omega) &= \frac{\rho c v_0(\omega)}{2\pi} \sum_{n=1}^{L_1} \sum_{l=1}^{L_2} \tilde{C}_n \tilde{C}_l \exp(i\omega \Delta t_{nl}) (-ik l_x l_y) \\ &\quad \cdot D_e(k U_x l_x, k U_y l_y) \frac{\exp(ikR)}{R} \exp[-ik(e_{nx} U_x + e_{ly} U_y)], \end{aligned} \quad (7.15)$$

where D_e is the element directivity, given by

$$D_e(k U_x l_x, k U_y l_y) = \frac{\sin(k U_x l_x / 2)}{(k U_x l_x / 2)} \frac{\sin(k U_y l_y / 2)}{(k U_y l_y / 2)}. \quad (7.16)$$

Placing the expressions for the centroid locations (see Eq. (7.2)) into Eq. (7.15) gives

$$p(\mathbf{x}, \omega) = \frac{\rho c v_0(\omega)}{2\pi} (-ik l_x l_y) D_e \frac{\exp(ikR)}{R} \exp\left[ik\left(\frac{L_1+1}{2}\right)s_x U_x\right] \exp\left[ik\left(\frac{L_2+1}{2}\right)s_y U_y\right] \cdot \sum_{n=1}^{L_1} \sum_{l=1}^{L_2} \tilde{C}_n \tilde{C}_l \exp(i\omega \Delta t_{nl}) \exp[-ik n s_x U_x] \exp[-ik l s_y U_y]. \quad (7.17)$$

If we set the amplitude weights and time delays equal to zero, then as shown in Chap. 4 we can sum the remaining series to find

$$p(\mathbf{x}, \omega) = \frac{\rho c v_0(\omega)}{2\pi} (-ik L_1 L_2 l_x l_y) D_e \frac{\sin[(L_1 k s_x U_x)/2]}{L_1 \sin[(k s_x U_x)/2]} \frac{\sin[(L_2 k s_y U_y)/2]}{L_2 \sin[(k s_y U_y)/2]} \frac{\exp(ikR)}{R}, \quad (7.18)$$

which shows that, as in the 2-D case, in the far field of the entire array we see both the element directivity, D_e , and directivity, D_s , associated with an array of point sources [1], where the point source directivity is

$$D_s(k s_x U_x, k s_y U_y) = \frac{\sin[(L_1 k s_x U_x)/2]}{L_1 \sin[(k s_x U_x)/2]} \frac{\sin[(L_2 k s_y U_y)/2]}{L_2 \sin[(k s_y U_y)/2]}. \quad (7.19)$$

Figure 7.3 shows the element directivity of a square element where the pitch is either one wavelength or two wavelengths. We see, as in the 2-D case, a very broad radiation pattern at the one wavelength case and that this radiation becomes more concentrated for the two wavelengths pitch. In the case of a linear array element, one dimension will typically have a length of several wavelengths or less while the other length will be many wavelengths. Figure 7.4 shows a contour plot of the far field directivity (looking down the z -axis) for an element where the length is two wavelengths in the x -direction and 15 wavelengths in the y -direction. As can be seen from that figure, the beam radiation is tightly confined in the y -direction but much broader in the x -direction, as expected.

7.1.2 Beam Steering in 3-D

In Chaps. 3–5, we showed for 2-D problems that beam steering could be generated by applying a spatially linear time delay to the face of a transducer or an array. In the next chapter, the corresponding steering time delays for 2-D arrays radiating a

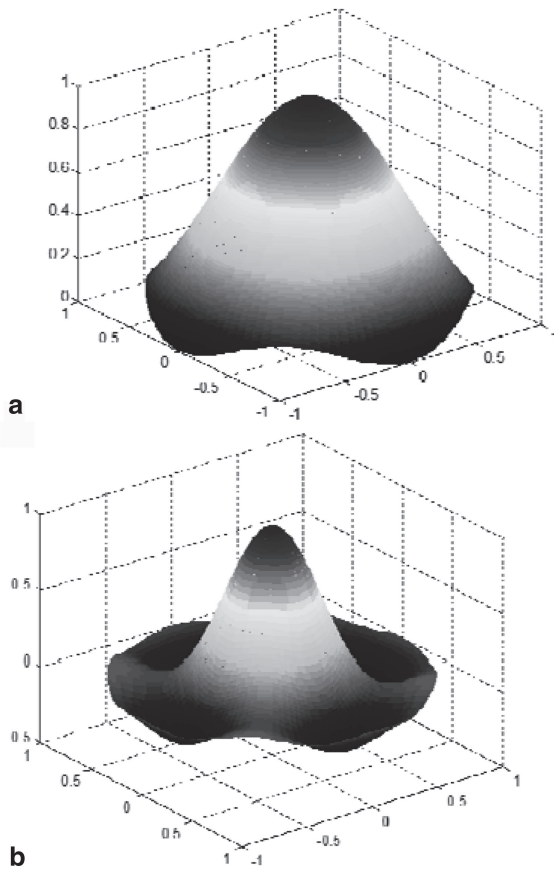


Fig. 7.3 The far field directivity of a square element when **a** the length of the element is one wavelength, and **b** when the length of the element is two wavelengths

3-D wave field are obtained, where it is shown that to steer a 2-D array (with pitch s_x and L_1 elements in the x -direction and pitch s_y and L_2 elements in the y -direction) in a single medium in a direction defined by the spherical coordinates (Θ, Φ) (see Fig. 7.5) requires the time delays, Δt_{nl} , given by

$$\begin{aligned} \Delta t_{nl} = & n \frac{s_x}{c} \sin \Theta \cos \Phi + l \frac{s_y}{c} \sin \Theta \sin \Phi \\ & - \frac{L_1 + 1}{2} \frac{s_x}{c} \sin \Theta \cos \Phi - \frac{L_2 + 1}{2} \frac{s_y}{c} \sin \Theta \sin \Phi, \end{aligned} \quad (7.20)$$

Fig. 7.4 Contour plot of the far field directivity of a linear array element, in a plane perpendicular to the z -axis, where the length of the element is two wavelengths in the x -direction and 15 wavelengths in the y -direction. The x - and y -coordinates of the plot are the unit vector components (U_x, U_y)

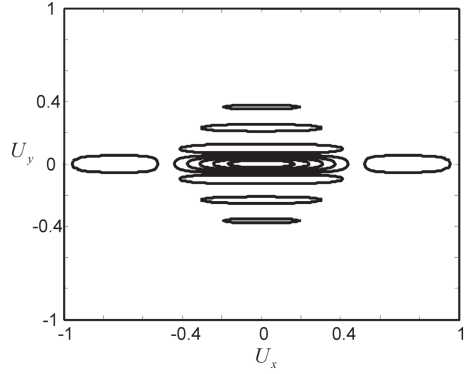
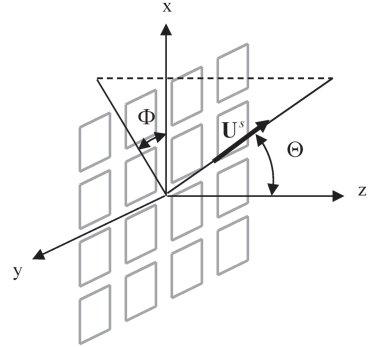


Fig. 7.5 The spherical coordinate steering angles, (Θ, Φ) , that define the unit vector, \mathbf{U}^s , in the steering direction



where c is the wave speed. This delay law can be put in the more compact form

$$\Delta t_{nl} = n \frac{S_x}{c} U_x^s + l \frac{S_y}{c} U_y^s - \frac{L_1 + 1}{2} \frac{S_x}{c} U_x^s - \frac{L_2 + 1}{2} \frac{S_y}{c} U_y^s, \quad (7.21)$$

where

$$\begin{aligned} U_x^s &= \sin \Theta \cos \Phi \\ U_y^s &= \sin \Theta \sin \Phi \end{aligned} \quad (7.22)$$

are components of a unit vector, \mathbf{U}^s , in the steering direction (Fig. 7.5). Placing this steering law into the far field pressure field of the array (Eq. (7.17) for a single point source) with no apodization terms gives

$$\begin{aligned}
p(\mathbf{x}, \omega) = & \frac{\rho c v_0(\omega)}{2\pi} (-ik l_x l_y) D_e \frac{\exp(ikR)}{R} \\
& \cdot \exp \left[ik \left(\frac{L_1+1}{2} \right) s_x (U_x - U_x^s) \right] \exp \left[ik \left(\frac{L_2+1}{2} \right) s_y (U_y - U_y^s) \right] \cdot \quad (7.23) \\
& \cdot \sum_{n=1}^{L_1} \sum_{l=1}^{L_2} \exp \left[-ik n s_x (U_x - U_x^s) \right] \exp \left[-ik l s_y (U_y - U_y^s) \right]
\end{aligned}$$

Again, the series can be summed directly, as shown in Chap. 4, to find

$$\begin{aligned}
p(\mathbf{x}, \omega) = & \frac{\rho c v_0(\omega)}{2\pi} (-ik L_1 L_2 l_x l_y) D_e \\
& \cdot \frac{\sin \left[L_1 k s_x (U_x - U_x^s) / 2 \right] \sin \left[L_2 k s_y (U_y - U_y^s) / 2 \right] \exp(ikR)}{L_1 \sin \left[k s_x (U_x - U_x^s) / 2 \right] L_2 \sin \left[k s_y (U_y - U_y^s) / 2 \right] R}. \quad (7.24)
\end{aligned}$$

Comparing Eq. (7.24) with the case of no steering (Eq. (7.18)) we can see that the time delays have caused a shifting of the point source directivity, i.e.

$$D_s(k s_x U_x, k s_y U_y) \rightarrow D_s(k s_x (U_x - U_x^s), k s_y (U_y - U_y^s))$$

so that this directivity will have its largest amplitude occur in the steering direction instead of along the z -axis. The magnitude of the point source directivity for a steered 2-D array is periodic since

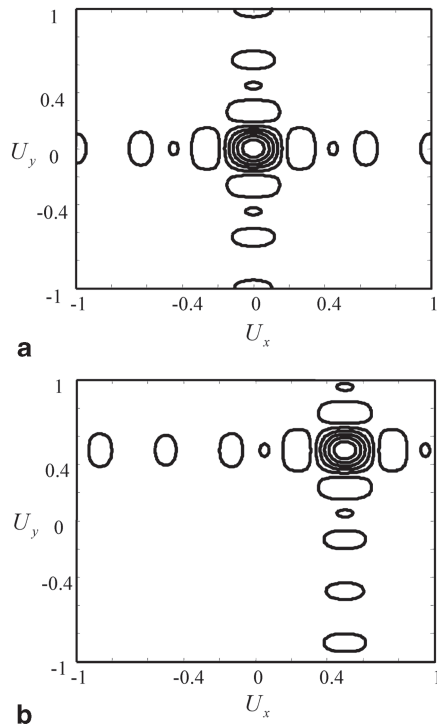
$$\begin{aligned}
\left| D_s(k s_x (U_x - U_x^s), k s_y (U_y - U_y^s)) \right| &= \left| D_s(k s_x (U_x - U_x^s) \pm 2n\pi, k s_y (U_y - U_y^s) \pm 2m\pi) \right| \\
(n=1, 2, \dots) \quad (m=1, 2, \dots) & \quad (7.25)
\end{aligned}$$

so that maxima other than in the steering direction can occur when

$$U_x = U_x^s \pm \frac{n\lambda}{s_x}, \quad U_y = U_y^s \pm \frac{m\lambda}{s_y} \quad (n=1, 2, \dots), (m=1, 2, \dots), \quad (7.26)$$

where λ is the wavelength. Any solutions of Eq. (7.26) will indicate the presence of grating lobes, similar to what was found in the 2-D case. But, since $|U_x| \leq 1$, $|U_x^s| \leq 1$ and $|U_y| \leq 1$, $|U_y^s| \leq 1$, we see that will be no values of (U_x, U_y) that can satisfy Eq. (7.26) if $s_x < \lambda/2$, $s_y < \lambda/2$. In the case of no steering, Eq. (7.26) shows that for no grating lobes we must have $s_x < \lambda$, $s_y < \lambda$ instead. Thus, the conditions for the absence of grating lobes follows the same criteria found earlier for 2-D problems. Figure 7.6a, b shows contour plots of the point source directivity of a

Fig. 7.6 Contour plots, in a plane perpendicular to the z -axis, of the point source directivity of a 11×11 square array with pitches equal to one half wavelength for **a** no steering, and **b** steering in the direction $\Theta = 45^\circ, \Phi = 45^\circ$. The x - and y -coordinates of the plot are the unit vector components (U_x, U_y)



square array when the pitches in both the x - and y -directions are equal to one half wavelength. It can be seen that the directivity with no steering in Fig. 7.6a is just shifted to the steering direction with no grating lobes when a steering law is applied, as shown in Fig. 7.6b. However, for the a 11×11 square array with pitches in both directions equal to 0.8 wavelength, while the point source directivity with no steering (Fig. 7.7a) is again shifted to the steering direction (Fig. 7.7b), grating lobes in other directions also appear, as predicted, and this can be clearly seen in Fig. 7.7b to be simply a consequence of the periodicity of the point source directivity of the array. Figure 7.8 shows the directivity for the 11×11 square array when the pitches in both directions are one and a half wavelengths. In this case, since the pitches are greater than a wavelength even with no steering the periodicity of the directivity will cause grating lobes to appear, as can be seen in Fig. 7.8.

7.2 Radiation Through a Planar Interface

From our results in Sect. 7.1 and following the same steps outlined Chap. 6, we can obtain multiple point source and single point source beam models for radiation through a planar interface. Consider first the immersion case. Using the superposition of multiple far field point sources of Eq. (6.64), we can generate a multiple

Fig. 7.7 Contour plots, in a plane perpendicular to the z -axis, of the point source directivity of a 11×11 square array with pitches equal to 0.8 wavelength for **a** no steering, and **b** steering in the direction $\Theta = 45^\circ, \Phi = 45^\circ$. The x - and y -coordinates of the plot are the unit vector components (U_x, U_y)

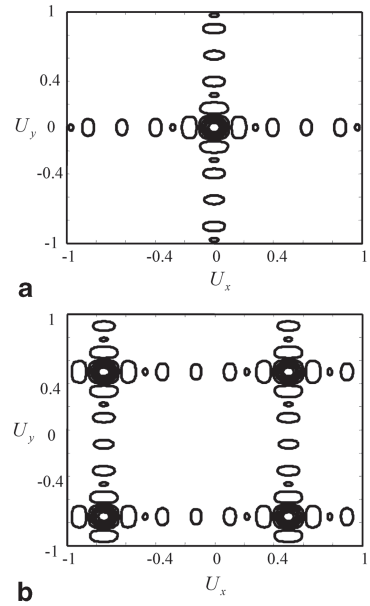
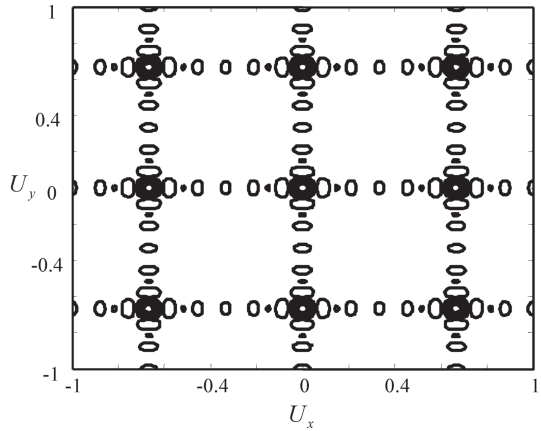


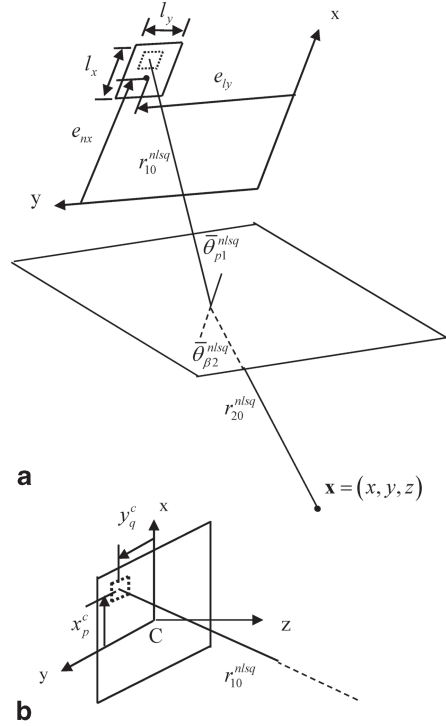
Fig. 7.8 Contour plots, in a plane perpendicular to the z -axis, of the point source directivity of a 11×11 square array with pitches equal to 1.5 wavelengths and no steering. The x - and y -coordinates of the plot are the unit vector components (U_x, U_y)



point source model for the velocity generated in the solid in a form very similar to the single medium case (see Fig. 7.9):

$$\mathbf{v}(\mathbf{x}, \omega) = \frac{v_0(\omega)}{2\pi} \sum_{n=1}^{L_1} \sum_{l=1}^{L_2} \tilde{C}_n \tilde{C}_l \exp(i\omega \Delta t_{nl}) \left\{ \sum_{s=1}^S \sum_{q=1}^Q (-ik_{p1} \Delta d_x \Delta d_y) \bar{T}_{fs;\beta}^{nlsq} \bar{\mathbf{d}}_{\beta 2}^{nlsq} \frac{\sin(k_{p1} u_x^{nlsq} \Delta d_x / 2) \sin(k_{p1} u_y^{nlsq} \Delta d_y / 2) \exp(ik_{p1} R_{\beta}^{nlsq})}{(k_{p1} u_x^{nlsq} \Delta d_x / 2) (k_{p1} u_y^{nlsq} \Delta d_y / 2) D_{\beta}^{nlsq}} \right\}, \quad (7.27)$$

Fig. 7.9 a Geometry parameters for an element of a 2-D array radiating through a planar interface, and **b** details of the segment parameters within each element



where $\bar{T}_{fs;\beta}^{nlsq}$ and $\bar{\mathbf{d}}_{\beta 2}^{nlsq}$ are sampled values of the fluid–solid transmission coefficient, $\bar{T}_{fs}^{\beta,p}$; and polarization, $\bar{\mathbf{d}}_{\beta 2}$, (in medium 2) for a wave of type β in the solid traveling from the centroid of the sq th segment of the n th element to point \mathbf{x} in the solid, respectively, and where the distances and angles in the definitions

$$ik_{p1}R_{\beta}^{nlsq} = ik_{p1}r_{10}^{nlsq} + ik_{\beta 2}r_{20}^{\beta,nlsq}$$

$$D_{\beta}^{nlsq} = \sqrt{\left(r_{10}^{nlsq} + \frac{c_{\beta 2}}{c_{p1}} \frac{\cos^2 \bar{\theta}_{p1}^{nlsq}}{\cos^2 \bar{\theta}_{\beta 2}^{nlsq}} r_{20}^{\beta,nlsq} \right) \left(r_{10}^{nlsq} + \frac{c_{\beta 2}}{c_{p1}} r_{20}^{\beta,nlsq} \right)} \quad (7.28)$$

are also measured from the segment centroid.

If we use a single point source for each element then Eq. (7.27) reduces to

$$\mathbf{v}(\mathbf{x}, \omega) = \frac{v_0(\omega)}{2\pi} \sum_{n=1}^{L_1} \sum_{l=1}^{L_2} \tilde{C}_n \tilde{C}_l \exp(i\omega \Delta t_{nl}) (-ik_{p1} l_x l_y) \bar{T}_{fs;\beta}^{nl} \bar{\mathbf{d}}_{\beta 2}^{nl}$$

$$\cdot \frac{\sin(k_{p1} u_x^{nl} l_x / 2) \sin(k_{p1} u_y^{nl} l_y / 2) \exp(ik_{p1} R_{\beta}^{nl})}{(k_{p1} u_x^{nl} l_x / 2) (k_{p1} u_y^{nl} l_y / 2) D_{\beta}^{nl}} \quad (7.29)$$

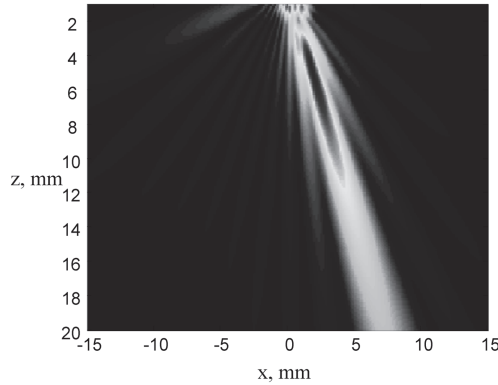


Fig. 7.11 The magnitude of the normalized pressure wave field of a 11×11 2-D array radiating into water with steering in the $\Phi = 0^\circ$, $\Theta = 20^\circ$ direction and no focusing ($Fl = \infty$). The other parameters are: $l_x = l_y = 0.15$ mm, $g_x = g_y = 0.05$ mm, $f = 5$ MHz, $c = 1480$ m/s, $z = \text{linspace}(1, 20, 200)$, $x = \text{linspace}(-15, 15, 300)$, $y = 0$. A rectangular window is used (no apodization)

7.3 Array Beam Modeling Examples

In this section, we will show some examples of the wave fields generated by arrays. First, consider the single medium case with the array radiating directly into a fluid medium (see Eq. 7.1). The MATLAB[®] script `mps_array_modeling` (Code Listing C.21) uses the multiple point source beam model, `ps_3Dv`, the delay laws contained in `delay_laws3D` (Code Listing C.22—see the next Chapter for more details), and the apodization laws of `discrete_windows` (Code Listing C.13) to simulate the normalized pressure wave field of an array. Figure 7.11 shows the pressure field in the x - z plane for a 11×11 2-D array where the element pitch is about one half a wavelength ($l_x = l_y = 0.15$ mm, $g_x = g_y = 0.05$ mm) so that there are at most weak grating lobes generated when the beam is steered in the $\Phi = 0^\circ$, $\Theta = 20^\circ$ direction (with no focusing). In Fig. 7.12a, one can see the 2-D steering of this beam in the x - y plane at $z = 8$ mm. Figure 7.12b also shows the beam in this same plane when the steering law is changed to $\Phi = 90^\circ$, $\Theta = 20^\circ$, while Fig. 7.12c shows the case for $\Phi = -90^\circ$, $\Theta = 20^\circ$, and Fig. 7.12d considers $\Phi = 0^\circ$, $\Theta = -20^\circ$.

Figure 7.13 shows the effects of steering and focusing of the same array considered in Fig. 7.11, where Fig. 7.13a shows the case of steering but no focusing (same configuration as in Fig. 7.11) but shown for a smaller range of depths), while Fig. 7.13b uses $Fl=3$ mm. Comparing Fig. 7.13a and b shows clearly the focusing effect. Note that the array in this example is very small so that near field of the array, where focusing is effective, is also quite small. Thus, the focal length specified here was chosen to demonstrate the effects of focusing but was not meant to illustrate a practical inspection case.

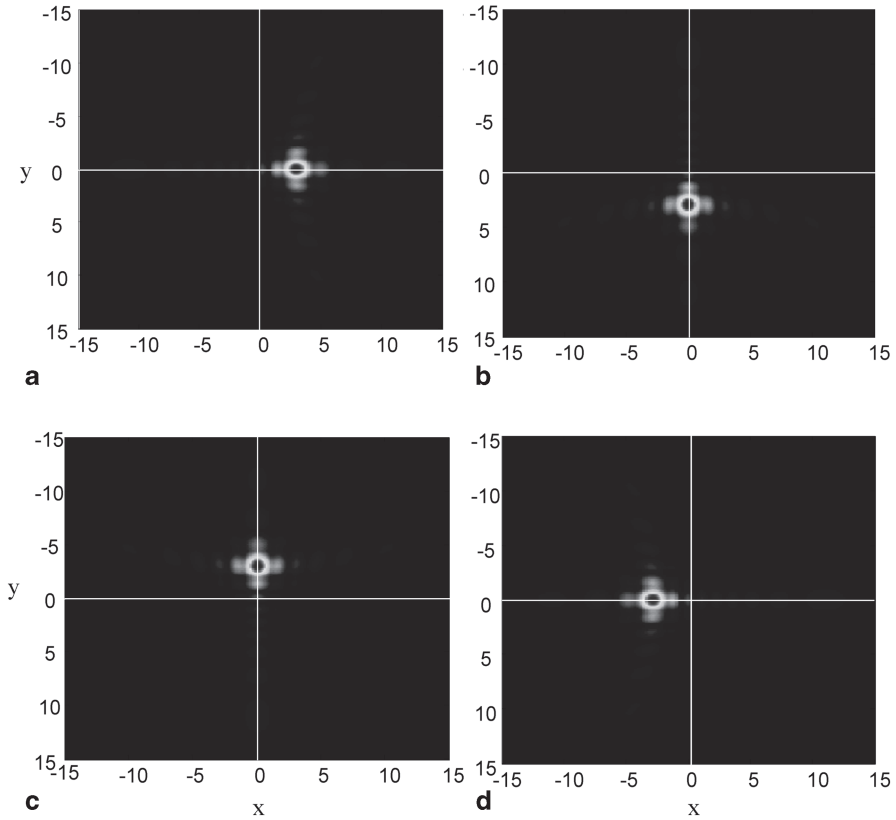


Fig. 7.12 The magnitude of the normalized pressure wave field of a 11×11 2-D array radiating into water with steering no focusing ($Fl = \inf$). The other parameters are $l_x = l_y = 0.15$ mm, $g_x = g_y = 0.05$ mm, $f = 5$ MHz, $c = 1480$ m/s, $z = 8$ mm, $x = \text{linspace}(-15, 15, 300)$, $y = \text{linspace}(-15, 15, 300)$. A rectangular window is used (no apodization). The steering in the four cases shown are: **a** $\Phi = 0^\circ$, $\Theta = 20^\circ$, **b** $\Phi = 90^\circ$, $\Theta = 20^\circ$, **c** $\Phi = -90^\circ$, $\Theta = 20^\circ$, and **d** $\Phi = 0^\circ$, $\Theta = -20^\circ$

The same small 11×11 array considered for a single medium was also used to describe cases where the array radiated waves through a plane water/steel interface. The MATLAB® script `mps_array_model_int` (Code Listing C.26) used the multiple point source beam model in `ps_3Dint` (Code Listing C.23) with the time delay laws of `delay_laws3D_int` (Code Listing C.27— see the next Chapter for more details) and apodization laws of discrete windows (Code Listing C.13). The parameters used in these interface cases were $l_x = l_y = 0.15$ mm, $g_x = g_y = 0.05$ mm, $f = 5$ MHz, $\rho_1 = 1 \text{ gm/cm}^3$, $c_{p1} = 1480$ m/s, $\rho_2 = 7.9 \text{ gm/cm}^3$, $c_{p2} = 5900$ m/s, $c_{s2} = 3200$ m/s. Figure 7.14a shows an image of the magnitude of the velocity of the wave field in the x - z plane where the array was at normal incidence ($\text{ang} = 0$) at a distance $D_{r0} = 50.8$ mm from the interface and no steering or focusing was present ($\Phi = 0^\circ$, $\Theta = 0^\circ$). The black arrow in this and some subsequent figures shows the

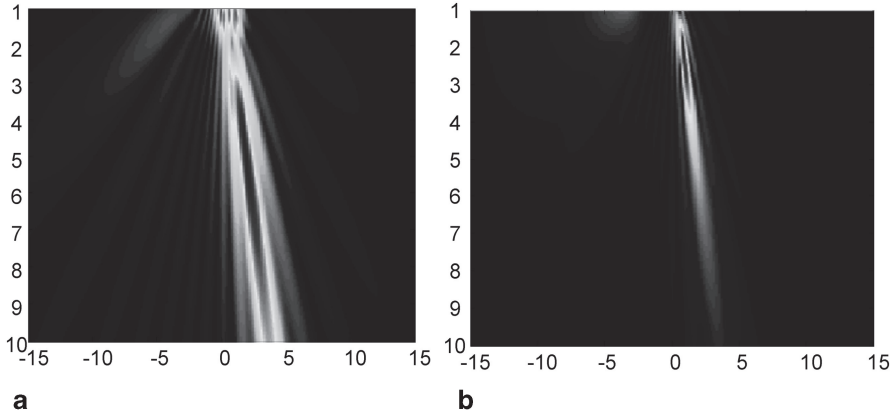


Fig. 7.13 The magnitude of the normalized pressure wave field of a 11×11 2-D array radiating into water with steering ($\Phi = 0^\circ$, $\Theta = 20^\circ$). The other parameters are $l_x = l_y = 0.15$ mm, $g_x = g_y = 0.05$ mm, $f = 5$ MHz, $c = 1480$ m/s, $x = \text{linspace}(-15, 15, 300)$, $z = \text{linspace}(1, 10, 300)$, $y = 0$. A rectangular window is used (no apodization). In case **a** $Fl = \text{inf}$, while in case **b** $Fl = 3$ mm

direction in which the beam is being steered in the steel. Figure 7.14b shows the wave field of this array in the x - z plane when it is steered ($\Phi = 0^\circ$, $\Theta = 30^\circ$) but not focused. Figure 7.14c and d shows the wave field in the x - y plane at $z = 4$ mm for this array when (c) the beam is steered in the x - z plane ($\Phi = 0^\circ$, $\Theta = 20^\circ$), and (d) steered in the x - y plane ($\Phi = 90^\circ$, $\Theta = 20^\circ$). All of these cases show that the beam is steered properly through the interface with the time delay laws. Figure 7.15 shows results for a 11×11 array, again at normal incidence to the interface, where the size of the element was increased to be one wavelength ($l_x = l_y = 0.3$ mm, $g_x = g_y = 0.05$ mm) and the array was moved closer to the interface ($D_0 = 2$ mm) so that the near field extends into the steel. Figure 7.15a shows the field in the x - z plane when the array simply radiates into the steel without steering, focusing, or apodization. Figure 7.15b shows the comparable beam when a Hamming window is applied to the elements in both the x - and y -directions. Comparing Fig. 7.15a and b, one can see that the apodization reduces the side lobes, as expected. Figure 7.15c shows the same array when it is focused (without steering or apodization) at $D_f = 2$ mm into the steel, thus concentrating the beam closer to the interface. The cases shown in Fig. 7.16 are again for the 11×11 array considered in Fig. 7.14 (pitch equal to one half wavelength), where the center of the array is located at $D_0 = 50.8$ mm again, but where the angle of array to the interface, $\theta_i = 10.217^\circ$, was chosen to generate a 45-degree P-wave in the steel (without steering). Figure 7.16a shows the wave field in the x - z plane where there is no steering, focusing or apodization so the beam does propagate at the 45° angle. The behavior of the same wave field as seen in the y - z plane at a distance $x = 15$ mm is shown in Fig. 7.16b. In Fig. 7.16c, the beam of the array is steered to an angle of 20° ($\Phi = 0^\circ$, $\Theta = 20^\circ$), showing the corresponding change of the direction of the wave field in the x - z plane. Finally, in Fig. 7.16d, the angle of the array is changed to an angle $\theta_i = -10.217^\circ$, so that with no steering or

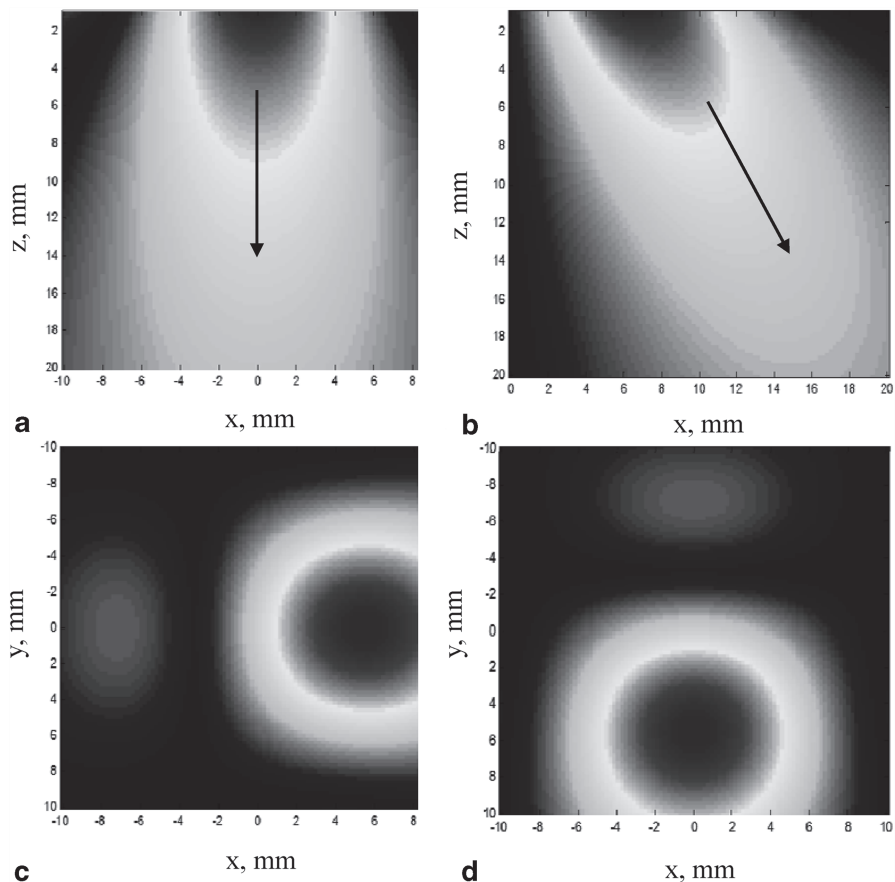


Fig. 7.14 The magnitude of the normalized velocity in steel for a 11×11 2-D array (element size approximately one half wavelength) normal to the interface at a distance $D_{r0} = 50.8$ mm, radiating a P-wave through a planar water/steel interface, for **a** the wave field in the x - z plane with no steering or focusing, **b** the wave field in the x - z plane with steering ($\Phi = 0^\circ$, $\Theta = 30^\circ$) but no focusing, **c** the wave field in the x - y plane at $z = 4$ mm with steering ($\Phi = 0^\circ$, $\Theta = 20^\circ$) but no focusing, and **d** the wave field in the x - y plane with steering ($\Phi = 90^\circ$, $\Theta = 20^\circ$) but no focusing. A rectangular window is used (no apodization) for all cases

focusing the beam propagates in the -45° direction instead. Note that as found in the 2-D case (see Chap. 5) the location of the first element relative to the interface is changed because the angle is negative. Figure 7.17 again considers the same array as in Fig. 7.16 but where now the angle of the array to the interface is taken as $\theta_i = 19.09^\circ$ to generate a shear wave traveling at an angle of 45° in the steel. Figure 7.17a shows the magnitude of the S-wave velocity field in the x - z plane when no steering, focusing or apodization laws are applied, while Fig. 7.17b shows the case when the S-wave is steered to 30° in the steel with no apodization. It can be seen that in addition to the main refracted beam there is also a relatively strong side

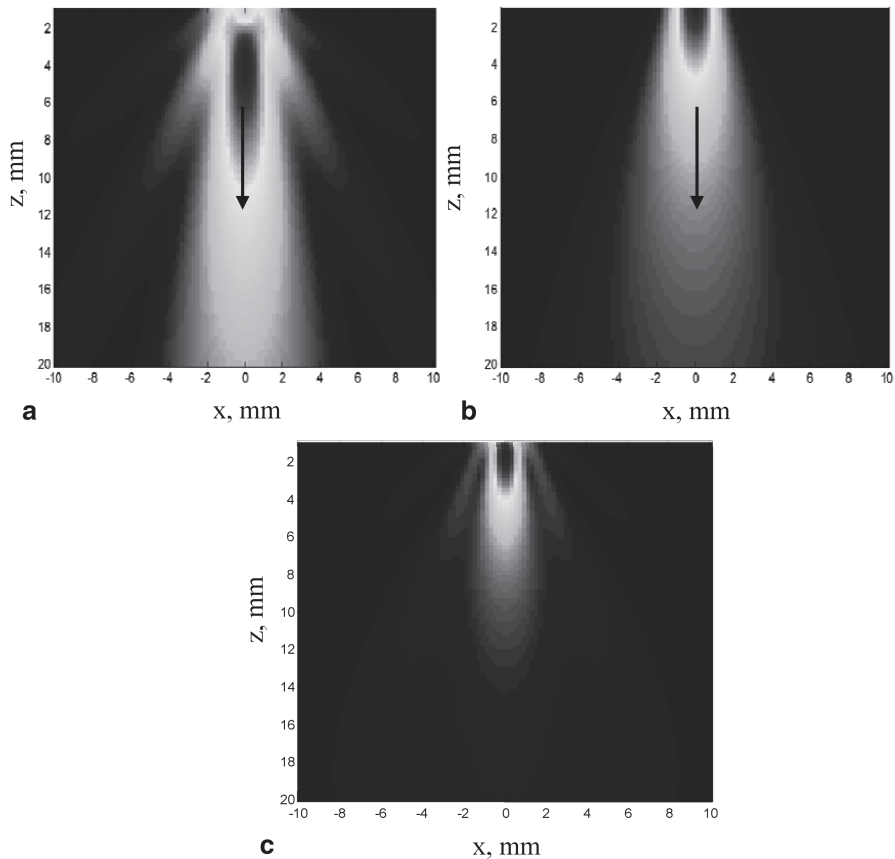


Fig. 7.15 The magnitude of the normalized velocity in steel for a 11×11 2-D array (element size one wavelength) normal to the interface at a distance $D_{i0} = 2$ mm, radiating a P-wave through a planar water/steel interface, for the wave field in the x - z plane with no steering or focusing or apodization, **b** the wave field in the x - z plane with no steering or focusing but with a Hamming window applied in the x - and y -directions, and **c** the wave field in the x - z plane with no steering or apodization but with focusing to a depth of 2 mm in the steel

lobe as well. Figure 7.17c shows beam with the same steering law as in Fig. 7.17b, but with a Blackman window applied in the x - and y -directions to the array, reducing somewhat the side lobe but also obviously broadening the main beam.

All of the cases examined so far in this section were chosen with small element sizes so that the array can effectively steer and focus the sound beam without grating lobes in the manner proscribed by the delay laws. Commercially available arrays, however, may use considerably larger element sizes which will limit their behavior and also introduce significant grating lobes. We will examine such effects with the use again of the script `mps_array_modeling`. Consider, for example, an 8×8 array of square elements radiating into water at 5 MHz, for example, where the

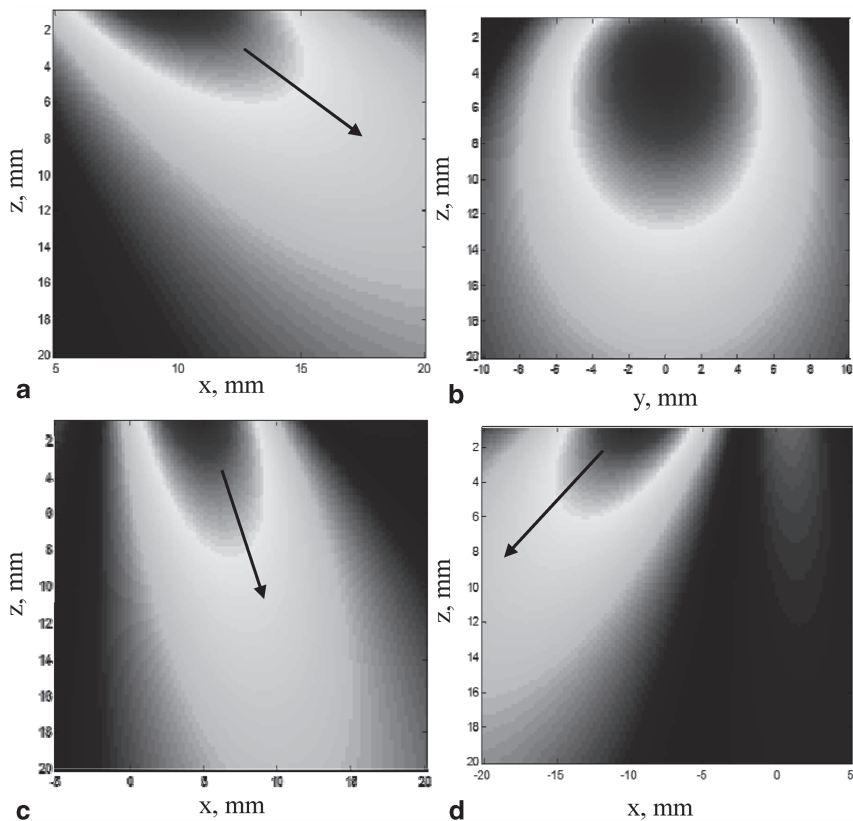


Fig. 7.16 The magnitude of the normalized velocity in steel for a 11×11 2-D array (element size one half wavelength) oriented at an angle of $\theta_i = 10.217^\circ$ to the interface with the array center at a distance $D_{i0} = 50.8$ mm, radiating a P-wave through a planar water/steel interface, for **a** the wave field in the x - z plane with no steering or focusing, **b** the wave field as seen in the y - z plane at a distance $x = 15$ mm, **c** the wave field in the x - z plane when the beam of the array is steered to an angle of 20° ($\Phi = 0^\circ$, $\Theta = 20^\circ$), and **d** the wave field in the x - z plane when $\theta_i = -10.217^\circ$, with no steering or focusing

length of the element is 0.9 mm and the gap length in both dimensions is 0.1 mm. Since the pitch of the array is about three wavelengths, there are multiple (but weak) grating lobes present (Fig. 7.18a). The directions of these grating lobes and the overall behavior of the sound beam can be understood by plotting the total far field directivity, D_t , of this array where $D_t = D_e D_s$ is the product of the element directivity and the point source directivity. The magnitude of this total directivity is plotted in Fig. 7.19a, where one can see three relatively weak grating lobes on both sides of the main beam that are difficult to see in Fig. 7.18a. If a delay law is applied to this array to try to steer it in the 45° direction, the wave field is as shown in Fig. 7.18b, and the corresponding total directivity is plotted in Fig. 7.19b. It can be seen that in this case the largest response occurs only at a small angle (less than 10°) and very

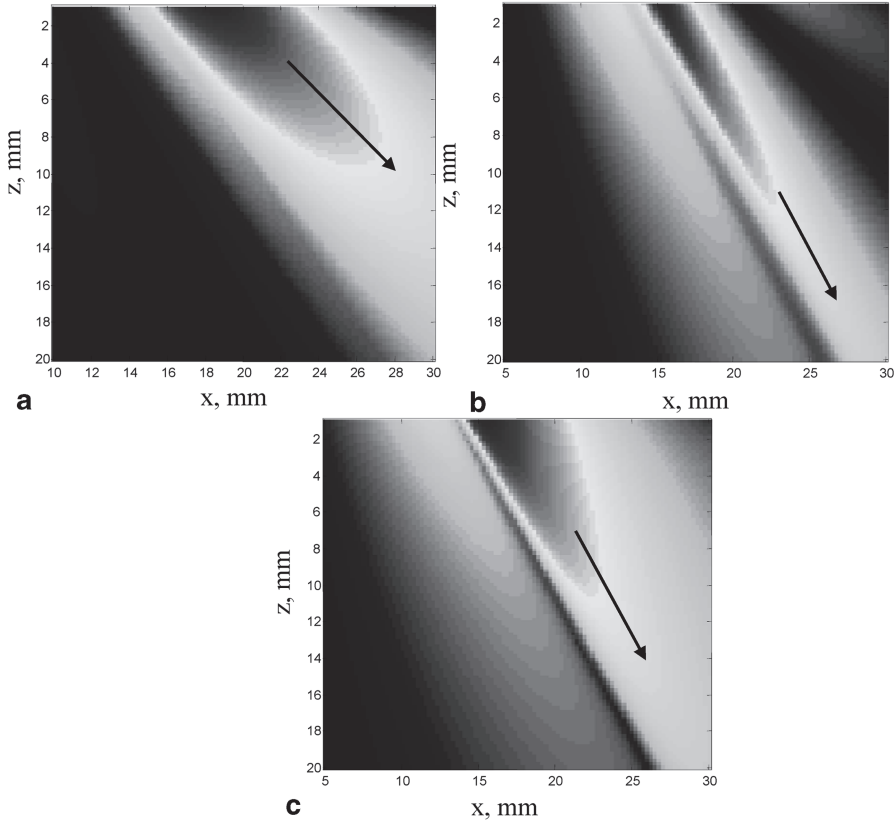


Fig. 7.17 The magnitude of the normalized velocity in steel for a 11×11 2-D array (element size one half wavelength) oriented at an angle of $\theta_i = 19.09^\circ$ to the interface with the array center at a distance $D_{i0} = 50.8$ mm, radiating an S-wave through a planar water/steel interface, for the wave field in the x - z plane with no steering or focusing, **b** the wave field in the x - z plane when the array is steered to 30° ($\Phi = 0^\circ$, $\Theta = 30^\circ$) with no focusing or apodization, and **c** the wave field in the x - z plane when the array is again steered to 30° without focusing but where a Blackman apodization law is applied in the x - and y -directions

little amplitude is near the steering direction. If the array is changed to be a 16×16 array of elements where the element length is reduced by a factor of two to a value of 0.45 mm and the gap length is held fixed at 0.1 mm, the radiated wave field is shown in Fig. 7.18c and the corresponding total directivity in Fig. 7.19c. It can be seen that the steering capability of the array is still very severely limited. If one goes to a 32×32 element array with an element length reduced by a factor of two again to a value of 0.225 mm with the gap length remaining at 0.1 mm, the resulting wave field and total directivity are shown in Figs. 7.18d and 7.19d, respectively. Now the element pitch is slightly larger than one wavelength and a relatively strong beam is

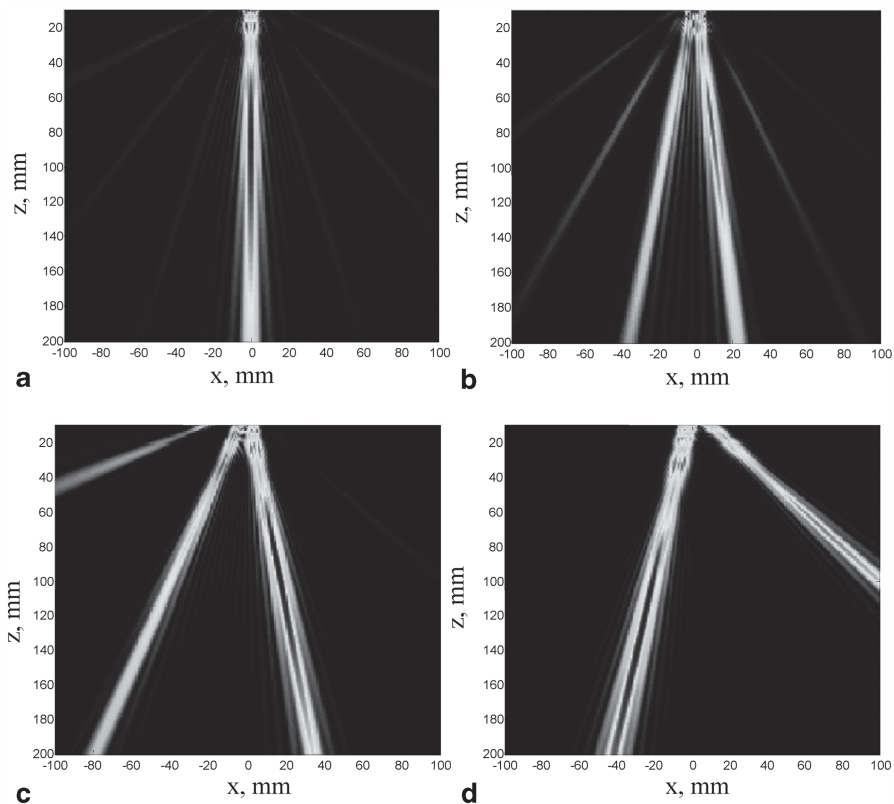


Fig. 7.18 An array radiating into water at 5 MHz for **a** 8×8 elements, $l_x = l_y = 0.9$ mm, $g_x = g_y = 0.1$ mm, no steering, **b** 8×8 elements, $l_x = l_y = 0.9$ mm, $g_x = g_y = 0.1$ mm, steered to 45° ($\Phi = 0^\circ$, $\Theta = 45^\circ$), **c** 16×16 elements, $l_x = l_y = 0.45$ mm, $g_x = g_y = 0.1$ mm, steered to 45° ($\Phi = 0^\circ$, $\Theta = 45^\circ$), and **d** 32×32 elements, $l_x = l_y = 0.225$ mm, $g_x = g_y = 0.1$ mm, steered to 45° ($\Phi = 0^\circ$, $\Theta = 45^\circ$). No focusing or apodization in all cases

steered closely to the proper angle of 45° . There is however, still a single remaining grating lobe that is in fact stronger than the main steered beam as seen in both Figs. 7.18d and 7.19d. These examples show that for arrays where the pitch is larger than a wavelength it is important to simulate the wave fields in this manner and examine the total directivity to understand the behavior of the array, which may be far from the “ideal” behavior seen for arrays with very small elements.

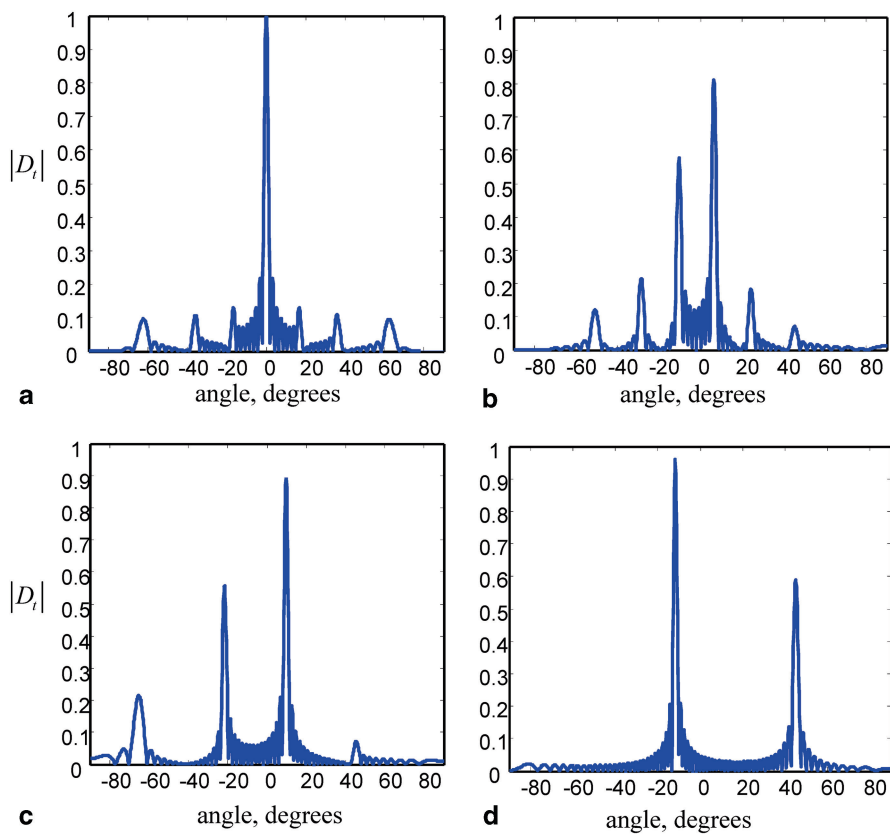


Fig. 7.19 The total far field directivities of the arrays considered in Fig. 7.18a–d

Reference

1. L.J. Ziomek, in *Fundamentals of Acoustic Field Theory and Space-Time Signal Processing* (CRC Press, Boca Raton, 1995)

Chapter 8

Time Delay Laws (3-D)

8.1 Beam Steering in 3-D

Consider an element of a 2-D array as shown in Fig. 8.1 where we want to steer the ultrasonic beam of the array in the direction of the unit vector, \mathbf{u} . We can express \mathbf{u} in spherical coordinates (Θ, Φ) as $\mathbf{u} = \sin \Theta \cos \Phi \mathbf{e}_x + \sin \Theta \sin \Phi \mathbf{e}_y + \cos \Theta \mathbf{e}_z$. Steering of the beam in this direction can be accomplished by applying a linearly varying time shift, $\Delta t = \mathbf{u} \cdot \mathbf{x} / c$, over the face of the array and evaluating that phase at the centroids of the individual elements. This results in the shifts, Δt_{mn} given by

$$\Delta t_{mn} = (e_{xm} \sin \Theta \cos \Phi + e_{yn} \sin \Theta \sin \Phi) / c. \quad (8.1)$$

The centroid locations are given by

$$\begin{aligned} e_{xm} &= [(m-1) - \bar{M}] s_x \\ e_{yn} &= [(n-1) - \bar{N}] s_y, \end{aligned} \quad (8.2)$$

where (s_x, s_y) are the pitches of the elements in the x - and y -directions, respectively, and M and N are the number of elements in the x - and y -directions, and where

$$\begin{aligned} \bar{M} &= \frac{(M-1)}{2} \\ \bar{N} &= \frac{(N-1)}{2}. \end{aligned} \quad (8.3)$$

Since the delays in Eq. (8.1) contain both positive and negative values, we can simply add a constant delay equal to the magnitude of largest negative value to obtain a proper time delay law, Δt_{mn}^d given by

$$\Delta t_{mn}^d = \left| \left\{ \Delta t_{mn} \right\}_{\min} \right| + \Delta t_{mn}. \quad (8.4)$$

Fig. 8.1 Parameters for steering a beam of a 2-D array in the direction of the unit vector, \mathbf{u}

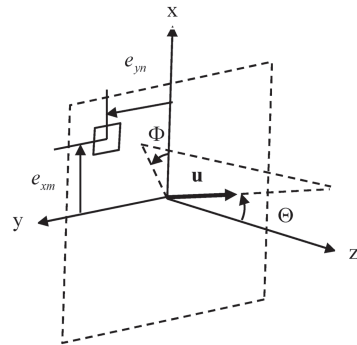
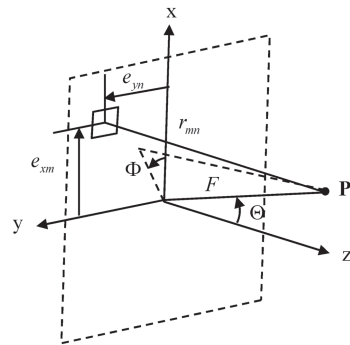


Fig. 8.2 Parameters for steering and focusing a 2-D array at a point, \mathbf{P} , as defined by the focal distance, F , and the angles (Θ, Φ)



8.2 Beam Steering and Focusing in 3-D

We can also consider steering and focusing of the array wave field to a point, \mathbf{P} , in the surrounding medium specified by the focal distance, F , and the steering angles (Θ, Φ) as shown in Fig. 8.2. In this case, the distance, r_{mn} , from an element to \mathbf{P} is given from the geometry as

$$r_{mn} = \sqrt{(F \sin \Theta \cos \Phi - e_{xm})^2 + (F \sin \Theta \sin \Phi - e_{ym})^2 + F^2 \cos^2 \Theta}. \quad (8.5)$$

A proper delay law, Δt_{mn}^d , can then be obtained from

$$\Delta t_{mn}^d = \max \{ r_{mn} / c \} - r_{mn} / c, \quad (8.6)$$

where c is the wave speed.

The MATLAB[®] function `delay_laws3D` (Code Listing C.22) implements the beam steering delay law of Eq. (8.4) and the steering/focusing law of Eq. (8.6) for a 2-D array. The function call is:

```
>> td=delay_laws3D(M, N, sx, sy, theta, phi, F, c);
```

Fig. 8.3 Time delays, t_d , (in μs) for steering the beam of a 2-D array parallel to the y -axis with $M=8$, $N=16$ elements, $s_x = s_y = 0.5$ mm, $\Theta = 30^\circ$, $\Phi = 90^\circ$, and $F = \text{inf}$, $c = 1480$ m/s

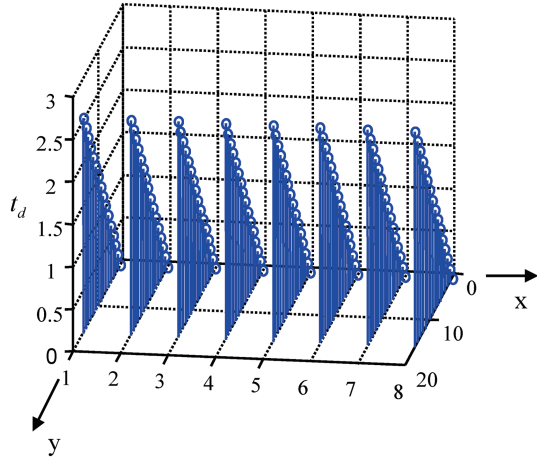
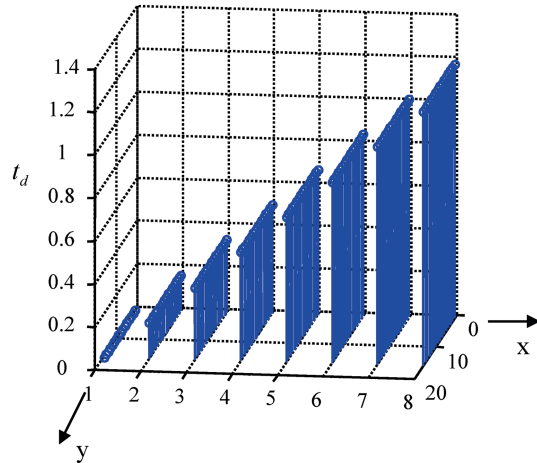


Fig. 8.4 Time delays, t_d , (in μs) for steering the beam of a 2-D array parallel to the x -axis with $M=8$, $N=16$ elements, $s_x = s_y = 0.5$ mm, $\Theta = 30^\circ$, $\Phi = 0^\circ$, and $F = \text{inf}$, $c = 1480$ m/s



where t_d is the matrix of delay times (in μs) for an array with M elements in the x -direction and N elements in the y -direction. The pitches of the array are $s_x = s_x$, and $s_y = s_y$ in the x - and y -directions, respectively (in mm), the steering angles $\theta = \Theta$, and $\phi = \Phi$ (in degrees), the focal distance is F (in mm), and the wave speed of the medium is c (in m/s). Figures 8.3–8.5 show some samples of delay laws for an array radiating into water ($c=1480$ m/s) with $M=8$, $N=16$ elements, $s_x = s_y = 0.5$ mm. Figure 8.3 shows the case of steering only parallel to the y -axis with $\Theta = 30^\circ$, $\Phi = 90^\circ$, $F = \text{inf}$, while Fig. 8.4 is for steering angles $\Theta = 30^\circ$, $\Phi = 0^\circ$ so that the steering is parallel to the x -axis. As seen in these figures in both these cases the time delays are purely the linear functions contained in Eq. (8.1). Figure 8.5 instead considers the case of focusing only of this same array where $\theta = \phi = 0^\circ$, $F = 10$ mm. In this case, there are approximately quadratic variations in the time delays in both the x - and y -directions.

Fig. 8.5 Time delays, t_d , (in μs) for focusing the beam of a 2-D array along the z -axis with $M=8$, $N=16$ elements, $s_x = s_y = 0.5$ mm, $\theta = 0^\circ$, $\phi = 0^\circ$, and $F = 10$ mm, $c = 1480$ m/s

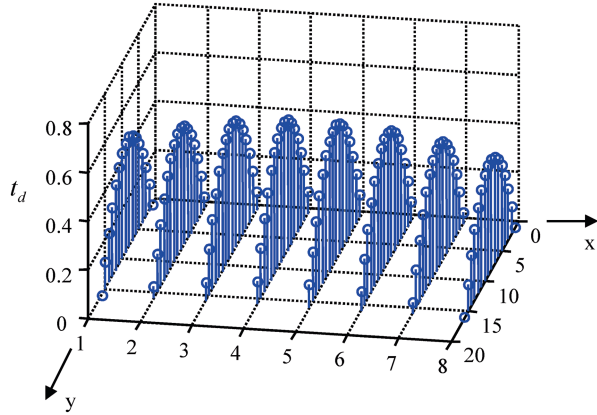
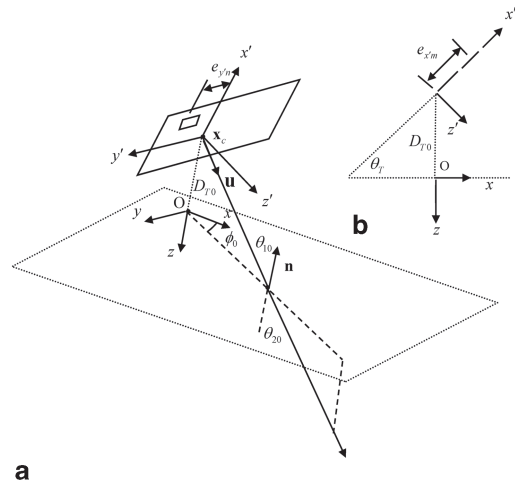


Fig. 8.6 **a** Geometry for beam steering, through a planar interface in three dimensions. **b** A side view, looking down the (y, y') axes



8.3 Beam Steering Through a Planar Interface

When a 2-D array is used in immersion testing or placed on the face of a solid wedge, the time delays needed to steer the beam in the adjacent solid are more complex than in the single medium case. Figure 8.6 shows an array whose face makes an angle θ_T with respect to the interface and whose center \mathbf{x}_c is located at a distance D_{T0} above the interface. In this configuration, we will specify the direction we want the beam to be steered in the second medium by giving the angles (ϕ_0, θ_{20}) , as shown in Fig. 8.6. If we can determine the unit vector, \mathbf{u} , in terms of these angles and the angle θ_T in the (x', y', z') coordinates, then as in the single medium case the corresponding time shifts are

$$\Delta t_{mn} = (u_{x'} e_{x'm} + u_{y'} e_{y'n}) / c_1, \quad (8.7)$$

where the location of the centroids of the elements $(e_{x'm}, e_{y'n})$ are again given by Eq. (8.2) and c_1 is the wave speed in the medium adjacent to the array. From Snell's law we have

$$\theta_{10} = \sin^{-1} \left[\frac{c_1 \sin \theta_{20}}{c_2} \right], \quad (8.8)$$

where c_2 is the wave speed of the transmitted wave in the second medium. From the geometry of Fig. 8.6 it is easy to show that in the (x, y, z) coordinates on the interface we have

$$\mathbf{u} = \sin \theta_{10} \cos \phi_0 \mathbf{e}_x + \sin \theta_{10} \sin \phi_0 \mathbf{e}_y + \cos \theta_{10} \mathbf{e}_z \quad (8.9)$$

with $(\mathbf{e}_x, \mathbf{e}_y, \mathbf{e}_z)$ being unit vectors along the (x, y, z) coordinates, respectively. These unit vectors can be written in terms of the unit vectors $(\mathbf{e}_{x'}, \mathbf{e}_{y'}, \mathbf{e}_{z'})$ along the (x, y, z) axes:

$$\begin{aligned} \mathbf{e}_x &= \cos \theta_T \mathbf{e}_{x'} + \sin \theta_T \mathbf{e}_{z'} \\ \mathbf{e}_z &= -\sin \theta_T \mathbf{e}_{x'} + \cos \theta_T \mathbf{e}_{z'} \\ \mathbf{e}_y &= \mathbf{e}_{y'} \end{aligned} \quad (8.10)$$

so one finds

$$\begin{aligned} \mathbf{u} &= (\sin \theta_{10} \cos \phi_0 \cos \theta_T - \cos \theta_{10} \sin \theta_T) \mathbf{e}_{x'} \\ &\quad + (\sin \theta_{10} \sin \phi_0) \mathbf{e}_{y'} \\ &\quad + (\cos \theta_{10} \cos \theta_T + \sin \theta_{10} \cos \phi_0 \sin \theta_T) \mathbf{e}_{z'} \end{aligned} \quad (8.11)$$

and the time shifts are then

$$\Delta t_{mn} = \left[(\sin \theta_{10} \cos \phi_0 \cos \theta_T - \cos \theta_{10} \sin \theta_T) e_{x'm} + (\sin \theta_{10} \sin \phi_0) e_{y'n} \right] / c_1, \quad (8.12)$$

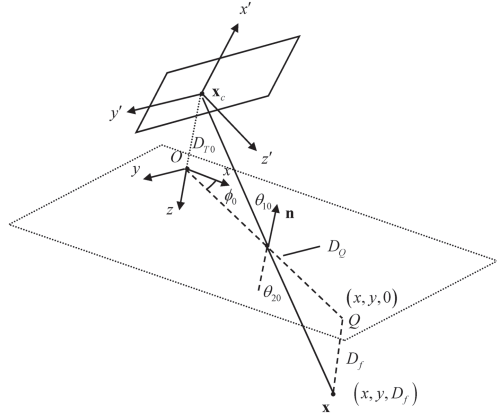
with the proper time delays, Δt_{mn}^d , given in terms of these time shifts again by Eq. (8.4):

$$\Delta t_{mn}^d = \left| \left\{ \Delta t_{mn} \right\}_{min} \right| + \Delta t_{mn}. \quad (8.13)$$

8.4 Beam Steering and Focusing Through a Planar Interface

The presence of an interface makes the time delays laws for steering and focusing much more complex than in the single medium case but one can use a very similar approach to the 2-D case discussed in Chap. 5. To begin with, we need to specify the

Fig. 8.7 The geometry parameters for steering and focusing an array through a planar interface



parameters we will use to define the steering and focusing. We will use the same angles (ϕ_0, θ_{20}) defined in the last section for a ray propagating from the center of the array as well as the distances (D_{T0}, D_f) to focus the beam at the point $\mathbf{x} = (x, y, D_f)$ as shown in Fig. 8.7. From that figure we can see that the distance, D_Q , from the origin of the (x, y, z) coordinates to the point $Q = (x, y, 0)$ is

$$D_Q = D_{T0} \tan \theta_{10} + D_f \tan \theta_{20} \quad (8.14)$$

and the coordinates of Q are

$$\begin{aligned} x &= D_Q \cos \phi_0 \\ y &= D_Q \sin \phi_0. \end{aligned} \quad (8.15)$$

If one then follows a ray path from the centroid of an element to $\mathbf{x} = (x, y, D_f)$, as shown in Fig. 8.8, the distance, \tilde{D}_{mn} , from point R (directly below the element centroid) to the point Q is given by

$$\tilde{D}_{mn} = |\mathbf{RQ}| = \sqrt{(x - e_{x'm} \cos \theta_T)^2 + (y - e_{y'n})^2} \quad (8.16)$$

and the vertical distance from the centroid of an element to the interface, D_{em} , is given by (see Fig. 8.8b)

$$D_{em} = D_{T0} + e_{x'm} \sin \theta_T. \quad (8.17)$$

Thus, in the plane of incidence containing the points $(\mathbf{x}_c, \mathbf{x}_I, \mathbf{x})$ as well as points R and Q we see the ray path appears as shown in Fig. 8.9. This is just the same configuration we encountered for 2-D problems in Chap. 5 (see Fig. 5.4) so that it can be solved in exactly the same fashion. Specifically, we can show that Snell's law for the ray path from \mathbf{x}_c to \mathbf{x} yields:

Fig. 8.10 Ray paths that define the time delay laws for a 4×4 array radiating through a water–steel interface ($c_1 = 1480$ m/s, $c_2 = 5900$ m/s) where $s_x = s_y = 0.5$ mm, $\theta_r = 20^\circ$, $\phi_0 = 0^\circ$, $\theta_{20} = 45^\circ$, $D_{T0} = 10$ mm, $D_f = 10$ mm

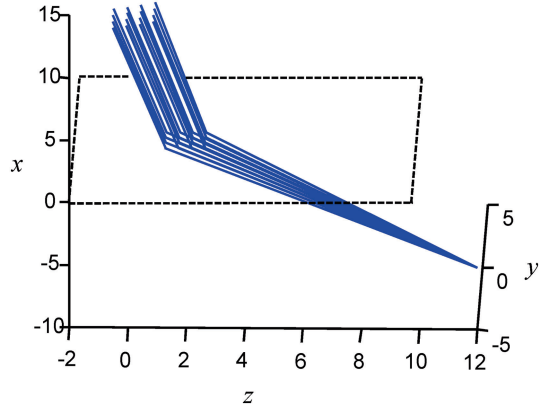
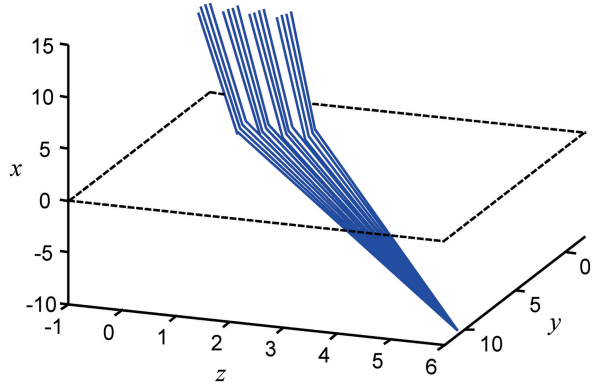


Fig. 8.11 Ray paths that define the time delay laws for a 4×4 array radiating through a water–steel interface ($c_1 = 1480$ m/s, $c_2 = 5900$ m/s), where $s_x = s_y = 0.5$ mm, $\theta_r = 20^\circ$, $\phi_0 = 30^\circ$, $\theta_{20} = 45^\circ$, $D_{T0} = 10$ mm, $D_f = 10$ mm



and the time of propagation from \mathbf{x}_e to \mathbf{x} is then

$$\Delta t_{mn} = \frac{\sqrt{(\tilde{x}_i^{mn})^2 + D_{em}^2}}{c_1} + \frac{\sqrt{D_f^2 + (\tilde{D}_{mn} - \tilde{x}_i^{mn})^2}}{c_2}, \quad (8.20)$$

which can be used to form the proper delay law

$$\Delta t_{mn}^d = (\Delta t_{mn})_{\max} - \Delta t_{mn}. \quad (8.21)$$

The MATLAB[®] function `delay_laws3Dint` (Code Listing C.27) implements Eq. (8.13) for steering through a planar interface and Eq. (8.21) for steering and focusing the beam through the interface. The calling sequence for this function is

```
>> td=delay_laws3Dint(Mx, My, sx, sy, thetat, phi, theta2, DT0, DF, c1, c2, plt);
```

where `td` is the matrix of delay times (in μ s) for an array with `Mx` elements in the x -direction and `My` elements in the y -direction. The pitches of the array are $s_x = s_y$,

and $sy = s_y$ in the x - and y -directions, respectively (in mm). The angle of the array from the interface is $\text{thetat} = \theta_t$ (in degrees) and the steering angles are $\text{phi} = \phi_0$ and $\text{theta2} = \theta_{20}$ (both in degrees). The height of the center of the array above the interface is $\text{DT0} = D_{t0}$ (in mm), and the depth to the focal point is $\text{DF} = D_f$ (in mm). See Figs. 8.7 and 8.8 for a description of these parameters. The arguments (c_1, c_2) are the wave speeds in the first and second media, respectively (in m/s). The final argument, `plt`, is a string used to optionally plot ray paths for the parameters chosen, where `plt='y'` or `'n'` for plot generation or not, respectively. Unlike the corresponding 2-D delay law function `delay_laws2Dint`, the plot option here is not implemented for the steering only case.

Figure 8.10 shows the ray paths for a 4×4 array radiating at oblique incidence through a planar interface between water and steel when the beam is steered and focused to $\phi_0 = 0^\circ$, $\theta_{20} = 45^\circ$ at a depth $D_f = 10\text{mm}$. The scales are unequal so the actual geometry is shown somewhat distorted in that figure. Figure 8.11 shows the rays where all the parameters are the same as in Fig. 8.10 except now $\phi_0 = 30^\circ$. Again, note the presence of unequal scales in Fig. 8.11.

Reference

1. J. Dziewierz, A. Gachagan, Computationally efficient solution of Snell's law of refraction. *IEEE Trans. Ultrason. Ferroelectr. Freq. Control* **60**, 1256–1259 (2013)

Chapter 9

Linear System Modeling of Phased Arrays

A phased array ultrasonic measurement system is a particularly complex collection of electrical, electromechanical, and acoustic/elastic processes because of the number of sending and receiving circuits and transducer elements present. In this chapter, we will use linear system theory concepts of two-port systems and single input–single output *linear time shift invariant (LTI) systems* to describe phased array measurement systems at different levels of detail, following an approach similar to that described in [Schmerr-Song] and [1, 2] for single element transducer systems. Our goal is to develop a model of a phased array flaw measurement system that can be used to predict quantitatively the signals that are produced in a given experiment in terms of parameters of the measurement system instrumentation and probes and the characteristics of the unknown flaw being examined.

In this chapter, we will develop a linear systems modeling framework that will allow us to ultimately describe a phased array system in terms of two types of terms:

- *System functions* that describe the electrical and electromechanical properties of the individual sending and receiving circuits and elements in the array being used. In Chap. 10, we will show how these system functions can be directly measured for a phased array in a calibration setup.
- *Acoustic/elastic transfer functions* that describe all the acoustic and elastic scattering processes present, including the sound beams generated and received by each element of the array(s) involved and the waves scattered from flaws that are present. In Chap. 11, expressions for these acoustic/elastic transfer functions will be obtained in terms of wave fields that can be described with the use of wave propagation and scattering models.

By combining measured system functions with these modeled acoustic/elastic transfer functions, we will have a complete and explicit model of an ultrasonic phased array measurement in a form that we will call an *ultrasonic measurement model* [Schmerr-Song]. As will be shown in Chap. 11 and later chapters, having a measurement model will be the key to quantitatively relating ultrasonic measurements to the properties of the flaw being examined and to give explicit meaning to the images of flaws that are obtained with arrays.

Fig. 9.1 The elements of a phased array immersion system, where a pair of sending and receiving elements are shown

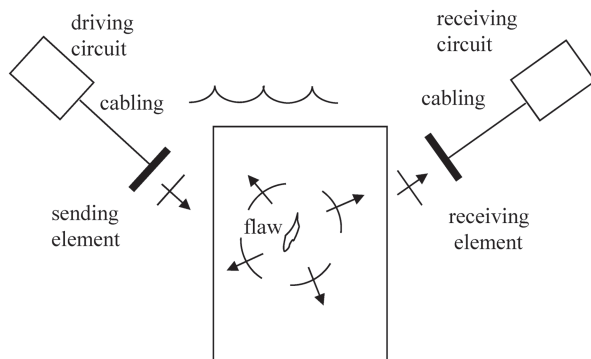
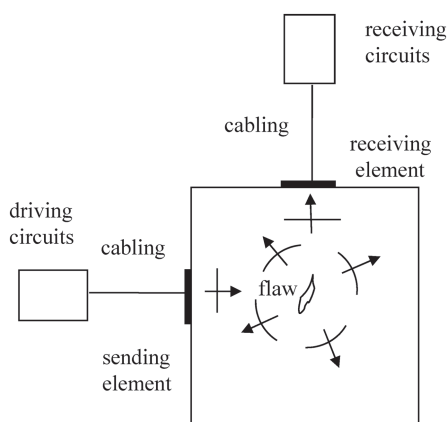


Fig. 9.2 The elements of a phased array contact testing system, where a pair of sending elements is shown



9.1 Linear System Modeling and Sound Generation

In a phased array system, the individual elements of the array(s) involved normally are assumed to act independently as drivers and receivers, so to analyze the system we can first consider only a single pair of sending and receiving elements. Figure 9.1 shows an immersion setup involving such a pair of elements, while Fig. 9.2 shows a corresponding contact testing setup. While both immersion and contact testing setups involve many of the same components, the physics of the sound generation and reception processes must be treated somewhat differently when modeling these setups, as we will see.

First consider the driving circuits in Figs. 9.1 and 9.2. If we assume that these driving circuits can be represented by a linear active network, then Thévenin's theorem says that in the frequency domain we can replace these driving circuits by an equivalent voltage source, $V_i(\omega)$, and electrical impedance, $Z_i^e(\omega)$, as shown in Fig. 9.3 [Schmerr-Song]. These equivalent circuit elements will generate the same output voltage, $V_1(\omega)$, and current, $I_1(\omega)$, as the original driving circuit. Note that these equivalent parameters are affected by the choice of the phased array instrument settings that control the driving circuits.

Fig. 9.3 An equivalent voltage source and electrical impedance model of the driving circuits

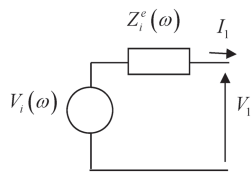
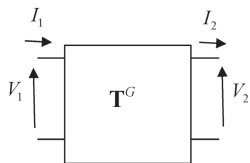


Fig. 9.4 A two-port representation of a cable as a 2×2 transfer matrix



The driving circuits are connected to the sending element through the cabling present in the sound generation process. The voltage and current (V_1, I_1) of the driving circuits at the input side of the cable produce corresponding voltage and current, (V_2, I_2) at the output side. At the typical MHz frequencies present in an ultrasonic experiment, the electrical characteristics of the cabling can be important if the cabling lengths are on the order of a meter or more in length since in these cases the cable does not just pass the inputs unchanged to the outputs. It is reasonable to assume the cable is a simple passive linear, and reciprocal device that can be treated as a two-port system [Schmerr-Song] where the inputs and outputs can be related through a 2×2 transfer matrix, \mathbf{T}^G , as shown in Fig. 9.4. More explicitly we can write

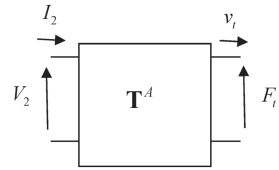
$$\begin{bmatrix} V_1 \\ I_1 \end{bmatrix} = \begin{bmatrix} T_{11}^G & T_{12}^G \\ T_{21}^G & T_{22}^G \end{bmatrix} \begin{bmatrix} V_2 \\ I_2 \end{bmatrix}, \quad (9.1)$$

where the elements of the transfer matrix are frequency dependent. Since the cable is assumed to be reciprocal, the determinant of the transfer matrix must be unity [Schmerr-Song], i.e.

$$\det[\mathbf{T}^G] = T_{11}^G T_{22}^G - T_{12}^G T_{21}^G = 1. \quad (9.2)$$

The array driving element is normally made of a piezoelectric material and is attached to both backing and facing materials. Its function is to transform the electrical inputs of the cable attached to the element, (V_2, I_2) , into mechanical outputs at its face. The face is in contact with either a fluid (for the immersion case) or a solid (for the contact case). In the contact case a thin fluid layer between the face of the driving array and the underlying solid is normally present to ensure good coupling of sound into the solid. For both the immersion and contact cases the acoustic output properties of the element can be characterized by two “lumped” acoustic parameters—a compressive force, $F_i(\omega)$, and velocity, $v_i(\omega)$, both acting on the adjacent material. However, the detailed physics of the acoustic fields on the face of the element is modeled differently in the immersion and contact cases. In the

Fig. 9.5 A two-port model of an array element as a 2×2 transfer matrix



immersion case, it is generally assumed that the face of the array at the element moves with the uniform velocity, $v_t(\omega)$, normal to the face of the transducer and generates a spatially varying pressure distribution, $p(\mathbf{x}, \omega)$, over its face. The force, F_t , is then just the integral of this pressure distribution over the active area, S_A , of the driving element, i.e.

$$F_t(\omega) = \int_{S_A} p(\mathbf{x}, \omega) dS(\mathbf{x}). \quad (9.3)$$

In contrast, in the contact case, since the face of the array is in contact with a stiff solid material through a thin fluid couplant, it is more reasonable to assume that piezoelectric element generates a constant pressure, $p(\omega)$, at its face and the total force is just $F_t(\omega) = p(\omega)S_A$, while the velocity field normal to the face has the distribution $v(\mathbf{x}, \omega)$. In this case the “lumped” parameter, $v_t(\omega)$, can be taken to be the average velocity at the face:

$$v_t(\omega) = \frac{1}{S_A} \int_{S_A} v(\mathbf{x}, \omega) dS(\mathbf{x}). \quad (9.4)$$

Thus, in either the immersion or contact testing setups, if we assume that the driving array element A acts as a linear reciprocal system that transforms the electrical inputs (V_2, I_2) to the mechanical outputs (F_t, v_t) we can model this element also as a two-port system as shown in Fig. 9.5.

Explicitly, we then have

$$\begin{bmatrix} V_2 \\ I_2 \end{bmatrix} = \begin{bmatrix} T_{11}^A & T_{12}^A \\ T_{21}^A & T_{22}^A \end{bmatrix} \begin{bmatrix} F_t \\ v_t \end{bmatrix}. \quad (9.5)$$

Since the array element is assumed to satisfy reciprocity, we also have

$$\det(\mathbf{T}^A) = T_{11}^A T_{22}^A - T_{12}^A T_{21}^A = 1. \quad (9.6)$$

At the acoustic output port of an array element the compressive force and velocity are not independent, reflecting the fact that if either the velocity on the face of the element or the pressure on the face of the element is specified then the other corresponding output parameter is also determined. This relationship is expressed as

$$F_t(\omega) = Z_r^{A;a}(\omega) v_t(\omega), \quad (9.7)$$

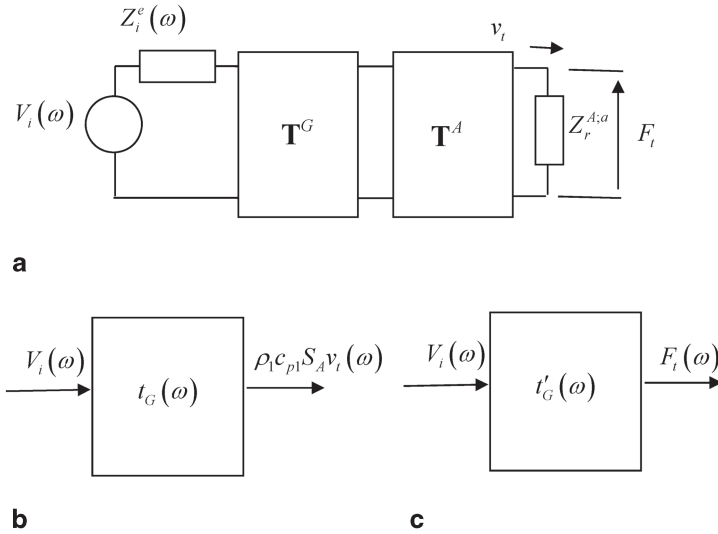


Fig. 9.6 **a** The sound generation process components, and **b** their replacement for an immersion inspection by a single input, single output linear time shift invariant system characterized by the transfer function, $t_G(\omega)$, and **c** their replacement for a contact inspection by the transfer function $t'_G(\omega)$

where $Z_r^{A;a}(\omega)$ is the *acoustic radiation impedance* of the element. For ultrasonic immersion measurement systems that use large, single element transducers of circular cross section one can derive an explicit expression for this radiation impedance as [3])

$$Z_r^{A;a} / \rho_1 c_{p1} S_A = 1 - [J_1(2ka) - iS_1(2ka)] / ka, \quad (9.8)$$

where J_1 is a Bessel function of order one and S_1 is a Struve function. Here (ρ_1, c_{p1}) are the density and compressional wave speed of the fluid, a is the radius of the transducer, $k = \omega / c_{p1}$ is the wave number, and $S_A = \pi a^2$. For most single element transducers ka can be a value of 100 or larger and Eq. (9.8) gives approximately $Z_r^{A;a} = \rho_1 c_{p1} S_A$, which is just the acoustic impedance of a plane wave. While this same plane wave limit is also true for rectangular elements that are many wavelengths long in both dimensions, the rectangular elements often used in linear and 2-D arrays have at least one dimension which is not many wavelengths in size so that the acoustic radiation impedance will inherently be a complex function of frequency.

Since the output force and velocity on the face of an element are related through the acoustic radiation impedance, we can model the driving circuits, cabling, and sending element as a series of two-port systems terminated at both ports, as shown in Fig. 9.6a, and we can replace this series of systems by a single input, single output linear time-shift invariant (LTI) system whose input is the Thevenin equivalent voltage, $V_i(\omega)$, of the driving circuits. On the output side, we can take either the

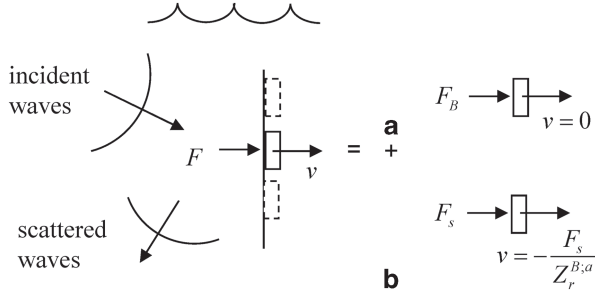


Fig. 9.7 Decomposition of the received waves at a receiving element in an immersion test into two cases. In case **a**, the incident waves are present and the face of the transducer is held rigidly fixed, and in case **b**, the incident waves are absent but the face of the transducer has the velocity present on the face of the element in the original problem

velocity, $v_i(\omega)$, or the compressive force on the face of the array element, $F_i(\omega)$, as the quantity to describe the acoustic fields. When modeling large, single element immersion transducers, it has been customary to use the force as the output [Schmerr-Song] where, as discussed above, the acoustic radiation impedance simply is a constant, i.e. $F_i(\omega) = \rho_1 c_{p1} S_A v_i(\omega)$. For array elements in immersion tests we will continue to take the output as $\rho_1 c_{p1} S_A v_i(\omega)$, as shown in Fig. 9.6b but one should realize that this is really just an output proportional to the velocity having the dimensions of a force and not the actual compressive force on the face of the array element, F_i , which is given as $F_i(\omega) = Z_r^{A:a}(\omega) v_i(\omega)$. We have made this choice because, as we will see, we can then develop complete models of ultrasonic phased arrays inspections without having to explicitly evaluate the radiation impedances of the elements. For array elements this evaluation must typically be done numerically, although it is not a difficult calculation for simple element shapes such as rectangles [4]. The transfer function for an immersion setup that describes the LTI system of Fig. 9.6b is denoted as $t_G(\omega)$. For a contact setup, since the pressure is modeled as given at the transducer face, we will instead take the output of our LTI model to be the actual force, $F_i(\omega)$, given by Eq. (9.3) and let $t'_G(\omega)$ be the transfer function in the contact case, as shown in Fig. 9.6c. Note that these transfer functions are explicit functions of all the system components shown in Fig. 9.6a but we will not need to write those explicit relationships here since t_G and t'_G will not need to be independently known in a complete description of the ultrasonic system, as will be discussed in Sect. 9.4.

9.2 Linear System Modeling and Sound Reception

The LTI models developed in the previous section can be used on sound generation for either immersion or contact phased array systems. In developing similar models for the sound reception processes it will be necessary to treat the immersion and contact cases separately. Consider first an immersion setup. Figure 9.7 shows the

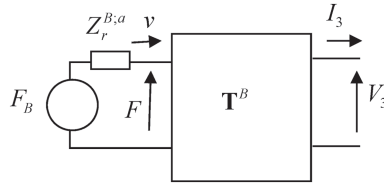


Fig. 9.8 A model of the receiving element in an immersion test as a two-port system driven by a force source of strength equal to the blocked force, F_B , on the face of the element in series with the acoustic radiation impedance, $Z_r^{B;a}$, of the receiving transducer

incident and scattered waves acting on an array element. These waves generate a compressive force, $F(\omega)$, and a normal velocity, $v(\omega)$, on the face of the element. This problem can be decomposed into the superposition of the two cases (a) and (b) shown in Fig. 9.7. In case (a), the incident waves are present and the face of the element is held rigidly fixed. The force exerted on the element in this case is called the *blocked force*, $F_B(\omega)$. In case (b), the incident waves are absent and the motion of the face of the element is assumed to be the total velocity, $v(\omega)$, of the original problem. In case (b), the waves generated are due solely to the motion of the face of the element so this case is just a radiation problem of the type considered for the transmitting array element where the force, $F_s(\omega)$, and velocity, $v(\omega)$, are related through the acoustic radiation impedance, $Z_r^{B;a}(\omega)$, of the receiving element, i.e.

$$F_s(\omega) = -Z_r^{B;a}(\omega)v(\omega). \quad (9.9)$$

The minus sign is present in Eq. (9.9) since the normal velocity here is assumed to act into the face of the element, as shown in Fig. 9.7. Since the total force, $F(\omega)$, in the original problem is just the sum of the forces in cases (a) and (b), we have

$$F(\omega) = F_B(\omega) - Z_r^{B;a}(\omega)v(\omega). \quad (9.10)$$

The meaning of Eq. (9.10) from a modeling standpoint can be seen more clearly by considering Fig. 9.8 where a receiving array element B is modeled as a two-port system with the 2×2 transfer matrix \mathbf{T}^B that transforms the acoustic input force and velocity (F, v) into the voltage and current outputs (V_3, I_3) . It can be seen from Fig. 9.8 that the relationship of Eq. (9.10) is satisfied if we assume the acoustic fields incident on the receiving element are modeled as a driving compressive force source, F_B , in series with an acoustic impedance, $Z_r^{B;a}$.

For the contact case shown in Fig. 9.9 the interaction of the incident and scattered waves are with an element sitting on an otherwise stress-free surface. The incident and scattered waves produce a force and average velocity given by (F, v) , respectively. Again we can decompose this problem into two cases. In case (a), the incident waves are assumed to excite the element when the contact surface is completely stress-free so that $F = 0$. The average free surface velocity on the face of the element is $v_{fs}(\omega)$. In case (b), the incident waves are absent and the waves generated

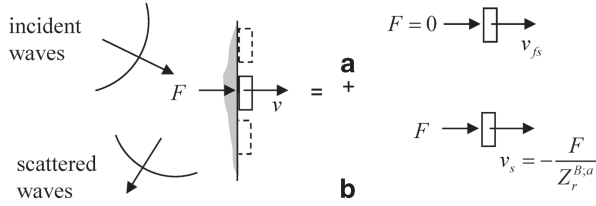


Fig. 9.9 Decomposition of the received waves in a contact measurement into two cases. In case **a**, the incident waves are present and the contact surface is assumed to be stress-free. The velocity at this free surface is v_{fs} . In case **b**, the incident waves are absent and all the waves generated are due to the motion of the face of the element

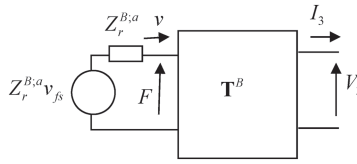


Fig. 9.10 A model of the receiving element in a contact test as a two-port system driven by a force source of strength equal to the acoustic impedance multiplied by the free-surface velocity on the face of the element, $Z_r^{B;a} v_{fs}$, in series with the acoustic radiation impedance, $Z_r^{B;a}$, of the receiving element

are solely due to the velocity v_s . Since again this case is identical to the radiation problem of a transmitting element we have $v_s = -F / Z_r^{B;a}$, where F is the total force on the element in the original problem. Since the velocities in these cases must add up to the total velocity $v(\omega)$ in the original problem, we find

$$v(\omega) = v_{fs}(\omega) - \frac{F(\omega)}{Z_r^{B;a}(\omega)} \quad (9.11)$$

or, equivalently,

$$F(\omega) = Z_r^{B;a}(\omega) v_{fs}(\omega) - Z_r^{B;a}(\omega) v(\omega). \quad (9.12)$$

Comparing Eq. (9.12) with Eq. (9.10) we see that in the contact case the waves interacting with the receiving element can be replaced by a force source $Z_r^{B;a} v_{fs}$ in series with an acoustic radiation impedance, $Z_r^{B;a}$, (see Fig. 9.10). Note that the mechanical sources and impedances appearing in Figs. 9.8 and 9.10 represent the mechanical analog to a Thévenin equivalent electrical circuit. We could also use a mechanical analog of a Norton equivalent current source and impedance. For example, we could represent the relations of either Eq. (9.11) or (9.12) in terms of a velocity source of strength $v_{fs}(\omega)$ in parallel with an acoustic radiation impedance, $Z_r^{B;a}(\omega)$, as shown in Fig. 9.11. This Norton-like equivalent system is the more “natural” model to use for the contact case since the acoustic source, $v_{fs}(\omega)$, that appears in the Norton model is a function only of the incident acoustic waves

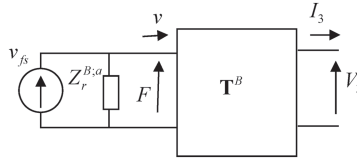


Fig. 9.11 A model of the receiving element in a contact test as a two-port system driven by a velocity source of strength v_{fs} in parallel with the acoustic radiation impedance, $Z_r^{B,a}$, of the receiving element

driving the receiving element, as is the blocked force, $F_B(\omega)$, in the immersion case. In fact, if we assume that we can represent the interaction of the incident waves with the element surfaces in these cases as plane wave interactions, then the blocked force (the force at a plane rigid, immobile surface) is just twice the force, $F_{inc}(\omega)$, generated on the face of the array element by the incident waves only (i.e. when the element receiving surface is absent) and the free-surface velocity (the velocity at a plane stress-free surface) is twice the velocity generated by only the incident waves, $v_{inc}(\omega)$, so that in both the immersion and the contact cases the acoustic equivalent sources shown in Figs. 9.8 and 9.11 become (see [Schmerr-Song] for an explicit proof in the immersion case; the contact case follows in a similar manner):

$$\begin{aligned} F_B(\omega) &= 2F_{inc}(\omega) \\ v_{fs}(\omega) &= 2v_{inc}(\omega). \end{aligned} \quad (9.13)$$

The voltage and current outputs (V_3, I_3) of the receiving array element in either the immersion or contact cases are the inputs that drive the cabling present between the element and the receiving circuits. If we let (V_4, I_4) be the voltage and current at the inputs to the receiving circuits then in the sound reception process we can represent the cabling as a 2×2 transfer matrix, \mathbf{T}^R , where

$$\begin{bmatrix} V_3 \\ I_3 \end{bmatrix} = \begin{bmatrix} T_{11}^R & T_{12}^R \\ T_{21}^R & T_{22}^R \end{bmatrix} \begin{bmatrix} V_4 \\ I_4 \end{bmatrix} \quad (9.14)$$

and, since the receiving cable is assumed to satisfy reciprocity,

$$T_{11}^R T_{22}^R - T_{12}^R T_{21}^R = 1. \quad (9.15)$$

The receiving components in a phased array system generally serve two functions: (1) they amplify the received low amplitude electrical signals, and (2) they can filter the low or high frequency content of the signals. Here, we will only model the amplification function since in many quantitative NDE measurements one does not normally want to further limit information present in the received signal beyond what is already inherently present in the measurement processes due to sources such

Fig. 9.12 A model of the receiving circuit for an array element as an electrical impedance, Z_0^e , and an amplification factor, $K(\omega)$

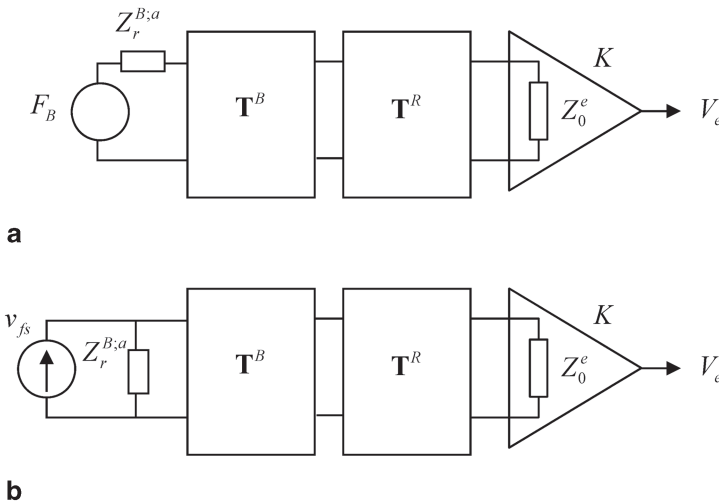
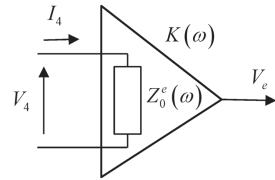


Fig. 9.13 Complete models of the reception process for an array element in **a** an immersion testing setup, and **b** in a contact testing setup

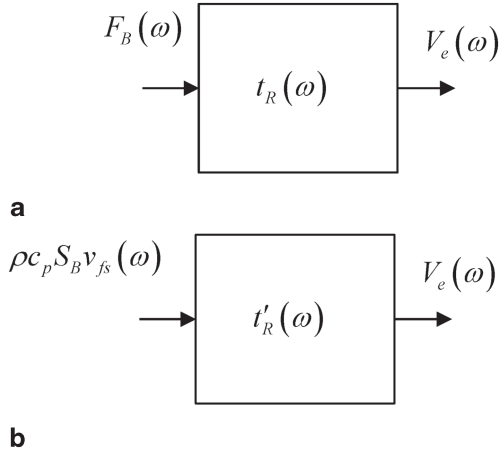
as material attenuation, for example. Any filtering of the signal by the receiving circuits, however, can always be introduced separately by modifying the amplified voltage, $V_e(\omega)$, received from an array element appropriately. Since we assume the receiving circuits act only as a linear electrical amplification network, we can characterize the receiving circuits as a receiving impedance, $Z_0^e(\omega)$, and a voltage amplification function, $K(\omega)$, as shown in Fig. 9.12, where

$$\begin{aligned} V_4(\omega) &= Z_0^e(\omega) I_4(\omega) \\ V_e(\omega) &= K(\omega) V_4(\omega). \end{aligned} \quad (9.16)$$

For both the immersion and contact cases, we can combine our acoustic source and array element models, cabling models, and receiving circuit models into a complete series of models that represent the sound reception process, as shown in Fig. 9.13a, b.

It then follows that we can replace the detailed models of Fig. 9.13 with the single input–single output LTI systems shown in Fig. 9.14 for the immersion and contact cases. The transfer function, $t_R(\omega)$, of the immersion case relates the blocked force input, $F_B(\omega)$, to the output voltage, $V_e(\omega)$. For the contact case we have chosen to

Fig. 9.14 LTI models of the reception process for **a** an immersion testing setup, and **b** a contact testing setup



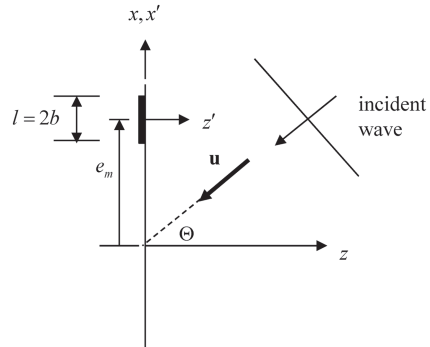
let the transfer function, $t'_R(\omega)$, relate a similar “force” input $\rho c_p S_B v_{fs}(\omega)$ to an output voltage, $V_e(\omega)$, where v_{fs} is the free-surface velocity, (ρ, c_p) are the density and compressional wave speed in the solid adjacent to the receiving transducer, and S_B is the area of the receiving transducer. Note that similar to the sound generation model, this “force”, $\rho c_p S_B v_{fs}(\omega)$, is not the actual force source term, which is $Z_r^{B;a} v_{fs}$, as shown in Fig. 9.10. By defining the input in this fashion, we see that the transfer functions in both the immersion and contact cases have the same dimensions and the acoustic radiation impedance does not appear. We can write down explicit expressions for the reception transfer functions in terms of the detailed system components shown in Fig. 9.13 but as done in our description of the sound generation process we will not give those expressions here as these transfer functions need not be obtained explicitly in a complete description of the measurement process, as will be discussed in Sect. 9.4.

9.3 The Reception Process and Grating Lobes

In Chap. 4, we considered in detail the sound field generated by arrays. We saw that for sufficiently large elements grating lobes were generated which travel in directions other than that of the main beam. Grating lobes can also appear in the reception process. We can demonstrate this fact in the simple reception problem outlined in Fig. 9.15 where a plane wave is incident on an element of a 1-D array in a fluid. In this case the incident pressure is given as

$$\begin{aligned} p_{inc} &= P \exp(ik \mathbf{u} \cdot \mathbf{x}) \\ &= P \exp[ik(-x \sin \Theta - z \cos \Theta)]. \end{aligned} \quad (9.17)$$

Fig. 9.15 A plane wave incident on a receiving array element



On the m th element of the array we have $(x, z) = (e_m + x', 0)$, where x' is measured from the center of the element which is located at $\mathbf{x}_m = (e_m, 0)$. Thus, the compressive force/unit length, exerted on this element by the incident wave is

$$\begin{aligned} f_{inc}(\mathbf{x}_m, \omega) &= \int_{-b}^b p_{inc} dx' \\ &= P \exp(-ik \sin \Theta e_m) \int_{-b}^b \exp(-ik \sin \Theta x') dx' \end{aligned} \quad (9.18)$$

and we will take the blocked force/unit length, $f_B(\mathbf{x}_m, \omega)$, as just twice this incident force so that performing the integration in Eq. (9.18) we find

$$\begin{aligned} f_B(\mathbf{x}_m, \omega) &= 2Pl \exp(-ik \sin \Theta e_m) \frac{\sin(kb \sin \Theta)}{kb \sin \Theta} \\ &= 2Pl \exp(-ik \sin \Theta e_m) D_b(\Theta) \end{aligned} \quad (9.19)$$

in terms of the far field directivity of the element, $D_b(\Theta)$, (see Eq. (2.39)) when it is acting as a transmitter. If the transfer function, $t_R(\omega)$, is the same for each element in the array then the received voltage from the m th element, $V_e = V(\mathbf{x}_m, \omega)$, is

$$V(\mathbf{x}_m, \omega) = t_R(\omega) f_B(\mathbf{x}_m, \omega) \quad (9.20)$$

and the received voltage from the entire array of M elements, $V_R(\omega)$, is given by

$$V_R(\omega) = 2Pl D_b(\Theta) t_R(\omega) \sum_{m=1}^M \exp(-ik \sin \Theta e_m). \quad (9.21)$$

Placing the expression for the centroid locations (Eq. (4.3)) into Eq. (9.21) then allows us to sum the resulting power series again and we have

$$\begin{aligned}
V_R(\omega) &= 2Pl t_R(\omega) D_b(\Theta) \exp \left[iks \sin \Theta \frac{M+1}{2} \right] \sum_{m=1}^M \exp(-iks \sin \Theta m) \\
&= 2Pl t_R(\omega) D_b(\Theta) \frac{\sin [Mks \sin \Theta / 2]}{\sin [ks \sin \Theta / 2]} \\
&= 2Pl M t_R(\omega) D_b(\Theta) D_s(ks \sin \Theta),
\end{aligned} \tag{9.22}$$

where the “point” source directivity, D_s , is the same directivity that appeared in the sound generation process (Eq. (4.22)). If on reception we steer the beam at an angle, Φ , with respect to the z -axis, then we need to include in Eq. (9.21) the steering delay law of Eq. (4.25). Again, as shown in Chap. 4, we can sum the series and find the total received voltage is instead

$$V_R(\omega) = 2Pl M t_R(\omega) D_b(\Theta) D_s[ks(\sin \Theta - \sin \Phi)]. \tag{9.23}$$

Because of the periodicity of D_s , as discussed in Chap. 4, Eq. (9.23) shows that if the array is steered in the incoming wave direction, there will be a large response, but for arrays with a pitch larger than one half a wavelength grating lobes can also appear that will produce enhanced responses in other directions as well. As in the sound generation case, apodization laws can be applied to the element responses in reception to help reduce these grating lobe contributions.

9.4 Linear System Model of the Complete Ultrasonic Measurement Process

Having obtained LTI models of both the sound generation and reception processes, to model the entire ultrasonic measurement process for a pair of sending/receiving elements requires that we relate the scaled output velocity or force of the sending element to the blocked force or input scaled free surface velocity of the receiving element in the immersion and contact cases, respectively. Thus, we need to model the complex acoustic/elastic propagation and scattering processes occurring between the sending and receiving elements by an appropriate acoustic/elastic transfer function. These transfer functions are shown in Fig. 9.16, where in the immersion case the acoustic/elastic transfer function, $t_A(\omega)$, is defined as

$$t_A(\omega) = \frac{F_B(\omega)}{\rho_1 c_{p1} S_A v_t(\omega)}, \tag{9.24}$$

and in the contact case the transfer function, $t'_A(\omega)$, is defined as

Fig. 9.16 Acoustic/elastic transfer functions for a pair of elements in **a** immersion testing setups, and **b** for contact testing setups

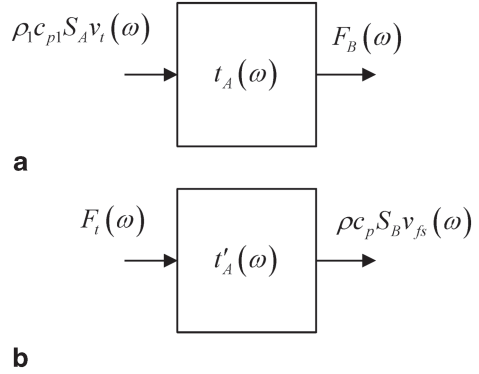
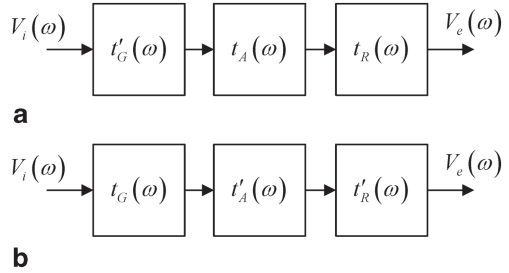


Fig. 9.17 Complete LTI models of a pair of elements for **a** an immersion measurement system, and **b** a contact measurement system



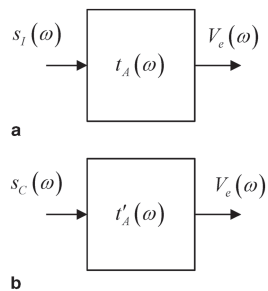
$$t'_A(\omega) = \frac{\rho c_p S_B v_{fs}(\omega)}{F_i(\omega)}. \quad (9.25)$$

While the Thevenin equivalent driving voltage, $V_i(\omega)$, and the sound generation and transfer functions can be measured with detailed electrical measurements [Schmerr-Song], [1, 2] the acoustic/elastic transfer functions are described by wave fields whose values are normally not measurable. Thus, accurate models of ultrasound propagation and scattering are needed to describe these functions. In Chap. 11, we will show explicitly what field values must be known in order to model these acoustic/elastic transfer functions in a flaw measurement experiment.

Figure 9.17 shows a complete model of either immersion or contact measurement systems as a series of the transfer functions discussed in this chapter. However, we can simplify these models even further by lumping the sound generation and reception transfer functions and the driving voltage into single *system functions*, defined as $s_i(\omega)$ for immersion testing and $s_c(\omega)$ for contact testing, where

$$\begin{aligned} s_i(\omega) &= t'_G(\omega) t_R(\omega) V_i(\omega) \\ s_c(\omega) &= t_G(\omega) t'_R(\omega) V_i(\omega). \end{aligned} \quad (9.26)$$

Fig. 9.18 Complete models of a pair of elements in terms of a system function and acoustic/elastic transfer function for **a** an immersion measurement system, and **b** a contact measurement system



Then the complete system models for either immersion or contact testing are given by

$$\begin{aligned} V_e(\omega) &= s_I(\omega)t_A(\omega) \\ V_e(\omega) &= s_C(\omega)t'_A(\omega). \end{aligned} \quad (9.27)$$

The complete ultrasonic system models in terms of the system functions are shown in Fig. 9.18. This combination of all these terms into a single function is important since, as shown in the next chapter, by making voltage measurements of a phased array system in a calibration setup where the acoustic/elastic transfer function can be modeled explicitly these system functions for each pair of sending/receiving elements in the array(s) present can be measured directly. By combining these measured system functions with models for the acoustic/elastic transfer function in more complex flaw measurements, we then have a viable approach to predict quantitatively the signals seen in many NDE phased array experiments.

References

1. C.J. Dang, L.W. Schmerr, A. Sedov, Modeling and measuring all the elements of an ultrasonic nondestructive evaluation system I: Modeling foundations. Res. NDE **14**, 141–176 (2002a)
2. C.J. Dang, L.W. Schmerr, A. Sedov, Modeling and measuring all the elements of an ultrasonic nondestructive evaluation system. II: Model-based measurements. Res. NDE **14**, 177–201 (2002b)
3. M. Greenspan, Piston radiator: Some extensions of the theory. J. Acoust. Soc. Am. **65**, 608–662 (1979)
4. K. Sha, J. Yang, W. Gan, A simple calculation method for the self- and mutual-radiation impedance of flexible rectangular patches in a rigid, infinite baffle. J. Sound Vib **282**, 179–195 (2005)

Chapter 10

Phased Array System Functions

As seen in the last chapter, the system function of a pair of phased array sending and receiving elements describes in a simple fashion all the electrical and electromechanical characteristics of the sound generation and sound reception process present in an ultrasonic measurement. In this chapter, we will show how system functions can be measured experimentally in a calibration setup where the corresponding acoustic/elastic functions are known.

10.1 Acoustic/Elastic Transfer Function Models

Since in phased arrays we can independently drive and receive with many different combinations of sending and receiving elements, in a phased array system with M sending elements and N receiving elements, we have $M \times N$ different system functions, $s_{mn}(\omega)$ and acoustic/elastic transfer functions, $t_A^{mn}(\omega)$ that generate the received voltages, $V_e^{mn}(\omega)$, where

$$V_e^{mn}(\omega) = s_{mn}(\omega)t_A^{mn}(\omega). \quad (10.1)$$

Equation (10.1) can be used to obtain these system functions experimentally if we measure the received voltages in a calibration setup and have explicit models for the acoustic/elastic transfer functions in that setup. The calibration setups we will use for immersion and contact tests are shown in Fig. 10.1, where a 2-D or linear array is placed parallel to a plane reflecting interface and the reflection of the waves generated by driving a single element of the array is received by a single receiving element. A more detailed description of the setup geometry is shown in Fig. 10.2 for a pair of sending and receiving rectangular elements.

Consider first an immersion setup. Our starting point in this case is the Rayleigh-Sommerfeld model for an element, Eq. (6.21), where the velocity is assumed to be constant over the face of the driving element, i.e. we will use a piston model. The pressure due to the waves generated by the driving element at a point (x_l, y_l, D) in the fluid at the location of the reflecting interface is given as

Fig. 10.1 Calibration setups for obtaining the system functions **a** for an immersion test, and **b** for a contact test

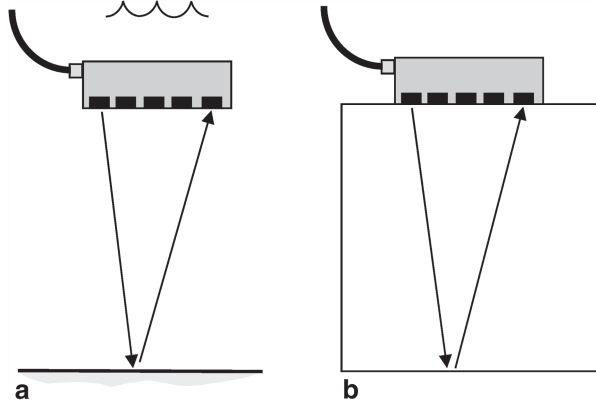
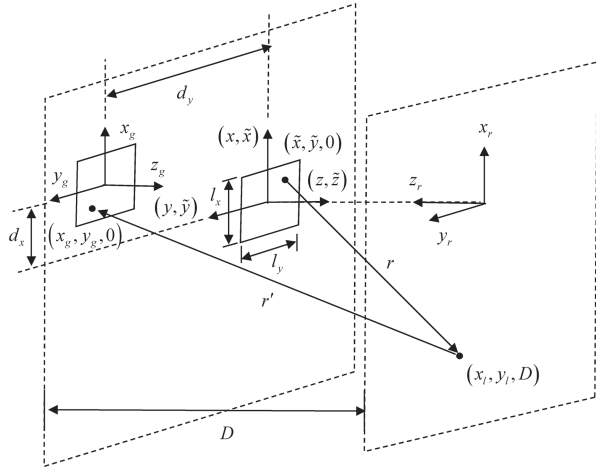


Fig. 10.2 A calibration setup geometry involving two rectangular array elements and a parallel plane reflecting interface



$$p(x_l, y_l, D, \omega) = \frac{-i\omega\rho_l v_0(\omega)}{2\pi} \int_{S_t} \frac{\exp(ikr)}{r} d\tilde{x}d\tilde{y}, \quad (10.2)$$

where S_t is the area of the transmitting element, the distance from a point $(\tilde{x}, \tilde{y}, 0)$ on the sending element to a point (x_l, y_l, D) on the reflecting interface is $r = \sqrt{(\tilde{x} - x_l)^2 + (\tilde{y} - y_l)^2 + D^2}$, $k = \omega/c_l$ is the wave number for the fluid, and ρ_l is the density of the fluid. If we assume the reflector is far enough away from the element so that $x, \tilde{x}, y, \tilde{y} \ll D$ then we can approximate this distance as $r \equiv D + [(\tilde{x} - x_l)^2 + (\tilde{y} - y_l)^2] / 2D$ (paraxial approximation) and we find

$$p(x_l, y_l, D, \omega) = \frac{-i\omega\rho_l v_0(\omega) \exp(ikD)}{2\pi D} \int_{S_t} \left[ik \frac{(\tilde{x} - x_l)^2 + (\tilde{y} - y_l)^2}{2D} \right] d\tilde{x} d\tilde{y}. \quad (10.3)$$

If we assume we can treat the interactions of these incident waves with the reflecting interface as a quasi-plane wave interaction at normal incidence, then pressure in the reflected wave at the interface, $p_R(x_l, y_l, D)$, is

$$p_R(x_l, y_l, D, \omega) = R_{12} p(x_l, y_l, D, \omega) = \frac{\rho_2 c_{p2} - \rho_1 c_{p1}}{\rho_2 c_{p2} + \rho_1 c_{p1}} p(x_l, y_l, D, \omega), \quad (10.4)$$

where R_{12} is the plane wave reflection coefficient at normal incidence (based on a pressure ratio) and $(\rho_1, c_{p1}), (\rho_2, c_{p2})$ are the density and compressional wave speed for the fluid and reflecting solid, respectively. The normal velocity, v_r , at the interface in the z_r -direction (directed towards the receiving element, see Fig. 10.2) is also given by the plane wave relationship

$$v_r(x_l, y_l, D, \omega) = R_{12} p(x_l, y_l, D, \omega) / \rho_1 c_{p1}. \quad (10.5)$$

Using this velocity field as specified on the entire interface, we can again use the Rayleigh-Sommerfeld integral to obtain the pressure, p_g , of the reflected waves at a point (x_r, y_r, D) on the plane of the receiving element:

$$p_g(x_r, y_r, D, \omega) = \frac{-i\omega\rho_1}{2\pi} \int_{-\infty}^{+\infty} \int_{-\infty}^{+\infty} v_r(x_l, y_l, D, \omega) \frac{\exp(ikr')}{r'} dx_l dy_l. \quad (10.6)$$

Applying the paraxial approximation to the distance r' then gives

$$p_g(x_r, y_r, D, \omega) = \frac{-ikR_{12} \exp(ikD)}{2\pi D} \int_{-\infty}^{+\infty} \int_{-\infty}^{+\infty} p(x_l, y_l, D, \omega) \exp\left(ik \frac{(x_r - x_l)^2 + (y_r - y_l)^2}{2D}\right) dx_l dy_l. \quad (10.7)$$

If the driving and receiving elements are separated by the distances (d_x, d_y) in the (x, y) directions, respectively, then

$$x_r = d_x + x_g, \quad y_r = d_y + y_g \quad (10.8)$$

(see Fig. 10.2) and we can rewrite Eq. (10.7) as

$$p_g(x_g, y_g, D, \omega) = \frac{-ikR_{12} \exp(ikD)}{2\pi D} \int_{-\infty}^{+\infty} \int_{-\infty}^{+\infty} [p(x_l, y_l, D, \omega) \exp\left(ik \frac{(x_g + d_x - x_l)^2 + (y_g + d_y - y_l)^2}{2D}\right)] dx_l dy_l. \quad (10.9)$$

If we assume the incident wave interactions with the receiving transducer can be treated approximately as plane wave interactions, an assumption that is likely satisfied for the setup of Fig. 10.2, we can take the blocked force, F_B , at the receiving element to be simply twice the force exerted on the element by the incident waves [Schmerr-Song] and we have

$$\begin{aligned} F_B(\omega) &= 2 \int_{S_r} p_g(x_g, y_g, D, \omega) dx_g dy_g \\ &= \frac{-2ikR_{12} \exp(ikD)}{2\pi D} \int_{S_r} \left\{ \int_{-\infty}^{+\infty} \int_{-\infty}^{+\infty} \left[p(x_l, y_l, D, \omega) \right. \right. \\ &\quad \left. \left. \exp\left(ik \frac{(x_g + d_x - x_l)^2 + (y_g + d_y - y_l)^2}{2D} \right) \right] dx_l dy_l \right\} dx_g dy_g, \end{aligned} \quad (10.10)$$

where S_r is the receiving area. Placing Eq. (10.3) into this result then gives

$$\begin{aligned} F_B(\omega) &= \frac{-2ikR_{12} \exp(2ikD)}{2\pi D} \frac{-ik\rho_1 c_{p1} v_0(\omega)}{2\pi D} \int_{S_r} \left[\int_{-\infty}^{+\infty} \int_{-\infty}^{+\infty} \left[\int_{S_t} \left[\exp\left(ik \frac{(\tilde{x} - x_l)^2 + (\tilde{y} - y_l)^2}{2D} \right) \right. \right. \right. \\ &\quad \left. \left. \exp\left(ik \frac{(x_g + d_x - x_l)^2 + (y_g + d_y - y_l)^2}{2D} \right) \right] d\tilde{x} d\tilde{y} \right] dx_l dy_l \right] dx_g dy_g. \end{aligned} \quad (10.11)$$

Since the acoustic/elastic transfer function, t_A , for the immersion case is defined as $t_A(\omega) = F_B(\omega) / \rho_1 c_{p1} v_0(\omega) S_t$, this transfer function is

$$\begin{aligned} t_A(\omega) &= 2R_{12} \left[\frac{-ik \exp(ikD)}{2\pi D} \right]^2 \frac{1}{S_t} \int_{S_r} \left[\int_{-\infty}^{+\infty} \int_{-\infty}^{+\infty} \left[\int_{S_t} \left[\exp\left(ik \frac{(\tilde{x} - x_l)^2 + (\tilde{y} - y_l)^2}{2D} \right) \right. \right. \right. \\ &\quad \left. \left. \exp\left(ik \frac{(x_g + d_x - x_l)^2 + (y_g + d_y - y_l)^2}{2D} \right) \right] d\tilde{x} d\tilde{y} \right] dx_l dy_l \right] dx_g dy_g. \end{aligned} \quad (10.12)$$

Now, consider the integrals in Eq. (10.12) over the interface, i.e.

$$\begin{aligned} I &= \int_{-\infty}^{+\infty} \int_{-\infty}^{+\infty} \exp\left(ik \frac{(\tilde{x} - x_l)^2 + (\tilde{y} - y_l)^2}{2D} \right) \exp\left(ik \frac{(x_g + d_x - x_l)^2 + (y_g + d_y - y_l)^2}{2D} \right) dx_l dy_l \\ &= \exp\left(ik \frac{(x_g + d_x)^2 + (y_g + d_y)^2}{2D} \right) \exp\left(ik \frac{\tilde{x}^2 + \tilde{y}^2}{2D} \right) \\ &\quad \int_{-\infty}^{+\infty} \exp\left(ik \frac{x_l^2}{D} \right) \exp\left(ik \frac{(x_g + d_x + \tilde{x})x_l}{D} \right) dx_l \\ &\quad \int_{-\infty}^{+\infty} \exp\left(ik \frac{y_l^2}{D} \right) \exp\left(ik \frac{(y_g + d_y + \tilde{y})y_l}{D} \right) dy_l. \end{aligned} \quad (10.13)$$

Both integrals appearing in Eq. (10.13) can be performed exactly since we have [Schmerr, Schmerr-Song]:

$$\int_{-\infty}^{+\infty} \exp(iAx^2) \exp(-iBx) dx = \sqrt{\frac{i\pi}{A}} \exp\left(\frac{-iB^2}{4A}\right) \quad \text{Im}(A) > 0, \quad (10.14)$$

where $\text{Im}()$ indicates “imaginary part of”. In Eq. (10.13) the corresponding A terms are purely real but if we add a small amount of “damping” by letting $A = A + i\varepsilon$ and then take the limit as $\varepsilon \rightarrow 0$, the result is the same as using Eq. (10.14) directly on the forms given in Eq. (10.13) and we find

$$I = \frac{i\pi D}{k} \exp\left(ik \frac{(x_g + d_x)^2 + (y_g + d_y)^2}{2D}\right) \exp\left(ik \frac{\tilde{x}^2 + \tilde{y}^2}{2D}\right) \exp\left(-ik \frac{(\tilde{x} + x_g + d_x)^2}{4D}\right) \exp\left(-ik \frac{(\tilde{y} + y_g + d_y)^2}{4D}\right). \quad (10.15)$$

Placing Eq. (10.15) into Eq. (10.12) gives

$$t_A(\omega) = 2R_{12} \frac{-ik \exp(2ikD)}{4\pi D S_t} \int_{S_t} \left[\int_{S_t} \exp\left(ik \frac{(x_g + d_x)^2 + (y_g + d_y)^2}{2D}\right) \exp\left(ik \frac{\tilde{x}^2 + \tilde{y}^2}{2D}\right) \exp\left(-ik \frac{(\tilde{x} + x_g + d_x)^2}{4D}\right) \exp\left(-ik \frac{(\tilde{y} + y_g + d_y)^2}{4D}\right) d\tilde{x} d\tilde{y} \right] dx_g dy_g. \quad (10.16)$$

When the exponential terms in Eq. (10.16) are combined, this equation simplifies to

$$t_A(\omega) = 2R_{12} \frac{-ik \exp(2ikD)}{4\pi D S_t} \int_{S_t} \left[\int_{S_t} \exp\left(ik \frac{[\tilde{x} - (x_g + d_x)]^2}{4D}\right) \exp\left(ik \frac{[\tilde{y} - (y_g + d_y)]^2}{4D}\right) d\tilde{x} d\tilde{y} \right] dx_g dy_g. \quad (10.17)$$

Since we are assuming that both the transmitting and receiving elements are of lengths (l_x, l_y) in the (x, y) directions, respectively, Eq. (10.17) can be rewritten more explicitly as

$$t_A(\omega) = 2R_{12} \frac{-ik \exp(2ikD)}{4\pi D S_t} \left[\int_{-l_x/2}^{l_x/2} \int_{-l_x/2}^{l_x/2} \exp\left(ik \frac{[\tilde{x} - (x_g + d_x)]^2}{4D}\right) dx_g d\tilde{x} \right] \left[\int_{-l_y/2}^{l_y/2} \int_{-l_y/2}^{l_y/2} \exp\left(ik \frac{[\tilde{y} - (y_g + d_y)]^2}{4D}\right) dy_g d\tilde{y} \right]. \quad (10.18)$$

Consider now the first double integral in Eq. (10.18) and make the change of variable from x_g to t , where

$$t = \sqrt{\frac{k}{2\pi D}} \left[\tilde{x} - (x_g + d_x) \right]. \quad (10.19)$$

Then we have

$$\begin{aligned} \int_{-l_x/2}^{l_x/2} \int_{-l_x/2}^{l_x/2} \exp \left(ik \frac{[\tilde{x} - (x_g + d_x)]^2}{4D} \right) dx_g d\tilde{x} &= \sqrt{\frac{2\pi D}{k}} \int_{-l_x/2}^{+l_x/2} \left[\int_{\sqrt{\frac{k}{2\pi D}}[\tilde{x}-l_x/2-d_x]}^{\sqrt{\frac{k}{2\pi D}}[\tilde{x}+l_x/2-d_x]} \exp \left(\frac{i\pi}{2} t^2 \right) dt \right] d\tilde{x} \\ &= \sqrt{\frac{2\pi D}{k}} \int_{-l_x/2}^{+l_x/2} \left[\int_0^{\sqrt{\frac{k}{2\pi D}}[\tilde{x}+l_x/2-d_x]} \exp \left(\frac{i\pi}{2} t^2 \right) dt - \int_0^{\sqrt{\frac{k}{2\pi D}}[\tilde{x}-l_x/2-d_x]} \exp \left(\frac{i\pi}{2} t^2 \right) dt \right] d\tilde{x} \end{aligned} \quad (10.20)$$

But the interior integrals are in the form of Fresnel integrals, $F(x)$, where

$$F(x) = \int_0^x \exp \left(\frac{i\pi}{2} t^2 \right) dt \quad (10.21)$$

so that we have

$$\begin{aligned} \int_{-l_x/2}^{l_x/2} \int_{-l_x/2}^{l_x/2} \exp \left(ik \frac{[\tilde{x} - (x_g + d_x)]^2}{4D} \right) dx_g d\tilde{x} \\ = \sqrt{\frac{2\pi D}{k}} \int_{-l_x/2}^{+l_x/2} \left[F \left(\sqrt{\frac{k}{2\pi D}} [\tilde{x} + l_x/2 - d_x] \right) - F \left(\sqrt{\frac{k}{2\pi D}} [\tilde{x} - l_x/2 - d_x] \right) \right] d\tilde{x}. \end{aligned} \quad (10.22)$$

Again, if we make a change of variables on each integrand in Eq. (10.22), namely,

$$\begin{aligned} w &= \sqrt{\frac{k}{2\pi D}} (\tilde{x} + l_x/2 - d_x) \\ q &= \sqrt{\frac{k}{2\pi D}} (\tilde{x} - l_x/2 - d_x) \end{aligned} \quad (10.23)$$

then Eq. (10.22) is of the form

$$\begin{aligned} \int_{-l_x/2}^{l_x/2} \int_{-l_x/2}^{l_x/2} \exp \left(ik \frac{[\tilde{x} - (x_g + d_x)]^2}{4D} \right) dx_g d\tilde{x} \\ = \frac{2\pi D}{k} \int_{\sqrt{\frac{k}{2\pi D}}[-d_x]}^{\sqrt{\frac{k}{2\pi D}}[l_x-d_x]} F(w) dw - \frac{2\pi D}{k} \int_{\sqrt{\frac{k}{2\pi D}}[-l_x-d_x]}^{\sqrt{\frac{k}{2\pi D}}[-d_x]} F(q) dq \end{aligned} \quad (10.24)$$

For these integrals of the Fresnel function we can use integration by parts to obtain the relationship

$$\int_{x_1}^{x_2} F(x) dx = \left[xF(x) + \frac{i}{\pi} \exp(i\pi x^2 / 2) \right]_{x_1}^{x_2} \quad (10.25)$$

so that we find

$$\begin{aligned} & \int_{-l_x/2}^{l_x/2} \int_{-l_x/2}^{l_x/2} \exp\left(ik \frac{[\tilde{x} - (x_g + d_x)]^2}{4D}\right) dx_g d\tilde{x} \\ &= \frac{2\pi D}{k} \left[\sqrt{\frac{k}{2\pi D}} (l_x + d_x) F\left((l_x + d_x) \sqrt{\frac{k}{2\pi D}}\right) + \sqrt{\frac{k}{2\pi D}} (l_x - d_x) F\left((l_x - d_x) \sqrt{\frac{k}{2\pi D}}\right) \right. \\ & \quad - 2d_x \sqrt{\frac{k}{2\pi D}} F\left((d_x) \sqrt{\frac{k}{2\pi D}}\right) - \frac{2i}{\pi} \exp\left(\frac{ik}{4D} (d_x)^2\right) \\ & \quad \left. + \frac{i}{\pi} \exp\left(\frac{ik}{4D} (l_x - d_x)^2\right) + \frac{i}{\pi} \exp\left(\frac{ik}{4D} (l_x + d_x)^2\right) \right]. \end{aligned} \quad (10.26)$$

Expanding the phase terms of the exponentials gives

$$\begin{aligned} & \frac{2i}{\pi} \exp\left(\frac{ik}{4D} (d_x)^2\right) + \frac{i}{\pi} \exp\left(\frac{ik}{4D} (l_x - d_x)^2\right) + \frac{i}{\pi} \exp\left(\frac{ik}{4D} (l_x + d_x)^2\right) \\ &= \frac{i}{\pi} \exp\left(\frac{ikd_x^2}{4D}\right) \left\{ -2 + \exp\left(\frac{ikl_x^2}{4D}\right) \left[\exp\left(\frac{ikl_x d_x}{2D}\right) + \exp\left(\frac{-ikl_x d_x}{2D}\right) \right] \right\} \\ &= \frac{2i}{\pi} \exp\left(\frac{ikd_x^2}{4D}\right) \left\{ \cos\left(\frac{kl_x d_x}{2D}\right) \exp\left(\frac{ikl_x^2}{4D}\right) - 1 \right\} \end{aligned} \quad (10.27)$$

and placing this result back into Eq. (10.26) we find

$$\begin{aligned} & \int_{-l_x/2}^{l_x/2} \int_{-l_x/2}^{l_x/2} \exp\left(ik \frac{[\tilde{x} - (x_g + d_x)]^2}{4D}\right) dx_g d\tilde{x} \\ &= \frac{2\pi D}{k} \left[\sqrt{\frac{k}{2\pi D}} (l_x + d_x) F\left((l_x + d_x) \sqrt{\frac{k}{2\pi D}}\right) + \sqrt{\frac{k}{2\pi D}} (l_x - d_x) F\left((l_x - d_x) \sqrt{\frac{k}{2\pi D}}\right) \right. \\ & \quad \left. - 2d_x \sqrt{\frac{k}{2\pi D}} F\left((d_x) \sqrt{\frac{k}{2\pi D}}\right) + \frac{2i}{\pi} \exp\left(\frac{ikd_x^2}{4D}\right) \left\{ \cos\left(\frac{kl_x d_x}{2D}\right) \exp\left(\frac{ikl_x^2}{4D}\right) - 1 \right\} \right]. \end{aligned} \quad (10.28)$$

In exactly the same fashion we can express the second double integral in Eq. (10.18) as

$$\begin{aligned}
 & \int_{-l_y/2}^{l_y/2} \int_{-l_y/2}^{l_y/2} \exp \left(ik \frac{[\tilde{y} - (y_g + d_y)]^2}{4D} \right) dy_g d\tilde{y} \\
 &= \frac{2\pi D}{k} \left[\sqrt{\frac{k}{2\pi D}} (l_y + d_y) F \left((l_y + d_y) \sqrt{\frac{k}{2\pi D}} \right) + \sqrt{\frac{k}{2\pi D}} (l_y - d_y) F \left((l_y - d_y) \sqrt{\frac{k}{2\pi D}} \right) \right. \\
 & \quad \left. - 2d_y \sqrt{\frac{k}{2\pi D}} F \left((d_y) \sqrt{\frac{k}{2\pi D}} \right) + \frac{2i}{\pi} \exp \left(\frac{ikd_y^2}{4D} \right) \left\{ \cos \left(\frac{kl_y d_y}{2D} \right) \exp \left(\frac{ikl_y^2}{4D} \right) - 1 \right\} \right] \quad (10.29)
 \end{aligned}$$

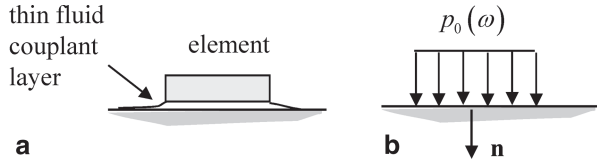
and the acoustic/elastic transfer function of Eq. (10.18) becomes, finally, an explicit expression in terms of Fresnel integrals and ordinary functions:

$$\begin{aligned}
 t_A(\omega) = R_{12} \frac{-2\pi i D \exp(2ikD)}{kl_x l_y} \\
 \left[\sqrt{\frac{k}{2\pi D}} (l_x + d_x) F \left((l_x + d_x) \sqrt{\frac{k}{2\pi D}} \right) + \sqrt{\frac{k}{2\pi D}} (l_x - d_x) F \left((l_x - d_x) \sqrt{\frac{k}{2\pi D}} \right) \right. \\
 \left. - 2d_x \sqrt{\frac{k}{2\pi D}} F \left((d_x) \sqrt{\frac{k}{2\pi D}} \right) + \frac{2i}{\pi} \exp \left(\frac{ikd_x^2}{4D} \right) \left\{ \cos \left(\frac{kl_x d_x}{2D} \right) \exp \left(\frac{ikl_x^2}{4D} \right) - 1 \right\} \right] \\
 \left[\sqrt{\frac{k}{2\pi D}} (l_y + d_y) F \left((l_y + d_y) \sqrt{\frac{k}{2\pi D}} \right) + \sqrt{\frac{k}{2\pi D}} (l_y - d_y) F \left((l_y - d_y) \sqrt{\frac{k}{2\pi D}} \right) \right. \\
 \left. - 2d_y \sqrt{\frac{k}{2\pi D}} F \left((d_y) \sqrt{\frac{k}{2\pi D}} \right) + \frac{2i}{\pi} \exp \left(\frac{ikd_y^2}{4D} \right) \left\{ \cos \left(\frac{kl_y d_y}{2D} \right) \exp \left(\frac{ikl_y^2}{4D} \right) - 1 \right\} \right]. \quad (10.30)
 \end{aligned}$$

Using Eq. (10.30) we can also obtain the results for a number of important special cases. For example, if we set $d_y = 0$ we can obtain the acoustic/elastic transfer function for a pair of elements in a linear array (where typically $l_y \gg l_x$).

$$\begin{aligned}
 t_A^{\text{linear}}(\omega) = R_{12} \frac{-2\pi i D \exp(2ikD)}{kl_x l_y} \\
 \left[\sqrt{\frac{k}{2\pi D}} (l_x + d_x) F \left((l_x + d_x) \sqrt{\frac{k}{2\pi D}} \right) + \sqrt{\frac{k}{2\pi D}} (l_x - d_x) F \left((l_x - d_x) \sqrt{\frac{k}{2\pi D}} \right) \right. \\
 \left. - 2d_x \sqrt{\frac{k}{2\pi D}} F \left((d_x) \sqrt{\frac{k}{2\pi D}} \right) + \frac{2i}{\pi} \exp \left(\frac{ikd_x^2}{4D} \right) \left\{ \cos \left(\frac{kl_x d_x}{2D} \right) \exp \left(\frac{ikl_x^2}{4D} \right) - 1 \right\} \right] \\
 \left[\sqrt{\frac{k}{2\pi D}} (2l_y) F \left((l_y) \sqrt{\frac{k}{2\pi D}} \right) + \frac{2i}{\pi} \left\{ \exp \left(\frac{ikl_y^2}{4D} \right) - 1 \right\} \right]. \quad (10.31)
 \end{aligned}$$

Fig. 10.3 **a** An array element in contact with an elastic solid, and **b** a model of this contact element as a constant pressure source



For a single element both sending and receiving (pulse-echo) we can set $d_x = d_y = 0$ and Eq. (10.30) reduces even further to:

$$t_A^{\text{pulse-echo}}(\omega) = R_{12} \frac{4}{i} \exp(2ikD) \left[F\left(\sqrt{\frac{kl_x^2}{2\pi D}}\right) + \frac{i}{\pi} \frac{1}{\sqrt{kl_x^2/2\pi D}} \left\{ \exp\left(\frac{ikl_x^2}{4D}\right) - 1 \right\} \right] \quad (10.32)$$

$$\left[F\left(\sqrt{\frac{kl_y^2}{2\pi D}}\right) + \frac{i}{\pi} \frac{1}{\sqrt{kl_y^2/2\pi D}} \left\{ \exp\left(\frac{ikl_y^2}{4D}\right) - 1 \right\} \right].$$

To obtain the acoustic/elastic transfer function for the contact case we must first treat the problem of an array element in contact with a solid surface (with a small fluid couplant layer between the array and the solid) as shown in Fig. 10.3a. As discussed in Chap. 6, we can model the element as a constant pressure source, $p_0(\omega)$, as shown in Fig. 10.3b acting over a rectangular area on the surface. Unlike the immersion case, this source generates a wide range of wave types in the solid, including bulk P- and S-waves, Head waves, and Rayleigh waves. However, if the distance to the reflecting surface (see Fig. 10.1b) is much larger than the separation distance between any pair of elements, then the P-wave interactions with the reflecting surface are the dominant waves and these waves travel at near normal incidence to the element. In this case, a high frequency approximation to the P-waves generated by the transmitting element at the location (x_l, y_l, D) of the reflecting surface can be expressed in the form of a Rayleigh/Sommerfeld integral (see Eq. 6.38) given by [Schmerr]

$$v_n(x_l, y_l, D, \omega) = \frac{-ikp_0(\omega)}{2\pi\rho_1 c_{p1}} \int_{S_l} \frac{\exp(ikr)}{r} d\tilde{x}d\tilde{y}, \quad (10.33)$$

where $k = \omega / c_{p1}$ is the wavenumber, v_n is the velocity in the solid in the direction \mathbf{n} normal to the face of the element, the distance $r = \sqrt{(x - x_l)^2 + (y - y_l)^2 + D^2}$ (same as in the immersion case) and (ρ_1, c_{p1}) are the density and compressional wave speed of the solid, respectively. We have set the directivity function $K_p(\theta) = 1$ in Eq. (6.38) in Eq. (10.33), because we are assuming all interactions of a sending element with the interface and then back to a receiving element occur at small angles relative to the normal, \mathbf{n} . In the paraxial approximation Eq. (10.33) becomes

$$v_n(x_l, y_l, D, \omega) = \frac{-ikp_0(\omega) \exp(ikD)}{2\pi\rho_1 c_{p1} D} \int_{S_l} \exp\left[ik \frac{(\tilde{x} - x_l)^2 + (\tilde{y} - y_l)^2}{2D}\right] d\tilde{x} d\tilde{y}. \quad (10.34)$$

Following exactly the same steps as in the immersion case we can find the incident velocity, $v_g(x_r, y_r, D, \omega)$ component of the reflected waves (acting in the $-\mathbf{n}$ direction) on the face of a receiving element as

$$v_g(x_r, y_r, D, \omega) = \frac{-ik}{2\pi\rho_1 c_{p1}} \int_{-\infty}^{+\infty} \int_{-\infty}^{+\infty} p_r(x_r, y_r, D, \omega) \frac{\exp(ikr')}{r'} dx_l dy_l \quad (10.35)$$

in terms of the reflected pressure

$$p_r(x_l, y_l, D, \omega) = R_{12} \rho_1 c_{p1} v_n(x_l, y_l, D, \omega) \quad (10.36)$$

which gives, in the paraxial approximation,

$$v_g(x_r, y_r, D, \omega) = \frac{-ikR_{12} \exp(ikD)}{2\pi D} \int_{-\infty}^{+\infty} \int_{-\infty}^{+\infty} \left[v_n(x_l, y_l, D, \omega) \exp\left(ik \frac{(x_r - x_l)^2 + (y_r - y_l)^2}{2D}\right) \right] dx_l dy_l. \quad (10.37)$$

Equation (10.37) can be expressed, as in the immersion case, in the form

$$v_g(x_g, y_g, D, \omega) = \frac{-ikR_{12} \exp(ikD)}{2\pi D} \int_{-\infty}^{+\infty} \int_{-\infty}^{+\infty} \left[v_n(x_l, y_l, D, \omega) \exp\left(ik \frac{(x_g + d_x - x_l)^2 + (y_g + d_y - y_l)^2}{2D}\right) \right] dx_l dy_l. \quad (10.38)$$

Placing Eq. (10.34) into (10.38) and computing the average velocity over the receiving element face:

$$\bar{v}_g(\omega) = \frac{1}{S_r} \int_{S_r} v_g(x_g, y_g, D, \omega) dx_g dy_g \quad (10.39)$$

we find

$$\bar{v}_g(\omega) = \frac{-ikR_{12} \exp(2ikD)}{2\pi D} \frac{-ikp_0(\omega)}{2\pi\rho_1 c_{p1} D} \frac{1}{S_r} \int_{S_r} \left[\int_{-\infty}^{+\infty} \int_{-\infty}^{+\infty} \left[\int_{S_l} \exp\left(ik \frac{(\tilde{x} - x_l)^2 + (\tilde{y} - y_l)^2}{2D}\right) \exp\left(ik \frac{(x_g + d_x - x_l)^2 + (y_g + d_y - y_l)^2}{2D}\right) d\tilde{x} d\tilde{y} \right] dx_l dy_l \right] dx_g dy_g. \quad (10.40)$$

We can take the free surface velocity, $v_{fs}(\omega)$, as just twice this average incident velocity, and note that for the contact case the acoustic/elastic transfer function, $t'_A(\omega)$, is defined as $t'_A(\omega) = \rho_1 c_{p1} S_B v_{fs}(\omega) / p_0(\omega) S_t$ so that this transfer function is

$$t'_A(\omega) = 2R_{12} \left[\frac{-ik \exp(ikD)}{2\pi D} \right]^2 \frac{1}{S_t} \int_{S_t} \left[\int_{-\infty}^{+\infty} \int_{-\infty}^{+\infty} \left[\int_{S_t} \left[\exp \left(ik \frac{(\tilde{x} - x_l)^2 + (\tilde{y} - y_l)^2}{2D} \right) \right. \right. \right. \\ \left. \left. \left. \exp \left(ik \frac{(x_g + d_x - x_l)^2 + (y_g + d_y - y_l)^2}{2D} \right) \right] d\tilde{x} d\tilde{y} \right] dx_l dy_l \right] dx_g dy_g. \quad (10.41)$$

If we compare Eq. (10.41) with Eq. (10.12) for the immersion case we see that they are identical forms so for this contact measurement configuration we can also use the immersion acoustic/elastic transfer functions.

When these acoustic/elastic transfer functions are used to determine the system function for a pair of elements from the measured voltage, $V_e(\omega)$, we have

$$\begin{aligned} V_e(\omega) &= s_i(\omega) t_A(\omega) \\ V_e(\omega) &= s_c(\omega) t'_A(\omega) = s_c(\omega) t_A(\omega) \end{aligned} \quad (10.42)$$

for the immersion and contact cases, respectively. Thus, we see that the system functions in both cases will have the same dimensions as $V_e(\omega)$, namely Volts/MHz or Volts- μ s. However, it is important to realize that in other contact and immersion setups $t'_A(\omega) \neq t_A(\omega)$ in general. Also, we should realize that in the setup of Fig. 10.2 being considered here, although the acoustic/elastic transfer functions are the same for both the immersion and contact case, when we measure the system function of the same array in both contact and immersion setups there will be differences in the measured voltage generated and we will find $s_c(\omega) \neq s_i(\omega)$ since the coupling of the sending and receiving elements to their adjacent media will be different in the two cases.

Note that the transfer functions derived here are for an “ideal” (loss-free) material. In any real material there will be ultrasonic attenuation of the waves present and if this attenuation is significant it must be included as part of the acoustic/elastic transfer function. If the attenuation is not too high then it is generally found that attenuation can be modeled as simply a multiplicative exponential term with a frequency dependent attenuation coefficient. For our calibration setups the acoustic/elastic transfer function with attenuation, t_A^{atten} , is then given in terms of the “ideal” transfer function, t_A^{ideal} , as

$$t_A^{\text{atten}}(\omega) = \exp[-2\alpha(\omega)D] t_A^{\text{ideal}}(\omega), \quad (10.43)$$

where $\alpha(\omega)$ is a measured frequency dependent attenuation coefficient, having dimensions of Nepers/unit length [Schmerr].

Table 10.1 Three linear arrays, each with N elements, a center frequency, f_c , a pitch, s_x , between elements and element lengths (l_x, l_y)

Serial number	Transducer type	N	f_c (MHz)	s_x (mm)	l_x (mm)	l_y (mm)
5L16-A1	Contact	16	5	0.60	0.55	10
10L32-A1	Contact	32	10	0.31	0.26	7
5L32E32-10	Immersion	32	5	1.0	0.8	10

10.2 Array Element System Functions

The calibration setups shown in Fig. 10.1 are simple to implement with immersion and contact arrays, but the number of system function measurements needed to fully characterize an array can be very large, since for every element pair (i, j) characterizing the i th and j th elements we need to measure a voltage, $V_{ij}(\omega)$, and relate it to a system function, $s_{ij}(\omega)$, and an acoustic/elastic transfer function, $t_{ij}(\omega)$, i.e.

$$V_{ij}(\omega) = s_{ij}(\omega)t_{ij}(\omega). \quad (10.44)$$

Then the system function can be obtained by deconvolution, i.e.

$$s_{ij}(\omega) = \frac{V_{ij}(\omega)}{t_{ij}(\omega)}. \quad (10.45)$$

However, convolution by direct division in this manner is severely contaminated by noise present outside the bandwidth of the measurement system so that the deconvolution is performed in practice with a Wiener filter, i.e.

$$s_{ij}(\omega) = V_{ij}(\omega)t_{ij}^*(\omega) / \left[|t_{ij}(\omega)|^2 + \varepsilon^2 \max\{|t_{ij}(\omega)|^2\} \right], \quad (10.46)$$

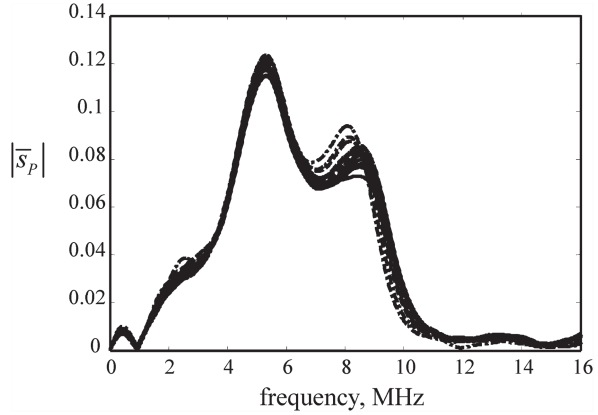
where ε is a small noise constant, and the $(\)^*$ represents the complex conjugate.

Even if the system function for the various element pairs are assumed to be symmetric ($s_{ij} = s_{ji}$) for N elements in an array there are still a total of $N(N+1)/2$ measurements needed to characterize all the possible element pairs. For a 32 element array, for example, a total of 528 measurements would be needed. Fortunately, a recent study of three commercial linear arrays [1] found little variation in these system functions. The three linear arrays (two contact and one immersion) listed in Table 10.1 were exhaustively tested to obtain all the system function pairs.

Representative data was shown in [1] for the first array listed in Table 10.1, as measured in a contact test setup with the array reflecting off the back face of a large aluminum block. To summarize the large number of results in an efficient manner, an average system function, $\bar{s}_p(\omega)$, was calculated over all element pairs with the same separation distance, i.e.

$$\bar{s}_p(\omega) = \frac{1}{N-P} \sum_{i=1}^{N-P} s_{ii+P}(\omega) \quad (P = 0, 1, 2, \dots, N-1), \quad (10.47)$$

Fig. 10.4 The magnitude of the average system function, $|\bar{s}_P|$, measured in volts- μ s, for two elements with P elements ($P=0, 1, \dots, 15$) between the sending and receiving element for the 16 element array of Table 10.1



where P is the number of elements between the transmitting and receiving elements. Thus for the 16 element transducer of Table 10.1, the data was reduced to only 16 average system functions. Figure 10.4 shows these average system functions with separation distances, in multiples of the pitch, s_x , between elements varying from $0 \cdot s_x$ ($P=0$) to $15 \cdot s_x$ ($P=15$), where $0 \cdot s_x$ represents pulse-echo cases (same element firing and receiving) and all the other separations are pitch-catch cases. It can be seen from Fig. 10.4 that the average system functions of various pairs were very similar to each other both in amplitude and shape, with generally less than seven percent overall variation, making it difficult to see all the curves present in Fig. 10.4. Similar consistency of all the system functions was found for the other two arrays shown in Table 10.1. This suggests that it may be adequate to determine just a single system function for the entire array that can be obtained with a single calibration measurement. However, since making phased arrays is still somewhat of an art, it is wise to conduct at least a partial characterization of all the system functions with the approach outlined here to ensure that the variations of the measured system functions are indeed small.

Going back to Eq. (10.1) and summing the received voltages for all sending/receiving element pairs, the total received voltage, $V_R(\omega)$, is given by

$$V_R(\omega) = \sum_{m=1}^{m=M} \sum_{n=1}^{n=N} s_{mn}(\omega) t_A^{mn}(\omega) \exp(i\omega\Delta t_m) \exp(i\omega\Delta t_n), \quad (10.48)$$

where we have also included the possibility of implementing time delay laws ($\Delta t_m, \Delta t_n$) on the sending and receiving elements in the calibration setups of Fig. 10.1. If all the system functions are nearly identical then we have

$$V_R(\omega) = s(\omega) t_\Sigma(\omega), \quad (10.49)$$

where

Fig. 10.5 The magnitude of a single system function, measured in volts- μ s, obtained with a linear phased array inspection system for various number of active elements—16 (*solid line*), 8 (*dotted line*), and 4 (*dashed line*)

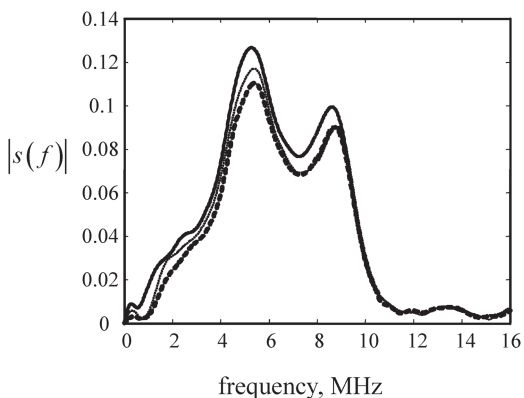
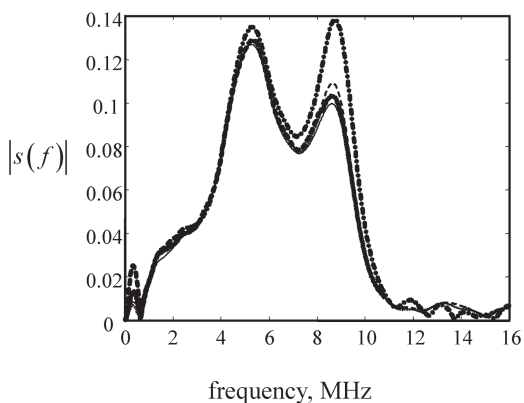


Fig. 10.6 A single system function obtained for a linear phased array inspection system for various focal lengths: 50.8 mm (*solid line*), 40 mm (*dotted line*), 30 mm (*dashed line*), and 20 mm (*dashed-dotted line*) (all 16 elements were used in these cases)



$$t_{\Sigma}(\omega) = \sum_{m=1}^M \sum_{n=1}^N t_A^{mn}(\omega) \exp(i\omega\Delta t_m) \exp(i\omega\Delta t_n) \quad (10.50)$$

and we can find this single system function by deconvolution with a Wiener filter, i.e.

$$s(\omega) = \frac{V_R(\omega) [t_{\Sigma}(\omega)]^*}{|t_{\Sigma}(\omega)|^2 + \varepsilon^2 \max\{|t_{\Sigma}(\omega)|^2\}}. \quad (10.51)$$

Figure 10.5 shows a single system function obtained in this fashion for the 16 element contact array of Table 10.1 placed on a two inch thick aluminum block. The three curves shown in Fig. 10.5 correspond to setups where the system function was obtained with all 16 elements firing/receiving, eight elements firing/receiving, and four elements firing/receiving. Time delay laws were implemented on sending and receiving to focus the array at the back surface of the aluminum block. It can be seen that again there is considerable consistency between the single system functions obtained in this manner.

The magnitude of a single system function, if it is representative of all the element pair system functions, should not depend on any time delay laws used in its determination. Figure 10.6 shows the same contact setup with the 16 element array of Table 10.1 where time delay laws were varied to attempt to focus the send/receive signals at focal depths of 50.8, 40, 30, and 20 mm with all elements of the array sending and receiving [note that all of these focal lengths except the 20 mm case were greater than one near field distance where true focusing is not possible. However, by including a focal law one can help reduce beam spread somewhat in these cases and make the use of the paraxial approximation more appropriate]. It can be seen from Fig. 10.6 that all the system functions were nearly identical except for the 20 mm focusing case. The differences seen in the 20 mm focusing case are likely due to errors in using the acoustic/elastic transfer functions derived here since those functions were obtained under the paraxial approximation, which is violated under such tight focusing conditions.

Reference

1. R. Huang, L.W. Schmerr, Characterization of the system functions of ultrasonic linear phased array inspection systems. *Ultrasonics* **49**, 219–225 (2009)

Chapter 11

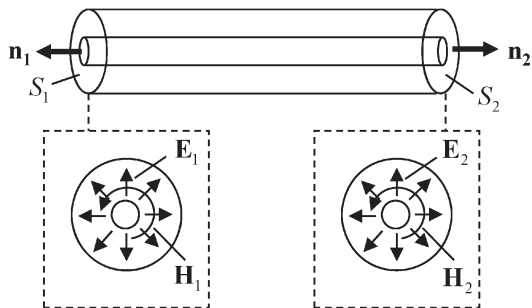
Measurement Models for Ultrasonic Arrays

In the previous two chapters we showed how the response of a pair of send-receive array elements can be modeled in terms of two components: (1) a system function that describes all the electrical and electromechanical parts of the elements and their driving/receiving sub-systems, and (2) an acoustic/elastic transfer function that describes all the acoustic and elastic wave propagation and scattering fields present between the sending/receiving elements. As seen in Chap. 10, the system functions can be measured directly in a calibration experiment where the acoustic/elastic transfer functions are known. If the same array elements and settings for the phased array instrument that are used in the calibration experiment are present when the array is used in an ultrasonic flaw measurement then the system functions remain unchanged. This is also true if the elements are part of separate sending and receiving arrays. Thus, if the acoustic/elastic transfer functions in the flaw measurement can also be expressed in terms of fields that can be modeled then one can determine the voltage signals received from the flaw from every element pair in the array(s).

Using general reciprocity relations, an explicit expression will be obtained in this chapter for the acoustic/elastic transfer function of a pair of sending and receiving elements in terms of the fields present in a flaw measurement. Multiplying this transfer function by the appropriate system function gives the measured voltage, as described in the previous chapters. This model of the received voltage is a complete *ultrasonic measurement model* for an arbitrary pair of array elements in a form similar to that developed by Auld [1]. Combining these measurement models for a collection of sending and receiving elements in a flaw measurement then gives us the corresponding measurement models for a complete phased array measurement system.

We will also develop a reduced form of measurement model of the Thompson–Gray type [2] where one assumes the flaw is small enough so that the incident fields from the array elements do not vary significantly over the flaw surface. The Thompson–Gray measurement model is less general than the Auld form of the measurement model but because the flaw response is contained in a Thompson–Gray measurement model explicitly in terms of the far field scattering amplitude of the flaw it is particularly useful for flaw characterization and sizing, probability of detection (POD) studies, and many other flaw-centered NDE applications.

Fig. 11.1 A “fields” parameter model of a coaxial cable showing the electrical and magnetic fields at the cable ends



Ultrasonic phased arrays, because of their ability to manipulate their ultrasonic wave fields, are inherently useful for generating images of flaws. Those images can be formed based on ad hoc methods or on more quantitative methods that relate the images directly to physical properties of the flaw being imaged. In this Chapter we will also develop approximate forms for both an Auld type measurement model and a Thompson–Gray model that are the bases for the generation of quantitative flaw images, as will be discussed in the following Chapters.

Finally, we will describe measurement models of both the Auld type and the Thompson–Gray type for 1-D arrays radiating into a fluid in two dimensions. These 1-D measurement models will, as done earlier for ultrasonic beam models, allow us to discuss phased array measurement systems and imaging principles in a much simpler context.

11.1 Reciprocity Relations

Reciprocity principles play a fundamental role in wave propagation studies [3, 4] and in modeling ultrasonic measurement systems [Schmerr–Song]. For example, these principles can be used when modeling how the electromagnetic fields in a cable behave (see Fig. 11.1). The electrical and magnetic fields at both ends of a cable can be shown to satisfy the reciprocity relationship

$$\begin{aligned} & \int_{S_1} (\mathbf{E}_1^{(2)} \times \mathbf{H}_1^{(1)} - \mathbf{E}_1^{(1)} \times \mathbf{H}_1^{(2)}) \cdot \mathbf{n}_1 dS \\ &= \int_{S_2} (\mathbf{E}_2^{(2)} \times \mathbf{H}_2^{(1)} - \mathbf{E}_2^{(1)} \times \mathbf{H}_2^{(2)}) \cdot \mathbf{n}_2 dS, \end{aligned} \quad (11.1)$$

where $(\mathbf{E}_1, \mathbf{H}_1)$ are the electrical and magnetic fields at one end of the cable and $(\mathbf{E}_2, \mathbf{H}_2)$ are the electrical and magnetic fields at the other end (Fig. 11.1). The unit vectors $(\mathbf{n}_1, \mathbf{n}_2)$ are the outward unit normals at the ends, as shown in Fig. 11.1, and (S_1, S_2) are the cross-sectional areas of the cables at their ends over which the

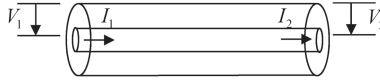


Fig. 11.2 A “lumped” parameter model of a coaxial cable showing the voltage and current at the cable ends

field values in Eq. (11.1) are calculated. The superscripts (1) and (2) on these fields denote two different driving/termination conditions under which these fields are measured.

Instead of using the field values explicitly in a reciprocity relationship, one can also use “lumped parameters.” For the cable, for example, we can express the voltages and currents produced by these underlying fields in a similar reciprocity relationship given as (see Fig. 11.2)

$$V_1^{(1)} I_1^{(2)} - V_1^{(2)} I_1^{(1)} = V_2^{(1)} I_2^{(2)} - V_2^{(2)} I_2^{(1)}, \quad (11.2)$$

where (V_1, I_1) and (V_2, I_2) are the voltages and currents at the cable ends, and (1) and (2) again denote two different “states” under which these lumped parameters are measured.

Reciprocity relations can also be developed that mix lumped parameters and field parameters. For example, in describing the inputs and outputs of a sending array element in an immersion test one can use lumped parameters of voltage and current (V, I) on the electrical driving side of the element and acoustic pressure and vector velocity fields $(p(\mathbf{x}, \omega), \mathbf{v}(\mathbf{x}, \omega))$ over the output face of the element to express the reciprocal theorem for an array element in the form

$$V^{(1)} I^{(2)} - V^{(2)} I^{(1)} = - \int_S (p^{(2)}(\mathbf{x}, \omega) \mathbf{v}^{(1)}(\mathbf{x}, \omega) - p^{(1)}(\mathbf{x}, \omega) \mathbf{v}^{(2)}(\mathbf{x}, \omega)) \cdot \mathbf{n} dS(\mathbf{x}), \quad (11.3)$$

where states (1) and (2) again are two different driving and termination conditions for the array element and \mathbf{n} is the unit outward normal to the element surface (Fig. 11.3a). Alternatively, reciprocity for the element could be expressed completely in terms of lumped parameters. If we assume the element in this immersion test acts a “piston”, for example, then $\mathbf{v}(\mathbf{x}, \omega) \cdot \mathbf{n} = v(\omega)$ and Eq. (11.3) reduces to

$$V^{(1)} I^{(2)} - V^{(2)} I^{(1)} = F^{(1)} v^{(2)} - F^{(2)} v^{(1)}, \quad (11.4)$$

where $F(\omega)$ is the force produced by the integral of the pressure over the face of the element and $v(\omega)$ is the (uniform) normal velocity (Fig. 11.3b).

In considering the acoustic and elastic wave fields between the sending and receiving array elements in a flaw measurement (see Fig. 11.4), it is possible to also derive a reciprocity relation that connects the fields on the flaw surface to the force and velocity on the face of the receiving element. The details of how this reciprocity relationship is obtained have been presented elsewhere [Schmerr–Song] so we will only state the reciprocity relationship here. It is

Fig. 11.3 **a** A “mixed” model of an array element with lumped parameters of voltage and current defining the inputs and pressure and velocity fields at the output face of the element, and **b** a model of an array element with voltage and currents at the input and compressive force and normal velocity at the output

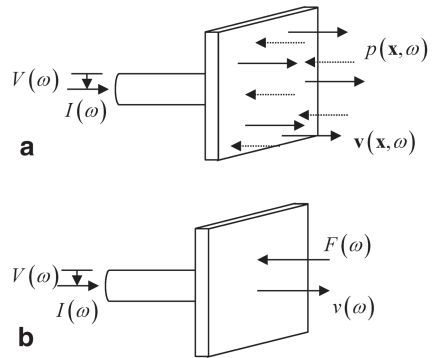
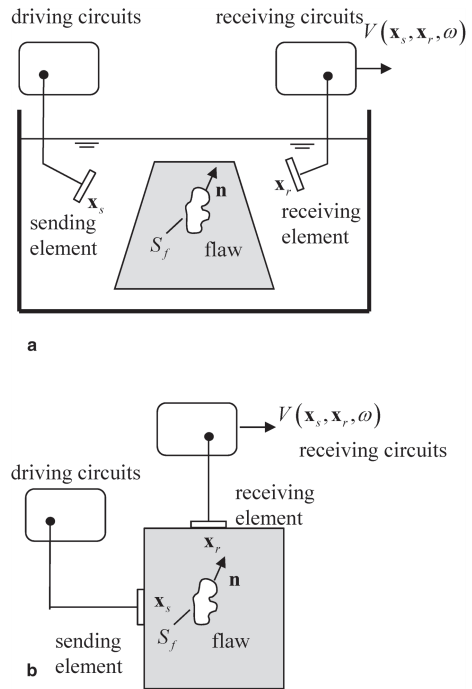


Fig. 11.4 **a** An immersion flaw inspection with a pair of sending and receiving array elements, and **b** a corresponding contact flaws inspection with sending and receiving elements



$$\left(F_R^f v_R^{(2)} - F_R^{(2)} v_R^f \right) = \int_{S_f} \left(\tau_{ji}^{(1)}(\mathbf{x}, \omega) v_i^{(2)}(\mathbf{x}, \omega) - \tau_{ji}^{(2)}(\mathbf{x}, \omega) v_i^{(1)}(\mathbf{x}, \omega) \right) n_j(\mathbf{x}) dS(\mathbf{x}). \quad (11.5)$$

Here states (1) and (2) are two specific states. State (1) is the actual flaw measurement setup where the flaw is present while state (2) is where the receiving element acts as a transmitter instead of a receiver, and the flaw is absent. The parameters (F_R^f, v_R^f) are the force and normal velocity on the receiving element produced by

the waves scattered from the flaw in state (1) while $(F_R^{(2)}, v_R^{(2)})$ are the force and normal velocity on the face of the receiving element when it acts as a transmitter in state (2). The fields $(\tau_{ij}(\mathbf{x}, \omega), v_j(\mathbf{x}, \omega))$ are the stresses and velocity components on the surface, S_f , of the flaw, whose outward unit normal components are $n_j(\mathbf{x})$ (see Fig. 11.4a, b). This reciprocity relationship can also be written in the alternate form

$$(F_R^f v_R^{(2)} - F_R^{(2)} v_R^f) = \int_{S_f} (\mathbf{t}^{(1)}(\mathbf{x}, \omega) \cdot \mathbf{v}^{(2)}(\mathbf{x}, \omega) - \mathbf{t}^{(2)}(\mathbf{x}, \omega) \cdot \mathbf{v}^{(1)}(\mathbf{x}, \omega)) dS(\mathbf{x}), \quad (11.6)$$

where $t_i^{(m)} = \tau_{ji}^{(m)} n_j$ ($m = 1, 2$) are the components of the traction vector, $\mathbf{t}^{(m)}$, acting on the surface of the flaw.

Although Eqs. (11.5) and (11.6) were derived in [Schmerr–Song] explicitly for the immersion case, both of these equations are applicable to either the immersion or contact testing setups shown in Fig. 11.4. This can be seen by writing these reciprocity relations entirely in terms of the underlying fields on the face of the receiving element. Equation (11.5), for example, then becomes

$$\begin{aligned} & \int_S (p^f(\mathbf{x}, \omega) \mathbf{v}^{(2)}(\mathbf{x}, \omega) - p^{(2)}(\mathbf{x}, \omega) \mathbf{v}^f(\mathbf{x}, \omega)) \cdot \mathbf{n} dS(\mathbf{x}) \\ &= \int_{S_f} (\tau_{ji}^{(1)}(\mathbf{x}, \omega) v_i^{(2)}(\mathbf{x}, \omega) - \tau_{ji}^{(2)}(\mathbf{x}, \omega) v_i^{(1)}(\mathbf{x}, \omega)) n_j(\mathbf{x}) dS(\mathbf{x}) \end{aligned} \quad (11.7)$$

which is true for both the contact and immersion cases since in the immersion case the stress fields at the acoustic port of the element are purely pressure fields and in the contact case there is a fluid couplant between the element and the adjacent solid so again there is only a pressure on the surface of the element. Here $(p^f(\mathbf{x}, \omega), \mathbf{v}^f(\mathbf{x}, \omega))$ are the pressure and velocity fields on the receiving element due to waves scattered from the flaw. But in the contact case, if we assume this pressure is uniform in both states, i.e. $p^f(\mathbf{x}, \omega) = p^f(\omega)$ and $p^{(2)}(\mathbf{x}, \omega) = p^{(2)}(\omega)$, then the forces on the receiving element face are just $F_R^f(\omega) = p^f(\omega) S_r$ and $F_R^{(2)}(\omega) = p^{(2)}(\omega) S_r$. Then, if we define the average normal velocities on the face of the receiving element in either state as

$$\begin{aligned} v_R^f(\omega) &= \frac{1}{S_r} \int_{S_r} \mathbf{v}^f(\mathbf{x}, \omega) \cdot \mathbf{n} dS(\mathbf{x}) \\ v_R^{(2)}(\omega) &= \frac{1}{S_r} \int_{S_r} \mathbf{v}^{(2)}(\mathbf{x}, \omega) \cdot \mathbf{n} dS(\mathbf{x}). \end{aligned} \quad (11.8)$$

Equation (11.7) again reduces to Eq. (11.5).

11.2 An Ultrasonic Measurement Model for Immersion Setups

Consider an immersion flaw measurement setup. In state (2) where the receiving element B is acting as a transmitter, the force $F_R^{(2)}$ and normal velocity $v_R^{(2)}$ are related through the acoustic radiation impedance, $Z_r^{B;a}$, of the receiving element, i.e.

$$F_R^{(2)}(\omega) = Z_r^{B;a}(\omega)v_R^{(2)}(\omega). \quad (11.9)$$

Placing Eq. (11.9) into Eq. (11.5) then gives

$$\left(F_R^f - Z_r^{B;a}v_R^f\right)v_R^{(2)} = \int_{S_f} \left(\tau_{ji}^{(1)}(\mathbf{x}, \omega)v_i^{(2)}(\mathbf{x}, \omega) - \tau_{ji}^{(2)}(\mathbf{x}, \omega)v_i^{(1)}(\mathbf{x}, \omega)\right)n_j(\mathbf{x})dS(\mathbf{x}). \quad (11.10)$$

But the quantity in parentheses on the left side of Eq. (11.10) is just the blocked force, $F_B(\omega)$, generated on the receiving element by the flaw fields (see Eq. (9.10), with $v = -v_R^f$ since v in that equation is directed inward to the element face) so that

$$F_B(\omega) = \frac{1}{v_R^{(2)}(\omega)} \int_{S_f} \left(\tau_{ji}^{(1)}(\mathbf{x}, \omega)v_i^{(2)}(\mathbf{x}, \omega) - \tau_{ji}^{(2)}(\mathbf{x}, \omega)v_i^{(1)}(\mathbf{x}, \omega)\right)n_j(\mathbf{x})dS(\mathbf{x}). \quad (11.11)$$

Dividing this result by $\rho_1 c_{p1} S_A v_T^{(1)}(\omega)$, where (ρ_1, c_{p1}) are the density and wave speed at the sending element A , which has an area, S_A , and a uniform velocity, $v_T^{(1)}(\omega)$, over that area in state (1), we find an expression for the acoustic/elastic transfer function (see Eq. (9.24)), namely

$$t_A(\omega) = \frac{1}{\rho_1 c_{p1} S_A v_T^{(1)}(\omega) v_R^{(2)}(\omega)} \int_{S_f} \left(\tau_{ji}^{(1)}(\mathbf{x}, \omega)v_i^{(2)}(\mathbf{x}, \omega) - \tau_{ji}^{(2)}(\mathbf{x}, \omega)v_i^{(1)}(\mathbf{x}, \omega)\right)n_j(\mathbf{x})dS(\mathbf{x}). \quad (11.12)$$

Since the received voltage, $V(\mathbf{x}_s, \mathbf{x}_r, \omega)$, for a sending element located at \mathbf{x}_s and a receiving element located at \mathbf{x}_r (see Fig. 11.4) is just proportional to this transfer function through the system function, $s_f(\omega)$, for the pair of sending and receiving elements present, we have

$$V(\mathbf{x}_s, \mathbf{x}_r, \omega) = s_f(\omega) \frac{1}{\rho_1 c_{p1} S_A v_T^{(1)}(\omega) v_R^{(2)}(\omega)} \cdot \int_{S_f} \left(\tau_{ji}^{(1)}(\mathbf{x}, \omega)v_i^{(2)}(\mathbf{x}, \omega) - \tau_{ji}^{(2)}(\mathbf{x}, \omega)v_i^{(1)}(\mathbf{x}, \omega)\right)n_j(\mathbf{x})dS(\mathbf{x}). \quad (11.13)$$

Equation (11.13) is an ultrasonic measurement model for an arbitrary pair of elements in an immersion flaw inspection (Fig. 11.4a). It predicts the frequency

spectrum of the measured voltage in terms of the system function, which can be measured in a calibration setup as shown in Chap. 10, and the fields on the surface of the flaw in states (1) and (2). These fields are normalized by driving velocities on the faces of the sending and receiving elements in states (1) and (2) respectively, so that one only needs to calculate the fields in Eq. (11.13) for cases where the driving velocity is unity on the faces of these elements. If appropriate ultrasonic beam models and flaw scattering models are available, these normalized fields can be directly calculated and one does not need to know the actual velocities on these element faces for the models involved.

11.3 An Ultrasonic Measurement Model for Contact Setups

One can again start with Eq. (11.10) since the force and average velocity lumped parameters are again related through the acoustic radiation impedance (Eq. 11.9 for state (2)). However, we can rewrite Eq. (11.10) as

$$\left(\frac{F_R^f}{Z_r^{B;a}} - v_R^f \right) F_R^{(2)} = \int_{S_f} \left(\tau_{ji}^{(1)}(\mathbf{x}, \omega) v_i^{(2)}(\mathbf{x}, \omega) - \tau_{ji}^{(2)}(\mathbf{x}, \omega) v_i^{(1)}(\mathbf{x}, \omega) \right) n_j(\mathbf{x}) dS(\mathbf{x}). \quad (11.14)$$

In the contact case, we can recognize the term in parentheses on the left side of Eq. (11.14) as the free surface velocity (see Eq. (9.11) with $v = -v_R^f$ again since v is directed inward to the transducer face) so we have

$$v_{fs} = \frac{1}{F_R^{(2)}} \int_{S_f} \left(\tau_{ji}^{(1)}(\mathbf{x}, \omega) v_i^{(2)}(\mathbf{x}, \omega) - \tau_{ji}^{(2)}(\mathbf{x}, \omega) v_i^{(1)}(\mathbf{x}, \omega) \right) n_j(\mathbf{x}) dS(\mathbf{x}). \quad (11.15)$$

In Chap. 10 we saw that a system function having the same dimensions as the measured voltage, could be obtained by using a non-dimensional transfer function in the contact case defined as $t'_A = \rho c_p S_B v_{fs} / F_T^{(1)}$ where $F_T^{(1)}$ is the compressive force exerted on the face of the driving element in state (1) and (ρ, c_p) are the density and compressional wave speed of the solid adjacent to the receiving element whose area is S_B . From Eq. (11.15) then we have

$$t'_A(\omega) = \frac{\rho c_p S_B}{F_T^{(1)} F_R^{(2)}} \int_{S_f} \left(\tau_{ji}^{(1)}(\mathbf{x}, \omega) v_i^{(2)}(\mathbf{x}, \omega) - \tau_{ji}^{(2)}(\mathbf{x}, \omega) v_i^{(1)}(\mathbf{x}, \omega) \right) n_j(\mathbf{x}) dS(\mathbf{x}). \quad (11.16)$$

and a complete measurement model for the received voltage for the contact case (Fig. 11.4b) is

$$V(\mathbf{x}_s, \mathbf{x}_r, \omega) = s_c(\omega) \frac{\rho c_p S_B}{F_T^{(1)} F_R^{(2)}} \int_{S_f} \left(\tau_{ji}^{(1)}(\mathbf{x}, \omega) v_i^{(2)}(\mathbf{x}, \omega) - \tau_{ji}^{(2)}(\mathbf{x}, \omega) v_i^{(1)}(\mathbf{x}, \omega) \right) n_j(\mathbf{x}) dS(\mathbf{x}). \quad (11.17)$$

In Eq. (11.17) we see the fields on the surface of the flaw are normalized by the forces on the faces of driving elements in states (1) and (2). Thus, as in the immersion case, we do not need to know the actual driving forces (or underlying pressures) in the contact case to model these wave fields.

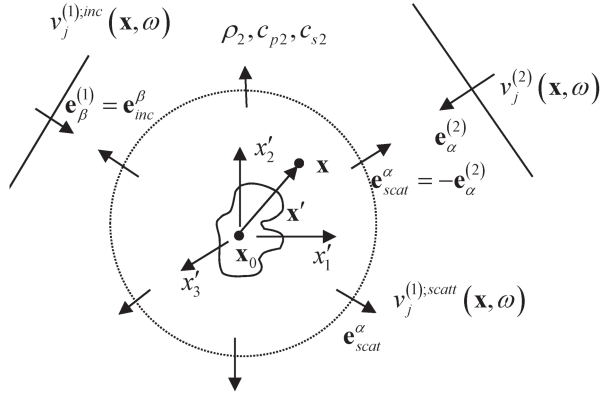
Measurement models similar to those given by Eqs. (11.13) and (11.17) were originally obtained by Auld [1] using general electromechanical reciprocity conditions. Because such measurement models are based primarily on assumptions of linearity and reciprocity they are applicable to almost all NDE inspections. Since Auld's seminal paper there have been numerous applications where these measurement models have been coupled with ultrasonic beam models and flaw scattering models to simulate the signals seen in NDE inspections. Many of these applications have been described in the Proceedings of the Review of Progress in Quantitative NDE meetings [5]. To date, measurement models have been mostly used to simulate inspections with large single element transducers but as we have seen here they are also applicable to any arbitrary pair of sending and receiving elements. By simply considering the ensemble of all pairs of sending/receiving element responses and by incorporating the appropriate time delay laws and/or apodization laws these measurement models are also applicable to virtually any ultrasonic inspection using one or more arrays.

11.4 A Reduced Measurement Model for Small Flaws

Although the measurement models of the Auld type discussed in the previous sections have the advantage of being very general, the flaw response is contained in those models only through the fields on the flaw surface, making it difficult to connect the measured voltage response with any specific flaw characteristic or flaw parameter. Since the purpose of most ultrasonic NDE flaw inspections is to make that connection and predict flaw properties from the measured signals, it would be useful to be able to have a measurement model that contains the flaw response in a more explicit fashion. Fortunately, this is possible with a relatively few additional assumptions. The details have been given elsewhere, [Schmerr], [Schmerr-Song], so here we will briefly outline the steps.

The basic assumptions we will make are (1) that the waves incident on the flaw in states (1) and (2) can be treated as quasi-plane waves, and (2) that the flaw is small enough so that the amplitude of these waves does not vary significantly over the flaw surface, so we can take the amplitude of these waves as evaluated at a fixed point, \mathbf{x}_0 , (see Fig. 11.5) which is usually taken to be the center of the flaw for simple

Fig. 11.5 The waves incident on a flaw from states (1) and (2) treated as quasi-plane waves



flaw shapes. Consider first the case of immersion testing where the waves are generated in states (1) and (2) by elements having uniform velocities ($v_T^{(1)}(\omega)$, $v_R^{(2)}(\omega)$) on their faces. The velocity components of the incident quasi-plane waves in states (1) and (2) on the flaw can be written as

$$\begin{aligned} v_j^{(1);inc}(\mathbf{x}, \omega) &= v_T^{(1)}(\omega) \hat{V}^{(1)}(\mathbf{x}_s, \mathbf{x}_0, \omega) d_{\beta j}^{(1)} \exp[ik_{\beta 2} \mathbf{e}_\beta^{(1)} \cdot (\mathbf{x} - \mathbf{x}_0)] \\ v_j^{(2)}(\mathbf{x}, \omega) &= v_R^{(2)}(\omega) \hat{V}^{(2)}(\mathbf{x}_r, \mathbf{x}_0, \omega) d_{\alpha j}^{(2)} \exp[ik_{\alpha 2} \mathbf{e}_\alpha^{(2)} \cdot (\mathbf{x} - \mathbf{x}_0)], \end{aligned} \quad (11.18)$$

where $(\mathbf{d}_\beta^{(1)}, \mathbf{d}_\alpha^{(2)})$ are the unit vector polarizations of the incident waves in states (1) and (2), which are traveling in the direction of the unit vectors $(\mathbf{e}_\beta^{(1)}, \mathbf{e}_\alpha^{(2)})$ and $k_{\beta 2} = \omega / c_{\beta 2}$, $k_{\alpha 2} = \omega / c_{\alpha 2}$ are the wave numbers of the incident waves, which can be of type β ($\beta = p, s$) for state (1) and type α ($\alpha = p, s$) for state (2) corresponding to either P-waves or S-waves where (ρ_2, c_{p2}, c_{s2}) are the density, compressional wave speed, and shear wave speed, respectively, for the medium surrounding the flaw. In Eq. (11.18) we will let (x'_1, x'_2, x'_3) be the coordinates of the position vector $\mathbf{x}' = \mathbf{x} - \mathbf{x}_0$ as measured with respect to the fixed point, \mathbf{x}_0 , as shown in Fig. 11.5. Note that the total velocity at the flaw in state (1) is given by the sum of the incident and scattered waves, i.e. $\mathbf{v}^{(1)} = \mathbf{v}^{(1);inc} + \mathbf{v}^{(1);scatt}$ (see Fig. 11.5), so we need to identify the waves in Eq. (11.18) as only those incident waves. In state (2) no flaw is present so the total velocity fields are just the incident fields of Eq. (11.18). Also, in state (2), the stresses, $\tau_{ij}^{(2)}$, can be calculated since

$$\begin{aligned} \tau_{ij}^{(2)} &= C_{ijkl} \frac{1}{-i\omega} \frac{\partial v_k^{(2)}}{\partial x'_l} \\ &= -C_{ijkl} \frac{e_{\alpha l}^{(2)}}{c_{\alpha 2}} v_k^{(2)}, \end{aligned} \quad (11.19)$$

where C_{ijkl} is the tensor of elastic constants [Schmerr]. Placing Eqs. (11.18) and (11.19) into the measurement model of Eq. (11.13) gives

$$\begin{aligned}
 V(\mathbf{x}_s, \mathbf{x}_r, \omega) = & s_I(\omega) \frac{\hat{V}^{(2)}(\mathbf{x}_r, \mathbf{x}_0, \omega)}{\rho_1 c_{p1} S_A v_T^{(1)}(\omega)} \\
 & \cdot \int_{S_f} \left(\tau_{ji}^{(1)}(\mathbf{x}, \omega) d_{ai}^{(2)}(\mathbf{x}, \omega) + C_{ijkl} \frac{e_{al}^{(2)}}{c_{a2}} d_{ak}^{(2)} v_i^{(1)}(\mathbf{x}, \omega) \right) \\
 & \cdot n_j(\mathbf{x}) \exp(ik_{a2} \mathbf{e}_\alpha^{(2)} \cdot \mathbf{x}') dS(\mathbf{x}')
 \end{aligned} \quad (11.20)$$

If we now normalize the stresses and velocity components in state (1) by the displacement amplitude, $v_T^{(1)} \hat{V}^{(1)} / (-i\omega)$, of the incident wave in that state, we can define these normalized fields as

$$\begin{aligned}
 \bar{\tau}_{ij}^{(1)} &= \frac{-i\omega \tau_{ij}^{(1)}}{v_T^{(1)} \hat{V}^{(1)}} \\
 \bar{v}_j^{(1)} &= \frac{-i\omega v_j^{(1)}}{v_T^{(1)} \hat{V}^{(1)}}.
 \end{aligned} \quad (11.21)$$

Then Eq. (11.20) can be rewritten as

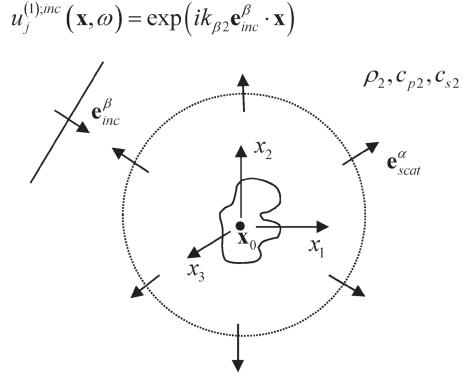
$$\begin{aligned}
 V(\mathbf{x}_s, \mathbf{x}_r, \omega) = & s_I(\omega) \frac{\hat{V}^{(1)}(\mathbf{x}_s, \mathbf{x}_0, \omega) \hat{V}^{(2)}(\mathbf{x}_r, \mathbf{x}_0, \omega)}{-i\omega \rho_1 c_{p1} S_A} \\
 & \cdot \int_{S_f} \left(\bar{\tau}_{ji}^{(1)}(\mathbf{x}, \omega) d_{ai}^{(2)}(\mathbf{x}, \omega) + C_{ijkl} \frac{e_l^{(2)}}{c_{a2}} d_{ak}^{(2)} \bar{v}_i^{(1)}(\mathbf{x}, \omega) \right) \\
 & \cdot n_j(\mathbf{x}) \exp[ik_{a2} \mathbf{e}_\alpha^{(2)} \cdot \mathbf{x}'] dS(\mathbf{x}')
 \end{aligned} \quad (11.22)$$

Equation (11.22) contains the flaw response in an explicit form. This can be seen by considering the canonical problem of a flaw in an infinite medium acted upon by a incident plane wave of type β ($\beta = P, S$) traveling in the $\mathbf{e}_\beta^{(1)} \equiv \mathbf{e}_{inc}^\beta$ direction and having a *unit displacement amplitude*, as shown in Fig. 11.6. In the far-field of the flaw a scattered wave of type α ($\alpha = P, S$) traveling in the $\mathbf{e}_{scat}^\alpha \equiv -\mathbf{e}_\alpha^{(2)}$ direction is a spherically spreading wave of polarization \mathbf{d}_s^α having the displacements

$$\mathbf{u}(\mathbf{x}, \omega) = A(\mathbf{e}_{inc}^\beta, \mathbf{e}_{scat}^\alpha, \omega) \mathbf{d}_s^\alpha \frac{\exp(ik_{a2} r)}{r}. \quad (11.23)$$

Here $\mathbf{A}(\mathbf{e}_{inc}^\beta, \mathbf{e}_{scat}^\alpha, \omega) = A(\mathbf{e}_{inc}^\beta, \mathbf{e}_{scat}^\alpha, \omega) \mathbf{d}_s^\alpha$ is the vector far-field scattering amplitude whose components are given by

Fig. 11.6 The far field scattering of a wave of type α due to a plane wave of type β having a unit displacement amplitude



$$A_n(\mathbf{e}_{inc}^\beta, \mathbf{e}_{scat}^\alpha, \omega) = -\frac{d_{s;n}^\alpha}{4\pi\rho_2 c_{a2}^2}$$

$$\int_{S_f} \left(\bar{\tau}_{ji}^{(1)}(\mathbf{x}, \omega) d_{s;i}^\alpha(\mathbf{x}, \omega) - C_{ijkl} \frac{e_{scat;l}^\alpha}{c_{a2}} d_{s;k}^\alpha \bar{v}_i^{(1)}(\mathbf{x}, \omega) \right) n_j(\mathbf{x}) \exp[-ik_{a2} \mathbf{e}_{scat}^\alpha \cdot \mathbf{x}'] dS(\mathbf{x}'). \quad (11.24)$$

Comparing this expression with the integral in Eq. (11.22), setting $\mathbf{d}_s^\alpha = -\mathbf{d}_\alpha^{(2)}$ and $\mathbf{e}_{scat}^\alpha = -\mathbf{e}_\alpha^{(2)}$ we see that

$$\int_{S_f} \left(\bar{\tau}_{ji}^{(1)}(\mathbf{x}, \omega) d_{sd}^{(2)}(\mathbf{x}, \omega) + C_{ijkl} \frac{e_{sd}^{(2)}}{c_{a2}} d_{sk}^{(2)} \bar{v}_i^{(1)}(\mathbf{x}, \omega) \right) n_j(\mathbf{x}) \exp[ik_{a2} \mathbf{e}_\alpha^{(2)} \cdot \mathbf{x}'] dS(\mathbf{x}') \\ = 4\pi\rho_2 c_{a2}^2 [\mathbf{A}(\mathbf{e}_{inc}^\beta, \mathbf{e}_{scat}^\alpha, \omega) \cdot (-\mathbf{d}^{(2)})] \quad (11.25)$$

and Eq. (11.22) becomes

$$V(\mathbf{x}_s, \mathbf{x}_r, \omega) = s_I(\omega) \hat{V}^{(1)}(\mathbf{x}_s, \mathbf{x}_0, \omega) \hat{V}^{(2)}(\mathbf{x}_r, \mathbf{x}_0, \omega) A(\mathbf{e}_{inc}^\beta, \mathbf{e}_{scat}^\alpha, \omega) \left[\frac{4\pi\rho_2 c_{a2}}{-ik_{a2} \rho_1 c_{p1} S_A} \right], \quad (11.26)$$

where $A(\mathbf{e}_{inc}^\beta, \mathbf{e}_{scat}^\alpha, \omega)$ is the scalar component of the vector scattering amplitude given as

$$A(\mathbf{e}_{inc}^\beta, \mathbf{e}_{scat}^\alpha, \omega) = [\mathbf{A}(\mathbf{e}_{inc}^\beta, \mathbf{e}_{scat}^\alpha, \omega) \cdot (-\mathbf{d}^{(2)})]. \quad (11.27)$$

The contact case follows similar steps. First, the incident waves are expressed as quasi-plane waves of the form

$$\begin{aligned} v_j^{(1);inc}(\mathbf{x}, \omega) &= \frac{F_T^{(1)}(\omega)}{\rho_1 c_{p1} S_A} \hat{V}^{(1)}(\mathbf{x}_s, \mathbf{x}_0, \omega) d_{\beta j}^{(1)} \exp(ik_{\beta 2} \mathbf{e}_{\beta}^{(1)} \cdot \mathbf{x}') \\ v_j^{(2)}(\mathbf{x}, \omega) &= \frac{F_R^{(2)}(\omega)}{\rho c_p S_B} \hat{V}^{(2)}(\mathbf{x}_r, \mathbf{x}_0, \omega) d_{\alpha j}^{(2)} \exp(ik_{\alpha 2} \mathbf{e}_{\alpha}^{(2)} \cdot \mathbf{x}'), \end{aligned} \quad (11.28)$$

where (ρ, c_p) are the density and compressional wave speed, respectively, in the solid adjacent to the receiving element and (ρ_1, c_{p1}) are the corresponding parameters at the sending element. These densities and wave speeds are the same in contact tests where the sending and receiving elements are in contact with the same medium but for generality we have left them different. Similarly, $(\rho_2, c_{\alpha 2})$ are denoted as the possibly different density and wave speed (of the scattered wave) surrounding the flaw.

Second, the stresses and velocities in state (1) are normalized so that the incident plane wave in that state is of unit displacement amplitude:

$$\begin{aligned} \bar{\tau}_{ij}^{(1)} &= \frac{-i\omega \rho_1 c_{p1} S_A \tau_{ij}^{(1)}}{F_T^{(1)} \hat{V}^{(1)}} \\ \bar{v}_j^{(1)} &= \frac{-i\omega \rho_1 c_{p1} S_A v_j^{(1)}}{F_T^{(1)} \hat{V}^{(1)}}. \end{aligned} \quad (11.29)$$

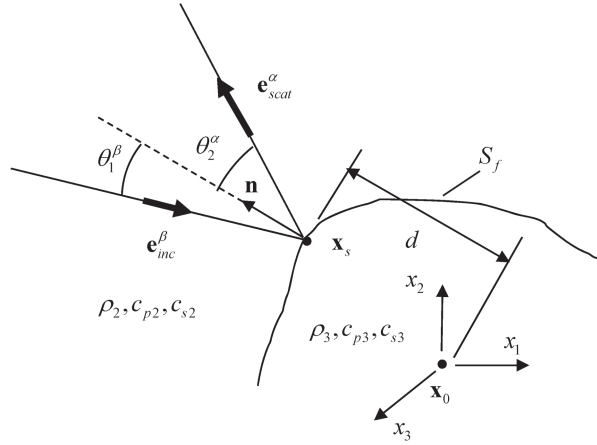
Then Eq. (11.17) reduces to

$$V(\mathbf{x}_s, \mathbf{x}_r, \omega) = s_c(\omega) \hat{V}^{(1)}(\mathbf{x}_s, \mathbf{x}_0, \omega) \hat{V}^{(2)}(\mathbf{x}_r, \mathbf{x}_0, \omega) A(\mathbf{e}_{inc}^{\beta}, \mathbf{e}_{scat}^{\alpha}, \omega) \left[\frac{4\pi \rho_2 c_{\alpha 2}}{-ik_{\alpha 2} \rho_1 c_{p1} S_A} \right], \quad (11.30)$$

which is of exactly the same form as Eq. (11.26) for the immersion case. Note that in both cases the fields $(\hat{V}^{(1)}, \hat{V}^{(2)})$ are non-dimensional.

A reduced measurement model in a form similar to Eqs. (11.26) and (11.30) was first obtained by Thompson and Gray [2] for immersion setups that used single element transducers. Because the received voltage is just proportional to the scattering amplitude $A(\mathbf{e}_{inc}^{\beta}, \mathbf{e}_{scat}^{\alpha}, \omega)$, if one measures the received voltage and the system function and models the incident fields present in $(\hat{V}^{(1)}, \hat{V}^{(2)})$ one can obtain the scattering amplitude by deconvolution [Schmerr-Song]. Numerous previous studies have used the Thompson–Gray measurement model to experimentally determine scattering amplitudes. Those scattering amplitudes then have been used as the basis for flaw sizing and flaw characterization methods, inverse scattering problems, and probability of detection (POD) studies [5]. We have shown here that the same type

Fig. 11.7 Scattering of a general shaped convex inclusion where the specular response at a stationary phase point is measured



of measurement model is directly applicable to elements of arrays in both immersion and contact testing.

To predict the voltage using a measurement model of this type, one needs a beam model for evaluating the fields and a flaw scattering model to predict the scattering amplitude $A(\mathbf{e}_{inc}^\beta, \mathbf{e}_{scat}^\alpha, \omega)$. The beam models discussed in Chap. 6 can be used effectively to compute the $(\hat{V}^{(1)}, \hat{V}^{(2)})$ terms, but flaw scattering processes are generally very complex, even for simple shaped scatterers. However, one scattering case of rather general complexity can be modeled explicitly, as shown in Fig. 11.7. Consider a general shaped elastic inclusion with density and wave speeds (ρ_3, c_{p3}, c_{s3}) embedded in an adjacent elastic medium with density and wave speeds (ρ_2, c_{p2}, c_{s2}) and let a plane wave of type β be incident on the flaw from a sending element of an array. If there is a point on the surface of the inclusion, \mathbf{x}_s , called a *specular point*, where the incident wave and scattered wave directions satisfy Snell's law, i.e.

$$\frac{\sin \theta_1^\beta}{c_{\beta 2}} = \frac{\sin \theta_2^\alpha}{c_{\alpha 2}}, \quad (11.31)$$

then one can use the Kirchhoff approximation and the method of stationary phase [Schmerr] to obtain an explicit expression for the *specular point response* of the flaw. For many flaws, this specular point response is the most significant scattered wave contribution to the entire flaw response. Specifically, one finds for the specular point response of a convex flaw

$$A(\mathbf{e}_{inc}^\beta, \mathbf{e}_{scat}^\alpha, \omega) = \frac{(\mathbf{e}_{scat}^\alpha \cdot \mathbf{n}) R_{23}^{\alpha\beta} \sqrt{R_1 R_2}}{|\mathbf{g}^{\alpha\beta} \cdot \mathbf{n}|} \exp[ik_{\alpha 2} \mathbf{g}^{\alpha\beta} \cdot \mathbf{x}_s], \quad (11.32)$$

where

$$\mathbf{g}^{\alpha\beta} = \frac{C_{\alpha 2}}{C_{\beta 2}} \mathbf{e}_{inc}^{\beta} - \mathbf{e}_{scat}^{\alpha} \quad (11.33)$$

is a vector parallel to the outward unit normal \mathbf{n} at the stationary phase point. The $R_{23}^{\alpha\beta}$ term is the plane wave reflection coefficient (based on velocity ratios) for an incident wave of type β and a reflected wave of type α for a wave incident in medium 2 (surrounding the flaw) and where medium 3 is designated as the material within the flaw. The lengths (R_1, R_2) are the principal radii of the convex flaw surface at the specular point \mathbf{x}_s . Another way to express this scattering amplitude is

$$A(\mathbf{e}_{inc}^{\beta}, \mathbf{e}_{scat}^{\alpha}, \omega) = \frac{(\mathbf{e}_{scat}^{\alpha} \cdot \mathbf{n}) R_{23}^{\alpha\beta} \sqrt{R_1 R_2}}{|\mathbf{g}^{\alpha\beta} \cdot \mathbf{n}|} \exp[-ik_{\alpha 2} |\mathbf{g}^{\alpha\beta}| d], \quad (11.34)$$

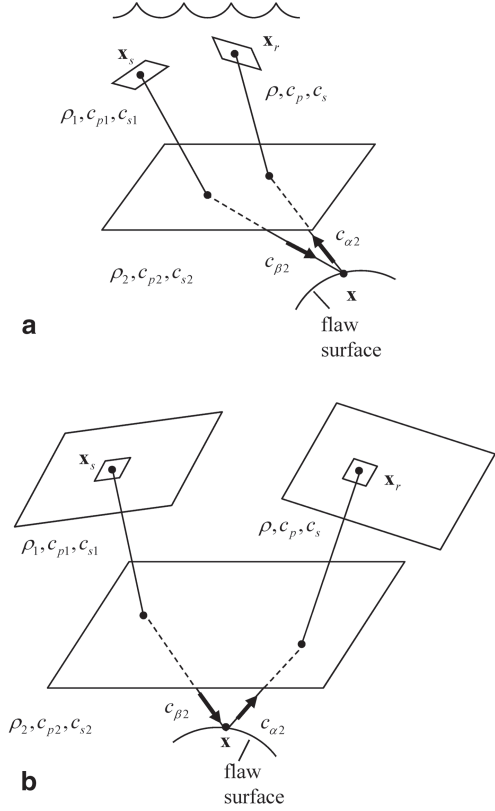
where $d = \mathbf{x}_s \cdot \mathbf{n}$ (see Fig. 11.7). For simple convex shapes like a sphere there is only one specular point on the flaw surface for a given pair of sending and receiving elements. For more complex shapes there may be more than one specular point contributions. Because the amplitude of the scattering amplitude of the specular point response is independent of frequency, in a real band-limited system the specular point pulse will act as a band-limited delta function in the time domain. Other flaw scattered wave responses often have a frequency content that is more significant at lower frequencies and so those responses may become very small in comparison to the specular point response(s) when band-limited.

11.5 Measurement Models for Quantitative Imaging

In the previous section we showed how a measurement model of the Auld type could be reduced to a more explicit Thompson–Gray type of form. In the reduced Thompson–Gray model the flaw response is just the far field scattering amplitude function of the flaw. We also showed how the specular point response from the flaw surface contribution to that scattering amplitude could be obtained explicitly.

When we use phased arrays for imaging flaws, those flaws may not be small enough to allow us to assume that the beam variations across the flaw surface are negligible. However, as discussed in more detail in the next Chapter, the specular point responses from points on the flaw surface are often still the primary signals received by an array from the flaw so that in an image formation process these specular responses waves play an important role. In this section we will use the Kirchhoff approximation and the stationary phase approximation to develop approximate measurement models of both the Auld and Thompson–Gray type that characterize the scattering of the flaw entirely in terms of these specular responses. In Chaps. 12 and 13 we will invert these measurement models to form an image of the surface reflectivity of the flaw.

Fig. 11.8 A pair of sending and receiving elements in either **a** an immersion testing setup, or **b** a contact testing setup. The densities and wave speeds at the sending element, for the material surrounding the flaw, and at the receiving element are (ρ_1, c_{p1}, c_{s1}) , (ρ_2, c_{p2}, c_{s2}) , and (ρ, c_p, c_s) , respectively, for an immersion setup where $c_{s1} = c_s = 0$. Normally, the density and wave speeds at the sending and receiving elements may be the same, but we have allowed them to be different for generality



Consider a general pair of sending and receiving array elements, either in an immersion test setup, as shown in Fig. 11.8a or the contact setup of Fig. 11.8b. The location of the centroid of the sending element is \mathbf{x}_s and the centroid of the receiving element is \mathbf{x}_r . The response of this pair of elements from a point \mathbf{x} on the surface of a flaw is also shown. We will develop approximate measurement models that will form the basis of imaging flaws for both cases. For the immersion case we found the measurement model in the form (see Eq. (11.13)):

$$V(\mathbf{x}_s, \mathbf{x}_r, \omega) = s_I(\omega) \frac{1}{\rho_1 c_{p1} S_A v_T^{(1)}(\omega) v_R^{(2)}(\omega)} \cdot \int_{S_f} \left(\tau_{ji}^{(1)}(\mathbf{x}, \omega) v_i^{(2)}(\mathbf{x}, \omega) - \tau_{ji}^{(2)}(\mathbf{x}, \omega) v_i^{(1)}(\mathbf{x}, \omega) \right) n_j(\mathbf{x}) dS(\mathbf{x}), \quad (11.35)$$

while for the contact case we had (see Eq. (11.17))

$$V(\mathbf{x}_s, \mathbf{x}_r, \omega) = s_C(\omega) \frac{\rho c_p S_B}{F_T^{(1)} F_R^{(2)}} \int_{S_f} \left(\tau_{ji}^{(1)}(\mathbf{x}, \omega) v_i^{(2)}(\mathbf{x}, \omega) - \tau_{ji}^{(2)}(\mathbf{x}, \omega) v_i^{(1)}(\mathbf{x}, \omega) \right) n_j(\mathbf{x}) dS(\mathbf{x}). \quad (11.36)$$

If we normalize Eqs. (11.35) and (11.36) appropriately, we can write these expressions in a common form. Specifically, we define a normalized voltage, $\widehat{V}(\mathbf{x}_s, \mathbf{x}_r, \omega)$, as

$$\widehat{V}(\mathbf{x}_s, \mathbf{x}_r, \omega) = \rho_1 c_{p1} S_A V(\mathbf{x}_s, \mathbf{x}_r, \omega) / s_I(\omega). \quad (11.37)$$

for the immersion case and

$$\widehat{V}(\mathbf{x}_s, \mathbf{x}_r, \omega) = V(\mathbf{x}_s, \mathbf{x}_r, \omega) / \rho c_p S_B s_C(\omega) \quad (11.38)$$

for the contact case. Similarly, we define normalized (but not necessarily non-dimensional) stress and velocity terms as

$$\begin{aligned} \tilde{\tau}_{ji}^{(1)} &= \tau_{ji}^{(1)} / v_T^{(1)}, \quad \tilde{v}_i^{(1)} = v_i^{(1)} / v_T^{(1)} \\ \tilde{\tau}_{ji}^{(2)} &= \tau_{ji}^{(2)} / v_R^{(2)}, \quad \tilde{v}_i^{(2)} = v_i^{(2)} / v_R^{(2)} \end{aligned} \quad (11.39)$$

for the immersion case and

$$\begin{aligned} \tilde{\tau}_{ji}^{(1)} &= \tau_{ji}^{(1)} / F_T^{(1)}, \quad \tilde{v}_i^{(1)} = v_i^{(1)} / F_T^{(1)} \\ \tilde{\tau}_{ji}^{(2)} &= \tau_{ji}^{(2)} / F_R^{(2)}, \quad \tilde{v}_i^{(2)} = v_i^{(2)} / F_R^{(2)} \end{aligned} \quad (11.40)$$

for the contact case. Then in either the immersion or contact case we have

$$\widehat{V}(\mathbf{x}_r, \mathbf{x}_s, \omega) = \int_{S_f} \left(\tilde{\tau}_{ji}^{(1)} \tilde{v}_i^{(2)} - \tilde{\tau}_{ji}^{(2)} \tilde{v}_i^{(1)} \right) n_j dS(\mathbf{x}). \quad (11.41)$$

Note that, as mentioned previously, since we have normalized the fields in both the immersion and contact cases by the driving velocities or forces acting on the transmitting element face, these normalized fields are those due to a transmitting element with either a unit velocity or unit force acting on its face. Thus, one can evaluate these normalized fields completely with models without having to know the actual velocity or force on the driving element.

We will use Eq. (11.41) as the starting point for developing a measurement model that evaluates the voltage response from points on the flaw surface shown in Fig. 11.8. At high frequencies the incident normalized displacement fields and their derivatives in configurations (1) and (2) can be written as

$$\begin{aligned} \tilde{u}_k^{(1);inc} &= \tilde{U}_\beta^{(1)}(\mathbf{x}_s, \mathbf{x}, \omega) d_{\beta k}^{(1)} \exp[i\omega T(\mathbf{x}_s, \mathbf{x})] \\ \frac{\partial \tilde{u}_k^{(1);inc}}{\partial x_j} &= i\omega \frac{\partial T(\mathbf{x}_s, \mathbf{x})}{\partial x_j} \tilde{U}_\beta^{(1)}(\mathbf{x}_s, \mathbf{x}, \omega) d_{\beta k}^{(1)} \exp[i\omega T(\mathbf{x}_s, \mathbf{x})] \\ &= ik_\beta e^{(1)}_{\beta j} \tilde{U}_\beta^{(1)}(\mathbf{x}_s, \mathbf{x}, \omega) d_{\beta k}^{(1)} \exp[i\omega T(\mathbf{x}_s, \mathbf{x})] \end{aligned} \quad (11.42)$$

(no sum on β)
and

$$\begin{aligned}\tilde{u}_k^{(2)} &= \tilde{U}_\alpha^{(2)}(\mathbf{x}_r, \mathbf{x}, \omega) d_{\alpha k}^{(2)} \exp[i\omega T(\mathbf{x}_r, \mathbf{x})] \\ \frac{\partial \tilde{u}_k^{(2)}}{\partial x_j} &= i\omega \frac{\partial T(\mathbf{x}_r, \mathbf{x})}{\partial x_j} \tilde{U}_\alpha^{(2)}(\mathbf{x}_r, \mathbf{x}, \omega) d_{\alpha k}^{(2)} \exp[i\omega T(\mathbf{x}_r, \mathbf{x})] \\ &= ik_\alpha e_{\alpha j}^{(2)} \tilde{U}_\alpha^{(2)}(\mathbf{x}_r, \mathbf{x}, \omega) d_{\alpha k}^{(2)} \exp[i\omega T(\mathbf{x}_r, \mathbf{x})],\end{aligned}\quad (11.43)$$

(no sum on α)

where again we have dropped the designation “inc” for the incident waves in configuration (2) since incident waves are the only types of waves present in that state (the flaw is assumed absent). Note that these normalized displacements, $\tilde{u}_k^{(1);inc}$ and $\tilde{u}_k^{(2)}$ are normalized in the same fashion as the normalized velocities given in Eqs. (11.39) and (11.40) for the immersion and contact cases, respectively. In Eqs. (11.42) and (11.43) the $\tilde{U}_\beta^{(1)}, \tilde{U}_\alpha^{(2)}$ terms denote the similarly normalized amplitudes of the incident waves, where (α, β) can take on either of the values (p, sv) to denote a P-wave or SV-wave mode, i.e. we have allowed for the transmitted and received waves to be either of these different types in the solid. The polarizations of these waves are the terms $d_{\beta k}^{(1)}, d_{\alpha k}^{(2)}$ for states (1) and (2) respectively. The phase terms $T(\mathbf{x}_s, \mathbf{x}), T(\mathbf{x}_r, \mathbf{x})$ represent the time delays associated with the travel to and from center of the elements to the flaw in states (1) and (2), respectively, and at high frequencies the derivatives of the fields are just proportional to the derivatives of these phase terms, as seen in Eqs. (11.42) and (11.43). Furthermore, we have used the relationships

$$\begin{aligned}i\omega \frac{\partial T(\mathbf{x}_s, \mathbf{x})}{\partial x_j} &= ik_\beta e_{\beta j}^{(1)} \\ i\omega \frac{\partial T(\mathbf{x}_r, \mathbf{x})}{\partial x_j} &= ik_\alpha e_{\alpha j}^{(2)},\end{aligned}\quad (11.44)$$

(no sum on α, β)

where $k_m = \omega / c_m$ ($m = \alpha, \beta$) are wave numbers associated with the corresponding wave speeds, c_m , and $(e_{\beta j}^{(1)}, e_{\alpha j}^{(2)})$ are unit vectors in the incident wave directions at the flaw for states (1) and (2), respectively.

To develop a more explicit measurement model we will assume the scattered waves in state (1) can be obtained at high frequencies from the Kirchhoff approximation. In the Kirchhoff approximation, the scattered waves at any point, \mathbf{x} , on that portion of the surface of the flaw where the incident waves can directly strike the surface (the so-called “lit” part of the surface, S_{lit}) are assumed to be identical to the reflected waves generated by a plane wave incident on a planar surface, where the planar surface is taken to be tangent to the flaw surface at point \mathbf{x} . These reflected

waves satisfy Snell's law and can be obtained from ordinary plane wave reflection coefficients, $R_{23}^{m;\beta}$ (based on displacement or velocity ratios), where $m = (p, sv)$ denotes the mode of the reflected wave while $\beta = (p, sv)$ is the mode of the incident wave in state (1). On the remainder of the surface the total fields are assumed to be identically zero. Thus, the normalized displacements and their derivatives on the lit surface for state (1) are given by

$$\begin{aligned}\tilde{u}_k^{(1)} &= \tilde{U}_\beta^{(1)}(\mathbf{x}_s, \mathbf{x}, \omega) \exp[i\omega T(\mathbf{x}_s, \mathbf{x})] \left(d_{\beta k}^{(1)} + \sum_{m=p,sv} R_{23}^{m;\beta} d_{mk}^r \right) \\ \frac{\partial \tilde{u}_k^{(1)}}{\partial x_j} &= \tilde{U}_\beta^{(1)}(\mathbf{x}_s, \mathbf{x}, \omega) \exp[i\omega T(\mathbf{x}_s, \mathbf{x})] \left(ik_\beta d_{\beta k}^{(1)} e_{\beta j}^{(1)} + \sum_{m=p,sv} ik_m R_{23}^{m;\beta} d_{mk}^r e_{mj}^r \right),\end{aligned}\quad (11.45)$$

where d_{mk}^r are the components of the polarization unit vector of a reflected wave of type m , and e_{mj}^r are the components of a unit vector in the direction of a reflected wave of type m . The stress and velocity fields appearing in Eq. (11.41) are given in terms of the displacements and displacement gradients by

$$\begin{aligned}\tilde{\tau}_{ji}^{(1)} &= C_{ijkl} \frac{\partial \tilde{u}_k^{(1)}}{\partial x_l} \\ \tilde{v}_i^{(1)} &= -i\omega \tilde{u}_i^{(1)} \\ \tilde{\tau}_{ji}^{(2)} &= C_{ijkl} \frac{\partial \tilde{u}_k^{(2)}}{\partial x_l} \\ \tilde{v}_i^{(2)} &= -i\omega \tilde{u}_i^{(2)},\end{aligned}\quad (11.46)$$

where C_{ijkl} is the fourth order tensor of elastic constants for the material surrounding the flaw [Schmerr]. Placing these results into Eq. (11.41) we then obtain

$$\hat{V}(\mathbf{x}_s, \mathbf{x}_r, \omega) = \omega^2 \int_{S_{lit}} \tilde{U}_\beta^{(1)}(\mathbf{x}_s, \mathbf{x}, \omega) \tilde{U}_\alpha^{(2)}(\mathbf{x}_r, \mathbf{x}, \omega) \exp[i\omega \phi(\mathbf{x}_s, \mathbf{x}_r, \mathbf{x})] I(\mathbf{x}) dS(\mathbf{x}), \quad (11.47)$$

where the integrand term, $I(\mathbf{x})$, is given by

$$I(\mathbf{x}) = n_j C_{ijkl} \left[\frac{d_{\beta k}^{(1)} d_{\alpha l}^{(2)} e_{\beta l}^{(1)}}{c_{\beta 2}} - \frac{d_{\beta l}^{(1)} d_{\alpha k}^{(2)} e_{\alpha l}^{(2)}}{c_{\alpha 2}} + \sum_{m=p,sv} \left(\frac{R_{23}^{m;\beta} d_{\alpha l}^{(2)} d_{mk}^r e_{ml}^r}{c_{m2}} - \frac{R_{23}^{m;\beta} d_{\alpha k}^{(2)} d_{mi}^r e_{\alpha l}^{(2)}}{c_{\alpha 2}} \right) \right] \quad (11.48)$$

and the phase term $\phi(\mathbf{x}_s, \mathbf{x}_r, \mathbf{x})$ is

$$\phi(\mathbf{x}_s, \mathbf{x}_r, \mathbf{x}) = T(\mathbf{x}_s, \mathbf{x}) + T(\mathbf{x}_r, \mathbf{x}). \quad (11.49)$$

To develop a measurement model form suitable for imaging, we will assume that the primary voltage response of the surface will be due to a collection of specular reflections from the surface, where Snell's law is satisfied, similar to what was discussed in the previous section for small flaws. This assumption corresponds to replacing $I(\mathbf{x})$ by its stationary phase value, $I(\mathbf{x}_{stat})$, a value that has been obtained previously [Schmerr] for a homogenous, isotropic elastic solid, where it is shown that the incident wave terms in Eq. (11.48) vanish at the stationary phase point and the remaining terms reduce to simply

$$I(\mathbf{x}_{stat}) = -2\rho_2 c_{\alpha 2} R_{23}^{\alpha;\beta} (e_{\alpha k}^r n_k), \quad (11.50)$$

where ρ_2 is the density of the material surrounding the flaw [Note: the minus sign in Eq. (11.50) is not present in [Schmerr] since the $I(\mathbf{x})$ considered there was the negative of the expression used here]. Although the algebra is lengthy for proving Eq. (11.50) in general testing setups, in pulse-echo cases only the same mode is present for both the incident and reflected waves ($\alpha = \beta$) since the normal incidence reflection coefficient is zero for mixed incident/reflected modes and we also have $e_{\beta}^{(1)} n_k = -1$, $e_{\alpha k}^r n_k = 1$. In this case we can directly evaluate $I(\mathbf{x}_{stat})$ in general for a homogeneous, anisotropic material. To see this, note that the equations of motion for the displacements of a homogeneous, anisotropic solid are [6]

$$C_{ijkl} \frac{\partial u_k}{\partial x_i \partial x_j} = -\rho_2 \omega^2 u_j. \quad (11.51)$$

For a plane wave of type β and polarization $d_{\beta k}$ traveling in the e_i direction we have

$$u_k = A d_{\beta k} \exp[ik(e_i x_i) - i\omega t] \quad (11.52)$$

and Eq. (11.51) reduces to

$$C_{ijkl} e_i e_j d_{\beta k} = \rho_2 c_{\beta 2}^2 d_{\beta j}. \quad (11.53)$$

From Eq. (11.53) it follows that

$$C_{ijkl} e_i e_j d_{\beta k} d_{\beta j} = \rho_2 c_{\beta 2}^2. \quad (11.54)$$

Also, for a wave of type α and polarization $d_{\alpha k}$ traveling in the e_i (or $e_i^r = -e_i$) direction we have

$$C_{ijkl} e_i e_j d_{\alpha k} = \rho_2 c_{\alpha 2}^2 d_{\alpha j}. \quad (11.55)$$

From Eqs. (11.53) and (11.55) and the symmetries of the C_{ijkl} tensor ($C_{ijkl} = C_{jikl} = C_{ijlk} = C_{klji}$) we have

$$\rho_2 (c_{\beta 2}^2 - c_{\alpha 2}^2) d_{\beta j} d_{\alpha j} = 0, \quad (11.56)$$

which shows that the polarizations of two different mode plane waves traveling in the same (or opposite) directions are orthogonal to each other, i.e.

$$d_{\beta j} d_{\alpha j} = 0 \quad (\alpha \neq \beta). \quad (11.57)$$

We can now use these results in the evaluation of $I(\mathbf{x})$ at the stationary phase point. In pulse-echo at this point we have (with $\alpha = \beta$) $e_{\beta i}^{(1)} = e_{\alpha i}^{(2)} = e_i$, $n_i = -e_i$, $e_{ml}^r = -e_i$, and $d_{\beta i}^{(1)} = d_{\beta i}^{(2)} = d_{\beta i}$ so that we find

$$\begin{aligned} I(\mathbf{x}_{stat}) = & -C_{ijkl} \left[\frac{d_{\beta k} d_{\beta l} e_{\beta l} e_{\beta j}}{c_{\beta 2}} - \frac{d_{\beta l} d_{\beta k} e_{\beta l} e_{\beta j}}{c_{\beta 2}} \right. \\ & \left. - \sum_{m=p,sv} \left(\frac{R_{23}^{m;\beta} d_{\beta l} d_{mk}^r e_{\beta l} e_{\beta j}}{c_{m2}} + \frac{R_{23}^{m;\beta} d_{\beta k} d_{mi}^r e_{\beta l} e_{\beta j}}{c_{\beta 2}} \right) \right]. \end{aligned} \quad (11.58)$$

The first two terms in Eq. (11.58) just cancel and using the symmetries of the C_{ijkl} tensor and Eq. (11.53) we find

$$I(\mathbf{x}_{stat}) = \rho_2 \sum_{m=p,sv} R_{23}^{m;\beta} (c_{m2} + c_{\beta 2}) d_{mj}^r d_{\beta j}. \quad (11.59)$$

But the polarizations of the reflected and incident waves will be orthogonal unless $m = \beta$ because of Eq. (11.56) so that

$$I(\mathbf{x}_{stat}) = 2\rho_2 c_{\beta 2} R_{23}^{\beta;\beta} d_{\beta j}^r d_{\beta j}. \quad (11.60)$$

We will take the polarization of the reflected wave opposite to that of the incident wave (an arbitrary assumption, but one that is commonly used—the final result, however, is independent of this choice since a change in sign of the assumed polarization will also result in a change in the sign of the reflection coefficient, leaving the product unchanged). Then $d_{\beta j}^r d_{\beta j} = -1$ and we find, finally

$$I(\mathbf{x}_{stat}) = -2\rho_2 c_{\beta 2} R_{23}^{\beta;\beta}(0^\circ), \quad (11.61)$$

which is just Eq. (11.50) for the pulse-echo case. We have written the reflection coefficient here as $R_{23}^{\beta;\beta}(0^\circ)$ to emphasize that we are dealing with the reflection coefficient at normal incidence to the flaw surface. Note, however, that while the pulse-echo result, Eq. (11.61), is valid for a general homogeneous, anisotropic elastic solid, the more general form of Eq. (11.50) was only obtained in [Schmerr] for a homogenous, isotropic elastic solid.

If we now place Eq. (11.50) into Eq. (11.47) we obtain

$$\begin{aligned} \widehat{V}(\mathbf{x}_s, \mathbf{x}_r, \omega) = & -2 \rho_2 c_{\alpha 2} \omega^2 \int_{S_{\text{fl}}}\left\{R_{23}^{\alpha \beta}\left(e_{\alpha k}^r n_k\right) \tilde{U}_{\beta}^{(1)}\left(\mathbf{x}_s, \mathbf{x}, \omega\right) \tilde{U}_{\alpha}^{(2)}\left(\mathbf{x}_r, \mathbf{x}, \omega\right)\right. \\ & \cdot \exp \left[i \omega \phi\left(\mathbf{x}_s, \mathbf{x}_r, \mathbf{x}\right)\right] d S(\mathbf{x})\left.\right\} \end{aligned} \quad (11.62)$$

In the case of a pulse-echo setup (with the same mode on sending and receiving), we have $e_{\alpha k}^r n_k = 1$, $\alpha = \beta$, $\tilde{U}_{\beta}^{(1)} = \tilde{U}_{\alpha}^{(2)}$, $\mathbf{x}_s = \mathbf{x}_r = \mathbf{x}_c$ (the common centroid location of the sending/receiving element), $\phi = 2T(\mathbf{x}_c, \mathbf{x})$. In this special case Eq. (11.62) becomes

$$\begin{aligned} \widehat{V}\left(\mathbf{x}_c, \omega\right) = & -2 \rho_2 c_{\beta 2} \omega^2 \int_{S_{\text{fl}}}\left\{R_{23}^{\beta, \beta}\left[\tilde{U}_{\beta}^{(1)}\left(\mathbf{x}_c, \mathbf{x}, \omega\right)\right]^2\right. \\ & \cdot \exp \left[2 i \omega T\left(\mathbf{x}_c, \mathbf{x}\right)\right] d S(\mathbf{x})\left.\right\}. \end{aligned} \quad (11.63)$$

Equations (11.62) and (11.63) are both approximate measurement models of the voltage received from a flaw in forms that describe the received voltage for a pair of sending and receiving elements in terms of the reflection coefficient and fields on the flaw surface. In the following chapters we will see how these models can be used to generate flaw images.

For the reduced case of a small flaw, the normalized displacements in the integrand of Eq. (11.62) are evaluated at a fixed point \mathbf{x}_0 so they can be removed from the integral and the phase $\phi(\mathbf{x}_s, \mathbf{x}_r, \mathbf{x}, \omega)$ is given to first order in the neighborhood of the fixed point as

$$\begin{aligned} \phi\left(\mathbf{x}_s, \mathbf{x}_r, \mathbf{x}\right) \cong & \phi\left(\mathbf{x}_s, \mathbf{x}_r, \mathbf{x}_0\right)+\left[\nabla T\left(\mathbf{x}_s, \mathbf{x}\right)+\nabla T\left(\mathbf{x}_r, \mathbf{x}\right)\right] \cdot\left(\mathbf{x}-\mathbf{x}_0\right) \\ = & \phi\left(\mathbf{x}_s, \mathbf{x}_r, \mathbf{x}_0\right)+\left(\mathbf{e}_{\beta}^{(1)} / c_{\beta 2}+\mathbf{e}_{\alpha}^{(2)} / c_{\alpha 2}\right) \cdot\left(\mathbf{x}-\mathbf{x}_0\right) \end{aligned} \quad (11.64)$$

so that we obtain

$$\begin{aligned} \widehat{V}\left(\mathbf{x}_s, \mathbf{x}_r, \omega\right) = & -2 \rho_2 c_{\alpha 2} \omega^2 \tilde{U}_{\beta}^{(1)}\left(\mathbf{x}_s, \mathbf{x}_0, \omega\right) \tilde{U}_{\alpha}^{(2)}\left(\mathbf{x}_r, \mathbf{x}_0, \omega\right) \exp \left[i \omega \phi\left(\mathbf{x}_s, \mathbf{x}_r, \mathbf{x}_0\right)\right] \\ & \cdot \int_{S_{\text{fl}}}\left\{R_{23}^{\alpha, \beta}\left(e_{\alpha k}^r n_k\right) \exp \left[i k_{\alpha 2} \mathbf{g}^{\alpha \beta} \cdot\left(\mathbf{x}-\mathbf{x}_0\right)\right] d S(\mathbf{x})\right\}, \end{aligned} \quad (11.65)$$

where $\mathbf{g}^{\alpha, \beta}$ is defined as

$$\mathbf{g}^{\alpha, \beta}=c_{\alpha 2} \mathbf{e}_{\beta}^{(1)} / c_{\beta 2}+\mathbf{e}_{\alpha}^{(2)} . \quad (11.66)$$

In the pulse-echo case with same sending and receiving modes ($\alpha = \beta$), Eq. (11.65) reduces to

$$\begin{aligned} \hat{V}(\mathbf{x}_c, \omega) = & -2\rho_2 c_{\beta 2} \omega^2 \left[\tilde{U}_{\beta}^{(1)}(\mathbf{x}_c, \mathbf{x}_0, \omega) \right]^2 \exp[2i\omega T(\mathbf{x}_c, \mathbf{x}_0)] \\ & \cdot \int_{S_{fl}} \left\{ R_{23}^{\beta, \beta} \exp[2ik_{\beta 2} \mathbf{e}^{(1)} \cdot (\mathbf{x} - \mathbf{x}_0)] \right\} dS(\mathbf{x}). \end{aligned} \quad (11.67)$$

As we will see in Chaps. 12 and 13, Eqs. (11.65) and (11.67) are approximate measurement models suitable for developing an image formation process for small flaws.

Equation (11.65) is closely related to the specular point response obtained in conjunction with the Thompson–Gray measurement model of the previous section. To see this relationship, we will assume the flaw is a small convex flaw and evaluate the surface integral by the method of stationary phase [Schmerr]. We find

$$\begin{aligned} \hat{V}(\mathbf{x}_s, \mathbf{x}_r, \omega) = & -\omega^2 \tilde{U}_{\beta}^{(1)}(\mathbf{x}_s, \mathbf{x}_0, \omega) \exp[i\omega T(\mathbf{x}_s, \mathbf{x}_0)] \tilde{U}_{\alpha}^{(2)}(\mathbf{x}_r, \mathbf{x}_0, \omega) \exp[i\omega T(\mathbf{x}_r, \mathbf{x}_0)] \\ & \cdot \frac{4\pi\rho_2 c_{\alpha 2} i \sqrt{R_1 R_2}}{k_{\alpha 2} |\mathbf{g}^{\alpha, \beta} \cdot \mathbf{n}|} R_{23}^{\alpha, \beta} (e_{\alpha k}^r n_k) \exp[ik_{\alpha 2} \mathbf{g}^{\alpha, \beta} \cdot (\mathbf{x}_{stat} - \mathbf{x}_0)]. \end{aligned} \quad (11.68)$$

Comparing this equation with Eq. (11.32) we see we can write Eq. (11.68) in terms of the far field scattering amplitude of the flaw as

$$\begin{aligned} \hat{V}(\mathbf{x}_s, \mathbf{x}_r, \omega) = & -\omega^2 \tilde{U}_{\beta}^{(1)}(\mathbf{x}_s, \mathbf{x}_0, \omega) \exp[i\omega T(\mathbf{x}_s, \mathbf{x}_0)] \tilde{U}_{\alpha}^{(2)}(\mathbf{x}_r, \mathbf{x}_0, \omega) \exp[i\omega T(\mathbf{x}_r, \mathbf{x}_0)] \\ & \cdot \frac{4\pi\rho_2 c_{\alpha 2}}{-ik_{\alpha 2}} A(\mathbf{e}_{inc}^{\beta}, \mathbf{e}_{scat}^{\alpha}, \omega), \end{aligned} \quad (11.69)$$

where, recall, $\mathbf{e}_{inc}^{\beta} \equiv \mathbf{e}_{\beta}^{(1)}$, $\mathbf{e}_{scat}^{\alpha} \equiv -\mathbf{e}_{\alpha}^{(2)}$.

We will put Eq. (11.69) in a more explicit form so that we can compare it to the Thompson–Gray form. Consider first the contact case where Eq. (11.30) is rewritten here again as

$$V(\mathbf{x}_s, \mathbf{x}_r, \omega) = s_C(\omega) \hat{V}^{(1)}(\mathbf{x}_s, \mathbf{x}_0, \omega) \hat{V}^{(2)}(\mathbf{x}_r, \mathbf{x}_0, \omega) A(\mathbf{e}_{inc}^{\beta}, \mathbf{e}_{scat}^{\alpha}, \omega) \left[\frac{4\pi\rho_2 c_{\alpha 2}}{-ik_{\alpha 2} \rho_1 c_{\beta 1} S_A} \right]. \quad (11.70)$$

Similarly, we can rewrite Eq. (11.69) as

$$\begin{aligned} V(\mathbf{x}_s, \mathbf{x}_r, \omega) = & -\omega^2 s_C(\omega) \tilde{U}_{\beta}^{(1)}(\mathbf{x}_s, \mathbf{x}_0, \omega) \exp[i\omega T(\mathbf{x}_s, \mathbf{x}_0)] \tilde{U}_{\alpha}^{(2)}(\mathbf{x}_r, \mathbf{x}_0, \omega) \exp[i\omega T(\mathbf{x}_r, \mathbf{x}_0)] \\ & \cdot A(\mathbf{e}_{inc}^{\beta}, \mathbf{e}_{scat}^{\alpha}, \omega) \left[\frac{4\pi\rho_2 c_{\alpha 2}}{-ik_{\alpha 2}} \rho_C S_B \right], \end{aligned} \quad (11.71)$$

where, recall (ρ, c_p) are the density and compressional wave speed at the contact receiving element, whose area is S_B . Equations (11.70) and (11.71) are equivalent since the incident velocity and displacement fields for state (1) were written in the two separate forms

$$\begin{aligned} v_j^{(1);inc}(\mathbf{x}, \omega) &= \frac{F_T^{(1)}}{\rho_1 c_{p1} S_A} \hat{V}^{(1)}(\mathbf{x}_s, \mathbf{x}_0, \omega) d_{\beta j}^{(1)} \exp[ik_{\beta 2}(\mathbf{e}^{(1)} \cdot \mathbf{x})] \\ u_j^{(1);inc}(\mathbf{x}, \omega) &= F_T^{(1)} \tilde{U}_{\beta}^{(1)}(\mathbf{x}_s, \mathbf{x}_0, \omega) d_{\beta j}^{(1)} \exp[i\omega T(\mathbf{x}_s, \mathbf{x}_0)] \exp[ik_{\beta 2}(\mathbf{e}^{(1)} \cdot \mathbf{x})]. \end{aligned} \quad (11.72)$$

Similarly, for state (2)

$$\begin{aligned} v_j^{(2)}(\mathbf{x}, \omega) &= \frac{F_R^{(2)}}{\rho c_p S_B} \hat{V}^{(2)}(\mathbf{x}_r, \mathbf{x}_0, \omega) d_{\alpha j}^{(2)} \exp[ik_{\alpha 2}(\mathbf{e}^{(2)} \cdot \mathbf{x})] \\ u_j^{(2)}(\mathbf{x}, \omega) &= F_R^{(2)} \tilde{U}_{\alpha}^{(2)}(\mathbf{x}_r, \mathbf{x}_0, \omega) d_{\alpha j}^{(2)} \exp[i\omega T(\mathbf{x}_r, \mathbf{x}_0)] \exp[ik_{\alpha 2}(\mathbf{e}^{(2)} \cdot \mathbf{x})]. \end{aligned} \quad (11.73)$$

But since $v_j^{(1);inc} = -i\omega u_j^{(1);inc}$, $v_j^{(2)} = -i\omega u_j^{(2)}$, we have

$$\begin{aligned} \hat{V}^{(1)}(\mathbf{x}_s, \mathbf{x}_0, \omega) &= -i\omega \rho_1 c_{p1} S_A \tilde{U}_{\beta}^{(1)}(\mathbf{x}_s, \mathbf{x}_0, \omega) \exp[i\omega T(\mathbf{x}_s, \mathbf{x}_0)] \\ \hat{V}^{(2)}(\mathbf{x}_r, \mathbf{x}_0, \omega) &= -i\omega \rho c_p S_B \tilde{U}_{\alpha}^{(2)}(\mathbf{x}_r, \mathbf{x}_0, \omega) \exp[i\omega T(\mathbf{x}_r, \mathbf{x}_0)]. \end{aligned} \quad (11.74)$$

Using the relations in Eq. (11.74) we see that Eqs. (11.70) and (11.71) are identical.

Similarly, in the immersion case, from Eq. (11.26) we found

$$V(\mathbf{x}_s, \mathbf{x}_r, \omega) = s_I(\omega) \hat{V}^{(1)}(\mathbf{x}_0, \omega) \hat{V}^{(2)}(\mathbf{x}_0, \omega) A(\mathbf{e}_{inc}^{\beta}, \mathbf{e}_{scat}^{\alpha}, \omega) \left[\frac{4\pi\rho_2 c_{\alpha 2}}{-ik_{\alpha 2} \rho_1 c_{p1} S_A} \right], \quad (11.75)$$

while from Eqs. (11.69) and (11.38) we obtain

$$\begin{aligned} V(\mathbf{x}_s, \mathbf{x}_r, \omega) &= -\omega^2 s_I(\omega) \tilde{U}_{\beta}^{(1)}(\mathbf{x}_s, \mathbf{x}_0, \omega) \exp[i\omega T(\mathbf{x}_s, \mathbf{x}_0)] \tilde{U}_{\alpha}^{(2)}(\mathbf{x}_r, \mathbf{x}_0, \omega) \\ &\quad \cdot \exp[i\omega T(\mathbf{x}_r, \mathbf{x}_0)] A(\mathbf{e}_{inc}^{\beta}, \mathbf{e}_{scat}^{\alpha}, \omega) \left[\frac{4\pi\rho_2 c_{\alpha 2}}{-ik_{\alpha 2} \rho_1 c_{p1} S_A} \right]. \end{aligned} \quad (11.76)$$

In this case the velocity and displacement fields were expressed in state (1) as

$$\begin{aligned} v_j^{(1);inc}(\mathbf{x}, \omega) &= v_T^{(1)} \hat{V}^{(1)}(\mathbf{x}_s, \mathbf{x}_0, \omega) d_{\beta j}^{(1)} \exp[ik_{\beta 2}(\mathbf{e}^{(1)} \cdot \mathbf{x})] \\ u_j^{(1);inc}(\mathbf{x}, \omega) &= v_T^{(1)} \tilde{U}_{\beta}^{(1)}(\mathbf{x}_s, \mathbf{x}_0, \omega) d_{\beta j}^{(1)} \exp[i\omega T(\mathbf{x}_s, \mathbf{x}_0)] \exp[ik_{\beta 2}(\mathbf{e}^{(1)} \cdot \mathbf{x})]. \end{aligned} \quad (11.77)$$

and in state (2) as

$$\begin{aligned} v_j^{(2)}(\mathbf{x}, \omega) &= v_r^{(2)} \hat{V}^{(2)}(\mathbf{x}_r, \mathbf{x}_0, \omega) d_{\alpha j}^{(2)} \exp[ik_{\alpha 2}(\mathbf{e}^{(2)} \cdot \mathbf{x})] \\ u_j^{(2)}(\mathbf{x}, \omega) &= v_r^{(2)} \tilde{U}_{\alpha}^{(2)}(\mathbf{x}_r, \mathbf{x}_0, \omega) d_{\alpha j}^{(2)} \exp[i\omega T(\mathbf{x}_r, \mathbf{x}_0)] \exp[ik_{\alpha 2}(\mathbf{e}^{(2)} \cdot \mathbf{x})] \end{aligned} \quad (11.78)$$

so that with $v_j^{(1);inc} = -i\omega u_j^{(1);inc}$, $v_j^{(2)} = -i\omega u_j^{(2)}$ we have

$$\begin{aligned} \hat{V}^{(1)}(\mathbf{x}_s, \mathbf{x}_0, \omega) &= -i\omega \tilde{U}_{\beta}^{(1)}(\mathbf{x}_s, \mathbf{x}_0, \omega) \exp[i\omega T(\mathbf{x}_s, \mathbf{x}_0)] \\ \hat{V}^{(2)}(\mathbf{x}_r, \mathbf{x}_0, \omega) &= -i\omega \tilde{U}_{\alpha}^{(2)}(\mathbf{x}_r, \mathbf{x}_0, \omega) \exp[i\omega T(\mathbf{x}_r, \mathbf{x}_0)]. \end{aligned} \quad (11.79)$$

Using Eq. (11.79) we see that Eqs. (11.75) and (11.76) are identical.

11.6 Measurement Models for 2-D Problems

In earlier chapters we have examined the responses of 1-D arrays radiating two-dimensional waves in a fluid since much of the physics associated with phased array can be discussed more clearly in those simpler problems. For imaging applications, 2-D problems have the added advantage of requiring much less computations. Thus, in this section we will describe measurement models for such 2-D cases.

It is relatively easy to transform a measurement model of the Auld type for a 3-D elastic wave problem to a corresponding 2-D problem of waves in fluid media. We can start with Eq. (11.13) for the immersion case and note that if all the wave fields are 2-D waves propagating in a fluid we have

$$\tau_{ji}^{(1)}(\mathbf{x}, \omega) = -p^{(1)}(\mathbf{X}, \omega) \delta_{ji}, \quad \tau_{ji}^{(2)}(\mathbf{x}, \omega) = -p^{(2)}(\mathbf{X}, \omega) \delta_{ji}, \quad (11.80)$$

where $(p^{(1)}, p^{(2)})$ are the pressures in states (1) and (2), respectively, $\mathbf{X} = (x_1, x_2)$ is a position vector in two dimensions, and δ_{ji} is the Kronecker delta. Also, the surface, S_f , of the flaw in 3-D problems becomes a counterclockwise line integral over the line, C_f , of the flaw and the area of the sending element, S_A , becomes the length of the element, l_A . With these changes, Eq. (11.13) becomes

$$\begin{aligned} V(\mathbf{x}_s, \mathbf{x}_r, \omega) &= s_I(\omega) \frac{1}{\rho_1 c_1 l_A v_r^{(1)}(\omega) v_r^{(2)}(\omega)} \\ &\cdot \int_{C_f} (p^{(2)}(\mathbf{X}, \omega) v_n^{(1)}(\mathbf{X}, \omega) - p^{(1)}(\mathbf{X}, \omega) v_n^{(2)}(\mathbf{X}, \omega)) ds(\mathbf{X}), \end{aligned} \quad (11.81)$$

where $(v_n^{(1)}, v_n^{(2)})$ are the (outward) normal components of the velocity in states (1) and (2), $ds(\mathbf{X})$ is an arc length along C_f , and we have set $c_{p1} = c_1$ since we only have compressional waves in a fluid. Since

$$v_n = \frac{1}{i\omega\rho_2} \frac{\partial p}{\partial n} \quad (11.82)$$

Equation (11.81) can be rewritten as

$$V(\mathbf{x}_s, \mathbf{x}_r, \omega) = s_I(\omega) \frac{1}{i\omega\rho_1 c_1 l_A v_T^{(1)}(\omega) \rho_2 v_R^{(2)}(\omega)} \cdot \int_{C_f} \left(p^{(2)}(\mathbf{X}, \omega) \frac{\partial p^{(1)}}{\partial n}(\mathbf{X}, \omega) - p^{(1)}(\mathbf{X}, \omega) \frac{\partial p^{(2)}}{\partial n}(\mathbf{X}, \omega) \right) ds(\mathbf{X}). \quad (11.83)$$

Equations (11.81) and (11.83) are complete measurement models for a 2-D scalar wave problem. To obtain a reduced measurement model, at high frequencies we can write the incident pressure wave fields in states (1) and (2) at the flaw as

$$\begin{aligned} p^{(1);inc} &= P^{(1)}(\mathbf{X}_s, \mathbf{X}, \omega) \exp[i\omega T(\mathbf{X}_s, \mathbf{X})] \\ p^{(2)} &= P^{(2)}(\mathbf{X}_r, \mathbf{X}, \omega) \exp[i\omega T(\mathbf{X}_r, \mathbf{X})] \\ \frac{\partial p^{(2)}}{\partial n} &= ik_2 (\mathbf{e}^{(2)} \cdot \mathbf{n}) P^{(2)}(\mathbf{X}_r, \mathbf{X}, \omega) \exp[i\omega T(\mathbf{X}_r, \mathbf{X})]. \end{aligned} \quad (11.84)$$

Placing these results into Eq. (11.83) gives the measured voltage received at the centroid, \mathbf{X}_r , of an element from a sending element whose centroid is at \mathbf{X}_s :

$$\begin{aligned} V(\mathbf{X}_s, \mathbf{X}_r, \omega) &= s_I(\omega) \frac{1}{ik_2 l_A \rho_1 c_1 v_T^{(1)}} \frac{1}{\rho_2 c_2 v_R^{(2)}} \int_{C_f} P^{(2)}(\mathbf{X}_r, \mathbf{X}, \omega) \exp[i\omega T(\mathbf{X}_r, \mathbf{X})] \\ &\cdot \left(\frac{\partial p^{(1)}}{\partial n}(\mathbf{X}, \omega) - ik_2 (\mathbf{e}^{(2)} \cdot \mathbf{n}) p^{(1)}(\mathbf{X}, \omega) \right) ds(\mathbf{X}). \end{aligned} \quad (11.85)$$

Now, if we assume that the flaw is small so that at a fixed point, \mathbf{X}_0 , near the surface of the flaw the incident fields behave like quasi-plane waves of constant amplitude we have

$$\begin{aligned} P^{(1)}(\mathbf{X}_s, \mathbf{X}, \omega) \exp[i\omega T(\mathbf{X}_s, \mathbf{X})] &\cong P^{(1)}(\mathbf{X}_s, \mathbf{X}_0, \omega) \exp[i\omega T(\mathbf{X}_s, \mathbf{X}_0)] \\ &\cdot \exp[ik_2 \mathbf{e}^{(1)} \cdot (\mathbf{X} - \mathbf{X}_0)] \\ P^{(2)}(\mathbf{X}_r, \mathbf{X}, \omega) \exp[i\omega T(\mathbf{X}_r, \mathbf{X})] &\cong P^{(2)}(\mathbf{X}_r, \mathbf{X}_0, \omega) \exp[i\omega T(\mathbf{X}_r, \mathbf{X}_0)] \\ &\cdot \exp[ik_2 \mathbf{e}^{(2)} \cdot (\mathbf{X} - \mathbf{X}_0)] \end{aligned} \quad (11.86)$$

so Eq. (11.85) becomes

$$V(\mathbf{X}_s, \mathbf{X}_r, \omega) = s_f(\omega) \hat{P}^{(1)}(\mathbf{X}_s, \mathbf{X}_0, \omega) \hat{P}^{(2)}(\mathbf{X}_r, \mathbf{X}_0, \omega) \frac{1}{ik_2 l_A} \frac{\rho c}{\rho_2 c_2} \cdot \int_{C_f} \left(\frac{\partial \bar{p}^{(1)}}{\partial n}(\mathbf{X}', \omega) - ik_2 (\mathbf{e}^{(2)} \cdot \mathbf{n}) \bar{p}^{(1)}(\mathbf{X}', \omega) \right) \exp[ik_2 \mathbf{e}^{(2)} \cdot \mathbf{X}'] ds(\mathbf{X}'), \quad (11.87)$$

where $\mathbf{X}' = \mathbf{X} - \mathbf{X}_0$ is the position vector to a point on C_f as measured from \mathbf{X}_0 and

$$\begin{aligned} \hat{P}^{(1)}(\mathbf{X}_s, \mathbf{X}_0, \omega) &= \frac{P^{(1)}(\mathbf{X}_s, \mathbf{X}_0, \omega)}{\rho_1 c_1 v_T^{(1)}} \exp[i\omega T(\mathbf{X}_s, \mathbf{X}_0)] \\ \hat{P}^{(2)}(\mathbf{X}_r, \mathbf{X}_0, \omega) &= \frac{P^{(2)}(\mathbf{X}_r, \mathbf{X}_0, \omega)}{\rho c v_R^{(2)}} \exp[i\omega T(\mathbf{X}_r, \mathbf{X}_0)] \end{aligned} \quad (11.88)$$

are non-dimensional pressure amplitudes of the incident waves in states (1) and (2) at point \mathbf{X}_0 , and

$$\bar{p}^{(1)} = \frac{p^{(1)}}{P^{(1)}(\mathbf{X}_s, \mathbf{X}_0, \omega) \exp i\omega T(\mathbf{X}_s, \mathbf{X}_0)} \quad (11.89)$$

is the pressure in state (1) normalized by the incident pressure of a quasi-plane wave at the flaw so that it is the pressure due to an incident wave of unit pressure amplitude. Note that the density and wave speed at the sending element, (ρ, c) are the values measured at the receiving element, and (ρ_2, c_2) are the density and wave speed in the material surrounding the flaw, which we have allowed again to be different for generality.

In two-dimensional fluid (scalar) problems the scattered pressure in the far field of a flaw, p_{scatt} , due to a planar pressure wave of unit amplitude is given by

$$p_{scatt} = A(\mathbf{e}_{inc}; \mathbf{e}_{scat}) \frac{\exp(ikR)}{\sqrt{R}}, \quad (11.90)$$

where the far field scattering amplitude, A , of the waves scattered in the \mathbf{e}_{scat} direction is given by

$$A(\mathbf{e}_{inc}; \mathbf{e}_{scat}) = -\sqrt{\frac{i}{8\pi k_2}} \int_{C_f} \left\{ \frac{\partial \bar{p}}{\partial n} + ik_2 (\mathbf{e}_{scat} \cdot \mathbf{n}) \bar{p} \right\} \exp[-ik_2 \mathbf{e}_{scat} \cdot \mathbf{X}'] ds. \quad (11.91)$$

Since $\mathbf{e}_{scat} = -\mathbf{e}^{(2)}$, placing Eq. (11.91) into Eq. (11.87) gives

$$V(\mathbf{X}_s, \mathbf{X}_r, \omega) = s_I(\omega) \hat{P}^{(1)}(\mathbf{X}_s, \mathbf{X}_0, \omega) \hat{P}^{(2)}(\mathbf{X}_r, \mathbf{X}_0, \omega) A(\mathbf{e}_{inc}; \mathbf{e}_{scat}) \left[\frac{1}{-ik_2 l_A} \frac{\rho c}{\rho_2 c_2} \sqrt{-8\pi i k_2} \right]. \quad (11.92)$$

Equation (11.92) is a measurement model of the Thompson–Gray type for 2-D problems.

We can also develop approximate measurement models suitable for imaging both large and small flaws. Consider first the large flaw case where we return to Eq. (11.85). In the Kirchhoff approximation on the lit face of the flaw we have

$$p^{(1)} = P^{(1)}(\mathbf{X}_s, \mathbf{X}, \omega) \exp[i\omega T(\mathbf{X}_s, \mathbf{X})] \{1 + R_{23}\} \\ \frac{\partial p^{(1)}}{\partial n} = ik_2 P^{(1)}(\mathbf{X}_s, \mathbf{X}, \omega) \exp[i\omega T(\mathbf{X}_s, \mathbf{X})] \{(\mathbf{e}_{inc} \cdot \mathbf{n}) + R_{23}(\mathbf{e}_r \cdot \mathbf{n})\}, \quad (11.93)$$

where R_{23} is the plane wave reflection coefficient (based on a pressure ratio) and \mathbf{e}_r is a unit vector in the direction of the specular reflected wave. Placing these results into Eq. (11.85) gives

$$V(\mathbf{X}_s, \mathbf{X}_r, \omega) = s_I(\omega) \frac{1}{l_A \rho_1 c_1 v_T^{(1)}} \frac{1}{\rho_2 c_2 v_R^{(2)}} \int_{C_{lit}} P^{(2)}(\mathbf{X}_r, \mathbf{X}, \omega) \exp[i\omega T(\mathbf{X}_r, \mathbf{X})] \\ \cdot P^{(1)}(\mathbf{X}_s, \mathbf{X}, \omega) \exp[i\omega T(\mathbf{X}_s, \mathbf{X})] \{(\mathbf{e}_{inc} \cdot \mathbf{n}) + R_{23}(\mathbf{e}_r \cdot \mathbf{n}) - (\mathbf{e}^{(2)} \cdot \mathbf{n})(1 + R_{23})\} ds(\mathbf{X}). \quad (11.94)$$

But at a stationary phase point Snell's law is satisfied and we have $\mathbf{e}_r = -\mathbf{e}^{(2)}$, $(\mathbf{e}_{inc} \cdot \mathbf{n}) = -(\mathbf{e}_r \cdot \mathbf{n})$ so that Eq. (11.94) becomes

$$V(\mathbf{X}_s, \mathbf{X}_r, \omega) = s_I(\omega) \frac{1}{l_A \rho_1 c_1 v_T^{(1)}} \frac{1}{\rho_2 c_2 v_R^{(2)}} \int_{C_{lit}} 2R_{23}(\mathbf{e}_r \cdot \mathbf{n}) P^{(1)}(\mathbf{X}_s, \mathbf{X}, \omega) \exp[i\omega T(\mathbf{X}_s, \mathbf{X})] \\ \cdot P^{(2)}(\mathbf{X}_r, \mathbf{X}, \omega) \exp[i\omega T(\mathbf{X}_r, \mathbf{X})] ds(\mathbf{X}). \quad (11.95)$$

Normalizing the pressure amplitude terms, i.e. defining

$$\tilde{P}^{(1)}(\mathbf{X}_s, \mathbf{X}, \omega) = \frac{P^{(1)}(\mathbf{X}_s, \mathbf{X}, \omega)}{\rho_1 c_1 v_T^{(1)}}, \quad \tilde{P}^{(2)}(\mathbf{X}_r, \mathbf{X}, \omega) = \frac{P^{(2)}(\mathbf{X}_r, \mathbf{X}, \omega)}{\rho c v_R^{(2)}} \quad (11.96)$$

and letting

$$\phi(\mathbf{X}_s, \mathbf{X}_r, \mathbf{X}) = T(\mathbf{X}_s, \mathbf{X}) + T(\mathbf{X}_r, \mathbf{X}) \quad (11.97)$$

we find

$$V(\mathbf{X}_s, \mathbf{X}_r, \omega) = s_I(\omega) \frac{2\rho c}{l_A \rho_2 c_2} \cdot \int_{C_{lit}} R_{23}(\mathbf{e}_r \cdot \mathbf{n}) \tilde{P}^{(1)}(\mathbf{X}_s, \mathbf{X}, \omega) \tilde{P}^{(2)}(\mathbf{X}_r, \mathbf{X}, \omega) \exp[i\omega\phi(\mathbf{X}_s, \mathbf{X}_r, \mathbf{X})] ds(\mathbf{X}). \quad (11.98)$$

For pulse-echo responses, $\tilde{P}^{(1)} = \tilde{P}^{(2)}$, $(\mathbf{e}_r \cdot \mathbf{n}) = 1$, $\phi = 2T(\mathbf{X}_c, \mathbf{X})$, with $\mathbf{X}_s = \mathbf{X}_r = \mathbf{X}_c$ and Eq. (11.98) becomes

$$V(\mathbf{X}_c, \omega) = s_I(\omega) \frac{2\rho c}{l_A \rho_2 c_2} \int_{C_{lit}} R_{23}[\tilde{P}^{(1)}(\mathbf{X}_c, \mathbf{X}, \omega)]^2 \exp[2i\omega T(\mathbf{X}_c, \mathbf{X})] ds(\mathbf{X}). \quad (11.99)$$

Equations (11.98) and (11.99) are approximate measurement models suitable for the development of images of large flaws in 2-D problems. These equations are the counterparts of Eqs. (11.62) and (11.63), respectively.

For the small flaw case, we have (see Eq. (11.64))

$$\begin{aligned} \phi(\mathbf{X}_s, \mathbf{X}_r, \mathbf{X}) &\cong \phi(\mathbf{X}_s, \mathbf{X}_r, \mathbf{X}_0) + [\nabla T(\mathbf{X}_s, \mathbf{X}) + \nabla T(\mathbf{X}_r, \mathbf{X})] \cdot (\mathbf{X} - \mathbf{X}_0) \\ &= \phi(\mathbf{X}_s, \mathbf{X}_r, \mathbf{X}_0) + (\mathbf{e}^{(1)} + \mathbf{e}^{(2)}) \cdot (\mathbf{X} - \mathbf{X}_0) / c_2. \end{aligned} \quad (11.100)$$

so that Eq. (11.99) becomes

$$\begin{aligned} V(\mathbf{X}_s, \mathbf{X}_r, \omega) &= s_I(\omega) \tilde{P}^{(1)}(\mathbf{X}_s, \mathbf{X}_0, \omega) \exp[i\omega T(\mathbf{X}_s, \mathbf{X}_0)] \tilde{P}^{(2)}(\mathbf{X}_r, \mathbf{X}_0, \omega) \exp[i\omega T(\mathbf{X}_r, \mathbf{X}_0)] \\ &\cdot \frac{2\rho c}{l_A \rho_2 c_2} \int_{C_{lit}} R_{23}(\mathbf{e}_r \cdot \mathbf{n}) \exp[ik_2(\mathbf{e}^{(1)} + \mathbf{e}^{(2)}) \cdot (\mathbf{X} - \mathbf{X}_0)] ds(\mathbf{X}). \end{aligned} \quad (11.101)$$

which reduces in pulse-echo to

$$\begin{aligned} V(\mathbf{X}_c, \omega) &= s_I(\omega) [\tilde{P}^{(1)}(\mathbf{X}_c, \mathbf{X}_0, \omega)]^2 \exp[2i\omega T(\mathbf{X}_c, \mathbf{X}_0)] \\ &\cdot \frac{2\rho c}{l_A \rho_2 c_2} \int_{C_{lit}} \exp[2ik_2 \mathbf{e}^{(1)} \cdot (\mathbf{X} - \mathbf{X}_0)] ds(\mathbf{X}). \end{aligned} \quad (11.102)$$

Equations (11.101) and (11.102) are the approximate measurement models suitable for generating images of small flaws for the 2-D scalar wave case being considered in this section. Note that

$$\begin{aligned} \tilde{P}^{(1)}(\mathbf{X}_s, \mathbf{X}_0, \omega) \exp[i\omega T(\mathbf{X}_s, \mathbf{X}_0)] &= \hat{P}^{(1)}(\mathbf{X}_s, \mathbf{X}_0, \omega) \\ \tilde{P}^{(2)}(\mathbf{X}_r, \mathbf{X}_0, \omega) \exp[i\omega T(\mathbf{X}_r, \mathbf{X}_0)] &= \hat{P}^{(2)}(\mathbf{X}_r, \mathbf{X}, \omega) \end{aligned} \quad (11.103)$$

(see Eqs. (11.88) and (11.96) with $\mathbf{X} = \mathbf{X}_0$) so that Eq. (11.101) also can be written as

$$V(\mathbf{X}_s, \mathbf{X}_r, \omega) = s_I(\omega) \hat{P}^{(1)}(\mathbf{X}_s, \mathbf{X}_0, \omega) \hat{P}^{(2)}(\mathbf{X}_r, \mathbf{X}_0, \omega) \cdot \frac{2\rho c}{l_A \rho_2 c_2 c_{th}} \int R_{23}(\mathbf{e}_r \cdot \mathbf{n}) \exp[ik_2(\mathbf{e}^{(1)} + \mathbf{e}^{(2)}) \cdot (\mathbf{X} - \mathbf{X}_0)] ds(\mathbf{X}), \quad (11.104)$$

which is in the same form as the Thompson–Gray type of measurement model of Eq. (11.92). The integral in Eq. (11.104) is of the form

$$I = \int_C f(X) \exp[ik_2 \mathbf{g} \cdot (\mathbf{X} - \mathbf{X}_0)] ds(\mathbf{X}) \quad (11.105)$$

which, when evaluated by the method of stationary phase for convex flaw, gives

$$I \cong f(\mathbf{X}_{stat}) \exp[ik_2 \mathbf{g} \cdot (\mathbf{X}_{stat} - \mathbf{X}_0)] \sqrt{\frac{2\pi i R_p}{k_2 |\mathbf{g} \cdot \mathbf{n}|}} \quad (11.106)$$

at the stationary phase point, \mathbf{X}_{stat} , with R_p the curvature of the flaw at that point and \mathbf{n} is the outward unit normal to the flaw surface. The vector \mathbf{g} is parallel to \mathbf{n} at the stationary phase point. Identifying

$$f = R(\mathbf{e}_r \cdot \mathbf{n}), \mathbf{g} = \mathbf{e}^{(1)} + \mathbf{e}^{(2)} = \mathbf{e}_{inc} - \mathbf{e}_r \quad (11.107)$$

Equation (11.104) becomes

$$V(\mathbf{X}_s, \mathbf{X}_r, \omega) = s_I(\omega) \hat{P}^{(1)}(\mathbf{X}_s, \mathbf{X}_0, \omega) \hat{P}^{(2)}(\mathbf{X}_r, \mathbf{X}_0, \omega) \left\{ \frac{\sqrt{R_p}}{\sqrt{|\mathbf{g} \cdot \mathbf{n}|}} R_{23}(\mathbf{e}_r \cdot \mathbf{n}) \exp[ik_2 \mathbf{g} \cdot (\mathbf{X}_{stat} - \mathbf{X}_0)] \right\} \cdot \left[\frac{1}{-ik_2 l_A} \frac{c}{\rho_2 c_2} \sqrt{-8\pi i k_2} \right]. \quad (11.108)$$

Comparing Eq. (11.108) with the Thompson–Gray model of Eq. (11.92) we see that the scattering amplitude is just

$$A(\mathbf{e}_{inc}, \mathbf{e}_{scat}) = \sqrt{\frac{R_p}{|\mathbf{g} \cdot \mathbf{n}|}} R_{23}(\mathbf{e}_r \cdot \mathbf{n}) \exp[ik_2 \mathbf{g} \cdot (\mathbf{X}_{stat} - \mathbf{X}_0)] \quad (11.109)$$

with $\mathbf{e}_{scat} = \mathbf{e}_r$. This result is the specular point response of the flaw in 2-D, comparable to the 3-D result obtained in Eq. (11.32).

References

1. B.A. Auld, General electromechanical reciprocity relations applied to the calculation of elastic wave scattering coefficients. *Wave Motion* **1**, 3–10 (1979)
2. R.B. Thompson, T.A. Gray, A model relating ultrasonic scattering measurements through liquid-solid interfaces to unbounded medium scattering amplitudes. *J. Acoust. Soc. Am.* **74**, 140–146 (1983)
3. J.D. Achenbach, *Reciprocity in Elastodynamics* (Cambridge University Press, Cambridge, 2003)
4. J.T. Fokkema, P.M. Van den Berg, *Seismic Applications of Acoustic Reciprocity* (Elsevier, New York, 1993)
5. D.O. Thompson, D.E. Chimenti (ed.), *Review of Progress in Quantitative Nondestructive Evaluation* (Plenum Press, New York, 1981–present) (American Institute of Physics, Melville, NY, Past volumes)
6. J.M. Carcione, *Wave Fields in Real Media: Wave Propagation in Anisotropic, Anelastic, and Porous Media* (Elsevier, Oxford, 2001)

Chapter 12

Imaging with Phased Arrays—An Introduction

The capabilities of a phased array to electronically tailor the ultrasonic waves on either transmission or reception (or both) also allow an array to have a rich set of imaging capabilities. In this chapter we will first describe several ad-hoc types of imaging methods that are widely used—the synthetic aperture focusing technique (SAFT) and the total focusing method (TFM). In both of those methods images are obtained by shifting and combining the measured time domain (A-scan) responses of the array elements. They are examples of a class of imaging techniques that are called *delay and sum imaging*. However, we will also examine the imaging process in more detail in this chapter to better understand how a flaw response contributes to an image. This perspective is important since in both this chapter and Chap. 13 we will use models to describe images of a flaw that can be explicitly related to the scattering properties of a flaw. We will call these models *imaging measurement models* (IMMs) since they will be based on inverting the measurement models of the Auld and Thompson-Gray types discussed in Chap. 11. Imaging measurement models will give us a clearer picture of why popular imaging methods such as SAFT and TFM work so well and they will allow us to delineate the capabilities and limitations of delay and sum imaging methods.

12.1 SAFT Imaging

The synthetic aperture focusing technique (SAFT) was originally developed as an imaging technique for use with single element transducers where the transducer was scanned along a line and, at a set of sampling points along that line, the pulse-echo responses from a scatterer were collected and used to form an image [1]. This same type of data collection procedure and imaging can obviously also be implemented with a linear array of N elements as shown in Fig. 12.1 where at each element, whose centroid is located at \mathbf{X}_{cn} $n = (1, \dots, N)$, the pulse-echo voltage response of the scatterer, $V(\mathbf{X}_{cn}, t)$, as a function of the time, t , is measured and stored. To form up a 2-D image one can set up a 2-D (x, z) grid of image points, such as the point \mathbf{Y} shown in Fig. 12.2 and calculate the travel time from the centroid \mathbf{X}_{cn} of each

Fig. 12.1 Collection of the pulse-echo responses of a flaw with a linear array

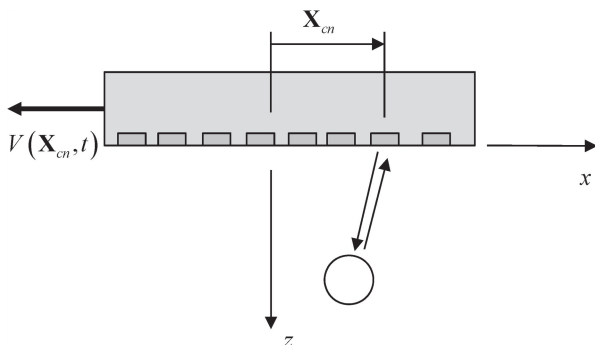
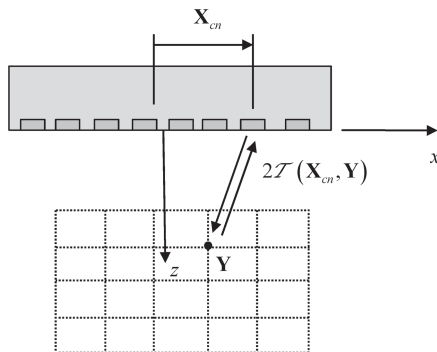


Fig. 12.2 The SAFT image formation process, where the two-way travel time from each element to an image point is calculated

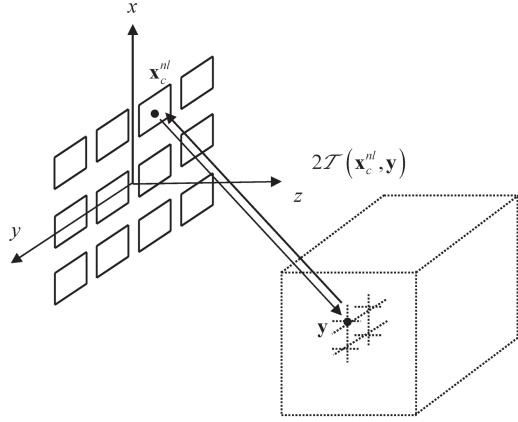


element to those image points and back, $2T(X_{cn}, Y)$, where $T(X_{cn}, Y)$ is the one-way travel time between these points. At each image point the stored voltage signals are then each advanced by these two-way travel times and summed. The amplitude of the summed signal at time $t = 0$ is then taken as the value of the image of the scatterer, $I_{SAFT}(Y)$, at that point, so that

$$I_{SAFT}(Y) = \sum_{n=1}^N V(X_{cn}, t + 2T(X_{cn}, Y)) \Big|_{t=0}. \quad (12.1)$$

This method can be understood in terms of our discussion of the time delay laws in Chaps. 5 and 8. On sound generation, application of the one-way time advances $T(X_{cn}, Y)$ would focus the waves from each element at point Y . Application of these same time advances on reception would likewise focus the received signals to appear as if they came from point Y . If a flaw scattering source exists at Y we would expect to see a large value for the summed signals at $t = 0$ and if a source was not present at this point, we would expect to see a correspondingly small value. Thus, it is reasonable to take the summed value of Eq. (12.1) as a value that describes the image of the flaw(s) present. Note that in this process we have not invoked the physics of the measurement process except for the travel times involved.

Fig. 12.3 The SAFT image formation process for generating a 3-D image with a 2-D array



Thus, the SAFT image is an ad-hoc approach and it is somewhat misleading to call the image formed an image of the flaw since the formed image also depends on the element system functions of the phased array measurement system, the wave propagation behavior to the flaw and back, and the interactions with the flaw, and the SAFT method does not characterize or compensate for any of those parameters. Even so, SAFT has proven to be a powerful imaging method that has been widely used for many years [2–4].

A frequency domain version of SAFT can also be developed since if we express the measured voltage signals in terms of their Fourier transforms, Eq. (12.1) becomes

$$I_{SAFT}(\mathbf{Y}) = \sum_{n=1}^N \frac{1}{2\pi} \int_{-\infty}^{+\infty} V(\mathbf{X}_{cn}, \omega) \exp[-i\omega(t + 2T(\mathbf{X}_{cn}, \mathbf{Y}))] d\omega \Big|_{t=0} \quad (12.2)$$

$$= 2\text{Re} \left\{ \sum_{n=1}^N \frac{1}{2\pi} \int_0^{+\infty} V(\mathbf{X}_{cn}, \omega) \exp[-2i\omega T(\mathbf{X}_{cn}, \mathbf{Y}_p)] d\omega \right\},$$

where Re indicates “real part of”. If we discretize the frequency integration, we have

$$I_{SAFT}(\mathbf{Y}) = 2\text{Re} \left\{ \frac{\Delta\omega}{2\pi} \sum_{m=1}^M \sum_{n=1}^N V(\mathbf{X}_{cn}, \omega_m) \exp[-2i\omega_m T(\mathbf{X}_{cn}, \mathbf{Y})] \right\}. \quad (12.3)$$

SAFT imaging can also be used with a 2-D array to generate a 3-D image of a flaw. The image formation process is identical to the 2-D case we just discussed. In this case, an image, $I_{SAFT}(\mathbf{y})$, at an image point, \mathbf{y} , in three dimensions (see Fig. 12.3) for an array with L_1 elements in the x -direction and L_2 elements in the y -direction is given by

$$I_{SAFT}(\mathbf{y}) = \sum_{n=1}^{L_1} \sum_{l=1}^{L_2} V(\mathbf{x}_c^{nl}, t + 2T(\mathbf{x}_c^{nl}, \mathbf{y})) \Big|_{t=0} \quad (12.4)$$

Fig. 12.4 Collection of the responses of all sending/receiving element pairs in an array (full matrix capture)

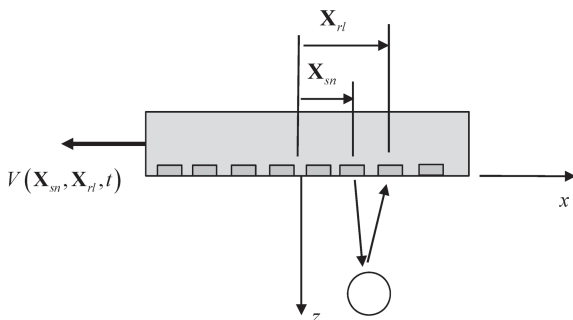
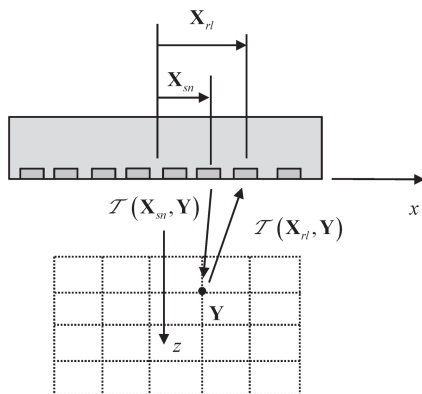


Fig. 12.5 The total focusing method (TFM) image formation process, where the travel times for various pairs of sending/receiving elements to an image point are calculated



or, in the frequency domain,

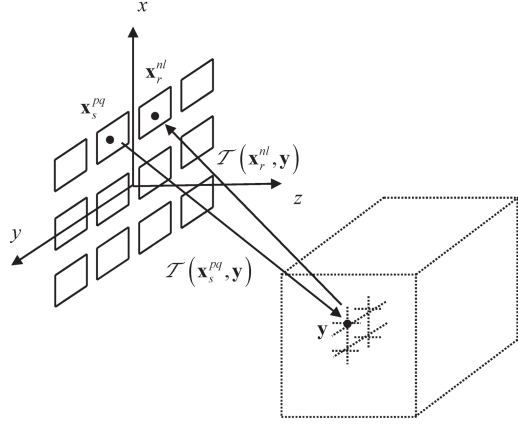
$$I_{SAFT}(\mathbf{y}) = 2\text{Re} \left\{ \frac{\Delta\omega}{2\pi} \sum_{m=1}^M \sum_{n=1}^{L_1} \sum_{l=1}^{L_2} V(\mathbf{x}_c^{nl}, \omega_m) \exp[-2i\omega_m T(\mathbf{x}_c^{nl}, \mathbf{y})] \right\}. \quad (12.5)$$

12.2 TFM Imaging

The SAFT method uses only the pulse-echo responses of the array so that it does not take advantage of the much larger number of responses for various pairs of elements that can be recorded with an array. The total focusing method (TFM) does utilize all combinations of sending and receiving elements, also called *full matrix capture*, to form an image [5].

Consider the formation of a TFM image with a linear array (Fig. 12.4) with N elements. In this case we record all the voltage time domain signals $V(\mathbf{X}_{sn}, \mathbf{X}_{rl}, t)$, ($n = 1, \dots, N$), ($l = 1, \dots, N$) for a sending element whose centroid is located at \mathbf{X}_{sn} and a receiving element whose centroid is at \mathbf{X}_{rl} as shown in Fig. 12.4. In the image formation process we again set up a grid of image points \mathbf{Y} as shown in Fig. 12.5,

Fig. 12.6 The total focusing method (TFM) imaging process for generating a 3-D image with a 2-D array



advance all these sending/receiving element pair responses by the travel times $T(\mathbf{X}_{sn}, \mathbf{Y}) + T(\mathbf{X}_{rl}, \mathbf{Y})$ and then calculate their sum at time $t = 0$ to form an image, $I_{TFM}(\mathbf{Y})$, giving

$$I_{TFM}(\mathbf{Y}) = \sum_{n=1}^N \sum_{l=1}^N V(\mathbf{X}_{sn}, \mathbf{X}_{rl}, t + T(\mathbf{X}_{sn}, \mathbf{Y}) + T(\mathbf{X}_{rl}, \mathbf{Y})) \Big|_{t=0}. \quad (12.6)$$

Transforming the measured time domain signals to the frequency domain and evaluating at M positive frequencies, as in the SAFT method, we find the alternate frequency domain TFM form:

$$I_{TFM}(\mathbf{Y}) = 2\text{Re} \left\{ \frac{\Delta\omega}{2\pi} \sum_{m=1}^M \sum_{n=1}^N \sum_{l=1}^N V(\mathbf{X}_{sn}, \mathbf{X}_{rl}, \omega_m) \exp[-i\omega_m T(\mathbf{X}_{sn}, \mathbf{Y}) - i\omega_m T(\mathbf{X}_{rl}, \mathbf{Y})] \right\}. \quad (12.7)$$

If 3-D TFM imaging is done with a 2-D array having L_1 elements in the x -direction and L_2 elements in the y -direction then the image formation process is shown in Fig. 12.6 and the image, $I_{TFM}(\mathbf{y})$, is

$$I_{TFM}(\mathbf{y}) = \sum_{n=1}^{L_1} \sum_{l=1}^{L_2} \sum_{p=1}^{L_1} \sum_{q=1}^{L_2} V(\mathbf{x}_s^{pq}, \mathbf{x}_r^{nl}, t + T(\mathbf{x}_s^{pq}, \mathbf{y}) + T(\mathbf{x}_r^{nl}, \mathbf{y})) \Big|_{t=0} \quad (12.8)$$

and in the frequency domain

$$I_{TFM}(\mathbf{y}) = 2\text{Re} \left\{ \frac{\Delta\omega}{2\pi} \sum_{m=1}^M \sum_{n=1}^{L_1} \sum_{l=1}^{L_2} \sum_{p=1}^{L_1} \sum_{q=1}^{L_2} V(\mathbf{x}_s^{pq}, \mathbf{x}_r^{nl}, \omega_m) \exp[-i\omega_m T(\mathbf{x}_s^{pq}, \mathbf{y}) - i\omega_m T(\mathbf{x}_r^{nl}, \mathbf{y})] \right\}. \quad (12.9)$$

But note that the large number of calculations involved makes these 2-D and 3-D TFM formulations computationally much more expensive than their SAFT counterparts.

Fig. 12.7 Waves of different types scattered from a flaw, including waves directly reflected from the flaw surface, waves that travel around the flaw surface, and waves that refract into the flaw and then re-emerge

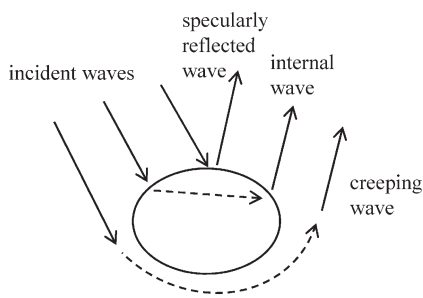
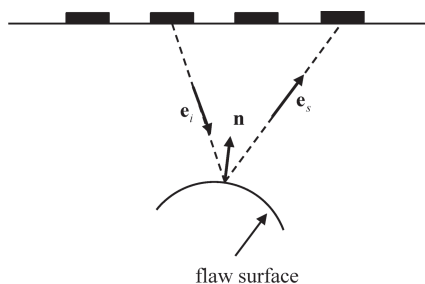


Fig. 12.8 Waves that travel from one element of an array to another via a direct reflection from the flaw surface



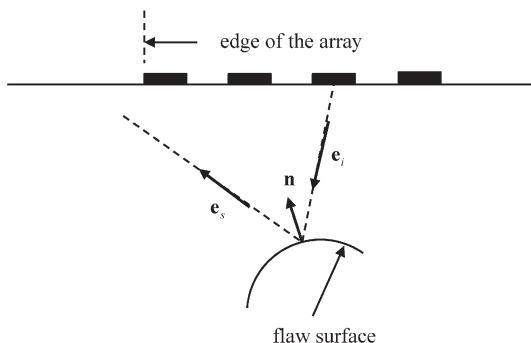
12.3 The Image Formation Process

While the images described in the previous sections of this Chapter can provide us with some visual measurements of a flaw response, all of those images are produced in ad-hoc fashion from the measured data and normally there is no significance placed on the values present in the image. In this section we want to describe in general terms some of the characteristics of the waves scattered from flaws and received by arrays so the underlying physics associated with image formation process can be better understood and used as the basis for more quantitative imaging.

When ultrasonic waves from an array (or in fact any type of transducer) interact with flaws, scattered waves of many different types may be present. By “type” we do not mean here just wave mode types such P-waves or S-waves but also different types of interactions of the incident wave with the flaw, as shown in Fig. 12.7. These interactions include waves directly reflected from the flaw surface, waves that travel around the flaw (so-called *creeping waves*), waves that may involve one or more internal interactions within the flaw itself (for inclusions), and others. However, the waves directly reflected (and possibly mode-converted) from the flaw surface have a special importance. Figure 12.8 shows a situation where a wave is generated by one element of an array and then is directly reflected by a flaw surface to another array element.

The unit vector \mathbf{e}_i describes the incident wave direction and a unit vector \mathbf{e}_s describes the scattering direction back to another element. The unit normal to the flaw where \mathbf{e}_i intersects the flaw surface is \mathbf{n} . At high frequencies, there are points on the flaw surface where these directly reflected waves have significant amplitudes

Fig. 12.9 The case where the scattered response from a specular point on the flaw surface returns to a point beyond the edge of the array and thus is not received



and these particular amplitudes are often larger than the amplitudes of any of the other wave types present. These are called *specular reflection points* and they occur when the vector $\mathbf{q} = \mathbf{e}_i / c_\beta - \mathbf{e}_s / c_\alpha$ is parallel to the unit normal, \mathbf{n} , where c_β is the wave speed of the incident wave and c_α is the wave speed of the scattered wave [Schmerr]. The incident and scattered waves at these specular points satisfy Snell's law since if

$$\mathbf{e}_i / c_\beta - \mathbf{e}_s / c_\alpha = \lambda \mathbf{n}, \quad (12.10)$$

then for any unit vector, \mathbf{t} , that is tangent to the surface and lies in the plane of incidence (the plane containing both \mathbf{e}_i and \mathbf{n}), we must have

$$(\mathbf{e}_i \cdot \mathbf{t}) / c_\beta = (\mathbf{e}_s \cdot \mathbf{t}) / c_\alpha, \quad (12.11)$$

which is just a statement of Snell's law.

These specular point responses play particularly important roles since, as mentioned in the previous chapter, when all the elements of the array are being used as transmitters and receivers the largest signals received by the array often come from a collection of these specular points on the flaw surface. Likewise, when an image is formed from the ultrasonic array data it is often predominantly an image of this collection of specular points. Of course, there may be specular points on the surface where the scattered direction for one or more elements that are transmitting lies outside the boundary of the array as shown in Fig. 12.9. In this case we expect the amplitude of the response seen in the image will be reduced and in the extreme case where no specular points exists for any combination of transmitting or receiving elements of the array, the contributions of these points to an image will be absent. This does not mean that in this case there will be no image generated at all because of the presence of responses from wave types other than these directly reflected waves. Figure 12.10 shows an example of this situation where a flat crack is oriented so that all the possible specular points on the crack will involve directly reflected waves that are not received by the array. However, cracks also generate waves that arise from the crack edges. Although these waves are typically smaller in amplitude than the directly reflected waves they can travel in many directions so that they can be received by the elements of the array (see Fig. 12.11) even when the

Fig. 12.10 A crack being interrogated by an array where the specular point responses are absent. However, waves also are generated by diffraction from the crack edges, as shown, which can be used to form an image of the crack edge

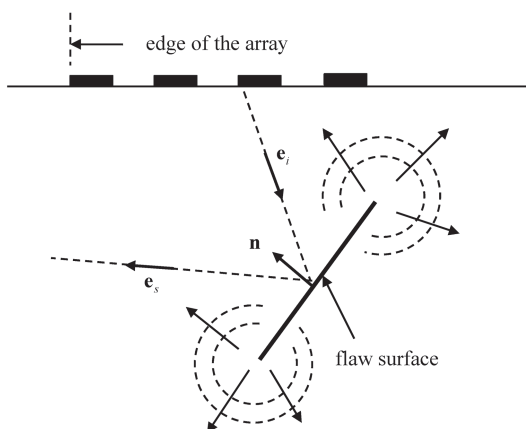
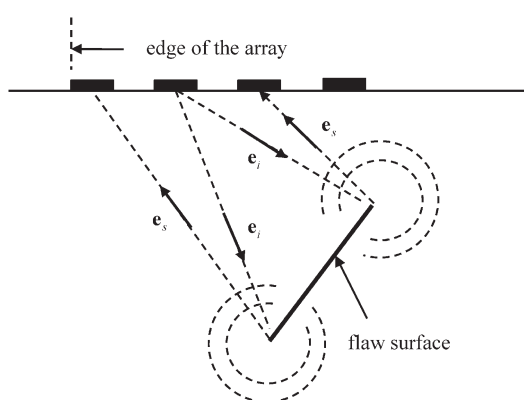


Fig. 12.11 The same configuration of Fig. 12.10 showing the generation and reception of the edge waves from the crack



specular point responses are absent. When processed, these edge waves can form up an image of the crack edge.

Both specularly reflected waves and edge waves play an important role in the development of the imaging measurement model (IMM) we will discuss in the next section and the more general models considered in Chap. 13. These imaging measurement models are based on the Kirchhoff approximation which can predict both specularly reflected and edge wave contributions to an image. We have discussed the Kirchhoff approximation in Chap. 11, where we showed that with this approximation we could extract explicitly the far field scattering amplitude specular response of a small flaw and develop measurement models for the specular responses of more general flaws. In Chap. 11 we saw that the Kirchhoff approximation is based on a *single scattering approximation*. By this we mean that the Kirchhoff approximation assumes that only waves that are directly reflected (scattered) from the flaw surface are considered. It is this single scattering nature of the Kirchhoff approximation that permits one to directly image explicit flaw properties from the measured flaw response and we will see that this single scattering approximation

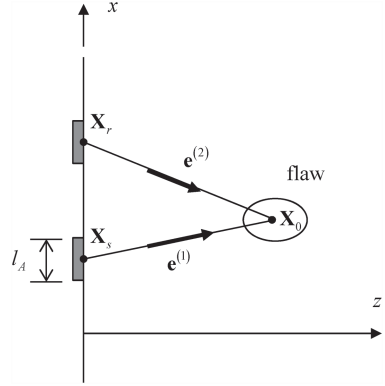
includes both the specular point responses and the responses of corners or edges of the flaws present. If other wave types are present they can also contribute to the images generated with an IMM, but in the form of image reconstruction artifacts or “noise”. Other wave types, such as the creeping waves of Fig. 12.7, for example, are not directly scattered from the flaw surface or edge so that they will appear in a flaw image as originating from some other location which may not coincide with any part of the real flaw geometry.

Considering the specular reflections and edge waves as the main contributors to the formation of ultrasonic images is only one view of how images are produced. In the geophysics community, for example, another viewpoint is to treat the image formation process as one where the scattering potential of the flaw is the fundamental quantity that is imaged instead [6]. In this view, one often uses the Born approximation instead of the Kirchhoff approximation to model how flaw responses and images are formed. Although the Born approximation is a low frequency, weak-scattering approximation that assumes that the flaw and the surrounding host material have nearly the same material properties, like the Kirchhoff approximation the Born approximation is a single scattering approximation where only direct interactions of the incident waves with the flaw surface are considered. Thus, it is not surprising that one can relate the scattering potential to the specular reflectivity of the flaw surface present in the Kirchhoff approximation [6] and thus connect the two viewpoints. However, the Born approximation viewpoint is somewhat misleading as it implies that for volumetric flaws in a band-limited and aperture-limited real measurement one is viewing a proper (but “fuzzy”) image of the entire flaw (or, to be more precise, a proper but “fuzzy” image of both the front and back surface of the flaw). We will see in Sect. 12.5, that this is not true except in the weak scattering limit. Like the Kirchhoff approximation, the Born approximation leads to a linear relationship between the specular reflectivity (or scattering potential) and the measured flaw response. To account for other types of flaw responses properly, (such as multiple internal reflections within a flaw, for example) one must resort to more complex (and likely non-linear) image formation methods. In this book we will only consider linear image formation methods as these linear methods form the basis of some of the most successful ultrasonic imaging algorithms in general use and are directly and simply related to the physics of the wave propagation and scattering present in an ultrasonic measurement system.

12.4 Far Field Imaging Measurement Models (2-D)

In Chap. 13 we will use the general measurement models developed in Chap. 11 to describe explicitly the formation of images of the surface reflectivity of flaws and of other surfaces present (such as the back surface of a part, for example) in an ultrasonic measurement. However, we can gain significant insight into these imaging methods by first considering the special cases considered in Chap. 11 where the flaw is small enough so that the incident wave fields do not vary significantly over

Fig. 12.12 A 1-D array radiating and receiving waves from a 2-D flaw in a fluid



the flaw surface. In this section we will examine this small flaw case for 2-D waves in a fluid (see Fig. 12.12) since this is a simple case but one that illustrates most of the central points in image formation in more complex problems. This approach to imaging follows the same approach we used in earlier Chapters where we first discussed sound beams, delay laws, etc. for 2-D fluid problems before considering the more complex 3-D cases.

We will assume that an element whose centroid is located on the x -axis at $\mathbf{X}_r = (x_r, 0)$ (Fig. 12.12) receives a scattered wave signal from a small flaw which is excited by an element whose centroid is also located on the x -axis at $\mathbf{X}_s = (x_s, 0)$. From Eqs. (11.102) and (11.104) the voltage received from the specular responses of the flaw surface for this pair of elements can be written as

$$V(\mathbf{X}_s, \mathbf{X}_r, \omega) = s_I(\omega) \hat{P}^{(1)}(\mathbf{X}_s, \mathbf{X}_0, \omega) \hat{P}^{(2)}(\mathbf{X}_r, \mathbf{X}_0, \omega) \cdot \frac{2\rho c}{l_A \rho_2 c_2 c_{lit}} \int R_{23}(\mathbf{e}_r \cdot \mathbf{n}) \exp i k_2 (\mathbf{e}^{(1)} + \mathbf{e}^{(2)}) \cdot (\mathbf{X} - \mathbf{X}_0) d\mathbf{s}(\mathbf{X}). \quad (12.12)$$

We will first specialize this equation to where we receive only pulse-echo responses in a single medium. Then $\rho = \rho_1 = \rho_2, c = c_1 = c_2, \mathbf{X}_r = \mathbf{X}_s = \mathbf{X}_c, \hat{P}^{(1)} = \hat{P}^{(2)} = \hat{P}(\mathbf{X}_c, \mathbf{X}_0, \omega)$, and $\mathbf{e}_r \cdot \mathbf{n} = 1, \mathbf{e}^{(1)} = \mathbf{e}^{(2)} = \mathbf{e}$, and we find

$$V(\mathbf{X}_c, \omega) = s_I(\omega) \hat{P}(\mathbf{X}_c, \mathbf{X}_0, \omega)^2 \frac{2}{l_A c_{lit}} \int R_{23} \exp 2ik_2 \mathbf{e} \cdot \mathbf{X}' d\mathbf{s}(\mathbf{X}'), \quad (12.13)$$

where $\mathbf{X}' = \mathbf{X} - \mathbf{X}_0$ is a 2-D position vector, $\mathbf{X}' = (x', z')$ measured from a fixed point, $\mathbf{X}_0 = (x_0, z_0)$, (usually taken as the “center” of the flaw). Here the pressure term, $\hat{P}(\mathbf{X}_c, \mathbf{X}_0, \omega)$, is just the normalized pressure of the incident wave generated at point \mathbf{X}_0 by an element whose centroid is located at point \mathbf{X}_c , i.e. (see Eq. (11.88))

$$\hat{P}(\mathbf{X}_c, \mathbf{X}_0, \omega) = \frac{P(\mathbf{X}_c, \mathbf{X}_0, \omega)}{\rho_1 c_1 v_T^{(1)}} \exp i\omega T(\mathbf{X}_c, \mathbf{X}_0). \quad (12.14)$$

Now, let the centroid of the element be allowed to vary continuously over all locations, $\mathbf{X}_c = (x_c, 0)$, along the line $z=0$, and let C be that part of the flaw surface from which all the specular responses can be received from elements along this line. Then we have

$$V(\mathbf{X}_c, \omega) = s_I(\omega) \hat{P}(\mathbf{X}_c, \mathbf{X}_0, \omega)^2 \frac{2}{l_A} \int_C R_{23} \exp i\mathbf{k} \cdot \mathbf{X}' ds(\mathbf{X}'), \quad (12.15)$$

where $\mathbf{k} = 2k_2 \mathbf{e}$. To put Eq. (12.15) in a more explicit form, we can define a singular function of the lit surface, $\gamma_C(\mathbf{X}')$, which has the property that [7]

$$\int_C f(\mathbf{X}') ds(\mathbf{X}') = \int \gamma_C(\mathbf{X}') f(\mathbf{X}') dA(\mathbf{X}'). \quad (12.16)$$

Using this singular function, Eq. (12.15) can be expressed as a 2-D Fourier transform of the function $R(\mathbf{X}') \equiv R_{23} \gamma_C(\mathbf{X}')$, which we will define as the *reflectivity* of the flaw surface in this pulse-echo response case. Denoting the Fourier transform of this function by $\bar{R}(\mathbf{k})$, we find

$$V(\mathbf{X}_c, \omega) = s_I(\omega) \hat{P}(\mathbf{X}_c, \mathbf{X}_0, \omega)^2 \frac{2}{l_A} \bar{R}(\mathbf{k}), \quad (12.17)$$

where

$$\bar{R}(\mathbf{k}) = \int R_{23} \gamma_C(\mathbf{X}') \exp i\mathbf{k} \cdot \mathbf{X}' dA(\mathbf{X}'). \quad (12.18)$$

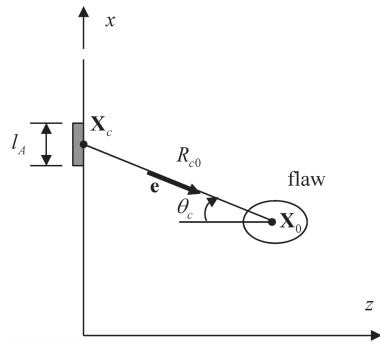
Since Eq. (12.18) shows that the measured voltage data is just proportional to the 2-D Fourier transform of the reflectivity, we can in principle obtain an image of that reflectivity, $I_R(\mathbf{X}')$, by simply performing an inverse Fourier transform of that data in the form

$$I_R(\mathbf{X}') \equiv R_{23} \gamma_C(\mathbf{X}') = \frac{l_A}{8\pi^2} \int \frac{V(\mathbf{X}_c, \omega)}{s_I(\omega) \hat{P}(\mathbf{X}_c, \mathbf{X}_0, \omega)^2} \exp -i\mathbf{k} \cdot \mathbf{X}' d^2\mathbf{k}, \quad (12.19)$$

where it is assumed that \mathbf{X}_c can take on any continuous values in the range $-\infty < x_c < +\infty$ and the frequency, ω , likewise can range over all values $-\infty < \omega < +\infty$ so that \mathbf{k} can take on any value in the entire \mathbf{k} -plane. In this formal result we see that we have deconvolved the measured voltage with the system function and the incident wave fields. Deconvolution by straight division, however, is unstable in the presence of noise. In ultrasonics, a common approach to remedy this problem is to use a Wiener filter [Schmerr-Song], i.e. we make the replacement

$$\frac{V(\mathbf{X}_c, \omega)}{s_I(\omega) \hat{P}(\mathbf{X}_c, \mathbf{X}_0, \omega)^2} \rightarrow V_W(\mathbf{X}_c, \mathbf{X}_0, \omega), \quad (12.20)$$

Fig. 12.13 Geometry parameters for the pulse-echo response of a typical array element



where

$$V_W(\mathbf{X}_c, \mathbf{X}_0, \omega) = \frac{V(\mathbf{X}_c, \omega) \{s_I(\omega) \hat{P}(\mathbf{X}_c, \mathbf{X}_0, \omega)^2\}^*}{|s_I(\omega) \hat{P}(\mathbf{X}_c, \mathbf{X}_0, \omega)^2|^2 + \varepsilon^2 \max \left\{ |s_I(\omega) \hat{P}(\mathbf{X}_c, \mathbf{X}_0, \omega)^2|^2 \right\}} \quad (12.21)$$

and where $()^*$ denotes the complex conjugate and ε is a noise constant. The effect of this replacement is to avoid division by small terms that can amplify the noise and instead drive the filtered response to zero whenever either the system function, $s_I(\omega)$, or the pressure wave field term, $\hat{P}(\mathbf{X}_c, \mathbf{X}_0, \omega)$, goes to zero. In terms of this replacement, Eq. (12.19) becomes

$$I_R(\mathbf{X}') = \frac{l_A}{8\pi^2} \int V_W(\mathbf{X}_c, \mathbf{X}_0, \omega) \exp(-i\mathbf{k} \cdot \mathbf{X}') d^2\mathbf{k}. \quad (12.22)$$

In this case, the Wiener filter will also modify the image generated so strictly speaking we should indicate this by a change in left side expression of Eq. (12.22) but to emphasize that we are still trying to image the reflectivity as defined in Eq. (12.19) we will leave this expression unchanged here. Equation (12.22) is still in terms of a 2-D integration over the 2-D wave number plane, $\mathbf{k} = (k_x, k_z)$, but we can transform it to an integration over the frequency, ω , and the angle, θ_c , (measured clockwise from a line passing through \mathbf{X}_0 parallel to the z -axis—see Fig. 12.13) by a change of variables to yield

$$I_R(\mathbf{X}') = \frac{l_A}{8\pi^2} \int V_W(\mathbf{X}_c, \mathbf{X}_0, \omega) \exp(-i\mathbf{k} \cdot \mathbf{X}') \left| \frac{(\partial k_x, \partial k_z)}{(\partial \omega, \partial \theta_c)} \right| d\omega d\theta_c, \quad (12.23)$$

where the Jacobian of the transformation is given by

$$\begin{aligned} \left| \frac{\partial(k_x, k_z)}{\partial(\omega, \theta_c)} \right| &= \left| \det \begin{bmatrix} \partial k_x / \partial \omega & \partial k_z / \partial \omega \\ \partial k_x / \partial \theta_c & \partial k_z / \partial \theta_c \end{bmatrix} \right| \\ &= \left| \det \begin{bmatrix} -2 \sin \theta_c / c & 2 \cos \theta_c / c \\ -2 \omega \cos \theta_c / c & -2 \omega \sin \theta_c / c \end{bmatrix} \right| = 4 |\omega| / c^2. \end{aligned} \quad (12.24)$$

Also, we can write the angle, θ_c , in terms of the x_c -coordinate along the line $z=0$, since

$$d\theta_c = \cos \theta_c \frac{dx_c}{R_{co}}, \quad (12.25)$$

(Fig. 12.13) so placing Eqs. (12.24) and (12.25) into Eq. (12.23) gives

$$I_R(\mathbf{X}') = \frac{l_A}{2\pi^2 c^2} \int \frac{\cos \theta_c}{R_{co}} V_W(\mathbf{X}_c, \mathbf{X}_0, \omega) \exp[-i\mathbf{k} \cdot \mathbf{X}'] |\omega| d\omega dx_c. \quad (12.26)$$

Equation (12.26) is an imaging model for a setup where the deconvolved voltage received by an element (whose centroid location is allowed to take on continuous values along a line) is used to form an image of the specular surface response of the flaw as defined in Eq. (12.19). In an array, of course, the element centroid locations only exist at N discrete locations, \mathbf{X}_{cn} , $n = (1, 2, \dots, N)$ and if we consider only M positive discrete frequencies, ω_m , ($m = 1, 2, \dots, M$), we can write Eq. (12.26) as a finite sum and form a band-limited and aperture-limited image of the flaw reflectivity, $I_R^{BA}(\mathbf{X}')$ at the points \mathbf{X}' as:

$$I_R^{BA}(\mathbf{X}') = \frac{2l_A \Delta f \Delta x_c}{c^2} 2\text{Re} \left\{ \sum_{m=1}^M \sum_{n=1}^N \frac{(\cos \theta_c)_n}{(R_{co})_n} f_m V_W(\mathbf{X}_{cn}, \mathbf{X}_0, \omega_m) \exp[-i\mathbf{k}_{nm} \cdot \mathbf{X}'] \right\}, \quad (12.27)$$

where Δf is the sampling spacing in the frequency domain and Δx_c is the pitch of the array.

Equation (12.27) is the discrete imaging measurement model counterpart of Eq. (12.26). Note that here we are treating “inversion” and “imaging” as essentially synonymous since we are using the inversion of a reduced measurement model to form an image of an explicit physical reflectivity response of the flaw. In practice, flaw images are often generated without placing a meaning on the amplitude values in the image or without taking into account the band limited system properties or wave processes that produced the image. B-scan, C-scan, S-scan, SAFT, and TFM images are all examples of such image formation methods. In fact, the SAFT imaging approach discussed in Sect. 12.1 is closely related to this imaging measurement model, as we will now show.

Since SAFT ignores system function properties and wave propagation processes, we can show how to reduce our imaging measurement model to SAFT by first setting the ε term in our Wiener filter (Eq. 12.21) equal to zero and use Eq. (12.14) to write Eq. (12.27) as

$$I_R^{BA}(\mathbf{X}') = \frac{2l_A \Delta f \Delta x_c}{c^2} 2\text{Re} \left\{ \sum_{m=1}^M \sum_{n=1}^N \frac{(\cos \theta_c)_n}{(R_{co})_n} f_m \frac{V(\mathbf{X}_{cn}, \omega_m)}{s_I(\omega_m) [P(\mathbf{X}_{cn}, \mathbf{X}_0, \omega_m) / \rho c v_T^{(1)}]^2} \right. \\ \left. \cdot \exp[-2i\omega_m T(\mathbf{X}_{cn}, \mathbf{X}_0) - 2ik_{2m} \mathbf{e}_n \cdot \mathbf{X}'] \right\}. \quad (12.28)$$

But, recall because of our small flaw assumption we expanded the total time travel function to first order so $\omega T(\mathbf{X}_c, \mathbf{X}) = \omega T(\mathbf{X}_c, \mathbf{X}_0) + k_2 \mathbf{e} \cdot \mathbf{X}'$ and if we simply ignore all system and wave terms not associated with the directly measured voltage response except the parameter $\Delta f = \Delta \omega / 2\pi$ we can recover the SAFT algorithm as discussed in Sect. 12.1:

$$I_{SAFT}(\mathbf{X}) = 2\text{Re} \left\{ \frac{\Delta \omega}{2\pi} \sum_{m=1}^M \sum_{n=1}^N V(\mathbf{X}_{cn}, \omega_m) \exp[-2i\omega_m T(\mathbf{X}_{cn}, \mathbf{X})] \right\}. \quad (12.29)$$

In both our imaging measurement model and the SAFT imaging approach, we are only using the pulse-echo responses of the array elements to form an image. This subset of all the possible sending and receiving pairs of elements we see is sufficient to reconstruct the reflectivity of the flaw with our imaging measurement model and a related image quantity in the SAFT approach. If we use a full matrix capture of all combinations of sending and receiving elements to form an image we expect to obtain a “better” image in some sense since we are summing over many more element pairs but how is such an image related to the reflectivity of the flaw? To answer this question, consider first the case where we have a single sending element and receive with all elements of the array. Going back to Eq. (12.12) we have for the voltage response from the specular reflections of the flaw in a single medium:

$$V(\mathbf{X}_s, \mathbf{X}_r, \omega) = s_I(\omega) \hat{P}^{(1)}(\mathbf{X}_s, \mathbf{X}_0, \omega) \hat{P}^{(2)}(\mathbf{X}_r, \mathbf{X}_0, \omega) \\ \cdot \frac{2}{l_A} \int_{C_{fl}} R_{23}(\mathbf{e}_r \cdot \mathbf{n}) \exp[ik_2(\mathbf{e}^{(1)} + \mathbf{e}^{(2)}) \cdot \mathbf{X}'] ds(\mathbf{X}'). \quad (12.30)$$

We introduce the singularity function of the surface again and now define the *reflectivity* as

$$R \equiv R_{23}(\mathbf{e}_r \cdot \mathbf{n}) \gamma_C(\mathbf{X}') \quad (12.31)$$

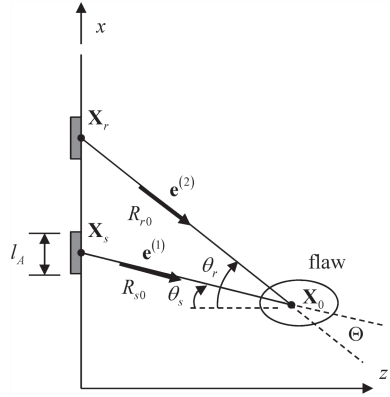
and let the wave number vector $\mathbf{k} = k_2(\mathbf{e}^{(1)} + \mathbf{e}^{(2)})$. Then, following the same steps as in the pulse-echo case, we find the measured voltage can be again expressed as a Fourier transform of this reflectivity in the form

$$V(\mathbf{X}_s, \mathbf{X}_r, \omega) = s_I(\omega) \hat{P}^{(1)}(\mathbf{X}_s, \mathbf{X}_0, \omega) \hat{P}^{(2)}(\mathbf{X}_r, \mathbf{X}_0, \omega) \frac{2}{l_A} \bar{R}(\mathbf{k}), \quad (12.32)$$

where now

$$\bar{R}(\mathbf{k}) = \int R_{23}(\mathbf{e}_r \cdot \mathbf{n}) \gamma_C(\mathbf{X}') \exp[i\mathbf{k} \cdot \mathbf{X}'] dA(\mathbf{X}'). \quad (12.33)$$

Fig. 12.14 Geometry parameters for sending and receiving with different element pairs



Performing an inverse Fourier transform on Eq. (12.32) then gives

$$R_{23}(\mathbf{e}_r \cdot \mathbf{n}) \gamma_C(\mathbf{X}') = \frac{l_A}{8\pi^2} \int \frac{V(\mathbf{X}_s, \mathbf{X}_r, \omega)}{s_l(\omega) [\hat{P}(\mathbf{X}_s, \mathbf{X}_0, \omega) \hat{P}(\mathbf{X}_r, \mathbf{X}_0, \omega)]} \exp[-i\mathbf{k} \cdot \mathbf{X}' d^2 \mathbf{k}]. \quad (12.34)$$

Changing the integration variables to the frequency, ω , and the angle measured from the z -axis to the receiving element, θ_r (see Fig. 12.14) gives

$$R_{23}(\mathbf{e}_r \cdot \mathbf{n}) \gamma_C(\mathbf{X}') = \frac{l_A}{8\pi^2} \int \frac{V(\mathbf{X}_s, \mathbf{X}_r, \omega)}{s_l(\omega) [\hat{P}(\mathbf{X}_s, \mathbf{X}_0, \omega) \hat{P}(\mathbf{X}_r, \mathbf{X}_0, \omega)]} \exp[-i\mathbf{k} \cdot \mathbf{X}'] \left| \frac{\partial(\mathbf{k})}{\partial(\omega, \theta_r)} \right| d\omega d\theta_r. \quad (12.35)$$

In two-dimensions the Jacobian of the coordinate transformation becomes

$$\begin{aligned} \left| \frac{\partial(\mathbf{k})}{\partial(\omega, \theta_r)} \right| &= \left| \frac{\omega}{c^2} \det \begin{bmatrix} \mathbf{e}^{(1)} + \mathbf{e}^{(2)} \\ \partial \mathbf{e}^{(2)} / \partial \theta_r \end{bmatrix} \right| = \left| \frac{\omega}{c^2} \mathbf{e}_y \cdot \left[(\mathbf{e}^{(1)} + \mathbf{e}^{(2)}) \times \frac{\partial \mathbf{e}^{(2)}}{\partial \theta_r} \right] \right| \\ &= \left| \frac{\omega}{c^2} (\mathbf{e}^{(1)} + \mathbf{e}^{(2)}) \cdot \left(\frac{\partial \mathbf{e}^{(2)}}{\partial \theta_r} \times \mathbf{e}_y \right) \right|, \end{aligned} \quad (12.36)$$

where $(\mathbf{e}_x, \mathbf{e}_y, \mathbf{e}_z)$ are unit vectors along the (x, y, z) axes, respectively, and we have used the distributional property of the triple product $\mathbf{a} \cdot (\mathbf{b} \times \mathbf{c})$ to obtain the final result shown in Eq. (12.36). Since $\mathbf{e}^{(2)} = -\sin \theta_r \mathbf{e}_x + \cos \theta_r \mathbf{e}_z$ is a unit vector, it is perpendicular to its derivative so we have

$$\frac{\partial \mathbf{e}^{(2)}}{\partial \theta_r} \times \mathbf{e}_y = -\cos \theta_r \mathbf{e}_z + \sin \theta_r \mathbf{e}_x = -\mathbf{e}^{(2)}. \quad (12.37)$$

But the sign is immaterial because of the absolute value present in the Jacobian so we have

$$\left| \frac{\partial(\mathbf{k})}{\partial(\omega, \theta_r)} \right| = \left| \frac{\omega}{c^2} (\mathbf{e}^{(1)} + \mathbf{e}^{(2)}) \cdot \mathbf{e}^{(2)} \right|, \quad (12.38)$$

If we express the dot product of the two incident unit wave vectors as $\mathbf{e}^{(1)} \cdot \mathbf{e}^{(2)} = \cos \Theta$, where Θ is the angle between them (Fig. 12.14) we find, finally

$$\left| \frac{\partial(\mathbf{k})}{\partial(\omega, \theta_r)} \right| = \left| \frac{\omega}{c^2} (1 + \cos \Theta) \right| \quad (12.39)$$

and Eq. (12.35) expresses the image $I_R \equiv R_{23}(\mathbf{e}_r \cdot \mathbf{n}) \gamma_C(\mathbf{X}')$ as

$$I_R = \frac{l_A}{8\pi^2} \int \left| \frac{\omega}{c^2} (1 + \cos \Theta) \right| \frac{V(\mathbf{X}_s, \mathbf{X}_r, \omega)}{s_l(\omega) [\hat{P}(\mathbf{X}_s, \mathbf{X}_0, \omega) \hat{P}(\mathbf{X}_r, \mathbf{X}_0, \omega)]} \exp[-i\mathbf{k} \cdot \mathbf{X}'] d\omega d\theta_r. \quad (12.40)$$

As in the pulse-echo case, we can write the angle θ_r in terms of the x -coordinate of the receiving element, x_r on the x -axis since $dx_r = R_{r0} d\theta_r / \cos \theta_r$ to obtain

$$I_R = \frac{l_A}{8\pi^2} \int \left| \frac{\omega}{c^2} (1 + \cos \Theta) \right| \frac{\cos \theta_r}{R_{r0}} \frac{V(\mathbf{X}_s, \mathbf{X}_r, \omega)}{s_l(\omega) [\hat{P}(\mathbf{X}_s, \mathbf{X}_0, \omega) \hat{P}(\mathbf{X}_r, \mathbf{X}_0, \omega)]} \exp[-i\mathbf{k} \cdot \mathbf{X}'] d\omega dx_r. \quad (12.41)$$

In Eq. (12.41) the sending element has been fixed and we have formed the image by integrating over the receiving elements. In seismology, this is called a *common shot response* [8]. Unlike the pulse-echo case the image now is a function also of the angle of the incident wave direction, θ_{inc} , which is the angle between the $\mathbf{e}^{(1)}$ unit vector and the unit normal of the flaw surface at \mathbf{X}' , i.e. $I_R = I_R(\mathbf{X}', \theta_{inc})$ since $R_{23}, (\mathbf{e}_r \cdot \mathbf{n})$ are both functions of θ_{inc} . If we now allow the sending element location to vary this incident angle will vary and we can define an angular independent image function, $\tilde{I}_R(\mathbf{X}')$ as

$$\tilde{I}_R(\mathbf{X}') = \int I_R(\mathbf{X}', \theta_{inc}) d\theta_{inc} \quad (12.42)$$

However, at a fixed image point, \mathbf{X}' , on the flaw the normal is also fixed, so we can replace the integration over θ_{inc} to one over the angle θ_s measured from the z -axis (Fig. 12.14). As with the receiving element this angle for the sending element can be related to a position of the sending element on the x -axis, since $dx_s = R_{s0} d\theta_s / \cos \theta_s$ so that we can express our image function as

$$\tilde{I}_R(\mathbf{X}') = \int I_R d\theta_{inc} = \int I_R d\theta_s = \int \frac{\cos \theta_s}{R_{s0}} I_R dx_s \quad (12.43)$$

and applying this result to Eq. (12.41) we have

$$\tilde{I}_r(\mathbf{X}') = \frac{l_A}{8\pi^2} \int \left\{ \left| \frac{\omega}{c^2} (1 + \cos \Theta) \right| \frac{\cos \theta_r}{R_{r0}} \frac{\cos \theta_s}{R_{s0}} \cdot \frac{V(\mathbf{X}_s, \mathbf{X}_r, \omega)}{s_I(\omega) [\hat{P}(\mathbf{X}_s, \mathbf{X}_0, \omega) \hat{P}(\mathbf{X}_r, \mathbf{X}_0, \omega)]} \exp[-i\mathbf{k} \cdot \mathbf{X}'] d\omega dx_r dx_s \right\}. \quad (12.44)$$

Equation (12.44) gives us an imaging measurement model for producing an image of a flaw with full matrix capture, i.e. using all pitch-catch combinations of sending and receiving elements along the x -axis. It shows that quantity being imaged in this case is an integrated reflectivity of the surface, specifically

$$\tilde{I}_r(\mathbf{X}') = \int R_{23}(\mathbf{e}_r \cdot \mathbf{n}) \gamma_C(\mathbf{X}') d\theta_{inc}. \quad (12.45)$$

We can again replace the deconvolution present in Eq. (12.44) by a Wiener-filtered version of the measured voltage given by

$$V_W(\mathbf{X}_s, \mathbf{X}_r, \mathbf{X}_0, \omega) = \frac{V(\mathbf{X}_s, \mathbf{X}_r, \omega) \{s_I(\omega) \hat{P}(\mathbf{X}_s, \mathbf{X}_0, \omega) \hat{P}(\mathbf{X}_r, \mathbf{X}_0, \omega)\}^*}{\left| s_I(\omega) \hat{P}(\mathbf{X}_s, \mathbf{X}_0, \omega) \hat{P}(\mathbf{X}_r, \mathbf{X}_0, \omega) \right|^2 + \varepsilon^2 \max \left\{ \left| s_I(\omega) \hat{P}(\mathbf{X}_s, \mathbf{X}_0, \omega) \hat{P}(\mathbf{X}_r, \mathbf{X}_0, \omega) \right|^2 \right\}} \quad (12.46)$$

to give

$$\tilde{I}_r(\mathbf{X}') = \frac{l_A}{8\pi^2} \int \left\{ \left| \frac{\omega}{c^2} (1 + \cos \Theta) \right| \frac{\cos \theta_r}{R_{r0}} \frac{\cos \theta_s}{R_{s0}} V_W(\mathbf{X}_s, \mathbf{X}_r, \mathbf{X}_0, \omega) \exp[-i\mathbf{k} \cdot \mathbf{X}'] d\omega dx_r dx_s \right\}. \quad (12.47)$$

Note that as in the pulse-echo case we can combine the phase terms $\omega T(\mathbf{X}_s, \mathbf{X}_0)$, $\omega T(\mathbf{X}_r, \mathbf{X}_0)$ present in the $\hat{P}(\mathbf{X}_s, \mathbf{X}_0, \omega)$, $\hat{P}(\mathbf{X}_r, \mathbf{X}_0, \omega)$, respectively, with the complex exponential term present in Eq. (12.44) and simply ignore all the amplitude and phase terms other than the measured voltage (and a factor of $1/2\pi$ which is kept for convenience) to obtain an image via

$$I(\mathbf{X}) = \frac{1}{2\pi} \int V(\mathbf{X}_s, \mathbf{X}_r, \omega) \exp[-i\omega T(\mathbf{X}_s, \mathbf{X}) - i\omega T(\mathbf{X}_r, \mathbf{X})] d\omega dx_r dx_s. \quad (12.48)$$

In this case Eq. (12.48) is a continuous version of the total focusing method (TFM) for full matrix capture [5]. In discrete form, similar to the pulse-echo SAFT result of Eq. (12.29) with N elements and M positive frequencies, we have (again, ignoring any additional terms except the frequency sampling interval, $\Delta\omega$) we recover the TFM result of Sect. 12.2:

$$I_{TFM}(\mathbf{X}) \equiv 2\text{Re} \left\{ \frac{\Delta\omega}{2\pi} \sum_{m=1}^M \sum_{n=1}^N \sum_{l=1}^N V(\mathbf{X}_{sl}, \mathbf{X}_{rn}, \omega_m) \exp[-i\omega_m T(\mathbf{X}_{sl}, \mathbf{X}) - i\omega_m T(\mathbf{X}_{rn}, \mathbf{X})] \right\}. \quad (12.49)$$

As in the SAFT approach, with the TFM we cannot identify a quantitative reflectivity that is being imaged but we see from our imaging measurement model that the focusing terms, which are crucial to the image formation process, are present in all of these imaging methods.

Our imaging measurement model approach can also show how images of crack tips can be formed. We will illustrate this for the pulse-echo case but a very similar analysis holds for full matrix capture. We first need to modify Eq. (12.15) since we will assume that there is no received specular response from the entire crack surface. In that case, Eq. (12.15) becomes (see Eq. 11.94)

$$V(\mathbf{X}_c, \omega) = s_I(\omega) \left[\hat{P}(\mathbf{X}_c, \mathbf{X}_0, \omega) \right]^2 \frac{1}{l_A} \int_C R_{23}(\mathbf{e}_r - \mathbf{e}) \cdot \mathbf{n} \exp[i\mathbf{k} \cdot \mathbf{X}'] ds(\mathbf{X}'). \quad (12.50)$$

First, note that Stokes' theorem two dimensions has the form

$$\int_C \mathbf{e}_y \cdot (\mathbf{n} \times \nabla f) ds(\mathbf{X}') = f(\mathbf{X}'_e) - f(\mathbf{X}'_b), \quad (12.51)$$

where \mathbf{e}_y is a unit vector in the y -direction and $(\mathbf{X}'_b, \mathbf{X}'_e)$ are the beginning and end points of the crack C . Since we assumed that there is no received specular response from the surface of the crack, $\mathbf{n} \times \mathbf{k}$ is never zero and we can let

$$f = \frac{R_{23}(\mathbf{e}_r - \mathbf{e}) \cdot \mathbf{n} \exp[i\mathbf{k} \cdot \mathbf{X}']}{i\mathbf{e}_y \cdot (\mathbf{n} \times \mathbf{k})}. \quad (12.52)$$

At high frequencies, however, we find

$$\mathbf{e}_y \cdot (\mathbf{n} \times \nabla f) \cong R_{23}(\mathbf{e}_r - \mathbf{e}) \cdot \mathbf{n} \exp[i\mathbf{k} \cdot \mathbf{X}'] \quad (12.53)$$

so Eq. (12.50) can be formally expressed as

$$V(\mathbf{X}_c, \omega) = s_I(\omega) \left[\hat{P}(\mathbf{X}_c, \mathbf{X}_0, \omega) \right]^2 \left\{ \frac{1}{l_A} \frac{R_{23}(\mathbf{e}_r - \mathbf{e}) \cdot \mathbf{n} \exp i\mathbf{k} \cdot \mathbf{X}'}{i\mathbf{e}_y \cdot (\mathbf{n} \times \mathbf{k})} \right\}_{\mathbf{X}'=\mathbf{X}'_e} - \left\{ \frac{R_{23}(\mathbf{e}_r - \mathbf{e}) \cdot \mathbf{n} \exp i\mathbf{k} \cdot \mathbf{X}'}{i\mathbf{e}_y \cdot (\mathbf{n} \times \mathbf{k})} \right\}_{\mathbf{X}'=\mathbf{X}'_b}. \quad (12.54)$$

Again, we can write this result as:

$$V(\mathbf{X}_c, \omega) = \frac{s_I(\omega)c}{i\omega} \left[\hat{P}(\mathbf{X}_c, \mathbf{X}_0, \omega) \right]^2 \frac{2}{l_A} \bar{R}_e(\mathbf{k}), \quad (12.55)$$

where $\bar{R}_e(\mathbf{k})$ formally looks like a Fourier transform of the reflectivity of the crack tips, R_e , i.e.

$$\bar{R}_e(\mathbf{k}) = \int R_e \exp[i\mathbf{k} \cdot \mathbf{X}'] dA(\mathbf{X}') \quad (12.56)$$

and

$$R_e = \frac{R_{23}(\mathbf{e}_r - \mathbf{e}) \cdot \mathbf{n}}{2\mathbf{e}_y \cdot (\mathbf{n} \times \mathbf{e})} \delta(\mathbf{X}' - \mathbf{X}'_e) - \frac{R_{23}(\mathbf{e}_r - \mathbf{e}) \cdot \mathbf{n}}{2\mathbf{e}_y \cdot (\mathbf{n} \times \mathbf{e})} \delta(\mathbf{X}' - \mathbf{X}'_b), \quad (12.57)$$

where $\delta(\mathbf{X}' - \mathbf{X}'_p)$ is a 2-D delta function located at $\mathbf{X}' = \mathbf{X}'_p$ ($p = e, b$). Unlike the specular surface response, the coefficients of these delta functions are functions of \mathbf{e} as well as $(\mathbf{X}', \mathbf{X}'_p)$ so that R_e is also a function of these variables as well. This means that Eq. (12.56) is not strictly speaking a Fourier transform. Also, we should note that the delta function coefficients in Eq. (12.57) were obtained with the Kirchhoff approximation so they are not the correct high frequency diffraction coefficients associated with the crack tips. However, in forming an image of the crack tips, the image will be defined primarily by the singular delta functions of Eq. (12.57). Thus, we expect that treating their coefficients as purely constants so that $R_e = R_e(\mathbf{X}', \mathbf{X}'_p)$ should still allow us to image these delta functions and hence the crack tips. Making that assumption, Eq. (12.56) is then indeed in the form of a Fourier transform and we can invert Eq. (12.55) to obtain

$$I_e(\mathbf{X}') \equiv R_e(\mathbf{X}', \mathbf{X}'_p) = \frac{l_A}{8\pi^2} \int \frac{(i\omega/c)V(\mathbf{X}_c, \omega)}{s_I(\omega) \left[\hat{P}(\mathbf{X}_c, \mathbf{X}_0, \omega) \right]^2} \exp[-i\mathbf{k} \cdot \mathbf{X}'] d^2\mathbf{k}. \quad (12.58)$$

Equation (12.58) is very similar to the expression for the surface reflectivity given by Eq. (12.19), which we rewrite here for comparison:

$$I_R(\mathbf{X}') = \frac{l_A}{8\pi^2} \int \frac{V(\mathbf{X}_c, \omega)}{s_I(\omega) \left[\hat{P}(\mathbf{X}_c, \mathbf{X}_0, \omega) \right]^2} \exp[-i\mathbf{k} \cdot \mathbf{X}'] d^2\mathbf{k}. \quad (12.59)$$

We see that in the crack tip case there is a frequency dependent factor, ω/c , present in the numerator as well as a $i = \sqrt{-1}$ factor, both of which are absent in the surface reflectivity expression. If we simply ignore this additional frequency factor when forming an image of the crack tips then we expect we will still see filtered crack tip images, which suggest that we can image both the specular surface response and the crack tips by using Eq. (12.59). Based on our results we would expect to see the surface response in the real part of the image formed by Eq. (12.59) and the crack tips in the imaginary part but since our results were based on a high frequency approximation we may not see that sort of strict separation in an image generated with frequency-band-limited and aperture-limited real data.

The pulse-echo imaging measurement model of Eq. (12.59) is also a relative of a well known imaging method—the Physical Optics Far Field Inverse Scattering (POFFIS) approach [7]. The POFFIS method was originally developed by Bojarski [9]. In its original form, POFFIS was an expression for imaging a characteristic function of the scatterer, which is a function that is one inside and zero outside the scatterer [10]. However, trying to image a characteristic function in real band-limited and aperture-limited systems is a task fraught with difficulty because these limits severely distort the characteristic function, making it unrecognizable. To overcome this difficulty, Bleistein reformulated the POFFIS relationship in terms of the singular function of the surface [7, 11], leading to a form which is closely related to our imaging measurement model. We can gain some additional insight into the meaning of our imaging measurement model by examining that relationship more closely. To compare with POFFIS, let us return to Eq. (12.17), i.e.

$$V(\mathbf{X}_c, \omega) = s_I(\omega) \left[\hat{P}(\mathbf{X}_c, \mathbf{X}_0, \omega) \right]^2 \frac{2}{l_A} \bar{R}(\mathbf{k}). \quad (12.60)$$

In a POFFIS formulation the frequency bandwidth is assumed to be infinite and the incident wave field is assumed to be from a concentrated “point” source [7]. In this case $s_I(\omega) = 1$ and if we use the far-field values of a line source for the radiation of an element (see Eqs. 2.37 and 2.38) with the far field directivity of the element $D_b(\theta_c, \omega) = 1$, we find

$$\hat{P}(\mathbf{X}_c, \mathbf{X}_0, \omega) = \sqrt{\frac{2k_2}{i\pi}} b \frac{\exp(ik_2 R_{c0})}{\sqrt{R_{c0}}}, \quad (12.61)$$

where $b = l_A / 2$ is one half the total element length. Equation (12.60) then becomes

$$V(\mathbf{X}_c, \omega) = \frac{2\omega}{i\pi c_2} b \frac{\exp(2ik_2 R_{c0})}{R_{c0}} \bar{R}(\mathbf{k}), \quad (12.62)$$

which is a 2-D version of the 3-D POFFIS identity obtained by Bleistein [7]. In the traditional way that POFFIS is derived [7] the left hand side of Eq. (12.62) is the scattered wave field, not the measured voltage but Eq. (12.62) shows that it is possible to derive an equivalent POFFIS form in terms of the actual voltage measurements.

If the system function and directivity of the element are retained, we have instead

$$V(\mathbf{X}_c, \omega) = s_I(\omega) \frac{2\omega}{i\pi c_2} b [D_b(\theta_c, \omega)]^2 \frac{\exp(2ik_2 R_{c0})}{R_{c0}} \bar{R}(\mathbf{k}). \quad (12.63)$$

When inverted, this gives

$$I_R(\mathbf{X}') \frac{c_2}{8\pi b} \int \frac{R_{c0} V(\mathbf{X}_c, \omega)}{-i\omega s_I(\omega) [D_b(\theta_c, \omega)]^2} \exp[-2ik_2 R_{c0} - 2ik_2 \mathbf{e} \cdot \mathbf{X}'] d^2 \mathbf{k}, \quad (12.64)$$

which is a more complete imaging measurement model form of POFFIS imaging. This form shows that in the deconvolution process we are (1) compensating for the frequency dependent system function effects on the measurements, (2) applying a propagation (gain) factor (R_{c0}) to compensate for the $1/\sqrt{R_{c0}}$ amplitude decay when the waves go from the sending element to the center of the flaw and a similar factor when going back to the receiving element, and (3) compensating for the directivity of the waves on both transmission and reception. We see from Eq. (12.62) that POFFIS includes a propagation gain factor but does not include a system function or directivity effects since the bandwidth was assumed infinite and the sending and receiving elements were considered to be omnidirectional concentrated sources. Our imaging measurement model approach shows that propagation, directivity and system functions are in general all important compensation factors that must be included to obtain an image of the flaw reflectivity (as defined here) and that all of these effects are contained more generally in the two terms

$$s_I(\omega) \left[\hat{P}(\mathbf{X}_c, \mathbf{X}_0, \omega) \right]^2, s_I(\omega) \hat{P}(\mathbf{X}_s, \mathbf{X}_0, \omega) \hat{P}(\mathbf{X}_r, \mathbf{X}_0, \omega)$$

for pulse-echo and full matrix capture imaging, respectively.

One can follow the approach of Bleistein [7] and test the consistency of this imaging model by going back to Eq. (12.19) (or, equivalently, Eq. (12.59)) and placing the explicit results found for the measured pulse-echo specular response of a small cylindrical reflector of radius a in the Kirchhoff approximation for a single medium (see Eq. (11.109) specialized for the pulse-echo case where $R_p = a$, $\mathbf{g} \cdot \mathbf{n} = 2$, $\mathbf{e}_r \cdot \mathbf{n} = 1$, and $\mathbf{g} \cdot (\mathbf{X}_{stat} - \mathbf{X}_0) = -2a$ when \mathbf{X}_0 is at the center of the cylinder). In this case Eq. (11.109) becomes

$$V(\mathbf{X}_c, \omega) = s_I(\omega) \left[\hat{P}^{(1)}(\mathbf{X}_c, \mathbf{X}_0, \omega) \right]^2 \left\{ \sqrt{\frac{a}{2}} R_{23} \exp[-2ik_2 a] \right\} \cdot \left[\frac{1}{-ik_2 l_A} \frac{\rho c}{\rho_2 c_2} \sqrt{-8\pi i k_2} \right]. \quad (12.65)$$

[Note: These results assume that the frequency is positive and in forming an image we will need to integrate over both positive and negative frequencies. Thus, formally we must be careful and express all our intermediate steps for both positive and negative values. However, if we use Eq. (12.65) and all intermediate steps for ω positive only we will see the end result is clearly valid for all frequencies.]

To evaluate Eq. (12.19) we will introduce polar coordinates for both \mathbf{X}' and \mathbf{k} :

$$\begin{aligned} \mathbf{X}' &= r \sin \alpha \mathbf{e}_x + r \cos \alpha \mathbf{e}_z, \\ \mathbf{k} &= \frac{2\omega}{c} [\sin \theta \mathbf{e}_x + \cos \theta \mathbf{e}_z]. \end{aligned} \quad (12.66)$$

Then we can express Eq. (12.19) as

$$I_R(\mathbf{X}') = \frac{l_A}{2\pi^2 c^2} \left\{ \int_{\omega=-\infty}^{\infty} \int_{\theta=0}^{2\pi} \frac{V(\mathbf{X}_c, \omega)}{s_I(\omega) \left[\hat{P}(\mathbf{X}_c, \mathbf{X}_0, \omega) \right]^2} \exp[-i\mathbf{k} \cdot \mathbf{X}'] \omega d\omega d\theta \right\}. \quad (12.67)$$

Placing Eq. (12.65) into this result then gives (with $\rho_2 c_2 = \rho c$)

$$I_R(\mathbf{X}') = R_{23} \frac{4}{\sqrt{8\pi\pi c^2}} \sqrt{\frac{a}{2}} \left\{ \int_{\omega=-\infty}^{\omega=\infty} \int_{\theta=0}^{\theta=2\pi} \sqrt{\frac{1}{-ik_2}} \exp(-2ik_2 a) \exp[-i\mathbf{k} \cdot \mathbf{X}'] \omega d\omega d\theta \right\}. \quad (12.68)$$

Using the explicit values in the exponential term gives

$$I_R(r, \alpha) = \frac{R_{23}}{c^2} \frac{4}{\sqrt{8\pi\pi}} \sqrt{\frac{a}{2}} \left\{ \int_{\omega=-\infty}^{\omega=\infty} \int_{\theta=0}^{\theta=2\pi} \sqrt{\frac{c}{-i\omega}} \exp(-2ia\omega/c) \exp[-(2i\omega r/c) \cos(\theta - \alpha)] \omega d\omega d\theta \right\} \quad (12.69)$$

and the θ -integration can be performed, yielding

$$I_R(r, \alpha) = \frac{2R_{23}}{c^2} \sqrt{\frac{a}{\pi}} \cdot \left\{ \int_{\omega=-\infty}^{\omega=\infty} \sqrt{\frac{c\omega}{-i}} \exp(-2ia\omega/c) J_0(2\omega r/c) d\omega \right\}. \quad (12.70)$$

But, consistent with the high frequency approximation for the specular response we can take the asymptotic expansion for the Bessel function:

$$J_0(2\omega r/c) \sim \sqrt{\frac{-ic}{\pi\omega r}} \frac{\exp(2i\omega r/c) + i \exp(-2i\omega r/c)}{2} \quad (12.71)$$

to obtain

$$I_R(r, \alpha) = \frac{2R_{23}}{c} \left\{ \sqrt{\frac{a}{r}} \frac{1}{2\pi} \int_{\omega=-\infty}^{\omega=\infty} \left\{ \exp[2i(r-a)\omega/c] + i \exp[-2i(r+a)\omega/c] \right\} d\omega \right\}. \quad (12.72)$$

We can recognize the two integrals as delta functions $\delta(2(r-a)/c)$, $\delta(2(r+a)/c)$ which have sampling properties at $r = a$, $r = -a$, respectively, so we can replace the square root term by its values at these locations, giving formally

$$\begin{aligned} I_R(r, \alpha) &= \frac{2R_{23}}{c} \left\{ \frac{1}{2\pi} \int_{\omega=-\infty}^{\omega=\infty} \left\{ \exp[2i(r-a)\omega/c] - \exp[-2i(r+a)\omega/c] \right\} d\omega \right\} \\ &= \frac{2R_{23}}{c} \left\{ \delta(2(r-a)/c) - \delta(2(r+a)/c) \right\} \\ &= R_{23} \left\{ \delta(r-a) - \delta(r+a) \right\}. \end{aligned} \quad (12.73)$$

But for all α and $r > 0$ $\delta(r+a)$ is identically zero so we do recover the reflectivity of the flaw surface. Of course, in practice one does not have data for all frequencies and angles when performing these inversions. To examine the effects of

limited bandwidth let the response be non-zero only in the finite bandwidth range $\omega_- < \omega < \omega_+$. Then the first term in Eq. (12.73) becomes

$$\begin{aligned} I_R &\cong \frac{2R_{23}}{c} \cdot 2\text{Re} \left\{ \frac{1}{2\pi} \int_{\omega=\omega_-}^{\omega=\omega_+} \exp[2i(r-a)\omega/c] d\omega \right\} \\ &= \frac{R_{23}}{\pi(r-a)} \left\{ \sin[2(r-a)\omega_+/c] - \sin[2(r-a)\omega_-/c] \right\}, \end{aligned} \quad (12.74)$$

which shows the delta function is now replaced by a pair of sinc-like functions. If the aperture of measurements is also limited, Bleistein [11] has shown with a stationary phase analysis that one recovers a form similar to Eq. (12.74) over the finite aperture.

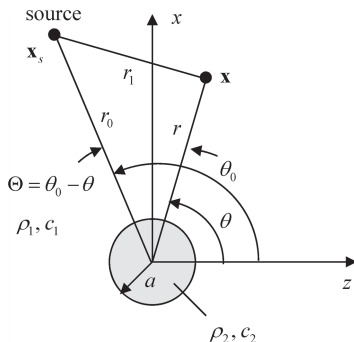
12.5 Imaging Simulations

In this section we will describe a simulation setup which will give us that capability to model the signals received from a flaw in a phased array inspection and use those signals to form images with the 2-D far field imaging methods just discussed. To simulate this problem we will first model the canonical problem of the pressure received from a 2-D circular inclusion in a fluid, where the incident waves are generated by an omni-directional line source, as shown in Fig. 12.15. This setup will allow us to model the response of the inclusion from an array since, as seen in earlier chapters, for very small array elements (whose size is on the order of a tenth of a wavelength or less), a single omni-directional line source can represent an individual element, while larger elements can be broken into segments which can also be modeled as a superposition of such sources. In our model the scattering of the incident waves from the circular inclusion will be treated with the use of the separation of variables method. Thus, in this simulation setup we will have the ability to synthesize the signals received by an array without introducing any high or low frequency approximations and without having to perform any detailed numerical integrations.

Consider first the incident pressure, p_{inc} , generated by a 2-D line source in a fluid whose density and wave speed are (ρ_1, c_1) , respectively (Fig. 12.15). This pressure can be written in terms of the Green function, G , for Helmholtz's equation, given by $G = iH_0^{(1)}(k_1 r_1) / 4$ [12]. This function in turn can be expanded in an infinite series of Bessel and Hankel functions in a polar coordinates with origin at the center of the circular inclusion (see Fig. 12.15) as [13]:

$$p_{\text{inc}} = \frac{iH_0(k_1 r_1)}{4} = \frac{i}{4} \begin{cases} \sum_{n=-\infty}^{\infty} J_n(k_1 r_0) H_n^{(1)}(k_1 r) \exp[in(\theta - \theta_0)] & r > r_0 \\ \sum_{n=-\infty}^{\infty} J_n(k_1 r) H_n^{(1)}(k_1 r_0) \exp[in(\theta - \theta_0)] & r < r_0 \end{cases} \quad (12.75)$$

Fig. 12.15 Scattering of a cylindrical fluid inclusion in a fluid of the waves generated by a line source



Since the incident fields immediately outside the circular inclusion will always be located at a radius $r < r_0$, we will take the second form in Eq. (12.75) and write the incoming waves near the cylinder as

$$p_{\text{inc}} = \frac{i}{4} \sum_{n=-\infty}^{\infty} J_n(k_1 r) H_n^{(1)}(k_1 r_0) \exp[in(\theta - \theta_0)]. \quad (12.76)$$

For the scattered waves we will take the scattered pressure, p_{scatt} , instead as a superposition of outgoing waves of the form

$$p_{\text{scatt}} = \sum_{n=-\infty}^{\infty} a_n H_n^{(1)}(k_1 r_0) \exp[in\theta], \quad (12.77)$$

while inside the flaw, whose density and wave speed are (ρ_2, c_2) , we will let the internal pressure, p_{int} , to be given as

$$p_{\text{int}} = \sum_{n=-\infty}^{\infty} b_n J_n(k_2 r) \exp[in\theta] \quad (12.78)$$

in terms of the unknown coefficients (a_n, b_n) . To determine these coefficients we must satisfy the boundary conditions at the radius $r = a$ of the inclusion, which are that the pressure and the normal (radial) velocity must be continuous. Written in terms of the pressures, these conditions are, at $r = a$:

$$\begin{aligned} p_{\text{inc}} + p_{\text{scatt}} &= p_{\text{int}} \\ \frac{1}{i\omega\rho_1} \frac{\partial p_{\text{inc}}}{\partial r} + \frac{1}{i\omega\rho_1} \frac{\partial p_{\text{scatt}}}{\partial r} &= \frac{1}{i\omega\rho_2} \frac{\partial p_{\text{int}}}{\partial r}. \end{aligned} \quad (12.79)$$

Placing Eqs. (12.76)–(12.78) into these boundary conditions, we find, in matrix form

$$\begin{bmatrix} H_n^{(1)}(k_1 a) & -J_n(k_2 a) \\ \frac{k_1}{\rho_1} \{H_n^{(1)}(k_1 a)\}' & -\frac{k_2}{\rho_2} \{J_n(k_2 a)\}' \end{bmatrix} \begin{bmatrix} a_n \\ b_n \end{bmatrix} = c_n \begin{bmatrix} J_n(k_1 a) \\ \frac{k_1}{\rho_1} \{J_n(k_1 a)\}' \end{bmatrix}, \quad (12.80)$$

where

$$c_n = \frac{-i}{4} H_n^{(1)}(k_1 r_0) \exp[-in\theta_0] \quad (12.81)$$

and

$$\left\{ H_n^{(1)}(x) \right\}' = \frac{dH_n^{(1)}(x)}{dx} \Big|_{r=a}, \quad \left\{ J_n(x) \right\}' = \frac{dJ_n(x)}{dx} \Big|_{r=a}, \quad (12.82)$$

with $x = k_1 r$ or $x = k_2 r$. Solving for (a_n, b_n) , we find

$$a_n = c_n \frac{\Delta_2(n)}{\Delta_1(n)}, \quad b_n = c_n \frac{\Delta_3(n)}{\Delta_1(n)}, \quad (12.83)$$

where

$$\begin{aligned} \Delta_1(n) &= \frac{k_1}{\rho_1} \left\{ H_n^{(1)}(k_1 a) \right\}' J_n(k_2 a) - \frac{k_2}{\rho_2} \left\{ J_n(k_2 a) \right\}' H_n^{(1)}(k_1 a), \\ \Delta_2(n) &= \frac{k_1}{\rho_1} \left\{ J_n(k_1 a) \right\}' J_n(k_2 a) - \frac{k_2}{\rho_2} \left\{ J_n(k_2 a) \right\}' J_n(k_1 a), \\ \Delta_3(n) &= \frac{k_1}{\rho_1} \left[\left\{ J_n(k_1 a) \right\}' H_n^{(1)}(k_1 a) - \left\{ H_n^{(1)}(k_1 a) \right\}' J_n(k_1 a) \right]. \end{aligned} \quad (12.84)$$

Substituting Eq. (12.83) into Eqs. (12.77) and (12.78) we obtain

$$\begin{aligned} p_{\text{scatt}} &= \frac{-i}{4} \sum_{n=-\infty}^{\infty} \frac{\Delta_2(n)}{\Delta_1(n)} H_n^{(1)}(k_1 r_0) H_n^{(1)}(k_1 r_0) \exp[in(\theta - \theta_0)], \\ p_{\text{int}} &= \frac{-i}{4} \sum_{n=-\infty}^{\infty} \frac{\Delta_3(n)}{\Delta_1(n)} H_n^{(1)}(k_1 r_0) J_n(k_2 r) \exp[in(\theta - \theta_0)]. \end{aligned} \quad (12.85)$$

We can use the following relations to express the scattered pressure in a more convenient form for numerical calculations. Specifically,

$$\left\{ Z_n(x) \right\}' = -Z_{n+1}(x) + \frac{n}{x} Z_n(x) = Z_{n-1}(x) - \frac{n}{x} Z_n(x) \quad (12.86)$$

and

$$Z_{-n}(x) = (-1)^n Z_n(x), \quad (12.87)$$

where $Z_n(x)$ can be either $H_n^{(1)}(x)$ or $J_n(x)$. First, we use the first equality in Eq. (12.86) to rewrite the $\Delta_m(n)$ ($m = 1, 2, 3$) coefficients as

$$\begin{aligned}
\Delta_1(n) &= \frac{k_2}{\rho_2} \left[J_{n+1}(k_2 a) - \frac{n}{k_2 a} J_n(k_2 a) \right] H_n^{(1)}(k_1 a) - \frac{k_1}{\rho_1} \left[H_{n+1}^{(1)}(k_1 a) - \frac{n}{k_1 a} H_n^{(1)}(k_1 a) \right] J_n(k_2 a), \\
\Delta_2(n) &= \frac{k_2}{\rho_2} \left[J_{n+1}(k_2 a) - \frac{n}{k_2 a} J_n(k_2 a) \right] J_n(k_1 a) - \frac{k_1}{\rho_1} \left[J_{n+1}(k_1 a) - \frac{n}{k_1 a} J_n(k_1 a) \right] J_n(k_2 a), \\
\Delta_3(n) &= \frac{k_1}{\rho_1} \left[H_{n+1}^{(1)}(k_1 a) J_n(k_1 a) - J_{n+1}(k_1 a) H_n^{(1)}(k_1 a) \right]. \tag{12.88}
\end{aligned}$$

Next, we will split the infinite sum for the scattered pressure into three parts as:

$$\begin{aligned}
p_{scatt} &= \frac{-i}{4} \sum_{n=1}^{\infty} \frac{\Delta_2(n)}{\Delta_1(n)} H_n^{(1)}(k_1 r_0) H_n^{(1)}(k_1 r) \exp[in(\theta - \theta_0)] \\
&\quad - \frac{i}{4} \frac{\Delta_2(0)}{\Delta_1(0)} H_0^{(1)}(k_1 r_0) H_0^{(1)}(k_1 r) \\
&\quad - \frac{i}{4} \sum_{n=-\infty}^{-1} \frac{\Delta_2(n)}{\Delta_1(n)} H_n^{(1)}(k_1 r_0) H_n^{(1)}(k_1 r) \exp[in(\theta - \theta_0)]. \tag{12.89}
\end{aligned}$$

But for the last semi-infinite sum of Eq. (12.89) if we replace n by $-n$ we can re-write it as

$$\frac{-i}{4} \sum_{n=\infty}^1 \frac{\Delta_2(-n)}{\Delta_1(-n)} H_{-n}^{(1)}(k_1 r_0) H_{-n}^{(1)}(k_1 r) \exp[-in(\theta - \theta_0)] \tag{12.90}$$

Then, using Eqs. (12.87) and (12.88) and the second equality relationship of Eq. (12.86), it is easy to show that $\Delta_m(-n) = \Delta_m(n)$ ($m = 1, 2$) so that Eq. (12.90) becomes

$$\frac{-i}{4} \sum_{n=1}^{\infty} \frac{\Delta_2(n)}{\Delta_1(n)} H_n^{(1)}(k_1 r_0) H_n^{(1)}(k_1 r) \exp[-in(\theta - \theta_0)]. \tag{12.91}$$

Placing Eq. (12.91) back into Eq. (12.89), we see we can combine the two semi-infinite sums and write

$$\begin{aligned}
p_{scatt} &= \frac{-i}{4} \frac{\Delta_2(0)}{\Delta_1(0)} H_0^{(1)}(k_1 r_0) H_0^{(1)}(k_1 r) \\
&\quad - \frac{i}{2} \sum_{n=1}^{\infty} \frac{\Delta_2(n)}{\Delta_1(n)} H_n^{(1)}(k_1 r_0) H_n^{(1)}(k_1 r) \cos n\Theta, \tag{12.92}
\end{aligned}$$

which also can be put in the more compact form

$$p_{scatt} = \frac{-i}{4} \sum_{n=0}^{\infty} \varepsilon_n \frac{\Delta_2(n)}{\Delta_1(n)} H_n^{(1)}(k_1 r_0) H_n^{(1)}(k_1 r) \cos[n\Theta], \tag{12.93}$$

where $\Theta = \theta_0 - \theta$ (see Fig. 12.15) and

$$\mathcal{E}_n = \begin{cases} 1 & n = 0 \\ 2 & \text{otherwise} \end{cases}. \quad (12.94)$$

Equation (12.92) or, equivalently, Eq. (12.93) can be used to model the received voltage response of a pair of elements in a phased array. To see this, note that from Eq. (2.28) we can write the incident wave pressure, p_s , generated by a sending element (acting as a piston source) in terms of the Green function as

$$p_s = -2i\omega\rho_1 v_l(\omega) \int_{-b}^b G \, ds, \quad (12.95)$$

where $v_l(\omega)$ is the uniform piston velocity on the face of the element, $l = 2b$ is the length of the element, and ds is a differential length along the element. Thus, the pressure at a receiving element, p_r , from Eq. (12.92) or (12.93) is, likewise,

$$p_r = -2i\omega\rho_1 v_l(\omega) \int_{-b}^b p_{\text{scatt}} \, ds \quad (12.96)$$

and, if we take the blocked force/unit length, $f_B(\omega)$, acting on the receiving element as just twice this received pressure integrated over the face of the receiving element, we find

$$f_B(\omega) = -4i\omega\rho_1 v_l(\omega) \int_{-b}^b \int_{-b}^b p_{\text{scatt}} \, ds \, ds', \quad (12.97)$$

where ds' is a differential length along the receiving element. Recall, from Eq. (9.24) for 3-D problems the acoustic/elastic transfer function, $t_A(\omega)$, was defined as

$$t_A(\omega) = \frac{F_B(\omega)}{\rho_1 c_1 S v_l(\omega)}, \quad (12.98)$$

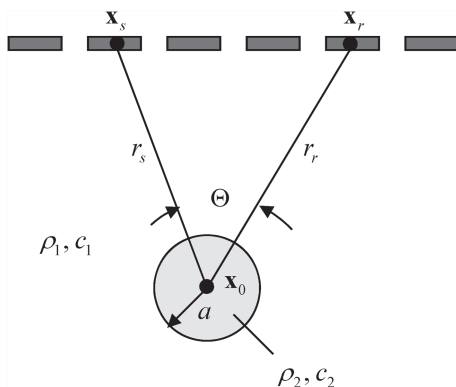
where $F_B(\omega)$ is the blocked force and S was the area of the sending element. For our 2-D problem, this transfer function is analogously defined in terms of the blocked force/unit length and the length of the element as

$$t_A(\omega) = \frac{f_B(\omega)}{\rho_1 c_1 l v_l(\omega)}. \quad (12.99)$$

Thus, we see the acoustic/elastic transfer function is

$$t_A(\omega) = \frac{-4ik_1}{l} \int_{-b}^b \int_{-b}^b p_{\text{scatt}} \, ds \, ds' \quad (12.100)$$

Fig. 12.16 Geometry for modeling the measured response of the circular inclusion by a pair of array elements



and the received voltage, $V(\mathbf{x}_s, \mathbf{x}_r, \omega)$, for a pair of sending and receiving elements located at $(\mathbf{x}_s, \mathbf{x}_r)$, respectively, (see Fig. 12.16) is

$$V(\mathbf{x}_s, \mathbf{x}_r, \omega) = s_I(\omega) \frac{-4ik_l}{l} \int_{-b}^b \int_{-b}^b p_{\text{scatt}}(r_s, r_r, \Theta, \omega) ds ds', \quad (12.101)$$

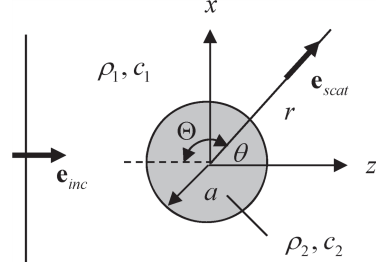
where $s_I(\omega)$ is the system function for this pair of elements and we have explicitly indicated the dependency of the pressure on the distances (r_s, r_r) from the sending and receiving elements to the center of the inclusion, respectively, and the angle, Θ , as shown in Fig. 12.16. These distances are the same distances (r_0, r) shown in Fig. 12.15 and which are present in Eqs. (12.92) and (12.93). If the elements are small enough so that we can neglect the field variations over the elements in Eq. (12.101), then we find simply

$$V(\mathbf{x}_s, \mathbf{x}_r, \omega) = s_I(\omega) \left[-4ik_l l p_{\text{scatt}}(r_s, r_r, \Theta, \omega) \right] \quad (12.102)$$

and we see that our scattered pressure expressions of Eq. (12.92) or (12.93) give us a model for the received voltage directly. For larger elements we can break the elements into segments and use Eq. (12.102) again, summing over those segments to again get an essentially exact separation of variable model for the received voltage. We can use this model to simulate the measured signals in NDE inspections and to analyze various NDE imaging methods so it is an important tool for studying phased array systems. A similar approach could also be used to simulate the response of linear or 2-D arrays to a spherical inclusion since those configurations can also be modeled with point sources and the method of separation of variables. However, this simpler 2-D model is computationally more efficient than a 3-D model while still describing much of the important physics of how array signals are generated, so it will be the only one considered in this book.

We can also use this separation of variables model to examine the 2-D far field imaging measurement models derived in the previous section. To do numerical simulations of images obtained with those imaging models, it is convenient first to write them in terms of the plane wave far field scattering amplitude, $A(\mathbf{e}_{\text{inc}}, \mathbf{e}_{\text{scat}}, \omega)$,

Fig. 12.17 A plane wave incident on a circular inclusion



of the flaw explicitly. This can be done since from Eq. (11.92) we found for the small flaw case:

$$V(\mathbf{X}_s, \mathbf{X}_r, \omega) = s_I(\omega) \hat{P}^{(1)}(\mathbf{X}_s, \mathbf{X}_0, \omega) \hat{P}^{(2)}(\mathbf{X}_r, \mathbf{X}_0, \omega) A(\mathbf{e}_{inc}; \mathbf{e}_{scat}, \omega) \left[\frac{1}{-ik_2 l_A} \frac{\rho c}{\rho_2 c_2} \sqrt{-8\pi i k_2} \right]. \quad (12.103)$$

Placing this result into the full matrix capture imaging measurement model, Eq. (12.44), for a single medium where $\rho = \rho_2 = \rho_1$ and $c = c_2 = c_1$ and taking the density and wave speed of the host material to be (ρ_1, c_1) , respectively, to be compatible with the separation of variables solution just given, gives

$$\tilde{I}_s(\mathbf{X}') = \frac{1}{8\pi^2} \int \left\{ \left| \frac{\omega}{c_1^2} (1 + \cos \Theta) \right| \frac{\cos \theta_r}{R_{r0}} \frac{\cos \theta_s}{R_{s0}} \sqrt{\frac{8\pi c_1}{-i\omega}} A(\mathbf{e}_{inc}; \mathbf{e}_{scat}, \omega) \exp[-i\mathbf{k} \cdot \mathbf{X}'] d\omega dx_r dx_s \right\}. \quad (12.104)$$

For the pulse-echo single medium case, from Eq. (12.26),

$$I_R(\mathbf{X}') = \frac{1}{2\pi^2 c_1^2} \int \frac{\cos \theta_c}{R_{co}} \sqrt{\frac{8\pi c_1}{-i\omega}} A(\mathbf{e}_{inc}; -\mathbf{e}_{inc}, \omega) \exp[-i\mathbf{k} \cdot \mathbf{X}'] |\omega| d\omega dx_c. \quad (12.105)$$

We can easily turn our previous results for the scattered pressure field for a pair of elements into the far field scattering amplitudes needed in Eqs. (12.104) and (12.105). However, the scattering amplitude here is the far field response of the flaw to an incident plane wave so we need to replace our line source with a plane wave. Consider, for example, a plane wave incident on the inclusion from the negative z -axis as shown in Fig. 12.17. In this case the plane wave can be expanded in a series of Bessel functions in the form [13]

$$\exp(ik_1 z) = \exp(ik_1 r \cos \theta) = \sum_{n=-\infty}^{\infty} i^n J_n(k_1 r) \exp[in\theta]. \quad (12.106)$$

To obtain a comparable plane wave from our point source incident wave, Eq. (12.76), we need to let $\theta_0 = \pi, r_0 \rightarrow \infty$ in that equation. For large arguments we have asymptotically

$$\begin{aligned}
 H_n^{(1)}(k_1 r_0) &\sim \sqrt{\frac{2}{\pi k_1 r_0}} \exp i(k_1 r_0 - n\pi/2 - \pi/4) \\
 &= (-i)^n \sqrt{\frac{2}{i\pi k_1 r_0}} \exp(ik_1 r_0)
 \end{aligned} \tag{12.107}$$

so Eq. (12.76) becomes

$$\begin{aligned}
 p_{\text{inc}} &= \frac{i}{4} \sum_{n=-\infty}^{\infty} J_n(k_1 r) H_n^{(1)}(k_1 r_0) \exp[in(\theta - \pi)] \\
 &= \frac{i}{4} \sum_{n=-\infty}^{\infty} (-1)^n J_n(k_1 r) H_n^{(1)}(k_1 r_0) \exp[in\theta] \\
 &= \sqrt{\frac{2}{i\pi k_1 r_0}} \exp(ik_1 r_0) \frac{i}{4} \sum_{n=-\infty}^{\infty} (i)^n J_n(k_1 r) \exp[in\theta].
 \end{aligned} \tag{12.108}$$

Comparing the third line of Eq. (12.108) with Eq. (12.106) we see that we need to remove the factor multiplying the infinite sum in that line and retain the $(-i)^n$ factor from the Hankel functions to obtain the plane wave result. From the second line of Eq. (12.108) we see we can accomplish this by simply making the replacement $iH_n^{(1)}(k_1 r_0)/4 \rightarrow (-i)^n$ in the infinite sum. It follows that if we make that same replacement in the expression for p_{scatt} , Eq. (12.93), we will obtain the scattered pressure due to a plane wave, $p_{\text{scatt}}^{\text{pw}}$, given by

$$p_{\text{scatt}}^{\text{pw}} = - \sum_{n=0}^{\infty} \varepsilon_n (-i)^n \frac{\Delta_2(n)}{\Delta_1(n)} H_n^{(1)}(k_1 r) \cos[n\Theta]. \tag{12.109}$$

In the far field we have

$$p_{\text{scat}}^{\text{pw}} = A(\mathbf{e}_{\text{inc}}; \mathbf{e}_{\text{scat}}, \omega) \frac{\exp(ik_1 r)}{\sqrt{r}}, \tag{12.110}$$

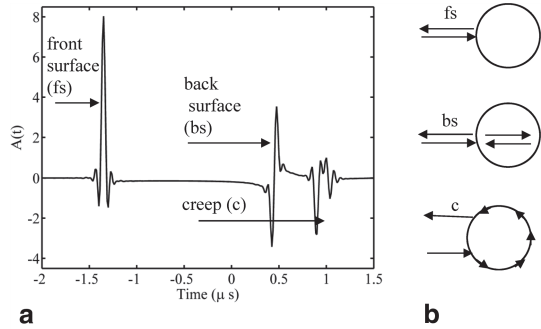
where $A(\mathbf{e}_{\text{inc}}; \mathbf{e}_{\text{scat}}, \omega)$ is the plane wave far field scattering amplitude, and we can recover that scattering amplitude from Eq. (12.109) by using the asymptotic form of the Hankel functions again, i.e.

$$H_n^{(1)}(k_1 r) \sim \sqrt{\frac{2}{i\pi k_1 r}} (-i)^n \exp(ik_1 r), \tag{12.111}$$

to obtain

$$A(\mathbf{e}_{\text{inc}}; \mathbf{e}_{\text{scat}}, \omega) = - \sqrt{\frac{2}{i\pi k_1}} \sum_{n=0}^{\infty} \varepsilon_n (-1)^n \frac{\Delta_2(n)}{\Delta_1(n)} \cos[n\Theta]. \tag{12.112}$$

Fig. 12.18 a The pulse-echo far field scattering amplitude as a function of time for a 1 mm radius inclusion, where the density of the inclusion is 1.5 times that of the host material (taken as water) and the wave speed is also 1.5 times that of the host, and **b** the paths followed by the three major responses identified in **a**.



The pulse-echo far field scattering amplitude, $A(\mathbf{e}_{\text{inc}}; -\mathbf{e}_{\text{inc}}, \omega)$ then follows directly by setting $\Theta = 0$ in Eq. (12.112) to find

$$A(\mathbf{e}_{\text{inc}}; -\mathbf{e}_{\text{inc}}, \omega) = -\sqrt{\frac{2}{i\pi k_1}} \sum_{n=0}^{\infty} \varepsilon_n (-1)^n \frac{\Delta_2(n)}{\Delta_1(n)}. \quad (12.113)$$

To see explicitly the nature of the waves scattered from the inclusion, we can invert the scattering amplitudes of either Eq. (12.112) or (12.113) into the time domain with an inverse FFT. For example, Fig. 12.18a shows a pulse-echo scattering amplitude versus time for a 1 mm radius circular inclusion whose density is twice that of the host material (taken here as water with $c_1 = 1480$ m/s) and wave speed 1.5 times that of the host. This time domain result was obtained by evaluating Eq. (12.113) for frequencies from zero to twenty MHz and then applying a Hanning filter to taper the response to zero between 10 and 20 MHz before inverting into the time domain with an FFT. The predominate waves seen can be identified by their time of arrivals as the front and back surface reflections and a creeping wave that originates from where the incident wave has struck the front surface at a critical angle and then has traveled around the circumference of the flaw at the wave speed of the flaw. These wave paths are shown in Fig. 12.18b. Later arriving waves are also present but these are much smaller responses involving multiply reflected waves, etc. that are not visible in the time window of Fig. 12.18a.

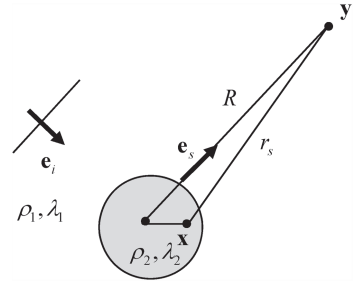
We can gain some additional understanding of the scattering amplitude response of the inclusion by considering this scattering problem in the Born approximation. First, we write the scattered pressure as an integral over the area of the flaw [Schmerr]:

$$p_{\text{scatt}} = \int \left(\gamma_{\rho} \nabla p \cdot \nabla G - \frac{\omega^2}{c_0^2} \gamma_{\lambda} p G \right) dA \quad (12.114)$$

in terms of the pressure and gradient of the pressure and Green's function, G , for Helmholtz's equation, and where

$$\gamma_{\rho} = \frac{\rho_2 - \rho_1}{\rho_2}, \quad \gamma_{\lambda} = \frac{\lambda_2 - \lambda_1}{\lambda_2} \quad (12.115)$$

Fig. 12.19 Scattering geometry for a circular inclusion, showing the incident and scattered wave directions



in terms of the densities (ρ_1, ρ_2) and bulk moduli (λ_1, λ_2) of the host and flaw, respectively. In the far field of the flaw we have (see Fig. 12.19)

$$G \sim \frac{i}{4} \left(\frac{2}{\pi k_1 R} \right)^{1/2} \exp(ik_1 R - i\pi/4) \exp(-ik_1 \mathbf{e}_s \cdot \mathbf{x}), \quad (12.116)$$

$$\nabla G \sim -ik_1 \mathbf{e}_s G,$$

where $\mathbf{e}_s \equiv \mathbf{e}_{\text{scat}}$ is a unit vector in the scattering direction. In the Born approximation we assume the material properties of the flaw and host material are nearly the same and we take the pressure wave field and its derivatives inside the flaw as just those of the incident waves. For an incident plane wave of unit pressure amplitude traveling in the $\mathbf{e}_i \equiv \mathbf{e}_{\text{inc}}$ direction we have

$$p = \exp(ik_1 \mathbf{e}_i \cdot \mathbf{x})$$

$$\nabla p = ik_1 \mathbf{e}_i p. \quad (12.117)$$

Placing Eqs. (12.116) and (12.117) into Eq. (12.114) then gives the scattered pressure in the far field form

$$p_{\text{scatt}} = A(\mathbf{e}_i, \mathbf{e}_s, \omega) \frac{\exp(ik_1 R)}{\sqrt{R}}, \quad (12.118)$$

where the scattering amplitude, $A(\mathbf{e}_i; \mathbf{e}_s, \omega)$, is given as

$$A(\mathbf{e}_i, \mathbf{e}_s, \omega) = -k_1^2 \left(\frac{i}{8\pi k_1} \right)^{1/2} \left[\gamma_\lambda - (\mathbf{e}_i \cdot \mathbf{e}_s) \gamma_\rho \right] \int \exp[ik_1 (\mathbf{e}_i - \mathbf{e}_s) \cdot \mathbf{x}] dA. \quad (12.119)$$

In pulse-echo $\mathbf{e}_s = -\mathbf{e}_i$ and the scattering amplitude is

$$A(\mathbf{e}_i, -\mathbf{e}_i, \omega) = -k_1^2 \left(\frac{i}{8\pi k_1} \right)^{1/2} \left[\gamma_\lambda + \gamma_\rho \right] \int \exp[2ik_1 \mathbf{e}_i \cdot \mathbf{x}] dA. \quad (12.120)$$

However, we note that in the weak scattering limit

$$\frac{\gamma_\rho + \gamma_\lambda}{4} = R_{12}, \quad (12.121)$$

where R_{12} is the plane wave reflection coefficient at normal incidence, so Eq. (12.120) becomes

$$A(\mathbf{e}_i, -\mathbf{e}_i, \omega) = -k_1^2 \left(\frac{2i}{\pi k_1} \right)^{1/2} R_{12} \int \exp[2ik_1 \mathbf{e}_i \cdot \mathbf{x}] dA. \quad (12.122)$$

Now, consider a circular inclusion of radius a . In this case, examine the integral:

$$\begin{aligned} I &= \int \exp(2ik_1 \mathbf{e}_i \cdot \mathbf{x}) dA \\ &= \int_{r=0}^{r=a} \int_{\theta=0}^{\theta=2\pi} \exp(2ik_1 r \cos \theta) r dr d\theta. \end{aligned} \quad (12.123)$$

The theta integration can be performed since

$$\int_{\theta=0}^{\theta=2\pi} \exp(2ik_1 r \cos \theta) d\theta = 2\pi J_0(2k_1 r), \quad (12.124)$$

Where J_0 is the Bessel function of order zero, so the integral becomes

$$I = 2\pi \int_{r=0}^{r=a} J_0(2k_1 r) r dr. \quad (12.125)$$

But the r integration can also be done, since

$$\int_0^1 J_0(bx) x dx = \frac{1}{b} J_1(b), \quad (12.126)$$

so letting $u = r / a$

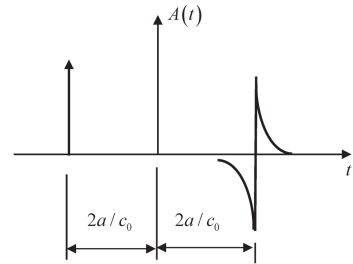
$$I = 2\pi a^2 \int_{u=0}^{u=1} J_0(2k_1 a u) u du = \frac{\pi a}{k_1} J_1(2k_1 a). \quad (12.127)$$

Placing this result into Eq. (12.121) we find

$$A(\mathbf{e}_i, -\mathbf{e}_i, \omega) = -k_1 a \left(\frac{2\pi i}{k_1} \right)^{1/2} R_{12} J_1(2k_1 a). \quad (12.128)$$

We can examine this result for large ka values. We have, asymptotically,

Fig. 12.20 The time domain pulse-echo response of a circular inclusion of radius a in the Born approximation



$$J_1(2k_1 a) \sim \sqrt{\frac{2}{\pi}} \frac{\cos(2k_1 a - 3\pi/4)}{\sqrt{2k_1 a}} \quad (12.129)$$

so

$$\begin{aligned} A(\mathbf{e}_i, -\mathbf{e}_i, \omega) &= -R_{12} \sqrt{2a} \left\{ \sqrt{i} \cos(2k_1 a - 3\pi/4) \right\} \\ &= -R_{12} \sqrt{\frac{a}{2}} \left\{ -i \exp(2ik_1 a) - \exp(-2ik_1 a) \right\} \quad (12.130) \\ &= R_{12} \sqrt{\frac{a}{2}} \left\{ \exp(-2ik_1 a) + i \exp(2ik_1 a) \right\}. \end{aligned}$$

There are two contributions to the scattering amplitude in the Born approximation. These terms represent the front and back surface reflections in the weak scattering limit. This can be seen more clearly by taking twice the real part of the inverse Fourier transform of Eq. (12.130) (which is valid for positive frequencies), giving

$$A(\mathbf{e}_i, -\mathbf{e}_i, t) = R_{12} \sqrt{\frac{a}{2}} \left\{ \delta(t + 2a/c_1) + \frac{1}{\pi(t - 2a/c_1)} \right\}. \quad (12.131)$$

Figure 12.20 shows these two contributions, where the front surface reflection is a delta function and the back surface is the negative of the Hilbert transform of a delta function. In fact the front surface response is identical to that predicted by the Kirchhoff approximation and used as the basis for our imaging measurement model. We can see in Fig. 12.19 that the separation of variables solution gives band limited versions of both the front and back surface waveforms. In the Born approximation the creeping waves and any later arrivals are missing. It can be seen from Eq. (12.130) that the amplitude coefficients of both the front surface and back surface reflections are identical in the Born approximation. However, for flaws that are not weak scatterers the strength of the back surface reflection can be much smaller than that of the front surface, a property also found for 3-D inclusions [Schmerr-Song].

We can use the pulse-echo separation of variables solution, Eq. (12.113) to form up an image with Eq. (12.105) which we write in discrete form for positive frequencies as:

Fig. 12.21 Image of a 1 mm radius circular inclusion obtained with the pulse-echo responses of a 32 element array with a 1 mm pitch, where the density of the inclusion is 1.5 times that of the host material (taken as water) and the wave speed is also 1.5 times that of the host

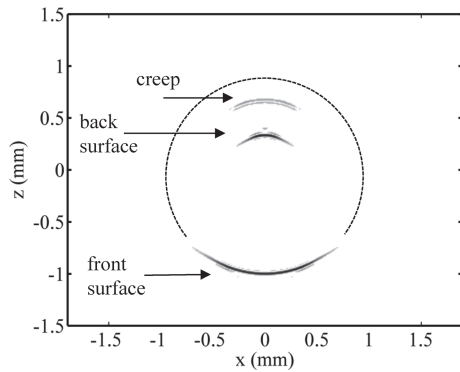
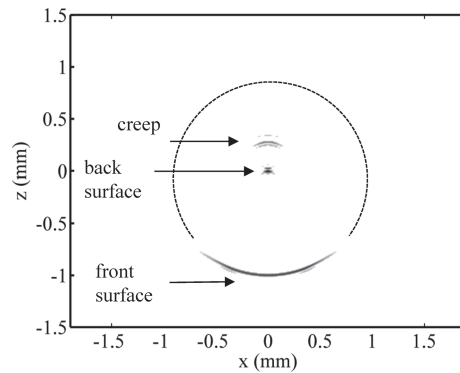


Fig. 12.22 Image of a 1 mm radius circular inclusion obtained with the pulse-echo responses of a 32 element array with a 1 mm pitch, where the density of the inclusion is twice that of the host material (taken as water) and the wave speed is also 2.0 times that of the host

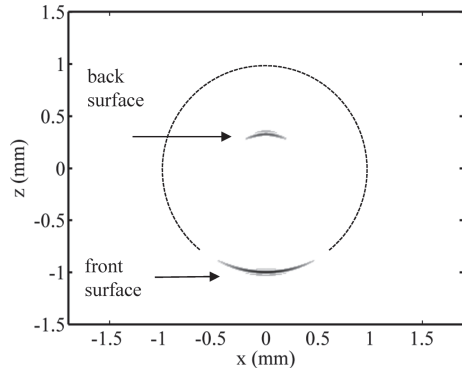


$$I_R(\mathbf{X}') = \frac{\Delta\omega_m \Delta x}{2\pi^2 c^2} 2\text{Re} \left\{ \sum_{m=1}^M \sum_{n=1}^N \omega_m \frac{(\cos \theta_c)_n}{(R_{co})_n} \sqrt{\frac{8\pi c}{-i\omega_m}} A(\mathbf{e}_{\text{inc}}^n; -\mathbf{e}_{\text{inc}}^n, \omega_m) \exp(-i\mathbf{k}_{mn} \cdot \mathbf{X}') \right\}, \quad (12.132)$$

where $\mathbf{e}_{\text{inc}}^n$ is a unit vector along a line from the center of the n th element to the center of the inclusion and $\mathbf{k}_{mn} = 2\omega_m \mathbf{e}_{\text{inc}}^n / c_1$.

Consider, for example, simulating the response of a 32 element array with a 1 mm pitch whose center is located a distance of one inch from the center of the circular inclusion. The resulting pulse-echo image is shown in Fig. 12.21 for the same flaw properties considered in Fig. 12.18. A dotted outline of the flaw is also shown on the image of Fig. 12.21 to help better identify the image features. As can be seen, the front surface of the flaw is imaged properly over the available aperture while both the back surface and creeping wave are misplaced artifacts in the image. This is to be expected since imaging is done using the velocity of the host material, not the flaw (the wave number of the host material, not the flaw, is contained in \mathbf{k}_{mn}). All delay and sum methods, including SAFT and TFM, form images using time delays involving the host velocity so that similar artifacts will appear in images generated with those methods as well. A striking example of this is shown in Fig. 12.22 where

Fig. 12.23 Image of a 1 mm radius circular inclusion obtained with full matrix capture of the responses of a 32 element array with a 1 mm pitch, where the density of the inclusion is 1.5 times that of the host material (taken as water) and the wave speed is also 1.5 times that of the host



the same array is used to image a flaw whose wave speed is twice that of the host material. In this case, when the waves from the back surface are imaged with the host wave speed, the waves appear to have originated from the center of the flaw so that the back surface appears as a point source located at the flaw center. Back surface reflections, creeping waves, and other multiply reflected waves will appear either inside the flaw or outside, depending on the wave speed of the flaw relative to the surrounding material. Thus, only the specular front surface reflections (or edge diffractions, in the case of cracks) are properly imaged with delay and sum methods.

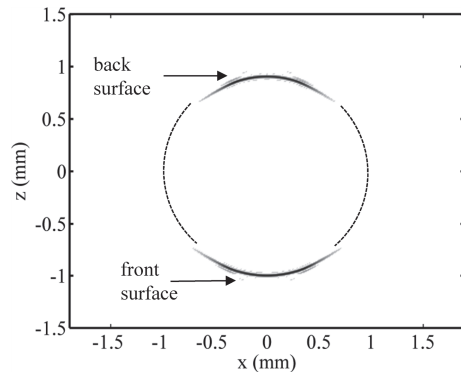
One can also use Eq. (12.104) to form up a full matrix capture image. In this case the discrete form of Eq. (12.104) is given by

$$\tilde{I}_R(\mathbf{X}') = \frac{\Delta\omega\Delta x_r\Delta x_s}{8\pi^2} 2\text{Re} \left\{ \sum_{m=1}^M \sum_{n=1}^N \sum_{p=1}^N \sqrt{\frac{8\pi c_1}{-i\omega_m}} \left| \frac{\omega_m}{c_1^2} (1 + \cos\Theta_{np}) \right| \frac{(\cos\theta_r)_n}{(R_{r0})_n} \frac{(\cos\theta_s)_p}{(R_{s0})_p} \right. \\ \left. \cdot A(\mathbf{e}_{inc}^n; \mathbf{e}_{scat}^p, \omega) \exp[-i\mathbf{k}_{mnp} \cdot \mathbf{X}'] \right\}, \quad (12.133)$$

where \mathbf{e}_{scat}^p is a unit vector along a line from the center of the flaw to the center of the p th array element and now $\mathbf{k}_{mnp} = \omega_m(\mathbf{e}_{inc}^n - \mathbf{e}_{scat}^p)/c_1$. For the same array and the same flaw imaged in pulse-echo in Fig. 12.21, Fig. 12.23 shows the corresponding full matrix capture image. Comparing Fig. 12.21 and Fig. 12.23 one can see that the creeping wave artifact has been essentially eliminated but that the back surface artifact remains. This is to be expected since the creeping waves travel along different path lengths for the various pitch-catch responses present in the full matrix imaging case and are averaged over the aperture, leading to a small response in the resulting image.

Finally, Fig. 12.24 shows the image of a weak scattering inclusion (density and wave speed 1.05 times that of the host material) generated with the simulated pulse-echo responses of the 32 element array. In this case the back surface is also imaged in essentially the correct location. There are also images of creep wave artifacts that are generated but these occur at sufficiently late times so that they are outside the displayed image window of Fig. 12.24.

Fig. 12.24 Image of a 1 mm radius circular inclusion obtained with the pulse-echo responses of a 32 element array with a 1 mm pitch, where the density of the inclusion is 1.05 times that of the host material (taken as water) and the wave speed is also 1.05 times that of the host



References

1. R.C. Fairchild, B.H. Anderson, J.R. Frederick, Synthetic aperture ultrasonic inspection of pressure vessels and piping. ASME Pressure Vessel and Piping Division Reprint, 77-PVP-23, 1977
2. K. Nagai, A new synthetic-aperture focusing method for ultrasonic B-scan imaging by the Fourier Transform. IEEE Trans. Sonics Ultrason. **32**(4), 531–536 (1985)
3. J.T. Ylitalo, H. Ermert, Ultrasound synthetic aperture imaging: monostatic approach. IEEE Trans. Ultrason. Ferroelectr. Freq. Control. **41**, 333–339 (1994)
4. J.A. Jensen, S.I. Nikolov, K.L. Gammelmark, M.H. Pedersen, Synthetic aperture ultrasound imaging. Ultrasonics **44**, e5–e15 (2006)
5. C. Holmes, B.W. Drinkwater, P.D. Wilcox, Post-processing of the full matrix of ultrasonic transmit-receive array data for non-destructive evaluation. NDT&E Int. **38**, 701–711 (2005)
6. R.H. Stolt, A.B. Weglein, *Seismic Imaging and Inversion—Application of Linear Inverse Theory* (Cambridge University Press, Cambridge, 2012)
7. N. Bleistein, *Mathematical Methods for Wave Phenomena* (Academic Press, New York, 1984)
8. N. Bleistein, J.K. Cohen, J.W. Stockwell, Jr., *Mathematics of Multidimensional Seismic Imaging, Migration, and Inversion* (Springer, New York, 2000)
9. N.N. Bojarski, A survey of the physical optics inverse scattering identity. IEEE T. Antenn. Propag. **30**, 980–989 (1982)
10. N. Bleistein, Direct image reconstruction in a plane via physical optics inverse scattering. J. Acoust. Soc. Am. **59**, 1259–1264 (1976)
11. J.K. Cohen, N. Bleistein, The singular function of a surface and physical optics inverse scattering. Wave Motion **1**, 153–161 (1979)
12. L.B. Felsen, N. Marcuvitz, *Radiation and Scattering of Waves* (Prentice-Hall, Englewood Cliffs, 1973), Chap. 4, p. 421
13. W.C. Chew, *Waves and Fields in Inhomogeneous Media* (Van Nostrand Reinhold, New York, 1990)

Chapter 13

Imaging Measurement Models

In Chap. 12, we described the ways in which images can be formed with phased arrays, including a two-dimensional (2-D) far field imaging measurement model. More general imaging measurement models will be developed in this chapter for forming images in 3-D with 2-D arrays and for forming images of 2-D scatterers with linear arrays. As found in Chap. 12 for the 2-D case, these imaging measurement models can be directly related to SAFT imaging and the total focusing method (TFM).

13.1 Pulse-Echo Imaging

In Chap. 11, we developed measurement models from general reciprocity relations and then used the Kirchhoff approximation to express those measurement models in terms of the specular response of the flaw surface (see Eqs. (11.62) and (11.63)). Consider first the case where each element fires and we receive only the collection of pulse echo responses as shown in Fig. 13.1. In Chap. 11, we found that we could express the pulse-echo received voltage of a single element for both immersion and contact testing cases in the form (Eq. (11.63)):

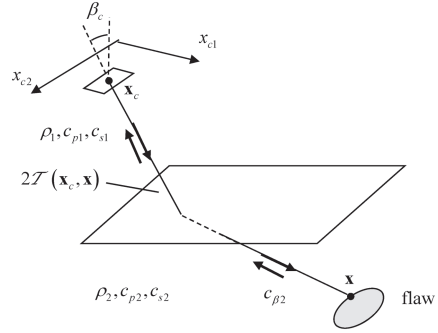
$$\hat{V}(\mathbf{x}_c, \omega) = -2\rho_2 c_{\beta 2} \omega^2 \int_{S_{lit}} \left\{ R_{23}^{\beta, \beta} \left[\tilde{U}_{\beta}^{(1)}(\mathbf{x}_c, \mathbf{x}, \omega) \right]^2 \cdot \exp[2i\omega T(\mathbf{x}_c, \mathbf{x})] dS(\mathbf{x}) \right\}. \quad (13.1)$$

We will replace the normalized displacement amplitude term $\tilde{U}_{\beta}^{(1)}(\mathbf{x}_c, \mathbf{x}, \omega)$ by the corresponding normalized velocity amplitude $\tilde{V}_{\beta}^{(1)}(\mathbf{x}_c, \mathbf{x}, \omega) = -i\omega \tilde{U}_{\beta}^{(1)}(\mathbf{x}_c, \mathbf{x}, \omega)$. Then Eq. (13.1) becomes

$$\hat{V}(\mathbf{x}_c, \omega) = 2\rho_2 c_{\beta 2} \int_{S_{lit}} \left\{ R_{23}^{\beta, \beta} \left[\tilde{V}_{\beta}^{(1)}(\mathbf{x}_c, \mathbf{x}, \omega) \right]^2 \cdot \exp[2i\omega T(\mathbf{x}_c, \mathbf{x})] dS(\mathbf{x}) \right\}. \quad (13.2)$$

As done in Chap. 12 for 2-D scalar problems (see Eq. 12.16), we can define a singular function, $\gamma_s(\mathbf{x})$, of the lit surface which in 3-D problems has sampling property [1]:

Fig. 13.1 A pulse-echo testing setup where an array element acts as both a sending and receiving element in examining a flaw through an interface



$$\int_S f(\mathbf{x}) dS(\mathbf{x}) = \int \gamma_S(\mathbf{x}) f(\mathbf{x}) dV(\mathbf{x}), \quad (13.3)$$

and also define the reflectivity of the surface as $R(\mathbf{x}) \equiv R_{23}^{\beta\beta} \gamma_S(\mathbf{x})$ to turn the surface integral in Eq. (13.3) into a volume integral of that reflectivity over all space, i.e.

$$\hat{V}(\mathbf{x}_c, \omega) = 2\rho_2 c_{\beta 2} \int \left\{ R(\mathbf{x}) \left[\tilde{V}_{\beta}^{(1)}(\mathbf{x}_c, \mathbf{x}, \omega) \right]^2 \exp[2i\omega T(\mathbf{x}_c, \mathbf{x})] dV(\mathbf{x}) \right\}. \quad (13.4)$$

We will now show how we can invert Eq. (13.4) to obtain an image of the flaw properties without making the small flaw assumption, as done in Chap. 12, following a similar approach to that of Bleistein et al. for scalar problems [2]. Specifically, we will again define that image, $I_R(\mathbf{x})$, to simply be the reflectivity of the flaw surface:

$$I_R(\mathbf{x}) \equiv R(\mathbf{x}) = R_{23}^{\beta\beta} \gamma_S(\mathbf{x}) \quad (13.5)$$

and obtain an expression for the image in terms of the measured values, $\hat{V}(\mathbf{x}_c, \omega)$.

In a real ultrasonic array, the values of $\hat{V}(\mathbf{x}_c, \omega)$ are only measured at the discrete locations of the array elements and at discretely sampled frequencies but in inverting Eq. (13.4) we will find it convenient to consider (\mathbf{x}_c, ω) as continuous variables. We will also parameterize the array element locations, \mathbf{x}_c , assumed here to lie on a planar surface, in terms of two auxiliary variables $\xi_c = (\xi_{c1}, \xi_{c2})$, i.e. $\mathbf{x}_c = \mathbf{x}_c(\xi_c)$. Since Eq. (13.4) is in a form similar to that of a 3-D Fourier transform, we will seek to obtain the image of the flaw at a point \mathbf{y} , $I_R(\mathbf{y})$, to be in the form of a similar inverse Fourier-like transform given by

$$I_R(\mathbf{y}) = \iint K(\mathbf{y}, \mathbf{x}_c, \omega) \hat{V}(\mathbf{x}_c, \omega) \exp[-2i\omega T(\mathbf{x}_c, \mathbf{y})] d^2 \xi_c d\omega. \quad (13.6)$$

To see if this representation of the flaw image is possible and to obtain the unknown function $K(\mathbf{y}, \mathbf{x}_c, \omega)$, we will place Eq. (13.4) into (13.6) to obtain

$$I_R(\mathbf{y}) = \iiint 2\rho_2 c_{\beta 2} K(\mathbf{y}, \mathbf{x}_c, \omega) \left[\tilde{V}_{\beta}^{(1)}(\mathbf{x}_c, \mathbf{x}, \omega) \right]^2 \cdot \exp[2i\omega T(\mathbf{x}_c, \mathbf{x}) - 2i\omega T(\mathbf{x}_c, \mathbf{y})] I_R(\mathbf{x}) d^2 \xi_c d\omega dV(\mathbf{x}). \quad (13.7)$$

Since in Eq. (13.7) we are relating the flaw image to a volume integral over itself, then in some sense we must have

$$I_R(\mathbf{y}) = \int \delta(\mathbf{x} - \mathbf{y}) I_R(\mathbf{x}) dV(\mathbf{x}) \quad (13.8)$$

or equivalently, in some sense

$$\delta(\mathbf{x} - \mathbf{y}) = \iint 2\rho_2 c_{\beta 2} K(\mathbf{y}, \mathbf{x}_c, \omega) [\tilde{V}_\beta^{(1)}(\mathbf{x}_c, \mathbf{x}, \omega)]^2 \cdot \exp[2i\omega T(\mathbf{x}_c, \mathbf{x}) - 2i\omega T(\mathbf{x}_c, \mathbf{y})] d^2 \xi_c d\omega, \quad (13.9)$$

where $\delta(\mathbf{x} - \mathbf{y})$ is the Dirac delta function. At least asymptotically at high frequencies Eq. (13.9) may be valid since at high frequencies the rapidly varying phase terms in the integrand will cause the integrals to be small except near the critical point $\mathbf{x} = \mathbf{y}$, where the phase term in Eq. (13.9) vanishes. Near this point, if we expand the phase term to first order and evaluate the amplitude at that point we have

$$T(\mathbf{x}_c, \mathbf{x}) - T(\mathbf{x}_c, \mathbf{y}) \cong \left. \frac{\partial T}{\partial x_i} \right|_{\mathbf{x}=\mathbf{y}} (x_i - y_i) \equiv \nabla_y T \cdot (\mathbf{x} - \mathbf{y}), \quad (13.10)$$

so that

$$\delta(\mathbf{x} - \mathbf{y}) = \iint 2\rho_2 c_{\beta 2} K(\mathbf{y}, \mathbf{x}_c, \omega) [\tilde{V}_\beta^{(1)}(\mathbf{x}_c, \mathbf{y}, \omega)]^2 \exp[2i\omega \nabla_y T \cdot (\mathbf{x} - \mathbf{y})] d^2 \xi_c d\omega. \quad (13.11)$$

If we now define a wave number vector, \mathbf{k} , as

$$\mathbf{k} = 2\omega \nabla_y T \quad (13.12)$$

we can transform the integral in Eq. (13.11) into one over 3-D k -space, i.e.

$$\delta(\mathbf{x} - \mathbf{y}) = \iint 2\rho_2 c_{\beta 2} K(\mathbf{y}, \mathbf{x}_c, \omega) [\tilde{V}_\beta^{(1)}(\mathbf{x}_c, \mathbf{y}, \omega)]^2 \left| \frac{\partial(\omega, \xi_{c1}, \xi_{c2})}{\partial(\mathbf{k})} \right| \exp[i\mathbf{k} \cdot (\mathbf{x} - \mathbf{y})] d^3 \mathbf{k}, \quad (13.13)$$

where the inverse of the Jacobian of the transformation for this pulse-echo case can be written as

$$\frac{\partial(\mathbf{k})}{\partial(\omega, \xi_{c1}, \xi_{c2})} = \omega^2 h_{pe}(\xi_{c1}, \xi_{c2}, \mathbf{y}) \quad (13.14)$$

with

$$h_{pe}(\xi_{c1}, \xi_{c2}, \mathbf{y}) = \det \begin{bmatrix} 2\nabla_y T \\ 2\frac{\partial}{\partial \xi_{c1}}(\nabla_y T) \\ 2\frac{\partial}{\partial \xi_{c2}}(\nabla_y T) \end{bmatrix} \quad (13.15)$$

which is called the Beylkin determinant [2]. If we take

$$K(\mathbf{y}, \mathbf{x}_c, \omega) = \frac{1}{8\pi^3} \frac{\omega^2 |h_{pe}(\xi_{c1}, \xi_{c2}, \mathbf{y})|}{2\rho_2 c_{\beta 2} [\tilde{V}_{\beta}^{(1)}(\mathbf{x}_c, \mathbf{y}, \omega)]^2} \quad (13.16)$$

then Eq. (13.13) becomes

$$\delta(\mathbf{x} - \mathbf{y}) = \frac{1}{8\pi^3} \iint \exp[i\mathbf{k} \cdot (\mathbf{x} - \mathbf{y})] d^3\mathbf{k}, \quad (13.17)$$

which is indeed just a k -space transform representation of the delta function. Thus, if we place Eq. (13.16) into (13.6) we now have an explicit expression for the image given by

$$I_R(\mathbf{y}) = \frac{1}{16\pi^3 \rho_2 c_{\beta 2}} \iint \frac{\omega^2 \hat{V}(\mathbf{x}_c, \omega)}{[\tilde{V}_{\beta}^{(1)}(\mathbf{x}_c, \mathbf{y}, \omega)]^2} |h_{pe}(\xi_{c1}, \xi_{c2}, \mathbf{y})| \exp[-2i\omega T(\mathbf{x}_c, \mathbf{y})] d^2\xi_c d\omega. \quad (13.18)$$

The evaluation of the Beylkin determinant can be made particularly easy by choosing the ξ -parameters to be the spherical coordinates (θ_c, ϕ_c) centered around a reference unit vector in the incident wave direction at point \mathbf{y} . Then, as shown in Appendix A, we have

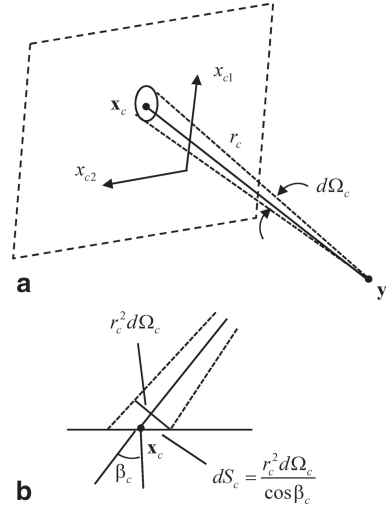
$$h_{pe} = \frac{8 \sin \theta_c}{c_{\beta 2}^3}. \quad (13.19)$$

In this case

$$I_R(\mathbf{y}) = \frac{1}{2\pi^3 \rho_2 c_{\beta 2}^4} \iint \frac{\omega^2 \hat{V}(\mathbf{x}_c, \omega)}{[\tilde{V}_{\beta}^{(1)}(\mathbf{x}_c, \mathbf{y}, \omega)]^2} \exp[-2i\omega T(\mathbf{x}_c, \mathbf{y})] \sin \theta_c d\theta_c d\phi_c d\omega, \quad (13.20)$$

where $\sin \theta_c d\theta_c d\phi_c = d\Omega_c$ is just a differential solid angle as measured in these spherical coordinates. If we let dS_c be a differential area element at the plane of the

Fig. 13.2 **a** Geometry for relating the solid angle coordinates to Cartesian coordinates on the face of the array, and **b** a side view, showing the angle of the array with the face of the array



array we can transform the integration over the solid angle to an integration over the array element coordinates to find

$$I_R(\mathbf{y}) = \frac{1}{2\pi^3 \rho_2 c_{\beta 2}^4} \iint \frac{\omega^2 \hat{V}(\mathbf{x}_c, \omega)}{[\tilde{V}_{\beta}^{(1)}(\mathbf{x}_c, \mathbf{y}, \omega)]^2} \exp[-2i\omega T(\mathbf{x}_c, \mathbf{y})] \frac{d\Omega_c}{dS_c} dS_c d\omega. \quad (13.21)$$

The ratio $d\Omega_c/dS_c$ (see Fig. 13.2a, b) is easy to calculate for an array radiating into a single medium. We find $d\Omega_c/dS_c = \cos \beta_c / r_c^2$, where r_c is the distance from the point \mathbf{x}_c on the plane of the array to an image point \mathbf{y} and β_c is the angle that the ray from \mathbf{y} to \mathbf{x}_c makes with respect to the normal to the plane of the array (Figs. 13.1 and 13.2b). For other more complex situations, such as the radiation of the array through a planar interface, as shown in Fig. 13.1, one can use ray tracing to calculate $d\Omega_c/dS_c$ (see Appendix B for details).

Equation (13.21) is essentially an imaging measurement model for forming an image of the reflectivity of a flaw from either immersion or contact pulse-echo measurements of the voltages $V(\mathbf{x}_c, \omega)$ received from a flaw over all locations in the plane of the array and at all frequencies. In practice, of course, if one only has the voltages measured at the discrete locations of the array elements $\mathbf{x}_c^{nl} = (x_{c1}^n, x_{c2}^l)$ ($n = 1, \dots, L_1$, $l = 1, \dots, L_2$) and at a finite set of positive frequencies, ω_m ($m = 1, \dots, M$), we can only obtain a band-limited and aperture-limited image, $I_R^{BA}(\mathbf{y})$, given by

$$I_R^{BA}(\mathbf{y}) = \frac{\Delta x_{c1} \Delta x_{c2} \Delta \omega}{2\pi^3 \rho_2 c_{\beta 2}^4} 2 \operatorname{Re} \left\{ \sum_{m=1}^M \sum_{n=1}^{L_1} \sum_{l=1}^{L_2} \frac{\omega_m^2 \hat{V}(\mathbf{x}_c^{nl}, \omega_m)}{[\tilde{V}_{\beta}^{(1)}(\mathbf{x}_c^{nl}, \mathbf{y}, \omega_m)]^2} \exp[-2i\omega_m T(\mathbf{x}_c^{nl}, \mathbf{y})] \frac{d\Omega_c}{dS_c}(\mathbf{x}_c^{nl}, \mathbf{y}) \right\}, \quad (13.22)$$

where $(\Delta x_{c1}, \Delta x_{c2})$ is the spacing between elements in the (x_{c1}, x_{c2}) directions, respectively, and $\Delta\omega$ is the spacing between sampled frequencies in rad/s. The term 2Re indicates twice the “real part” and is present because we are only summing over positive frequencies to generate the image of the flaw reflectivity. As discussed in Chap. 12, the measured voltages here are being divided (deconvolved) with a system function and an incident beam wave field term so that we must stabilize that deconvolution process to make it well behaved. Consider, for example, the immersion case where $\hat{V}(\mathbf{x}_c, \omega) = \rho_1 c_{p1} S_A V(\mathbf{x}_c, \omega) / s_I(\omega)$ (see Eq. (11.37) with $\mathbf{x}_s = \mathbf{x}_r = \mathbf{x}_c$). Then

$$I^{BA}(\mathbf{y}) = \frac{\Delta x_{c1} \Delta x_{c2} \Delta\omega}{2\pi^3 \rho_2 c_{\beta 2}^4} 2 \text{Re} \left\{ \sum_{m=1}^M \sum_{n=1}^{L_1} \sum_{l=1}^{L_2} \frac{\rho_1 c_{p1} S_A \omega_m^2 V(\mathbf{x}_c^{nl}, \omega_m)}{s_I(\omega_m) [\tilde{V}_{\beta}^{(1)}(\mathbf{x}_c^{nl}, \mathbf{y}, \omega_m)]^2} \right. \\ \left. \cdot \exp[-2i\omega_m T(\mathbf{x}_c^{nl}, \mathbf{y})] \frac{d\Omega_c}{dS_c}(\mathbf{x}_c^{nl}, \mathbf{y}) \right\}. \quad (13.23)$$

In implementing Eq. (13.23) we can replace the deconvolution by division again with a Wiener filter, i.e.

$$\frac{V(\mathbf{x}_c^{nl}, \omega_m)}{s_I(\omega_m) [\tilde{V}_{\beta}^{(1)}(\mathbf{x}_c^{nl}, \mathbf{y}, \omega_m)]^2} \rightarrow V_W(\mathbf{x}_c^{nl}, \mathbf{y}, \omega_m), \quad (13.24)$$

where the filtered voltage is

$$V_W(\mathbf{x}_c^{nl}, \mathbf{y}, \omega_m) = \frac{V(\mathbf{x}_c^{nl}, \omega_m) \left\{ s_I(\omega_m) [\tilde{V}_{\beta}^{(1)}(\mathbf{x}_c^{nl}, \mathbf{y}, \omega_m)]^2 \right\}^*}{\left| s_I(\omega_m) [\tilde{V}_{\beta}^{(1)}(\mathbf{x}_c^{nl}, \mathbf{y}, \omega_m)]^2 \right|^2 + \varepsilon^2 \max \left\{ \left| s_I(\omega_m) [\tilde{V}_{\beta}^{(1)}(\mathbf{x}_c^{nl}, \mathbf{y}, \omega_m)]^2 \right|^2 \right\}} \quad (13.25)$$

so that in the immersion case we would find

$$I_R^{BA}(\mathbf{y}) = \frac{\Delta x_{c1} \Delta x_{c2} \Delta\omega}{2\pi^3 \rho_2 c_{\beta 2}^4} 2 \text{Re} \left\{ \sum_{m=1}^M \sum_{n=1}^{L_1} \sum_{l=1}^{L_2} \rho_1 c_{p1} S_A \omega_m^2 V_W(\mathbf{x}_c^{nl}, \mathbf{y}, \omega_m) \right. \\ \left. \cdot \exp[-2i\omega_m T(\mathbf{x}_c^{nl}, \mathbf{y})] \frac{d\Omega_c}{dS_c}(\mathbf{x}_c^{nl}, \mathbf{y}) \right\}. \quad (13.26)$$

This 3-D imaging measurement model can also be related to a corresponding SAFT algorithm, as done in Chap. 12 for the simpler 2-D problems. If we set $\varepsilon = 0$ in the Wiener filter and simply ignore all the terms in Eq. (13.26) except the constant

$\Delta\omega/2\pi$, the measured voltages, and the phase terms involving the propagation terms T we find the SAFT image (see Eq. (12.5)):

$$I_{SAFT}(\mathbf{y}) = 2 \operatorname{Re} \left\{ \frac{\Delta\omega}{2\pi} \sum_{m=1}^M \sum_{n=1}^{L_1} \sum_{l=1}^{L_2} V(\mathbf{x}_c^{nl}, \omega_m) \exp \left[-2i\omega_m T(\mathbf{x}_c^{nl}, \mathbf{y}) \right] \right\}. \quad (13.27)$$

The imaging measurement model of Eq. (13.21) is applicable to the imaging of large or small surfaces. When the flaw is small enough so that the incident wave fields do not vary significantly over the flaw surface we have

$$\begin{aligned} \tilde{V}_\beta^{(1)}(\mathbf{x}_c, \mathbf{y}) &\equiv \tilde{V}_\beta^{(1)}(\mathbf{x}_c, \mathbf{y}_0) \\ T(\mathbf{x}_c, \mathbf{y}) &\equiv T(\mathbf{x}_c, \mathbf{y}_0) + \mathbf{e}_\beta^{(1)} \cdot (\mathbf{y} - \mathbf{y}_0) / c_{\beta 2} \end{aligned} \quad (13.28)$$

for a fixed image point \mathbf{y}_0 near the flaw surface and Eq. (13.21) becomes

$$\begin{aligned} I_R(\mathbf{y}) &= \frac{1}{2\pi^3 \rho_2 c_{\beta 2}^4} \iint \left\{ \frac{\omega^2 \tilde{V}(\mathbf{x}_c, \omega)}{\left[\tilde{V}_\beta^{(1)}(\mathbf{x}_c, \mathbf{y}_0, \omega) \exp \{ i\omega T(\mathbf{x}_c, \mathbf{y}_0) \} \right]^2} \right. \\ &\quad \left. \cdot \exp \left[-2ik_{\beta 2} \mathbf{e}_\beta^{(1)} \cdot (\mathbf{y} - \mathbf{y}_0) \right] \frac{d\Omega_c}{dS_c} dS_c d\omega \right\}, \end{aligned} \quad (13.29)$$

which is a POFFIS-style imaging expression, similar to the 2-D case considered in Chap. 12. Computationally, Eq. (13.29) requires much less effort than Eq. (13.21) to implement since one needs to calculate the incident wave field terms only for the one fixed point \mathbf{y}_0 for all image points \mathbf{y} . However, in implementing Eq. (13.29) one should only use images points near the flaw surface so that Eq. (13.28) is not violated. Thus, with multiple flaws that are widely separated one should locally image each flaw individually with Eq. (13.29).

As done in Chap. 12 for the 2-D scalar case, we can write Eq. (13.29) in terms of the far field scattering amplitude of the flaw by using the Thompson-Gray measurement model (Eqs. (11.26) and (11.30)) for either an immersion or contact setup. In the pulse-echo case we have $\rho_1 c_{\beta 1} S_A = \rho c_p S_B$, and $A = A(\mathbf{e}_{inc}^\beta; -\mathbf{e}_{inc}^\beta)$, so that we find that for both the immersion and contact cases

$$I_R(\mathbf{y}) = \frac{2}{\pi^2 c_{\beta 2}} \iint ik_{\beta 2} A(\mathbf{e}_{inc}^\beta; -\mathbf{e}_{inc}^\beta) \exp \left[-2i\omega \mathbf{e}_\beta^{(1)} \cdot (\mathbf{y} - \mathbf{y}_0) \right] \frac{d\Omega_c}{dS_c} dS_c d\omega. \quad (13.30)$$

Equation (13.30) can be used to simulate POFFIS-style images generated by an imaging measurement model for a flaw whose far field scattering amplitude can be modeled by semi-analytical or numerical means. When discussing POFFIS imaging, Bleistein [3] obtained this result for 3-D scalar wave problems (see Eq. 9.2.9 in [3]), a result which we see here is also directly applicable to imaging with elastic waves.

We can also develop an imaging measurement model for the pulse-echo edge response of cracks following similar steps to those used in Chap. 12 for the scalar 2-D case. We will again assume that there is no specular response from the crack surface (which will be assumed to be entirely lit by the incident waves) so that we must start by modifying Eq. (13.2) to reflect that fact. In Chap. 11, we obtained this form of an approximate measurement model by using the Kirchhoff approximation to obtain (see Eq. (11.47), written here in terms of velocities)

$$\hat{V}(\mathbf{x}_c, \omega) = - \int_S \left\{ I(\mathbf{x}) \left[\tilde{V}_\beta^{(1)}(\mathbf{x}_c, \mathbf{x}, \omega) \right]^2 \exp[i\omega\phi(\mathbf{x}_c, \mathbf{x})] dS(\mathbf{x}) \right\}, \quad (13.31)$$

where $\phi(\mathbf{x}_c, \mathbf{x}) = 2T(\mathbf{x}_c, \mathbf{x})$. The integrand term $I(\mathbf{x})$ was evaluated at the stationary phase points on the flaw surface to model the specular response of the surface. Here, instead we keep the original integral term, Eq. (11.48), which for pulse-echo, same mode responses reduces to

$$I(\mathbf{x}) = n_j C_{ijkl} \left[\sum_{m=p,sv} \left(\frac{R_{23}^{m;\beta} d_{\beta l}^{(2)} d_{mk}^r e_{ml}^r}{c_{m2}} - \frac{R_{23}^{m;\beta} d_{\beta k}^{(2)} d_{mi}^r e_{\beta l}^{(2)}}{c_{\beta 2}} \right) \right]. \quad (13.32)$$

Now, let us define a vector field, \mathbf{F} , as

$$\mathbf{F} = - \frac{1}{i\omega} \frac{\mathbf{n} \times \nabla \phi}{|\nabla \phi|^2 - (\nabla \phi \cdot \mathbf{n})^2} I(\mathbf{x}) \left[\tilde{V}_\beta^{(1)} \right]^2 \exp[i\omega\phi], \quad (13.33)$$

which is possible since if there are no specular points on the crack surface the denominator in Eq. (13.33) never vanishes. At high frequencies the derivatives of this field come from derivatives of the phase term so that we have, approximately

$$\mathbf{n} \cdot (\nabla \times \mathbf{F}) = -I(\mathbf{x}) \left[\tilde{V}_\beta^{(1)} \right]^2 \exp[i\omega\phi], \quad (13.34)$$

where we have used the vector identity

$$(\mathbf{n} \times \nabla \phi) \cdot (\mathbf{n} \times \nabla \phi) = \nabla \phi \cdot \nabla \phi - (\mathbf{n} \cdot \nabla \phi)(\mathbf{n} \cdot \nabla \phi). \quad (13.35)$$

Thus, using Stokes theorem

$$\int_S \mathbf{n} \cdot (\nabla \times \mathbf{F}) dS = \int_C \mathbf{F} \cdot \mathbf{t} ds, \quad (13.36)$$

where \mathbf{t} is a unit tangent vector to the crack edge, C , we can rewrite Eq. (13.31) as

$$\hat{V}(\mathbf{x}_c, \omega) = - \frac{1}{i\omega} \int_C \frac{(\mathbf{n} \times \nabla \phi) \cdot \mathbf{t}}{|\nabla \phi|^2 - (\nabla \phi \cdot \mathbf{n})^2} I(\mathbf{x}) \left[\tilde{V}_\beta^{(1)} \right]^2 \exp[i\omega\phi] ds. \quad (13.37)$$

If we introduce the singular function of the crack edge, $\gamma_c(\mathbf{x})$, where for any function $f(\mathbf{x})$

$$\int_c f(\mathbf{x}) ds(\mathbf{x}) = \int \gamma_c(\mathbf{x}) f(\mathbf{x}) dV(\mathbf{x}), \quad (13.38)$$

Equation (13.37) can be rewritten in a form very similar to Eq. (13.4), namely

$$\hat{V}(\mathbf{x}_c, \omega) = \frac{2\rho_2 c_{\beta 2}^2}{i\omega} \int R_e \left\{ \left[\tilde{V}_{\beta}^{(1)}(\mathbf{x}_c, \mathbf{x}, \omega) \right]^2 \exp[2i\omega T(\mathbf{x}_c, \mathbf{x})] dV(\mathbf{x}) \right\} \quad (13.39)$$

where the reflectivity of the crack edge, R_e , is defined here as

$$R_e = \frac{-(\mathbf{n} \times \nabla \phi) \cdot \mathbf{t}}{|\nabla \phi|^2 - (\nabla \phi \cdot \mathbf{n})^2} \frac{I(\mathbf{x})}{2\rho_2 c_{\beta 2}^2} \gamma_c(\mathbf{x}). \quad (13.40)$$

As discussed in Chap. 12 for the 2-D case, we cannot expect to image explicitly this reflectivity at each point on the edge because of the dependence of the coefficients of $\gamma_c(\mathbf{x})$ in Eq. (13.40) on the incident and scattering directions, but we can ignore those dependencies and write $R_e = R_e(\mathbf{x})$ only in trying to image the crack edge singularities. In that case Eqs. (13.39) and (13.4) are nearly identical. In fact, we can make the forms identical by making the replacement $\hat{V} \rightarrow (i\omega/c_{\beta 2})\hat{V}$ in Eq. (13.4). Thus, making the same replacement in the imaging measurement model of Eq. (13.21), we obtain for an image of the crack edge

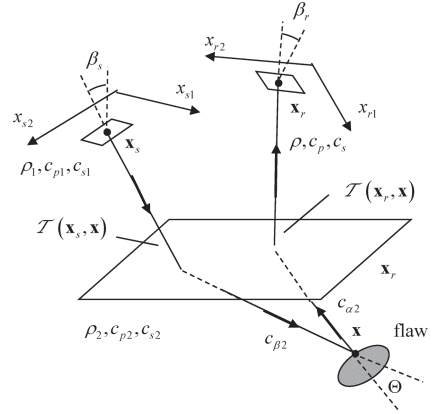
$$I_e(\mathbf{y}) = \frac{1}{2\pi^3 c_{\beta 2}^4} \iint \frac{(i\omega/c_{\beta 2}) \omega^2 \hat{V}(\mathbf{x}_c, \omega)}{\left[\tilde{V}_{\beta}^{(1)}(\mathbf{x}_c, \mathbf{y}, \omega) \right]^2} \exp[-2i\omega T(\mathbf{x}_c, \mathbf{y})] \frac{d\Omega_c}{dS_c} dS_c d\omega, \quad (13.41)$$

with $I_e(\mathbf{y}) \equiv R_e(\mathbf{y})$. As found in Chap. 12 for the 2-D scalar case, we see that a 3-D crack image involves an additional $i\omega/c_{\beta 2}$ factor not present in the image of the specular surface response. Although we have only considered the pulse-echo case here, following the same steps for the full matrix imaging approach described in the next section also leads to a crack edge image that is related to the specular flaw response by making the replacement $\hat{V} \rightarrow (i\omega/c_{\alpha 2})\hat{V}$.

13.2 Full Matrix Imaging

The previous section showed that measuring all the pulse-echo responses from an array of elements in a 2-D array was sufficient to generate a 3-D image of a flaw. If instead, one captures all combinations of responses from element pairs (full-matrix capture) then one can also form up an image. The element pairs can be on the same array or on separate arrays, as shown in Fig. 13.3. As done in Chap. 12 for the scalar

Fig. 13.3 A pitch-catch setup where separate array elements are used as senders and receivers



problem, we will first consider the case where we have a single sending element and receive with all elements of the receiving array. Again, we will consider the parameters $(\mathbf{x}_s, \mathbf{x}_r, \omega)$ as continuous variables. From Eq. (11.62) we had

$$\begin{aligned} \widehat{V}(\mathbf{x}_s, \mathbf{x}_r, \omega) = & -2\rho_2 c_{\alpha 2} \omega^2 \int_{S_{in}} \left\{ R_{23}^{\alpha; \beta} (e_{\alpha k}^r n_k) \tilde{U}_{\beta}^{(1)}(\mathbf{x}_s, \mathbf{x}, \omega) \tilde{U}_{\alpha}^{(2)}(\mathbf{x}_r, \mathbf{x}, \omega) \right. \\ & \left. \cdot \exp[i\omega\phi(\mathbf{x}_s, \mathbf{x}_r, \omega)] dS(\mathbf{x}) \right\}, \end{aligned} \quad (13.42)$$

which, in terms of the velocities $\tilde{V}_{\beta}^{(1)} = -i\omega\tilde{U}_{\beta}^{(1)}$, $\tilde{V}_{\alpha}^{(2)} = -i\omega\tilde{U}_{\alpha}^{(2)}$ becomes

$$\begin{aligned} \widehat{V}(\mathbf{x}_s, \mathbf{x}_r, \omega) = & 2\rho_2 c_{\alpha 2} \int_{S_{in}} \left\{ R_{23}^{\alpha; \beta} (e_{\alpha k}^r n_k) \tilde{V}_{\beta}^{(1)}(\mathbf{x}_s, \mathbf{x}, \omega) \tilde{V}_{\alpha}^{(2)}(\mathbf{x}_r, \mathbf{x}, \omega) \right. \\ & \left. \cdot \exp[i\omega\phi(\mathbf{x}_s, \mathbf{x}_r, \omega)] dS(\mathbf{x}) \right\}. \end{aligned} \quad (13.43)$$

Introducing the singular function of the surface again we can write Eq. (13.43) as

$$\begin{aligned} \widehat{V}(\mathbf{x}_s, \mathbf{x}_r, \omega) = & 2\rho_2 c_{\alpha 2} \int \left\{ R_{23}^{\alpha; \beta} (e_{\alpha k}^r n_k) \gamma_S(\mathbf{x}) \tilde{V}_{\beta}^{(1)}(\mathbf{x}_s, \mathbf{x}, \omega) \tilde{V}_{\alpha}^{(2)}(\mathbf{x}_r, \mathbf{x}, \omega) \right. \\ & \left. \cdot \exp[i\omega\phi(\mathbf{x}_s, \mathbf{x}_r, \mathbf{x})] dV(\mathbf{x}) \right\}. \end{aligned} \quad (13.44)$$

We will parameterize the receiving array element locations, \mathbf{x}_r , assumed here to lie on a planar surface, in terms of two auxiliary variables $\xi_r = (\xi_{r1}, \xi_{r2})$, i.e. $\mathbf{x}_r = \mathbf{x}_r(\xi_r)$, and in this case define the flaw image as

$$I_R(\mathbf{y}) \equiv R(\mathbf{y}) = R_{23}^{\alpha; \beta} (e_{\alpha k}^r n_k) \gamma_S(\mathbf{y}), \quad (13.45)$$

which reduces to our previous definition, Eq. (13.5), for the pulse-echo case. Since Eq. (13.44) is again a Fourier-like integral we will attempt to invert that equation and form an image via the relation

$$I_R(\mathbf{y}) = \iint K(\mathbf{y}, \mathbf{x}_s, \mathbf{x}_r, \omega) \widehat{V}(\mathbf{x}_s, \mathbf{x}_r(\xi_r), \omega) \cdot \exp[-i\omega\phi(\mathbf{x}_s, \mathbf{x}_r(\xi_r), \mathbf{y})] d^2\xi_r d\omega \quad (13.46)$$

Placing Eq. (13.44) into (13.46) gives formally

$$I_R(\mathbf{y}) = \iiint K(\mathbf{y}, \mathbf{x}_s, \mathbf{x}_r, \omega) \{2\rho_2 c_{\alpha 2} I_R(\mathbf{x}) \tilde{V}_\beta^{(1)}(\mathbf{x}_s, \mathbf{x}, \omega) \tilde{V}_\alpha^{(2)}(\mathbf{x}_r, \mathbf{x}, \omega) \cdot \exp[i\omega\phi(\mathbf{x}_s, \mathbf{x}_r, \mathbf{x}) - i\omega\phi(\mathbf{x}_s, \mathbf{x}_r(\xi_r), \mathbf{y})]\} d^2\xi_r d\omega dV(\mathbf{x}) \quad (13.47)$$

As in the pulse-echo case Eq. (13.47) can be true if in some sense we have

$$\delta(\mathbf{x} - \mathbf{y}) = \iint K(\mathbf{y}, \mathbf{x}_s, \mathbf{x}_r, \omega) \{2\rho_2 c_{\alpha 2} \tilde{V}_\beta^{(1)}(\mathbf{x}_s, \mathbf{x}, \omega) \tilde{V}_\alpha^{(2)}(\mathbf{x}_r, \mathbf{x}, \omega) \cdot \exp[i\omega\phi(\mathbf{x}_s, \mathbf{x}_r, \mathbf{x}) - i\omega\phi(\mathbf{x}_s, \mathbf{x}_r(\xi_r), \mathbf{y})] d^2\xi_r d\omega\}. \quad (13.48)$$

This is possible since at high frequencies again we expect the major contribution to come from this highly oscillatory integrand around the critical point $\mathbf{x} = \mathbf{y}$. Evaluating the amplitude of the integrand of the integral at that critical point and expanding the phase to first order, i.e.

$$\phi(\mathbf{x}_s, \mathbf{x}_r, \mathbf{x}) - \phi(\mathbf{x}_s, \mathbf{x}_r, \mathbf{y}) \cong \left. \frac{\partial \phi}{\partial x_i} \right|_{\mathbf{x}=\mathbf{y}} (x_i - y_i) = \nabla_y \phi(\mathbf{x} - \mathbf{y}). \quad (13.49)$$

Equation (13.48) becomes

$$\delta(\mathbf{x} - \mathbf{y}) = \iint K(\mathbf{y}, \mathbf{x}_s, \mathbf{x}_r, \omega) \{2\rho_2 c_{\alpha 2} \tilde{V}_\beta^{(1)}(\mathbf{x}_s, \mathbf{y}, \omega) \tilde{V}_\alpha^{(2)}(\mathbf{x}_r, \mathbf{y}, \omega) \cdot \exp[i\omega \nabla_y \phi \cdot (\mathbf{x} - \mathbf{y})]\} d^2\xi_r d\omega. \quad (13.50)$$

Now, defining a wave vector, \mathbf{k} , as

$$\mathbf{k} = \omega \nabla_y \phi, \quad (13.51)$$

we transform the integral in Eq. (13.50) to one over 3-D \mathbf{k} -space:

$$\delta(\mathbf{x} - \mathbf{y}) = \iint K(\mathbf{y}, \mathbf{x}_s, \mathbf{x}_r, \omega) \{2\rho_2 c_{\alpha 2} \tilde{V}_\beta^{(1)}(\mathbf{x}_s, \mathbf{y}, \omega) \tilde{V}_\alpha^{(2)}(\mathbf{x}_r, \mathbf{y}, \omega) \cdot \left. \frac{\partial(\omega, \xi_{r1}, \xi_{r2})}{\partial(\mathbf{k})} \right| \exp[i\mathbf{k} \cdot (\mathbf{x} - \mathbf{y})]\} d^3\mathbf{k}, \quad (13.52)$$

where the inverse of the Jacobian of the transformation can be written as

$$\frac{\partial(\mathbf{k})}{\partial(\omega, \xi_{r1}, \xi_{r2})} = \omega^2 h(\mathbf{x}_s, \mathbf{x}_r, (\xi_{r1}, \xi_{r2}), \mathbf{y}) = \omega^2 h(\xi_{r1}, \xi_{r2}, \mathbf{y}) \quad (13.53)$$

in terms of the Beylkin determinant, $h(\xi_{r1}, \xi_{r2}, \mathbf{y})$. Thus, if one takes the function K as

$$K(\mathbf{y}, \mathbf{x}_s, \mathbf{x}_r, \omega) = \frac{\omega^2 |h(\xi_{r1}, \xi_{r2}, \mathbf{y})|}{16\pi^3 \rho_2 c_{\alpha 2} \tilde{V}_\beta^{(1)}(\mathbf{x}_s, \mathbf{y}, \omega) \tilde{V}_\alpha^{(2)}(\mathbf{x}_r, \mathbf{y}, \omega)} \quad (13.54)$$

one obtains the k-space transform representation of the delta function again (see Eq. (3.17)) and Eq. (13.46) becomes

$$I_R(\mathbf{y}) = \frac{1}{16\pi^3 \rho_2 c_{\alpha 2}} \iint \frac{\omega^2 |h(\xi_{r1}, \xi_{r2}, \mathbf{y})| \tilde{V}(\mathbf{x}_s, \mathbf{x}_r(\xi_r), \omega)}{\tilde{V}_\beta^{(1)}(\mathbf{x}_s, \mathbf{y}, \omega) \tilde{V}_\alpha^{(2)}(\mathbf{x}_r(\xi_r), \mathbf{y}, \omega)} \cdot \exp[-i\omega\phi(\mathbf{x}_s, \mathbf{x}_r(\xi_r), \mathbf{y})] d^2 \xi_r d\omega. \quad (13.55)$$

If one chooses the parameters (ξ_{r1}, ξ_{r2}) to be spherical coordinates (θ_r, ϕ_r) at the image point \mathbf{y} , as shown in Appendix A the magnitude of this Beylkin determinant simply becomes

$$|h(\mathbf{x}_s, \mathbf{x}_r(\theta_r, \phi_r), \mathbf{y})| = \left| 1 + \frac{c_{\alpha 2}}{c_{\beta 2}} \cos \Theta \right| \frac{\sin \theta_r}{c_{\alpha 2}^3}, \quad (13.56)$$

where Θ is the angle at \mathbf{y} between a ray path from the source to that point and a ray path from the receiver to that point (see Fig. 13.3). Then Eq. (13.55) is

$$I_R(\mathbf{y}) = \frac{1}{16\pi^3 \rho_2 c_{\alpha 2}^4} \iint \left| 1 + \frac{c_{\alpha 2}}{c_{\beta 2}} \cos \Theta \right| \frac{\omega^2 \tilde{V}(\mathbf{x}_s, \mathbf{x}_r(\xi_r), \omega)}{\tilde{V}_\beta^{(1)}(\mathbf{x}_s, \mathbf{y}, \omega) \tilde{V}_\alpha^{(2)}(\mathbf{x}_r(\xi_r), \mathbf{y}, \omega)}, \quad (13.57)$$

$$\cdot \exp[-i\omega\phi(\mathbf{x}_s, \mathbf{x}_r(\xi_r), \mathbf{y})] d\Omega_r d\omega$$

where $d\Omega_r = \sin \theta_r d\theta_r d\phi_r$ is a solid angle corresponding to different $\mathbf{e}_\alpha^{(2)}$ directions at \mathbf{y} from the receivers. If we relate this solid angle to a corresponding area, dS_r , on the plane of the receiving elements then we have

$$I_R(\mathbf{y}) = \frac{1}{16\pi^3 \rho_2 c_{\alpha 2}^4} \iint \left| 1 + \frac{c_{\alpha 2}}{c_{\beta 2}} \cos \Theta \right| \frac{\omega^2 \tilde{V}(\mathbf{x}_s, \mathbf{x}_r(\xi_r), \omega)}{\tilde{V}_\beta^{(1)}(\mathbf{x}_s, \mathbf{y}, \omega) \tilde{V}_\alpha^{(2)}(\mathbf{x}_r(\xi_r), \mathbf{y}, \omega)} \cdot \exp[-i\omega\phi(\mathbf{x}_s, \mathbf{x}_r(\xi_r), \mathbf{y})] \frac{d\Omega_r}{dS_r} dS_r d\omega. \quad (13.58)$$

Equation (13.58) shows that we can form an image of the reflectivity of a flaw with only one element firing but with many receiving elements. However, in practice one uses an array with some or all elements both firing and receiving to have as high a signal-to-noise ratio as possible. To simulate this case we can write the position of

the sending element, \mathbf{x}_s , in terms of parameters (ξ_{s1}, ξ_{s2}) and consider varying those parameters. If we choose these auxiliary parameters to be spherical coordinates (θ_s, ϕ_s) , as similarly done with the receiving elements, then $I_R = I_R(\mathbf{y}, \theta_s, \phi_s)$ and we can define the integral of this image over a solid angle as measured to the sending elements as

$$\bar{I}_R(\mathbf{y}) = \int I_R(\mathbf{y}, \theta_s, \phi_s) d\Omega_s \quad (13.59)$$

where $d\Omega_s = \sin \theta_s d\theta_s d\phi_s$. Using that definition and Eq. (13.58) we find

$$\begin{aligned} \bar{I}_R(\mathbf{y}) = & \frac{1}{16\pi^3 \rho_2 c_{\alpha 2}^4} \iiint \left| 1 + \frac{c_{\alpha 2}}{c_{\beta 2}} \cos \Theta \right| \frac{\omega^2 \hat{V}(\mathbf{x}_s(\xi_s), \mathbf{x}_r(\xi_r), \omega)}{\tilde{V}_{\beta}^{(1)}(\mathbf{x}_s(\xi_s), \mathbf{y}, \omega) \tilde{V}_{\alpha}^{(2)}(\mathbf{x}_r(\xi_r), \mathbf{y}, \omega)} \\ & \cdot \exp[-i\omega\phi(\mathbf{x}_s(\xi_s), \mathbf{x}_r(\xi_r), \mathbf{y})] \frac{d\Omega_r}{dS_r} \frac{d\Omega_s}{dS_s} dS_r dS_s d\omega \end{aligned} \quad (13.60)$$

in terms of an integral over both the sending and receiving element surfaces. The angle–area ratios $d\Omega_r / dS_r$, $d\Omega_s / dS_s$ can again be easily obtained with ray theory for a single medium or radiation through a planar interface, as shown in Fig. 13.3. The details are given in Appendix B where it is shown that the angles (β_s, β_r) between the normal to the arrays and the Snell's law rays to the flaw (see Fig. 13.3) appear.

Equation (13.60) shows that in a full matrix imaging approach the explicit image generated in the continuous case is the flaw reflectivity integrated over the angular directions associated with the sending elements. For a real array, this image will become a band-limited and aperture-limited (on both the sending and receiving sides) version, \bar{I}_R^{BA} , of this integrated reflectivity. Implementing Eq. (13.60) is computationally challenging since it involves a total of five integrations. We can relate this image to one obtained with the total focusing method, replacing the integrations with finite sums over the element locations and positive frequencies, and ignoring all the parameters except a $\Delta\omega / 2\pi$ factor, the measured voltage, and phase term in Eq. (13.60), to obtain the TFM image generated by an array with L_1 elements in the x_1 -direction and L_2 elements in the x_2 -direction at M positive frequencies (see Eq. 12.2.4):

$$I_{TFM}(\mathbf{y}) = 2 \operatorname{Re} \left\{ \frac{\Delta\omega}{2\pi} \sum_{m=1}^M \sum_{n=1}^{L_1} \sum_{l=1}^{L_2} \sum_{p=1}^{L_1} \sum_{q=1}^{L_2} V(\mathbf{x}_s^{pq}, \mathbf{x}_r^{nl}, \omega_m) \exp[-i\omega_m\phi(\mathbf{x}_s^{pq}, \mathbf{x}_r^{nl}, \mathbf{y})] \right\}. \quad (13.61)$$

If the flaw is small enough we can reduce the computational burden of computing Eq. (13.60) somewhat by using a POFFIS-style imaging model for full matrix imaging. In this case, we assume that the incident fields can be evaluated at a fixed image

point, \mathbf{y}_0 , near the scatterer and the phase term in Eq. (13.60) expanded to first order, so making the replacements

$$\begin{aligned}\tilde{V}_\beta^{(1)}(\mathbf{x}_s, \mathbf{y}, \omega) &\equiv \tilde{V}_\beta^{(1)}(\mathbf{x}_s, \mathbf{y}_0, \omega) \\ \tilde{V}_\alpha^{(2)}(\mathbf{x}_r, \mathbf{y}, \omega) &\equiv \tilde{V}_\alpha^{(2)}(\mathbf{x}_r, \mathbf{y}_0, \omega) \\ \phi(\mathbf{x}_s, \mathbf{x}_r, \mathbf{y}) &\equiv T(\mathbf{x}_s, \mathbf{y}_0) + T(\mathbf{x}_r, \mathbf{y}_0) \\ &\quad + \mathbf{e}_\beta^{(1)} \cdot (\mathbf{y} - \mathbf{y}_0) / c_{\beta 2} + \mathbf{e}_\alpha^{(2)} \cdot (\mathbf{y} - \mathbf{y}_0) / c_{\alpha 2}\end{aligned}\quad (13.62)$$

in Eq. (13.60) gives

$$\begin{aligned}\bar{I}_R(\mathbf{y}) = & \frac{1}{16\pi^3 \rho_2 c_{\alpha 2}^4} \iiint \frac{\omega^2 \hat{V}(\mathbf{x}_s, \mathbf{x}_r, \omega)}{\tilde{V}_\beta^{(1)}(\mathbf{x}_s, \mathbf{y}_0, \omega) \exp[i\omega T(\mathbf{x}_s, \mathbf{y}_0)] \tilde{V}_\alpha^{(2)}(\mathbf{x}_r, \mathbf{y}_0, \omega) \exp[i\omega T(\mathbf{x}_r, \mathbf{y}_0)]} \\ & \cdot \left| 1 + \frac{c_{\alpha 2}}{c_{\beta 2}} \cos \Theta \right| \exp[-i\omega \mathbf{s} \cdot (\mathbf{y} - \mathbf{y}_0)] \frac{d\Omega_r}{dS_r} \frac{d\Omega_s}{dS_s} dS_r dS_s d\omega,\end{aligned}\quad (13.63)$$

where

$$\mathbf{s} = \mathbf{e}_\beta^{(1)} / c_{\beta 2} + \mathbf{e}_\alpha^{(2)} / c_{\alpha 2} . \quad (13.64)$$

Equation (13.63) can also be written in terms of the far field scattering amplitude since we found previously in Chap. 11 the measured voltage in the Thompson-Gray measurement model written in our current notation is

$$\begin{aligned}\hat{V}(\mathbf{x}_s, \mathbf{x}_r, \omega) &= \tilde{V}_\beta^{(1)}(\mathbf{x}_s, \mathbf{y}_0, \omega) \exp[i\omega T(\mathbf{x}_s, \mathbf{y}_0)] \tilde{V}_\alpha^{(2)}(\mathbf{x}_r, \mathbf{y}_0, \omega) \exp[i\omega T(\mathbf{x}_r, \mathbf{y}_0)] \\ &\quad \cdot \frac{4\pi \rho_2 c_{\alpha 2}}{-ik_{\alpha 2}} A(\mathbf{e}_\beta^{(1)}, -\mathbf{e}_\alpha^{(2)}, \omega)\end{aligned}\quad (13.65)$$

so that Eq. (13.63) becomes

$$\begin{aligned}\bar{I}_R(\mathbf{y}) = & \frac{1}{4\pi^2 c_{\alpha 2}} \iiint (ik_{\alpha 2}) A(\mathbf{e}_\beta^{(1)}; -\mathbf{e}_\alpha^{(2)}, \omega) \left| 1 + \frac{c_{\alpha 2}}{c_{\beta 2}} \cos \Theta \right| \\ & \cdot \exp[-i\omega \mathbf{s} \cdot (\mathbf{y} - \mathbf{y}_0)] \frac{d\Omega_r}{dS_r} \frac{d\Omega_s}{dS_s} dS_r dS_s d\omega,\end{aligned}\quad (13.66)$$

which can be compared to the pulse-echo case of Eq. (13.30). Equation (13.66) is valid for both immersion and contact setups.

Fig. 13.4 A sending and receiving element of two linear arrays interrogating a 2-D scatterer through a planar interface, where the long axis of the scatterer is parallel to the long dimensions of the elements. The polarizations of P- and S-waves incident on the scatterer in states (1) and (2) are shown explicitly, as well as other pertinent geometric parameters

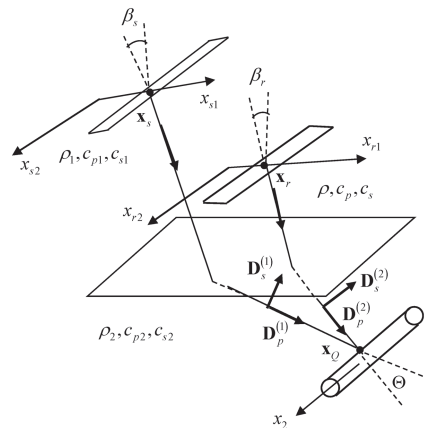
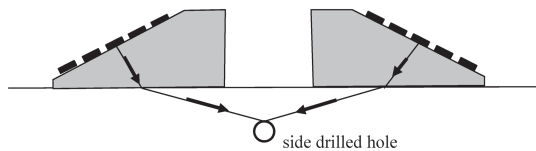


Fig. 13.5 An example inspection setup of the type shown in Fig. 13.4 where a pair of linear arrays placed on wedges are used in a pitch-catch calibration setup with a side-drilled hole



13.3 2-D Imaging with a Linear Array

In Sect. 13.1, we showed how to form a 3-D image of a flaw from 3-D data consisting of the pulse-echo responses as measured over the planar area of a 2-D array and at all frequencies. This is the minimum amount of data needed for 3-D imaging. For a linear array, we only have elements distributed in one dimension so that it is not possible to develop a 3-D image without physically moving the array to obtain additional data measured in a second spatial dimension. However, one can use linear arrays without any motion to form 2-D images of 2-D scatterers such as side-drilled holes, which are commonly used as reference scatterers in evaluating imaging parameters. Figure 13.4 shows a pitch-catch setup where separate sending and receiving elements of a linear array are interrogating a 2-D scatterer. The centroids of the sending and receiving elements are located at the points $(\mathbf{x}_s, \mathbf{x}_r)$ respectively. It is assumed that both these centroids and the point \mathbf{x}_Q on the scatterer all lie in a common plane given as $x_{s2} = x_{r2} = x_2 = 0$, which is also the common plane of incidence in this setup. An example inspection problem of this type is shown in Fig. 13.5 where a pair of linear arrays are used in a calibration setup with a side-drilled hole. We will find it convenient to use capital letters to distinguish quantities that only have 2-D coordinates in that common plane. Thus, since the centroids $(\mathbf{x}_s, \mathbf{x}_r)$ are also assumed to lie along the (x_{s1}, x_{r1}) axes, respectively, we have $\mathbf{x}_s = (\mathbf{X}_s, x_{s2} = 0)$ where $\mathbf{X}_s = (x_{s1}, x_{s3} = 0)$, and $\mathbf{x}_r = (\mathbf{X}_r, x_{r2} = 0)$ where $\mathbf{X}_r = (x_{r1}, x_{r3} = 0)$. Similarly, we can write $\mathbf{x}_Q = (\mathbf{X}, x_2 = 0)$ where $\mathbf{X} = (x_1, x_3)$ and a generic point \mathbf{x} anywhere on the scatterer is $\mathbf{x} = (\mathbf{X}, x_2)$.

We begin with our previous result for full matrix imaging given by Eq. (13.43):

$$\begin{aligned} \widehat{V}(\mathbf{x}_s, \mathbf{x}_r, \omega) = 2\rho_2 c_{\alpha 2} \int_{S_{\text{lit}}} \left\{ R_{23}^{\alpha;\beta} \left(e_{\alpha k}^r n_k \right) \tilde{V}_{\beta}^{(1)}(\mathbf{x}_s, \mathbf{x}, \omega) \tilde{V}_{\alpha}^{(2)}(\mathbf{x}_r, \mathbf{x}, \omega) \right. \\ \left. \cdot \exp[i\omega\phi(\mathbf{x}_s, \mathbf{x}_r, \mathbf{x})] dS(\mathbf{x}) \right\}. \end{aligned} \quad (13.67)$$

and note that we can write it in terms of the incident velocities in states (1) and (2) as (see Eqs. (11.42) and (11.43), which are for the corresponding displacements):

$$\widehat{V}(\mathbf{x}_s, \mathbf{x}_r, \omega) = 2\rho_2 c_{\alpha 2} \int_{S_{\text{lit}}} R_{23}^{\alpha;\beta} \left(e_{\alpha k}^r n_k \right) \left[\tilde{\mathbf{v}}_{\beta}^{(1);inc} \cdot \mathbf{d}_{\beta}^{(1)} \right] \left[\tilde{\mathbf{v}}_{\alpha}^{(2)} \cdot \mathbf{d}_{\alpha}^{(2)} \right] dS(\mathbf{x}), \quad (13.68)$$

where

$$\begin{aligned} \tilde{\mathbf{v}}_{\beta}^{(1);inc} &= \tilde{V}_{\beta}^{(1)}(\mathbf{x}_s, \mathbf{x}, \omega) \mathbf{d}_{\beta}^{(1)} \exp[i\omega T(\mathbf{x}_s, \mathbf{x})] \\ \tilde{\mathbf{v}}_{\alpha}^{(2)} &= \tilde{V}_{\alpha}^{(2)}(\mathbf{x}_r, \mathbf{x}, \omega) \mathbf{d}_{\alpha}^{(2)} \exp[i\omega T(\mathbf{x}_r, \mathbf{x})], \end{aligned} \quad (13.69)$$

For our linear arrays we will write these velocity fields instead as

$$\begin{aligned} \tilde{\mathbf{v}}_{\beta}^{(1);inc} &= \tilde{V}_{\beta}^{(1)}(\mathbf{X}_s, \mathbf{x}, \omega) \mathbf{D}_{\beta}^{(1)} \exp[i\omega T(\mathbf{X}_s, \mathbf{X})], \\ \tilde{\mathbf{v}}_{\alpha}^{(2)} &= \tilde{V}_{\alpha}^{(2)}(\mathbf{X}_r, \mathbf{x}, \omega) \mathbf{D}_{\alpha}^{(2)} \exp[i\omega T(\mathbf{X}_r, \mathbf{X})], \end{aligned} \quad (13.70)$$

where we have used the fact that the long length of the array elements produces a wave field from an element polarized essentially in the plane of incidence (the polarizations $\mathbf{D}_{\beta}^{(1)}, \mathbf{D}_{\alpha}^{(2)}$ (see Fig. 13.4) lie in those planes for the sending and receiving elements, respectively) and the major time delays are also primarily those measured in that plane since there is little beam spreading in the x_2 -direction. Thus, Eq. (13.68) becomes

$$\widehat{V}(\mathbf{x}_s, \mathbf{x}_r, \omega) = 2\rho_2 c_{\alpha 2} \int_{S_{\text{lit}}} R_{23}^{\alpha;\beta} \left(e_{\alpha k}^r n_k \right) \left[\tilde{\mathbf{v}}_{\beta}^{(1);inc} \cdot \mathbf{D}_{\beta}^{(1)} \right] \left[\tilde{\mathbf{v}}_{\alpha}^{(2)} \cdot \mathbf{D}_{\alpha}^{(2)} \right] dS(\mathbf{x}) \quad (13.71)$$

or, equivalently,

$$\begin{aligned} \widehat{V}(\mathbf{x}_s, \mathbf{x}_r, \omega) = 2\rho_2 c_{\alpha 2} \int_{S_{\text{lit}}} R_{23}^{\alpha;\beta} \left(e_{\alpha k}^r n_k \right) \tilde{V}_{\beta}^{(1)}(\mathbf{X}_s, \mathbf{x}, \omega) \tilde{V}_{\alpha}^{(2)}(\mathbf{X}_r, \mathbf{x}, \omega) \\ \exp[i\omega\phi(\mathbf{X}_s, \mathbf{X}_r, \mathbf{X})] dS(\mathbf{x}) \end{aligned} \quad (13.72)$$

with

$$\phi(\mathbf{X}_s, \mathbf{X}_r, \mathbf{X}, \omega) = T(\mathbf{X}_s, \mathbf{X}) + T(\mathbf{X}_r, \mathbf{X}). \quad (13.73)$$

If we ignore the ends of the scatterer, the response of the linear array element from the specular points is independent of the x_2 -coordinate and so that $R_{23}^{\alpha;\beta}(e_{\alpha k}^r n_k)$ does not depend on x_2 but the incident fields are still 3-D. This means that we can separate

Eq. (13.73) into an integral of the wave fields over the length of the scatterer and a counterclockwise integral over the “lit” circumference of the flaw, in the form

$$\begin{aligned} \widehat{V}(\mathbf{x}_s, \mathbf{x}_r, \omega) = 2\rho_2 c_{\alpha 2} \int_{C_{lit}} R_{23}^{\alpha;\beta} (e_{\alpha k}^r n_k) \tilde{V}_{\alpha\beta}^L(\mathbf{X}_s, \mathbf{X}_r, \mathbf{X}, \omega) \\ \exp[i\omega\phi(\mathbf{X}_s, \mathbf{X}_r, \mathbf{X})] ds(\mathbf{X}), \end{aligned} \quad (13.74)$$

where

$$\tilde{V}_{\alpha\beta}^L(\mathbf{X}_s, \mathbf{X}_r, \mathbf{X}) = \int_L \tilde{V}_{\beta}^{(1)}(\mathbf{X}_s, \mathbf{X}, x_2) \tilde{V}_{\alpha}^{(2)}(\mathbf{X}_r, \mathbf{X}, x_2) dx_2 \quad (13.75)$$

Introducing the singular function $\gamma_C(\mathbf{X})$ of the lit circumference of the scatter then transforms Eq. (13.74) into an integral over the entire (x_1, x_3) plane at $x_2 = 0$ and we have

$$\widehat{V}(\mathbf{X}_s, \mathbf{X}_r, \omega) = 2\rho_2 c_{\alpha 2} \int R_{2D}(\mathbf{X}) \tilde{V}_{\alpha\beta}^L(\mathbf{X}_s, \mathbf{X}_r, \mathbf{X}, \omega) \exp[i\omega\phi(\mathbf{X}_s, \mathbf{X}_r, \mathbf{X})] d^2\mathbf{X} \quad (13.76)$$

in terms of the 2-D reflectivity

$$R_{2D}(\mathbf{X}) = R_{23}^{\alpha;\beta} (e_{\alpha k}^r n_k) \gamma_c(\mathbf{X}). \quad (13.77)$$

Comparing Eq. (13.76) with (13.44) we see that Eq. (13.76) is the comparable starting point for describing full matrix imaging of 2-D scatterers with linear arrays. Thus, we can follow the same steps used for 3-D imaging suitably modified to account for the fact that we are now working strictly with 2-D terms in Eq. (13.76). In this case we will define a 2-D image, $I_{2D}(\mathbf{X})$, as $I_{2D}(\mathbf{X}) = R_{2D}(\mathbf{X})$, and for a fixed sending element and varying receiving elements attempt to obtain this image through an integral of the form

$$\begin{aligned} I_{2D}(\mathbf{Y}) = \iint K(\mathbf{X}_s, \mathbf{X}_r(\xi_{r1}), \mathbf{Y}, \omega) \widehat{V}(\mathbf{X}_r, \mathbf{X}_s, \omega) \\ \cdot \exp[-i\omega\phi(\mathbf{X}_s, \mathbf{X}_r(\xi_{r1}), \mathbf{Y})] d\omega d\xi_{r1}, \end{aligned} \quad (13.78)$$

where the location of the centroid of the receiving element (assumed to be a continuous variable here again) is parameterized by the variable ξ_{r1} , i.e. $\mathbf{X}_r(\xi_{r1}) = (x_{r1}(\xi_{r1}), 0)$. If we place Eq. (13.76) into Eq. (13.78) we obtain formally

$$\begin{aligned} I_{2D}(\mathbf{Y}) = 2\rho_2 c_{\alpha 2} \iint \iint K(\mathbf{X}_s, \mathbf{X}_r, \mathbf{Y}, \omega) \tilde{V}_{\alpha\beta}^L(\mathbf{X}_r, \mathbf{X}_s, \mathbf{X}, \omega) I_{2D}(\mathbf{X}) \\ \cdot \exp[i\omega\phi(\mathbf{X}_s, \mathbf{X}_r, \mathbf{X}) - i\omega\phi(\mathbf{X}_s, \mathbf{X}_r, \mathbf{Y})] d\omega d\xi_{r1} d^2\mathbf{X}, \end{aligned} \quad (13.79)$$

which suggests we must have

$$\begin{aligned} \delta(\mathbf{X} - \mathbf{Y}) = & \int \int 2\rho_2 c_{\alpha 2} K(\mathbf{X}_s, \mathbf{X}_r, \mathbf{Y}, \omega) \tilde{V}_{\alpha\beta}^L(\mathbf{X}_s, \mathbf{X}_r, \mathbf{X}, \omega) \\ & \cdot \exp[i\omega\phi(\mathbf{X}_s, \mathbf{X}_r, \mathbf{X}) - i\omega\phi(\mathbf{X}_s, \mathbf{X}_r, \mathbf{Y})] d\omega d\xi_{r1}. \end{aligned} \quad (13.80)$$

Again, as in the 3-D imaging case we expect at high frequencies the major contributions to the integrals in Eq. (13.80) to occur around the critical point $\mathbf{X} = \mathbf{Y}$. Expanding the phase term about this point we have

$$\phi(\mathbf{X}_s, \mathbf{X}_r, \mathbf{X}) = \phi(\mathbf{X}_s, \mathbf{X}_r, \mathbf{Y}) + \nabla_Y \phi \cdot (\mathbf{X} - \mathbf{Y}) \quad (13.81)$$

and defining a 2-D \mathbf{k} -vector, \mathbf{k}_{2D} , as

$$\mathbf{k}_{2D} = \omega \nabla_Y \phi \quad (13.82)$$

we can rewrite Eq. (13.80) as approximately

$$\begin{aligned} \delta(\mathbf{X} - \mathbf{Y}) = & \int \int 2\rho_2 c_{\alpha 2} K(\mathbf{X}_s, \mathbf{X}_r, \mathbf{Y}, \omega) \tilde{V}_{\alpha\beta}^L(\mathbf{X}_s, \mathbf{X}_r, \mathbf{Y}, \omega) \\ & \cdot \left| \frac{\partial(\omega, \xi_{r1})}{\partial(\mathbf{k}_{2D})} \right| \exp[i\mathbf{k}_{2D} \cdot (\mathbf{X} - \mathbf{Y})] d^2\mathbf{k}_{2D} \end{aligned} \quad (13.83)$$

As in the 3-D case, we can write the inverse of the Jacobian appearing in Eq. (13.83) in terms of a Beylkin determinant, $H(\xi_{r1}, \mathbf{Y})$, where now

$$\frac{\partial(\mathbf{k}_{2D})}{\partial(\omega, \xi_{r1})} = \omega H(\xi_{r1}, \mathbf{Y}) \quad (13.84)$$

and

$$H(\xi_{r1}, \mathbf{Y}) = \det \left[\begin{array}{c} \nabla_Y \phi \\ \frac{\partial}{\partial \xi_{r1}} (\nabla_Y \phi) \end{array} \right] \quad (13.85)$$

which shows that if we take

$$K(\mathbf{X}_s, \mathbf{X}_r, \mathbf{Y}, \omega) = \frac{1}{4\pi^2} \frac{|\omega H(\xi_{r1}, \mathbf{Y})|}{2\rho_2 c_{\alpha 2} \tilde{V}_{\alpha\beta}^L(\mathbf{X}_s, \mathbf{X}_r, \mathbf{Y}, \omega)} \quad (13.86)$$

we indeed have valid representation of a delta function, i.e.

$$\delta(\mathbf{X} - \mathbf{Y}) = \frac{1}{4\pi^2} \int \int \exp[i\mathbf{k}_{2D} \cdot (\mathbf{X} - \mathbf{Y})] d^2\mathbf{k}_{2D}. \quad (13.87)$$

Placing Eq. (13.86) into Eq. (13.78) gives

$$I_{2D}(\mathbf{Y}) = \frac{1}{8\pi^2 \rho_2 c_{\alpha 2}} \iint \frac{|\omega H(\xi_{r1}, \mathbf{Y})|}{\tilde{V}_{\alpha\beta}^L(\mathbf{X}_s, \mathbf{X}_r, \mathbf{Y}, \omega)} \hat{V}(\mathbf{X}_r, \mathbf{X}_s, \omega) \cdot \exp[-i\omega\phi(\mathbf{X}_s, \mathbf{X}_r, \mathbf{Y})] d\omega d\xi_{r1}. \quad (13.88)$$

As shown in Appendix A, if we take the parameter ξ_{r1} to be associated with the incident angle, θ_r , of a wave in the plane of incidence coming from the receiving element to the image point, \mathbf{Y} , the Beylkin determinant can be easily evaluated (see Eq. (A.34) and the image is given by

$$I_{2D}(\mathbf{Y}) = \frac{1}{8\pi^2 \rho_2 c_{\alpha 2}^3} \iint |\omega| \left| 1 + \frac{c_{\alpha 2}}{c_{\beta 2}} \cos \Theta \right| \frac{\hat{V}(\mathbf{X}_r, \mathbf{X}_s, \omega)}{\tilde{V}_{\alpha\beta}^L(\mathbf{X}_s, \mathbf{X}_r, \mathbf{Y}, \omega)} \cdot \exp[-i\omega\phi(\mathbf{X}_s, \mathbf{X}_r, \mathbf{Y})] d\omega d\theta_r. \quad (13.89)$$

If through ray tracing, following the same procedures as done for the solid angle/area ratios in Appendix B, we relate the angle parameter θ_r to the location of the receiving element in the x_{r1} -direction by evaluating $d\theta_r / dx_{r1}$ then we have

$$I_{2D}(\mathbf{Y}) = \frac{1}{8\pi^2 \rho_2 c_{\alpha 2}^3} \iint |\omega| \left| 1 + \frac{c_{\alpha 2}}{c_{\beta 2}} \cos \Theta \right| \frac{\hat{V}(\mathbf{X}_r, \mathbf{X}_s, \omega)}{\tilde{V}_{\alpha\beta}^L(\mathbf{X}_s, \mathbf{X}_r, \mathbf{Y}, \omega)} \cdot \exp[-i\omega\phi(\mathbf{X}_s, \mathbf{X}_r, \mathbf{Y})] d\omega \frac{d\theta_r}{dx_{r1}} dx_{r1}. \quad (13.90)$$

Equation (13.90) shows that, similar to what was found in the 3-D imaging case, with a linear array we can form a 2-D image with only one element firing and receiving with many elements. To simulate the full matrix imaging case where there are multiple sending elements firing, we can use Eq. (13.90) and parameterize $\mathbf{X}_s = \mathbf{X}_s(x_{s1})$ by an incident angle, θ_s , at the image point of a wave coming from the sending element which also causes the image of Eq. (13.90) to be a function of that angle, i.e. $I_{2D} = I_{2D}(\mathbf{Y}, \theta_s)$. If we integrate these images over that incident angle, we obtain the 2-D image

$$\bar{I}_{2D}(\mathbf{Y}) = \int I_{2D}(\mathbf{Y}, \theta_s) d\theta_s, \quad (13.91)$$

where

$$\bar{I}_{2D}(\mathbf{Y}) = \frac{1}{8\pi^2 \rho_2 c_{\alpha 2}^3} \iint |\omega| \left| 1 + \frac{c_{\alpha 2}}{c_{\beta 2}} \cos \Theta \right| \frac{\hat{V}(\mathbf{X}_r, \mathbf{X}_s, \omega)}{\tilde{V}_{\alpha\beta}^L(\mathbf{X}_s, \mathbf{X}_r, \mathbf{Y}, \omega)} \cdot \exp[-i\omega\phi(\mathbf{X}_s, \mathbf{X}_r, \mathbf{Y})] d\omega \frac{d\theta_r}{dx_{r1}} \frac{d\theta_s}{dx_{s1}} dx_{r1} dx_{s1}. \quad (13.92)$$

Equation (13.92) is an imaging measurement model for full matrix imaging. If one replaces the integrals by sums over the array elements and positive frequencies only and ignores all the terms except a $\Delta\omega/2\pi$ parameter, the measured voltage, and the phase term, Eq. (13.92) becomes the 2-D image generated by the total focusing method:

$$I_{TFM}^{2D}(\mathbf{Y}) = 2 \operatorname{Re} \left\{ \frac{\Delta\omega}{2\pi} \sum_{m=1}^M \sum_{n=1}^N \sum_{l=1}^N V(\mathbf{X}_{rn}, \mathbf{X}_{sl}, \omega_m) \exp[-i\omega_m \phi(\mathbf{X}_{sl}, \mathbf{X}_{rn}, \mathbf{Y})] \right\}, \quad (13.93)$$

which can be compared with the total focusing result for 2-D scalar problems given by Eq. (12.49).

A 2-D image of a 2-D scatterer can also be generated with the pulse-echo responses of a linear array. Many details follow closely that of the full matrix imaging approach so we will only outline the highlights here. The pulse-echo case can be obtained from our full matrix case by letting $\alpha = \beta$ and making the following replacements:

$$\begin{aligned} \mathbf{X}_s &= \mathbf{X}_r \rightarrow \mathbf{X}_c = (x_{c1}, x_{c3} = 0), \\ \hat{V}(\mathbf{X}_s, \mathbf{X}_r, \omega) &\rightarrow \hat{V}(\mathbf{X}_c, \omega), \\ \tilde{V}_{\alpha\beta}^L &\rightarrow \tilde{V}_{\beta}^L(\mathbf{X}_c, \mathbf{X}, \omega) = \int_L \left[\tilde{V}_{\beta}(\mathbf{X}_c, \mathbf{X}, x_2, \omega) \right]^2 dx_2, \\ I_{2D}(\mathbf{X}) &= R_{2D}(\mathbf{X}) \rightarrow R_{23}^{\beta;\beta} \gamma_c(\mathbf{X}), \\ \phi(\mathbf{X}_s, \mathbf{X}_r, \mathbf{X}) &\rightarrow \phi(\mathbf{X}_c, \mathbf{X}) = 2T(\mathbf{X}_c, \mathbf{X}). \end{aligned} \quad (13.94)$$

Then the equation for the received voltage, Eq. (13.74), becomes

$$\hat{V}(\mathbf{X}_c, \omega) = 2\rho_2 c_{\beta 2} \int_{C_{lit}} R_{2D}(\mathbf{X}) \tilde{V}_{\beta}^L(\mathbf{X}_c, \mathbf{X}, \omega) \exp[2i\omega T(\mathbf{X}_c, \mathbf{X})] d^2\mathbf{X}, \quad (13.95)$$

where, recall, the integration is counterclockwise over the lit surface. This equation can then be inverted, as before, to form the 2-D image as

$$\begin{aligned} I_{2D}(\mathbf{Y}) &= \frac{1}{8\pi^2 \rho_2 c_{\beta 2}} \iint \frac{|\omega H_{pe}(\xi_{c1}, \mathbf{Y})|}{\tilde{V}_{\beta}^L(\mathbf{X}_c, \mathbf{Y}, \omega)} \hat{V}(\mathbf{X}_c, \omega) \\ &\quad \cdot \exp[-2i\omega T(\mathbf{X}_c, \mathbf{Y})] d\omega d\xi_{c1}, \end{aligned} \quad (13.96)$$

where the location of the centroid of the element has been parameterized in terms of the variable ξ_{c1} , i.e. $x_{c1} = x_{c1}(\xi_{c1})$. As shown in Appendix A, the Beylkin determinant for the pulse-echo case, $H_{pe}(\xi_{c1}, \mathbf{Y})$, can be easily evaluated if we take $\xi_{c1} = \theta_c$, where θ_c is an angle defining the incident wave direction at the image point. Then $H_{pe} = 4/c_{\beta 2}^2$ and we find

$$I_{2D}(\mathbf{Y}) = \frac{1}{2\pi^2 \rho_2 c_{\beta 2}^3} \iint \frac{|\omega| \hat{V}(\mathbf{X}_c, \omega)}{\tilde{V}_{\beta}^L(\mathbf{X}_c, \mathbf{Y}, \omega)} \exp[-2i\omega T(\mathbf{X}_c, \mathbf{Y})] d\omega d\theta_c. \quad (13.97)$$

Again, using ray tracing we can turn the integration over θ_c into one over the centroid location, x_{c1} , of the element, to obtain the pulse-echo imaging measurement model:

$$I_{2D}(\mathbf{Y}) = \frac{1}{2\pi^2 \rho_2 c_{\beta 2}^3} \iint \frac{|\omega| \tilde{V}(\mathbf{X}_c, \omega)}{\tilde{V}_{\beta}^L(\mathbf{X}_c, \mathbf{Y}, \omega)} \exp[-2i\omega T(\mathbf{X}_c, \mathbf{Y})] \frac{d\theta_c}{dx_{c1}} d\omega dx_{c1}. \quad (13.98)$$

Two-dimensional SAFT imaging with a linear array is a highly simplified version of this imaging model where only the measured voltage and phase terms are retained and the integrations are replaced by sums over the discrete elements and at discrete positive frequencies, giving

$$I_{SAFT}^{2D}(\mathbf{Y}) = 2 \operatorname{Re} \left\{ \frac{\Delta\omega}{2\pi} \sum_{m=1}^M \sum_{n=1}^N V(\mathbf{X}_{cn}, \omega_m) \exp[-2i\omega_m T(\mathbf{X}_{cn}, \mathbf{Y})] \right\}, \quad (13.99)$$

which is the same expression as developed for 2-D scalar problems in Eq. (12.29).

Finally, a 2-D POFFIS-style imaging model can again be obtained for both full matrix and pulse-echo imaging with a linear array. Consider first the pulse-echo case, Eq. (13.98), and assume the flaw is small enough so that the fields can be evaluated at a fixed point, \mathbf{Y}_0 , at the flaw and the phase term expanded to first order. Then

$$\begin{aligned} \tilde{V}_{\beta}^L(\mathbf{X}_c, \mathbf{Y}, \omega) &\cong \tilde{V}_{\beta}^L(\mathbf{X}_c, \mathbf{Y}_0, \omega), \\ T(\mathbf{X}_c, \mathbf{Y}) &\cong T(\mathbf{X}_c, \mathbf{Y}_0) + \mathbf{e}_{\beta}^{(1)} \cdot (\mathbf{Y} - \mathbf{Y}_0) / c_{\beta 2}, \end{aligned} \quad (13.100)$$

(see the corresponding 3-D case in Eq. (13.28)), to give

$$\begin{aligned} I_{2D}(\mathbf{Y}) &= \frac{1}{2\pi^2 \rho_2 c_{\beta 2}^3} \iint \frac{|\omega| \tilde{V}(\mathbf{X}_c, \omega)}{\tilde{V}_{\beta}^L(\mathbf{X}_c, \mathbf{Y}_0, \omega) \exp[2i\omega T(\mathbf{X}_c, \mathbf{Y}_0)]} \\ &\quad \cdot \exp[-2ik_{\beta 2} \mathbf{e}_{\beta}^{(1)} \cdot (\mathbf{Y} - \mathbf{Y}_0)] \frac{d\theta_c}{dx_{c1}} d\omega dx_{c1}. \end{aligned} \quad (13.101)$$

To compare this result to that of the scalar 2-D problem in a single medium considered in Chap. 12, consider the immersion case version of Eq. (13.101), which is

$$\begin{aligned} I_{2D}(\mathbf{Y}) &= \frac{1}{2\pi^2 \rho_2 c_{\beta 2}^3} \iint \frac{\rho_1 c_{\rho 1} S_A |\omega| V(\mathbf{X}_c, \omega)}{s_I(\omega) \tilde{V}_{\beta}^L(\mathbf{X}_c, \mathbf{Y}_0, \omega) \exp[2i\omega T(\mathbf{X}_c, \mathbf{Y}_0)]} \\ &\quad \cdot \exp[-2ik_{\beta 2} \mathbf{e}_{\beta}^{(1)} \cdot (\mathbf{Y} - \mathbf{Y}_0)] \frac{d\theta_c}{dx_{c1}} d\omega dx_{c1}. \end{aligned} \quad (13.102)$$

Letting $\rho_1 = \rho_2 = \rho$, $c_{p1} = c_{\beta 2} = c$, $2k_{\beta 2} \mathbf{e}_{\beta}^{(1)} = \mathbf{k}$, $\mathbf{Y} - \mathbf{Y}_0 = \mathbf{X} - \mathbf{X}_0 = \mathbf{X}'$ and writing the area $S_A = l_A L_2$, where L_2 is a large characteristic length in the x_2 -direction, we have

$$I_{2D}(\mathbf{Y}) = \frac{l_A}{2\pi^2 c^2} \iint \frac{L_2 |\omega| V(\mathbf{X}_c, \omega)}{s_I(\omega) \tilde{V}_{\beta}^L(\mathbf{X}_c, \mathbf{Y}_0, \omega) \exp[2i\omega T(\mathbf{X}_c, \mathbf{Y}_0)]} \cdot \exp[-i\mathbf{k} \cdot \mathbf{X}'] \frac{d\theta_c}{dx_{cl}} d\omega dx_{cl}. \quad (13.103)$$

To compare the non-dimensional field terms in the two cases we need to make the replacement

$$\tilde{V}_{\beta}^L(\mathbf{X}_c, \mathbf{Y}_0, \omega) \exp[2i\omega T(\mathbf{X}_c, \mathbf{Y}_0)] \rightarrow [\hat{P}(\mathbf{X}_c, \mathbf{Y}_0, \omega)]^2 L_2, \quad (13.104)$$

where the L_2 length appears because of the integration of the 3-D fields in \tilde{V}_{β}^L that is absent for the 2-D case of Chap. 12. Then Eq. (13.103) becomes

$$I_{2D}(\mathbf{Y}) = \frac{l_A}{2\pi^2 c^2} \iint \frac{|\omega| V(\mathbf{X}_c, \omega)}{s_I(\omega) [\hat{P}(\mathbf{X}_c, \mathbf{X}_0, \omega)]^2} \exp[-i\mathbf{k} \cdot \mathbf{X}'] d\theta_c d\omega. \quad (13.105)$$

Finally, transforming back to a \mathbf{k} -space integration through (see Eq. (12.25))

$$d\theta_c d\omega = \frac{c^2}{4|\omega|} d^2\mathbf{k}, \quad (13.106)$$

we obtain

$$I_{2D}(\mathbf{Y}) = \frac{l_A}{8\pi^2} \iint \frac{V(\mathbf{X}_c, \omega)}{s_I(\omega) [\hat{P}(\mathbf{X}_c, \mathbf{X}_0, \omega)]^2} \exp[-i\mathbf{k} \cdot \mathbf{X}'] d^2\mathbf{k}, \quad (13.107)$$

which is just Eq. (12.19). A similar set of steps for the contact case can also transform it into this equation.

In the full matrix imaging case we have

$$\begin{aligned} \tilde{V}_{\alpha\beta}^L(\mathbf{X}_s, \mathbf{X}_r, \mathbf{Y}, \omega) &\equiv \tilde{V}_{\alpha\beta}^L(\mathbf{X}_s, \mathbf{X}_r, \mathbf{Y}_0, \omega) \\ \phi(\mathbf{X}_s, \mathbf{X}_r, \mathbf{Y}) &\equiv T(\mathbf{X}_s, \mathbf{Y}_0) + T(\mathbf{X}_r, \mathbf{Y}_0) \\ &\quad + \mathbf{e}_{\beta}^{(1)} \cdot (\mathbf{Y} - \mathbf{Y}_0) / c_{\beta 2} + \mathbf{e}_{\alpha}^{(2)} \cdot (\mathbf{Y} - \mathbf{Y}_0) / c_{\alpha 2} \end{aligned} \quad (13.108)$$

and Eq. (13.92) becomes

$$\begin{aligned} \bar{T}_{2D}(\mathbf{Y}) = & \frac{1}{8\pi^2 \rho_2 c_{\alpha 2}^3} \iiint \frac{|\omega| \bar{V}(\mathbf{X}_r, \mathbf{X}_s, \omega)}{\tilde{V}_{\alpha\beta}^L(\mathbf{X}_s, \mathbf{X}_r, \mathbf{Y}_0, \omega) \exp[i\omega T(\mathbf{X}_s, \mathbf{Y}_0)] \exp[i\omega T(\mathbf{X}_r, \mathbf{Y}_0)]} \\ & \cdot \left| 1 + \frac{c_{\alpha 2}}{c_{\beta 2}} \cos \Theta \right| \exp[-i\omega \mathbf{S} \cdot (\mathbf{Y} - \mathbf{Y}_0)] d\omega \frac{d\theta_r}{dx_{r1}} \frac{d\theta_s}{dx_{s1}} dx_{r1} dx_{s1}, \end{aligned} \quad (13.109)$$

where, as in 3-D imaging,

$$\mathbf{S} = \mathbf{e}_{\beta}^{(1)} / c_{\beta 2} + \mathbf{e}_{\alpha}^{(2)} / c_{\alpha 2}, \quad (13.110)$$

but now \mathbf{S} is a 2-D vector in the plane perpendicular to the x_2 -axis of the scatterer. Equation (13.109) is our POFFIS type of imaging measurement model for full matrix imaging 2-D flaws with linear arrays.

We can use the Thompson-Gray measurement model for 2-D scatterers to write the image in terms of the far field scattering amplitude of the flaw as done previously in the 2-D and 3-D cases. Recall, in the case of a 3-D scatterer in an elastic solid, we found (see Eq. 11.69):

$$\begin{aligned} \hat{V}(\mathbf{x}_s, \mathbf{x}_r, \omega) = & \tilde{V}_{\beta}^{(1)}(\mathbf{x}_s, \mathbf{x}_0, \omega) \exp[i\omega T(\mathbf{x}_s, \mathbf{x}_0)] \tilde{V}_{\alpha}^{(2)}(\mathbf{x}_r, \mathbf{x}_0, \omega) \exp[i\omega T(\mathbf{x}_r, \mathbf{x}_0)] \\ & \cdot \frac{4\pi\rho_2 c_{\alpha 2}}{-ik_{\alpha 2}} A(\mathbf{e}_{inc}^{\beta}, \mathbf{e}_{scat}^{\alpha}, \omega) \end{aligned} \quad (13.111)$$

in terms of the velocity fields $\tilde{V}_{\beta}^{(1)} = -i\omega\tilde{U}_{\beta}^{(1)}$, $\tilde{V}_{\alpha}^{(2)} = -i\omega\tilde{U}_{\alpha}^{(2)}$. For a 2-D scatterer a corresponding measurement model can be derived in our current notation as (see [Schmerr-Song] for the assumptions that go into the derivation):

$$\begin{aligned} \hat{V}(\mathbf{X}_s, \mathbf{X}_r, \omega) = & \tilde{V}_{\alpha\beta}^L(\mathbf{X}_s, \mathbf{Y}_0, \omega) \exp[i\omega T(\mathbf{X}_s, \mathbf{Y}_0)] \exp[i\omega T(\mathbf{X}_r, \mathbf{Y}_0)] \\ & \cdot \frac{4\pi\rho_2 c_{\alpha 2}}{-ik_{\alpha 2}} \frac{A(\mathbf{e}_{inc}^{\beta}, \mathbf{e}_{scat}^{\alpha}, \omega)}{L}. \end{aligned} \quad (13.112)$$

for the general pitch-catch case and

$$\begin{aligned} \hat{V}(\mathbf{X}_c, \omega) = & \tilde{V}_{\beta}^L(\mathbf{X}_c, \mathbf{Y}_0, \omega) \exp[2i\omega T(\mathbf{X}_c, \mathbf{Y}_0)] \\ & \cdot \frac{4\pi\rho_2 c_{\beta 2}}{-ik_{\beta 2}} \frac{A(\mathbf{e}_{inc}^{\beta}, -\mathbf{e}_{inc}^{\alpha}, \omega)}{L} \end{aligned} \quad (13.113)$$

for the pulse-echo-case, where L is the length of the 2-D scatterer and A is the 3-D scattering amplitude. In the full matrix imaging case then, from Eq. (13.109) we obtain

$$\begin{aligned} \bar{I}_{2D}(\mathbf{Y}) = & \frac{1}{2\pi c_{\alpha 2} L} \iiint i \operatorname{sgn}(\omega) A(\mathbf{e}_{inc}^{\beta}, \mathbf{e}_{scatt}^{\alpha}, \omega) \\ & \cdot \left| 1 + \frac{c_{\alpha 2}}{c_{\beta 2}} \cos \Theta \right| \exp[-i\omega \mathbf{S} \cdot (\mathbf{Y} - \mathbf{Y}_0)] d\omega \frac{d\theta_r}{dx_{r1}} \frac{d\theta_s}{dx_{s1}} dx_{r1} dx_{s1}. \end{aligned} \quad (13.114)$$

and for the pulse-echo case, from Eq. (13.101):

$$\begin{aligned} I_{2D}(\mathbf{Y}) = & \frac{2}{\pi c_{\beta 2} L} \iint i \operatorname{sgn}(\omega) A(\mathbf{e}_{inc}^{\beta}, -\mathbf{e}_{inc}^{\beta}, \omega) \\ & \cdot \exp[-2ik_{\beta 2} \mathbf{e}_{\beta}^{(1)} \cdot (\mathbf{Y} - \mathbf{Y}_0)] \frac{d\theta_c}{dx_{c1}} d\omega dx_{c1}. \end{aligned} \quad (13.115)$$

13.4 Discussion

This chapter has shown that SAFT, TFM, and POFFIS methods image different ad-hoc or filtered versions of the reflectivity images that are described explicitly in our imaging measurement model approach. All of these methods fall under the category of *delay and sum methods* which have been some of the most successful imaging techniques used to date. These methods are, however, ultimately constrained by the fundamental fact, as discussed in Chap. 12, that *they can only reconstruct proper images of flaw properties that are directly or indirectly related to the specular response of flaw surfaces and/or the response of flaw edges*. It is important to remember this limitation when trying to use these methods for flaw characterization or sizing applications. For example, having a one-sided aperture-limited image of only the front surface for volumetric flaws is generally inadequate to deduce flaw size information, regardless of how detailed the image resolution might be. If delay and sum methods are used with data obtained from both front and back surface specular responses, however, then sizing volumetric flaws from an image is certainly possible. In contrast, it is possible in principle to image a crack edge with a one-sided aperture-limited setup and still obtain crack size information from that image. A simple example where SAFT is used in this manner to calculate crack lengths and compared to time-of-flight diffraction (TOFD) sizing is given in [4]. For flaw characterization studies, the situation is similar. For example, in POFFIS-style imaging the image is directly related to the inverse Fourier transform of the far field scattering amplitude of the flaw. However, again this yields correct images only of the specular surface or edge diffracted parts of the scattering amplitude. Other responses seen in the image are artifacts of the delay and sum image formation process and not related to the flaw properties in a usable fashion.

In Chap. 12, a striking example of this fact was demonstrated for a cylindrical inclusion having a wave speed twice that of the surrounding material. In that case, the back surface response was imaged as a fictitious point scatterer located at the center of the inclusion! These limitations of the delay and sum methods may not be widely realized because of (1) their long history of successful use in medical and seismology applications where scatterers may be large enough so that the specular surface and edge responses inherently play key roles in directly interpreting the images generated and (2) a tradition of using the weak scattering Born approximation to describe how the measured signals are formed. Within the Born approximation, for example, it is possible to properly image both front and back surface reflections since the wave speed of the flaw is assumed to differ little from that of the host material. In that case, an image of the scattering potential may be reasonably connected to a quantitative image of the entire flaw geometry. An example of this case was shown in Chap. 12 where the image of a weak scattering inclusion was given. In NDE applications, however, where flaws are typically not weak scatterers and they may be small, irregular and with few other distinguishing characteristics, images obtained with delay and sum methods may often be of more limited value. Thus, it is important to examine other ways in which the underlying array data may be used. The work of Wilcox and his colleagues [5–7], for example, are excellent examples of advanced flaw characterization methods that attempt to find other patterns and features that can be extracted from phased array inspections. The equivalent flaw sizing approach of Engle et al. [8] is also a case where an array is used not to form crack images but to act instead as a steerable single element transducer that can effectively collect crack scattering data in multiple directions that can then be used to obtain crack size and orientation information.

Another limitation of delay and sum imaging methods that may not be frequently understood is that the images they produce may be statistically unstable [9]. This means that in a random or inhomogeneous material where the material properties are not known explicitly, it is not sufficient to form images with some “equivalent” model of the material properties since the images depend crucially on the particular realization of those properties present in the actual material. The work by Borcea and her colleagues have studied this issue in depth and offered some solutions that might be useful in NDE inspections of welds and composites [10–12].

In this chapter, we have not discussed computational efficiency issues or concentrated on imaging methods that are optimized for speed of computation. There are two reasons for this. First, in NDE applications speed is not nearly as critical as in the medical world since most NDE measurements are done in a static environment. Second, a focus on speed issues tends to neglect the basic elements of the imaging process and instead concentrate on implementation details. As the title of this book implies, we have chosen to describe in depth the fundamentals of how flaw signals are generated with phased arrays and how one can use that knowledge of the measurement process to produce quantitative flaw images. That being said, we do recognize the importance that speed plays in making imaging with phased arrays practical and cost-effective. This is especially true for 3-D imaging which is computationally challenging even with modern high speed computers. There are versions

of pulse-echo and full matrix imaging, for example, that can take advantage of FFTs in forming images [13–16]. See also Wilcox [17] for a discussion of other speed issues. Also, in Chaps. 5 and 8, we noted that the solution of a large number of ray paths when calculating either time delay laws or the fields produced through planar interfaces does benefit greatly by the use of high speed methods.

The delay and sum methods we have discussed are only a small subset of the world of possible imaging methods that we could have chosen to describe. There are imaging methods based on time-reversal, singular value decomposition, and tomography, as well as topological methods, statistical methods, and many more that are available or are being developed [18–22]. The challenge for all of those methods, in our view, is to demonstrate that they can provide practical improvements to the delay and sum methods commonly in use today. Those improvements must come not just in terms of resolution but also in terms of the flaw information they provide, i.e. information that the NDE community can use for quantitative flaw detection, sizing, and characterization studies. Thus, although we could have analyzed image resolution by evaluating point response functions with our imaging measurement models, we chose instead to concentrate on what flaw properties are being imaged.

The imaging measurement approach we used in this chapter gives us a very effective tool for understanding the images that are generated with common methods such as SAFT, TFM, and POFFIS and our approach shows how those methods must be modified to obtain images that are truly images of flaw properties and not the entire measurement system. There are other analytical and semi-analytical methods that are used in practice that can also help us to understand the imaging process [23–27]. Some of these are based on the Born approximation rather than the Kirchhoff approximation. Here, we sought to concentrate on a fundamental approach that is compatible with the frequencies and types of flaws and flaw images that can be expected in NDE tests and is based on the physics of how the flaw signals are generated in ultrasonic NDE measurement systems.

13.5 Summary of Imaging Measurement Models

In the previous sections of this chapter, we have derived a number of imaging models. Those models contain a relatively large number of parameters which are defined in this chapter and others. In this section, we will summarize all the results of this chapter in a consistent fashion and reiterate the meaning of all the defining parameters in terms of quantities that can be measured or modeled. In all cases, we will use forms that involve direct deconvolutions (without a Wiener filter) to simplify the expressions.

Consider, first the case of pulse echo imaging with a 2-D array. In this case, we can use Eq. (13.22):

$$I_R^{BA}(\mathbf{y}) = \frac{\Delta x_{c1} \Delta x_{c2} \Delta \omega}{2\pi^3 \rho_2 c_{\beta 2}^4} 2 \operatorname{Re} \left\{ \sum_{m=1}^M \sum_{n=1}^{L_1} \sum_{l=1}^{L_2} \omega_m^2 \frac{\widehat{V}(\mathbf{x}_c^{nl}, \omega_m)}{\left[\tilde{V}_{\beta}^{(l)}(\mathbf{x}_c^{nl}, \mathbf{y}, \omega_m) \right]^2} \cdot \frac{d\Omega_c}{dS_c}(\mathbf{x}_c^{nl}, \mathbf{y}) \exp \left[-2i\omega_m T(\mathbf{x}_c^{nl}, \mathbf{y}) \right] \right\}. \quad (13.116)$$

Here, $(\Delta x_{c1}, \Delta x_{c2})$ are the spacing between the centroids of the array elements in the (x_1, x_2) directions, respectively, so they are just the arrays pitches in those directions. The quantity $\Delta \omega$ is the spacing of frequency components (in rad/s) and $(\rho_2, c_{\beta 2})$ are the density and wave speed in the medium surrounding the flaw for an incident wave of type β . The points $\mathbf{x}_c^{nl} = (x_{c1}^{nl}, x_{c2}^{nl})$ are the discrete locations of the element centroids, ω_m are the discrete sampled frequencies, and \mathbf{y} is the image point (which will also be sampled discretely in practice). The quantity $d\Omega_c / dS_c$ is a solid angle–area ratio that is calculated from an element centroid to an image point, as shown in Appendix B for various cases, while $T(\mathbf{x}_c^{nl}, \mathbf{y})$ is the time it takes for a wave to travel from the centroid of an element to the image point. The normalized voltages, $\widehat{V}(\mathbf{x}_c^{nl}, \omega_m)$, are given in terms of the real measured voltages, $V(\mathbf{x}_c^{nl}, \omega_m)$, for immersion cases, by

$$\widehat{V}(\mathbf{x}_c^{nl}, \omega_m) = \rho_1 c_{p1} S_A V(\mathbf{x}_c^{nl}, \omega_m) / s_I(\omega_m) \quad (13.117)$$

and, for contact cases, by

$$\widehat{V}(\mathbf{x}_c^{nl}, \omega_m) = V(\mathbf{x}_c^{nl}, \omega_m) / \rho c_p S_B s_C(\omega_m), \quad (13.118)$$

where (ρ_1, c_{p1}) are the density and (compressional) wave speed at the transmitting element and S_A is the area of that element. Similarly, (ρ, c_p) are the density and (compressional) wave speed at the receiving element, and S_B is the area of that element. For the pulse-echo case considered here, $\rho = \rho_1, c_p = c_{p1}, S_A = S_B$. The quantities $(s_I(\omega_m), s_C(\omega_m))$ are the system functions for an element in immersion or contact testing, respectively, at the discrete sampled frequencies. The normalized velocity terms, $\tilde{V}_{\beta}^{(l)}(\mathbf{x}_c^{nl}, \mathbf{y}, \omega_m)$, are related to the actual incident velocity, $\mathbf{v}_{\beta}^{(1);inc}(\mathbf{x}_c^{nl}, \mathbf{y}, \omega_m)$, generated by the transmitting elements at the image point, \mathbf{y} , for immersion problems, by

$$\mathbf{v}_{\beta}^{(1);inc}(\mathbf{x}_c^{nl}, \mathbf{y}, \omega_m) = v_T^{(1)} \tilde{V}(\mathbf{x}_c^{nl}, \mathbf{y}, \omega_m) \mathbf{d}_{\beta}^{(1)} \exp \left[i\omega_m T(\mathbf{x}_c^{nl}, \mathbf{y}) \right] \quad (13.119)$$

and, for contact problems, by

$$\mathbf{v}_{\beta}^{(1);inc}(\mathbf{x}_c^{nl}, \mathbf{y}, \omega_m) = F_T^{(1)} \tilde{V}(\mathbf{x}_c^{nl}, \mathbf{y}, \omega_m) \mathbf{d}_{\beta}^{(1)} \exp \left[i\omega_m T(\mathbf{x}_c^{nl}, \mathbf{y}) \right], \quad (13.120)$$

where $(v_T^{(1)}, F_T^{(1)})$ are the velocity and force, respectively, on the face of the transmitting elements and where $\mathbf{d}_\beta^{(1)}$ is the polarization (unit vector). Note that these normalized velocity terms can be calculated directly from Eqs. (13.119) (13.120) using the ultrasonic beam models discussed in previous chapters and are not dependent on $(v_T^{(1)}, F_T^{(1)})$. Note also that Eq. (13.116) can be used to image the edge of a crack, as previously discussed, (see Eq. 13.41) with the replacement $\hat{V} \rightarrow (i\omega_m / c_{\beta 2}) \hat{V}$.

In the case of a small flaw, this pulse-echo imaging measurement model reduces, from Eq. (13.29) to a POFFIS-style discrete form:

$$I_R^{BA}(\mathbf{y}) = \frac{\Delta x_{c1} \Delta x_{c2} \Delta \omega}{2\pi^3 \rho_2^4 c_{\beta 2}^4} 2 \operatorname{Re} \left\{ \sum_{m=1}^M \sum_{n=1}^{L_1} \sum_{l=1}^{L_2} \omega_m^2 \frac{\hat{V}(\mathbf{x}_c^{nl}, \omega_m)}{\left[\tilde{V}_\beta^{(1)}(\mathbf{x}_c^{nl}, \mathbf{y}_0, \omega_m) \right]^2} \frac{d\Omega_c(\mathbf{x}_c^{nl}, \mathbf{y}_0)}{dS_c} \right. \\ \left. \cdot \exp \left[-2i\omega_m T(\mathbf{x}_c^{nl}, \mathbf{y}_0) \right] \exp \left[-2i\omega_m \mathbf{e}_\beta^{(1)}(\mathbf{x}_c^{nl}, \mathbf{y}_0) \cdot (\mathbf{y} - \mathbf{y}_0) / c_{\beta 2} \right] \right\}, \quad (13.121)$$

where the point \mathbf{y}_0 is a fixed point close to the flaw and \mathbf{y} is the image point. All of the quantities in Eq. (13.121) have been described previously for Eq. (13.116) except $\mathbf{e}_\beta^{(1)}(\mathbf{x}_c^{nl}, \mathbf{y}_0)$ which is a unit vector in the direction of the incident wave for a wave traveling from an element to the fixed point, \mathbf{y}_0 .

For the case of full matrix imaging with a 2-D array we have from Eq. (13.60)

$$\bar{I}_R^{BA}(\mathbf{y}) = \frac{\Delta x_{s1} \Delta x_{s2} \Delta x_{r1} \Delta x_{r2} \Delta \omega}{16\pi^3 \rho_2^4 c_{\alpha 2}^4} 2 \operatorname{Re} \left\{ \sum_{m=1}^M \sum_{n=1}^{L_1} \sum_{l=1}^{L_2} \sum_{p=1}^{L_1} \sum_{q=1}^{L_2} \omega_m^2 \left| 1 + \frac{c_{\alpha 2}}{c_{\beta 2}} \cos \Theta_{nlpq} \right| \right. \\ \cdot \exp \left[-i\omega_m \phi(\mathbf{x}_s^{pq}, \mathbf{x}_r^{nl}, \mathbf{y}) \right] \frac{d\Omega_r(\mathbf{x}_r^{nl}, \mathbf{y})}{dS_r} \frac{d\Omega_s(\mathbf{x}_s^{pq}, \mathbf{y})}{dS_s} \\ \left. \cdot \frac{\hat{V}(\mathbf{x}_s^{pq}, \mathbf{x}_r^{nl}, \omega_m)}{\tilde{V}_\beta^{(1)}(\mathbf{x}_s^{pq}, \mathbf{y}, \omega_m) \tilde{V}_\alpha^{(2)}(\mathbf{x}_r^{nl}, \mathbf{y}, \omega_m)} \right\}. \quad (13.122)$$

Here $(\Delta x_{s1}, \Delta x_{s2})$ are the pitches of the transmitting elements and $(\Delta x_{r1}, \Delta x_{r2})$ are the pitches of the receiving elements and $\Delta \omega$ is again the frequency spacing. The quantities $(\rho_2, c_{\beta 2}, c_{\alpha 2})$ are the density, the wave speed of the incident wave (of type β), and the wave speed of the scattered wave (of type α) for the material surrounding the flaw, and ω_m again are the sampled frequencies. The discrete locations of the transmitting elements are $\mathbf{x}_s^{pq} = (x_{s1}^{pq}, x_{s2}^{pq})$, the locations of the receiving elements are $\mathbf{x}_r^{nl} = (x_{r1}^{nl}, x_{r2}^{nl})$, and \mathbf{y} again is the image point. The terms $d\Omega_s / dS_s$ and $d\Omega_r / dS_r$ are the solid angle-area ratios as calculated for the sending and receiving elements, respectively, as calculated in Appendix B, and Θ_{nlpq} are the angles between the various discrete sending and receiving elements (see Fig. 13.3). The phase term $\phi(\mathbf{x}_s^{pq}, \mathbf{x}_r^{nl}, \mathbf{y}) = T(\mathbf{x}_s^{pq}, \mathbf{y}) + T(\mathbf{x}_r^{nl}, \mathbf{y})$ is the total time it takes to travel from a sending element to an image point and back to a receiving element. The normalized voltages, $\hat{V}(\mathbf{x}_s^{pq}, \mathbf{x}_r^{nl}, \omega_m)$ are again related to the actual voltages, $V(\mathbf{x}_s^{pq}, \mathbf{x}_r^{nl}, \omega_m)$, for various element pairs by relations similar to Eqs. (13.117) (13.118), i.e.

$$\widehat{V}(\mathbf{x}_s^{pq}, \mathbf{x}_r^{nl}, \omega_m) = \rho_1 c_{p1} S_A V(\mathbf{x}_s^{pq}, \mathbf{x}_r^{nl}, \omega_m) / s_I(\omega_m) \quad (13.123)$$

for the immersion case and

$$\widehat{V}(\mathbf{x}_s^{pq}, \mathbf{x}_r^{nl}, \omega_m) = (\omega_m) V(\mathbf{x}_s^{pq}, \mathbf{x}_r^{nl}, \omega_m) / \rho c_p S_B s_C(\omega_m) \quad (13.124)$$

for the contact case where again (ρ_1, c_{p1}) are the density and (compressional) wave speed at the transmitting element and S_A is the area of that element. Similarly, (ρ, c_p) are the density and (compressional) wave speed at the receiving element and S_B is the area of that element. The normalized velocity terms, $\tilde{V}_\beta^{(1)}(\mathbf{x}_s^{pq}, \mathbf{y}, \omega_m)$, and $\tilde{V}_\alpha^{(2)}(\mathbf{x}_r^{nl}, \mathbf{y}, \omega_m)$, are related to the velocity at the image point for the incident wave (of type β) from the sending element, $\mathbf{v}_\beta^{(1);inc}(\mathbf{x}_s^{pq}, \mathbf{y}, \omega_m)$, and the velocity at the image point for an incident wave (of type α) from the receiving transducer, $\mathbf{v}_\alpha^{(2)}(\mathbf{x}_r^{nl}, \mathbf{y}, \omega_m)$, when it is acting as a transmitter as

$$\mathbf{v}_\beta^{(1);inc}(\mathbf{x}_s^{pq}, \mathbf{y}, \omega_m) = v_T^{(1)} \tilde{V}_\beta^{(1)}(\mathbf{x}_s^{pq}, \mathbf{y}, \omega_m) \mathbf{d}_\beta^{(1)} \exp[i\omega_m T(\mathbf{x}_s^{pq}, \mathbf{y})] \quad (13.125)$$

and

$$\mathbf{v}_\alpha^{(2)}(\mathbf{x}_r^{nl}, \mathbf{y}, \omega_m) = v_R^{(2)} \tilde{V}_\alpha^{(2)}(\mathbf{x}_r^{nl}, \mathbf{y}, \omega_m) \mathbf{d}_\alpha^{(2)} \exp[i\omega_m T(\mathbf{x}_r^{nl}, \mathbf{y})] \quad (13.126)$$

for immersion problems where $(v_T^{(1)}, v_R^{(2)})$ are the driving velocities on the faces of the sending and receiving elements, respectively, and $(\mathbf{d}_\beta^{(1)}, \mathbf{d}_\alpha^{(2)})$ are the polarization unit vectors. For the contact case, we have similarly,

$$\mathbf{v}_\beta^{(1);inc}(\mathbf{x}_s^{pq}, \mathbf{y}, \omega_m) = F_T^{(1)} \tilde{V}_\beta^{(1)}(\mathbf{x}_s^{pq}, \mathbf{y}, \omega_m) \mathbf{d}_\beta^{(1)} \exp[i\omega_m T(\mathbf{x}_s^{pq}, \mathbf{y})] \quad (13.127)$$

and

$$\mathbf{v}_\alpha^{(2)}(\mathbf{x}_r^{nl}, \mathbf{y}, \omega_m) = F_R^{(2)} \tilde{V}_\alpha^{(2)}(\mathbf{x}_r^{nl}, \mathbf{y}, \omega_m) \mathbf{d}_\alpha^{(2)} \exp[i\omega_m T(\mathbf{x}_r^{nl}, \mathbf{y})] \quad (13.128)$$

in terms of the forces $(F_T^{(1)}, F_R^{(2)})$ on the faces of the sending and receiving elements respectively. Once again these normalized velocity terms can be calculated by beam models. For this full matrix imaging case we can also use Eq. (13.122) for imaging the edge of a crack with the replacement $\widehat{V} \rightarrow (i\omega / c_{\alpha 2}) \widehat{V}$.

For POFFIS-style full matrix imaging we have from Eq. (13.63)

$$\begin{aligned} \bar{I}_R^{BA}(\mathbf{y}) = & \frac{\Delta x_{s1} \Delta x_{s2} \Delta x_{r1} \Delta x_{r2} \Delta \omega}{16\pi^3 \rho_2 c_{\alpha 2}^4} 2 \operatorname{Re} \left\{ \sum_{m=1}^M \sum_{n=1}^{L_1} \sum_{l=1}^{L_2} \sum_{p=1}^{L_1} \sum_{q=1}^{L_2} \omega_m^2 \left| 1 + \frac{c_{\alpha 2}}{c_{\beta 2}} \cos \Theta_{nlpq} \right| \right. \\ & \cdot \exp[-i\omega_m \phi(\mathbf{x}_s^{pq}, \mathbf{x}_r^{nl}, \mathbf{y})] \exp[-i\omega_m \mathbf{s}(\mathbf{x}_s^{pq}, \mathbf{x}_r^{nl}, \mathbf{y}_0) \cdot (\mathbf{y} - \mathbf{y}_0)] \\ & \cdot \left. \frac{d\Omega_r}{dS_r}(\mathbf{x}_r^{nl}, \mathbf{y}_0) \frac{d\Omega_s}{dS_s}(\mathbf{x}_s^{pq}, \mathbf{y}_0) \frac{\widehat{V}(\mathbf{x}_s^{pq}, \mathbf{x}_r^{nl}, \omega_m)}{\tilde{V}_\beta^{(1)}(\mathbf{x}_s^{pq}, \mathbf{y}_0, \omega_m) \tilde{V}_\alpha^{(2)}(\mathbf{x}_r^{nl}, \mathbf{y}_0, \omega_m)} \right\}, \end{aligned} \quad (13.129)$$

where the point \mathbf{y}_0 is a fixed point close to the image point, \mathbf{y} . All of the quantities in Eq. (13.129) have been described previously for Eq. (13.122) except the vector $\mathbf{s}(\mathbf{x}_s^{pq}, \mathbf{x}_r^{nl}, \mathbf{y}_0)$ which is given by

$$\mathbf{s}(\mathbf{x}_s^{pq}, \mathbf{x}_r^{nl}, \mathbf{y}_0) = \mathbf{e}_\beta^{(1)}(\mathbf{x}_s^{pq}, \mathbf{y}_0) / c_{\beta 2} + \mathbf{e}_\alpha^{(2)}(\mathbf{x}_r^{nl}, \mathbf{y}_0) / c_{\alpha 2}, \quad (13.130)$$

where $\mathbf{e}_\beta^{(1)}(\mathbf{x}_s^{pq}, \mathbf{y}_0)$ is a unit vector in the direction of the incident wave for a wave traveling from an sending element to the fixed point, \mathbf{y}_0 , and similarly $\mathbf{e}_\alpha^{(2)}(\mathbf{x}_r^{nl}, \mathbf{y}_0)$ is a unit vector in the direction of the incident wave for a wave traveling from an receiving element to the fixed point.

For imaging 2-D flaws with a linear array most of the quantities previously defined also appear in these cases so we will just outline the main differences here. First, we summarize the three cases we considered. For the pulse-echo case we have (see Eq. (13.98))

$$I_{2D}^{BA}(\mathbf{Y}) = \frac{\Delta x_{c1} \Delta \omega}{2\pi^2 \rho_2 c_{\beta 2}^3} 2 \operatorname{Re} \left\{ \sum_{m=1}^M \sum_{n=1}^N |\omega_m| \frac{\widehat{V}(\mathbf{X}_c^n, \omega_m)}{\widehat{V}_{\beta}^L(\mathbf{X}_c^n, \mathbf{Y}, \omega_m)} \cdot \frac{d\theta_c}{dx_{c1}}(\mathbf{X}_c^n, \mathbf{Y}) \exp[-2i\omega_m T(\mathbf{X}_c^n, \mathbf{Y})] \right\}, \quad (13.131)$$

which reduces, for POFFIS-style pulse-echo imaging (Eq. (13.101)), to

$$I_{2D}^{BA}(\mathbf{Y}) = \frac{\Delta x_{c1} \Delta \omega}{2\pi^2 \rho_2 c_{\beta 2}^3} 2 \operatorname{Re} \left\{ \sum_{m=1}^M \sum_{n=1}^N |\omega_m| \frac{\widehat{V}(\mathbf{X}_c^n, \omega_m)}{\widehat{V}_{\beta}^L(\mathbf{X}_c^n, \mathbf{Y}_0, \omega_m)} \frac{d\theta_c}{dx_{c1}}(\mathbf{X}_c^n, \mathbf{Y}_0) \cdot \exp[-2i\omega_m T(\mathbf{X}_c^n, \mathbf{Y}_0)] \exp[-2i\omega_m \mathbf{e}_\beta^{(1)}(\mathbf{X}_c^n, \mathbf{Y}_0) \cdot (\mathbf{Y} - \mathbf{Y}_0) / c_{\beta 2}] \right\}. \quad (13.132)$$

In the full matrix imaging case, from Eq. (13.102) we find

$$\bar{I}_{2D}^{BA}(\mathbf{Y}) = \frac{\Delta x_{s1} \Delta x_{r1} \Delta \omega}{8\pi^2 \rho_2 c_{\alpha 2}^3} 2 \operatorname{Re} \left\{ \sum_{m=1}^M \sum_{n=1}^N \sum_{l=1}^N |\omega_m| \left| 1 + \frac{c_{\alpha 2}}{c_{\beta 2}} \cos \Theta_{nl} \right| \frac{\widehat{V}(\mathbf{X}_r^l, \mathbf{X}_s^l, \omega_m)}{\widehat{V}_{\alpha\beta}^L(\mathbf{X}_r^l, \mathbf{X}_s^l, \mathbf{Y}, \omega_m)} \cdot \frac{d\theta_r}{dx_{r1}}(\mathbf{X}_r^l, \mathbf{Y}) \frac{d\theta_s}{dx_{s1}}(\mathbf{X}_s^l, \mathbf{Y}) \exp[-i\omega_m \phi(\mathbf{X}_s^l, \mathbf{X}_r^l, \mathbf{Y})] \right\} \quad (13.133)$$

and for POFFIS-style full matrix imaging (Eq. (13.109))

$$\bar{I}_{2D}^{BA}(\mathbf{Y}) = \frac{\Delta x_{s1} \Delta x_{r1} \Delta \omega}{8\pi^2 \rho_2 c_{\alpha 2}^3} 2 \operatorname{Re} \left\{ \sum_{m=1}^M \sum_{n=1}^N \sum_{l=1}^N |\omega_m| \left| 1 + \frac{c_{\alpha 2}}{c_{\beta 2}} \cos \Theta_{nl} \right| \frac{\widehat{V}(\mathbf{X}_r^l, \mathbf{X}_s^l, \omega_m)}{\widehat{V}_{\alpha\beta}^L(\mathbf{X}_s^l, \mathbf{X}_r^l, \mathbf{Y}_0, \omega_m)} \cdot \frac{d\theta_r}{dx_{r1}}(\mathbf{X}_r^l, \mathbf{Y}_0) \frac{d\theta_s}{dx_{s1}}(\mathbf{X}_s^l, \mathbf{Y}_0) \exp[-i\omega_m \phi(\mathbf{X}_s^l, \mathbf{X}_r^l, \mathbf{Y}_0)] \cdot \exp[-i\omega_m \mathbf{S}(\mathbf{X}_s^l, \mathbf{X}_r^l, \mathbf{Y}_0) \cdot (\mathbf{Y} - \mathbf{Y}_0)] \right\}. \quad (13.134)$$

For these 2-D imaging cases the array centroid locations are all along the x_1 axis in the (x_1, x_3) plane at the center of the linear array so \mathbf{X}_c^l , \mathbf{X}_s^l , and \mathbf{X}_r^n all are discrete locations of the elements along the x_1 -axis. All the capitalized vectors also lie in the (x_1, x_3) plane, including the image point, \mathbf{Y} , and the fixed point, \mathbf{Y}_0 . The unit vector $\mathbf{e}_\beta^{(1)}(\mathbf{X}_c^n, \mathbf{Y}_0)$ and the vector $\mathbf{S}(\mathbf{X}_s^l, \mathbf{X}_r^n, \mathbf{Y}_0)$, given by

$$\mathbf{S}(\mathbf{X}_s^l, \mathbf{X}_r^n, \mathbf{Y}_0) = \mathbf{e}_\beta^{(1)}(\mathbf{X}_s^l, \mathbf{Y}_0) / c_{\beta 2} + \mathbf{e}_\alpha^{(2)}(\mathbf{X}_r^n, \mathbf{Y}_0) / c_{\alpha 2}, \quad (13.135)$$

also lie in the (x_1, x_3) plane and the angle Θ_{nl} is the angle between the incident and scattered directions in the (x_1, x_3) plane (see Fig. 13.4). In this 2-D case, the solid angle–area ratios are replaced by angle–length ratios such as $d\theta_c / dx_{c1}$, $d\theta_s / dx_{s1}$, $d\theta_r / dx_{r1}$, which can be calculated explicitly for the case of a single medium, as shown in Chap. 12, or they can be calculated by the ray methods of Appendix B.

One major difference between these 2-D problems for a linear array and the 2-D array cases considered previously is in the beam correction terms, which now are integrated field values given by quantities such as \tilde{V}_β^L and $\tilde{V}_{\alpha\beta}^L$. These quantities are defined as

$$\tilde{V}_\beta^L(\mathbf{X}_c^n, \mathbf{Y}, \omega_m) = \int_L \left[\tilde{V}_\beta^{(1)}(\mathbf{X}_c^n, \mathbf{Y}, y_2, \omega_m) \right]^2 dy_2 \quad (13.136)$$

and

$$\tilde{V}_{\alpha\beta}^L(\mathbf{X}_s^l, \mathbf{X}_r^n, \mathbf{Y}) = \int_L \tilde{V}_\beta^{(1)}(\mathbf{X}_s^l, \mathbf{Y}, y_2) \tilde{V}_\alpha^{(2)}(\mathbf{X}_r^n, \mathbf{Y}, y_2) dy_2 \quad (13.137)$$

and they can be calculated again by a beam model for the 3-D incident fields which, for the full matrix, immersion case are written as

$$\begin{aligned} \mathbf{v}_\beta^{(1);inc}(\mathbf{X}_s^l, \mathbf{y}, \omega_m) &= \mathbf{v}_T^{(1)} \tilde{V}_\beta^{(1)}(\mathbf{X}_s^l, \mathbf{y}, \omega_m) \mathbf{D}_\beta^{(1)} \exp[i\omega_m T(\mathbf{X}_s^l, \mathbf{Y})] \\ \mathbf{v}_\alpha^{(2)}(\mathbf{X}_r^n, \mathbf{y}, \omega_m) &= \mathbf{v}_R^{(2)} \tilde{V}_\alpha^{(2)}(\mathbf{X}_r^n, \mathbf{y}, \omega_m) \mathbf{D}_\alpha^{(2)} \exp[i\omega_m T(\mathbf{X}_r^n, \mathbf{Y})] \end{aligned} \quad (13.138)$$

and for the full matrix, contact case

$$\begin{aligned} \mathbf{v}_\beta^{(1);inc}(\mathbf{X}_s^l, \mathbf{y}, \omega_m) &= F_T^{(1)} \tilde{V}_\beta^{(1)}(\mathbf{X}_s^l, \mathbf{y}, \omega_m) \mathbf{D}_\beta^{(1)} \exp[i\omega_m T(\mathbf{X}_s^l, \mathbf{Y})] \\ \mathbf{v}_\alpha^{(2)}(\mathbf{X}_r^n, \mathbf{y}, \omega_m) &= F_R^{(2)} \tilde{V}_\alpha^{(2)}(\mathbf{X}_r^n, \mathbf{y}, \omega_m) \mathbf{D}_\alpha^{(2)} \exp[i\omega_m T(\mathbf{X}_r^n, \mathbf{Y})] \end{aligned} \quad (13.139)$$

at the 3-D point $\mathbf{y} = (\mathbf{Y}, y_2)$. The pulse-echo case follows similarly with the replacements $\mathbf{X}_s^l \rightarrow \mathbf{X}_c^n$, $\mathbf{X}_r^n \rightarrow \mathbf{X}_c^n$ and $\alpha = \beta$. Here the polarization vectors $\mathbf{D}_\beta^{(1)}, \mathbf{D}_\alpha^{(2)}$ lie in the (x_1, x_3) plane and the integrations are along the x_2 -axis, which is parallel to the long axis of the linear array and the 2-D scatterer (see Fig. 13.4). For POFFIS-style imaging we must let $\mathbf{Y} = \mathbf{Y}_0$ in all these expressions.

References

1. J.K. Cohen, N. Bleistein, The singular function of a surface and physical optics inverse scattering. *Wave Motion* **1**, 153–161 (1979)
2. N. Bleistein, J.K. Cohen, J.W. Stockwell Jr., *Mathematics of Multidimensional Seismic Imaging, Migration, and Inversion* (Springer, New York, 2000)
3. N. Bleistein, *Mathematical Methods for Wave Phenomena* (Academic, New York, 1984)
4. J. Kitze, D. Brackrock, G. Brekow, J. Prager, M. Gaal, M. Kreutzbruck, D. Szado, K. Kuti, G. Paczolay, SAFT and TOFD—compared in ultrasonic defect detection. <http://www.ndt.net/article/jrc-nde2010/papers/64.pdf>. (8th Int'l Conference on NDE in relation to structural integrity for nuclear and pressurized components, Oct. 29–Nov. 1, 2010, Berlin, Germany)
5. C. Holmes, B.W. Drinkwater, P.D. Wilcox, Advanced post-processing for scanned ultrasonic arrays: application to defect detection and classification in non-destructive evaluation. *Ultrasonics* **48**, 636–642 (2008)
6. P.D. Wilcox, C. Holmes, B.W. Drinkwater, Advanced reflector characterization with ultrasonic phased arrays in NDE applications. *IEEE Trans. Ultrason. Ferroelectr. Freq. Control* **54**, 1541–1550 (2007)
7. A. Velichko, P.D. Wilcox, An analytical comparison of ultrasonic array imaging algorithms. *J. Acoust. Soc. Am.* **127**, 2377–2384 (2010)
8. B.J. Engle, L.W. Schmerr, A. Sedov, in *Equivalent Flaw Time-of-Flight Diffraction Sizing with Ultrasonic Phased Arrays*, ed. by D.O. Thompson, D.E. Chimenti. *Review of Progress in Quantitative Nondestructive Evaluation*, vol. 32A (American Institute of Physics, Melville, 2013) pp. 895–901
9. L. Borcea, G. Papanicolaou, C. Tsogka, Theory and applications of time reversal and interferometric imaging. *Inverse Probl.* **19**, S139–S164 (2003)
10. L. Borcea, G. Papanicolaou, C. Tsogka, Interferometric array imaging in clutter. *Inverse Probl.* **21**, 1419–1460 (2005)
11. L. Borcea, G. Papanicolaou, C. Tsogka, Optimal waveform design for array imaging. *Inverse Probl.* **23**, 1973–2020 (2007)
12. L. Borcea, T. Callaghan, J. Garnier, G. Papanicolaou, A universal filter for enhancing imaging with small arrays. *Inverse Probl.* **26**, 1–29 (2010)
13. P.T. Gough, D.W. Hawkins, Unified framework for modern synthetic aperture imaging algorithms. *Int. J. Imag. Syst. Technol.* **8**, 343–358 (1997)
14. K. Nagai, A new synthetic aperture focusing method for ultrasonic B-scan imaging by the Fourier transform. *IEEE Trans. Son. Ultrason.* **SU-32**, 531–536 (1985)
15. K.J. Langenberg, R. Marklein, K. Mayer, in *Ultrasonic Nondestructive Testing of Materials—Theoretical Foundations* (CRC Press, Boca Raton, 2012)
16. A.J. Hunter, B.W. Drinkwater, P.D. Wilcox, The wavenumber algorithm for full-matrix imaging using an ultrasonic array. *IEEE/Trans. Ultrason. Ferroelectr. Freq. Control* **55**, 2450–2462 (2008)
17. P.D. Wilcox, in *Ultrasonic Arrays in NDE: Beyond the B-scan*, ed. by D.O. Thompson, D.E. Chimenti. *Review of Progress in Quantitative Nondestructive Evaluation*, vol. 32A (American Institute of Physics, Melville, 2013) pp. 33–50
18. F.K. Gruber, E.A. Marengo, A.J. Devaney, Time-reversal imaging with multiple signal classification considering multiple scattering between targets. *J. Acoust. Soc. Am.* **115**, 3042–3047 (2004)
19. J.G. Berryman, L. Borcea, G. Papanicolaou, C. Tsongka, Statistically stable ultrasonic imaging in random media. *J. Acoust. Soc. Am.* **112**, 1509–1522 (2002)
20. F. Simonetti, L. Huang, From beamforming to diffraction tomography. *J. Appl. Phys.* **103**, 103110-5–103110-7 (2008)
21. N. Dominguez, V. Gippiat, Non-destructive imaging using the time domain topological energy method. *Ultrasonics* **50**, 367–372 (2010)

22. F. Lingvall, T. Olofsson, On time-domain model-based ultrasonic array imaging. *IEEE Trans. Ultrason. Ferroelectr. Freq. Control* **54**, 1623–1633 (2007)
23. R.H. Stolt, A.B. Weglein, *Seismic Imaging and Inversion – Application of Linear Inverse Theory* (Cambridge University Press, Cambridge, 2012)
24. R.Y. Chiao, L.J. Thomas, Analytical evaluation of sampled aperture ultrasonic imaging techniques for NDE. *IEEE Trans. Ultrason. Ferroelectr. Freq. Control* **41**, 484–493 (1994)
25. H.H. Barrett, K.J. Myers, *Foundations of Image Science* (Wiley, New York, 2004)
26. S.J. Norton, M. Linzer, Ultrasonic reflectivity imaging in three dimensions: exact solutions for plane, cylindrical, and spherical apertures. *IEEE Trans. Biomed. Eng.* **BME-28**, 202–220 (1981)
27. A.J. Devaney, *Mathematical Foundations of Imaging, Tomography and Wavefield Inversion* (Cambridge University Press, Cambridge, 2012)

Chapter 14

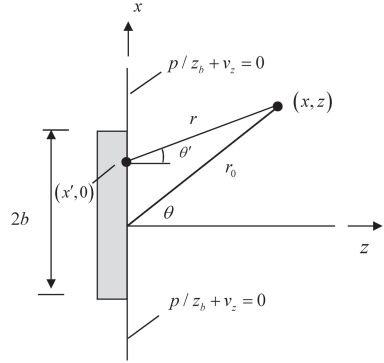
Element Boundary Conditions and Other Modeling Issues

As seen in previous chapters, single element beam models form the fundamental building blocks for developing complete phased array transducer beam models. In all the cases considered previously, an element was modeled either as a velocity distribution on a planar surface embedded in an infinite, rigid baffle (immersion cases) or as a pressure distribution on an otherwise stress-free surface (contact cases). For large, single element transducers, those models describe very well the transducer wave fields. However, as discussed in Chap. 1, the construction characteristics of phased arrays may bring the basic assumptions of those models into question. In this chapter, we will examine the consequences of using more general models that describe how array elements produce sound in the adjacent material.

14.1 Finite Impedance Baffle Model

In this section, we will use two-dimensional (2-D) beam models similar to those discussed in Chap. 2 to illustrate in a simple context the effects of different modeling assumptions. In particular, we will again assume that a 1-D element is located on the plane $z=0$ and radiates pressure waves into a fluid. Most single element beam models assume that when the piezoelectric element is driven electrically, a pressure distribution, $p(x, y, t)$, and a normal velocity, $v_z(x, y, t)$, are produced over the face of the element and that over the remainder of the plane $z=0$ outside the element either the velocity or pressure (or combinations of velocity and pressure) are specified. If the surface outside the element is a pressure-free surface, then we would have $p(x, y, t) = 0$ on that surface. If instead the element is imbedded in a rigid “baffle”, then we would have $v_z(x, y, t) = 0$ on the baffle. Although both of these types of conditions are commonly used in modeling large, single element transducers, neither of these extreme conditions may hold for an element in an array since the array elements are often embedded in a surrounding matrix of material that has a different acoustic impedance from the piezoelectric element or has facing layers that have a different acoustic impedance from either the element or the surrounding fluid. Techniques such as finite elements can be used to model in detail these

Fig. 14.1 A 1-D array element in a finite impedance baffle radiating into a fluid



features of an array element but here we want to develop a much simpler model that can examine the effects of the boundary conditions surrounding an element (see Pesque and Fink [1] for a similar approach). Specifically, we will model the array element as embedded in a baffle having a finite specific acoustic impedance, z_b , where on the baffle the condition

$$p(x, y, t) / z_b + v_z(x, y, t) = 0 \quad (14.1)$$

is satisfied (see Fig. 14.1). The case $z_b \rightarrow \infty$ then corresponds to the rigid baffle and the case $z_b \rightarrow 0$ models the pressure-free surface. Other finite values of the baffle impedance can then be used to model conditions that are in between these two extreme limits.

In the 2-D model discussed in this section, we will assume that the length of the element is of length $2b$ over the interval $[-b, b]$ in the x -direction. On the plane $z=0$, we will specify the pressure and velocity fields as

$$\frac{p(x, z=0, t)}{z_b} + v_z(x, z=0, t) = \begin{cases} v_0(x, t) & -b \leq x \leq b \\ 0 & \text{otherwise} \end{cases}, \quad (14.2)$$

which satisfies Eq. (14.1) on the surface outside the element and assumes that the pressure and velocity fields on the face of the element combine to generate a net non-zero driving term, $v_0(x, t)$, having the dimensions of a velocity, but which we see from Eq. (14.2) is not the actual velocity on the face of the element. Taking the Fourier transform of Eq. (14.2) gives

$$\frac{p(x, z=0, \omega)}{z_b} + v_z(x, z=0, \omega) = \begin{cases} v_0(x, \omega) & -b \leq x \leq b \\ 0 & \text{otherwise} \end{cases}. \quad (14.3)$$

To obtain solutions for the sound beam generated by this element, as done in Chap. 2, we will express the pressure field $p(x, z, \omega)$ in the form of an angular spectrum of plane waves. Specifically, we will write:

$$p(x, z, \omega) = \frac{1}{2\pi} \int_{-\infty}^{+\infty} [P(k_x) / z_b + V(k_x)] G(k_x) \exp(ik_x x + ik_z z) dk_x, \quad (14.4)$$

where

$$k_z = \begin{cases} \sqrt{k^2 - k_x^2} & k \geq k_x \\ i\sqrt{k_x^2 - k^2} & k < k_x \end{cases} \quad (14.5)$$

and $k = \omega / c$ is the wave number for pressure waves in the fluid. Since the right side of Eq. (14.4) is a superposition of plane waves and inhomogeneous waves, both of which are exact solutions of the Helmholtz equation, the pressure $p(x, z, \omega)$ in Eq. (14.4) will also be an exact solution to that equation. The “amplitude” terms $P(k_x)$, $V(k_x)$, $G(k_x)$ in Eq. (14.4) are at present undefined. The particular combination of these terms given in Eq. (14.4) was chosen simply to help satisfy the boundary conditions of Eq. (14.3), as we will now show. First, we note that from the equation of motion of the fluid in the z -direction, the pressure and the z -velocity must satisfy the differential relationship [Schmerr]

$$-\frac{\partial p(x, z, t)}{\partial z} = \rho \frac{\partial v_z(x, z, t)}{\partial t}. \quad (14.6)$$

Taking the Fourier transform of both sides of this equation and solving for $v_z(x, z, \omega)$ we find

$$v_z(x, z, \omega) = \frac{1}{ik_z z_f} \frac{\partial p(x, z, \omega)}{\partial z}, \quad (14.7)$$

where $z_f = \rho c$ is the specific impedance of the fluid.

Thus, using Eqs. (14.4) and (14.7), we can write the left-hand side of Eq. (14.3) as

$$p(x, z, \omega) / z_b + v_z(x, z, \omega) = \frac{1}{2\pi} \int_{-\infty}^{+\infty} [P(k_x) / z_b + V(k_x)] G(k_x) \left[\frac{1}{z_b} + \frac{k_z}{k z_f} \right] \exp(ik_x x + ik_z z) dk_x. \quad (14.8)$$

However, if we let

$$G(k_x) = \frac{1}{\frac{1}{z_b} + \frac{k_z}{k z_f}} \quad (14.9)$$

we see that on $z=0$, Eq. (14.8) is in the form of an inverse spatial Fourier transform, i.e.

$$p(x, z=0, \omega) / z_b + v_z(x, z=0, \omega) = \frac{1}{2\pi} \int_{-\infty}^{+\infty} [P(k_x) / z_b + V(k_x)] \exp(ik_x x) dk_x, \quad (14.10)$$

so that from an inverse spatial Fourier transform we have

$$P(k_x) / z_b + V(k_x) = \int_{-\infty}^{+\infty} [p(x, z=0, \omega) / z_b + v_z(x, z=0, \omega)] \exp(ik_x x) dx. \quad (14.11)$$

Equation (14.11) shows that the boundary conditions of Eq. (14.3) will be satisfied if we let

$$P(k_x) / z_b + V(k_x) = V_0(k_x), \quad (14.12)$$

where the term $V_0(k_x)$ is just the spatial Fourier transform of the right side of Eq. (14.3), i.e.

$$V_0(k_x) = \int_{-b}^{+b} v_0(x', \omega) \exp(-ik_x x') dx', \quad (14.13)$$

and from Eq. (14.11) it can be seen that $P(k_x)$ and $V(k_x)$ can be identified as the spatial Fourier transforms of the fields $p(x, z=0, \omega)$ and $v_z(x, z=0, \omega)$, respectively, given by

$$\begin{aligned} P(k_x) &= \int_{-\infty}^{+\infty} p(x, z=0, \omega) \exp(-ik_x x) dx, \\ V(k_x) &= \int_{-\infty}^{+\infty} v_z(x, z=0, \omega) \exp(-ik_x x) dx. \end{aligned} \quad (14.14)$$

Collecting all these results we then can obtain the pressure wave field of Eq. (14.4) explicitly as

$$p(x, z, \omega) = \frac{1}{2\pi} \int_{-\infty}^{+\infty} V_0(k_x) \left[\frac{z_b z_f}{z_f + z_b k_z / k} \right] \exp(ik_x x + ik_z z) dk_x. \quad (14.15)$$

Equation (14.15) is an angular plane wave spectrum representation for the wave field of a transducer element embedded in an infinite baffle of acoustic impedance, z_b . If we also assume that the driving velocity term, $v_0(x, z=0, \omega)$, is spatially uniform over the face of the transducer, i.e.

$$v_0(x, z=0, \omega) = \begin{cases} v_0(\omega) & -b \leq x \leq b \\ 0 & \text{otherwise} \end{cases}, \quad (14.16)$$

then the inverse Fourier transform of this velocity term can be performed analytically, giving

$$V_0(k_x) = 2bv_0(\omega) \frac{\sin(k_x b)}{k_x b} = 2bv_0(\omega) \text{sinc}(k_x b) \quad (14.17)$$

in terms of the sinc function $\text{sinc}(x) = \sin(x)/x$. This case is similar to a model of a single element piston transducer in a rigid baffle where the normal velocity is assumed to be uniform on the face of the transducer. Thus, we will also refer to our model of an element in a finite impedance baffle that satisfies Eq. (14.16) as a piston model.

Since on the face of the element we have

$$p(x, z=0, \omega) / z_b + v_z(x, z=0, \omega) = v_0(\omega), \quad (14.18)$$

if we integrate Eq. (14.18) over the element face we find

$$\frac{1}{z_b(2b)} \int_{-b}^{+b} p(x, \omega) dx + \frac{1}{2b} \int_{-b}^{+b} v_z(x, \omega) dx = v_0(\omega), \quad (14.19)$$

which can be written in terms of the force/unit length, $F_t(\omega)$, acting on the element face and the average velocity in the z -direction, $\bar{v}_z(\omega)$, on the face as

$$\frac{F_t(\omega)}{z_b(2b)} + \bar{v}_z(\omega) = v_0(\omega). \quad (14.20)$$

If we define the acoustic radiation impedance/unit length, $Z_t(\omega)$, as

$$Z_t(\omega) = F_t(\omega) / \bar{v}_z(\omega) \quad (14.21)$$

we then have

$$\left(\frac{Z_t(\omega)}{z_b(2b)} + 1 \right) \bar{v}_z(\omega) = v_0(\omega). \quad (14.22)$$

Equation (14.22) shows how the source term, $v_0(\omega)$, for a piston element in a finite impedance baffle is related to the average velocity on the element face. Similarly,

we could write a relationship between the average pressure in the z -direction, $\bar{p}(\omega)$, and the source term $v_0(\omega)$ as

$$\left(1 + \frac{z_b(2b)}{Z_t(\omega)}\right) \bar{p}(\omega) = z_b v_0(\omega), \quad (14.23)$$

so that if we instead define a source term, $p_0(\omega) = z_b v_0(\omega)$ for our finite impedance baffle model which has the dimensions of a pressure, Eq. (14.23) shows we can relate that pressure source term to the average pressure through

$$\left(1 + \frac{z_b(2b)}{Z_t(\omega)}\right) \bar{p}(\omega) = p_0(\omega). \quad (14.24)$$

14.2 Line Source Model of an Element in a Finite Impedance Baffle

It is possible to perform the angular plane wave spectrum integral of Eq. (14.15) numerically, leading to an “exact” solution for the wave field generated by the element. However, we can instead obtain some approximate results that allow us to describe the acoustic field more explicitly. First, we rewrite Eq. (14.15) in terms of the source velocity, $v_0(x', \omega)$ by using Eq. (14.13) to obtain

$$p(x, z, \omega) = \frac{1}{2\pi} \int_{-b}^{+b} \int_{-\infty}^{+\infty} v_0(x', \omega) \left[\frac{z_b z_f}{z_f + z_b k_z / k} \right] \exp[ik_x(x - x') + ik_z z] dk_x dx'. \quad (14.25)$$

At high frequencies the integration over k_x can be performed approximately by the method of stationary phase [Schmerr], which for 1-D integrals states that the integral, I , is given by

$$\begin{aligned} I &= \int_{-\infty}^{+\infty} f(k_x) \exp[i\phi(k_x)] dk_x \\ &\cong f(k_x^s) \exp[i\phi(k_x^s)] \sqrt{\frac{2\pi}{|\phi''(k_x^s)|}} \exp\left[i\pi \operatorname{sgn}(\phi''(k_x^s)) / 4\right] \end{aligned} \quad (14.26)$$

where k_x^s is the stationary phase point where $\phi'(k_x^s) = 0$ and ϕ', ϕ'' are the first and second derivatives of the function $\phi(k_x)$. The $\operatorname{sgn}()$ function is simply

$$\operatorname{sgn}(u) = \begin{cases} +1 & u > 0 \\ -1 & u < 0 \end{cases}. \quad (14.27)$$

In our case we have

$$f(k_x) = \frac{z_b z_f}{z_f + z_b k_z / k}$$

$$\phi(k_x) = k_x(x - x') + k_z z \quad (14.28)$$

and it is easy to show that at the stationary phase point

$$k_x^s = k \frac{(x - x')}{r}, \quad k_z^s = k \frac{z}{r}, \quad (14.29)$$

where (see Fig. 14.1)

$$r = \sqrt{(x - x')^2 + z^2} \quad (14.30)$$

is the distance from a point $(x', 0)$ on the plane $z=0$ to a point $\mathbf{x} = (x, z)$ in the fluid. We then also find

$$\phi''(x_s) = \frac{-r}{k \cos^2(\theta')}, \quad (14.31)$$

where $\cos(\theta') = z/r$ (see Fig. 14.1). Using all of these results the stationary phase evaluation of Eq. (14.25) gives

$$p(\mathbf{x}, \omega) = \sqrt{\frac{k}{2i\pi}} \int_{-b}^{+b} v_0(x', \omega) \frac{z_b z_f \cos(\theta')}{z_f + \cos(\theta') z_b} \frac{\exp(ikr)}{\sqrt{r}} dx'. \quad (14.32)$$

Equation (14.32) represents the transducer wave field as a superposition of waves arising from line sources acting on the $z=0$ plane over the region $-b < x' < b$, where the remainder of the plane is a baffle of finite impedance. For a piston source we have

$$p(\mathbf{x}, \omega) = z_f v_0(\omega) \sqrt{\frac{k}{2i\pi}} \int_{-b}^{+b} \frac{z_b \cos(\theta')}{z_f + \cos(\theta') z_b} \frac{\exp(ikr)}{\sqrt{r}} dx'. \quad (14.33)$$

Since the term $\exp(ikr)/\sqrt{r}$ in Eq. (14.33) represents a cylindrically spreading wave we see that the amplitude of this cylindrical wave is modified by the angle-dependent term,

$$D_{bf}(\theta') = \frac{z_b \cos(\theta')}{z_f + z_b \cos(\theta')}, \quad (14.34)$$

which we refer to as the directivity function for the finite impedance baffle. For the case of the rigid baffle ($z_b / z_f \rightarrow \infty$), we have simply $D_{bf} = 1$ and Eq. (14.33) reduces to the Rayleigh-Sommerfeld equation (also called the Rayleigh equation) for a piston velocity source in a rigid baffle:

$$p(\mathbf{x}, \omega) = z_f v_0(\omega) \sqrt{\frac{k}{2i\pi}} \int_{-b}^{+b} \frac{\exp(ikr)}{\sqrt{r}} dx'. \quad (14.35)$$

Similarly, if we let $v_0(\omega) = p_0(\omega) / z_b$ and consider the case of the pressure-free surface outside the element ($z_b / z_f \rightarrow 0$), we obtain the Rayleigh-Sommerfeld equation (also called the Sommerfeld equation) for a constant pressure source on a stress-free surface:

$$p(\mathbf{x}, \omega) = p_0(\omega) \sqrt{\frac{k}{2i\pi}} \int_{-b}^{+b} \cos(\theta') \frac{\exp(ikr)}{\sqrt{r}} dx'. \quad (14.36)$$

Our result, Eq. (14.33), thus is the generalization of these Rayleigh/Sommerfeld equations to the more general case of the finite impedance baffle.

Since most testing will be done at distances from an element where the far field approximation is valid, we can examine the effects of a finite impedance baffle by considering that case. The details of obtaining the far field for the Rayleigh-Sommerfeld equation have been given for a piston element in a rigid baffle so we will summarize the same results here. In the far field, we can make the replacements $r \rightarrow r_0$, $\theta' \rightarrow \theta$ (see Fig. 14.1) in the amplitude parts of Eq. (14.32) and keep two terms in the expansion of the phase to give

$$p(\mathbf{x}, \omega) = \sqrt{\frac{k}{2i\pi}} \frac{z_b z_f \cos(\theta)}{z_f + \cos(\theta) z_b} \frac{\exp(ikr_0)}{\sqrt{r_0}} \int_{-b}^{+b} v_0(x', \omega) \exp(-ik \sin \theta x') dx'. \quad (14.37)$$

And, for piston behavior, we find

$$p(\mathbf{x}, \omega) = \sqrt{\frac{2}{i\pi}} v_0(\omega) z_f (kb) \frac{z_b \cos(\theta)}{z_f + \cos(\theta) z_b} D_b(\theta) \frac{\exp(ikr_0)}{\sqrt{kr_0}}, \quad (14.38)$$

where $D_b(\theta)$ is the far field directivity of a piston element in a rigid baffle (Eq. (2.39)). Comparing Eq. (14.38) with the equivalent result for a piston source in a rigid baffle (Eq. (2.38)), we see that the finite impedance of the baffle introduces an additional directivity term

$$D_i(\theta) = \frac{z_b \cos \theta}{z_f + z_b \cos \theta}. \quad (14.39)$$

Fig. 14.2 The far field directivity versus angle due to a finite impedance baffle (*solid line*) and the far field directivity of a piston element in a rigid baffle (*dashed line*) for an element length equal to one wave length ($2b / \lambda = 1$). The baffle impedance $z_b = 2.85\text{MRayls}$ and the impedance of the fluid (water) $z_f = 1.48\text{MRayls}$

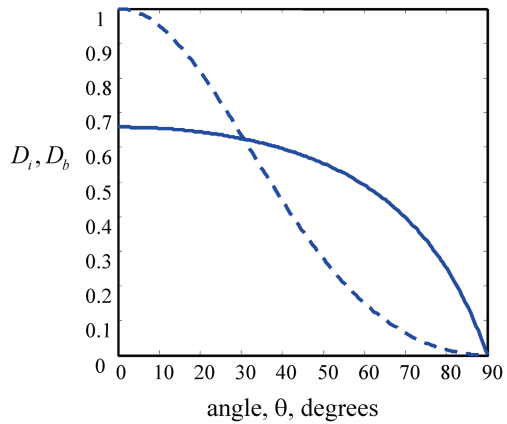
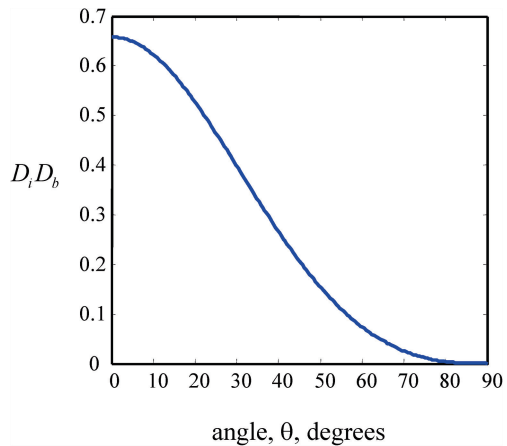


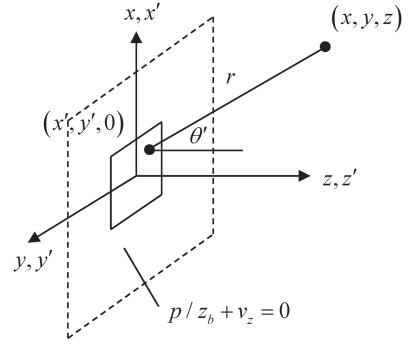
Fig. 14.3 The total directivity of the element considered in Fig. 14.2



[Note that the $v_0(\omega)$ source term here is not the same as the normal velocity term denoted by the same symbol in Eq. (2.37) because of Eq. (14.22)].

Figure 14.2 plots this additional directivity term for a baffle of impedance $z_b = 2.85\text{MRayls}$ (which is typical of the impedance of an epoxy-like filling around an array element) adjacent to water with $z_f = 1.48\text{MRayls}$. Also plotted in Fig. 14.2 is the far field directivity, D_b , of a piston element in a rigid baffle for an element length equal to one wavelength ($2b / \lambda = 1$). The product of these two directivities, which is the total far field directivity, is plotted in Fig. 14.3. It can be seen that the additional directivity term from the finite impedance baffle will produce an amplitude change but very little angular changes in the total directivity of the element in the far field. The same behavior will be true for element sizes larger than a wave length where the directivity, D_b , will be even more concentrated around $\theta = 0$. Thus, for arrays radiating into water, it is only for element sizes significantly smaller than a wavelength where we would expect to see any effects on the directivity of the element and hence the radiated field of the entire array. Although we have

Fig. 14.4 A 2-D array element in a finite impedance baffle



only considered a 1-D element radiating in two dimensions, we can also examine a 2-D array element radiating into a fluid (immersion case). Since the analysis for a 2-D array element can be performed with an angular plane wave spectrum approach in exactly the same fashion (see Chap. 6 for the piston element in a rigid baffle), we simply write the end result here for the pressure in the fluid for a 2-D element in a finite impedance baffle (see Fig. 14.4). We find

$$p(\mathbf{x}, \omega) = \frac{-ik}{2\pi} \int_{-\infty}^{+\infty} \int_{-\infty}^{+\infty} v_0(x', y', 0, \omega) D_i(\theta') \frac{\exp(ikr)}{r} dx' dy'. \quad (14.40)$$

Because the same directivity $D_i(\theta')$ appears in Eq. (14.40) as in Eq. (14.32), this directivity will affect the total far field directivity of the 2-D element only when the dimensions of the element are significantly less than a wavelength.

We can also examine the use of our finite impedance model for a 1-D element radiating into a fluid to consider a case similar to that of a contact array element radiating into a solid. Since a contact element on the free surface of a solid is normally modeled as a constant pressure source on a stress-free surface, we can emulate that case with our 1-D model with a finite impedance by setting $v_0(\omega) = p_0(\omega)/z_b$ in Eq. (14.33) to obtain

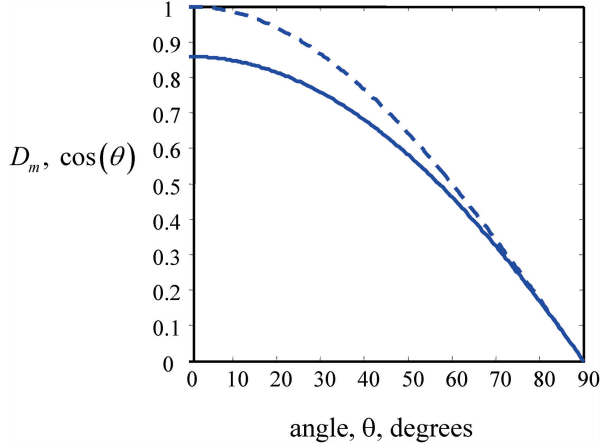
$$p(\mathbf{x}, \omega) = z_f p_0(\omega) \sqrt{\frac{k}{2i\pi}} \int_{-b}^{+b} \frac{\cos(\theta')}{z_f + \cos(\theta')z_b} \frac{\exp(ikr)}{\sqrt{r}} dx'. \quad (14.41)$$

In the far field, then we find

$$p(\mathbf{x}, \omega) = \sqrt{\frac{2}{i\pi}} p_0(\omega) (kb) \frac{z_f \cos(\theta)}{z_f + \cos(\theta)z_b} D_b(\theta) \frac{\exp(ikr_0)}{\sqrt{kr_0}}, \quad (14.42)$$

which shows that the finite impedance baffle model contains directivity, $D_m(\theta)$, given by

Fig. 14.5 The far field directivity, D_m , versus angle for a source having the dimensions of pressure in a finite impedance baffle (*solid line*) and the corresponding directivity, $\cos(\theta)$, for a constant pressure on a free surface (fluid model). The baffle impedance $z_b = 2.85\text{MRayls}$ and the impedance of the “fluid” is taken to be $z_f = 17.33\text{MRayls}$, the P-wave impedance of aluminum



$$D_m(\theta) = \frac{z_f \cos \theta}{z_f + z_b \cos \theta}. \quad (14.43)$$

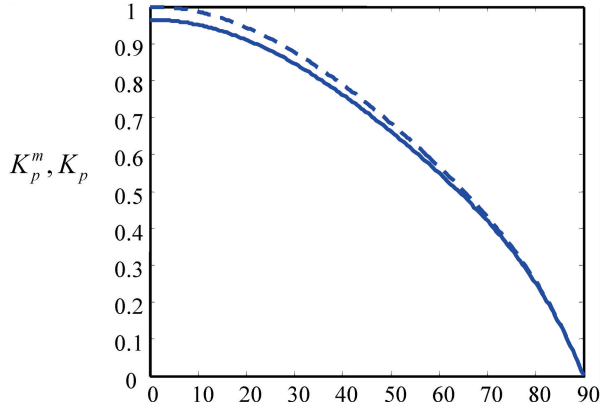
But for a constant pressure source acting on a free surface, a far field free surface directivity, $D_{fs}(\theta) = \cos \theta$ also exists because of the presence of the $\cos \theta'$ term in Eq. (14.36) so that D_m simply modifies that free surface directivity. Figure 14.5 plots these two directivities for a baffle impedance of an epoxy material again, but where the fluid impedance is taken as that of a P-wave in aluminum. Except for a small amplitude change, there is very little difference between these two directivities, which are frequency independent, so one would conclude that baffle impedance effects are very small even for very small elements in contact testing setups. Although this conclusion is based on a fluid model of a contact element, one can also use an angular plane wave spectrum approach to model a contact 2-D element as a constant source (having dimensions of a pressure) on a finite impedance surface of an elastic solid, following the same approach in [Schmerr] for a constant pressure source on an otherwise stress-free surface of a solid. Again, we will not present all the details here, but just give the final result as:

$$\mathbf{v}(\mathbf{x}, \omega) = \frac{-ik_{p1} p_0(\omega)}{2\pi \rho_1 c_{p1}} \int_S K_p^m(\theta') \mathbf{d}_p' \frac{\exp(ik_{p1} r)}{r} dS, \quad (14.44)$$

where $\mathbf{v}(\mathbf{x}, \omega)$ is the velocity in the solid due to P-waves generated by a constant source, $p_0(\omega)$, acting on the surface of an elastic solid having a finite impedance. The directivity, $K_p^m(\theta')$, is given as

$$K_p^m(\theta') = \frac{\cos \theta' \kappa^2 (\kappa^2 / 2 - \sin^2 \theta')}{2G_m(\sin \theta')}, \quad (14.45)$$

Fig. 14.6 The far field directivity, K_p^m , versus angle for a source having the dimensions of pressure in a finite impedance baffle on an elastic solid (*solid line*) and the corresponding directivity, K_p , for a constant pressure on a free surface of the solid. The baffle impedance $z_b = 2.85\text{MRayls}$ and the impedance of the solid is taken to be $z_f = 17.33\text{MRayls}$, the P-wave impedance of aluminum



where

$$G_m(x) = (\kappa^2 / 2 - x^2)^2 + x^2 \sqrt{1 - x^2} \sqrt{\kappa^2 - x^2} + (\kappa^2 z_b / 4z_p) \sqrt{1 - x^2} \quad (14.46)$$

and z_p is the impedance of a P-wave traveling in the elastic solid and $\kappa = c_{p1} / c_{s1}$ is the ratio of compressional to shear wave speeds of the solid. One can compare this result to the corresponding contact model presented in Chap. 6 (see Eqs. (6.38)–(6.40)) which is of identical form but where $z_b = 0$. Like the fluid model case just discussed, we see that the finite impedance simply modifies a directivity term, $K_p(\theta')$, (see Eq. (6.39)) which is present for a contact model of a constant pressure on a stress-free interface. Figure 14.6 compares the finite impedance baffle far field directivity K_p^m (for a baffle having an impedance of epoxy) with K_p when the elastic solid is aluminum. As in the corresponding fluid model case the finite impedance baffle only has a minor impact on the far field directivity.

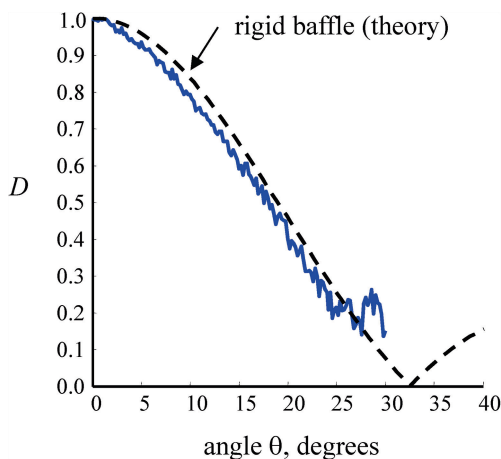
Note that for 2-D arrays we can relate the source terms (v_0, p_0) to the average velocity and pressure on the face of the element in similar forms to the ones found for 1-D elements. We find (see Eqs. 14.22 and 14.24):

$$\left(\frac{Z_t(\omega)}{z_b S} + 1 \right) \bar{v}_z(\omega) = v_0(\omega) \quad (14.47)$$

and

$$\left(1 + \frac{z_b S}{Z_t(\omega)} \right) \bar{p}(\omega) = p_0(\omega), \quad (14.48)$$

Fig. 14.7 Measurement of the total far field directivity of the eighth element of a 16-element linear array at a frequency of 5 MHz (*solid line*) compared to the behavior of a piston velocity source in a rigid baffle (*dashed line*). Pitch=0.6 mm, element length=0.5 mm, element height=10 mm



where Z_i is the radiation impedance of the element and S is the element area. To obtain this impedance numerically for a rectangular piston element is not difficult, as shown by Sha et al. [2].

From the above discussion, it is more likely that we will see far field directivity effects in the case of an array used in immersion testing. Fortunately, in the immersion case we can actually measure the total far field directivity of a single element experimentally to see how well the assumption that the element acts as a piston velocity source in a rigid baffle is satisfied. Figure 14.7 shows an example of such measurements taken at a frequency of 5 MHz for a single element of a 16-element linear array, where the pitch of the array was 0.6 mm, the length of the element was 0.5 mm, and the element height was 10 mm. In this case, it is seen that piston behavior and a rigid baffle assumption matches well the measured directivity of the central lobe of the element.

14.3 Other Modeling Issues

Besides the impedance of the baffle surrounding a transducer element, there are other modeling issues that one must be aware of when modeling arrays. In some cases, when a single element of array is excited by a voltage pulse, nearby elements may also exhibit some motion, as illustrated in Fig. 14.8 for a given element and its adjacent neighbors. This coupling may be due to the exciting electrical fields extending over more than one element, as shown in Fig. 14.8a, or it may be due to acoustic waves generated by the excited element that travel across the filler and/or facing materials to other elements, as shown in Fig. 14.8b. Needless to say, both electrical and acoustic types of interactions between elements are very complicated to describe. Baer and Kino [3] have given a relatively simple theory for acoustic cross coupling and Assaad and Bruneel [4] have used finite element models to ana-

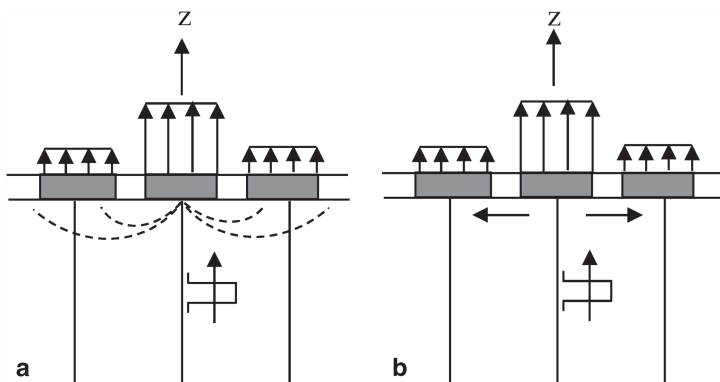


Fig. 14.8 A single element being excited where there are adjacent element excitations through **a** electrical interactions, and **b** through acoustic interactions

lyze such element-to-element couplings in detail. Although we will not examine these couplings in this book, we can note that if a single element of the array is excited and the far field directivity of the element is measured, any significant coupling to adjacent elements should be evident in changes of this directivity. Thus, as in the case of the baffle impedance, one could in principle take these couplings effects into account, at least partially, by measurements of the total directivity of an element in the far field, as discussed in the previous section, and use those measurements to define an *effective length* of an element that would produce the measured directivity. A similar approach has been used in large, single element transducers to define similar effective parameters [Schmerr].

References

1. P. Pesque, M. Fink, *Effect of the planar baffle impedance in acoustic radiation of a phased array element—theory and experimentation*. IEEE Ultrasonics Symposium Proceedings, Dallas, Texas, 14–16 Nov 1984 (Institute of Electrical and Electronic Engineers, Piscataway, NJ, 1984), pp. 1034–1038
2. K. Sha, J. Yang, W.-S. Gan, A simple calculation method for the self- and mutual-radiation impedance of flexible rectangular patches in a rigid baffle. *J. Sound Vibr.* **282**, 179–185 (2005)
3. R.L. Baer, G.S. Kino, Theory for cross coupling in ultrasonic transducer arrays. *Appl. Phys. Lett.* **44**, 954–956 (1984)
4. J. Assaad, C. Bruneel, Radiation from finite phased and focused linear array including interaction. *J. Acoust. Soc. Am.* **101**, 1859–1867 (1997)

Appendices

A The Beylkin Determinant

A.1 The Beylkin Determinant for 3-D Imaging (Common Source Case)

In forming an imaging measurement model for a fixed sending element and varying receiving elements we defined a 3-D wave vector, \mathbf{k} , as

$$\mathbf{k} = \omega \nabla_y \phi(\mathbf{x}_s, \mathbf{x}_r, \mathbf{y}, \omega), \quad (\text{A.1})$$

where ϕ represents the total travel time from the centroid of a sending element located at \mathbf{x}_s to an image point \mathbf{y} and then back to the centroid of a receiving element at \mathbf{x}_r , i.e.

$$\phi(\mathbf{x}_s, \mathbf{x}_r(\xi_r), \mathbf{y}, \omega) = T(\mathbf{x}_s, \mathbf{y}) + T(\mathbf{x}_r(\xi_r), \mathbf{y}), \quad (\text{A.2})$$

and where the variable receiving element centroid location is parameterized in terms of the ξ_r variables. The transformation from integrations over the (ξ_r, ω) variables to the \mathbf{k} wave vector coordinates then involves the magnitude of the Jacobian, $|J|$, of this transformation, i.e.

$$|J| = \left| \frac{\partial(\omega, \xi_{1r}, \xi_{2r})}{\partial(\mathbf{k})} \right| \quad (\text{A.3})$$

and the inverse of this Jacobian can be written as

$$\frac{\partial(\mathbf{k})}{\partial(\omega, \xi_{1r}, \xi_{2r})} = \omega^2 h(\xi_{1r}, \xi_{2r}, \omega), \quad (\text{A.4})$$

where the Beylkin determinant [1], h , is given by

$$h(\xi_r, \mathbf{y}) = \det \begin{bmatrix} \nabla_y \phi \\ \frac{\partial}{\partial \xi_{1r}} (\nabla_y \phi) \\ \frac{\partial}{\partial \xi_{2r}} (\nabla_y \phi) \end{bmatrix}. \quad (\text{A.5})$$

If we define slowness vectors $(\mathbf{p}_s, \mathbf{p}_r)$ as

$$\mathbf{p}_s = \nabla_y T(\mathbf{x}_s, \mathbf{y}), \mathbf{p}_r = \nabla_y T(\mathbf{x}_r, \mathbf{y}) \quad (\text{A.6})$$

and their derivatives as

$$\mathbf{v}_r = \frac{\partial \mathbf{p}_r}{\partial \xi_{1r}}, \mathbf{w}_r = \frac{\partial \mathbf{p}_r}{\partial \xi_{2r}}, \quad (\text{A.7})$$

then the Beylkin determinant becomes

$$h(\xi_{1r}, \xi_{2r}, \mathbf{y}) = \det \begin{bmatrix} \mathbf{p}_s + \mathbf{p}_r \\ \frac{\partial \mathbf{p}_r}{\partial \xi_{1r}} \\ \frac{\partial \mathbf{p}_r}{\partial \xi_{2r}} \end{bmatrix} = (\mathbf{p}_s + \mathbf{p}_r) \cdot (\mathbf{v}_r \times \mathbf{w}_r). \quad (\text{A.8})$$

At high frequencies these slowness vectors satisfy the eikonal equations

$$\mathbf{p}_s \cdot \mathbf{p}_s = \frac{1}{c_\beta^2(\mathbf{y})}, \mathbf{p}_r \cdot \mathbf{p}_r = \frac{1}{c_\alpha^2(\mathbf{y})} \quad (\text{A.9})$$

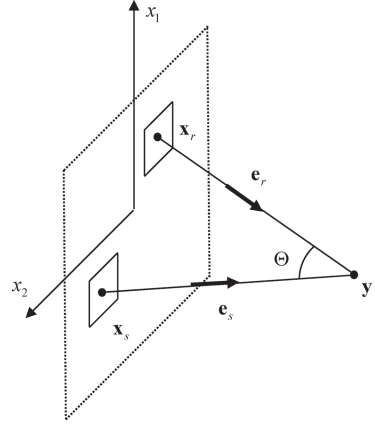
so that the slowness vectors are orthogonal to their derivatives. In particular

$$\mathbf{p}_r \cdot \mathbf{v}_r = \mathbf{p}_r \cdot \mathbf{w}_r = 0. \quad (\text{A.10})$$

Thus, the cross product in Eq. (A.8) must be parallel to \mathbf{p}_r and we have

$$\mathbf{v}_r \times \mathbf{w}_r = \pm c_\alpha(\mathbf{y}) \mathbf{p}_r |\mathbf{v}_r \times \mathbf{w}_r|. \quad (\text{A.11})$$

Fig. A.1 Parameters associated with the determination of the Beylkin determinant



Since we are only interested in the absolute value of the Beylkin determinant (see Eq. (A.3)), the plus or minus sign here is immaterial and will henceforth be dropped. Thus, the determinant can be written

$$h(\xi_{1r}, \xi_{2r}, \mathbf{y}) = c_\alpha(\mathbf{y}) (\mathbf{p}_s + \mathbf{p}_r) \cdot \mathbf{p}_r |\mathbf{v}_r \times \mathbf{w}_r|. \quad (\text{A.12})$$

If we let Θ be the angle between the two slowness vectors (see Fig. A.1), then

$$\begin{aligned} h(\xi_{1r}, \xi_{2r}, \mathbf{y}) &= \frac{1}{c_\alpha(\mathbf{y})} \left[1 + \frac{c_\alpha(\mathbf{y})}{c_\beta(\mathbf{y})} \cos \Theta \right] |\mathbf{v}_r \times \mathbf{w}_r| \\ &= \left[1 + \frac{c_\alpha(\mathbf{y})}{c_\beta(\mathbf{y})} \cos \Theta \right] \mathbf{p}_r \cdot (\mathbf{v}_r \times \mathbf{w}_r). \end{aligned} \quad (\text{A.13})$$

We can write Eq. (A.13) for the determinant in our original notation as

$$h(\xi_{1r}, \xi_{2r}, \mathbf{y}) = \left[1 + \frac{c_\alpha(\mathbf{y})}{c_\beta(\mathbf{y})} \cos \Theta \right] h_r(x_{1r}, x_{2r}, \mathbf{y}), \quad (\text{A.14})$$

where $h_r(x_{1r}, x_{2r}, \mathbf{y})$ is defined as

$$h_r(\xi_{1r}, \xi_{2r}, \mathbf{y}) \equiv \det \begin{bmatrix} \nabla_y T(\mathbf{x}_r, \mathbf{y}) \\ \frac{\partial}{\partial \xi_{1r}} [\nabla_y T(\mathbf{x}_r, \mathbf{y})] \\ \frac{\partial}{\partial \xi_{2r}} [\nabla_y T(\mathbf{x}_r, \mathbf{y})] \end{bmatrix} = \frac{1}{c_\alpha^3} \det \begin{bmatrix} \mathbf{e}_r \\ \frac{\partial \mathbf{e}_r}{\partial \xi_{1r}} \\ \frac{\partial \mathbf{e}_r}{\partial \xi_{2r}} \end{bmatrix}, \quad (\text{A.15})$$

and where $\mathbf{e}_r = \mathbf{e}_\alpha^{(2)}$ is the unit vector along the incident wave direction at the image point \mathbf{y} coming from the receiving element (acting as a transmitter). This determinant can be easily evaluated if we choose $(\xi_{1r}, \xi_{2r}) = (\theta_r, \phi_r)$ where (θ_r, ϕ_r) are spherical coordinates at the image point \mathbf{y} with the polar “ z ” axis taken along a fixed reference \mathbf{p}_r direction. Then we have

$$\mathbf{e}_r = \sin \theta_r \cos \phi_r \mathbf{e}_x + \sin \theta_r \sin \phi_r \mathbf{e}_y + \cos \theta_r \mathbf{e}_z \quad (\text{A.16})$$

and

$$h_r(\xi_{1r}, \xi_{2r}, \mathbf{y}) = \frac{1}{c_\alpha^3} \det \begin{bmatrix} \sin \theta_r \cos \phi_r & \sin \theta_r \sin \phi_r & \cos \theta_r \\ \cos \theta_r \cos \phi_r & \cos \theta_r \sin \phi_r & -\sin \theta_r \\ -\sin \theta_r \sin \phi_r & \sin \theta_r \cos \phi_r & 0 \end{bmatrix} = \frac{1}{c_\alpha^3} \sin \theta_r, \quad (\text{A.17})$$

so the complete Beylkin determinant is given by

$$h(\mathbf{x}_s, \mathbf{x}_r(\theta_r, \phi_r), \mathbf{y}) = \left(1 + \frac{c_\alpha}{c_\beta} \cos \Theta \right) \frac{1}{c_\alpha^3} \sin \theta_r. \quad (\text{A.18})$$

A.2 The Beylkin Determinant for 3-D Imaging (Pulse-Echo Case)

When an image is formed with the pulse-echo responses of the individual elements of an array, a 3-D wave vector, \mathbf{k} , is defined as

$$\mathbf{k} = 2\omega \nabla_y T(\mathbf{x}_c, \mathbf{y}). \quad (\text{A.19})$$

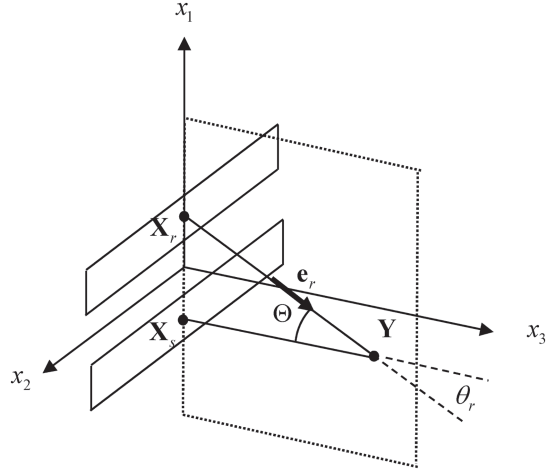
Where $T(\mathbf{x}_c, \mathbf{y})$ is the one-way travel time from the centroid, \mathbf{x}_c , of the element to an image point \mathbf{y} . As in the general case we will assume this centroid location is parameterized in terms of $\xi_c = (\xi_{1c}, \xi_{2c})$ variables and we will write the inverse Jacobian as (see Eq. (A.4)):

$$\frac{\partial(\mathbf{k})}{\partial(\omega, \xi_{1c}, \xi_{2c})} = \omega^2 h_{pe}(\xi_{1c}, \xi_{2c}, \omega), \quad (\text{A.20})$$

where the Beylkin determinant is now

$$h_{pe}(\xi_{1c}, \xi_{2c}, \mathbf{y}) = \det \begin{bmatrix} 2\nabla_y T(\mathbf{x}_c, \mathbf{y}) \\ 2\frac{\partial}{\partial \xi_{1c}} [\nabla_y T(\mathbf{x}_c, \mathbf{y})] \\ 2\frac{\partial}{\partial \xi_{2c}} [\nabla_y T(\mathbf{x}_c, \mathbf{y})] \end{bmatrix}. \quad (\text{A.21})$$

Fig. A.2 Parameters for defining the Beylkin determinant for 2-D imaging with linear arrays



We can evaluate the determinate in Eq. (A.21) by starting from Eq. (A.5) and letting $\mathbf{p}_r = \mathbf{p}_s = \mathbf{p}_c$ so that $\Theta = 0$ and set $\alpha = \beta$ (same mode on sending and receiving). We simply replace the parameters (ξ_{1r}, ξ_{2r}) in the general case by the parameters (ξ_{1c}, ξ_{2c}) and as before we let these parameters be spherical coordinates (θ_c, ϕ_c) defined at the image point \mathbf{y} . Then following all the same steps as before we find

$$h_{pe}(\theta_c, \phi_c, \mathbf{y}) = \frac{8 \sin \theta_c}{c_\beta^3}. \quad (\text{A.22})$$

A.3 The Beylkin Determinant for 2-D Imaging

Linear arrays can be used to form 2-D images of 2-D scatterers such as side-drilled holes, as shown in Chap. 13. In this case one defines a 2-D wave vector, \mathbf{k}_{2D} , as

$$\mathbf{k}_{2D} = \omega \nabla_Y \phi(\mathbf{X}_s, \mathbf{X}_r, \mathbf{Y}), \quad (\text{A.23})$$

where $(\mathbf{X}_s, \mathbf{X}_r, \mathbf{Y})$ are all 2-D vectors associated with the centroid of the sending element, the centroid of the receiving element, and the image point, respectively. For a linear array the element centroids can be parameterized in terms of the variables (ξ_{1s}, ξ_{1r}) , i.e. $\mathbf{X}_s = (X_{1s}(\xi_{1s}), X_{3s} = 0)$, $\mathbf{X}_r = (X_{1r}(\xi_{1r}), X_{3r} = 0)$ but the image point $\mathbf{Y} = (Y_1, Y_3)$ is a general point in a plane at the center of the array (see Fig. A.2). If one fixes the sending element and lets the location of the receiving element vary then in forming an imaging measurement model one needs to determine the inverse of the Jacobian defined as

$$\frac{\partial(\mathbf{k}_{2D})}{\partial(\omega, \xi_{1r})} = \omega H(\xi_{1r}, \mathbf{Y}), \quad (\text{A.24})$$

where

$$H(\xi_{lr}, \mathbf{Y}) = \det \left[\begin{array}{c} \nabla_Y \phi \\ \frac{\partial}{\partial \xi_{lr}} (\nabla_Y \phi) \end{array} \right]. \quad (\text{A.25})$$

Now, as in the 3-D case define the 2-D slowness vectors $(\mathbf{p}_s, \mathbf{p}_r)$ as

$$\mathbf{p}_s = \nabla_Y T(\mathbf{X}_s, \mathbf{Y}), \mathbf{p}_r = \nabla_Y T(\mathbf{X}_r, \mathbf{Y}). \quad (\text{A.26})$$

Then the determinant becomes

$$\begin{aligned} H(\xi_{lr}, \mathbf{Y}) &= \det \left[\begin{array}{c} \mathbf{p}_s + \mathbf{p}_r \\ \frac{\partial \mathbf{p}_r}{\partial \xi_{lr}} \end{array} \right] = \mathbf{e}_y \cdot \left[(\mathbf{p}_s + \mathbf{p}_r) \times \frac{\partial \mathbf{p}_r}{\partial \xi_{lr}} \right] \\ &= (\mathbf{p}_s + \mathbf{p}_r) \cdot \left(\frac{\partial \mathbf{p}_r}{\partial \xi_{lr}} \times \mathbf{e}_y \right), \end{aligned} \quad (\text{A.27})$$

where we have used the distributional property of the triple product and \mathbf{e}_y is a unit vector along the x_2 -axis (or y -axis, i.e. perpendicular to the imaging plane). These 2-D slowness vectors still satisfy the eikonal equations, Eq. (A.9), so the slowness vectors are orthogonal to their derivatives and we have

$$H(\xi_{lr}, \mathbf{Y}) = \pm c_\alpha (\mathbf{p}_s + \mathbf{p}_r) \cdot \mathbf{p}_r \left| \frac{\partial \mathbf{p}_r}{\partial \xi_{lr}} \times \mathbf{e}_y \right|. \quad (\text{A.28})$$

As before, we can ignore the sign indeterminacy here since we are only interested in the absolute value of the determinant, and if we let Θ be the angle between the two slowness vectors we have

$$\begin{aligned} H(\xi_{lr}, Y) &= \frac{1}{c_\alpha(Y)} \left[1 + \frac{c_\alpha(Y)}{c_\beta(Y)} \cos \Theta \right] \left| \frac{\partial \mathbf{p}_r}{\partial \xi_{lr}} \times \mathbf{e}_y \right| \\ &= \left[1 + \frac{c_\alpha(Y)}{c_\beta(Y)} \cos \Theta \right] \mathbf{p}_r \cdot \left(\frac{\partial \mathbf{p}_r}{\partial \xi_{lr}} \times \mathbf{e}_y \right) \\ &= \left[1 + \frac{c_\alpha(Y)}{c_\beta(Y)} \cos \Theta \right] \mathbf{e}_y \cdot \left(\mathbf{p}_r \times \frac{\partial \mathbf{p}_r}{\partial \xi_{lr}} \right) \\ &= \left[1 + \frac{c_\alpha(Y)}{c_\beta(Y)} \cos \Theta \right] H_r(\xi_{lr}, \mathbf{Y}), \end{aligned} \quad (\text{A.29})$$

where

$$H_r(\xi_{lr}, \mathbf{Y}) = \det \left[\begin{array}{c} \nabla_Y T(\mathbf{X}_r(\xi_{lr}), \mathbf{Y}) \\ \frac{\partial}{\partial \xi_{lr}} [\nabla_Y T(\mathbf{X}_r(\xi_{lr}), \mathbf{Y})] \end{array} \right]. \quad (\text{A.30})$$

Equation (A.30) can be rewritten as

$$H_r(\xi_{lr}, \mathbf{Y}) = \frac{1}{c_\alpha^2} \det \left[\begin{array}{c} \mathbf{e}_r \\ \frac{\partial \mathbf{e}_r}{\partial \xi_{lr}} \end{array} \right], \quad (\text{A.31})$$

where \mathbf{e}_r is a unit vector along the incident wave direction at the image point \mathbf{Y} coming from the receiving element location, \mathbf{X}_r . Now, suppose we use as the parameter ξ_{lr} the angle θ_r that this unit vector makes with respect to the x_3 -axis (see Fig. A.2). Then

$$\begin{aligned} \mathbf{e}_r &= -\sin \theta_r \mathbf{e}_x + \cos \theta_r \mathbf{e}_z \\ \frac{\partial \mathbf{e}_r}{\partial \theta_r} &= -\cos \theta_r \mathbf{e}_x - \sin \theta_r \mathbf{e}_z \end{aligned} \quad (\text{A.32})$$

so that

$$H_r(\theta_r, \mathbf{Y}) = \frac{1}{c_\alpha^2} \det \left[\begin{array}{cc} -\sin \theta_r & \cos \theta_r \\ -\cos \theta_r & -\sin \theta_r \end{array} \right] = \frac{1}{c_\alpha^2} \quad (\text{A.33})$$

and, finally,

$$H(\theta_r, \mathbf{Y}) = \frac{1}{c_\alpha^2} \left(1 + \frac{c_\alpha}{c_\beta} \cos \Theta \right). \quad (\text{A.34})$$

For pulse-echo 2-D imaging with a linear array, the 2-D \mathbf{k} -vector is instead given by

$$\mathbf{k}_{2D} = 2\omega \nabla_Y T(\mathbf{X}_c, \mathbf{Y}) \quad (\text{A.35})$$

and the inverse Jacobian becomes

$$\frac{\partial(\mathbf{k})}{\partial(\omega, \xi_{lc})} = \omega^2 H_{pe}(\xi_{lc}, \omega), \quad (\text{A.36})$$

where

$$H_{pe}(\xi_{lc}, \mathbf{Y}) = \det \left[2 \frac{\partial}{\partial \xi_{lc}} (\nabla_Y T) \right]. \quad (\text{A.37})$$

Equation (A.37) again can be expressed in terms of a unit vector and its derivatives (see Eq. (A.31), and letting $\xi_{lc} = \theta_c$ allows us to evaluate the determinant simply and we find (with $\alpha = \beta$ for the pulse-echo case)

$$H_{pe}(\theta_c, \mathbf{Y}) = \frac{4}{c_\beta^2}. \quad (\text{A.38})$$

A.4 References

1. N. Bleistein, J.K. Cohen, J.W. Stockwell, *Mathematics of Multidimensional Seismic Imaging, Migration, and Inversion* (Springer-Verlag, New York, 2001)

B Angle-Area Ratios

In developing imaging measurement models, it was convenient to parameterize the locations of the array elements by spherical coordinates at the image point, as this choice made the evaluation of the Beylkin determinant very simple. However, to express the final imaging models in terms of integrations over the element coordinates it is necessary to determine the angle-area ratios, $d\Omega/dS$, where $d\Omega$ is a solid angle measured at the image point and dS is an area element on the plane of the array [1, 2].

B.1 Ratios for Inspection in a Single Medium

For an array radiating into a single medium this ratio is simple to evaluate, as shown explicitly in Chap. 12 for 2-D scalar problems. In three dimensions, we have (see Fig. B.1)

$$\frac{d\Omega_s}{dS_s} = \frac{\cos \beta_s}{r_s^2}, \quad \frac{d\Omega_r}{dS_r} = \frac{\cos \beta_r}{r_r^2}, \quad (\text{B.39})$$

where r_s is the distance from the image point to the centroid, \mathbf{x}_s , of a sending element and β_s is the angle that the normal to the plane of the array at \mathbf{x}_s makes with

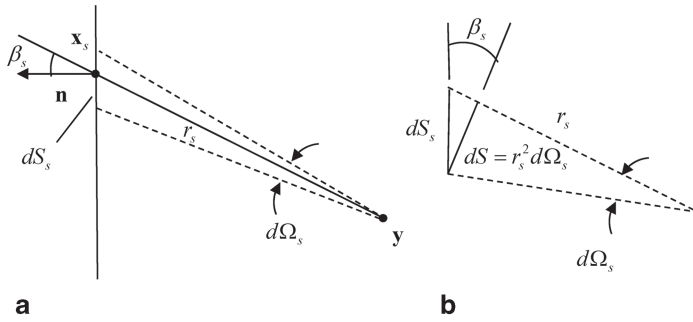


Fig. B.1 **a** Geometry for computing the angle-area ratio, $d\Omega/dS_s$, at a sending element in a single medium, and **b** detailed elements in the computation. Note that an entirely similar set of figures also hold for computing $d\Omega_r/dS_r$ at a receiving element

respect to a ray along the propagating wave direction from the element to the image point, \mathbf{y} . Similarly, r_r is the distance from the image point to the centroid, \mathbf{x}_r , of a receiving element and β_r is the angle that the normal to the plane of the array at \mathbf{x}_r makes with respect to a ray along the propagating wave direction from the element to the image point, \mathbf{y} . The relations of Eq. (B.39) are easily derivable from the geometry of Fig. B.1b. If one considers a bundle of rays of solid angle $d\Omega_s$ extending from the image point \mathbf{y} to the point \mathbf{x}_s , the cross-sectional area of this bundle is $dS = r_s^2 d\Omega_s$ and the corresponding area of the bundle on the plane of the element is $dS_s = dS / \cos \beta_s$, which leads directly to Eq. (B.39) for the sending element. A completely identical process yields the angle-area ratio at a receiving element.

B.2 Ratios for Inspection Through a Planar Interface

For immersion testing or testing with an array on wedge, the waves from the array must pass through an interface for both the sending and receiving elements. The angle-area ratios in this case are more complex than in the single medium case but they still can be easily calculated with a ray theory approach that follows a bundle of rays along the sound generation or reception propagation paths to the element of the array. Figure B.2 shows the geometry for a two medium problem for relating the solid angle $d\Omega_s$ to the area dS_s at a sending element across a planar interface, where a compressional wave is traveling with a wave speed c_{p1} in medium one and a wave of type β ($\beta = p, s$) is propagating in medium two with wave speed $c_{\beta 2}$. To analyze this problem it is convenient to consider first a spherical bundle of rays when it reaches the interface at point \mathbf{P} , as shown in Fig. B.3. The cross-sectional area of the bundle is just $dS_1 = (r_{s2}^\beta)^2 d\Omega_s$ and the projected area on the interface, dA , as shown in Fig. B.3 is just $dA = dS_1 / \cos \theta_{s2}^\beta$, where θ_{s2}^β is the angle that the wave front area makes with respect to the interface (which is also the angle that the ray along the propagation path makes with respect to the normal to the interface).

Fig. B.2 Geometry for calculating the angle-area ratio for a sending element in immersion or angle beam inspection problems

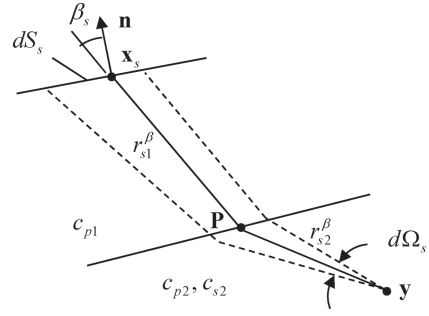
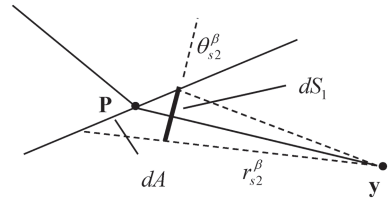


Fig. B.3 Geometry of a spherical bundle of rays in medium two



The bundle of rays in medium one has a wave front that is no longer spherical. At point **P** on the interface, let the principal radii of curvature of the refracted wave front be $(\rho_{si}^\alpha, \rho_{so}^\alpha)$, in the plane of incidence and perpendicular to that plane, respectively. These radii are given by

$$\rho_{si}^\beta = \frac{c_{\beta 2}}{c_{p1}} \frac{\cos^2 \theta_{s1}^\beta}{\cos^2 \theta_{s2}^\beta} r_{s2}^\beta \quad (\text{B.40})$$

$$\rho_{so}^\beta = \frac{c_{\beta 2}}{c_{p1}} r_{s2}^\beta,$$

where $(\theta_{s2}^\beta, \theta_{s1}^\beta)$ are the angles that the wave fronts make with respect to the plane of the interface in medium two and medium one, respectively. It is relatively easy to prove these relations. Consider first rays propagating in the plane of incidence, as shown in Fig. B.4. From the geometry for medium two we have

$$r_{s2}^\beta d\theta_{s2}^\beta = dl_1 = dl \cos \theta_{s2}^\beta. \quad (\text{B.41})$$

If we let ρ_{si}^β be the distance from the interface to the virtual source point \mathbf{V}_1 which the rays in medium one appear to originate from, we likewise have

$$\rho_{si}^\beta d\theta_{s1}^\beta = dl_2 = dl \cos \theta_{s1}^\beta \quad (\text{B.42})$$

Fig. B.4 Rays propagating in the plane of incidence

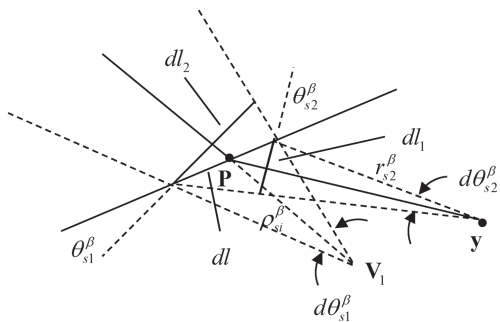
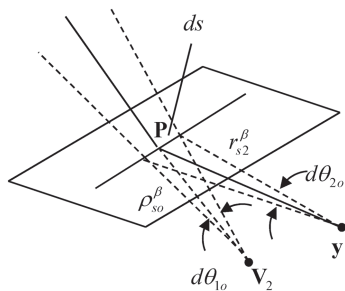


Fig. B.5 Rays propagating out of the plane of incidence



so that

$$\rho_{si}^\beta = r_{s2}^\beta \frac{\cos \theta_{s1}^\beta}{\cos \theta_{s2}^\beta} \frac{d\theta_{s2}^\beta}{d\theta_{s1}^\beta}. \quad (\text{B.43})$$

But, from Snell's law we have

$$\frac{\sin \theta_{s1}^\beta}{c_{p1}} = \frac{\sin \theta_{s2}^\beta}{c_{\beta2}}, \quad (\text{B.44})$$

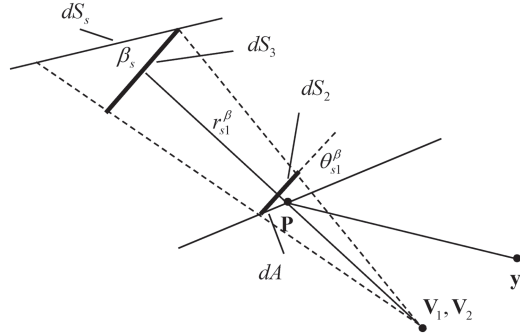
which implies that

$$\frac{d\theta_{s2}^\beta}{d\theta_{s1}^\beta} = \frac{c_{\beta2}}{c_{p1}} \frac{\cos \theta_{s1}^\beta}{\cos \theta_{s2}^\beta} \quad (\text{B.45})$$

so that combining Eq. (B.45) and Eq. (B.43) we obtain the expression for ρ_{si}^β given in Eq. (B.40).

Now, consider rays that are traveling out of the plane of incidence, as shown in Fig. B.5. In this case we have

Fig. B.6 The geometry of the bundle of rays in medium one



$$ds = r_{s2}^{\beta} d\theta_{2o} = \rho_{so}^{\beta} d\theta_{1o}, \quad (\text{B.46})$$

where ρ_{so}^{β} is the distance from the interface to the virtual source point \mathbf{V}_2 from which these rays appear to originate in medium two. However, for these rays and small angles, Snell's law is simply

$$\frac{d\theta_{2o}}{d\theta_{1o}} = \frac{c_{\beta 2}}{c_{\beta 1}}, \quad (\text{B.47})$$

so that combining Eq. (B.47) with Eq. (B.46) we also obtain the relationship for ρ_{so}^{β} given in Eq. (B.40).

The cross-sectional area of the bundle of rays at point \mathbf{P} on the interface is just $dS_2 = \rho_{si}^{\beta} \rho_{so}^{\beta} d\theta_{s1}^{\beta} d\theta_{1o}$ (see Fig. B.6). The projection of this cross-sectional area onto the plane of the interface is $dA = dS_2 / \cos \theta_{s2}^{\beta}$. Similarly, at the sending element, the cross-sectional area of the bundle is just $dS_3 = (\rho_{si}^{\beta} + r_{s1}^{\beta})(\rho_{so}^{\beta} + r_{s1}^{\beta}) d\theta_{s1}^{\beta} d\theta_{1o}$ and the projected area of this bundle onto the plane of the sending element is $dS_s = dS_3 / \cos \beta_s$. With all these results we can then calculate the angle-area ratio as

$$\begin{aligned} \frac{d\Omega_s}{dS_s} &= \frac{d\Omega_s}{dS_1} \frac{dS_1}{dA} \frac{dA}{dS_2} \frac{dS_2}{dS_3} \frac{dS_3}{dS_s} \\ &= \frac{1}{(r_{s2}^{\beta})^2} \cos \theta_{s2}^{\beta} \frac{1}{\cos \theta_{s1}^{\beta}} \frac{\rho_{si}^{\beta} \rho_{so}^{\beta}}{(\rho_{si}^{\beta} + r_{s1}^{\beta})(\rho_{so}^{\beta} + r_{s1}^{\beta})} \cos \beta_s. \end{aligned} \quad (\text{B.48})$$

Using Eq. (B.40) in this ratio, we find

$$\frac{d\Omega_s}{dS_s} = \left(\frac{c_{\beta 2}}{c_{\beta 1}} \right)^2 \frac{\cos \theta_{s1}^{\beta}}{\cos \theta_{s2}^{\beta}} \cos \beta_s \frac{1}{\left(r_{s1}^{\beta} + \frac{c_{\beta 2}}{c_{\beta 1}} r_{s2}^{\beta} \right) \left(r_{s1}^{\beta} + \frac{c_{\beta 2}}{c_{\beta 1}} \frac{\cos^2 \theta_{s1}^{\beta}}{\cos^2 \theta_{s2}^{\beta}} r_{s2}^{\beta} \right)} \quad (\text{B.49})$$

C MATLAB® Functions and Scripts

In this Appendix we will summarize the MATLAB® functions and scripts that appear throughout the book and give detailed listings of the codes. The MATLAB® m-files are also available by sending an e-mail with subject titled “Phased Array Codes” to the author at lschmerr@cnde.iastate.edu.

C.1 Beam Models for Single Elements

rs_2Dv (Code Listing C.1) A function which calculates the normalized pressure wave field of a 1-D element radiating waves in 2-D into a fluid as calculated by a superposition of Hankel functions over the face of the element.

ls_2Dv (Code Listing C.2) A function which calculates the normalized pressure wave field of a 1-D element radiating waves in 2-D into a fluid as calculated by a superposition of high frequency line sources over the face of the element.

ls_2D_int (Code Listing C.3) A function which calculates the normalized pressure wave field of a 1-D element radiating waves in 2-D across a plane interface between two fluids as calculated by a superposition of high frequency line sources over the face of the element and propagating the waves from those sources across the interface with ray theory.

fresnel_2D (Code Listing C.7) A function which calculates the normalized pressure wave field of a large 1-D element radiating waves in 2-D into a fluid as calculated by Fresnel integrals in the paraxial approximation.

on_axis_foc2D (Code Listing C.9) A function which calculates the normalized pressure wave field along the central axis of a large, focused 1-D element radiating waves in 2-D into a fluid as calculated by Fresnel integrals in the paraxial approximation.

Gauss_2D (Code Listing C.10) A function which calculates the normalized pressure wave field of a large 1-D element radiating waves in 2-D into a fluid as calculated by a superposition of Gaussian beams in the paraxial approximation.

NPGauss2D (Code Listing C.16) A function which calculates the normalized pressure wave field of a 1-D element radiating waves in 2-D into a fluid as calculated by a superposition of non-paraxial Gaussian beams.

ps_3Dv (Code Listing C.20) A function which calculates the normalized pressure wave field of a 2-D rectangular element radiating waves in 3-D into a fluid as calculated by a superposition of point sources over the face of the element.

ps_3Dint (Code Listing C.23) A function which calculates the normalized velocity components in an elastic solid for a 2-D rectangular element radiating waves

in 3-D across a plane fluid/solid interface as calculated by a superposition of high frequency point sources over the face of the element and propagating the waves from those sources across the interface with ray theory.

C.2 Delay Laws and Apodization Laws

delay_laws2D (Code Listing C.12) A function which generates the time delay laws for steering and focusing of an array of 1-D elements radiating waves in 2-D into a single medium. The function can also be used to generate delay laws for a linear array of 2-D elements.

discrete_windows (Code Listing C.13) A function which generates 1-D apodization laws for an array using cosine, Hanning, Hamming, Blackman, triangular, or rectangular weights.

delay_laws2D_int (Code Listing C.19) A function which generates the time delay laws for steering and focusing of an array of 1-D elements radiating waves in 2-D across a plane interface between two fluids. The function can also be used to generate delay laws for a linear array of 2-D elements.

delay_laws3D (Code Listing C.22) A function which generates the time delay laws for steering and focusing of an array of rectangular 2-D elements radiating waves in 3-D into a single medium.

delay_laws3D_int (Code Listing C.27) A function which generates the time delay laws for steering and focusing of an array of 2-D elements radiating waves in 3-D across a plane interface between two media.

C.3 Beam Models for Arrays

mls_array_modeling (Code Listing C.14) A script which models the normalized pressure wave field an array of 1-D elements radiating waves into a fluid, using a superposition of multiple line sources for each element. Steering, focusing, and apodization parameters for the array are specified.

mls_array_model_int (Code Listing C.18) A script which models the normalized pressure wave field an array of 1-D elements radiating waves across a plane interface between two fluids, using a superposition of multiple line sources for each element. Steering, focusing, and apodization parameters for the array are specified.

mps_array_modeling (Code Listing C.21) A script which models the normalized pressure wave field an array of 2-D rectangular elements radiating waves into a fluid, using a superposition of multiple point sources for each element. Steering, focusing, and apodization parameters for the array are specified.

mps_array_model_int (Code Listing C.26) A script which models the normalized velocity components in an elastic solid for an array of 2-D rectangular elements radiating waves across a fluid solid/solid interface, using a superposition of multiple point sources for each element. Steering, focusing, and apodization parameters for the array are specified.

C.4 Miscellaneous Functions

pts_2Dintf (Code Listing C.4) A function which uses Snell's law to determine the intersection points of rays traveling in 2-D across a plane interface between two media from the centroid of a 1-D element in an array to points (x, z) in the second medium. This function uses the helping functions *ferrari2* and *init_xi*.

ferrari2 (Code Listing C.5) A function which uses the input parameters of the functions *pts_2Dintf* or *pts_3Dint* to express Snell's law for a plane interface as the problem of finding the appropriate root of a quartic equation. Ferrari's method is used to obtain the roots of the quartic and return the location of the *single* intersection point on the interface of a ray path that goes from the centroid of an array element or element segment to a specified *single* point in the second medium.

init_xi (Code Listing C.6) A function which examines the sizes of the variables describing the points (x, z) in the input parameters of *pts_2Dintf* and generates the consistent size needed for the intersection points on the interface that define Snell's law ray paths and the number of calls needed to the function *ferrari2*, which can only return a single intersection point at a time.

fresnel_int (Code Listing C.8) A function which evaluates the Fresnel integral numerically.

gauss_c15 (Code Listing C.11) A function which returns fifteen Gaussian coefficients developed by Wen and Breazeale, which can be used to describe the wave field of an 1-D element with a multi-Gaussian beam model. See also *gauss_c10*.

elements (Code Listing C.15) A function which allows specification of array element sizes and gap sizes in normalized form and returns the actual element sizes and centroid locations. This function is used in the script *mls_array_modeling* to perform parametric studies.

gauss_c10 (Code Listing C.17) A function which returns ten Gaussian coefficients developed by Wen and Breazeale, which can be used to describe the wave field of an 1-D element with a multi-Gaussian beam model.

pts_3Dint (Code Listing C.24) A function which uses Snell's law to determine the intersection points of rays traveling in 3-D across a plane interface between two media from the centroid of a 2-D element in an array to points (x, y, z) in the second medium. This function uses the helping functions *ferrari2* and *init_xi3D*.

init_xi3D (Code Listing C.25) A function which examines the sizes of the variables describing the points (x, y, z) in the input parameters of `pts_3Dint` and generates the consistent empty matrix needed to hold the intersection points on the interface that define Snell's law ray paths. The function also returns the dimensions of the matrix holding the interface points, parameters which are used in calling the function `ferrari2`.

interface2 (Code Listing C.28) A function which expresses Snell's law in terms of the location of the point of intersection of a ray path with a planar interface. The value of the function is zero when Snell's law is satisfied. This function is used in the function `ferrari2` as a back-up evaluation in the event Ferrari's method does not give a sufficiently accurate solution. In that case the intersection point on the interface is calculated iteratively with the built-in MATLAB function `fzero`, using the call

```
>>xi=fzero(@interface2,[0,DX],[ ], cr, DF, DT, DX);
```

Note that this call to `fzero` can also be used as a direct replacement for the call to `ferrari2`:

```
>>xi=ferrari2(cr, DF, DT, DX);
```

but the use of `fzero` in this manner is typically much less efficient.

T_fluid_solid (Code Listing C.29) A function which computes the P-P (compressional wave to compressional wave) and P-S (compressional wave to vertical-shear wave) transmission coefficients, based on velocity ratios, for the oblique incidence of a plane wave on a fluid-solid interface.

C.5 Code Listings

Code Listing C.1. The function `rs_2DV` which calculates the normalized pressure wave field of a 1-D element radiating waves in 2-D into a fluid as calculated by a superposition of Hankel functions over the face of the element.

```
function p = rs_2Dv(b, f, c, e, x, z, varargin)
% p= rs_2Dv(b, f, c, e, x, z, Nopt) computes the normalized
% pressure, p, at a location (x, z) (in mm)
% in a fluid for a 1-D element of length
% 2b (in mm) along the x-axis at a frequency, f, (in MHz).
% and for a wave speed, c, (in m/sec) of the fluid. This
% function can be used to describe an element in an array by
% specifying a non-zero value for e (in mm), which is the offset
% of the center of the element along the x-axis.
% The assumed harmonic time dependency is exp(-2i*pi*f*t) and
% the 2-D version of the Rayleigh-Sommerfeld integral for a
% piston source is used as the model.
% Nopt gives the number of segments to use. If Nopt is not
% given as an input argument the function uses 10 segments
% per wavelength, based on the input frequency, f, which must
% be a scalar when Nopt is not given.
```

```

% compute wave number
kb = 2000*pi.*b.*f./c ;
% if number of segments is specified, use
if nargin == 7
    N = varargin{1};
else
% else choose number of segments so that the size of each segment
% is one-tenth a wavelength
N = round((20000)*f*b/c);
    if N <= 1
        N = 1;
    end
end
% use normalized positions in the fluid
xb = x./b;
zb = z./b;
eb = e./b;
% compute normalized centroid locations for the segments
xc=zeros(1,N);
for jj=1:N
    xc(jj) = -1 + 2*(jj-0.5)/N;
end
% calculate normalized pressure as a sum over all the
% segments as an approximation of the Rayleigh-Sommerfeld
% type of integral
p=0;
for kk = 1:N
    rb = sqrt((xb-xc(kk)-eb).^2 + zb.^2);
    p = p + besselh(0, 1,kb.*rb);
end
p = p.*(kb./N); % include external factor

```

Code Listing C.2. The function `ls_2Dv` which calculates the normalized pressure wave field of a 1-D element radiating waves in 2-D into a fluid as calculated by a superposition of high frequency line sources over the face of the element.

```

function p = ls_2Dv(b, f, c, e, x, z, varargin)
% p= ls_2Dv(b, f, c, e, x, z, Nopt) computes the normalized
% pressure, p, at a location (x, z) (in mm) in a fluid
% for a two-dimensional source of length
% 2b (in mm) along the x-axis at a frequency, f, (in MHz)
% and for a wave speed, c, (in m/sec) of the fluid. This
% function can be used to describe an element in an array by
% specifying a non-zero value for e (in mm), which is the offset
% of the center of the element along the x-axis.
% The assumed harmonic time dependency is exp(-2i*pi*f*t) and
% the 2-D version of the Rayleigh-Sommerfeld integral for a
% piston source is used as the model where the Hankel function

```

```
% is approximated by its asymptotic cylindrical wave form for
% large wave numbers.
% Nopt gives the number of segments to use. If Nopt is not
% given as an input argument the function uses 1 segment
% per wavelength, based on the input frequency, f, which must
% be a scalar in the case where Nopt is not given.

% compute wave number
kb = 2000*pi*b*f/c ;

% if number of segments is specified, use

if nargin == 7
    N = varargin{1};
else
% else choose number of terms so that the size of each segment
% is a wavelength
    N = round((2000)*f*b/c);
    if N < 1
        N=1;
    end
end
% use normalized positions in the fluid
xb = x/b;
zb = z/b;
eb=e/b;
% compute normalized centroid locations for the segments
xc=zeros(1,N);
for jj=1:N
    xc(jj) = -1 + 2*(jj-0.5)/N;
end
% calculate normalized pressure as a sum over all the
% segments as an approximation of the Rayleigh-Sommerfeld
% type of integral
p=0;
for kk = 1:N
    ang =atan((xb-xc(kk) -eb)./zb);
    ang = ang + eps.*( ang == 0);
    dir =sin(kb.*sin(ang)/N)./(kb.*sin(ang)/N);
    rb = sqrt((xb-xc(kk)- eb).^2 + zb.^2);
    ph = exp(1i*kb.*rb);
    p= p + dir.*exp(i*kb.*rb)./sqrt(rb);
end
p = p.*(sqrt(2*kb./(i*pi)))/N; % include external factor
```

Code Listing C.3. The function `ls_2Dint` which calculates the normalized pressure wave field of a 1-D element radiating waves in 2-D across a plane interface between two fluids as calculated by a superposition of high frequency line sources over the face of the element and propagating the waves from those sources across the interface with ray theory.

```
function p = ls_2Dint(b, f, mat,e, angt, Dt0, x, z, varargin)
% p= ls_2Dint(b, f, mat, e, angt, Dt0, x, z, Nopt) computes the normalized
% pressure, p, for an element in a 1-D array radiating waves across
% a plane fluid/fluid interface where p is calculated
% at a location (x, z) (in mm) in the second fluid for a
% source of length 2b (in mm) at a frequency, f, (in MHz).
% The vector mat = [d1, c1, d2, c2] where d1 is the density in the first
% medium (in gm/cm^3), c1 is the wave speed in the first medium
% (in m/sec) and similarly d2 is the density in the second medium (in
% gm/cm^3) and c2 is the wave speed in the second medium (in m/sec).
% The distance e (in mm) is the offset of the center of the element from
% the center of the array. The parameter angt(in degrees)
% specifies the angle of the array with respect to the x-axis
% and Dt0 (in mm) is the distance of the center of the array from the
% interface. The assumed harmonic time dependency is exp(-2i*pi*f*t).
% The model used is a Rayleigh-Sommerfeld type of integral for a
% piston source where ray theory has been used to propagate the cylindrical
% waves generated by the element across the interface.
% Nopt gives the number of segments to use. If Nopt is not
% specified as an input argument the function uses one segment
% per wavelength, based on the input frequency, f, which must
% be a scalar when Nopt is not given.

% extract material parameters
d1 = mat(1) ;
c1 = mat(2);
d2 = mat(3) ;
c2 = mat(4);
% compute wave numbers
k1b = 2000*pi*b*f/c1 ;
k2b=2000*pi*b*f/c2;

% if number of segments is specified, use
if nargin == 9
    N = varargin{1};
else
% else choose number of segments so that the size of each segment
% is a wavelength
    N = round((2000)*f*b/c1);
    if N < 1
        N=1;
    end
end

% compute centroid locations for the segments
xc = zeros(1,N);
for jj=1:N
    xc(jj) = b*(-1 + 2*(jj-0.5)/N);
end

% calculate normalized pressure as a sum over all the segments
```

```

p=0;
for nn= 1:N
    % find the distance, xi, where the ray from the center of a segment
    % to point(x,z) intersects the interface
    xi = pts_2Dintf(e, xc(nn), ang, Dt0, c1,c2, x, z);
    % compute the distances and angles needed in the model
    Dtn=Dt0+(e+xc(nn)).*sin(ang*pi/180);
    Dxn = x-(e+xc(nn)).*cos(ang*pi/180);
    r1 = sqrt(xi.^2.+ Dtn.^2)./b;
    r2 = sqrt((Dxn -xi).^2 +z.^2)./b;
    ang1 = asin(xi./(b*r1));
    ang2 =asin((Dxn-xi)./(b*r2));
    ang = ang*pi/180 -ang1;
    ang = ang + eps.*( ang == 0);
    % form up the segment directivity
    dir =sin(k1b.*sin(ang)/N)./(k1b.*sin(ang)/N);
    % compute plane wave transmission coefficient(based on pressure ratio)
    Tp = 2*d2*c2.*cos(ang1)./(d1.*c1.*cos(ang2) +d2.*c2.*cos(ang1));
    % compute phase term and denominator
    ph =exp(1i*k1b.*r1 + 1i*k2b.*r2);
    den =r1+(c2/c1).*r2.*((cos(ang1)).^2)./(cos(ang2)).^2;
    % put terms together for pressure due to each segment
    p= p + Tp.*dir.*ph./sqrt(den);
end
p = p.*(sqrt(2*k1b./(1i*pi)))/N; % include external factor

```

Code Listing C.4. The function `pts_2Dintf` which uses Snell's law to determine the intersection points of rays traveling in 2-D across a plane interface between two media from the centroid of a 1-D element in an array to points (x, z) in the second medium. This function uses the helping functions `ferrari2` and `init_xi`.

```

function xi = pts_2Dintf( e, xn, ang, Dt0, c1,c2, x, z)
% xi = pts_2Dintf(e, xn, ang, Dt0, c1, c2, x, z) calculates the
% intersection of a ray from the center of a segment of an array element in
% one fluid to a point (x, z) (in mm) in a second fluid across a plane
% interface, where e is the offset of the element from the center of the
% array and xn is the offset of the segment from the center of the element.
% (both in mm). The parameter ang is the angle (in degrees) that the array
% makes with respect to the x-axis (the interface) and Dt0 is the distance
% of the center of the array above the interface (in mm). The parameters
% c1, c2 are the wave speeds in the first and second medium, respectively,
% (both in m/sec). This function uses the function init_xi(x,z) to examine
% the sizes of the (x,z) variables to decide on the corresponding number
% of rows and columns needed to calculate the locations xi (in mm) at
% which rays from the center of a segment to the points (x,z) intersect the
% interface. The function ferrari2 is then used with the appropriate input
% arguments to calculate the xi values (in mm).

% calculate wave speed ratio
cr =c1/c2;

% based on sizes of (x, z), determine corresponding number of rows and
% columns (P,Q) needed for xi calculations and initialize xi as zeros.
[xi,P,Q]=init_xi(x,z);

```

```

% obtain sizes of (x,z) so appropriate arguments can be found in the calls
% to the function ferrari2 when making the xi calculations
[nrx,ncx]=size(x);
[nrz,ncz]=size(z);

% calculate xi locations using Ferrari's method
for pp=1:P
    for qq=1:Q
        Dtn=Dt0+(e+xn)*sin(angt*pi/180);
        % if x is a point, and z is a row or column vector
        if nrx ==1 && ncx == 1
            Dxn= x -(e+xn)*cos(angt*pi/180);
            xi(pp,qq)=ferrari2(cr, z(pp,qq), Dtn,Dxn);
            % if z is a point, and x is a row or column vector
        elseif nrz ==1 && ncz ==1
            Dxn = x(pp,qq) -(e+xn)*cos(angt*pi/180);
            xi(pp,qq)=ferrari2(cr, z, Dtn,Dxn);
            % if x and z are equal size PxQ matrices
        else
            Dxn = x(pp,qq) -(e+xn)*cos(angt*pi/180);
            xi(pp,qq)=ferrari2(cr, z(pp,qq), Dtn,Dxn);
        end
    end
end
end

```

Code Listing C.5. The function `ferrari2` which uses the input parameters of the functions `pts_2Dintf` or `pts_3Dint` to express Snell's law for a plane interface as the problem of finding the appropriate root of a quartic equation. Ferrari's method is used to obtain the roots of the quartic and return the location of the *single* intersection point on the interface of a ray path that goes from the centroid of an array element or element segment to specified *single* point in the second medium.

```

function xi= ferrari2(cr,DF,DT,DX)
% xi = ferrari2(cr, DF, DT, DX) solves for the intersection point, xi, on
% a plane interface along a Snell's law ray path from a point located a
% distance DT (in mm) above the interface to a point located a
% distance DF (in mm) below the interface.
% Both DT and DF must be positive. DX (in mm) is the separation
% distance between the points along the plane interface and can be positive
% or negative. cr = c1/c2 is the ratio of the wave speed in medium 1 to
% that of the wave speed in medium 2.
% The intersection point, xi, is obtained by writing Snell's law as a quartic
% equation in xi and solving the quartic with Ferrari's method. Of the
% four roots, two will be complex, one will be the wanted real solution
% in the interval [0,DX] and one will be real but outside that interval.
% reference: http://exampleproblems.com/wiki/index.php/Quartic\_equation
% If the root returned by Ferrari's method lies inside the permissible
% interval, [0, DX], and is essentially real (set by a tolerance value
% in line 76), the solution obtained by Ferrari's method is used.
% Otherwise, the MATLAB function fzero is used instead to find the
% intersection point.

% if two media are identical, use explicit solution for the interface point
% along a straight ray
if abs(cr-1) < 10^(-6)
    xi = DX*DT/(DF+DT);
% otherwise, use Ferrari's method
else

```

```

cri=1/cr; % cri = c2/c1
% define coefficients of quartic Ax^4 +Bx^3 +Cx^2 + Dx + E =0
A = 1-cri^2;
B = (2*(cri)^2*DX -2*DX)/DT;
C = (DX^2 +DT^2 -(cri)^2*(DX^2 +DF^2))/(DT^2);
D = -2*DX*DT^2/(DT^3);
E = DX^2*DT^2/(DT^4);
% begin Ferrari's solution
alpha = -3*B^2/(8*A^2) + C/A;
beta = B^3/(8*A^3) - B*C/(2*A^2) + D/A;
gamma = -3*B^4/(256*A^4) + C*B^2/(16*A^3) - B*D/(4*A^2) + E/A;
% if beta =0 the quartic is a bi-quadratic whose solution is easier
if(beta == 0)
x(1) = -B/(4*A) + sqrt( (-alpha + sqrt(alpha^2-4*gamma))/2);
x(2) = -B/(4*A) + sqrt( (-alpha - sqrt(alpha^2-4*gamma))/2);
x(3) = -B/(4*A) - sqrt( (-alpha + sqrt(alpha^2-4*gamma))/2);
x(4) = -B/(4*A) - sqrt( (-alpha - sqrt(alpha^2-4*gamma))/2);
% otherwise, proceed with Ferrari's method
else

P= -alpha^2/12 - gamma;
Q= -alpha^3/108 + alpha*gamma/3 - beta^2/8;
%

Rm= Q/2 - sqrt(Q^2/4 + P^3/27);
%
U=Rm^(1/3);
%
if(U == 0)
    y=-5/6*alpha - U;
else
    y=-5/6*alpha - U + P/(3*U);
end
%
W=sqrt(alpha + 2*y );
%
x(1) = -B/(4*A) + 0.5*( + W + sqrt(-(3*alpha + 2*y + 2*beta/W )));
x(2) = -B/(4*A) + 0.5*( - W + sqrt(-(3*alpha + 2*y - 2*beta/W )));
x(3) = -B/(4*A) + 0.5*( + W - sqrt(-(3*alpha + 2*y + 2*beta/W )));
x(4) = -B/(4*A) + 0.5*( - W - sqrt(-(3*alpha + 2*y - 2*beta/W )));
end
% end of bi-quadratic solution or Ferrari's method with four roots

% find root that is real, lies in the interval [0, DX]
flag =0;
for nn=1:4
    xr=real(x(nn));
    axi= DT*abs(imag(x(nn)));
    xt=xr*DT;
    tol = 10^( -6);
    % f is a function which should be zero if Snell's law
    % is satisfied and can also be used to check the
    % accuracy of Ferrari's solution. Currently not used.
    % f = (DX -xt)*sqrt(xt^2+DT^2)-cri*xt*sqrt((DX -xt)^2+DF^2);

```

```

        if DX >=0 && (xt >=0 && xt<= DX) && axi < tol
            xi = xr*DT;
            flag =1;

        elseif DX <0 && (xt <=0 && xt >= DX) && axi < tol

            xi = xr*DT;
            flag =1;

        end

    end

    if flag == 0

        % if interface intersection value returned by Ferrari's
        % method lies outside the permissible region or the
        % tolerance on being real is not met, use fzero instead

        xi=fzero(@interface2,[0,DX], [], cr, DF, DT, DX);

    end

end

end
end

```

Code Listing C.6. The function `init_xi` which examines the sizes of the variables describing the points (x, z) in the input parameters of `pts_2Dintf` and generates the consistent size needed for the intersection points on the interface that define Snell's law ray paths and the number of calls needed to the function `ferrari2`, which can only return a single intersection point at a time.

```

function [xi, P, Q] = init_xi(x,z)
% [xi,P,Q] =init_xi(x,z) examines the points(x,z), where x can be a row
% or column vector and z a scalar, or z a row or column vector and x a
% scalar, or both x and z can be equal sized scalars, vectors or matrices.
% The dimensions (P,Q) of xi are chosen accordingly so that calls to
% functions of (x, z, xi) can be made transparently and consistently
% if one is evaluating that function along an axis, a line, or over a 2-D
% array of points. An empty xi matrix of dimensions PxQ is returned, along
% with the dimensions P and Q.

% get sizes of x and z variables
[nrx, ncx] =size(x);
[nrz, ncz] = size(z);

% if x and z are equal sized matrices, vectors, or scalars, xi is of the
% same size
if nrx == nrz && ncx ==ncz
    xi=zeros(nrx, ncx);
    P=nrx;
    Q=ncx;
% if x is a column vector and z a scalar, xi is the same size column vector
elseif nrx > 1 && ncx ==1 && nrz ==1 && ncz ==1
    xi=zeros(nrx,1);
    P=nrx;
    Q=1;

```



```
% if z is a column vector and x a scalar, xi is the same size column vector
elseif nrz > 1 && ncx == 1 && nrx == 1 && ncx == 1
    xi=zeros(nrz,1);
    P=nrz;
    Q=1;
% if x is a row vector and z a scalar, xi is the same size row vector
elseif ncx > 1 && nrx == 1 && nrz == 1 && ncx == 1
    xi=zeros(1,ncx);
    P=1;
    Q=ncx;
% if z is a row vector and x a scalar, xi is the same size row vector
elseif ncx > 1 && nrz == 1 && nrx == 1 && ncx == 1
    xi=zeros(1,ncz);
    P=1;
    Q=ncz;
% other combinations are not supported
else error('(x,z) must be (vector,scalar) pairs or equal matrices')
end
```

Code Listing C.7. The function `fresnel_2D` which calculates the normalized pressure wave field of a large 1-D element radiating waves in 2-D into a fluid as calculated by Fresnel integrals in the paraxial approximation.

```
function p = fresnel_2D(b, f, c, x, z)
% p = fresnel_2D(b, f, c, x, z) calculates the normalized pressure
% field at a point (x, z), (in mm), of a 1-D element of
% length 2b(in mm), at a frequency, f,(in MHz) radiating
% into a fluid with wave speed, c, (in m/sec). This function uses the
% fresnel_int function to calculate the Fresnel integral numerically.

% calculate wave number
kb =2000*pi*f*b/c;

% put (x, z) coordinates in normalized form
xb=x/b;
zb=z/b;
% calculate term in Fresnel integral argument
arg = sqrt(kb./(pi*zb));

% calculate normalized pressure
p=sqrt(1/(2*i)).*exp(i*kb*zb).*(fresnel_int(arg.*(xb+1))...
    -fresnel_int(arg.*(xb-1)));
```

Code Listing C.8. The function `fresnel_int` which evaluates the Fresnel integral numerically.

```
function y=fresnel_int(x)
% y = fresnel_int(x) computes the Fresnel integral defined as the integral
% from t = 0 to t = x of the function exp(i*pi*t^2/2). Uses the approximate
% expressions given by Abramowitz and Stegun, Handbook of Mathematical
% Functions, Dover Publications, 1965, pp. 301-302.

% separate arguments into positive and negative values, change sign
% of the negative values
xn =-x(x<0);
xp=x(x >=0);
```

```

% compute cosine and sine integrals of the negative values, using the
% oddness property of the cosine and sign integrals

[cn,sn] =cs_int(xn);
cn= -cn;
sn = -sn;

% compute cosine and sine integrals of the positive values

[cp, sp]=cs_int(xp);

% combine cosine and sine integrals for positive and negative
% values and return the complex Fresnel integral
ct =[cn cp];
st =[sn sp];
y=ct+i*st;

% cs_int(xi) calculates approximations of the cosine and sine integrals
% for positive values of xi only(see Abramowitz and Stegun reference above)
function [c, s]=cs_int(xi)
f =(1+0.926.*xi)./(2+1.792.*xi +3.104.*xi.^2);      % f function (see ref.)
g=1./(2+4.142.*xi+3.492.*xi.^2+6.67.*xi.^3);        % g function (see ref.)
c=0.5 +f.*sin(pi.*xi.^2./2) -g.*cos(pi.*xi.^2./2);  % cos integral approx.
s = 0.5 -f.*cos(pi.*xi.^2./2)-g.*sin(pi.*xi.^2./2); % sin integral approx.

```

Code Listing C.9. The function `on_axis_foc_2D` which calculates the normalized pressure wave field along the central axis of a large, focused 1-D element radiating waves in 2-D into a fluid as calculated by Fresnel integrals in the paraxial approximation.

```

function p = on_axis_foc2D(b, R, f, c, z)
% p = on_axis_foc2D(b,R,f,c,z) computes the on-axis normalized
% pressure for a 1-D focused piston element of length 2b
% and focal length R (in mm).
% The frequency is f (in MHz), b is the transducer half-length
% (in mm), c is the wave speed of the surrounding fluid
% (in m/sec), and z is the on-axis distance (in mm). The
% paraxial approximation is used to write the pressure field in terms
% of a Fresnel integral. Note: the propagation term exp(ikz) is removed
% from the wave field calculation.

% ensure no division by zero at z =0
z = z +eps*(z == 0);

% define transducer wave number
kb = 2000*pi*f*b/c;

% define u and prevent division by zero
u =(1-z/R);
u = u + eps*( u == 0);

% argument of the Fresnel integral and denominator in on-axis pressure
% equation
x = sqrt((u.*kb.*b)./(pi.*z)).*( z <= R)+...
    sqrt((-u.*kb.*b)./(pi.*z)).*(z > R);
denom = sqrt(u).*(z <= R) + sqrt(-u).*( z > R);
Fr = fresnel_int(x).*( z <= R) + conj(fresnel_int(x)).*(z >R);

% compute normalized on-axis pressure (p/rho*c*v0) with
% the propagation phase term exp(ikz) removed. Use analytical
% values near the focus and the numerical Fresnel integral values
% away from the focus
p=(sqrt(2/i).*sqrt((b/R).*kb/pi)).*( abs(u) <= .005) + ...
    (sqrt(2/i).*Fr./denom).*(abs(u) > .005);

```

Code Listing C.10. The function Gauss_2D which calculates the normalized pressure wave field of a large 1-D element radiating waves in 2-D into a fluid as calculated by a superposition of Gaussian beams in the paraxial approximation.

```
function p=Gauss_2D(b, f, c, x, z)
% p = Gauss_2D(b,f,c,x,z) calculates the normalized pressure at a
% point (x, z) (in mm) in a fluid whose wave speed is c (in m/sec)
% for a 1-D element of length 2b (in mm) radiating at a frequency, f,
% (in MHz). The function uses a paraxial multi-Gaussian beam model and
% 15 Gaussian coefficients developed by Wen and Breazeale that are
% contained in the MATLAB function gauss_c15.

% retrieve Wen and Breazeale coefficients
[A, B] = gauss_c15;

% calculate the wave number
kb = 2000*pi*f*b/c;

% normalize the (x,z) coordinates
xb = x/b;
zb = z/b;

% initialize the pressure to zero and then superimpose 15
% Gaussian beams to calculate the pressure wave field
p=0;
for nn = 1:15
    qb=zb-i*1000*pi*f*b./(B(nn)*c);
    qb0 = -i*1000*pi*f*b./(B(nn)*c);
    p=p+sqrt(qb0./qb) .* A(nn) .* exp(i*kb*xb.^2./(2*qb));
end
```

Code Listing C.11. The function gauss_c15 which returns fifteen Gaussian coefficients developed by Wen and Breazeale, which can be used to describe the wave field of an 1-D element with a multi-Gaussian beam model.

```
function [a, b] = gauss_c15
% [a,b] = gauss_c15 returns the 15 "optimized" coefficients
% obtained by Wen and Breazeale to simulate the wave field
% of a circular planar piston transducer radiating into a fluid.
% Reference:
% Wen, J.J. and M. A. Breazeale, "Computer optimization of the
% Gaussian beam description of an ultrasonic field," Computational
% Acoustics, Vol.2, D. Lee, A. Cakmak, R. Vichnevetsky, Eds.
% Elsevier Science Publishers, Amsterdam, 1990, pp. 181-196.

a = zeros(15,1);
b = zeros(15,1);
a(1) = -2.9716 + 8.6187*i;
a(2) = -3.4811 + 0.9687*i;
a(3) = -1.3982 - 0.8128*i;
a(4) = 0.0773 - 0.3303*i;
a(5) = 2.8798 + 1.6109*i;
a(6) = 0.1259 - 0.0957*i;
a(7) = -0.2641 - 0.6723*i;
```

```

a(8) = 18.019 + 7.8291*i;
a(9) = 0.0518 + 0.0182*i;
a(10) = -16.9438 - 9.9384*i;
a(11) = 0.3708 + 5.4522*i;
a(12) = -6.6929 + 4.0722*i;
a(13) = -9.3638 - 4.9998*i;
a(14) = 1.5872 - 15.4212*i;
a(15) = 19.0024 + 3.6850*i;
b(1) = 4.1869 - 5.1560*i;
b(2) = 3.8398 - 10.8004*i;
b(3) = 3.4355 - 16.3582*i;
b(4) = 2.4618 - 27.7134*i;
b(5) = 5.4699 + 28.6319*i;
b(6) = 1.9833 - 33.2885*i;
b(7) = 2.9335 - 22.0151*i;
b(8) = 6.3036 + 36.7772*i;
b(9) = 1.3046 - 38.4650*i;
b(10) = 6.5889 + 37.0680*i;
b(11) = 5.5518 + 22.4255*i;
b(12) = 5.4013 + 16.7326*i;
b(13) = 5.1498 + 11.1249*i;
b(14) = 4.9665 + 5.6855*i;
b(15) = 4.6296 + 0.3055*i;

```

Code Listing C.12. The function `delay_laws2D` which generates the time delay laws for steering and focusing of an array of 1-D elements radiating waves in 2-D into a single medium. The function can also be used to generate delay laws for a linear array of 2-D elements.

```

function td=delay_laws2D(M, s, Phi, F, c)
% td = delay_laws2D(M,s,Phi,F,c) generates the time delay
% td (in microsec) for an array with M elements, pitch s
% (in mm), where we want to steer the beam at the angle Phi
% (in degrees) and focus it at the distance F (in mm)
% in a single medium of wave speed c (in m/sec). For steering
% at an angle Phi only the focal length, F, must be set equal
% to inf.

Mb=(M-1)/2;
m=1:1:M ;
em=s*((m-1)-Mb); % location of centroids of elements

switch (F)
    % steering only case
    case inf
        if Phi > 0
            td=1000*s*sind(Phi)*(m-1)/c;
        else
            td=1000*s*sind(abs(Phi))*(M-m)/c;
        end

```

```

        % steering and focusing case
    otherwise,
        r1=sqrt(F^2 +(Mb*s)^2 + 2*F*Mb*s*sind(Phi));
        rm = sqrt(F^2+em.^2 - 2*F*em*sind(Phi));
        rM=sqrt(F^2 +(Mb*s)^2 + 2*F*Mb*s*sind(abs(Phi)));
        if Phi > 0
            td=1000*(r1-rm)/c;
        else
            td=1000*(rM-rm)/c;
        end
    end
end

```

Code Listing C.13. The function `discrete_windows` which generates 1-D apodization laws for an array using cosine, Hanning, Hamming, Blackman, triangular, or rectangular weights.

```

function amp=discrete_windows(M, type)
% amp = discrete_windows(M, type) returns the discrete apodization
% amplitudes for M elements of type 'cos' (cosine), 'Han' (Hanning)
% 'Ham' (Hamming), 'Blk' (Blackman), 'tri' (triangle),
% and 'rect' (a window with all ones, i.e. no apodization)

m=1:M;
switch type
    case 'cos'
        amp = sin(pi*(m-1)/(M-1));
    case 'Han'
        amp =(sin(pi*(m-1)/(M-1))).^2;
    case 'Ham'
        amp= 0.54 -0.46*cos(2*pi*(m-1)/(M-1));
    case 'Blk'
        amp=0.42 -0.5*cos(2*pi*(m-1)/(M-1)) + ...
            0.08*cos(4*pi*(m-1)/(M-1));
    case 'tri'
        amp =1 - abs(2*(m-1)/(M-1) -1);
    case 'rect'
        amp = ones(1,M);
    otherwise
        disp(' Wrong type. Choices are ''cos'', ''Han'', ''Ham'', ''Blk'',
            ''tri'', ''rect'' ')
end

```

Code Listing C.14. The script `mls_array_modeling` which models the normalized pressure wave field an array of 1-D elements radiating waves into a fluid, using a superposition of multiple line sources for each element. Steering, focusing, and apodization parameters for the array are specified.

```

% script mls_array_modeling
clear

% give input parameters
f= 5;           % frequency (MHz)
c=1480;         % wave speed (m/sec)

```

```

M =32;           % number of elements
dl =0.5;         % element length, d, divided by wave length
gd =0.1;         % gap between elements, g, divided by d
Phi =20.;        % steering angle, degrees
F = inf;         % focal length (mm), F = inf for no focusing
type ='rect';    % type of amplitude weighting function

% calculate size of array, A, element length, d, gap size, g,
% and location of element centroids, e.
[A, d, g, e] = elements(f, c, dl, gd, M);
b=d/2;
s=d+g;

% generate 2-D area for field calculations
z= linspace(1, 100*dl, 500);
x=linspace(-50*dl,50*dl,500);
[xx,zz]=meshgrid(x,z);

% generate time delays, put in exponential
% and calculate amplitude weights
td =delay_laws2D(M,s,Phi,F,c);
delay = exp(1i.*2.*pi.*f.*td);
Ct=discrete_windows(M,type);

% generate normalized pressure wave field
p = 0;
for mm = 1:M
p=p + Ct(mm).*delay(mm).*ls_2Dv(b, f, c, e(mm), xx, zz);
end

% generate wave field image
imagesc(x, z, abs(p))
xlabel( ' x , mm')
ylabel( ' z , mm')

```

Code Listing C.15. The function `elements` which allows specification of array element sizes and gap sizes in normalized form and returns the actual element sizes and centroid locations. Used in the script `mls_array_modeling` to perform parametric studies.

```

function [ A, d, g, xc]=elements(f, c, dl, gd, N)
% [A,d,g,xc]=elements(f,c,dl,gd,N) calculates the
% total length of an array,A (in mm),the element size,d=2b,
% (in mm), the gap size, g, (in mm) and the location of the
% centroids of the array elements, xc, (in mm) for an array
% with N elements. The inputs are the frequency, f, (in MHz)
% the wave speed, c, (in m/sec), the element length divided
% by the wavelength, dl, the gap size divided by the element
% length,gd, and the number of elements, N.

```

```

% dl is the element diameter, d, divided by the
% wavelength, l, i.e. dl = d/l.
d=dl.*c./(1000*f);
% gd is the gap size, g, between elements as a fraction of the
% element size, i.e. gd =g/d
g=gd.*d;
% A is the total aperture size of the array
A = N*d + (N-1)*g;
% x= xc is the location of the centroid of each element
% where x = 0 is at the center of the array
for nn = 1:N
    xc(nn) = (g+d)*((2*nn -1)/2 - N/2);
end

```

Code Listing C.16. The function NPGauss_2D which calculates the normalized pressure wave field of a 1-D element radiating waves in 2-D into a fluid as calculated by a superposition of non-paraxial Gaussian beams.

```

function p = NPGauss_2D(b,f,c,e,x,z)
% p = NPGauss_2D(b,f,c,e,x,z) calculates the normalized pressure
% of an element of length 2b (in mm), at a frequency, f, (in MHz), in a
% fluid whose wave speed is c (in m/sec). The offset of the center of
% the element in the x-direction is e (in mm) and the pressure is
% calculated at a point (x,z) (in mm). The function uses a non-paraxial
% expansion of a cylindrical wave and 10 Gaussians to model piston
% behavior of the element.

% get the Gaussian coefficients of Wen and Breazeale
[A, B] = gauss_c10;

% define non-dimensional quantities
xb=x/b;
zb=z/b;
eb=e/b;
Rb=sqrt((xb-eb).^2 +zb.^2);
kb= 2000*pi*f*b/c;
Db = kb/2;
cosp=zb./Rb;

% calculate normalized pressure field from 10 Gaussians
p =0;
for nn= 1:10
    arg =(cosp.^2 +1i*B(nn).*Rb./Db);
    Dn = sqrt(arg);
    amp = A(nn).*exp(1i.*kb.*Rb)./Dn;
    p = p + amp.*exp(-1i.*kb.*(xb.^2)/(2.*Rb.*arg));
end

```

Code Listing C.17. The function `gauss_c10` which returns ten Gaussian coefficients developed by Wen and Breazeale, which can be used to describe the wave field of an 1-D element with a multi-Gaussian beam model.

```
function [a, b] = gauss_c10
% [a, b] = gauss_c10 returns the ten Wen and Breazeale
% coefficients for a multi-Gaussian beam model

a = zeros(10,1);
b = zeros(10,1);
% enter Wen and Breazeale Coefficients
a(1) = 11.428 + 0.95175*i;
a(2) = 0.06002 - 0.08013*i;
a(3) = -4.2743 - 8.5562*i;
a(4) = 1.6576 +2.7015*i;
a(5) = -5.0418 + 3.2488*i;
a(6) = 1.1227 - 0.68854*i;
a(7) = -1.0106 - 0.26955*i;
a(8) = -2.5974 + 3.2202*i;
a(9) = -0.14840 -0.31193*i;
a(10) = -0.20850 - 0.23851*i;
b(1) = 4.0697 + 0.22726*i;
b(2) = 1.1531 - 20.933*i;
b(3) = 4.4608 + 5.1268*i;
b(4) = 4.3521 +14.997*i;
b(5) = 4.5443 + 10.003*i;
b(6) = 3.8478 + 20.078*i;
b(7) = 2.5280 -10.310*i;
b(8) = 3.3197 - 4.8008*i;
b(9) = 1.9002 - 15.820*i;
b(10) = 2.6340 + 25.009*i;
```

Code Listing C.18. The script `mls_array_model_int` which models the normalized pressure wave field an array of 1-D elements radiating waves across a plane interface between two fluids, using a superposition of multiple line sources for each element. Steering, focusing, and apodization parameters for the array are specified.

```
% script mls_array_model_int
% This script solves for the normalized pressure wave field of
% an array of 1-D elements radiating waves through a fluid/fluid
% interface using the MATLAB function ls_2D_int. Both time delay
% and apodization laws can be specified for the array to steer
% it and focus it in the second medium.
```



```
clear

% -----give input parameters -----
f = 5;           % frequency (MHz)
d1 = 1.0;        % density gm/cm^3 of first medium
c1 = 1480;       % wave speed (m/sec) of first medium
d2 = 7.9;        % density gm/cm^3 of second medium
c2 = 5900;       % wave speed (m/sec) of second medium
M = 32;          % number of elements
d = 0.25;        % element length (mm)
g = 0.05;        % gap length (mm)
angt = 0;        % angle of array
ang20 = 30.0;    % steering angle, degrees in second medium
DF = 8;          % focal depth (mm) DF = inf for no focusing
DT0 = 25.4;      % distance of array from interface (mm). It must be >0
type = 'rect';   % type of amplitude weighting function

% generate 2-D area in second medium for field calculations or replace
% with other specifications for x and z, where z is measured from the
% interface into the second medium and must be >0.
x = linspace(-5, 15, 200);
z = linspace(1,20,200);
[xx,zz]=meshgrid(x,z);

% ----- end of input parameters -----

b = d/2;         % element half length
s = d + g;       % pitch of the array
mat = [ d1 c1 d2 c2]; % material properties

% calculate distances to element centers
for mm = 1:M
    e(mm) = s*((2*mm-1)/2 -M/2);
end

% generate time delays, put in exponential
% and calculate amplitude weights
td =delay_laws2D_int(M,s,angt, ang20, DT0, DF, c1, c2, 'n');
delay = exp(1i.*2.*pi.*f.*td);
Ct=discrete_windows(M,type);

% generate normalized pressure wave field
p = 0;
for mm = 1:M
p=p + Ct(mm).*delay(mm).*ls_2Dint(b, f, mat, e(mm), angt,DT0,xx, zz, 1);
end

% ----- outputs -----
% generate wave field image from x,z specifications. This must be changed
% if (x,z) input specifications are changed.
imagesc(x, z, abs(p))
xlabel( ' x , mm')
ylabel( ' z , mm')
```

Code Listing C.19. The function `delay_laws2D_int` which generates the time delay laws for steering and focusing of an array of 1-D elements radiating waves in 2-D across a plane interface between two fluids. The function can also be used to generate delay laws for a linear array of 2-D elements.

```
function td=delay_laws2D_int( M, s, angt,ang20,DT0,DF, c1, c2, plt)
% td = delay_laws2D_int(M,s,angt, an20, DT0, DF,c1,c2, plt) calculates
% the delay laws for steering and focusing an array of 1-D elements
```

```

% through a planar interface between two media in two dimensions. The
% number of elements is M, the pitch is s (in mm), the angle that array
% makes with the interface is angt(in degrees). The height of the
% center of the array above the interface is DT0 (in mm). Steering and
% focusing to a point in the second medium are specified by giving the
% refracted angle, ang20, (in degrees) and the depth in the second
% medium, DF, (in mm). For steering only to the angle ang20, DF = inf.
% The wave speeds of the first and second media
% are (c1, c2), respectively (in m/sec). The plt argument is a string
% ('y' or 'n') that specifies if a plot of the rays from the centroids
% of the elements to the point in the second medium is wanted ('y') or
% not ('n')

cr = c1/c2; % wave speed ratio
Mb=(M-1)/2;
% compute location of element centroids, e
m=1:1:M;
e =(m-1-Mb)*s;
% computed parameters:
% angl0, incident angle of central ray, deg
% DX0, distance along interface from center of array to focal point, mm
% DT, heights of elements above interface, mm
% DX, distances along interface from elements to focal point, mm
    angl0 = asind((c1/c2).*sind(ang20));
    DX0 = DF.*tand(ang20) + DT0.*tand(angl0);
    DT = DT0 + e.*sind(angt);
    DX =DX0 - e.*cosd(angt);
switch (DF)
% steering only case, use linear law
    case inf
        if (angl0 -angt)>0
            td = 1000*(m-1)*s*sind(angl0-angt)/c1;
        else
            td = 1000*(M-m)*s*abs(sind(angl0-angt))/c1;
        end
% plotting rays option
        if strcmp(plt,'y')
            for nn = 1:M
                xp2(1, nn) = e(nn)*cosd(angt);
                yp2(1, nn) = DT(nn);
                xp2(2, nn) = e(nn)*cosd(angl0 - angt)/cosd(angl0) +DT0*tand(angl0);
                dm=e(nn)*cosd(angl0 - angt)/cosd(angl0);
                if ang20 >0
                    dM = e(M)*cosd(angl0 - angt)/cosd(angl0);
                else
                    dM =e(1)*cosd(angl0 - angt)/cosd(angl0) ;
                end
                yp2(2, nn) = 0;
                xp2(3, nn) = xp2(2,nn) + (dM -dm)*sind(ang20)*sind(ang20);
                yp2(3, nn) = - (dM -dm)*sind(ang20)*cosd(ang20);
            end
        plot(xp2, yp2, 'b')
        end
% end plotting rays option

% steering and focusing case
    otherwise,

% solve for ray intersection locations on interface, xi, (in mm)
% and path lengths in medium 1 and medium 2, r1, r2 (mm)

```

```

        xi=zeros(1,M);
        r1=zeros(1,M);
        r2=zeros(1,M);
        for mm = 1:M
            xi(mm) = ferrari2(cr,DF,DT(mm),DX(mm));
            r1(mm) =sqrt(xi(mm)^2 +(DT0+e(mm)*sind(angt))^2);
            r2(mm) =sqrt( (xi(mm) +e(mm)*cosd(angt) - DX0)^2 +DF^2);
        end

% solve for time advances (in microsec), turn into delays, and
% make the delays ,td, positive
        t= 1000*r1/c1 +1000*r2/c2;
        td=max(t) -t;
% plotting rays option
        if strcmp(plt, 'y')

            for nn = 1:M
                xp(1, nn) = e(nn)*cos(angt*pi/180);
                yp(1, nn) = DT(nn);
                xp(2, nn) = e(nn)*cos(angt*pi/180) +xi(nn);
                yp(2, nn) = 0;
                xp(3, nn) = DX0;
                yp(3, nn) = -DF;
            end
            plot(xp, yp, 'b')
        end
% end plotting rays option

end
end

```

Code Listing C.20. The function `ps_3Dv` which calculates the normalized pressure wave field of a 2-D rectangular element radiating waves in 3-D into a fluid as calculated by a superposition of point sources over the face of the element.

```

function p = ps_3Dv(lx,ly,f,c,ex,ey,x,y,z, varargin )
% p =ps_3Dv(lx, ly, f, c, ex, ey, x,y,z,Popt,Qopt) computes the normalized
% pressure, p, at a location (x,y,z) (in mm) in a fluid
% for a rectangular element of lengths (lx, ly)
% (in mm) along the x- and y-axes, respectively, at a frequency, f, (in MHz)
% ,and for a wave speed, c, (in m/sec) of the fluid. This
% function can be used to describe an element in an array by
% specifying non-zero values for (ex,ey) (in mm), which are the offsets
% of the center of the element along the x- and y-axes, respectively.
% The assumed harmonic time dependency is  $\exp(-2i\pi f t)$  and
% the Rayleigh-Sommerfeld integral for a piston source is used
% as the beam model.
% Popt and Qopt are optional arguments. Popt specifies the number of
% segments to use in the x-direction while Qopt specifies the number of
% segments in the y-direction. If either Popt or Qopt are not
% given as input arguments for a given direction the function uses
% one segment per wavelength in that direction, based on the input
% frequency, f, which must be a scalar when either Popt or
% Qopt are not given.

```

```

% compute wave number
k=2000*pi*f/c;

% if number of x-segments is specified then use
if nargin > 9
    P = varargin{1};
% else choose number of terms so each segment
% length is at most a wave length
else
    P=ceil(1000*f*lx/c);
    if P < 1
        P=1;
    end
end

% if number of y-segments is specified then use
if nargin >10
    Q = varargin{2};
% else choose number of terms so that each segment
% is a wave length or less
else
    Q=ceil(1000*f*ly/c);
    if Q < 1
        Q=1;
    end
end

% compute centroid locations of segments in x- and y-directions
xc=zeros(1,P);
yc=zeros(1,Q);
for pp=1:P
    xc(pp) = -lx/2 + (lx/P)*(pp-0.5);
end
for qq=1:Q
    yc(qq) = -ly/2 + (ly/Q)*(qq-0.5);
end

% calculate normalized pressure as a sum over all the
% segments as an approximation of the Rayleigh-Sommerfeld
% integral
p=0;
for pp = 1:P
    for qq = 1:Q
        rpq=sqrt((x-xc(pp)-ex).^2 + (y-yc(qq)-ey).^2 + z.^2);
        ux= (x -xc(pp)-ex)./rpq;
        uy = (y-yc(qq)-ey)./rpq;
        ux =ux+eps*(ux == 0);
        uy =uy+eps*(uy == 0);
        dirx = sin(k.*ux.*lx/(2*P))./(k.*ux.*lx/(2*P));
        diry =sin(k.*uy.*ly/(2*Q))./(k.*uy.*ly/(2*Q));
        p=p + dirx.*diry.*exp(1i*k.*rpq)./rpq;
    end
end
p = p.*(-1i*k*(lx/P)*(ly/Q))/(2*pi); % include external factor

```

Code Listing C.21. The script `mps_array_modeling` which models the normalized pressure wave field an array of 2-D rectangular elements radiating waves into a fluid, using a superposition of multiple point sources for each element. Steering, focusing, and apodization parameters for the array are specified.

```
% script mps_array_modeling
% This script solves for the normalized pressure wave field of a 2-D
% array of rectangular elements radiating waves in a fluid using the
% MATLAB function ps_3Dv. Both time delay and apodization laws can
% be specified for the array to steer it and focus it.

clear

% ----- give input parameters -----
lx = 0.15; % element length in x-direction (mm)
ly = 0.15; % element length in y-direction (mm)
gx=0.05; % gap length in x-direction (mm)
gy = 0.05; % gap length in y-direction (mm)
f= 5; % frequency (MHz)
c = 1480; % wave speed (m/sec)
L1 =11; % number of elements in x-direction
L2 =11; % number of elements in y-direction
theta =20; % steering angle in theta direction (deg)
phi =0; % steering angle in phi direction (deg)
Fl = 3; % focal distance (mm)
% weighting choices are 'rect','cos', 'Han', 'Ham', 'Blk', 'tri'
ampx_type = 'rect'; % weighting coefficients in x-direction
ampy_type = 'rect'; % weighting coefficients in y-direction

% field points (x,y,z) to evaluate
xs= linspace(-15,15, 300);
zs= linspace(1, 10, 200);
y=0;
[x,z]=meshgrid(xs,zs);

% ----- end input parameters -----

% calculate array pitches
sx = lx+gx;
sy = ly+gy;

% compute centroid locations for the elements
Nx = 1:L1;
Ny = 1:L2;
ex =(2*Nx -1-L1)*(sx/2);
ey =(2*Ny -1 -L2)*(sy/2);

% generate time delays, put in exponential
% and calculate amplitude weights
td =delay_laws3D(L1,L2,sx,sy,theta,phi,Fl,c);
delay = exp(1i.*2.*pi.*f.*td);
Cx = discrete_windows(L1,ampx_type);
Cy = discrete_windows(L2,ampy_type);

% calculate normalized pressure
p=0;
for nn=1:L1
    for ll=1:L2
        p = p + Cx(nn)*Cy(ll)*delay(nn,ll)...
            *ps_3Dv(lx,ly,f,c,ex(nn),ey(ll),x,y,z);
    end
end

% ----- outputs -----
% plot results based on specification of (x,y,z) points
imagesc(xs,zs,abs(p))
```

Code Listing C.22. The function `delay_laws3D` which generates the time delay laws for steering and focusing of an array of rectangular 2-D elements radiating waves in 3-D into a single medium.

```
function td= delay_laws3D(M, N, sx, sy, theta, phi, F, c)
% td = delay_laws3D(M,N,sx,sy,theta, phi, F, c) generates the time delays
% td (in microseconds) for a 2-D array of MxN elements in a single medium
% with elements whose pitches are (sx,sy) in the x- and
% y-directions, respectively(in mm). The steering direction is
% specified by the spherical coordinate angles (theta, phi) (both in
% degrees) and the focusing distance is specified by F (in mm). For steering
% only, F = inf. The wave speed of medium is c (in m/sec).

% calculate locations of element centroids in x- and y-directions
m=1:M;
n=1:N;
Mb = (M-1)/2;
Nb= (N-1)/2;
exm=(m-1-Mb)*sx;
eyn=(n-1-Nb)*sy;

% calculate delays (in microseconds)
switch(F)
% if steering only specified, use explicit steering law
case(inf)
    for mm=1:M
        for nn=1:N
            dt(mm,nn)=1000*(exm(mm)*sind(theta)*cosd(phi) + ...
                eyn(nn)*sind(theta)*sind(phi))/c;
        end
    end
    % make delays all positive
    td = abs(min(min(dt))) + dt;
% otherwise, if steering and focusing specified, use time delays to
% the specified point
otherwise,
    for mm=1:M
        for nn=1:N
            r(mm,nn) = sqrt((F*sind(theta)*cosd(phi) -exm(mm))^2 ...
                +(F*sind(theta)*sind(phi)-eyn(nn))^2 +F^2*(cosd(theta))^2);
        end
    end
    td = max(max(1000*r/c)) -1000*r/c;
end
end
```

Code Listing C.23. The function `ps_3Dint` which calculates the normalized velocity components in an elastic solid for a 2-D rectangular element radiating waves in 3-D across a plane fluid/solid interface as calculated by a superposition of high frequency point sources over the face of the element and propagating the waves from those sources across the interface with ray theory.

```
function [vx,vy,vz] = ps_3Dint(lx,ly,f,mat,ex,ey,angt, Dt0,x,y,z, varargin )
% [vx,vy,vz] = ps_3Dint(lx,ly,f,mat,ex,ey,angt, Dt0, x,y,z,Ropt, Qopt)
% calculates the normalized velocity components (vx,vy,vz) of a rectangular
```

```
% array element radiating waves through a planar fluid/solid interface. The
% parameters (lx, ly) are the lengths of the element in the x'- and y'-
% directions, respectively (in mm), f is the frequency (in MHz), and mat is
% a vector mat = [d1, cp1, d2, cp2, cs2, type] where (d1, cp1) are the
% density (in gm/cm^3) and compressional wave speed (in m/sec) for the
% fluid and (d2, cp2, cs2) are similarly the density, P-wave speed, and
% S-wave speed for the solid, and type ='p' or 's' for a P-wave or
% S-wave, respectively, in the solid. The distances (ex, ey) are the
% x'- and y'- coordinates of the centroid of the element relative to the
% center of the array (in mm). The parameters angt is the angle
% (in degrees) the array makes with respect to the interface, and Dt0
% is the distance of the center of the array above the interface (in mm).
% The parameters (x,y,z) specify the point(s) in the second medium at
% which the fields are to be calculated (in mm), where x and y are
% parallel to the interface and z is normal to the interface, pointing
% into the second medium.
% Ropt and Qopt are optional arguments. Ropt specifies the number of
% segments to use in the x'-direction while Qopt specifies the number of
% segments in the y'-direction. If either Ropt or Qopt are not
% given as input arguments for a given direction then the function uses
% one segment per wavelength in that direction, based on the input
% frequency, f, which must be a scalar when either Ropt or Qopt
% are not given.

% extract material densities, wave speeds, and the type of wave in the
% second medium from mat vector
d1 =mat(1);
cp1=mat(2);
d2 =mat(3);
cp2=mat(4);
cs2 =mat(5);
type =mat(6);

% wave speed in the first medium (a fluid) is for compressional waves
c1 =cp1;
% decide which wave speed to use in second medium for specified wave type
if strcmp(type, 'p')
    c2 =cp2;
elseif strcmp(type, 's')
    c2=cs2;
else error(' type must be 'p' or 's' ')
end

% compute wave numbers for waves in first and second medium
k1=2000*pi*f/c1;
k2 =2000*pi*f/c2;

% if number of x-segments is specified then use
if nargin > 11
    R = varargin{1};

% else choose number of terms so each segment
% is a wave length or less
else
    R=ceil(1000*f*lx/c1);
    if R < 1
        R=1;
    end
end

% if number of y-segments is specified then use
if nargin >12
    Q = varargin{2};
```

```

% else choose number of terms so that each segment
% is a wave length or less
else
    Q=ceil(1000*f*ly/cl);
    if Q < 1
        Q=1;
    end
end

% compute centroid locations of segments in x'- and y'-directions
% relative to the element centroid
xc=zeros(1,R);
yc=zeros(1,Q);
for rr=1:R
    xc(rr) = -lx/2 + (lx/R)*(rr-0.5);
end
for qq=1:Q
    yc(qq) = -ly/2 + (ly/Q)*(qq-0.5);
end

% calculate normalized velocity components as a sum over all the
% segments as an approximation of the Rayleigh-Sommerfeld
% integral
vx=0;
vy=0;
vz=0;

for rr = 1:R
    for qq = 1:Q
        % calculate distance xi along the interface for a ray from a
        % segment to the specified point in the second medium
        Db = sqrt((x-(ex+xc(rr)).*cosd(angt)).^2 + (y-(ey+yc(qq))).^2);
        Ds = Dt0 + (ex +xc(rr)).*sind(angt);
        xi = pts_3Dint(ex,ey,xc(rr),yc(qq),angt,Dt0,c1,c2,x,y,z);

        % calculate incident and refracted angles along the ray,
        % including the special case when ray is at normal incidence
        if Db ==0
            angl =0;
        else
            angl = atand(xi./Ds);
        end

        if angl == 0
            ang2 =0;
        else
            ang2=atand((Db-xi)./z);
        end

        % calculate ray path lengths in each medium
        r1 =sqrt(Ds.^2 +xi.^2);
        r2=sqrt((Db-xi).^2 +z.^2);
        % calculate segment sizes in x'- and y'- directions
        dx=lx/R;
        dy =ly/Q;

        % calculate (x', y') components of unit vector along the ray in the
        % first medium
        if Db ==0
            uxt =-sind(angt);
            uyt = 0;
        else
            uxt=xi.*(x-(ex+xc(rr)).*cosd(angt)).*cosd(angt)./(Db.*r1) ...
                -Ds.*sind(angt)./r1;
            uyt = xi.*(y - (ey+yc(qq)))./(Db.*r1);
        end
    end
end

```



```

% calculate polarization components for P- and S-waves in the
% second medium, including special case of normal incidence
if Db == 0
    dpx =0;
    dpy=0;
    dpz=1;
    dsx =1;
    dsy =0;
    dsz=0;
else
    dpx = (1-xi./Db).*(x-(ex+xc(rr)).*cosd(angt))./r2;
    dpy = (1 -xi./Db).*(y-(ey+yc(qq)).)/r2;
    dpz=z./r2;
    dsx = sqrt(dpy.^2 +dpz.^2);
    dsy= -dpx.*dpy./dsx;
    dsz = -dpx.*dpz./dsx;
end
% choose polarization components to use based on wave type in the
% second medium
if strcmp(type, 'p' )
    px=dpx;
    py=dpy;
    pz =dpz;
elseif strcmp(type, 's')
    px = dsx;
    py = dsy;
    pz =dsz;
else error('wrong type')
end
% calculate transmission coefficients (based on velocity ratios)
% for P- and S-waves and choose appropriate coefficient for the
% specified wave type
[tppt, tps]= T_fluid_solid(d1,cp1,d2,cp2,cs2, angl);

if strcmp(type, 'p')
    T=tppt;
elseif strcmp(type, 's')
    T = tps;
end
% form up the directivity term
argx = k1.*uxt.*dx/2;
argx =argx +eps.*(argx == 0);
argy = k1.*uyt.*dy/2;
argy = argy + eps.*( argy == 0);
dir = (sin(argx)./argx).*(sin(argy)./argy);
% form up the denominator term
D1 = r1 + r2.*(c2/c1).*(cosd(ang1)./cosd(ang2)).^2;
D2 = r1 + r2.*(c2/c1);
% put transmission coefficient, polarization, directivity, phase
% term and denominator together to calculate velocity components.
vx = vx + T.*px.*dir.*exp(1i.*k1.*r1 +1i.*k2.*r2)./sqrt(D1.*D2);
vy = vy + T.*py.*dir.*exp(1i.*k1.*r1 +1i.*k2.*r2)./sqrt(D1.*D2);
vz = vz + T.*pz.*dir.*exp(1i.*k1.*r1 +1i.*k2.*r2)./sqrt(D1.*D2);
end
end
% include external factor for these components
vx = vx.*(-1i*k1*dx*dy)/(2*pi);
vy = vy.*(-1i*k1*dx*dy)/(2*pi);
vz = vz.*(-1i*k1*dx*dy)/(2*pi);

```

Code Listing C.24. The function `pts_3Dint` which uses Snell's law to determine the intersection points of rays traveling in 3-D across a plane interface between two media from the centroid of a 2-D element in an array to points (x, y, z) in the second medium. This function uses the helping functions `ferrari2` and `init_xi3D`.

```
function xi = pts_3Dint(ex, ey, xn, yn, angt, Dt0, c1, c2, x, y, z)
% xi = pts3Dint(ex, ey, xn,yn,angt,Dt0, c1,c2,x,y,z) calculates the
% distance, xi, (in mm) along the interface in the plane of incidence,
% at which a ray from the center of an array element segment to a point
% in the second medium intersects the interface. The parameters
% (ex, ey) are the element offsets (in mm) from the center of the
% entire array to the center of the element in the x'- and y'-directions,
% respectively, and (xn,yn) are similarly the offsets as measured
% to the center of the element segment from the center of the
% element in the x'- and y'-directions (in mm). The parameter angt, is the
% angle of the array (in degrees) from the interface, and Dt0 is the
% distance (in mm) of the center of the array from the interface. (c1,c2)
% are the wave speeds in the first and second medium (in m/sec) and
% (x,y,z) are the coordinates of end point of the ray in the second medium
% (all in mm).

% calculate wave speed ratio
cr=c1/c2;
% determine size of array needed for xi calculations based on the sizes of
% the (x,y,z) variables) and also determine those sizes
[xi, P, Q] = init_xi3D(x,y,z);

[nrx,ncx] =size(x);
[nry,ncy] =size(y);
[nrz,ncz] =size(z);

% call ferrari2 function to compute xi with the arguments of that function
% determined by the sizes of the (x,y,z) variables.
De = Dt0 +(ex + xn)*sind(angt);
for pp=1:P
    for qq = 1:Q

        % x and y are points, z is a row or column vector
        if nrx ==1 && ncx ==1 && nry ==1 && ncy ==1
            Db=sqrt((x-(ex +xn)*cosd(angt)).^2 +(y-(ey+yn)).^2);
            xi(pp,qq) =ferrari2(cr, z(pp,qq), De, Db);
        % y and z are points, x is a row or column vector
        elseif nry == 1 && ncy ==1 && nrz ==1 && ncz ==1
            Db=sqrt((x(pp,qq)-(ex +xn)*cosd(angt)).^2 +(y-(ey+yn)).^2) ;
            xi(pp,qq) =ferrari2(cr, z, De, Db);
        % x and z are points, y is a row or column vector
        elseif nrx ==1 && ncx ==1 && nrz ==1 && ncz ==1
            Db=sqrt((x-(ex +xn)*cosd(angt)).^2 +(y(pp,qq)-(ey+yn)).^2);
            xi(pp,qq) =ferrari2(cr, z, De, Db);
        % y is a point, x and z are equal size PxQ matrices
        elseif nry ==1 && ncy ==1 && nrx == nrz && ncx == ncz
            Db=sqrt((x(pp,qq)-(ex +xn)*cosd(angt)).^2 +(y-(ey+yn)).^2);
            xi(pp,qq) = ferrari2(cr, z(pp,qq), De, Db);

        % z is a point, x and y are equal size PxQ matrices
        elseif nrz == 1 && ncz ==1 && nrx == nry && ncx == ncy
            Db=sqrt((x(pp,qq)-(ex +xn)*cosd(angt)).^2 +(y(pp,qq)-
(ey+yn)).^2);
            xi(pp,qq) = ferrari2(cr, z, De, Db);
        % x is a point, y and z are equal size PxQ matrices
        elseif nrx ==1 && ncx ==1 && nry == nrz && ncy == ncz
            Db=sqrt((x-(ex +xn)*cosd(angt)).^2 +(y(pp,qq)-(ey+yn)).^2);
            xi(pp,qq) = ferrari2(cr, z(pp,qq), De, Db);
        % x, y, z are all equal size row or column vectors
        else
            Db=sqrt((x(pp,qq)-(ex +xn)*cosd(angt)).^2 +(y(pp,qq)-
(ey+yn)).^2);
            xi(pp,qq) = ferrari2(cr, z(pp,qq),De, Db);
        end
    end
end
end
```

Code Listing C.25. The function `init_xi3D` which examines the sizes of the variables describing the points (x, y, z) in the input parameters of `pts_3Dint` and generates the consistent size needed for the intersection points on the interface that define Snell's law ray paths and the number of calls needed to the function `ferrari2`, which can only return a single intersection point at a time.

```
function [xi, P, Q] = init_xi3D(x,y,z)
% [xi, P, Q] = init_xi3D(x,y,z) examines the sizes of the (x,y,z) variables
% (which specify points in the second medium, across a plane interface,
% to which a ray must travel from an array element or element segment)
% and returns a PxQ array of zero values to hold the distances xi
% at which the ray intersects an interface, as well as the values (P,Q).
% Eleven different combinations of sizes for (x,y,z) are
% allowed, which permits (x,y,z) to represent values in planes parallel
% to the x-,y-,or z-axes (three cases), or values along lines parallel to
% the x-, y-,or z-axes (six cases since the line could be represented
% as row or column vectors),or values along an inclined line
% in 3-D (two cases since the line could be represented as row or column
% vectors).

% get sizes of (x,y,z)
[nrx,ncx] = size(x);
[nry,ncy] = size(y);
[nrz,ncz] = size(z);

% if x,z are equal size [nrx,ncx] matrices and y is single value, make
% xi a [nrx, ncx] matrix
if nrx == nrz && ncx == ncx && nry == 1 && ncy == 1
    xi = zeros(nrx,ncx);
    P = nrx;
    Q = ncx;
% if x, y are equal size [nrx, ncx] matrices and z is a single value, make
% xi a [ nrx, ncx] matrix
elseif nrx == nry && ncx == ncy && nrz == 1 && ncx == 1
    xi = zeros(nrx,ncx);
    P = nrx;
    Q = ncx;
% if y, z are equal size [nry,ncy] matrices and x is a single value, make
% xi a [nry, ncy] matrix
elseif nry == nrz && ncy == ncx && nrx == 1 && ncx == 1
    xi=zeros(nry, ncy);
    P = nry;
    Q = ncy;

% if z is a [1,ncz] vector and x and y are single values, make
% xi a [1,ncz] vector
elseif nrz == 1 && ncx > 1 && nrx == 1 && ncx == 1 && nry == 1 && ncy == 1
    xi =zeros(1, ncx);
    P = 1;
    Q = ncx;
% if z is a [nrz, 1] vector and x and y are single values, make
% xi a [nrz,1] vector
elseif ncx == 1 && nrz > 1 && nrx == 1 && ncx == 1 && nry == 1 && ncy == 1
    xi =zeros(nrz,1);
    P = nrz;
    Q = 1;
% if x is a [1,ncx] vector and y and z are single values, make
% xi a [1,ncx] vector
elseif nrx == 1 && ncx > 1 && nry == 1 && ncy == 1 && nrz == 1 && ncx == 1
    xi =zeros(1,ncx);
    P = 1;
    Q = ncx;
```

```

% if x is a [nrx, 1] vector and y and z are single values, make
% xi a [nrx, 1] vector
elseif ncx == 1 && nrx > 1 && nry == 1 && ncy == 1 && nrz == 1 && ncz == 1
    xi = zeros(nrx, 1);
    P = nrx;
    Q = 1;
% if y is a [1, ncy] vector and x and z are single values, make
% xi a [1, ncy] vector
elseif nry == 1 && ncy > 1 && nrx == 1 && ncx == 1 && nrz == 1 && ncz == 1
    xi = zeros(1, ncy);
    P = 1;
    Q = ncy;
% if y is a [nry, 1] vector and x and z are single values, make
% xi a [nry, 1] vector
elseif nry > 1 && ncy == 1 && nrx == 1 && ncx == 1 && nrz == 1 && ncz == 1
    xi = zeros(nry, 1);
    P = nry;
    Q = 1;
% if x, y, z are equal size [1, ncx] vectors, make
% xi a [1, ncx] vector
elseif nrx == nry && ncx == ncy && nrz == nrx && ncx == ncx && nrx == 1
    xi = zeros(1, ncx);
    P = 1;
    Q = ncx;
% if x, y, z are equal size [nrx, 1] vectors, make
% xi a [nrx, 1] vector
elseif nrx == nry && ncx == ncy && nrz == nrx && ncx == ncx && ncx == 1
    xi = zeros(nrx, 1);
    P = nrx;
    Q = 1;
else error(' (x,y,z) combination given is not supported')
end

```

Code Listing C.26. The script `mps_array_model_int` which models the normalized velocity components in an elastic solid for an array of 2-D rectangular elements radiating waves across a fluid solid/solid interface, using a superposition of multiple point sources for each element. Steering, focusing, and apodization parameters for the array are specified.

```

% script mps_array_model_int
% This script solves for the normalized velocity wave field of
% an array of 1-D elements radiating waves through a fluid/solid
% interface using the MATLAB function ps_3Dint. Both time delay
% and apodization laws can be specified for the array to steer
% it and focus it in the solid.

clear
% -----input parameters -----
tic          % time the calculations
lx = 0.15;   % element length in x-direction (mm)
ly = 0.15;   % element length in y-direction (mm)
gx=0.05;     % gap length in x-direction (mm)
gy = 0.05;   % gap length in y-direction (mm)
f= 5;        % frequency (MHz)
dl=1.0;      % density, medium one (arbitrary units)
cp1 = 1480;  % compressional wave speed, medium one (m/sec)
d2=7.9;     % density, medium two (same arbitrary units)
cp2 = 5900;  % compressional wave speed, medium two (m/sec)
cs2=3200;    % shear wave speed, medium two (m/sec)
type='p';    % wave type, medium two
mat=[dl,cp1,d2,cp2,cs2,type]; % form material vector

```

```

L1 =11;          % number of elements in x-direction
L2 =11;          % number of elements in y-direction
angt =10.217;    % angle of the array (deg)
Dt0=50.8;        % height of array center from interface (mm)

theta2 =0;       % steering angle in theta direction (deg)
phi =0;          % steering angle in phi direction (deg)
DF = inf;        % focal distance (mm)
% weighting choices are 'rect','cos', 'Han', 'Ham', 'Blk', 'tri'
ampx_type='rect'; % weighting coefficients in x-direction
ampy_type='rect'; % weighting coefficients in y-direction

% field points to evaluate
xs= linspace(-5,20, 100);
zs= linspace(1, 20, 100);
y=0;
[x,z]=meshgrid(xs,zs);

% ----- end input parameters -----
cl=cpl;
if strcmp(type,'p')
    c2=cp2;
elseif strcmp(type,'s')
    c2=cs2;
else
    error('type incorrect')
end

% calculate array pitches
sx = lx+gx;
sy = ly+gy;

% compute centroid locations for the elements
Nx = 1:L1;
Ny = 1:L2;
ex = (2*Nx -1-L1)*(sx/2);
ey = (2*Ny -1 -L2)*(sy/2);

% generate time delays, put in exponential
% and calculate amplitude weights
td =delay_laws3Dint(L1,L2,sx,sy,angt,phi,theta2,Dt0,DF,c1,c2,'n');
delay = exp(1i.*2.*pi.*f.*td);
Cx = discrete_windows(L1,ampx_type);
Cy = discrete_windows(L2,ampy_type);

% calculate normalized velocities
vx=0;
vy=0;
vz=0;
for nn=1:L1
    for ll=1:L2
        [vxe,vye,vze]= ps_3Dint(lx,ly,f,mat,ex(nn),ey(ll),angt,Dt0,x,y,z,1,1);
        vx = vx + Cx(nn)*Cy(ll)*delay(nn,ll)*vxe;
        vy = vy + Cx(nn)*Cy(ll)*delay(nn,ll)*vye;
        vz = vz + Cx(nn)*Cy(ll)*delay(nn,ll)*vze;
    end
end

% ----- outputs -----
% plot results
vmag=sqrt(abs(vx).^2 +abs(vy).^2 +abs(vz).^2);
imagesc(xs,zs,vmag)
toc      % end of time calculations

```

Code Listing C.27. The function `delay_laws3Dint` which generates the time delay laws for steering and focusing of an array of 2-D elements radiating waves in 3-D across a plane interface between two media.

```
function td = delay_laws3Dint(Mx,My,sx,sy,thetat, phi, ...
    theta2,DT0, DF, c1,c2, plt)
% td = delay_laws3Dint(Mx,My,sx,sy,thetat,phi, theta2, DT0,DF,c1,c2,plt)
% calculates the delay laws for steering and focusing a 2-D array
% through a planar interface between two media in three dimensions.
% (Mx, My) are the number of elements in the (x', y') directions, (sx, sy)
% are the pitches (in mm), and thetat is the angle that array
% makes with the interface (in degrees). Steering and focusing to a point in
% the second medium is specified by giving the angles theta2 and
% phi, (both in degrees). The height of the center of the array above
% the interface is DT0 (in mm). The wave speeds of the first and second
% media are (c1, c2), respectively (in m/sec). The plt argument is a string
% ('y' or 'n') that specifies if a plot of the rays from the centroids
% of the elements to the point in the second medium is wanted ('y') or
% not ('n'). Plotting is not done if steering only (DF = inf) is specified.

% compute wave speed ratio
cr=c1/c2;

% compute element centroid locations
Mbx=(Mx-1)/2;
Mby=(My-1)/2;
mx=1:Mx;
ex=(mx-1-Mbx)*sx;
my=1:My;
ey=(my-1-Mby)*sy;

% initialize variables to be used
t=zeros(Mx,My);
Db=zeros(Mx,My);
De=zeros(1,Mx);
xi=zeros(Mx,My);

angl = asind(c1*sind(theta2)/c2); % angle in first medium (in degrees)

switch(DF)
    % steering only case, use linear steering law
    case inf
        ux= sind(angl)*cosd(phi)*cosd(thetat) -cosd(angl)*sind(thetat);
        uy =sind(angl)*sind(phi);
        for m =1:Mx
            for n = 1:My
                t(m,n)= 1000*(ux*ex(m)+uy*ey(n))/c1; %time in microsec
            end
        end
        td = abs(min(min(t))) +t; % make sure delay is positive

    % steering and focusing case
    otherwise
        % determine distances De, Db needed in arguments of ferrari2
        % function
        DQ=DT0*tand(angl)+DF*tand(theta2);
        x=DQ*cosd(phi);
        y=DQ*sind(phi);
        for m=1:Mx
            for n = 1:My
                Db(m,n) = sqrt((x-ex(m)*cosd(thetat))^2 +(y-ey(n))^2);
            end
        end
    end
end
```

```

De = DT0 +ex*sind(thetat);
% use ferrari2 method to determine distance, xi, where a ray from an
% element to the point (x, y, DF) intersects the interface
% in the plane of incidence
for m=1:Mx
    for n = 1:My
        xi(m,n) = ferrari2(cr,DF,De(m),Db(m,n));
    end
end
% use ray distances to calculate time advances (in microsec)
for m=1:Mx
    for n=1:My
        t(m,n) = 1000*sqrt(xi(m,n)^2 +De(m)^2)/c1 +...
            1000*sqrt(DF^2+(Db(m,n) -xi(m,n))^2)/c2;
    end
end
% turn time advances into delays and make all delays positive
td =max(max(t)) -t;

% plotting rays option
if strcmp(plt, 'y')

    for m=1:Mx
        for n = 1:My
            xp(1,1) = ex(m)*cosd(thetat);
            zp(1,1)=DT0 +ex(m)*sind(thetat);
            yp(1,1) = ey(n);
            xp(2,1) = ex(m)*cosd(thetat) + xi(m,n)*(x-
ex(m)*cosd(thetat))/Db(m,n);
            yp(2,1) = ey(n) + xi(m,n)*(y-ey(n))/Db(m,n);
            zp(2,1) =0;
            xp(3,1) = x;
            yp(3,1) = y;
            zp(3,1) =-DF;
            plot3(xp,yp,zp)
            hold on
        end
    end
    hold off
end
% end plotting rays option
end

```

Code Listing C.28. The function interface2 which expresses Snell's law in terms of the location of the point of intersection of a ray path with a planar interface. The value of the function is zero when Snell's law is satisfied. This function is used in the function ferrari2 as a back-up evaluation method when Ferrari's method does not give an accurate solution. In that case the intersection point on the interface is calculated iteratively with the built-in MATLAB function fzero, using the call

`xi=fzero(@interface2,[0,DX],[], cr, DF, DT, DX);`

```

function y =interface2(x, cr, df, dp, dpf)
% y = interface2(x, cr, df, dp, dpf) outputs the value of a function, y,
% which is zero if the input argument,x,is the location along an interface

```

```
% where Snell's law is satisfied. The input parameter cr=c1/c2, where c1
% is the wave speed in medium one, and c2 is the wave speed in medium 2,
% The other input parameters (df, dp, dpf) define a ray which goes from
% a point in medium one to the interface and then to a point in medium
% two, where df = DF is the depth of the point in medium two,
% dp = DT is the height of the point in medium one, and dpf = DX is the
% separation distance between the points in medium one and two
% (see Fig 5.4 in the text). The function y used here is c1 times the
% function defined in Eq.(5.2.6) in the text.

% the function,y,

y =x./sqrt(x.^2+dp^2)-cr*(dpf-x)./sqrt((dpf-x).^2 +df^2);
```

Code Listing C.29 The function `T_fluid_solid` which computes the plane wave transmission coefficients at a plane fluid-solid interface, based on velocity ratios, for both P-to-P waves and P-to-SV waves.

```
function [tpp,tps]= T_fluid_solid(d1,cp1,d2,cp2,cs2, thetal)
% T_fluid_solid(d1,cp1,d2,cp2,cs2, thetal) computes the P-P (tpp)
% and P-S (tps) transmission coefficients based on velocity ratios
% for a plane fluid-solid interface. (d1,cp1) are the density and wave
% speed of the fluid. (d2,cp2,cs2) are the density, compressional wave
% speed and shear wave speed of the solid, and thetal is the incident angle
% (in degrees)

% put incident angle in radians
iang = (thetal.*pi)./180;
% calculate sin(theta) for refracted p- and s-waves
sinp = (cp2/cp1)*sin(iang);
sins = (cs2/cp1)*sin(iang);

% calculate cos(theta) for refracted p- and s-waves
% for angles beyond critical, the value of the cosine is
% computed for positive frequencies only
cosp = 1i*sqrt(sinp.^2 - 1).*(sinp >= 1) + sqrt(1 - sinp.^2).*(sinp < 1);
coss = 1i*sqrt(sins.^2 - 1).*(sins >= 1) + sqrt(1 - sins.^2).*(sins < 1) ;

% calculate transmission coefficients
denom = cosp + (d2/d1)*(cp2/cp1)*sqrt(1-
sin(iang).^2).*(4.*(cs2/cp2)^2).*(sins.*coss.*sinp.*cosp) ...
+ 1 - 4.*(sins.^2).*(coss.^2));
tpp = (2*sqrt(1 - sin(iang).^2).*(1 - 2*(sins.^2)))./denom;
tps = -(4*cosp.*sins.*sqrt(1 - sin(iang).^2))./denom;
```


Index

A

- Acoustic cross-talk, 325
- Acoustic/elastic transfer function
 - defined for contact testing, 191
 - defined for immersion testing, 191
 - model for contact testing, 193
 - model for immersion testing, 193
- Acoustic radiation impedance, 183, 185, 186, 189, 216, 217
- Amplitude weighing *See* Apodization laws, 4
- Angle/area ratios, 297
- Angular spectrum of plane waves (2-D), 20
- Angular spectrum of plane waves (3-D), 314
- Apodization laws
 - continuous, 75
 - discrete, 73, 94
- Auld measurement model *See* Ultrasonic measurement model, 14

B

- Bessel function, 183, 262, 269
- Beylkin determinant, 282, 290, 296–298
- Blackman window, 88, 164
- Blocked force, 8, 9, 185, 187, 191, 198, 216, 267
- Born approximation, 249
 - far field scattering amplitude, inclusion (2-D), 271

C

- Convolution theorem, 116, 117
- Crack tip diffraction *See* Edge waves, 258
- Creeping waves, 246, 249

D

- Deconvolution, 10, 206, 208, 222, 251, 257, 261, 284, 304
- Delay and sum imaging methods, 241, 303

Delay laws:

- paraxial, steering *See* Paraxial, 91
- steering and focusing, single medium (2-D), 84, 99
- steering and focusing, single medium (3-D), 101, 170
- steering and focusing through a planar interface (3-D), 94, 95, 174
- steering, single medium (2-D), 83, 86
- steering, single medium (3-D), 99
- steering through a plane interface (2-D), 172, 173
- steering through a plane interface (3-D), 107

E

- Edge waves, 248, 249
- Effective length of an element, 326
- Electrical cross-talk, 8
- Element directivity (1-D element), 165
- Element directivity (2-D element)
 - rectangle, 141, 184
 - triangle, 141

F

- Far field scattering amplitude
 - defined, 211, 232
 - for an inclusion (separation of variables), 263
 - specular point response, 224
- Far field waves (2-D), 23
- Far field waves (3-D), 117, 118
- Ferrari method, 106, 175
- Finite impedance baffle, 313, 314, 317, 320, 321, 324
- Fourier transform, 115, 118, 254, 259, 316
- Free surface velocity, 185, 187, 191, 217
- Fresnel integral, 202

Full matrix capture (FMC), 12, 13, 244, 254, 257, 261, 269

G

Gaussian beam, 138, 139, 142, 143
 Gaussian beam equivalent point source (GBEPS) model, 139, 142, 144, 146
 Grating lobes, 13, 76, 79, 80
 sound generation, 191
 sound reception, 156, 191
 Green's function for the Helmholtz equation (2-D), 271

H

Hamming Window, 63, 88
 Hankel function, 263, 270
 Hankel function beam model, 94
 Hanning window, 87, 88
 Helmholtz equation (2-D), 271, 315
 Helmholtz equation (3-D), 113, 114

I

Imaging measurement model (IMM), 14
 edge waves (3-D), 249
 edge waves, scalar (2-D), 248
 full matrix capture (3-D), 287, 288, 289, 290, 291, 292
 linear array and a 2-D scatterer, 293, 294, 295, 296, 297, 298, 299, 300, 301
 pulse-echo (3-D), 260, 285, 286
 pulse-echo, scalar (2-D), 260, 279, 280, 281, 282, 283, 285, 287
 Information matrix, 12
 Inhomogeneous waves, 114, 315
 Inverse Fourier transform, 114, 116, 251, 255, 302, 317

K

Kerf, 5
 Kirchhoff approximation, 223, 224, 227, 237, 248, 249, 261, 286, 304

L

Linear array, 5, 6, 10, 101, 152, 169, 202, 206, 279, 293, 294
 Linear time-shift invariant (LTI) system, 184, 188
 Line source beam model *See* Multiple line source element beam model, 89

M

Measurement models *See* Ultrasonic measurement model, 14
 Multi-Gaussian element beam model, 91, 138

Multiple line source array beam model
 fluid, 76
 fluid-fluid interface, 140
 Multiple line source element beam model
 fluid, 28
 finite impedance baffle, 318
 fluid-fluid interface, 140
 Multiple point source array beam model
 contact, 182
 fluid/solid interface, 182
 immersion (single medium), 151, 181
 solid/solid interface, 187
 Multiple point source element beam model
 contact, 122, 123, 132
 fluid-solid interface, 132
 immersion (single medium), 120–122, 131
 solid-solid interface, 133

N

Near field distance, 209
 Non-paraxial Gaussian model, 93, 94
 Norton equivalent circuit of a receiving element, 186

P

Paraxial approximation, 86, 87, 91, 101, 102, 138, 197, 203, 209
 Physical Optics Far Field Inverse Scattering (POFFIS), 14, 260
 Piston model, 114, 195, 317
 Pitch of an array, 5
 Point source beam models *See* Multiple point source beam model, 138
 Point source directivity, 81, 84, 152, 154, 155, 165
 Prony's method, 142, 143

R

Rayleigh distance, 93
 Rayleigh-Sommerfeld equation, 124, 320
 Ray theory, 124, 125, 138, 139, 291
 Reciprocal theorem, 213
 Reciprocity
 for a cable, 187, 213
 for a flaw measurement system, 213
 for an element, 182, 213
 Reflectivity of a flaw (pitch-catch), 257
 Reflectivity of a flaw (pulse-echo), 241
 Rigid baffle model, 12, 113

S

Scattering amplitude *See* Far field scattering amplitude, 221
 Separation of variables, 263, 268

Single line source array beam model, 75, 76, 86
 Single point source array beam model, 151, 154, 156
 Single point source element beam model
 contact, 124
 fluid/solid interface, 135, 136
 immersion (single medium), 150
 Singular function of a surface, 251, 260, 288
 Snell's law, 97, 103, 104, 125, 127, 138, 140, 174, 223, 237, 291
 Sound generation transfer function
 (see Transfer function – sound generation)
 Sound reception transfer function (see Transfer function – sound reception)
 Specular point response, 223, 224, 232, 247, 249
 Specular reflection points, 247
 Synthetic Aperture Focusing Technique (SAFT), 14, 241
 System function, 9, 10, 13, 179, 193, 195, 205–207, 305

T

Thévenin equivalent
 circuit of a receiving element, 186
 voltage of a driving circuit, 8
 Thévenin's theorem, 180
 Thompson-Gray measurement model *See*
 Ultrasonic measurement model—
 reduced, 14

Total Focusing Method (TFM), 14, 241, 244, 257, 279, 291
 Transfer function
 acoustic/elastic *See* Acoustic/elastic
 transfer function, 9
 sound generation, 8
 sound reception, 8
 Transfer matrix, 181, 187
 Triangular window, 88
 Two port system, 179, 182, 183, 185

U

Ultrasonic measurement model, 14, 179, 211
 contact (3-D), 217, 218
 for imaging (3-D), 229
 for imaging, scalar (2-D), 308
 immersion (3-D), 216, 217
 reduced (3-D) (Thompson-Gray), 14, 222
 reduced, scalar (2-D), 218, 235

W

Wave equation (2-D), 18
 Wave equation (3-D), 113
 Wave number, 20
 Wen and Breazeale coefficients, 93
 Weyl representation of spherical wave, 117
 Wiener filter, 10, 206, 208, 251, 252, 253, 284, 304

